Emanuel Abreu Antunes Carlos

Mestre em Engenharia de Micro e Nanotecnologias

Design and synthesis of low temperature printed metal oxide electronic devices

Dissertação para obtenção do Grau de Doutor em
Nanociências e Nanotecnologias

Orientadora: Doutora Elvira Maria Correia Fortunato, Professora Catedrática, Faculdade de Ciências e Tecnologia da Universidade Nova de Lisboa

Co-orientadora: Doutora Rita Maria Mourão Salazar Branquinho, Professora Auxiliar Convidada, Faculdade de Ciências e Tecnologia da Universidade Nova de Lisboa

Júri:

Presidente: Prof. Doutor João Carlos da Palma Goes

Arguentes: Prof. Doutora Maria Lourdes Calzada

Prof. Doutor Henrique Leonel Gomes

Vogais: Prof. Doutora Florinda Mendes da Costa

Prof. Doutora Elvira Maria Correia Fortunato

Prof. Doutor Rodrigo Ferrão Paiva Martins

Doutora Maria Smolander

FACULDADE DE CIÊNCIAS E TECNOLOGIA
UNIVERSIDADE NOVA DE LISBOA

Novembro, 2020

Emanuel Abreu Antunes Carlos

Mestre em Engenharia de Micro e Nanotecnologias

Design and synthesis of low temperature printed metal oxide electronic devices

Dissertação para obtenção do Grau de Doutor em
Nanociências e Nanotecnologias

Orientadora: Doutora Elvira Maria Correia Fortunato, Professora Catedrática, Faculdade de Ciências e Tecnologia da Universidade Nova de Lisboa

Co-orientadora: Doutora Rita Maria Mourão Salazar Branquinho, Professora Auxiliar Convidada, Faculdade de Ciências e Tecnologia da Universidade Nova de Lisboa

Júri:

Presidente: Prof. Doutor João Carlos da Palma Goes

Arguentes: Prof. Doutora Maria Lourdes Calzada

Prof. Doutor Henrique Leonel Gomes

Vogais: Prof. Doutora Florinda Mendes da Costa

Prof. Doutora Elvira Maria Correia Fortunato

Prof. Doutor Rodrigo Ferrão Paiva Martins

Doutora Maria Smolander

FACULDADE DE CIÊNCIAS E TECNOLOGIA
UNIVERSIDADE NOVA DE LISBOA

Novembro, 2020

Design and synthesis of low temperature printed metal oxide electronic devices

Acknowledgements

"Discovery consists of seeing what everybody has seen and thinking what nobody else has thought." – Albert Szent-Györgyi

First, I would like to thank my institution the Faculdade de Ciências e Tecnologias da Universidade NOVA de Lisboa, and my department, Materials Science, for all the experiences provided over these years.

I want to acknowledge my supervisors (Prof. Elvira Fortunato and Prof. Rita Branquinho) for their support, guidance, and advice during this significant step of my life.

To Prof. Elvira Fortunato, for the chance to develop this work in an amazing group and facilities (CENIMAT/i3N and CEMOP), the pioneers of transparent and paper electronics. Thank you for the trust deposited in me and in my work offering me the opportunity to go for international conferences where I had the chance to learn so much and share knowledge. Also, for pushing me to achieve more and pay attention to the smallest details that make a difference.

To Prof. Rita Branquinho for her friendship during these wonderful 5 years where I grow up so much and had the pleasure to share the best office of CENIMAT. Thank you for the encouragement, the helpful discussions and feedback when I need it most. Also, for her trust to let me teach master students on their thesis as well as my participation on international projects which lead to the establishment of great networks.

I am proud for having them as the advisors of this research work and hope that the results achieved after these years meet their expectations.

To Prof. Rodrigo Martins for the advices and aim to push me to achieve greatness being possible due to the people involved, tools and exceptional research facilities of CENIMAT/i3N and CEMOP.

To Asal Kiazadeh and Jonas Deuermeier for their friendship and for making resistive switching devices clearer to me by showing their potential.

To Prof. Demosthenes Koutsogeorgis for the opportunity to do an internship on Nottingham Trent University, learn about laser processing technology and fruitful discussions. Also, I like to thank to Dr. Nikolaus Kalfagiannis for teaching me how to use the amazing excimer laser. To Jacob Spear for showing me the iSMART facilities procedures and for being always willing to help. To James, Patrick and Franka for their friendship and gatherings after work. To my housemates Thuy

and Odette for their friendship, dinners, and tours during this time out. It was a great pleasure and I hope to see you one day again.

To VTT Technical Research Centre of Finland for the opportunity to do an internship and get a more profound knowledge on printing techniques. I thank and appreciate the time that Liam Gillan and Asko Sneck spent to show me the labs and introduce me to flexographic printing, respectively. A special thanks to Dr. Jaakko Leppäniemi and Dr. Ari Alastalo for the productive discussions where I learned so much. Also, I would like to thank the rest of the team which receive me so well and were always open to help. To my friend José Rosa who is living in Finland for the interesting cross-country tours and talks.

To the Fundação para a Ciência e Tecnologia for the fellowship (SFRH/BD/116047/2016) and IDS-funMat-INNO project from EIT RawMaterials program (15015).

To the European Community H2020 NMP-22-2015 project 1D-NEON (685758); To the European Institute of Innovation and Technology (EIT RawMaterials, Horizon 2020) Supersmart, Scale-Up of Printed Electronics (17161); To the European Commission under the project BET-EU (H2020-TWINN-2015, GA 692373).

This work was also supported by FEDER funds through the COMPETE 2020 Programme and National Funds through FCT - Portuguese Foundation for Science and Technology under project number POCI-01-0145-FEDER-007688, Reference UID/CTM/50025.

To all my colleagues in the Advanced Functional Materials for Micro and Nanotechnologies (AFMMN) group that direct or indirectly, contributed to this work: MSc. Alexandre Fonseca, MSc. Alexandra Gonçalves, MSc. Ana Marques, Dr. Ana Batista, Dr. Ana Pimentel, Dr. Ana Rovisco, MSc. Ana Santa, MSc. André Moura, MSc. Andreia Santos, MSc. Ângelo Santos, Dr. Asal Kiazadeh, MSc. Beatriz Coelho, Dr. Bruno Veigas, Dr. Cristina Gaspar, Dr. Daniela Gomes, Dr. Diana Gaspar, MSc. Gonçalo Narciso, MSc. Guilherme Ferreira, MSc. Guilherme Ribeiro, Dr. Hugo Águas, MSc. Inês Cunha, Dr. Joana Pinto, MSc. Joana Figueira, Dr. Joana Neto, Dr. João Coelho, Dr. Jonas Deuermeier, MSc. Jorge Martins, MSc. José Carvalho, Dr. Luís Pereira, Dr. Manuel Mendes, MSc. Maria Pereira, MSc. Maria Oliveira, MSc. Mariana Matias, MSc. Miguel Franco, MSc. Miguel Alexandre, MSc. Paul Grey, MSc. Pedro Centeno, Dr. Pedro Barquinha, MSc. Raquel Barras, Dr. Rui Igreja, Dr. Santanu Jana, MSc. Sara Silvestre, Dr. Shrabani Panigrahi, MSc. Sirazul Haque, Dr. Suman Nandy, Dr. Sumita Goswami, MSc. Tiago Mateus, MSc. Tomás Freire, MSc. Tomás Pinheiro, MSc. Tomás Calmeiro and Dr. Ugur Menda. Of course, I cannot forget the people that left us for new adventures: MSc. Adriana Costa, MSc. Alexandra Fernandes, Dr. Hasan Yetkin, Dr. Oluwayomi Oluwabi, Dr. Andriy Lyubchyk, Dr.

António Vicente, MSc. Cátia Figueiredo, MSc. Cristina Fernandes, MSc. Daniela Salgueiro, Dr. Hasan Yetkin, MSc. Inês Martins, MSc. João Ribas, Dr. Kasra Kardarian, Dr. Lidia Santos, MSc. Manuel Chapa, MSc. Marco Moreira, MSc. Marta Ferreira, Msc. Neusmar Cordeiro, MSc. Nuno Branca, Dr. Oluwabi Titilope, MSc. Pedro Ivo, MSc. Pedro Trigo, Dr. Pydi Ganga, MSc. Raquel Maricato, MSc. Raquel Martins, MSc. Ricardo Farinha, MSc. Rodrigo Santos, Dr. Rogério Morais and MSc. Sónia Pereira.

To Alexandra Gonçalves, Sónia Pereira and Ricardo Ferreira for all the help in solving technical issues in the lab, without you, science need more time to really happen.

To Lucia Mendes, Susana Mendes, Valéria Gomes, Luís Milhano, Sara Oliveira and Sónia Soares for their friendship and professionalism, making logistics a lot easier.

To Paulo Manteigas for his availability to help me solving administrative issues required for conferences and internships.

To Joana Neto for the friendship, great discussions and advices in the best office of CENIMAT.

To all the students that I help monitoring, it was a great pleasure we learned a lot together and I desire the best luck in your future lives: Marco Moreira, Pedro Trigo, Tomás Vasconcelos, Matteo Giangolini, Carlos Dias, João Silva, Hadassa Valle, Rita Pereira, José Menezes, Raquel Martins, André Sá, Fabio Caldeira, Tomás Fernandes, José Barnabé, Guilherme Coelho, Dmytro Chervonovskyy, Laura Pires, Diogo Ferreira, Rita Firmino, Francisco Sousa and Manuel Pereira.

A special thank you to my friends Inês Cunha, Paul Grey, Carolina Marques, Jorge Martins, Sofia Ferreira and Maria Oliveira that are finishing the same journey for the great discussions and friendship along these 4 years. To my open space friends Maria Pereira, Gonçalo Narciso, Inês Martins, Pedro Trigo, Ana Samouco, Eduardo Duarte, Vasco Caniça, Cátia Figueiredo, Tomás Pinheiro, Ricardo Farinha, Carolina Natal, João Ribas e Marco Moreira for parties, beers and dinners.

To my housemates Paul Grey, Tobias Simon, Rogério Morais, João Loureiro, Nil Lozano, Pedro Centeno, Miguel Alexandre during a part of my PhD a big hug from the amazing times spent together (meals, beers, discussions, barbecues, travels and friendship).

To former colleagues (but lifelong friends) that help and teach me so much before or during this journey: Farah Alimagham, Daniel Pereira, Diogo Lima, Ana Figueiredo, Catarina Rodrigues, and Miguel Farto.

To all my friends for their comprehension and support, with you everything was easier.

To family Gameiro for their friendship and support in this last two years.

To my girlfriend Estefânia, for all the support and patient during this important step of my life. Without you by my side it would be a longer way to go, thank you my love.

Finally, but not least I want to thank my family for all the support during these tough years, without you will not be possible. Mom (Ana) and Dad (Ludgero) you gave to me, to my sister and my brother the best gift in life, an amazing education inside and outside of the classroom. I know that was not easy to have three “little” kids studying at the same time, but you did it and I am really proud of you. To my sister Joana for her caring and positive energy when my battery was lower. To my brother Ludgero for giving me strength to keep going, you are the next engineer in the list, so you know what that means. To my aunt Silvia, my cousin Margarida and my cousin Santiago for caring and support. To my grandparents, Fernanda, Quitas, António and Inácio for all the caring and teaching over all my life. It is a blessing to have all of you in my life until now and I hope to continue much more years. Love you all, family is everything.

Abstract

Printed electronics have led to new possibilities in the development of low-cost and low-temperature methods for materials production and processing. Inorganic oxide devices that are totally solution-processed offer an appealing approach, overcoming some limitations of organic electronics, such as performance and stability. Solution processes are simple and versatile however, there are still some drawbacks that need to be addressed. Currently, synthesis of these materials usually needs higher temperatures and longer annealing time which limits their use on flexible substrates being crucial for flexible and wearable device applications.

In this thesis, a general overview is made to solution combustion synthesis (SCS) method to synthetize nanostructures, thin films and their application in thin film transistors (TFTs) with a low thermal budget. Also, new strategies towards processing of solution-based metal oxide TFTs such as, oxide synthesis, post deposition treatments, low temperature high-κ dielectrics and emerging printing techniques are discussed.

Relevant steps to boost solution-based metal oxide TFTs are analysed, since the optimization of metal oxide (MO) thin films processed at low temperature until their printability in Roll-to-Roll (R2R) compatible techniques. To go even further some tests are performed to decrease the processing time required for the formation of MO thin films.

To finalize, special attention is given to solution-based metal oxide resistive switching devices in which the resistive states are quite important to represent different logic states (e.g. binary code) being useful for many digital applications.

Resumo

A eletrónica impressa tem aberto novas possibilidades para o desenvolvimento de métodos de baixo custo e a baixa temperatura para a produção e processamento de materiais. Dispositivos à base óxidos inorgânicos que são processados totalmente por solução oferecem uma abordagem atraente, superando algumas limitações existentes na eletrónica orgânica, como o desempenho e a estabilidade dos dispositivos. Os processos de solução são simples e versáteis, no entanto, tem algumas desvantagens que devem ser consideradas. Atualmente, a síntese desses materiais geralmente necessita de temperaturas mais altas e tempos mais longos de recozimento que suprimem a sua utilização em substratos flexíveis sendo crucial para a sua aplicação em dipositivos flexíveis.

Nesta tese é utilizado o método de síntese de combustão em solução (SCS) para sintetizar nano-estruturas, filmes finos e a sua aplicação em transístores de filme fino (TFFs) utilizando baixas temperaturas. Além disso, são discutidas novas estratégias para o processamento de TFFs baseados em óxidos metálicos por solução tal como a síntese dos óxidos, os tratamentos pós-deposição, dielétricos com alta constante dielétrica a baixa temperatura e técnicas de impressão emergentes.

São também analisadas as etapas relevantes para impulsionar TFFs de óxidos metálicos processados por solução, desde a otimização de filmes finos de óxidos metálicos (OM) a baixa temperatura até à sua capacidade de impressão em técnicas compatíveis com rolo a larga escala. Para ir ainda mais longe, alguns testes são feitos para diminuir o tempo de processamento necessário para a formação de filmes finos de OM.

Para finalizar, é dada especial atenção a dispositivos de comutação resistiva produzidos por solução nas quais os estados resistivos são muito importantes para representar diferentes estados lógicos (i.e., código binário) sendo úteis para diversas aplicações digitais.

Symbols

μ – mobility

μ_{FE} – field effect mobility

μ_{SAT} – saturation mobility

A – optical absorption

c – concentration (mol)

C_{ox} – oxide capacitance per unit area

d – insulator thickness

E_a – activation energy

E_g – bandgap energy

g_m – transconductance

h – Planck´s constant (4.135×10^{-15} eV.s)

I_D or I_{DS} – drain-to-source current

I_G – gate leakage current

$I_{ON/OFF}$ – current on-off ratio

J – current density

k – extinction coefficient

L – channel length

n – number of moles

ϕ – stoichiometry ratio/reducer to oxidizer ratio

q – elementary charge of a particle (1.6×10^{-19} C)

r – cation size

S or SS – subthreshold slope

T – Transmittance

T_A – annealing temperature

T_d – decomposition temperature

T_{exp} – experimental temperature of the reaction

$T_{ignition}$ – temperature required for the ignition of the combustion reaction

T_{low} – lowest temperature

T_{MAX} – maximum annealing temperature

T_{th} – theoretical temperature

V_D or V_{DS} – drain voltage

V_G or V_{DS} – gate voltage

V_{Hyst} – hysteresis

V_{ON} – turn-on voltage

V_T or V_{TH} – threshold voltage

W – channel width

z – valence states

α – absorption coefficient

ΔG – Gibbs free energy

ΔG_{hyd} – the standard molar Gibbs free energies of hydration

ΔV_T – threshold voltage variation

ε_0 – permittivity of free space (8.854×10^{-12} F.m^{-1})

λ – wavelength of electromagnetic wave

κ – dielectric constant

k_{H_2O} – water exchange rate

Abbreviations

1D – one dimensional

2D – two-dimensional

2-ME – 2-methoxyethanol

Aa – ascorbic acid

AA – aspartic acid

Ac – acetylacetone

Ace – acetamide

ACO – aluminium doping in cadmium oxide

AFM – atomic force microscopy

AG – artocarpus gomezeanus

AI – abutilon indicum

Ala – alanine

ALD – atomic layer deposition

Arg – arginine

ATR –attenuated total reflectance

AZO – aluminium-doped zin oxide

Blade – blade-coating

CA – citric acid

CAF – cassia fistula

CB – cross-bar

CBE – common bottom electrode

CB-PVS – current-blind pulse voltage stress

CC – current compliance

CD – charge density

CEMOP – Centre of Excellence in Microelectronics, Optoelectronics and Processes

CENIMAT – Centro de Investigação de Materiais

Cf – capacitance-frequency

CF – conductive filament

CG – calotropis gigantean

CMOS – complementary metal oxide semiconductor

CP – cross-point

CS – combustion synthesis

CTA – conventional thermal annealing

CTE – coefficient of thermal expansion

CV – capacitance-voltage

CVD – chemical vapor deposition

CV-PVS – current-visible pulse voltage stress

D – dielectric

DC – direct current

DEA – diethanolamine

DOD – drop-on-demand

DSC – differential scanning calorimetry

DUV – deep-ultraviolet

E – electrode

ECM – electrochemical metallization

EDS – energy-dispersive X-ray spectroscopy

EDTA – ethylene diamine tetra acetic acid

EFD – extremely fuel deficient

EFE – extremely fuel excess

EG – ethylene glycol

EGCG – Epigallocatechin gallate

EGT – electrolyte gate transistor

EHD – electrohydrodynamic printing

ELA – excimer laser annealing

EOT – effective oxide thickness

ETL – electron transport layer

FD – fuel deficient

FE – fuel excess

FIB – focused ion beam

Flexo – flexo-printing

Fru – frutose

FTIR – fourier transform infrared

FUV – far ultraviolet

GA – glutamic acid

GAXRD – glancing angle X-ray diffraction

Glu – glucose

Glyc – glycerine

GPTMS – (3-glycidoxy- propyl) trimethoxysilane

GZO – gallium-doped zinc oxide

GZTO – gallium−zinc-tin oxide

Hid – hydrazine

HMT – hexamethylenetetramine

HRS – high resistive state

IGO – indium gallium oxide

IGZO – indium gallium zinc oxide

IJ – inkjet printing

IoT – internet of things

IPA – isopropyl alcohol

IPL – intense pulse light

IT – indigofera tinctorial

ITO – tin-doped indium oxide

IV – current-voltage

IZO – indium zinc oxide

LA – laser annealing

LAT – lactose

LRS – low resistive state

LSA – laser spike annealing

MA – malic acid

MEA – monoethanolamine

MF – muffle furnace

MIM – metal-insulator-metal

MIS – metal-insulator-semiconductor

MLA – melia azedarach

MLC – multi-level cell

MO – metal oxide

M-O-M – metal-oxygen-metal

MOSFET – metal-oxide-semiconductor filed-effect transistor

MRAM – magnetoresistive random-access memory

MW – microwave

NA – nitric acid

NAc – nitroacetylacetone

NB – nanobelt

NBS – negative bias stress

NF – nanoflake

NFW – nanoflower

NiO – nickel oxide

NIR – near infrared

NN – nanoneedle

NP – nanoparticle

NPT – nanoplate

NPW – nanopowder

NS – nanosheet

NVM – non-volatile memory

OA – oxalic acid

ODH – oxalyal dihydrazide

OEL – oxygen exchange layer

OLA – oleic acid

OV – oxidizing valence

PA – phenylalanine

PANI – polyaniline

PBS – positive bias stress

PCRAM – phase change random-access memory

PDMS – polydimethylsiloxane

PEG – polyethylene glycol

PET – polyethylene terephthalate

PI – polyimide

PLD – pulsed laser deposition

PMMA – poly(methylmethacrylate)

PVA – polyvinyl alcohol

PVD – physical vapor deposition

PVK – poly(N-vinylcarbazole)

PVP – poly(4-vinylphenol)

PVS – pulse voltage stress

QD – quantum dot

r.f. – radio-frequency

R2R – roll-to-roll

rms – root mean square

ROP – reverse offset printing

rpm – rotations per minute

RRAM – resistive random-access memory

RS – raphanus sativus

RS – resistive switching

RV – reducing valence

SA – succinic acid

SAM – self-assembled monolayers

SC – semiconductor

sccm – standard cubic centimetres per minute

SCLC – space-charge-limited conduction

SCS – solution combustion synthesis

SEM – scanning electron microscopy

Ses – sesame

SHS – self-propagating high-temperature synthesis

SPCS – solid phase combustion synthesis

Spin – spin-coating

Spray – spray-coating

S-RRAM – solution-based metal oxide resistive random-access memory

Sta – starch

STT – spin transfer torque

Suc – sucrose

TA – tartaric acid

TAB – trimethylammonium bromide

TC – tinospora cordifolia

TCM – thermochemical mechanism

TCO – transparent conductive oxide

TCR – temperature coefficient of resistance

TEA – triethanolamine

TEG – tetra ethylene glycol

TEM – transmission electron microscopy

TFT – thin-film transistor

TG – thermogravimetry

TMO – transition metal oxide

U – urea

UV – ultraviolet

VCM – valence change mechanism

VCS – volume combustion synthesis

VG – vetiver grass

Vis – visible

W – water

XPS – X-ray photoelectron spectroscopy

XRD – X-ray diffraction

XRR – X-Ray Reflectivity

ZTO – zinc-tin oxide

Table of Contents

List of Figures

List of Tables

Chapter 1

Motivation

The production of inorganic electronic devices is a complex multistep process that resides mostly on vacuum deposition techniques and comprises patterning by several photolithographic processes. Research efforts have been focused on solution-based fabrication processes, such as printed electronics, which avoid most of the expensive production steps (reduction of 64 %).[1] Lately, there has been remarkable development in solution processed semiconductors, however the development of insulator materials for such applications is still a step behind which can delay the realization of fully printed electronics.

High-κ metal oxides are key materials in several applications: gate dielectrics for thin film transistors (TFTs) and more recently as non-volatile memories. Regardless of application, thin films of these materials must be smooth, dense and exhibit low leakage current. The search for high quality insulator oxides that can be processed at low temperatures and by cost effective techniques is thus extremely important and highly required for a more sustainable world.

1.1. Introduction

Inorganic metal oxide based transparent devices that can be solution processed have demonstrated impressive results in the last decade[2–5]. The synthesis of metal oxides via solution reactions is a promising alternative to high vacuum deposition processes currently used in conventional microelectronics fabrication. Synthesis via solution is a low-cost, simple and versatile method. However, it requires large stabilizing organic molecules and solvents. The decomposition process can lead to poor uniformity, impurities and film cracking. These effects can be minimized by reducing the organic content in the precursor solutions by using smaller molecules, adjusting the stoichiometry of the reaction chemistry and with ultraviolet treatment. Other variables (precursor salts, concentration, humidity, solvent and pH) must also be considered and optimized.

The constant demands for new applications and high-throughput fabrication of electronic devices has led to the development of new materials and techniques. The current fabrication techniques applied in the optoelectronic industry usually require high vacuum and photolithographic processes which are expensive and consequently keep production at high costs. Solution based fabrication methods have been pursued as an alternative for economically viable large-scale electronics, without using high vacuum[2,6–8].

Recently the development of solution based oxide semiconductors[2,3,9] and conductors[10] has been well reported however for dielectric materials, which are a crucial component in electronic devices, such as capacitors and transistors, the development of a low temperature synthetic route still needs to be further investigated.

Organic dielectrics have been studied for this purpose however they suffer from low dielectric permittivity and operational stability issues, falling short in performance when compared to inorganic materials[2,3]. High-κ dielectrics have demonstrated high performance and suitability for such applications. These materials are also at the basis of the performance of sensor interface circuits[11], driving circuits[12] and non-volatile resistive switching memory devices[13–15].

Solution processed oxides precursor routes based on sol-gel or hydrolysis reactions have been reported for several high-κ dielectrics; however high temperatures (>400 °C), incompatible with flexible substrates, are still required for degradation of the organic load[16–19].

Lowering the organic content can be achieved with a new synthetic route, solution combustion synthesis[2], which leads to a lower process temperature (<300 °C). This method takes advantage of the chemistry of the solution precursors as a source of energy for localized heating. The exothermic reaction generates energy that can convert precursors into oxides at low process

temperatures. Moreover, the solution based amorphous metal oxides thin films possess a substantial amount of residual organic components and the exposure to high energy photons can improve film densification by cleavage of alkoxy groups, activate metals and oxygen atoms to simplify metal-oxygen-metal (M-O-M) network formation[20]. In order to achieve the desired film properties at lower temperatures an ultraviolet (UV) treatment is required to improve condensation and film densification in amorphous metal-oxide dielectrics[3,21].

The properties and quality of the oxide thin films is highly dependent on precursor solution characteristics, therefore the development and understanding of the solution chemistry for low temperature dielectric oxides is currently a challenging target and a key development milestone to allow application in printable flexible electronics.

1.2. Objectives

In this PhD thesis, a low-cost process suitable to synthetize a variety of high-κ insulator metal oxides for electronic applications is proposed. This process relies on combustion synthesis of precursor solutions containing the metal ion that undergo reduction/oxidation reactions upon annealing assisted by different photonic curing tool processes on low-temperature substrates.

The research was divided into three main objectives:

- Precursor solutions development and optimization to produce dielectric oxides such as, Al_2O_3, HfO_2 and ZrO_2 using solution combustion synthesis (SCS) method;
- Optimization of annealing methods and deposition methods for the thin films' formation at low temperature;
- Production of solution based electronic devices (capacitors, thin film transistors (TFTs), and non-volatile resistive switching (RS) devices) by spin-coating and printing techniques (flexographic and inkjet printing).

1.3. Thesis outline

The structure of the work presented in this dissertation is divided in seven chapters where I set out to accomplish each one of the mentioned tasks.

- **Chapter 1** provides the motivation and aims of this study.
- **Chapter 2** summarizes solution combustion synthesis (SCS) method approach to produce metal oxides with different morphologies, mainly nanostructures and thin films for diverse applications. Special attention is given to thin films application in thin film transistors (TFTs).
- **Chapter 3** focuses on recent approaches to achieve solution-based oxides at low temperature such as, SCS and post processing irradiation (UV, NIR) treatments which allow their implementation in printable flexible TFTs. An appropriate concern is given to solution-based high-κ oxide dielectrics that play a critical role to achieve low power consumption. Also, a detailed discussion of emerging printing techniques and current challenges is presented.
- **Chapter 4** describes the main results obtained for solution based TFTs. This chapter is subdivided in three sections: the optimization of solution-based high-κ dielectrics at low temperature for their application in electronic structures, the printing of metal oxides and the enhancement of the processing time of solution-based metal oxides using UV laser irradiation.
- **Chapter 5** focuses on the state-of-the-art of solution-based metal oxide resistive random-access memory (S-RRAM). A detailed description of the solution synthesis parameters influence on S-RRAMs is performed, as well as the study of interface interaction between the layers. Then, the figures of merit and the main challenges in S-RRAMs are discussed and future trends are proposed.
- **Chapter 6** focuses on the main results achieved with solution-processed resistive switching memories based on metal oxides. This chapter is subdivided in two sections: the number of layers effect on spin-coated solution-based aluminum oxide (AlO_x) memories and the response of low temperature printed AlO_x resistive switching devices.
- **Chapter 7** is devoted to the main conclusions of this dissertation and further applications of the results and concepts reached.

1.4. Research impact

The main results attained during this dissertation were presented in several international conferences (6 oral presentations) and published in peer-reviewed publications (10 articles, 2 review articles and 1 book chapter). Also, some of this work was distinguished internationally, which empathizes the relevance of this thesis to the field.

1.4.1. Publications

- **Emanuel Carlos,** Jonas Deuermeier, Rita Branquinho, Cristina Gaspar, Rodrigo Martins, Asal Kiazadeh, Elvira Fortunato. "Design and synthesis of low temperature printed metal oxide memristors", Journal of Materials Chemistry C, **2021** (DOI: 10.1039/D0TC05368F);
- Santanu Jana, **Emanuel Carlos**, Shrabani Panigrahi, Rodrigo Martins, Elvira Fortunato. "Towards Stable Solution-Processed High Mobility p-Type Thin Film Transistors Based on Halide Perovskites", ACS Nano, **2020** (DOI: 10.1021/acsnano.0c02862);
- **Emanuel Carlos,** Rita Branquinho, Rodrigo Martins, Asal Kiazadeh, Elvira Fortunato. "Recent Progress in Solution-Based Metal Oxide Resistive Switching Devices", Review, Advanced Materials, **2020** (DOI: 10.1002/adma.202004328);
- **Emanuel Carlos**, Rita Branquinho, Pedro Barquinha, Rodrigo Martins, Elvira Fortunato. "New strategies towards high performance and low temperature processing of solution based metal oxide TFTs", Book Chapter Review, Elsevier, **2021** (DOI: 10.1016/B978-0-12-819718-9.00003-0);
- **Emanuel Carlos,** Rodrigo Martins, Elvira Fortunato, Rita Branquinho. "Solution Combustion Synthesis: Towards a Sustainable Approach for Metal Oxides", Review, Chemistry – A European Journal, **2020** (DOI: 10.1002/chem.202000678);
- **Emanuel Carlos**, Spilios Dellis, Nikolaos Kalfagiannis, Loukas Koutsokeras, Demosthenes C. Koutsogeorgis, Rita Branquinho, Rodrigo Martins, Elvira Fortunato. "Laser induced ultrafast combustion synthesis of solution-based AlO_x for thin film transistors", Journal of Materials Chemistry C, **2020**, (DOI: 10.1039/D0TC01204A);
- **Emanuel Carlos**, Jaakko Leppäniemi, Asko Sneck, Ari Alastalo, Jonas Deuermeier, Rita Branquinho, Rodrigo Martins, Elvira Fortunato. "Printed, Highly Stable Metal Oxide TFTs with Ultra-Thin High-κ Oxide Dielectric", Advanced Electronic Materials, **2020** (DOI: 10.1002/aelm.201901071);
- Abayomi Oluwabi, Atanas Katerski, **Emanuel Carlos**, Rita Branquinho, Arvo Mere, Malle Krunks, Elvira Fortunato, Luis Pereira, Rodrigo Martins, Elvira Fortunato, Ilona Acik. "Application of ultrasonic sprayed zirconium oxide dielectric in zinc tin oxide-based thin film transistor", Journal of Materials Chemistry C, **2020** (DOI: 10.1039/C9TC05127A);

- Nuno Branca, Jonas Deuermeier, Jorge Martins, **Emanuel Carlos**, Maria Pereira, Rodrigo Martins, Elvira Fortunato, Asal Kiazadeh. "2D Resistive Switching Based on Amorphous Zinc–Tin Oxide Schottky Diodes", Advanced Electronic Materials, **2019** (DOI: 10.1002/aelm.201900958);
- Marco Moreira, **Emanuel Carlos**, Carlos Dias, Jonas Deuermeier, Maria Pereira, Pedro Barquinha, Rita Branquinho, Rodrigo Martins, Elvira Fortunato. "Tailoring IGZO Composition for Enhanced Fully Solution-Based Thin Film Transistors", Nanomaterials, **2019** (DOI: 10.3390/nano9091273);
- Ghisman Plescan Viorica, Viorica Musat, Ana Pimentel, Tomas Calmeiro, **Emanuel Carlos**, Liliana Baroiu, Rodrigo Martins, Elvira Fortunato. "Hybrid (Ag) ZnO/Cs/PMMA nanocomposite thin films", Journal of Alloys and Compounds, **2019** (DOI: 10.1016/j.jallcom.2019.06.373);
- Raquel Barros, Kachirayil Saji, João Waerenborgh, Pedro Barquinha, Luís Pereira, **Emanuel Carlos**, Rodrigo Martins, Elvira Fortunato. "Role of Structure and Composition on the Performances of P-Type Tin Oxide Thin-Film Transistors Processed at Low-Temperatures", Nanomaterials, **2019** (DOI: 10.3390/nano9030320);
- **Emanuel Carlos**, Asal Kiazadeh, Jonas Deuermeier, Rita Branquinho, Rodrigo Martins, Elvira Fortunato. "Critical role of a double-layer configuration in solution-based unipolar resistive switching memories", Nanotechnology IOP, **2018** (DOI: 10.1088/1361-6528/aac9fb);
- **Emanuel Carlos**, Rita Branquinho, Asal Kiazadeh, Jorge Martins, Pedro Barquinha, Rodrigo Martins, Elvira Fortunato. "Boosting Electrical Performance of High-κ Nanomultilayer Dielectrics and Electronic Devices by Combining Solution Combustion Synthesis and UV Irradiation", ACS Applied Materials & Interfaces, **2017** (DOI: 10.1021/acsami.7b11752);

1.4.2. Presentations

1.4.2.1. Oral presentations

- Elvira Fortunato, **Emanuel Carlos**, Rita Branquinho, Pedro Barquinha, Rodrigo Martins. "Metal Oxides: A family of materials that is full of potentialities" - Oxide Semiconductor for Display, Electronics and Energy Applications (Symposium 7) - The 5th International Conference on Advanced Electromaterials (ICAE) – Jeju – Korea **2019**; **(Invited)**
- **Emanuel Carlos**, Rita Branquinho, Asal Kiazadeh, Pedro Barquinha, Nikolaos Kalfagiannis, Demosthenes C. Koutsogeorgis, Asko Sneck, Jaakko Leppäniemi, Ari Alastalo, Rodrigo Martins, Elvira Fortunato. "How to go further in printable oxide electronic materials" - Synthesis, processing and characterization of nanoscale multi functional oxide films VII (Symposium A) - E-MRS Spring Meeting - Nice - France **2019;**

- **Emanuel Carlos**, Rita Branquinho, Asal Kiazadeh, Pedro Barquinha, Nikolaos Kalfagiannis, Demosthenes C. Koutsogeorgis, Asko Sneck, Jaakko Leppäniemi, Ari Alastalo, Rodrigo Martins, Elvira Fortunato. "How to go further in printable oxide electronic materials" – Functional Materials (Symposium A) - Materiais - Lisbon - Portugal **2019;**
- **Emanuel Carlos**, Rita Branquinho, Pedro Trigo, Asal Kiazadeh, Jorge Martins, Pedro Barquinha, Rodrigo Martins, Elvira Fortunato. "Boosting electrical performance of solution-based high-κ dielectrics to apply in electronic devices using low cost processes" - Solution processing and properties of functional oxide thin films and nanostructures-III (Symposium P), E-MRS Spring Meeting - Strasbourg - France **2018; (Invited)**
- **Emanuel Carlos**, Asal Kiazadeh, Rita Branquinho, Jonas Deuermeier, Rodrigo Martins, Elvira Fortunato. "Coexistence of unipolar and bipolar resistive switching properties in fully solution-based aluminum oxide device" - Solution processing and properties of functional oxide thin films and nanostructures-III (Symposium P), E-MRS Spring Meeting - Strasbourg - France **2018;**
- Rita Branquinho, **Emanuel Carlos**, Ana Santa, Daniela Salgueiro, Spilios Dellis, Nikolaos Kalfagiannis, Asal Kiazadeh, Pedro Barquinha, Demosthenes C. Koutsogeorgis, Rodrigo Martins, Elvira Fortunato. "Solution Combustion Synthesis: Applications in Oxide Electronics" - Solution processing and properties of functional oxide thin films and nanostructures-III (Symposium P), E-MRS Spring Meeting - Strasbourg - France **2018;**

1.4.2.2. Poster presentations

- **Emanuel Carlos**, Spilios Dellis, Nikolaos Kalfagiannis, Loukas Koutsokeras, Demosthenes C. Koutsogeorgis, Rita Branquinho, Rodrigo Martins, Elvira Fortunato. "Ultrafast photonic curing of solution-based aluminium oxide for thin film transistors" - Innovations in Large-Area Electronics (innoLAE) – Cambridge – UK **2019**; **(Best poster award)**
- **Emanuel Carlos**, Asal Kiazadeh, Jonas Deuermeier, Rita Branquinho, Rodrigo Martins, Elvira Fortunato. "Opportunities with solution-processed high-κ dielectrics for ReRAM applications"- New Memory Paradigms: Memristive Phenomena and Neuromorphic Applications, Faraday Discussion - Aachen – Germany **2018**;
- **Emanuel Carlos**, Rita Branquinho, Asal Kiazadeh, Jorge Martins, Pedro Barquinha, Rodrigo Martins, Elvira Fortunato. "Boosting the Electrical Performances of Solution-Based High-κ Multilayer Dielectrics at Low Temperature and Their Application in Electronic Structures" - Solution-Processed Inorganics for Electronic and Photonic Device Applications, MRS Fall Meeting - Boston - USA **2017**; **(Best poster award nominee)**

- **Emanuel Carlos**, Rita Branquinho, Asal Kiazadeh, Pedro Barquinha, Rodrigo Martins, Elvira Fortunato. "Improvement of solution-based high-κ dielectrics at low temperature for electronic structures" – 5th Dresden Nanoanalysis Symposium: In-situ Microscopy, Fraunhofer Campus - Dresden - Germany **2017**;
- Daniela Salgueiro, **Emanuel Carlos**, Ana Santa, Asal Kiazadeh, Pedro Barquinha, Rita Branquinho, Rodrigo Martins, Elvira Fortunato " Solution Based Thin Film Transistors: From Lab To Fab" - Ciência, Lisbon - Portugal **2017**;

1.4.3. Master thesis guidance

- Marco Moreira, "Composition ratio effect in IGZO using solution combustion synthesis for TFT applications", 2017;
- Pedro Trigo, "Oxide transistors produced by Combustion Synthesis: Influence of the PVP on the properties of the insulator", 2017;
- Rita Pereira, "Printing of eco-friendly solution based zinc-tin oxide for device applications", 2019;
- Hadassa Valle, "Effect of eco-friendly solvents in solution-based ZrO_x dielectrics", 2019;
- Carlos Dias, "Fully Solution-based Thin Film Transistors", 2019;
- João Silva, "Effect of eco-friendly solvents in solution-based AlO_x dielectrics at low temperature", 2020;
- José Menezes "Solution-based zinc-tin oxide diodes under infrared irradiation", 2020
- Raquel Martins "Solution based metal oxide semiconductor memristors", 2020

1.4.4. Impact of this work in the field

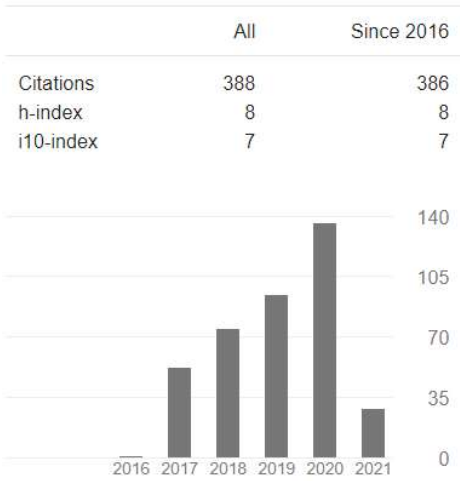

Figure 1.1. Number of citations achieved during this dissertation work until now (February, 2021) on the field of oxide electronic materials.

1.4.5. Soft skills

During the PhD acquiring soft skills is essential and highly valuable for the next career steps. They help us to develop character traits and interpersonal skills that will influence how well a person can work or interact with others. So, during this thesis some courses were performed:

- "Technology Intelligence", Raw Materials - IDS FunMat programme, Bordeaux – France, **2018**
- "Material Selection and Processing & Scientific Communication", Raw Materials - IDS FunMat programme, Hirschegg – Austria, **2018**
- "Entrepreneurship and Innovation", Raw Materials - IDS FunMat programme, Bilbao – Spain, **2017**
- "Life Cycle of Materials and Project & Risk Management", Raw Materials - IDS FunMat programme, Lisbon – Portugal, **2017**
- European Advanced Training Course, "Nanoscale Materials Characterization – Techniques and Applications", Dresden – Germany, **2017**

Chapter 2

Solution combustion synthesis (SCS) of metal oxides

Solution combustion synthesis (SCS) has been widely used to produce simple and complex oxides with a desired morphology (size and shape). SCS is valuable due to low cost, simplicity and energy efficiency synthesis. To guarantee the best molecular-level mixing of reactants in an aqueous or solvent-based solution some parameters need to be controlled, such as fuel type, metal cations precursors, stoichiometry ratio (ϕ), pH effect, atmosphere and initiation type. These determine the final properties of the oxide materials, having the potentiality to reach different morphologies, which are essential for their final applications. This review focuses on the crucial parameters in SCS and how these affect the overall materials properties from nanostructures to thin films. To finalize, special attention is given to the application of SCS to form metal oxide thin films at low temperature and their application in thin film transistors (TFTs).

Keywords: solution combustion synthesis, fuel, metal oxides, nanostructures, thin film transistors.

The literature presented in this chapter is published in:

- ✓ *Emanuel Carlos, Rodrigo Martins, Elvira Fortunato, Rita Branquinho. "Solution Combustion Synthesis: Towards a Sustainable Approach for Metal Oxides", Review, Chemistry – A European Journal, 2020.*

2.1. Introduction

Combustion is a universal technology, supplying most of the primary energy worldwide.[22] For combustion to occur a fuel (oil, coal, natural gas, hydroelectricity, nuclear energy and renewables) is burnt with an oxidizer, commonly air, to generate heat being passed down for different purposes, for heating, propulsion and energy production.[22,23] Also, combustion is useful to destroy harmful pollutants and to eliminate of biomass waste. Combustion is defined by a redox reaction or electron transfer process in which the fuel is oxidized (electropositive element), and the oxidizer is reduced (electronegative element) leading to an exothermic reaction. The equation 2.1 that describes the formation of water from the redox reaction of hydrogen and oxygen is an example:

$$2H_2^{[0]} + O_2^{[0]} \rightarrow 2H_2^{[1+]}O^{[2-]} \quad (2.1)$$

The small subscripts in brackets refer to the oxidation state. The oxidation is related with an increase of the oxidation state from [0] to [+1] in hydrogen (fuel) and a decrease in the oxidation state in oxygen (oxidizer) from [0] to [2-]. Combustion processes that are common in society as wildfires, factories, vehicle exhausts, power generation and are characterized essentially by high temperatures, usually combined with high pressures and transient conditions.

In general, products are typically pollutants; like carbon monoxide (CO), carbon dioxide (CO_2), nitrogen oxide (NO), nitrogen dioxide (NO_2), sulphur dioxide (SO_2) and ammonia (NH_3) which are harmful for public health.[24] However, when combustion is applied for synthesis it allows a variety of inorganic materials to be produced at lower temperatures, such as ceramics powders and catalysts.[25,26] To generate combustion three elements are required, an oxidizer, a fuel (reducer) and the necessary temperature, as depicted in Figure 2.1.

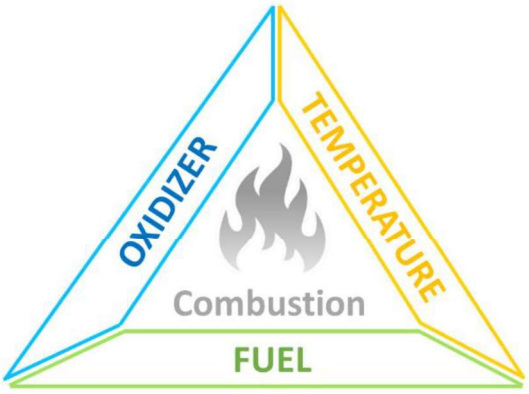

Figure 2.1. Demanded elements to occur combustion synthesis.[27] Copyright © 2020, Wiley-VCH Verlag GmbH & Co. KGaA, Weinheim.

Although, this synthesis has been used since the prehistoric times to produce carbon black from the fires for caves painting. The first real implementation of combustion synthesis was performed by Pechini in 1967. The Pechini process consist on resin intermediates to form oxides and which are sintered them into a dense ceramic to form capacitors.[28] In the early seventies, Merzhanov pioneered self-propagating high-temperature synthesis, also known as combustion synthesis to produce refractory inorganic compounds.[25] The process requires high-purity fine precursors which ignite at high temperatures (> 1000 °C) and is highly exothermic reaching temperatures of 4000 °C to form oxides and non-oxide materials. However, it does not lead to homogeneous products resulting in coarse powders and low surface areas since it is a solid-state reaction.[29]

The combustion synthesis (CS) processes depend on the nature of the reactants which can be gaseous, liquids or solids. For that reason CS processes are classified into gas phase combustion synthesis, solid phase combustion synthesis (subdivided into, the self-propagating high-temperature synthesis (SHS) and volume combustion synthesis (VCS)) and liquid phase combustion synthesis.[23] Gas phase combustion synthesis is not just a synthesis process where all the reactants are gaseous but also combustion processes that involve the gas phase through some part of the synthesis. This synthesis relies on a wide range of conditions, as the reactant concentration, the control particle morphology and temperature applied. The capability to produce nanometre particles is highly useful to promote the catalytic activity, superplasticity and lower reaction sintering temperatures.[30,31] In solid phase combustion synthesis (SPCS) the solid reactants (powder mixture) are pressed into a cylindrical pellet and ignited by an energy source (tungsten coil, laser or another suitable sources). In the case of self-propagating high-temperature synthesis the energy source acts locally (focus on a spot) igniting a highly exothermic reaction that self-propagates through the mixture, as shown in Figure 2.2 (a).[25] For the VCS, the entire volume of the powder mixture sample is heated uniformly in a controlled way, as depicted in

Figure 2.2 (b). In this type of solid phase combustion synthesis, the reaction occurs simultaneously in the entire volume and is more convenient for a weak exothermic reaction and thus SPCS is normally used to synthetize single and multiphase ceramic nanocomposites.[32] Figure 2.2 (c) show the liquid phase combustion synthesis, also named solution combustion synthesis (SCS) which start to be implemented in 1981 with the Jain method.[33] The method consist on the stoichiometric proportion between the oxidizer and the fuel for SCS, which is based on propellant chemistry. This allows the calculation of the oxidizing/reducing valences (OV/RV) of a redox mixture being applied by Patil and co-workers in 1988 to produce metal oxides.[34] The Jain method involve an exothermic reaction of metal nitrates (oxidants) and an organic fuel which should be a source of carbon and hydrogen. Most of metal oxides can be achieved by combining a metal nitrate, and fuel. Nitrates are preferred as the metal precursor because these provide a metal ion that is water/alcohol soluble and guarantee homogeneity. In general, SCS is a common method for the preparation of a wide variety of materials due to its simplicity, broad range of applicability and the possibility of easily obtaining products in the desired composition allowing diverse applications.[32,35].

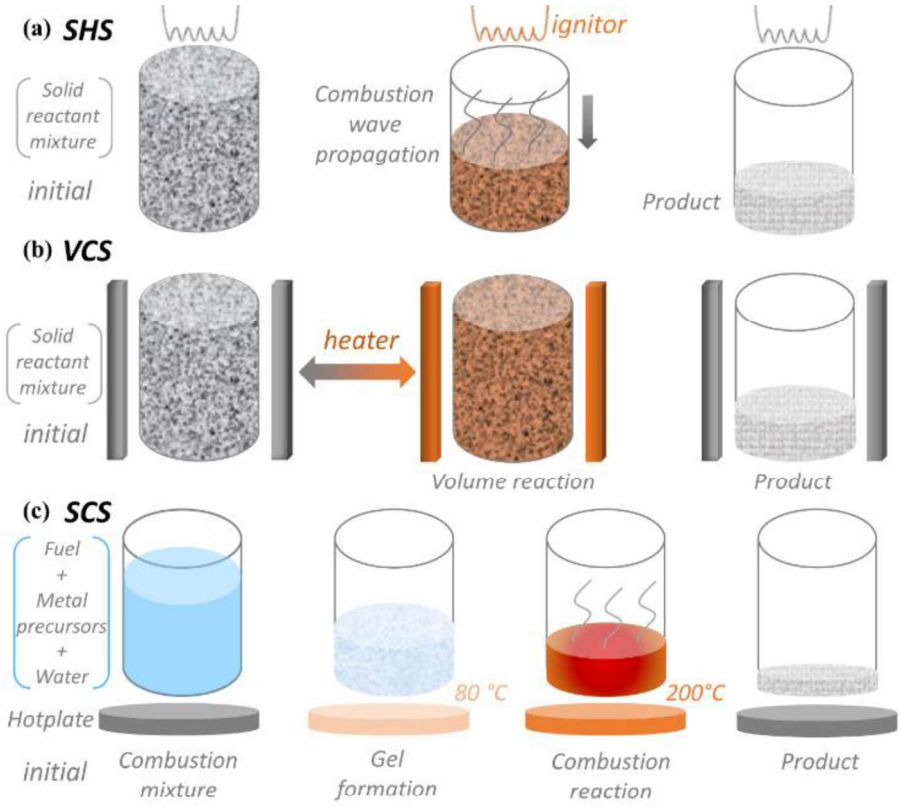

Figure 2.2. Schematic representation of (a) self-propagating high-temperature synthesis (SHS), (b) volume combustion synthesis (VCS) and (c) solution combustion synthesis (SCS) method.[27] Copyright © 2020, Wiley-VCH Verlag GmbH & Co. KGaA, Weinheim.

In this review, we cover why SCS is so relevant to produce metal oxides (section 2.2) and examine the crucial parameters, such as fuel, metal cations precursors, pH, concentration, oxidizer to reducer ratio (ϕ), atmosphere environment and initiation type. These parameters are truly relevant to determine the oxide materials morphology and possible applications. SCS is becoming one of the most-convenient methods for the preparation of simple and multicomponent oxides thin films at lower temperatures. Thus, in section 2.3 we will cover their application in thin film transistors (TFTs) and discuss the implementation of UV irradiation in the annealing process to solve some of the current issues in low temperature combustion solution processed TFTs. In section 2.4 a brief conclusion and outlook on the possibilities of SCS are presented.

2.2. Solution combustion synthesis (SCS) of oxides

Solution combustion synthesis is a fast, simple, efficient and versatile method becoming highly popular globally for the preparation of oxide materials with controlled properties (high purity and homogeneity) for a wide number of applications, such as catalysts, solid fuel cells and electronics.[4,36–39] SCS derives from sol-gel and propellant chemistry, however SCS is faster when compared to sol-gel and can provide higher quality final products.[33,40] Solution combustion

synthesis is subdivided in three main steps, i) combustion mixture formation, ii) gel formation and iii) combustion of the gel. In a simple way SCS consists on a self-sustained redox reaction initiated by a source of energy (thermal or electric) between a fuel and an oxidant (usually metal nitrates) in the presence of metal cations. The fuel is typically composed by organics containing carbon and hydrogen that facilitate the liberation of heat by the formation of CO_2 and H_2O during the combustion process.[41] Like previously mention, *Patil et al.* firstly reported the SCS of oxides by combining aluminum nitrate nonahydrate ($Al(NO_3)_3 \cdot 9H_2O$), the oxidant and urea ($CO(NH_2)_2$), the fuel, based on a stoichiometric balance of the redox mixture to attain aluminum oxide.[29] In this method, the ignition temperature is not high, just a moderate temperature is required to trigger the combustion reaction leading to a strong exothermic redox reaction that deliver enough energy to form the metal oxide lattices. This allows the use of low process temperatures to convert the solution precursors into oxides.

2.2.1. Crucial parameters in solution combustion synthesis

The final characteristics of the resultant oxides from the SCS are highly dependent on the synthesis parameters, namely, the fuel type, the metal cations precursors, the pH, the reducer to oxidizer ratio (ϕ), the atmosphere environment and initiation type.

2.2.1.1. Role of the fuel

The fuel plays a central role in the final product properties and even act not just as reducer, but also as complexing agent and microstructural template. It is composed by organic compounds, usually carboxylate (urea, glycine, and citric acid) and aliphatic amine (hydrazides) groups, that can react with an oxidant initializing the combustion reaction. Fuels contain chelating agents that prevent precipitation of metal ions and preserve the compositional homogeneity between all the constituents which helps create strong coordinate bonds.[42,43] For this reason fuels are widely used for the synthesis of metal oxides promoting a gel network after solvent evaporation that maintains the metal cations homogenously fixed in their position during the combustion process.

The fuel type greatly affects the microstructure of the final oxide material which is related with the gel network formed by the fuel and its decomposition features.[35,44–46] To clarify the different fuel types *Deganello et al.* established a multiple classification to select the right fuel mixture for diverse metal cations and ionic potentials.[47] The fuels were divided in four categories depending on their functional groups: carboxylic, hydroxyl, amino and multifunctional. As reported by *Varma et al.* fuels containing amino groups ($–NH_2$) are more reactive in the combustion reaction compared to hydroxyl groups (–OH) and carboxylic groups (–COOH), the less reactive redox.[48] Taking that into account the combination of different functional groups in the same fuel can be useful to improve the coordination with metal salts to form distinctive oxides.

Carboxylic functional groups (–C(=O)OH or –COOH) consist on a carbon atom double bonded to an oxygen atom and single bonded to a hydroxyl group. These fuel groups ionize by releasing the hydrogen atom from the –OH group. Therefore, carboxyl groups are found in acids, such as citric, ascorbic, tartaric, oxalic, glutamic and aspartic acid. Citric acid ($C_6H_8O_7$) is a widely used fuel since it is inexpensive and request low ignition temperature when combusted with nitrate salts precursors to form metal oxides.[35,49] Also, it is a high carbon fuel composed by three carboxylic and one hydroxyl groups, and has the lowest decomposition temperature compared to other carboxylic fuels, as shown in Figure 2.3 (a). Nevertheless, citric acid directly affects the pH of the solution when mixed with metal salts thus disturbing the stability and homogeneity of the gel.[50,51] Also, the combustion of citric acid generates higher amount of gaseous products being more favourable for the production of oxides powders than thin films.[35]

Ascorbic acid ($C_6H_8O_6$), also known as Vitamin C and tartaric acid ($C_4H_6O_6$), which are extracted from oranges and grapes, respectively, have a high carbon content and are nitrogen free as is citric acid. The main issue of these fuels is the weak complexation capability of metal cations leading to an early precipitation if several cation oxidants are used.[52,53] Nevertheless, they provide a slow combustion reaction which can be profitable for a more controlled oxide formation and the resultant oxide nanoparticles can be interesting for photocatalytic, sensor and antibacterial applications.

Oxalic acid ($C_2H_2O_4$), a dicarboxylic acid, is a strong and toxic organic compound with low molecular weight (Figure 2.3 (a)) widely distributed in nature. This fuel has been used for the production of oxide nanostructures, cathodes in batteries and solid oxide fuel cells.[54–56]

Glutamic acid ($C_5H_9NO_4$), aspartic acid ($C_4H_7NO_4$) and ethylene diamine tetra acetic acid (EDTA) ($C_{10}H_{16}N_2O_8$) are mostly constituted by carboxylic functional groups but also contain amino groups. EDTA has two amino groups and is a widely used complexing agent to avoid the precipitation of insoluble metal compounds. As a result, the coordination with the metal ions is improved assuming homogeneity during the gel formation. Carboxylic fuels are typically inexpensive and offer low ignition temperatures ($\leq$ 250 °C), leading to nanopowders and nanomaterials with varied applications, such as thermoelectrics, ceramics and perovskite oxides.[57–63]

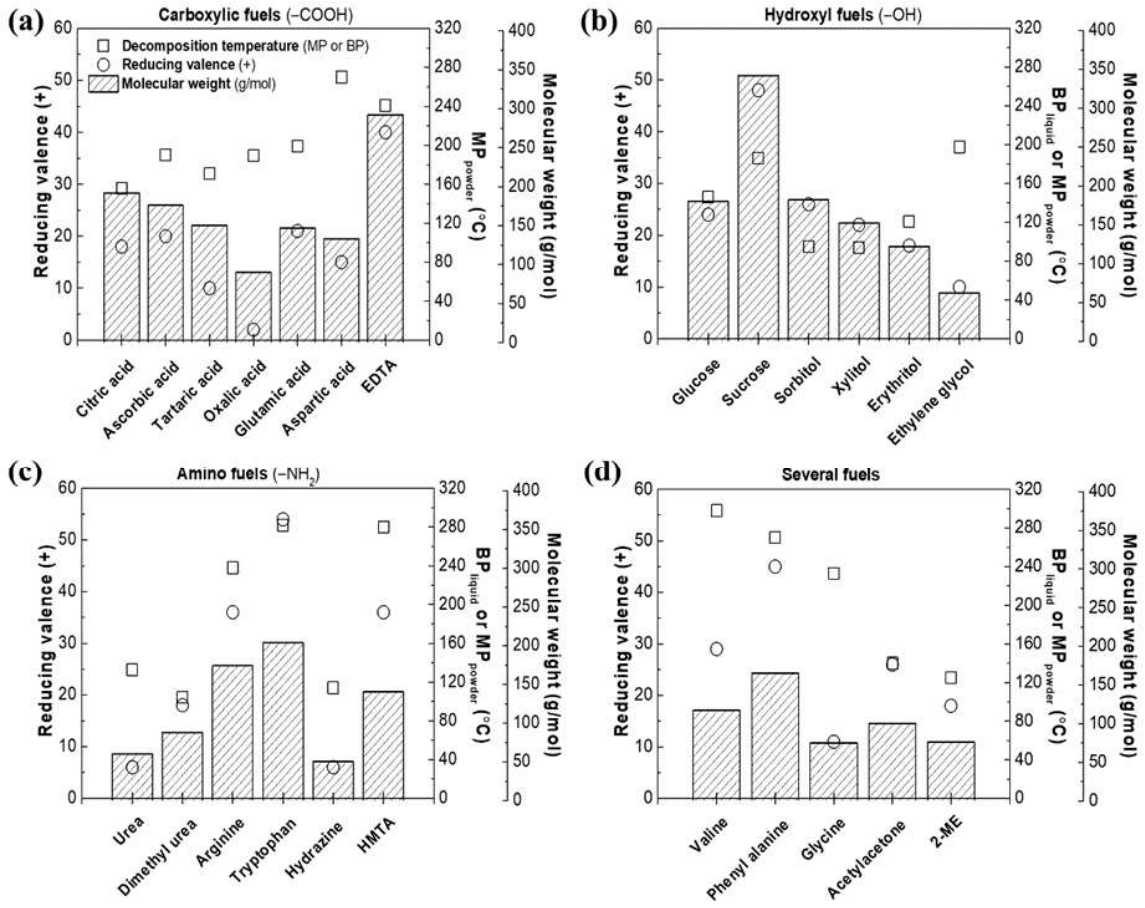

Figure 2.3. Reducing valence (+), decomposition temperature (melting point (MP) or boiling point (BP)) , and molecular weight for different fuel types applied in SCS: (a) carboxylic functional gro ups (–COOH); (b) hydroxyl groups (–OH); (c) amino functional groups (–NH_2); (d) several functional groups. The boiling point is show only for liquid fuels (ethylene glycol, hydrazine, acetylacetone and 2 -methoxyethanol (2-ME)). The melting point, boiling point and molecular weight data of the fuels were taken from the Sigma Aldrich website. The reducing valence of each fuel was determined considering the Jain method.[27] Copyright © 2020, Wiley-VCH Verlag GmbH & Co. KGaA, Weinheim.

When the hydroxyl groups (–OH) are predominant in the organic compound the combustion reaction is more intense compared to the carboxylic groups and the decomposition temperature is lower in overall, as depicted in Figure 2.3 (b). Carbohydrates, such as glucose ($C_6H_{12}O_6$), sucrose ($C_{12}H_{22}O_{11}$), sorbitol ($C_6H_{14}O_6$), xylitol ($C_5H_{12}O_5$), erythritol ($C_4H_{10}O_4$) and ethylene glycol (EG) ($C_2H_6O_2$) are in this category. EG behaves as a gelating agent by the formation of an organic ester with the creation of a homogeneous network with the metal ions leading to an organize polymerization.[64,65] Porous and thin film oxide materials have been obtained to produce nanocatalysts, supercapacitors and thin film transistors using these fuels group.[65–69]

Organic fuels comprising mostly amino groups (–NH_2) present a high exothermicity when the combustion reaction occurs and the lowest molecular weights compared to carboxylic and

hydroxyl functional groups, as shown in Figure 2.3 (c). Example of fuels in this category for oxides production are urea (CH_4N_2O), dimethyl urea ($C_3H_8N_2O$), arginine ($C_6H_{14}N_4O_2$), tryptophan ($C_{10}H_{10}N_2O_2$), hydrazine monohydrate ($N_2H_4{\cdot}H_2O$) and hexamethylene tetraamine (HMTA)($(CH_2)_6N_4$).[47] Urea is the most commonly used in SCS due to its abundant availability, low cost, high exothermic reaction at a low ignition temperature, and enhanced coordination ability relative to metal nitrate precursors.[70] Arginine and tryptophan can form a homogeneous gel due to the good correlation between them and metal ions. Arginine has the same number of amino groups as urea but also contains a carboxyl group which leads to an increase of decomposition temperature. Dimethyl urea should be selected if is desirable a very high exothermicity.[62] HMTA and hydrazine monohydrate are rather unsafe as these can form highly exothermic explosive reactions.[71–73] Nevertheless, hydrazine monohydrate has the lowest molecular weight and is an optimal fuel to avoid carbon impurities in the final product however a controlled environment must be used.

In terms of fuels with equal proportion of various functional groups, some examples can be found for the oxides production, such as valine ($C_5H_{11}NO_2$), phenyl alanine ($C_9H_{11}NO_2$) and glycine ($C_2H_5NO_2$).[62] Valine has the highest decomposition temperature used in SCS, as depicted in Figure 2.3 (d), which is not ideal for the production of low temperature oxides. Glycine is a commonly used fuel like urea with high coordination ability toward nitrates, low cost, high exothermicity, however instead of two amino groups, it is constituted by one amino group and one carboxylic group at opposite ends of the chemical structure.[74] Since glycine has carbon bonds the final product will have higher probability of carbon impurities compared to urea.[75] Interestingly, glycine is a zwitterionic molecule (has more than one functional group which contain at least one positive and one negative charge, being the molecule electrically neutral) which helps prevent selective precipitation and maintain a compositional equilibrium between the constituents.[26]

Another interesting organic liquid fuel in SCS is acetylacetone ($C_5H_8O_2$) that in the presence of metal nitrate ions result in a sharp combustion process with low activation temperature. This fuel has been used to perform not just metal oxide powders, but widely used to produce metal oxide thin films.[76,77] 2-methoxyethanol (2-ME) ($C_3H_8O_2$) is generally used as solvent for the production of oxide thin films but recently was proven that it can also act as fuel, preventing the need of other fuels.[78]

A mixture of fuels is sometimes required where a secondary fuel is demanded to stabilize metal complexes in multicomponent oxides. However, a good interaction between the primary and the secondary fuel, and with the metal cations needs to be assured.[67,79]

In general, organic fuels with different functional groups can achieve various phase formations and morphologies for diverse metal cations. The fuel selection plays a critical role in relation to the type of compound for the final product requirements, as the ignition temperature and presence of carbon impurities.

2.2.1.2. Role of the metal cation precursors

The metal precursors are the source of the metal cations in the solution combustion synthesis, thus determining the final metal oxide. The metal precursor are typically salts and can have three types of counter anions groups: oxidants, reducers or neutrals.[80] From these ones, the oxidants, hydrated nitrates are preferable not just because of the high oxidizing power (negative charge), but also due to their great solubility in water or polar organic solvents and their low decomposition temperature, as depicted Figure 2.4.[81–83]

Reducers as the case of oxalates, alkoxides, acetates and acetylacetonates precursors need additional oxidants to the combustion process regulation.[77,84–88] The most common combustion aid are nitric acid (HNO_3) and ammonium nitrate (NH_4NO_3).[86,89,90] Neutral precursors are chlorine-based, since the anions do not contribute to the redox reaction during the combustion process. However, chlorine-based precursors are not desirable for SCS due to possible contaminations in the final powder or film and the release of HCl as a by-product.[82,91,92]

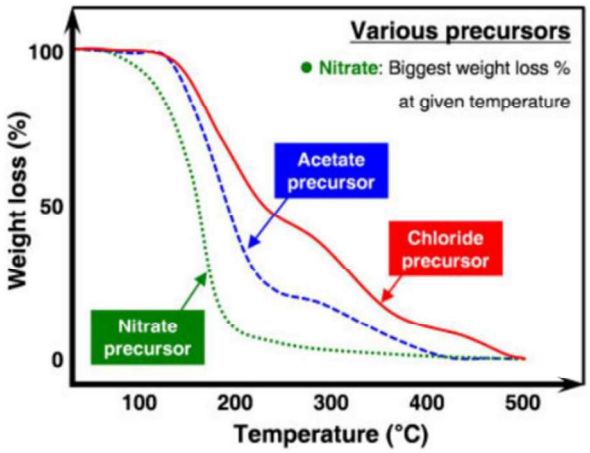

Figure 2.4. Schematic diagram of thermogravimetric analyses of various precursors.[93] Copyright © 2019, IOP Publishing Ltd.

As observed in Figure 2.4, metal nitrate salts precursors have a lower decomposition temperature (T_d) due to the electronic interactions between the metal and the nitrate group.[94] Their low processing temperatures is related to the high volatility of the decomposition by-products leading to a higher purity in the final product.[95] The nitrate thermal decomposition is related with the dissociation of the N–O bond and its bond order.[96,97] The molecular orbital theory or also called

band theory provides a model of metallic bonding and for the case of the nitrate anion will have a bond order of 4/3.[98] This can be reduced by the back-donation of the nitrate electron cloud to a vacant *d*-orbital of the metal ion or by the electronic cloud polarization of the nitrate ion through the high charge density of the metal ion decreasing the T_d.[94] The metal-ion charge density (CD) as shown in equation 2.2 is the ion charge divided by the ion volume which allows to infer on the covalent nature of the metal and nitrate interaction.[99]

$$CD = \frac{(number\ of\ ion\ charge\ units) \times (proton\ charge)}{(bond\ order) \times \pi \times (atomic\ radius\ in\ nm)^3} \qquad (2.2)$$

The positive charged cations of the metals ions with high charge density (CD) can polarize effectively the electron cloud of the negative charged nitrates ions (NO_3^-) as defined by Fajans´ rule.[98] *Yuvaraj et al.* observed that when low CD metal cations are used, the nitrate-salt decomposition occurs at higher temperature and the opposite occurs for high CD metal cation, as depicted in Figure 2.5 (a).[94] Recently, *Boettcher et al.* studied the decomposition behaviour of different metal-nitrate hydrate salts to confirm the correlation between CD and T_d.[99,100] For that was defined T_d as the temperature where a loss of 75 % of the metal salt volatile mass was achieved, as depicted in Figure 2.5 (b).

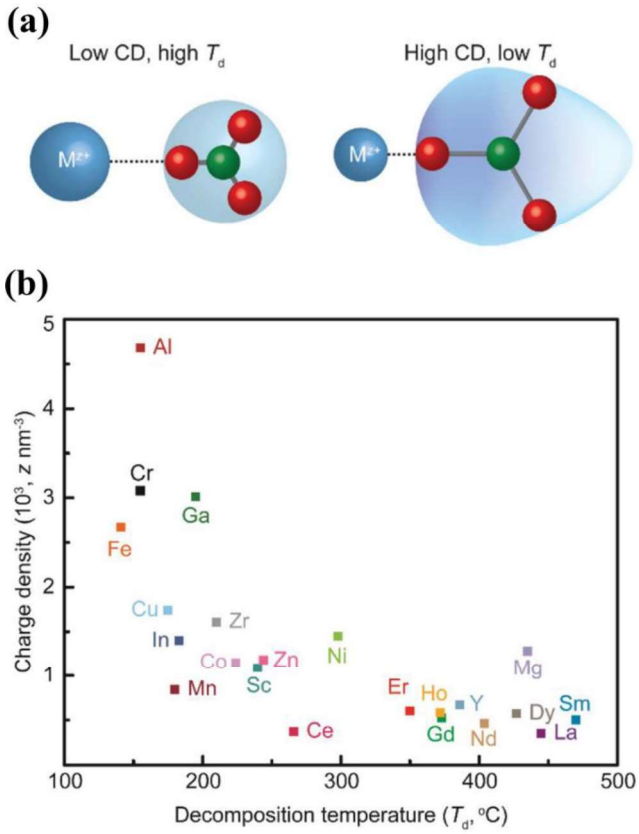

Figure 2.5. a) Schematic depicting the electronic interaction between positively-charged metal cations (M^{z+}) and nitrate. Low charge-density (CD) metals are unable to polarize the nitrate electron cloud, resulting in high T_d (left), whereas high-CD metals attract the electron density of nitrate (indicated by distortion and shading of the electron cloud), which lowers T_d (right); **b)** Metal-nitrate decomposition temperature (T_d) as a function of metal-cation charge density (CD). Metal-nitrate salts exhibit a broad range of decomposition temperatures due to differing electronic interactions between the metal and nitrate. As a general trend, *Td* increases with decreasing CD (i.e. the cation polarizing ability decreases). T_d is defined as the temperature at which the salt has lost 75 % of its volatile mass.[99] Copyright © The Royal Society of Chemistry 2019.

To understand how the nitrate and metal ionic species interact in solution, some metal-nitrate (M-NO_3) complexes have been identified and quantified using Raman spectroscopy by *Rudolph et al.*[101–104] The concentration conditions clearly impact the metal-anion complexes form in aqueous solutions. For all these metal cations, the quantity of metal nitrate-complexes formed decrease with decline of positively-charged metal cations (M^{z+}) and nitrates in solution. The relative thermodynamic stability of the aquo cations (M-H_2O) and the M-NO_3 complex can clarify the dependence between the metal cation and the M-NO_3 complex formation. As described by *Marcus et al.* the standard molar Gibbs free energies of hydration (ΔG_{hyd}) provides a measure of the thermodynamic stability of hydrated metal cations.[99,105] The Al^{3+} and Ga^{3+} metal cations are strongly hydrated which leads to a more negative ΔG_{hyd} and consequently are more thermodynamically stable and decompose at lower temperatures. This is explained through their

high charge densities which result in strong M-H_2O bonds forming fewer and lower equilibrium concentrations of M-NO_3 complexes. In Figure 2.6 (a) a linear relationship between the ΔG_{hyd} and the cation size (r) can be observed.[99]

Exchange kinetics allow determining how quickly equilibrium concentrations of M-NO_3 complex are settled in aqueous solution, considering the water exchange rate (k_{H_2O}). The k_{H_2O} for metal cations tend to increase with the increasing ionic radius due to the weakening of the first hydration sphere M-H_2O bond strengths.[106] In general, k_{H_2O} for the reported metal cations occur in a matter of seconds leading to fast equilibrium of the aqueous metal nitrate solutions as shown in Figure 2.6 (b).[99]

In summary, chemical factors such as: i) the metal-nitrate decomposition temperature as a function of metal-cation charge density; ii) the relationship between cation radius and the standard molar Gibbs free energies of hydration; and iii) exchange kinetics play a critical role on the decomposition behaviour of metal nitrates and processing conditions to form different morphologies.

2.2.1.3. Fuel to oxidizer ratio (ϕ)

In 1981, Jain and co-authors define a new approach to calculate the ratio of the oxidizing (commonly, nitrates) to reducing (fuel) elemental composition to reach a stochiometric proportion in the combustion mixture.[33] In this method, oxygen (O) and nitrogen (N) are considered oxidizers with the respective valence of −2 and 0. The metal ions are considered as reducing elements with their final valences corresponding to the metal valence. Carbon (C) and hydrogen (H) are treated as reducing elements with a valence of +4 and +1, respectively. The relation between the amount of reagents and their reducing and oxidizing valences (RV/OV) is shown in equation 2.3:

$$\phi = \frac{(-1) \cdot RV}{OV} n \qquad (2.3)$$

where is ϕ the fuel(reducer)/oxidizer ratio and n is the number of moles of fuel per mole of oxidizer.[35,77] For the stochiometric ratio with balanced reducing and oxidizing species (ϕ =1) atmospheric oxygen is not required for the reaction to occur. This stochiometric state indicates an intense and complete combustion of the precursor materials resulting in the conversion to metal oxide and gaseous products (H_2O, CO_2 and N_2). If ϕ > 1 or ϕ < 1, indicates a fuel rich or a fuel lean mixture, respectively.

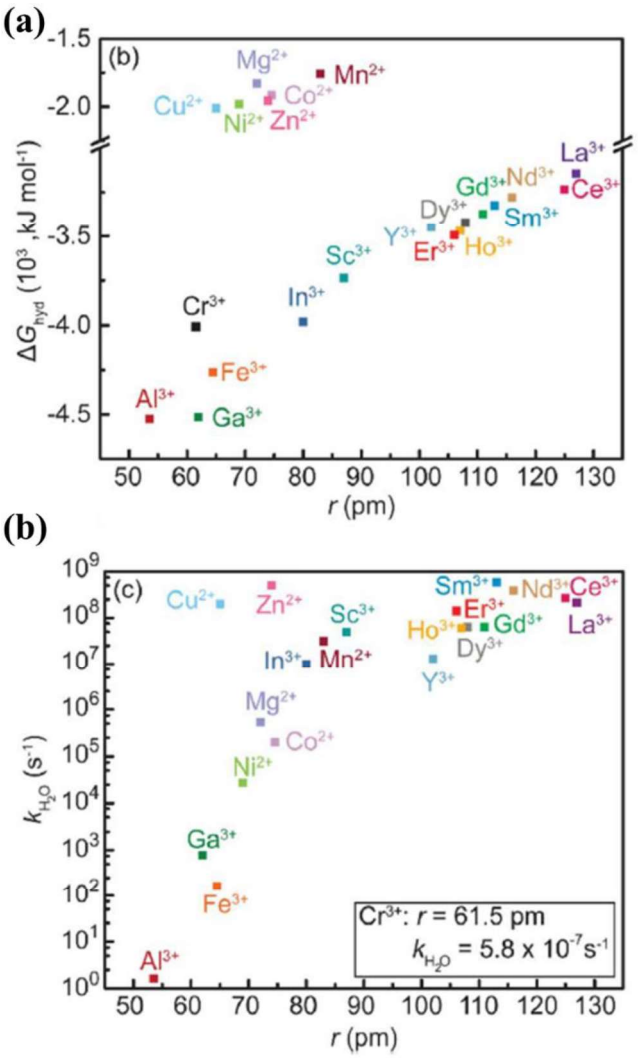

Figure 2.6. Metal-nitrate (M-NO_3) complex formation. (a) Relationship between cation radius (r) and ΔG_{hyd}. Cations that are more strongly hydrated (i.e. more negative ΔG_{hyd}) are thermodynamically stable and tend to form fewer M-NO_3 complexes. Deviation of z = +2 first-row transition metals from this trend is due to weak ligand-field effects, which results in cation radius expansion when e_g orbitals are filled. (b) Relationship between cation radius (r) and k_{H_2O}. Exchange kinetics will dictate how quickly equilibrium concentrations of M-NO_3 complex will be established in aqueous solution.[99] Copyright © The Royal Society of Chemistry 2019.

Overall, SCS is not a complete adiabatic process so the experimental temperature of the reaction (T_{exp}) is always lower when compared to the theoretical temperature (T_{th}), since heat losses are not consider.[107] Figure 2.7 shows the experimental and theoretical trend of temperature versus the ϕ ratio. SCS can be classified in five main categories from fuel deficient to fuel excess ratio.[47]

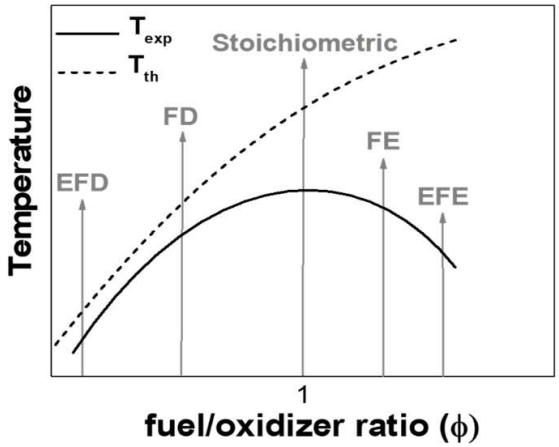

Figure 2.7. Theoretical and the experimental trend of temperature versus the fuel oxidizer ratio (extremely fuel deficient (EFD), fuel deficient (FD), stochiometric, fuel excess (FE) and extremely fuel excess (EFE) combustion reaction).[27] Copyright © 2020, Wiley-VCH Verlag GmbH & Co. KGaA, Weinheim.

In extremely fuel deficient (EFA) combustion reaction almost no fuel is present, and an external heating is required to complete the reaction. This category is flameless and leads to massive evolution of gases.[108] In fuel deficient (ED) combustion the slightly higher fuel amount leads to a slow combustion reaction which also requires an external heating to complete the reaction. The stoichiometric fuel/oxidizer ratio grant a self-combustion reaction and auto ignition process with an highly exothermic behaviour reaching high temperatures through a uniform distribution.[2] Thus, when a stoichiometric combustion occurs an optimal amount of oxygen and fuel mix generates the most heat possible and maximum combustion efficiency is reached. In fuel rich conditions, the fuel excess (FE) and extremely fuel excess combustion reaction (EFE), the probability of tracing impurities (carbon and carbonates) in the final product is higher due to the larger quantity of fuel.[92,108]

In the fuel/oxidizer ratio, the fuel should be always carefully chosen to have the best correlation with the metal nitrate precursor in order to accomplish the highest temperature of the reaction.

2.2.1.4. Effect of pH

The pH level of the metal precursors solution also plays a crucial role in SCS and should be maintained slight acidic to avoid the formation of metal hydroxides or other salts. When metal salts are dissolved in water normally a hydrolysis reaction occur which is the origin of metal cation acidity. The reaction depends on the oxidation state of the metal cation and the solution pH, according to charge-pH diagram defined by *C. K. Jorgensen* (Figure 2.8).[109] Therefore, the existence of hydroxyl ligands (OH) enhances the formation of soluble, polynuclear cationic species through condensation reactions.[99] These reactions have two mechanisms, olation (M-OH-M + H_2O) and oxolation (M-O-M + H_2O).[110,111] The olation products usually occur for metal

nitrate solutions, since most of the metal nitrates salts have a low valence states (z = 2 or 3).[99] In the case of oxolation reactions with low-valence cations ($z \leq 4$) usually occurs the precipitation of (oxy)hydroxides. Also, for a constant metal cation concentration, the solution pH can be changed by adding acidic or alkaline species. However, excess of acidic/alkaline species in the solution can affect the structure morphology of the final product. For solution combustion synthesis the pH control is crucial by the choice of a proper organic fuel (acidic or alkaline moieties) to have good interaction with the metal cations in solution. The fuel-to-metal cations ratio will regulate the pH for an efficient fuel dissociation and their chelating abilities to the metal cations. In SCS the precursor solution pH can mainly affect the intensity of the combustion process and the structure morphology of the final oxide material.[50,112–114]

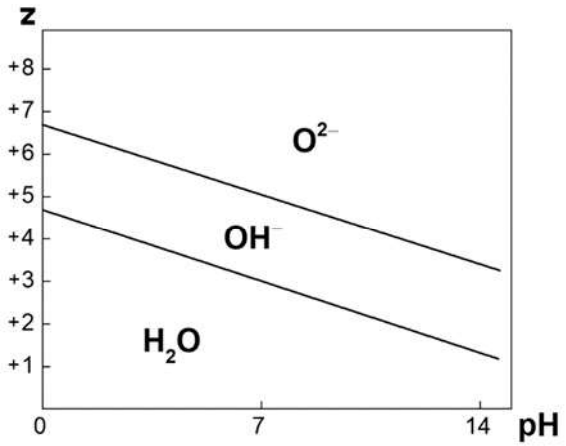

Figure 2.8. The charge-pH diagram according to C. K. Jorgensen. Condensation reactions are expected to occur when the system is brought from the aquo (low-valent cations) or oxo (high-valent cations) domains into the hydroxo one (middle domain).[27,111] Copyright © 2020, Wiley-VCH Verlag GmbH & Co. KGaA, Weinheim.

2.2.1.5. Atmosphere environment and initiation type

The atmosphere environment is quite relevant in the quality of the combustion reaction, although it is not well explored. *Yu et al.* noticed that a faster reaction process occurs when was flowing air in comparison to nitrogen environment.[115] Nonetheless, the mass-changing rate in nitrogen atmosphere is almost doubled, which is explained by the supply of N ions when nitrogen gas is in contact with the gel. This enhances the formation of NO_3^- ions that act as oxidants and subsequently improves the mass-changing rate in SCS.[115,116]

For SCS different heating sources can be used to initiate the combustion reaction, such as muffle, hotplate, microwave and laser annealing. The most used initiation source is the muffle furnace, where a uniform heating is applied to the precursor solution resulting in a violent combustion reaction. However, some of the powder is lost during the reaction in the muffle which can

contaminate it.[34,117,118] For the production of powders and mainly thin films, hotplate annealing has been quite used as initiation source in SCS.[2,77,119,120] In microwave heating source, the radiation is absorbed and converted to thermal energy inside the xerogel. This initiation type results in a homogeneous heat distribution with fast reaction kinetics leading to interesting microstructural and textural properties, such as surface area, grain and crystal uniform size distribution by controlling the power and exposure time with a very high yield.[69,121–124] However, some limitations exits like the high equipment cost and the scale-up to industry due to the small quantities produced.[124]

2.2.2. Oxides` morphology and applications

As observed previously, there are crucial parameters in solution combustion synthesis that determine the final morphology of the metal oxide materials. The most promising products are nanostructured materials and thin films that have a high versatility for a wide range of applications, which tend to increase. In the last 15 years the number of oxide nanostructures and thin films produced via SCS has increased, as depicted in Figure 2.9.

2.2.2.1. Nanostructures

A vast effort has been made to define and control the morphology of metal oxides using SCS. Metal oxide nanostructures processed by SCS have an enormous potential due to the simple control, low-cost, versatility, scalability and higher purity compared to conventional sol-gel. These nanostructures can be formed with various controlled shapes, such as nanobelts[125,126], nanoflakes[127–133], nanoflowers[134–137], nanoneedles[138], nanosheets[138,139], nanoplates[140–143], nanorods[124,144–149], nanowires[150–153], nanopowders and nanoparticles. For nanobelts (NBs) as shown in Figure 2.10 (a) has been reported the use of triethanolamine (TEA), as organic fuel, which provides not only a homogeneous distribution of metal ions in solution, but also serves as shape-controlling agent.[125,126] These nanostructures are mainly used for optoelectronic applications; however further studies are required to produce new metal oxides and boost their upcoming impact using SCS.

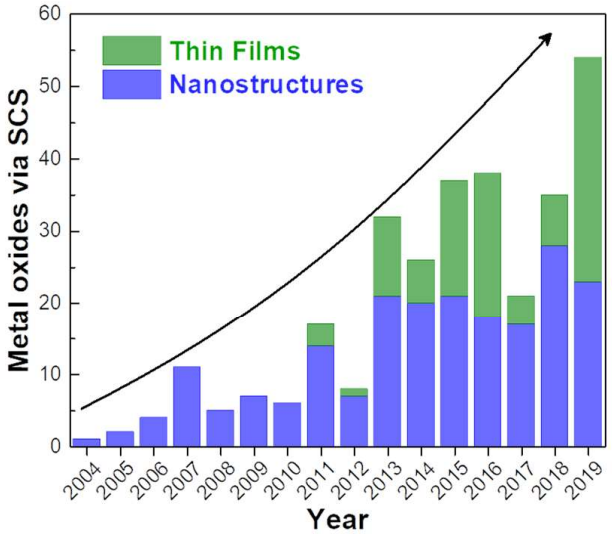

Figure 2.9. Metal oxides nanostructures and thin films produced via SCS in the last 15 years.[27] Copyright © 2020, Wiley-VCH Verlag GmbH & Co. KGaA, Weinheim.

The nanoflakes (NFs) have at least one nanometric dimension (1 – 100 nm) and are not perfectly flat being handled in different kind of applications, such as photocatalysis, spintronics, optoelectronics, chemical sensing, biomedical, battery electrodes and supercapacitors.[127,129–133] As observed, in Table 2.1 various fuels have been implemented in the production of diverse metal oxides NFs to improve the ignition temperature required. To go even further instead of using the most common initiation type, the muffle furnace (MF), microwave (MW) is used allowing a short-time consumption for the combustion reaction. *Köseoğlu et al.* promote a fast synthesis of nickel doped zinc oxide (Ni:ZnO) magnetic semiconductor adopting MW oven for 20 min.[129] The resultant grain structure is mainly composed by NFs with some voids and pores in the formed network, as depicted in Figure 2.10 (b). The porous structure is due to the gaseous products release during the combustion reaction. It was noticed that the energy bandgap of the semiconductor decreases with the increment of Ni concentration related with the increase of the carrier concentration on the Ni:ZnO which present a ferromagnetic behaviour. Recently, *Sharma et al.* reported highly pseudocapacitive nickel oxide (NiO) NFs with 10 nm for supercapacitor cells with mesoporous channels and high surface area produced by microwave-assisted route and using urea as fuel.[133] The large surface area and porosity is highly demanded of an electrode material for charge storage devices. Since the obtained NiO NFs electrodes possess these characteristics the penetration of the electrolyte in the electrodes is facilitated, promoting the ion migration which improves the power capability and energy density. These NiO electrodes exhibited good electrochemical response leading to high specific capacitance, being then applied in a symmetric supercapacitor, that revealed an excellent cycling stability.

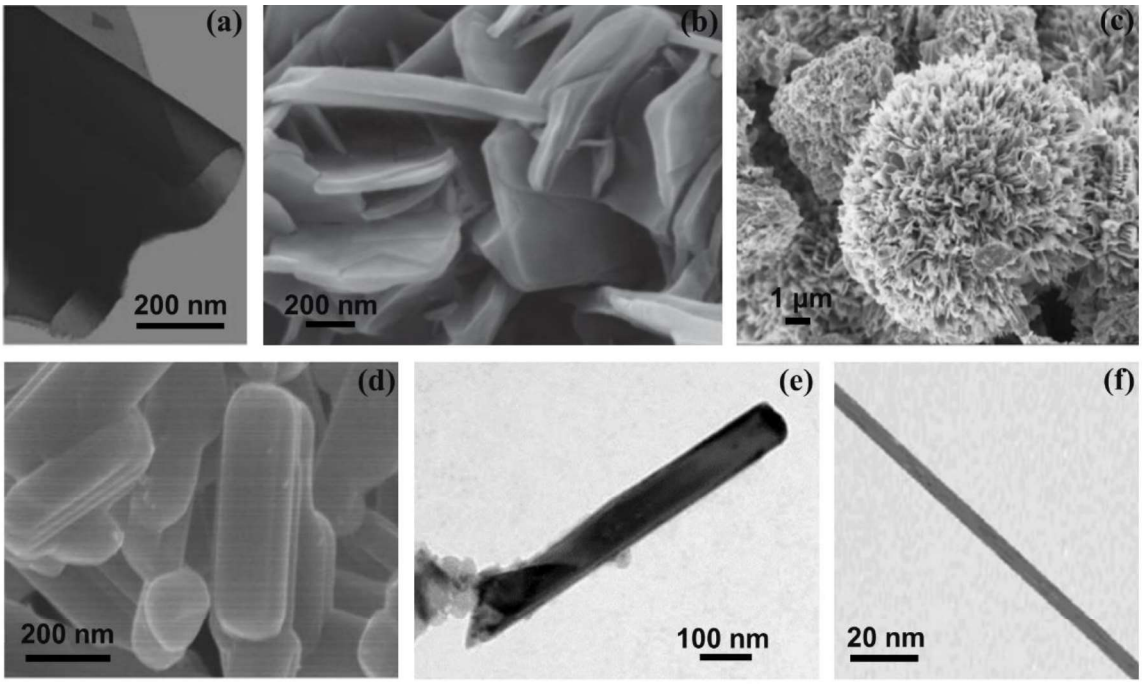

Figure 2.10. Various nanostructures via SCS: (a) Transmission electron microscopy images of $SrAl_2O_4:Eu^{2+},Dy^{3+}$ nanobelts;[126] Copyright © Materials Research Society 2011. (b) SEM picture of $Ni_xZn_{1-x}O$ nanoflakes;[129] Copyright © 2014 Elsevier Ltd and Techna Group S.r.l. (c) FESEM image of CuO nanoflower;[134] Copyright © 2013 Elsevier B.V. (d) High-magnification FESEM of NaV_6O_{15} nanoplates;[141] Copyright © 2015 The Electrochemical Society. (e) TEM images of a single VO_2 nanorod;[147] Copyright © The Royal Society of Chemistry 2013. (f) TEM image of MgO nanowire.[151] Copyright © 2012 Elsevier Ltd.

SCS of metal oxide nanoflowers (NFWs) structures have been applied as photocatalysts, cathodes for lithium ion batteries and biomedical applications, such as cancer detection and drug delivery for specific targets.[134–137] In 2013, *Umavedi et al.* produced copper oxide (CuO) NFWs by SCS using glycine as fuel, which guarantee a good mixing of cations in the solution.[134] These CuO NFWs as shown in Figure 2.10 (c) are composed by nanopetals and present excellent photocatalytic activity.

The metal oxide nanoplates (NPTs) structure is similar to the NFs being mostly used for batteries and supercapacitors electrodes which demand high surface area and pores, enhancing the electrode-electrolyte interface.[140,141] In 2015, *Jiang et al.* reported self-combustion synthesis of NaV_6O_{15} nanoplates as cathode materials for sodium-ion batteries being quite relevant taking into account the toxicity of lithium-ion batteries currently used.[141] These NPTs depicted in Figure 2.10 (d) present a uniform size and shape with an average width of 100 nm and length of 400 nm and, when used as cathode, a high discharge capacity is achieved being comparable to hydrothermal

synthesis methods. This is reached due to the large specific surface area on these structures providing more sites for sodium ions exchange in the cathode-electrolyte interface.

Nanosheets (NSs) are two-dimensional (2D) nanostructures and have been recently produced using SCS, but only iron oxides (Fe_2O_3) NSs were developed as anode in lithium ion batteries showing potential for other applications, such as energy conversion and storage, water treatment and gas sensors.[138,139] *Qin et al.* reported the use of glycine as fuel and glucose as carbon source for the formation of network-like porous hematite NSs defined by a large quantity of well-formed round single pores with 40 nm in diameter.[139] This structure formed in simple way has a high potential for gas sensor applications. In 2018, the same group tested different molar ratios (ϕ) of glycine to ferric nitrate and the morphology evolved from uniform to porous nanoneedles (NNs) (ϕ = 0.5; 1). For a fuel rich condition (ϕ>1) the morphology changed to aggregated nanoparticles. The stoichiometric product composed by porous NNs displays the best electrochemical properties, showing a high reversible capacity and superior recovery. This is attributed to the porous nanosheet structure and high specific surface area which guarantee an improved electrode-electrolyte interface and lead to a fast charge transfer reducing the polarization effects.[138]

Table 2.1. Developments of metal oxide nanobelts (NBs), nanoflakes (NFs), nanoflowers (NFWs), nanoplates (NPTs) and nanosheets (NSs) using SCS for different applications. Copyright © 2020, Wiley-VCH Verlag GmbH & Co. KGaA, Weinheim.

Year	Structure	Metal oxide	$T_{ignition}$ (°C)	Fuel(s)	Particle/ Crystallite Size (nm)
2010 [125]	NBs	$ZnO:Eu^{3+}$	400	TEA	50 – 300
2011 [126]		$SrAl_2O_4:Eu^{2+}$ $SrAl_2O_4:Dy^{3+}$	300	TEA	< 100
2012 [127]	NFs	Fe_2O_3	300	Gly	17
2014 [129]		$Ni_xZn_{1-x}O$ (x = 0.0 – 0.2)	1000 W	U	33 – 44
2015 [130]		CeO_2	400	Glu	35.5
2017 [131]		V_2O_5	400	CA	37
2018 [133]		NiO	800 W	Gly/ U	10
2018 [132]		MgO	400	VG	20 – 25
2013 [134]	NFWs	CuO	300	Gly	50
2014 [135]	NFWs	$Si:MnZnFe_2O_4$	350	Gly	10 – 40
2016 [136]	NFWs	ZnO	470	TEA/ CA/EG	23
2019 [137]	NFWs	V_2O_5	900 W	EDTA	20
2014 [140]	NPTs	Bi_2MoO_6	300	U	90 – 500
2015 [141]	NPTs	NaV_6O_{15}	450	CA	Width (100) Length (400)
2016 [139]	NSs	α-Fe_2O_3	500	Gly/ Glu	18
2018 [138]	NSs	α-Fe_2O_3/ Fe_3O_4	300	Gly	50 – 100

$T_{ignition}$: temperature required for the ignition of the combustion reaction; VG: Vetiver grass; Gly: Glycine; Glu: Glucose; U: Urea; TEA: triethanolamine; CA: citric acid; EG: ethylene glycol; EDTA: ethylenediamine tetraacetic acid.

Metal oxide nanorods (NRs) applications are vast, as shown in Table 2.2; they can be used in photocatalysis, antimicrobial, photoluminescence, nanoelectronics, UV sensors, filters, solar control and antireflection coatings.[124,144–149] *Umadevi et al.* reported a novel combustion method to produce copper oxide (CuO) NRs with surface area using citric acid as fuel.[144] Since copper presents a high antibacterial activity compared to organic antibacterial agents, these CuO NRs were tested against *E. Coli* and other microorganisms showing enhanced antimicrobial activity. In the same year, *Chandrappa et al.* produced vanadium dioxide (VO_2) NRs in a faster way via SCS and at relative low temperature using malic acid as fuel, as shown in Figure 2.10 (e).[147] Lately, *Hussain et al.* reported one dimensional (1D) nanocrystalline molybdenum trioxide (MoO_3) NRs synthesized by SCS using urea as fuel for high performance supercapacitors.[149] These NRs present 50 nm diameter and few microns long, and were tested as counter electrode in electrochemical measurements. A high specific capacitance and good cycling stability were reached with these NRs paste (PVDF + carbon black + MoO_3 NRs) due to the increment of the surface to volume ratio leading to an easier ion exchange.

Table 2.2. Developments of metal oxide nanorods (NRs), nanowires (NWs) and nanoneedles (NNs) using SCS for different applications. Copyright © 2020, Wiley-VCH Verlag GmbH & Co. KGaA, Weinheim.

Year	Structure	Metal oxide	$T_{ignition}$ (°C)	Fuel(s)	Width/ Length (nm)
2013 [144]	NRs	CuO	300	CA	(10–20)/ (100-250)
2013 [145]		MAl_2O_4:Eu MAl_2O_4:Dy M = Ba, Ca, Sr	500	U	(40)/ (1000)
2013 [146]		SnREO RE = Y,La,Gd, and Nd	400*	NA/ EG	(8–12)/ (100–200)
2013 [147]		VO_2	470	MA	(60)/ (600)
2015 [148]		MoO_3	250	CA/NA	(15)/ (>50)
		WO_3	250	CA/NA	(8)/ (40–100)
2015 [154]		Fe^{3+}-$W_{18}O_{49}$	nd	Glu	(50 – 250)/ (4000 –10000)
2018 [124]		Co_3O_4	850 W	Starch	n.d.
2018 [149]		α-MoO_3	500	U	(50 nm)/ n.d.

2007 [150]	NWs	$Al_4B_2O_9$ $Al_{18}B_4O_{33}$	1050	CA	(50 – 200) (80 – 250)/ n.d.
2012 [151]		MgO	1000 W	U	(6)/ (10000)
2019 [153]		$NiMoO_4$	200	U	(35)/ (700)
2018 [138]	NNs	Fe_2O_3	300	Gly	(5)/ (100)

$T_{ignition}$: temperature required for the ignition of the combustion reaction; Gly: Glycine; Glu: Glucose; U: Urea; CA: citric acid; EG: ethylene glycol; MA: malic acid; NA: nitric acid; nd: not defined.

In the last two decades nanowires (NWs) have been widely used in nanodevices (nanowire field effect transistors (FETs), complementary logic gates), sensing, biological control and energy conversion applications.[150,151,153,155] The NWs have diameters from one to hundreds of nanometres and lengths of tens to hundreds of microns offering a high surface-area-to-volume ratio which makes them very sensitive to changes in surface chemistry.[155] They have been synthesized via several approaches such as thermal evaporation, sol-gel, and chemical vapor deposition (CVD). These methods normally require high temperature, catalyst particles or a series of steps. SCS allows a cost-effective method, usually more homogeneous and with fewer impurities.[150,151,153] *El-Tantawy et al.* reported the first 1D magnesium oxide (MgO) NWs via SCS as depicted in Figure 2.10 (f) using microwave hydrothermal process and urea as fuel.[151] These NWs exhibit a diameter of 6 nm and lengths of microns with high surface area and enriched surface chemistry being susceptible for biological control due to their non-toxicity to human beings. Considering this, MgO NWs were tested in some bacterial species revealing a high antibacterial efficiency.

Regarding the various metal oxide nanostructures mentioned above, nanopowders and nanoparticles are the most common outcome from SCS, as shown in Table 2.3 and 2.4, respectively. Nanopowders (NPWs) include nanoparticles (NPs) since they consist on solid powders or agglomerates of NPs. The NPWs are suitable for a wide range of applications such as, solid electrolytes for solid oxide fuel cells, catalysis, sensors (gas; humidity), laser, superconductors, dielectric resonators, photocatalysts, spintronics, superconductors, luminescence, hydrogen production, drug delivery and energy storage.[156–194]

Table 2.3. Developments of metal oxide nanopowders (NPw) using SCS for different applications. Copyright © 2020, Wiley-VCH Verlag GmbH & Co. KGaA, Weinheim.

Year	Metal oxide	$T_{ignition}$ (°C)	Fuel(s)	Particle/ Crystallite Size (nm)
2004 [187]	ZrO_2:CeO_2	200	NA/ Gly	20 – 50
2006 [184]	CeO_2	110	EG	7 – 10
2006 [166]	$CeREO_2$ RE = Sm or Gd	110	EG	5 – 7
2008 [156]	Y_2O_3 Yb-Y_2O_3	500	U	40 – 100
	Y_2O_3 Yb-Y_2O_3	200	CA	40 – 100
	Y_2O_3 Yb-Y_2O_3	500	Gly	40 – 100
2009 [179]	$LaAlO_3$	700	OLA	60
2009 [159]	YAG:Ce	900 W	Glyc Fru	--
2009 [189]	ZrO_2–Al_2O_3	400	CA	69 – 87
2010 [167]	$LaMnO_x$	300	ODH	30 – 50
2010 [186]	Lu_2O_3:Sm^{3+} Lu_2O_3:Tb^{3+}	800	NA	30 – 50
2010 [162]	$LaAlO_3$	345	CA/OA	41
2011 [178]	ZnO	300	ODH	14 – 50
2011 [194]	ZnO	100	Gly	25
2011 [177]	CuO Cu_2O	440	Gly	150 – 200
2011 [185]	NiO	327	Gly	150 – 200
2011 [165]	$MgAl_2O_4$	300	Gly/ U	3.9 – 13.6
2011 [176]	Al:$BiFeO_3$	200	CA	13 – 20
2011 [181]	YAG	700	Gly/ U	40 – 60
2011 [171]	$BiFeO_3$	300	Ala Gly	32
2011 [161]	ZnO:Cu	200	ODH	40
2012 [158]	α -Al_2O_3	900 W	U	18 – 20
2012 [174]	Fe_3O_4	400	Suc CA Glu	15 18 10
2013 [170]	AZO	500*	Gly	11 – 25
2013 [190]	$CeMO_3$ M = Ni, Cu, V, Fe	220	Gly	5 – 200
2014 [180]	Al:ZrO_2	500	Gly	17 – 44
2014 [183]	Y_2SiO_5	500	DFH Sugar U	34 – 40 35 – 42 45 – 50
2014 [173]	Ir:CeO_2	350	Gly	14 – 54
2015 [175]	ZnO	400	EGCG	10 – 20
2015 [191]	$Y_2Ce_2O_7$:Eu^{3+}	550	PEG/ NA/U	40
2016 [157]	$CaTiO_3$	nd	U CA	20

			Gly	
2018 [188]	ZnO	250	TAB	20 – 31
2018 [169]	La_2O_3:Mo	160	Gly	20 – 40
2018 [193]	CeO_2	210 135	Gly Hyd	21.7 – 38.7 10.2 – 14.8
2018 [172]	VO_2	200	Gly Gly/CA	40 20
2018 [160]	α -Fe_2O_3	350	ODH	-
2018 [195]	$NaAl_{11}O_{17}$	259 189 169	U Gly CA	56 55 44
2018 [164]	ZrO_2	400	Gly/ ODH	26
	$ZrTiO_4$	500	Gly	19
2019 [192]	Fe-Mo/MgO	400	Gly PEG	-
2019 [168]	$Ni_{0.5}Zn_{0.5}Fe_2O_4$	270	Gly U	11 – 30
2019 [182]	$ZnAl_2O_4$:Eu	900 W	EG CA	100
	$ZnAl_2O_4$:Eu	900 W	Gly Glu	2 – 50
2019 [163]	$La_2Ce_2O_7$:Eu^{3+}	550	U	15 – 120

$T_{ignition}$: temperature required for the ignition of the combustion reaction; Gly: Glycine; U: Urea; Glu: Glucose; CA: citric acid; EG: ethylene glycol; OLA: Oleic acid; W: width; L: length; NA: nitric acid; ODH: oxalyal dihydrazide; OA: Oxalic acid; EGCG: Epigallocatechin gallate; PEG: polyethylene glycol; TAB: trimethylammonium bromide; Hid: Hydrazine; Suc: Sucrose; Fru: Frutose; Glyc: Glycerine; Ala: Alanine.

In 2006, *Chen et al.* reported a novel route to achieve high surface area ceria-based nanopowders by salt-assisted SCS using ethylene glycol as fuel.[166] The salts inclusion, mainly potassium chloride (KCl), helps to break up the three-dimensional porous structure by splitting the particles composed of agglomerated nanocrystallites into well-dispersed nanoparticles which improves the specific surface area. Later, *Yang et al.* reported the importance of the fuel type and amount to reach pure phase magnetic bismuth ferric oxide ($BiFeO_3$) nanopowders by SCS.[171] Among all the tested fuels, glycine and L-α-alanine reach the optimal fuel to oxidizer ratio for the formation of $BiFeO_3$ phase. However, when fuel lean conditions are used only amorphous phase powders are obtained and in a fuel rich condition the appearance of impurities increases due to the high flame temperature involved. The ideal stoichiometric $BiFeO_3$ nanopowders were applied as catalyst to degrade rhodamine B in the presence of hydrogen peroxide being highly efficient. In 2012, *Laishram et al.* reported a novel method for combustion synthesis of α-Al_2O_3 nanopowders in a single step via microwave annealing using urea as fuel.[158] This method is energy and time efficient (3 – 5 min), and results in even finer particles (18 – 20 nm) compared to NPWs produced in a

muffle furnace (50 – 90 nm). Recently, *Qin et al.* reported the direct synthesis of vanadium oxide nanopowders via SCS adjusting the fuel type, atmosphere and fuel to oxidizer ratio.[172] When glycine was added as fuel the average particle size of vanadium dioxide (VO_2) was 40 nm. However, to decrease the particle size a mixture of fuels (glycine and citric acid) was used yielding an average particle size of 20 nm and increasing the specific surface area. Also, vanadium trioxide (V_2O_3) nanopowders were accomplished using an inert atmosphere. The adoption of SCS can be an essential approach to design a variety of nanostructures transition metal oxides leading to a wide range of applications. In the same year, *Madhusudhana et al.* reported the use of glycine to synthetize nanopowders of ZrO_2 and $ZrTiO_4$ for humidity sensing.[164] The $ZrTiO_4$ nanopowders present a higher dielectric constant (50), conductivity and linear response to atmospheric humidity (25 – 80 %) compared to ZrO_2. Lately, *Mollazadeh et al.* reported $Ni_{0.5}Zn_{0.5}Fe_2O_4$ nanopowders to test antibacterial and photocatalytic activity.[168] To synthetize these NPWs the effect of fuel to oxidizer ratio (0.8 – 1.4), fuel type (glycine and urea) and their mixture were studied, as shown in Figure 2.11. It was noticed that a higher amount of oxygen vacancies is generated in NPWs using a high molar proportion of urea leading to better magnetization saturation, antibacterial activity against *E. coli* and *S. aureus* bacterium, and photocatalytic activity.

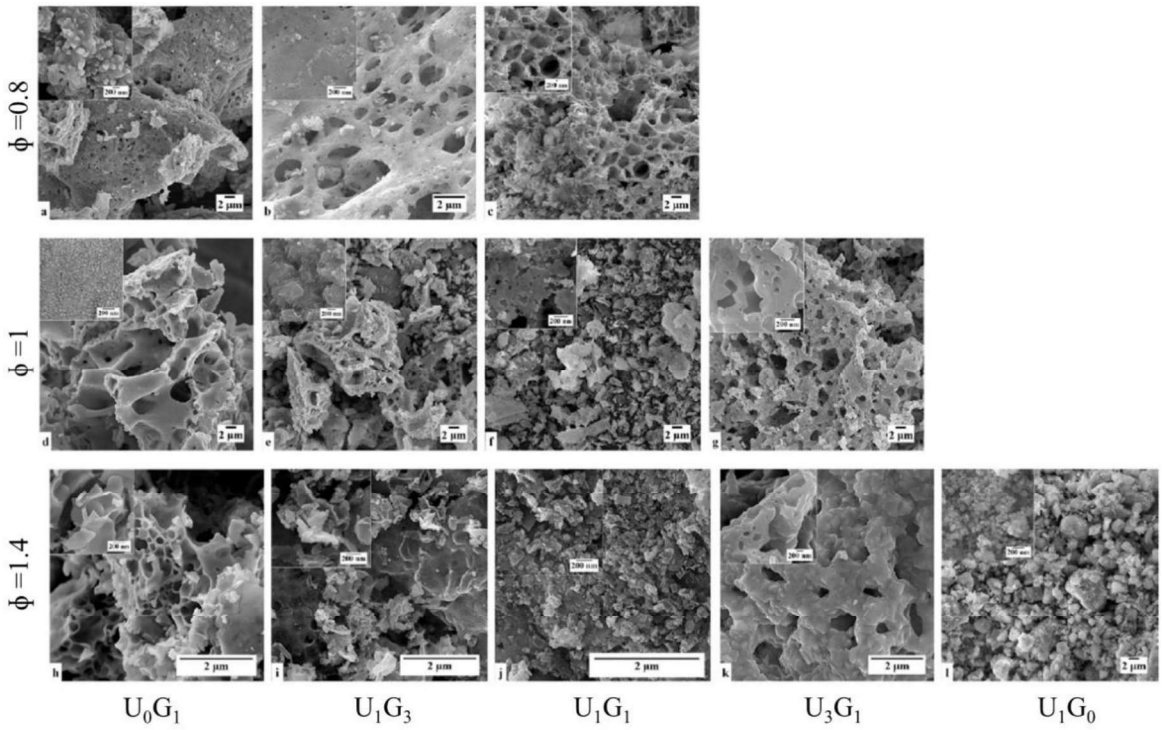

Figure 2.11. FESEM images of $Ni_{0.5}Zn_{0.5}Fe_2O_4$ nanopowders synthesized with various fuel to oxidizer ratio (ϕ) utilizing single and mixed fuels (U = Urea; G = Glycine).[168]

Nanoparticles (NPs) are the most typically obtained nanostructures using SCS. NPs have an extraordinarily high surface area-to-volume ratio and novel physical-chemical properties due to their very small sizes (1 – 100 nm). These properties allow broad applications, such as catalytic, photocatalytic, spintronics, solid oxide fuel cell, water splitting, photoluminescence, magnetic memories, anticancer activity, biomedical, medical diagnosis, gas sensors, bioimaging, antioxidant, antibacterial, magnetic drug delivery, electrochromic and electrodes for batteries, supercapacitors and solar cells.[152,154,196–262] In 2014, *Ayeshamariam et al.* reported tin-doped indium oxide (ITO) nanoparticles with various levels of Sn content for gas sensing.[210] This method results on a ITO nanopowder with a large surface area being highly required for sensing applications. The resultant gas sensor showed an increase of the sensitivity with the increment of the indium content (Figure 2.12) and temperature.

Table 2.4. Developments of metal oxide nanoparticles (NPs) using SCS for different applications. Copyright © 2020, Wiley-VCH Verlag GmbH & Co. KGaA, Weinheim.

Year	Metal oxide	$T_{ignition}$ (°C)	Fuel(s)	Particle/ Crystallite Size (nm)
2005 [206]	NiO	600 W	Gly U	30
2006 [217]	$CoFe_2O_4 - SiO_2$	300	CA	3 – 30
2007 [228]	$TiO_2:Sm^{3+}$	250	EG/CA	12.8 – 16.3
2007 [239]	$Gd_{3-x}Ln_xGa_5O_{12}$, $x \approx 0.3$ Ln = Pr; Tm	500	NA	30 – 100
2007 [250]	$MAl_2O_4:Eu^{2+},R^{3+}$ M = Sr, Ba R = Dy, Nd, La	600	U	20 – 44
2008 [260]	ZrO_2-Al_2O_3	500	U U/Sta	48/32 23/21
2008 [261]	MgO	100	U	15 – 60
2009 [262]	$(In_{1-x}Fe_x)_2O_3$ x = 0 –0.45	-	Gly	40 – 50
2009 [196]	LiMNC	200	Suc	20 – 50
2009 [197]	LSCM	400	TA	95 – 220
2010 [198]	Bi_2WO_6	200	Gly	20 – 30
2011 [200]	$ZnO:Eu^{3+}$	350	CA	30 – 80
2012 [202]	Co_3O_4	400	CA	30 – 40
2013 [203]	NiO	300	CA/ Gly	100 – 250
2013 [204]	$(La_{1-x}Sr_x)(Fe_{1-x}Ni_x)O_3$ x = 0.0, 0.1 & 0.2	120	CA	12.7 – 21.9
2013 [205]	α -Fe_2O_3	300	ODH	44
2014 [209]	Au-ZnO	450	PEG	8.5 – 15.5
2014 [210]	ITO	350	U	10 – 20
2014 [207]	$NiAl_2O_4$	950 W	*Ses*	15.2 – 18.2
2014 [211]	Co_3O_4	350	CA	15 – 110
2014 [208]	Y_2O_3:(Eu,Dy,Tb)	200	AA Arg GA PA Gly	10 12 14 25 29
2014 [212]	$BiFeO_3$	105	TRIS	100 – 120
2014 [213]	γ-Fe2O3	400	Glu	12

2014 [214]	$SrGdZrO_3$	300	CA	120
2015 [224]	$LaFeO_3$:Ce	120	CA/ EG	24.1 – 28.7
2015 [218]	CuO	400	CG	20 – 30
2015 [222]	MgO:Fe^{3+}	400	Aloe vera	12 – 22
2015 [215]	Ag_2WO_4 $CuWO_4$ $ZnWO_4$	350	U	33 22 32
2015 [220]	Gd_2O_3:(Er^{3+},Yb^{3+},Zn^{2+})	750 W	U	33 – 52
2015 [223]	CuO	400	TC	6 – 8
2015 [225]	ZnO	400	CF	5 – 15
2015 [216]	MnO	300	Gly	50 – 400
2015 [219]	ZnO	400	AG	4 – 20
2015 [221]	$MnFe_2O_4$	300	Gly/ TEG	30 – 35
2016 [233]	$Mn_{1-x}Zn_xFe_2O_4$ x= 0 – 1	450	U/ Glu	25 – 35
2016 [227]	$CoFe_2O_4$	750 W	CA U	57 32
2016 [226]	SnO_2	345	CA	11 – 30
2016 [235]	ZnO	375	Sugar	96
2016 [231]	TiO_2:Sn	450	U	12 – 24
2016 [229]	LR-SN	450	Suc	200
2016 [230]	$CuNb_2O_6$	350	U	8.3 – 20.3
	$ZnNb_2O_6$	350	U	4.1 –15.8
2016 [232]	α -Fe_2O_3	400	Gly Glu	21 – 62
2016 [234]	Cr_2O_3	300	ODH	20 – 40
2017 [242]	Fe_3O_4	160	Gly	39.1 – 87.4
2017 [238]	$Li_{0.5}Fe_{2.5}O_4$	157 403	Gly CA	12 – 20 16 – 21
2017 [240]	$Bi_2Ti_2O_7$	350	U HMT	61
	$M_xBi_{2-x}Ti_2O_7$ (M: Fe, Mn)	350	U HMT	57 – 63
2017 [237]	ZnO	300	Gly CA U RS	50
2017 [241]	$CoFe_2O_4$	250	Gly CA U	20 – 41 30 – 52 9 – 15
2017 [236]	ZnO	500	SA	19

2018 [245]	CeO_2	150	Gly	20
2018 [249]	Fe_3O_4	190	CA	13 – 20
2018 [248]	$ZnAl_2O_3$	600	U	23.6
2018 [243]	ZnO:Eu	nd	CA/Gly	30
2018 [247]	CeO_2:Cr	400	Gly	19.1 – 21.8
2018 [251]	$Bi_{1-x}Al_xFeO_3$ ($0.0 \leq x \leq 0.15$)	550	U	80
2018 [244]	ZnO	375	LA	13
			AI	7 – 12
			MA	7 – 18
			IT	8 – 12
2018 [246]	La_2O_3	600	Ace	42
2018 [263]	$NiCo_2O_4$	250	TA	4
2019 [256]	ZnO	500	U	17.3 – 28
2019 [258]	Cr_2O_3	800 W	Gly	< 100
2019 [257]	ZnO	600	U Gly CA	26 – 40
2019 [252]	CuO/Cu_2O/C	400	Glu	~ 20 nm
2019 [253]	CuO (NRS) ZnO	300	U	60 – 100 15 – 19
2019 [255]	CeO_2	250	Gly U	9 – 14
2020 [259]	WO_3	200	OA Gly CA	18.4 nd 11.5
		500	OA Gly CA	22.9 16.7 18.3

Init: Initiation; $T_{ignition}$: temperature required for the ignition of the combustion reaction; Gly: Glycine; U: Urea; Glu: Glucose; Suc: Sucrose; Sta: Starch; Arg: Arginine; TEA: triethanolamine; CA: citric acid; EG: ethylene glycol; EDTA: ethylenediamine tetraacetic acid; MA: malic acid; OLA: Oleic acid; Ses: Sesame; NA: nitric acid; ODH: oxalyal dihydrazide; OA: Oxalic acid; EGCG: Epigallocatechin gallate; PEG: polyethylene glycol; TAB: trimethylammonium bromide; TA: Tartaric acid; AA: Aspartic acid; GA: Glutamic acid; PA: Phenylalanine; TRIS: 2-amino-2-hydroxy- methyl-propane-1,3-diol; CG: Calotropis gigantean; TC: Tinospora cordifolia; CAF: Cassia fistula; AG: Artocarpus gomezeanus; TEG: tetra ethylene glycol; HMT: hexamethylenetetramine; RS: raphanus sativus; SA: succinic acid; AI: Abutilon indicum; MLA: Melia azedarach L; IT: Indigofera tinctorial; Ace: Acetamide; LAT: Lactose.

In the same year, *Tyagi et al.* reported the SCS of yttrium oxide (Y_2O_3) NPs doped with Dy^{3+}, Eu^{3+} and Tb^{3+} together using various amino-acid fuels (glycine, phenyl alanine, arginine, glutamic and aspartic acids) for luminescence applications.[208] These NPs processed with glycine and arginine lead to a smooth surface as a result from the higher heat generated. Nevertheless, NPs produced with glycine as fuel had lower surface area and smooth surface providing better luminescence properties, as shown in Figure 2.13 (a) and (b).

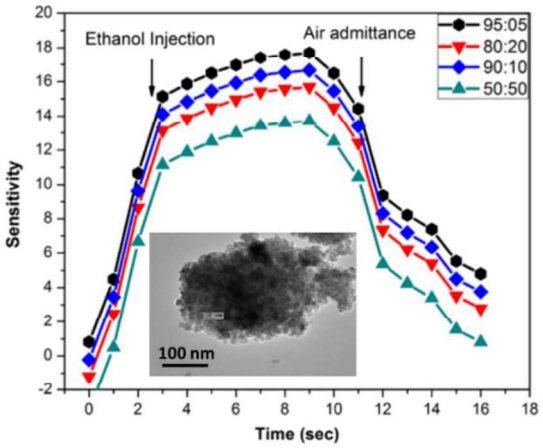

Figure 2.12. Time response curve of Sn doped of In_2O_3 for 1000 ppm ethanol concentration at 200 °C (inset shows TEM image of Sn (5%) doped In_2O_3 of ITO).[210] Copyright © 2013 Elsevier Ltd and Techna Group S.r.l.

Later, *Manoharan et al.* reported an interesting topic to produce Au-ZnO nanocomposites (clusters and nanoparticles) via SCS that act as an anticancer agent.[209] The percentage of gold was varied from 0 to 5 % and it was observed that the most effective Au-ZnO nanoagent to destroy cancer cells has between 1.5–2 % of gold with the highest concentration (200 µg/mL). In 2015, *Rajeshwar et al.* reported time and energy efficient via SCS of binary metal tungstate (Ag_2WO_4, $CuWO_4$ and $ZnWO_4$) NPs using urea as fuel.[215] In the synthesis of all these, the type of tungsten precursor, sodium or ammonium based, played a crucial role in their photocatalytic activity. $ZnWO_4$ showed the highest photodegradation (90 % in 20 min) of methyl orange under UV/Vis light irradiation using the sodium-based tungsten precursor. The results even surpass the reference (90 % in 50 min) due to the pure, monoclinic single-phase and relatively small particle size being a good approach for environmental remediation applications. In terms of photoelectrochemical performance, the highest photocurrent was observed for the $CuWO_4$ NPs showing potential for solar energy conversion. In 2017, *Masoudpanah et al.* reported the effect of the fuel type (citric acid, glycine and urea) for different fuel to oxidizer ratios (0.5, 0.75, 1 and 1.25) on $CoFe_2O_4$ NPs using SCS.[241] Apart from the fuel type the specific surface area of the combusted NPs decrease with the increase of fuel to oxidant ratio. Since using glycine leads to a highly exothermic peak

compared to the other fuels, more gaseous products are released resulting in a higher specific surface area. Also, $CoFe_2O_4$ NPs using glycine as fuel revealed a higher saturation magnetization due to their particle size and crystallinity.

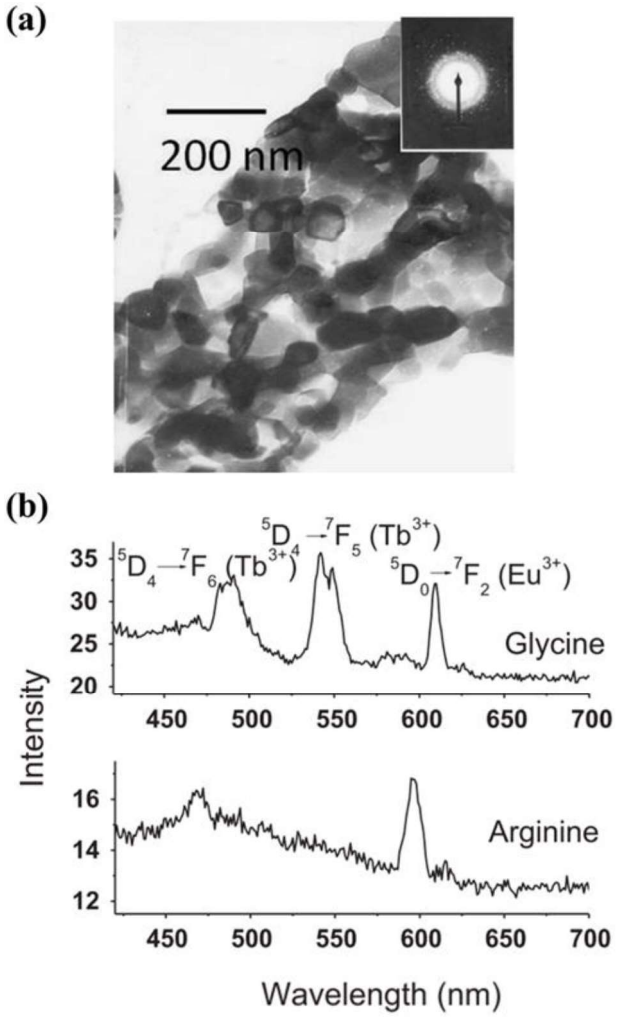

Figure 2.13. (a) TEM images of Y_2O_3:Eu, Dy, Tb (2.5 at%) nanoparticles prepared using glycine as fuel and heated at 600 °C for 30 min; (b) Emission spectrum from Y_2O_3:Eu, Dy, Tb(2.5 at%) nanoparticles prepared using glycine and arginine as fuels and annealed at 600 °C (The samples were excited at 300 nm).[208] Copyright © 2013 Elsevier B.V.

Later, *Prashanth et al. reported* a green synthesis of biocompatible ZnO NPs via SCS using leaf extracts as biofuels for anticancer activity.[244] The results achieved proved that the use of biofuels have potential for anticancer and biocompatible ZnO NPs to substitute conventional fuels in the near future.[254] *AlDahoudi et al.* reported the synthesis of ZnO NPs via SCS for photoanode of solar cells by the changing percentage of urea (stochiometric and fuel rich) in solution.[256] The ZnO NPs processed in fuel rich condition lead to lower crystallite sizes and higher bandgap.

Furthermore, when these ZnO NPs were applied as photoanode in dye synthetized solar cells increased efficiency and current density were achieved, as depicted in Figure 2.14.

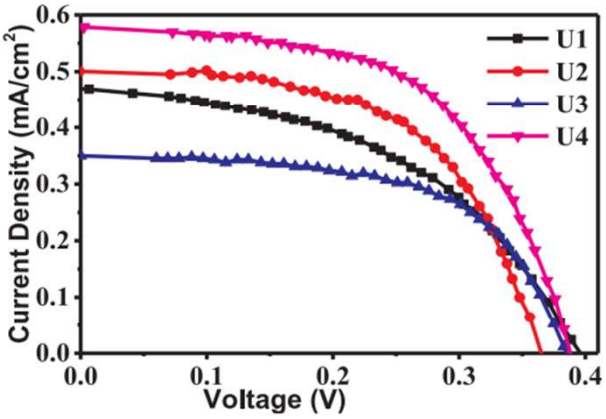

Figure 2.14. Current density-voltage characteristic curves of the dye sensitized solar cells for different urea percentages.[256] Copyright © *2019 Elsevier B.V.*

Varma et al. reported the SCS of $CuO/Cu_2O/C$ anode for long cycle lithium ion batteries using glucose as fuel.[252] The fuel to oxidizer ratio ranged from 0.8 to 50 and the ideal condition to form $CuO/Cu_2O/C$ composite was fuel rich ($\phi = 10$) which lead to 26 % carbon content. The CuO/Cu_2O nanoparticles displayed uniform spherical morphology in the carbon matrix and the composite offered high cyclability and rate capabilities in lithium ion batteries. The synergistic effect of anodes porous structure help to reach this high performance being SCS a promising method for anode materials applied in batteries. Lately, *Haratizadeh et al.* reported a novel approach for SCS of tungsten oxide (WO_3) NPs testing different fuels (oxalic acid, glycine and citric acid) and heat sources (hotplate and muffle furnace) for photocatalytic and electrochromic applications.[259] By changing the fuel type, different morphologies were achieved such as, sponge-like (glycine), rock style (citric acid), spherical (citric acid) and irregular shapes. The SCS using hotplate annealing results on orthorhombic and amorphous WO_3 structures while using furnace annealing yield stable tetragonal WO_3 structures. The WO_3 NPs produced with both heat sources using glycine demonstrate a good electrochromic response.

SCS has also been used to produce metal oxide quantum dots (QDs) are nanoparticles in quantum size regime characterized by the discretization of the energy levels inside the material. For semiconductor nanoparticles, the quantum size regime is reached when their dimensions are smaller than the exciton Bohr radius.[264] The simple QDs synthesis via SCS significantly boost their application in biosensing, imaging, photocatalysis and solar energy.[265–270]

In overview, all the above nanostructures are mainly produced in bulk using muffle furnace annealing and, in most cases, require a maximum temperature of 400 °C to convert precursors

into metal oxide nanostructures. Also, the most commonly used fuel is glycine a zwitterion molecule, which helps to maintain a compositional equilibrium between all the constituents. To further enhance their incredible properties such as, high specific surface area or porosity, the metal oxides have been mixed in pastes and solutions to allow their deposition in film form to boost functional devices.[141,149,215,256,259,263]

2.2.2.2. Thin films

As previously mentioned SCS is mainly used to produce materials in form of powders from micro to nanostructures. Nevertheless, almost two decades ago *Epifani et al.* reported using a chelating agent, acetylacetone, the formation of sol-gel based indium oxide (In_2O_3) thin films.[271] Here, an intense exothermic reaction at 180 °C and significant mass loss was observed in the thermal analysis differential scanning calorimetry/thermogravimetry (DSC/TG). Then, a few years later, the same author formally reported for the first time the production of metal oxides via SCS using acetylacetone as fuel.[77] The self-generated heat from SCS provides a localized energy supply, eliminating the need for high processing temperatures, not requiring external energy input once ignited. In 2011, *Marks et al.* adopt a new general route to produce various metal oxide thin films of In_2O_3, ZTO, ITO and IZO via SCS using different fuels (acetylacetone and urea) for thin film transistors (TFTs) application, as depicted in Figure 2.15 (a).[2] All the thin films were processed at low temperatures (200 °C) presented lower thickness, smooth surface and negligible porosity. In_2O_3 semiconductor thin films of were applied in TFTs showing a high mobility of 13 cm^2/Vs and a low operating voltage at low processing temperatures. This allowed a tremendous reduction of the required temperature to process metal oxide thin films compared the conventional sol-gel method opening the window for different electronic applications (Figure 2.15 (a)).

In 2013, *Li et al.* reported the use of SCS to fabricate molybdenum oxide (MoO_3) as hole selective layer for polymer solar cells using acetylacetone as fuel.[272] To improve the film morphology a small amount of PEDOT:PSS was added to the combustion system to help supressing significant heat losses, which results in high charge transporting performance at low annealing temperature (150 °C). The simplicity of this method can boost their application in roll-to-roll (R2R) manufacture of polymer solar cells. In 2014, using the same fuel *Gao et al.* reported the SCS of nickel oxide (NiO) thin films as hole transport interlayers for optoelectronic devices processed at low temperature.[273] One year later *Jen et al.* reported low-temperature Cu-doped nickel oxide ($Cu:NiO_x$) as hole-transporting layer via SCS for perovskite solar cells.[274] The $Cu:NiO_x$ thin films possess a homogeneous morphology, high crystallinity and better photoluminescent compared to sol-gel based $Cu:NiO_x$. SCS showed a high potential for n-type flexible printed thermoelectric devices. In 2016, *Cho et al.* explored a new application via SCS as thermoelectric generators using

highly conductive indium zinc oxide (IZO) thin films.[275] During SCS a strong exothermic reaction occurred using acetylacetonate as fuel decreasing the annealing temperature, which is essential for the formation of conductive metal oxides. These thin films retained a large power factor, exhibited a good Seebeck coefficient and an enhanced electrical conductivity for a composition ratio of In:Zn = 6:2 at low annealing temperature, as shown in Figure 2.15 (b). In 2017, *Xu et al.* reported that the use of SCS can produce AZO thin films at low temperature (250 °C) with high potential for transparent conductive films on flexible substrates.[276] Later, *Ullah et al.* reported the influence of rapid thermal annealing on conductive IZO thin films with different In:Zn ratios through SCS.[277] In the same year, *Hsu et al.* reported low temperature (180 °C) conductive p-type Cu:CrO_x thin films via SCS using glycine as fuel, allowing their application for large scale manufacturing on solar cells.[278] *Fortunato et al.* reported for the first time aluminum oxide (Al_2O_3) thin films for resistive switching memories via SCS as depicted in Figure 2.15 (c) using urea as fuel.[279] In 2019, *Song et al.* reported the production of high-quality NiO thin films via SCS using acetylacetone as fuel by spray pyrolysis.[280] These films were produced at relative low temperature and presented better results than films processed by spin-coating. A dense and uniform NiO thin film was achieved being incorporated as hole transport layer in perovskite solar cells, leading to an efficiency of 12.7 %.

Also, recently *Fachetti et al.* reported the production of zinc oxide (ZnO) through SCS and its application as electron transport layer (ETL) for stable and efficient perovskite solar cells.[37] These devices present large power conversion efficiencies reaching almost 20 % using SCS ZnO without the need of ETL doping or surface functionalization, as shown in Figure 2.15 (d). In the same year *Mandal et al.* reported a highly conductive titanium doped indium oxide and copper oxide for electrode applications.[281,282]

As observed the production of thin films via SCS has been widely used in the last decade for various applications such as, solar cells, memories, thermoelectrics and thin film transistors due to their numerous advantages (simple, low temperature compatibility and cost) allowing further implementation in R2R based techniques.

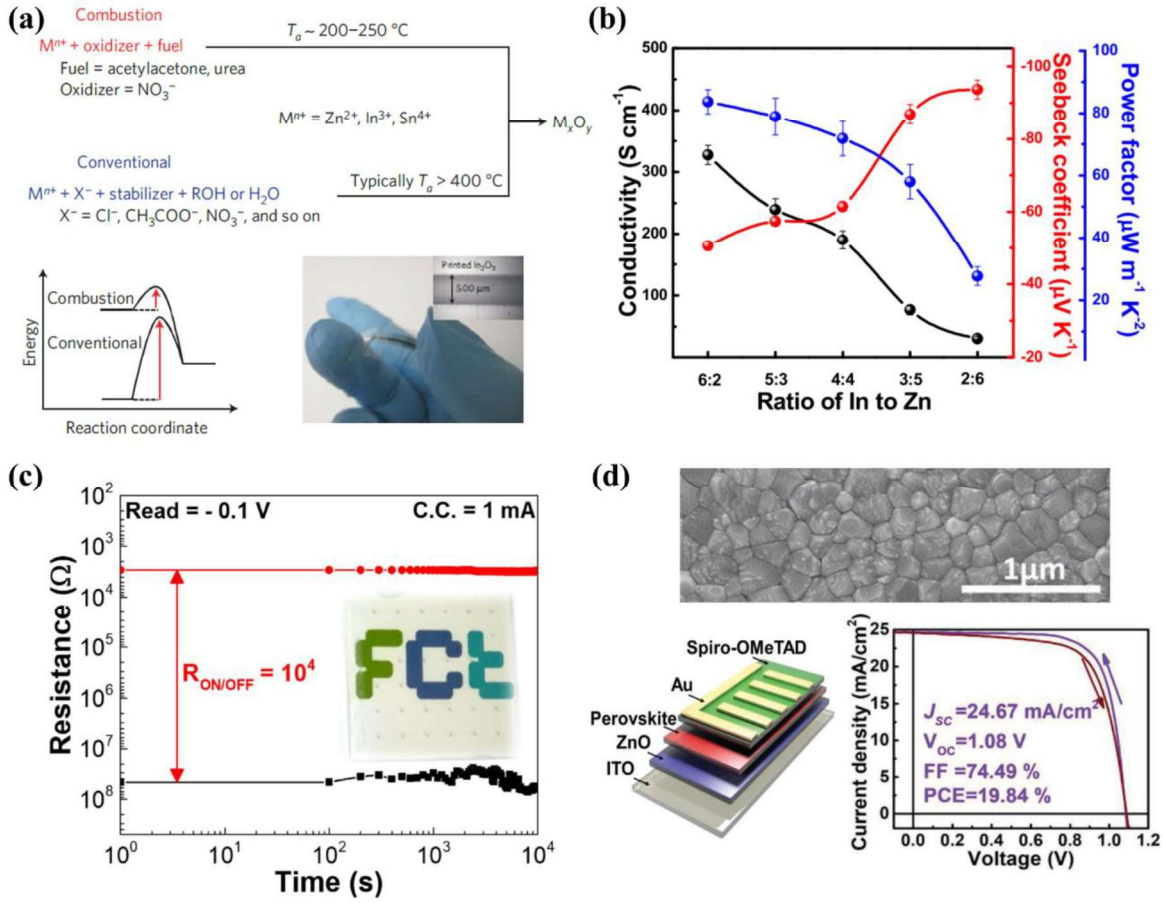

Figure 2.15. Various applications of metal oxide thin films produced via SCS: (a) Low-temperature solution-processing principles for metal oxides. Depiction of the two different synthetic approaches; Energetics of combustion synthesis-based processes versus conventional processes; Optical image of a flexible combustion-processed In_2O_3 device on AryLite (30nm Al gate electrode/41nm a-alumina dielectric, with 30nm Al source and drain electrodes) and optical image of an inkjet printed In_2O_3 line on n++Si/41nm a-alumina (inset);[2] Copyright © 2011, Springer Nature. (b) Thermoelectric properties of the IZO thin films according to composition ratio of In to Zn: electrical conductivity (black circles), Seebeck coefficient (red circles), and power factor (blue circles);[275] Copyright © 2016, American Chemical Society. (c) Retention of the transparent memory (ITO/Al_2O_3/IZO) with the respective optical image;[279] Copyright © 2018 IOP Publishing Ltd. (d) SEM images of perovskite P3 films deposited on combustion ZnO (c-ZnO); Structure of perovskite solar cells (PSCs); Forward and reverse scan J–V curves of champion devices with c-ZnO based on P3.[37] Copyright © 2019 WILEY-VCH Verlag GmbH & Co. KGaA, Weinheim.

2.3. Application in oxide thin film transistors (TFTs)

Amongst all the applications discussed in section 2.2.2.2 the most common use of SCS is to produce oxide thin films for electronic devices, namely thin film transistors (TFTs). Amorphous oxide thin film constituent layers of the TFTs are highly desirable since the electronic performances do not depend on the degree of films disorder and have ultra-smooth surfaces for

supressing interface traps and scattering centres.[1,283] Also, these oxides can be produced with low temperature deposition routes such as, spin-coating or roll-to-roll techniques, being a viable option to implement in flexible electronics industry allowing a reduction of the associated costs and human footprint. Taking this into account, a more detailed outlook will be performed on this topic, as shown in Table 2.5. In general, it can be observed that spin-coating technique followed by a maximum annealing temperature of 300 °C is widely used for the constituent layers production (i.e. dielectrics, semiconductors, and transparent conductive oxides) of TFTs.

2.3.1. TFTs via solution combustion synthesis (SCS)

As mentioned earlier, *Marks et al.* implemented for the first-time metal oxide (MO) thin films via SCS in TFTs at lower processing temperatures. Since then, different TFTs constituent layers have been developed using SCS. In 2013, the same group tested the influence of the oxygen binding metal ion ("oxygen getter", such as X = Ga^{3+}, Sc^{3+}, Y^{3+}, La^{3+}) to control oxygen vacancies and improve lattice formation on microstructure and carrier transport of indium zinc oxide (IXZO).[284] High performance was achieved for the various oxygen binding metal ions, however the Ga^{3+} showed the highest metal oxide lattice enthalpy and the lowest metal ionic radius being the most efficient oxygen getter. IGZO TFTs presented the highest mobility of 5.4 cm^2/Vs and the smallest threshold voltage shift under stress. *Facchetti et al.* reported the importance of bilayer metal oxides to boost the performance in TFT architectures processed a low temperature (250 °C).[285] In_2O_3/IGO TFTs with a mobility of 2.56 cm^2/Vs and I_{on}/I_{off} ratio of 10^8 surpass the monolayered In_2O_3 TFTs in terms of I_{on}/I_{off} ratio (10^4) due to their higher off current. *Marks et al.* reported the first inkjet printed IGZO through SCS using acetylacetone as fuel on solution-based hafnia self-assembled nanodielectrics.[286] By using this high-κ gate dielectric low operating voltage TFTs were achieved with a high electron mobility of 20.6 ± 4.3 cm^2/Vs. In 2014, high-κ dielectrics start to be developed for TFTs application via SCS by *Branquinho et al.* and *Cho et al.* for TFTs application.[7,287] *Branquinho et al.* reported aqueous combustion synthesis of aluminum oxide (AlO_x) dielectric using urea as fuel for solution-based gallium−zinc-tin oxide (GZTO) TFTs.[7] The water-based AlO_x thin films exhibited high stability, capacitance and negligible hysteresis compared to the toxic 2-methoxyethanol (2-ME) based thin films. This study represents a new and green route for amorphous metal oxide thin films. *Cho et al.* reported the incorporation of (3-glycidoxy- propyl)trimethoxysilane (GPTMS) as polymeric binders into the oxide network to improve the surface morphology of the dielectric layer avoiding pores and cracks generated during the annealing, as depicted Figure 2.16 (a).[287] By choosing the right molar ratio between the AlO_x precursor and GPTMS (1:8) the lowest leakage current density was achieved for the dielectric layer, and applied in ZnO TFTs reaching a high mobility of 24.7 cm^2/Vs. In 2015, *Facchetti et al.* developed a new low temperature route to reach high-mobility amorphous indium

oxide semiconductor films via SCS and doping with poly(4-vinylphenol) (PVP), an insulating polymer.[288] The addition of PVP suppresses crystallization, retains conducting pathways for efficient charge transport and improves mechanical properties, which is crucial for flexible applications, as shown in Figure 2.16 (b). In the same year, *Facchetti et al.* reported the first-time spray-combustion synthesis of metal oxide semiconductors (In_2O_3, IZO and IGZO) and conductors using acetylacetone as fuel for TFTs.[289] The devices with IGZO as semiconductor processed at low temperatures provide high performance and stability similar to the results reached by sputtering. In 2015 and 2016, *Branquinho et al.* reported the influence of different solvents (Figure 2.16 (c)), fuels, temperatures and MO thin films via SCS for TFTs.[6,35] This simple, friendly and low temperature annealing process is demanded for the application in low cost flexible substrates. *Facchetti et al.* explored the use of carbohydrates (sorbitol, glucose and sucrose) as assisting fuels to decrease the ignition threshold temperature compared to acetylacetonate without sugar through SCS to reach high-quality IGZO TFTs.[66] In this work a correlation between precursor combustion enthalpy, M-O-M lattice content, microstructural densification and IGZO electron mobility was established. From all the fuels tested, sorbitol (10 %) revealed the highest precursor combustion enthalpy leading to a higher mobility of 7.5 cm^2/Vs and better stability. In 2017, *Fortunato et al.* reported the dual role of 2-ME as solvent and fuel for the production of solution-based ZTO TFTs.[78] The devices produced without urea as fuel and only with 2-ME as solvent had lower variability and higher stability compared to the fuel rich condition whilst the thermal analysis of precursor showed high exothermic reaction.

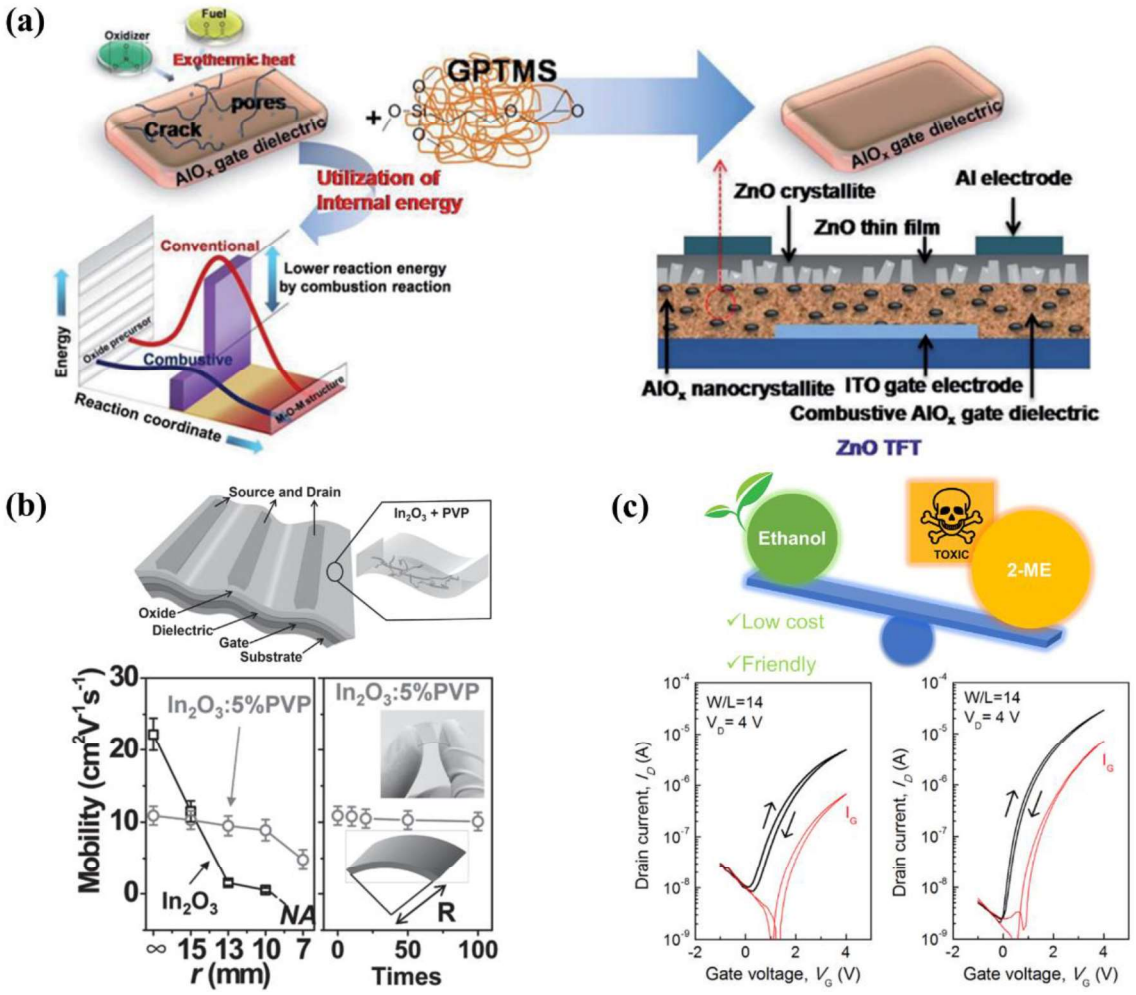

Figure 2.16. (a) Schematic diagram of the AlO_x gate dielectric film prepared by self-combustion of metal precursors mixed with organic compounds;[287] Copyright © The Royal Society of Chemistry 2014. (b) Schematic representation of the flexible, transparent TFT structure based on a metal oxide:polymer (In_2O_3:*x*%PVP) semiconductor blend; Dependence of TFT mobilities on bending radius of both neat In_2O_3 TFTs and all-amorphous In_2O_3:5% PVP TFTs (left), and mobilities on all-amorphous TFT bending cycles at a radius of 10 nm (Optical image of transparent flexible TFTs);[288] Copyright © 2015 WILEY-VCH Verlag GmbH & Co. KGaA, Weinheim. (c) Schematic of two solvents with different toxicities; Electrical characterization of bottom gate ethanol and 2-methoxyethanol (2-ME) based solution processed ZTO/AlO_x TFTs produced on highly doped p-Si (gate).[6] Copyright © 2015 IOP Publishing Ltd.

In 2018, *Facchetti et al.* reported the addition of nitroacetylacetone (NAcAcH) as cofuel of acetylacetone for SCS of high performance IGZO TFTs, as shown in Figure 2.17 (a).[290] The combination of these fuels lead to a reduction of the ignition temperature and increment in the enthalpy of combustion, similar to the work performed with carbohydrate fuels.[66] The TFTs with an optimal molar ratio between the fuels contribute to a large electron mobility of 7.5 cm^2/Vs and

enhanced bias stress stability, being the combustion synthesis reagents design crucial for high quality MO thin films.

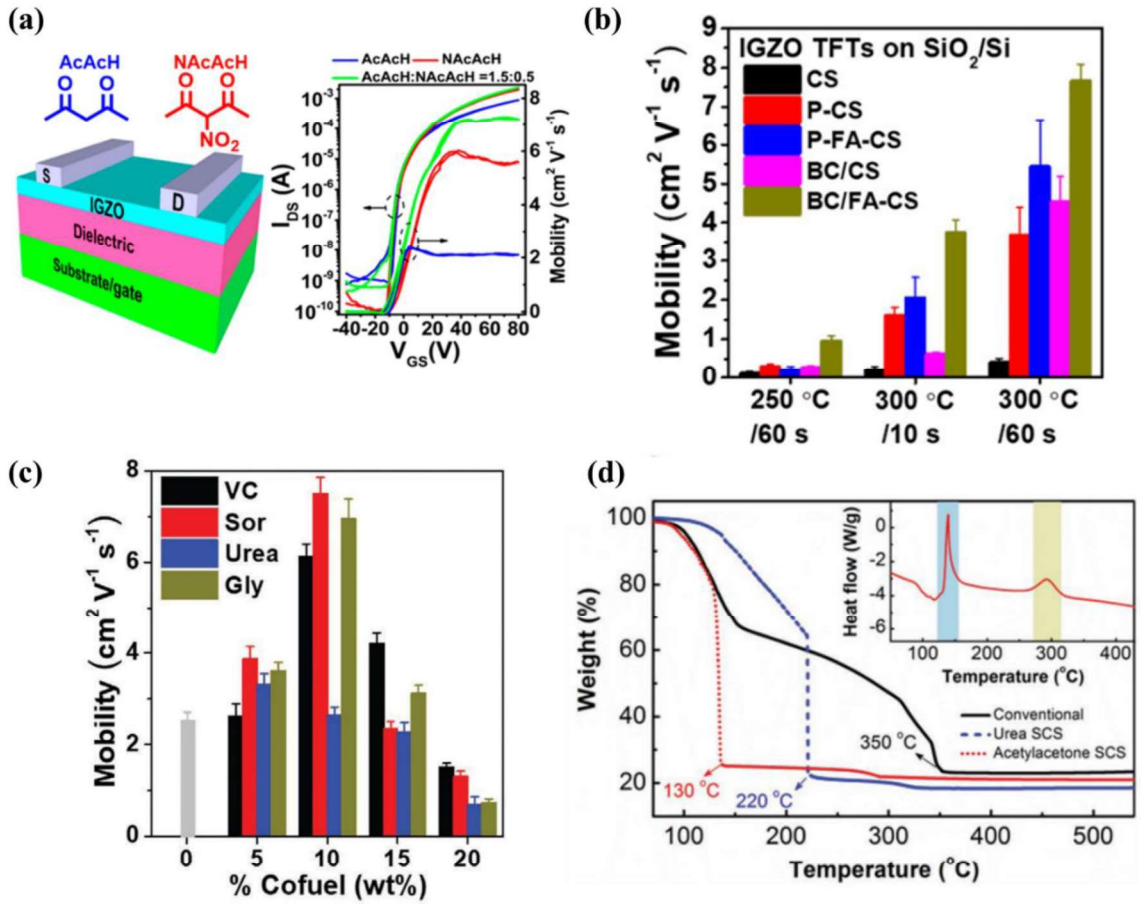

Figure 2.17. (a) Top-contact, bottom-gate MO TFT geometry, transfer curves and chemical structures of fuel used;[290] Copyright © 2018, American Chemical Society. (b) Comparison of IGZO TFT performance and stability. IGZO TFT mobilities on 300-nm SiO_2/Si with IGZO films processed by the indicated methods (Combustion synthesis (CS), fuel-assisted CS (FA-CS), preannealed CS (P-CS), and preannealed FA-CS (P-FA-CS) processes are done by spin-coating). Note "BC" indicates "blade-coating," while all other devices were fabricated by spin-coating unless otherwise noted;[291] © 2019 Published under the PNAS license. (c) Electron mobility statistics for *x* wt% cofuel/IGZO TFTs, with the indicated cofuel compositions.[67] Copyright © 2019 WILEY-VCH Verlag GmbH & Co. KGaA, Weinheim. (d) The TGA curves of the acetylacetone- and urea-involved combustive and conventional Cu:NiO (5 at% Cu) precursors. The inset shows the corresponding DSC curve of acetylacetone-involved precursor;[292] Copyright © 2017 WILEY-VCH Verlag GmbH & Co. KGaA, Weinheim.

In 2019, *Facchetti et al.* reported a highly efficient combustion blade coating by using a fluorinated fuel as cofuel for metal oxides.[291] Also, an ultrafast reaction and metal-oxygen-metal (M-O-M) lattice condensation occurs with just 10–60 s at 200–350 °C for MO semiconductor (IZO, IGZO) and dielectric (Al_2O_3) films, reaching higher TFT mobilities for the blade coating

process, as depicted in Figure 2.17 (b). The resultant IGZO/Al_2O_3 TFTs exhibit a low operating voltage (<2 V) and high field effect mobilities with a maximum value of 25.2 cm^2/Vs. The same group also reported the boost of combustion synthesis pathways by using various cofuels (sorbitol, L-ascorbic acid, urea, glycine, glucose, sucrose, xylitol, erythritol) to produce metal oxide semiconductor films and their use in TFTs, as shown in Figure 2.17 (c).[67] Recently, *Branquinho et al.* reported the importance of adding urea to the IGZO for a precursor solution uniform distribution of the metal cations within the gel phase reaction, which clearly affect the performance of solution-based IGZO TFTs.[293] Lately, *Skafidas et al.* reported the printing of all metal oxide thin films for TFT by direct electrohydrodynamic patterning using acetylacetone as fuel.[294] Fully transparent printed TFTs reached high electron mobilities of 117 cm^2/Vs and low operating voltage. These devices were applied on logic gates being a relevant path to achieve large area and high-performance transparent electronics. Similarly, to the conventional vacuum based oxide materials, the majority of developments focus on n-type materials. Nevertheless, *Shan et al.* implemented the SCS method to produce p-type Cu-doped NiO (Cu:NiO) TFTs at low temperature (150 °C) using acetylacetone as fuel (Figure 2.17 (d)).[292] The $Cu_{5\%}$NiO TFTs showed a good performance with hole mobility of 1.5 cm^2/Vs, large on/off current ratio of ~10^4 and low operating voltage. Also, the resultant TFTs were incorporated into a driving circuit to turn on a green light emitting diode. These results open the window for the production of low-temperature-processed p-type oxides via SCS and their implementation on complementary metal oxide semiconductor (CMOS) circuits on flexible substrates.

Table 2.5. Recent developments of oxide thin films using solution combustion synthesis for TFTs application. (T_{low}: low temperature used for an active TFT; SC: Semiconductor; D: Dielectric; E: Electrode; Spin: Spin-coating; Spray: Spray-coating; Blade: Blade-coating; Ac: Acetylacetone; AcA: Acetic acid; AN: Acetonitrile; U: Urea; 2-ME: 2-methoxyethanol; MEA: mono- ethanolamine; NAc: Nitroacetylacetone ; W: Water; Sor: Sorbitol; Glu: Glucose; Suc: Sucrose; FA: 1,1,1 – Trifluoroacetylacetone; Aa: Ascorbic acid; Gly: Glycine; P: Pre-annealing; EHD: Electrohydrodynamic printing; IJ: Inkjet printing).

Year	Deposition Technique	Layer	Fuel/ Solvent	Material	T_{low} (°C)	I_{on}/I_{off}	μ_{SAT} ($cm^2 \cdot V^{-1} \cdot s^{-1}$)
2011 [2]	Spin	SC	Ac or U/2-ME	In_2O_3	200	10^6	0.81
	Spin	SC	Ac or U/2-ME	ZTO	225	10^4	0.29
	Spin	SC	Ac or U/2-ME	IZO	225	10^6	0.25
2012 [295]	Spin	SC	Ac/2-ME	IYO	250	10^6	5
2013 [284]	Spin	SC	Ac/2-ME	IGZO	250	10^7	1.28
	Spin	SC	Ac/2-ME	IScZO	250	10^7	0.45
	Spin	SC	Ac/2-ME	IYZO	250	10^8	0.35

	Spin	SC	Ac/2-ME	ILaZO	250	10^8	0.65
	Spin	SC	Ac/2-ME	IZO	250	10^6	0.42
2013 [285]	Spin	SC	Ac/2-ME	In_2O_3	200	10^3	0.63
	Spin	SC	Ac/2-ME	IGO	250	10^6	0.78
	Spin	SC	Ac/2-ME	In_2O_3/IGO	200	10^7	0.36
2013 [286]	IJ	SC	Ac/2-ME	IGZO	300	10^7	20
2013 [296]	Spin	SC	MEA and AcA/ 2-ME	IGZO	350	10^7	1.15
	Spin	SC	Ac/2-ME	In_2O_3	250	10^8	2.24
2014 [7]	Spin	D	U/2-ME or W	Al_2O_3	350	~10^5	1.3
2014 [297]	Spin	SC	Ac/2-ME	In_2O_3	300	~10^5	2.5
2014 [287]	Spin	D	Ac/2-ME	Al_2O_3	250	10^5	24.7
2014 [297]	Spin	SC	Ac/2-ME	In_2O_3	250	~10^6	2.5
2015 [288]	Spin	SC	Ac/2-ME	In_2O_3:PVP	225	~10^5	11
2015 [298]	Spin	SC/D	Ac/2-ME	IGZO/Al_2O_3	300	10^5	7.3
2015 [289]	Spray	SC	Ac/2-ME	In_2O_3	200	~10^6	1.44
	Spin	SC	Ac/2-ME	In_2O_3	200	~10^6	0.83
	Spray	SC	Ac/2-ME	IZO	225	~10^7	0.52
	Spin	SC	Ac/2-ME	IZO	225	~10^7	0.29
	Spray	SC	Ac/2-ME	IGZO	225	~10^6	0.18
	Spin	SC	Ac/2-ME	IGZO	225	~10^6	0.01
2015 [6]	Spin	SC/D	U/2-ME	ZTO/Al_2O_3	350	10^4	2.6
	Spin	SC/D	U/Et	ZTO/Al_2O_3	350	~10^3	0.8
2016 [66]	Spin	SC	Ac/2-ME	IGZO	300	~10^7	2.1
	Spin	SC	Ac and Sor /2-ME	IGZO	300	~10^6	7.5
	Spin	SC	Ac and Glu /2-ME	IGZO	300	~10^6	5.7
	Spin	SC	Ac and Suc /2-ME	IGZO	300	~10^7	3.2
2016 [35]	Spin	D	U/2-ME	Al_2O_3	200	10^4	13.5
	Spin	D	U/Water	Al_2O_3	200	10^3	12.9
2016 [299]	Spin	E	Ac/2-ME	ITO	250	~10^7	2.1
2016 [300]	Spray	SC	Ac/2-ME	IZO	250	~10^6	1.3
	Spray	SC	Ac/2-ME	IGZO	350	~10^6	3.2
	Spray	SC/D	Ac/2-ME	IZO/ Al_2O_3	250	~10^4	6.5
	Spray	SC/D	Ac/2-ME	IZO/ ZrO_2	250	~10^4	9.3
	Spray	E/SC/D	Ac/2-ME	ITO/ IGZO/ ZrO_2	350	~10^5	5.3
	Spray	E/SC/D	Ac/2-ME	ITO/ IGZO/ Al_2O_3	350	~10^5	3.5

2017 [292]	Spin	SC	Ac/ 2-ME	Cu:NiO	150	~10^4	1.5 (p-type)
2017 [78]	Spin	SC	2-ME/2-ME	ZTO	350	~10^6	~4.5
	Spin	SC	U/2-ME	ZTO	350	10^6	~3
2017 [301]	Spin	E	Ac/2-ME	IZTO	400	10^3	0.44
2018 [290]	Spin	SC	Ac/2-ME	IGZO	300	~10^7	2.7
	Spin	SC	Ac and NAc/2-ME	IGZO	300	~10^7	7.5
	Spin	SC	NAc/2-ME	IGZO	300	~10^7	5.7
2019 [302]	Spin	SC/ D	U/2-ME	IGZO/ Al_2O_3	300	10^6	3.2
2019 [303]	Spin	SC	2-ME/2-ME	IZTO	200	10^2	4.21
	Spin	D	EG/AN	$NaAl_{11}O_{17}$			
2019 [291]	Blade	SC	Ac/2-ME	IGZO	225	10^6	0.17
	Blade	SC	FA and Ac/ 2-ME	IGZO	225	10^6	0.19
	Blade	SC	P(Ac)/2-ME	IGZO	225	10^7	0.78
	Blade	SC	P(FA and Ac)/ 2-ME	IGZO	225	10^7	0.92
	Blade	SC	Ac/2-ME	In_2O_3	225	10^4	0.21
	Blade	SC	FA and Ac/ 2-ME	In_2O_3	225	10^5	0.24
	Blade	SC	P(Ac)/2-ME	In_2O_3	225	10^4	2.96
	Blade	SC	P(FA and Ac)/ 2-ME	In_2O_3	225	10^3	3.82
	Blade	SC	Ac/2-ME	IZO	250	10^5	0.33
	Blade	SC	FA and Ac/ 2-ME	IZO	250	10^6	0.28
	Blade	SC	P(Ac)/2-ME	IZO	250	10^6	2.32
	Blade	SC	P(FA and Ac)/ 2-ME	IZO	250	10^6	2.11
	Blade	SC/D	P(FA and Ac)/ 2-ME	IGZO/ Al_2O_3	350	10^4	~18
2019 [67]	Spin	SC	Ac/2-ME	IGZO	300	~10^7	2.54
	Spin	SC	Ac and Aa/ 2-ME and W	IGZO	300	~10^7	6.12
	Spin	SC	Ac and Sor/ 2-ME and W	IGZO	300	~10^7	7.50
	Spin	SC	Ac and U/ 2-ME and W	IGZO	300	~10^7	3.32
	Spin	SC	Ac and Gly/ 2-ME and W	IGZO	300	~10^7	6.95
2019 [293]	Spin	SC	AcA	IGZO	400	~10^6	4.4
	Spin	SC	Ac	IGZO	400	~10^7	5.5
2019 [294]	EHD	SC/ D	Ac	In_2O_3/ Al_2O_3	350	~10^6	117
	EHD	SC/ D	Ac	IGZO/ Al_2O_3	350	~10^6	81

2.3.2. Combination of SCS and ultraviolet irradiation

Ultraviolet (UV) irradiation have high-energy photons which induce photochemical cleavage of alkoxy groups homogeneously, and activate metal and oxygen atoms to facilitate M–O–M network formation.[304–306] Further irradiation leads to a rapid decrease of oxygen and carbon contents promoting a near-complete condensation and a transition to film densification. In 2012, *Park et al.* reported the use of deep-ultraviolet (DUV) irradiation to induce efficient condensation and densification of oxide semiconductor films (IGZO and IZO) through photochemical activation at low temperature (150 °C).[3] In order to improve the quality, i.e. higher densification of the MO thin films at low processing temperatures, ultraviolet irradiation (UV) can be used simultaneously with SCS method, as depicted in Table 2.6.

Table 2.6. Recent developments of oxide thin films using solution combustion synthesis combined with UV irradiation for TFTs application. (T_{low}: low temperature used for an active TFT; SC: Semiconductor; D: Dielectric; E: Electrode; Spin: Spin-coating; Ac: Acetylacetone; U: Urea; 2-ME: 2-methoxyethanol; Flexo: Flexo-printing)

Year	Deposition Technique	Layer	Fuel/ Solvent	Material	T_{low} (°C)	I_{on}/I_{off}	μ_{SAT} ($cm^2 \cdot V^{-1} \cdot s^{-1}$)
2016 [307]	Spin	D	U/2-ME	Al_2O_3	150	10^4	23.8
2017 [92]	Spin	D	U/2-ME	AlO_x	150	10^5	17.7
	Spin	D	U/2-ME	HfO_x	150	10^5	31.2
	Spin	D	U/2-ME	HfO_x/ HfO_x	150	10^6	43.9
	Spin	D	U/2-ME	HfO_x/ AlO_x	150	10^5	23.6
	Spin	D	U/2-ME	HfO_x/ AlO_x/ HfO_x	150	10^5	37.5
	Spin	D	U/2-ME	AlO_x/ HfO_x	150	10^5	37.2
	Spin	D	U/2-ME	AlO_x/ HfO_x/ AlO_x	150	10^5	30.5
2018 [308]	Spin	SC	Ac/2-ME	Li:NiO_x	150	~10^7	1.7 **(p-type)**
2020 [309]	Flexo	D	U/2-ME	Al_2O_3	180	10^7	2.7

In 2016, *Carlos et al.* reported the combination of SCS and far ultraviolet (FUV) irradiation to boost the dielectric properties of aluminum oxide for TFT applications, as depicted in Figure 2.18 (a).[307] The devices had a high reproducibility and mobility, low operation voltage and good stability (under stress and ageing). One year later the same group studied the relevance of multilayer oxide dielectrics (AlO_x and HfO_x) at low temperatures using deep-ultraviolet instead

of FUV.[92] For HfO_x thin films, a fuel rich condition was required to decrease the processing temperature the metal oxide formation compared to the stoichiometric condition. IGZO TFTs with a bilayer of HfO_x exhibited the best electrical performance (mobility, stability, and uniformity) being applied in a basic electronic building block, an inverter. In 2018, *Zhang et al.* reported the combination of low temperature SCS (150 °C) and UV irradiation to process p-type Li:NiO_x active semiconductors for TFTs.[308] In these devices the doping of NiO_x with Li the was relevant to improve the p-type conductivity of NiO_x at low temperatures. The $Li_{5\%}$:NiO_x/ZrO_2 TFTs presented a good field effect mobility, a high on/off current ratio (8×10^6) and low operating voltage.

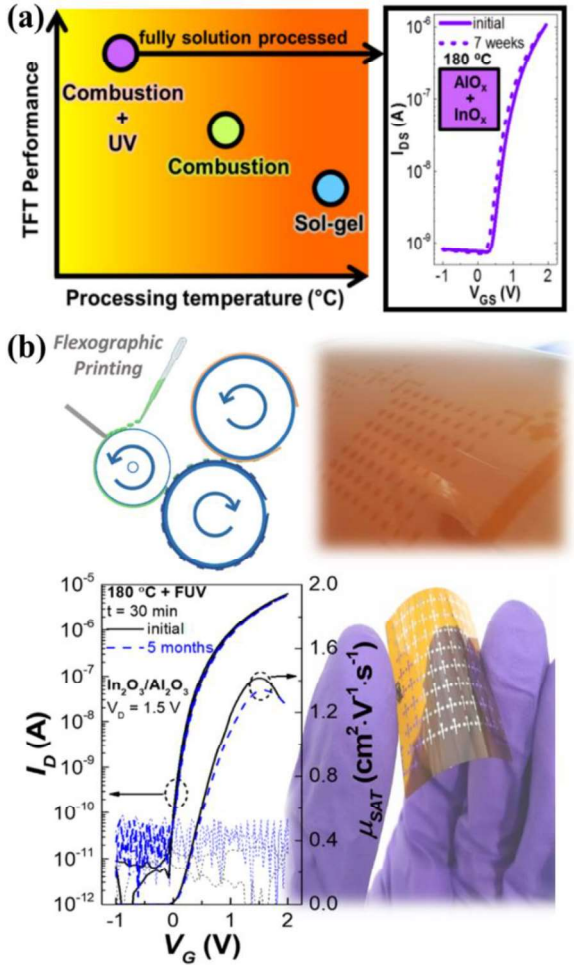

Figure 2.18. (a) Proposed mechanism of the low temperature photoactivation combined with the combustion synthesis of metal oxide thin films for TFT performance;[307] Copyright © 2016, American Chemical Society. (b) Schematic image of flexographic printing process of the Al_2O_3 dielectric ink on top of the bottom electrode deposited by thermal evaporation; Photograph after the dielectric printing in the

flexographic machine; Ageing effect of In_2O_3/Al_2O_3 TFT after 5 months.[309] Copyright © 2020 WILEY-VCH Verlag GmbH & Co. KGaA, Weinheim.

The high performance achieved with low temperature solution-based n-type and p-type MO TFTs allows compatibility with flexible substrates consequently, the next step is their implementation in large area processing techniques. *Fortunato et al.* recently reported for the first-time flexographic printing of a highly-stable aluminum-oxide dielectric with a high-throughput (50 m/min) while simultaneously demonstrating low-temperature processing ($\leq$ 200 °C), as shown in Figure 2.18 (b).[309] This low temperature process was achieved due to the combination between SCS and UV irradiation. The printed In_2O_3/Al_2O_3 TFTs presented high stability under electrical and mechanical stress which can redefine printed flexible applications for large area manufacturing.

2.4. Summary and Outlook

This review enhances the potentialities of solution combustion synthesis (SCS) to produce metal oxides giving a special attention to crucial parameters that influence the final structures such as, fuel type, metal cation precursor, fuel to oxidizer ratio, pH, atmosphere and initiation type. The fuel serves as reducer and complexing agent avoiding the precipitation of metal cations thus ensuring compositional homogeneity. The choice of organic fuel or mixture of fuels depends on their specific interaction with the metal cations and solvent which determine the final morphology and application of the oxides. The metal nitrate-based precursors are preferable due to the high oxidizing power, vast solubility and low decomposition temperature. For these precursors the charge density of the metal ions, the standard molar Gibbs free energies of hydration and the exchange kinetics play a critical role. The fuel to oxidizer ratio is quite important to define the final oxide structure and the intensity of the exothermic reaction. The atmosphere environment can effectively influence the process time and mass degradation during the combustion reaction.

Typically, a muffle furnace is used as initiation of SCS in bulk however, microwave radiation can improve the yield and lower the processing time to a few minutes. For metal oxides thin films via SCS annealing is preferably performed using a hotplate or its combination with UV irradiation. All these parameters influence the final metal oxides morphology, of which nanoparticles and thin films are the most exciting due to their versatility. Nanoparticles are the most common nanostructures produced showing a high-surface area-to-volume ratio which is highly demanded for sensors, catalysis and biomedical applications. Besides nanostructures, in the last decade a significant effort has been made to implement SCS in thin films to reduce the processing temperature as this will allow large area manufacturing of simple devices (memories, TFTs, solar cells) and further wearable applications. Nevertheless, the prevalent application of MO thin films

via SCS method is thin film transistors and these devices performances have been enhanced by combining annealing with UV irradiation.

Certainly, SCS is a suitable method for the production of metal oxides providing a high reliability, versatility and efficiency for different demands at low processing temperatures. Moreover, the resultant nanostructures can even be applied on pastes or solutions to upscale and boost for various applications. SCS will become essential for printing solution-based metal oxides allowing a good homogeneity and controllability of the process. SCS is certainly becoming a fundamental piece for next-generation large-scale electronics and IoT clearly contributing to a more sustainable society.

Chapter 3

New strategies towards processing of solution-based metal oxide TFTs

Solution-based metal oxides have been attracting a lot of attention due to the low cost, high throughput and simple chemical composition control when compared with vacuum-based systems. These materials have outstanding properties such as high optical transparency, chemical and thermal stability and mechanical toughness. Also, facile tailoring of solution-based metal oxides leads to multifunctionality allowing their application in different areas, like sensing, energy and flexible displays. Particularly for large-area electronics the exploration of a crucial component, the thin film transistor (TFT) and their key materials components, the semiconductor, the dielectric, the conductor as well as substrate are demanded. To boost the implementation of TFTs emerging printing techniques and low thermal budget, novel approaches have been and need to be further explored. This chapter review focuses on recent low temperature approaches as combustion synthesis, irradiation (UV, NIR) post annealing treatments which allow their implementation in printable flexible TFTs. Next, special attention is given to solution-based high-κ oxide dielectrics that play a critical role to achieve low power consumption. Finally, a detailed discussion of emerging printing techniques and current challenges are discussed.

Keywords: oxides, solution synthesis, high-κ dielectrics, metal oxide thin films, thin film transistors, low temperature, printing electronics

The results presented in this chapter is published in:

- ✓ *Emanuel Carlos, Rita Branquinho, Pedro Barquinha, Rodrigo Martins, Elvira Fortunato. "New strategies towards high performance and low temperature processing of solution based metal oxide TFTs", Book Chapter 18, Review, Elsevier, 2021.*

3.1. Introduction

Nowadays, energy management plays a crucial role for the internet of things (IoT) growing with the increment of the amount of data to handle. The pursue of more and more comfort in society will lead to an exponentially increase of IoT nodes, since almost every device has embedded electronics. This caught the attention of companies, investors and manufactures to invest and follow up the market expansion, as shown in Figure 3.1. [310,311] Many approaches have a clear focus on lowering the power consumption which is a basic requirement for IoT. Also, in terms of an economic point of view it is required to sell millions of units to cut down the production costs and establish IoT in our society in a reachable state.[310]

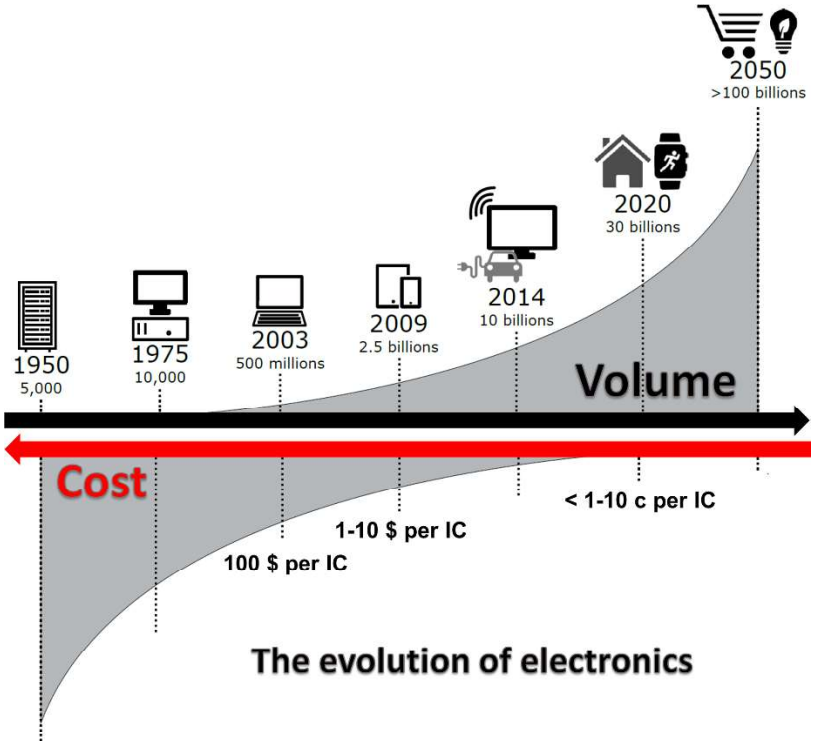

Figure 3.1. Expected adoption growth of IoT devices relating volume and cost. Reproduced with permission and adapted from [310]. Copyright © 2021 Elsevier B.V. All rights reserved.

To promote sustainability, solution processing has been considered as key to surpass the high production costs and large area application concerns in vacuum-based systems. Several flexible application devices, like circuits, sensors and displays using vacuum-based or solution-based techniques are currently under development, as depicted in Figure 3.2.[312–315] From all these applications, oxide thin film transistors (TFTs) present a vital position in IoT based on high uniformity over large areas, low temperature process, low power consumption and suitability for different fabrication methodologies.[1,314] Nonetheless, a high thermal budget is typically required to achieve a high film quality in solution-based oxide thin film transistors compared to vacuum-based techniques.[8,316–320] Some drawbacks persist when low temperature solution processing is

adopted, like low thin film densification, which can affect the general devices stability, time to process and reproducibility. However, these limitations can be surpassed by the adoption of different approaches as the solution synthesis details (metal salt precursor, combustion process, doping, solvents, concentration, pH, humidity and temperature environment)[4,321–325] and post-treatment processes (lamp and laser irradiation).[3,20,326–329] By improving the films´ quality with these notable approaches, the great potential to perform a simple fabrication process in flexible substrates by decreasing the associated cost and the applicability for high throughput techniques was demonstrated. Printing techniques minimize material waste via selective area deposition compared to coating techniques.[330] The printing speed and resolution features are the most critical points that need to be enhanced, however, new emerging approaches have been developed to settle these issues as will be introduced further in this chapter review.

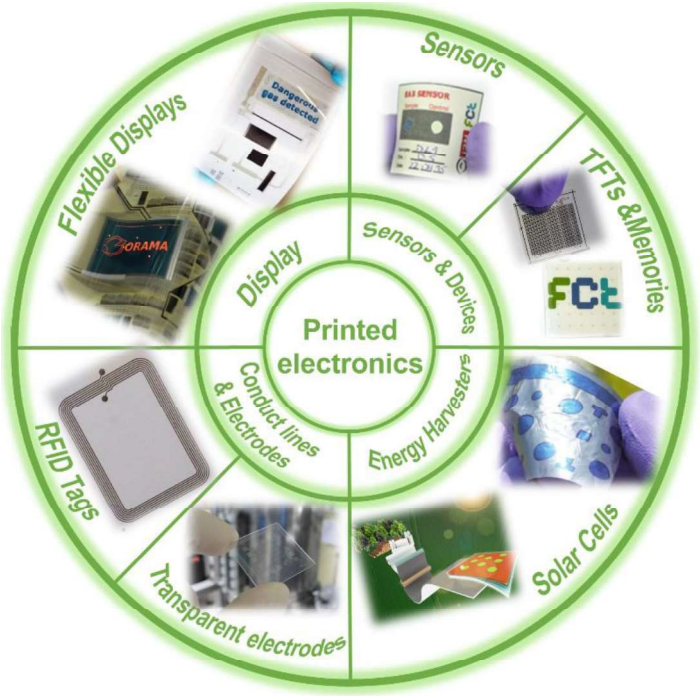

Figure 3.2. Diverse applications with potential for printed electronics. Reproduced and adapted with permission.[331] Copyright © 2015, Royal Society of Chemistry; Copyright © 2021 Elsevier B.V. All rights reserved.

High-κ oxide dielectrics are highly demanded to boost microelectronics, wearables and sensors since the high permittivity helps to supress the tunnelling effect compared to SiO_2 dielectric and allow low power consumption.[332] So, considerable efforts have been made to implement high-κ oxide dielectrics in printable flexible electronics. Nevertheless, most of printable dielectrics require an increase film thickness to avoid high leakage currents (pinholes, defects) being affordable for roll-to-roll (R2R) techniques. Lately, a huge attempt to decrease the thickness (< 20 nm) of printed high-κ oxide dielectrics and at the same time guarantee a good thin film quality

with large capacitance per unit area (C_{ox}) and low current density (J) has been developed to empower low consumption devices.[309,333,334]

In this work, an overview of low temperature approaches in solution-based metal oxide TFTs is performed and the importance of high-κ oxide dielectrics for low operation voltage and miniaturization was highlighted. To clearly understand the integration of these metal oxide inks for large-scale manufacturing further studies on advanced printing techniques are reported. To finalize, the current challenges of low temperature solution-based metal oxide TFTs to be up-scaled for printing industry are discussed.

3.2. Low temperature approaches for solution processed oxide TFTs

3.2.1. Oxides synthesis design

Solution synthesis process of oxides play a crucial role in the metal-oxygen-metal (M-O-M) frameworks formation improving the purity, condensation, and densification of the thin films at low temperature. However, usually high temperature annealing (> 300 °C) is required to avoid metal-hydroxyl (M-OH) bonds presence in low temperature films arrangement, which will affect the modulation and stability of oxide TFTs. In the last decade, novel approaches regarding the solution synthesis manipulation have been developed to overcome these challenges as depicted in Figure 3.3.

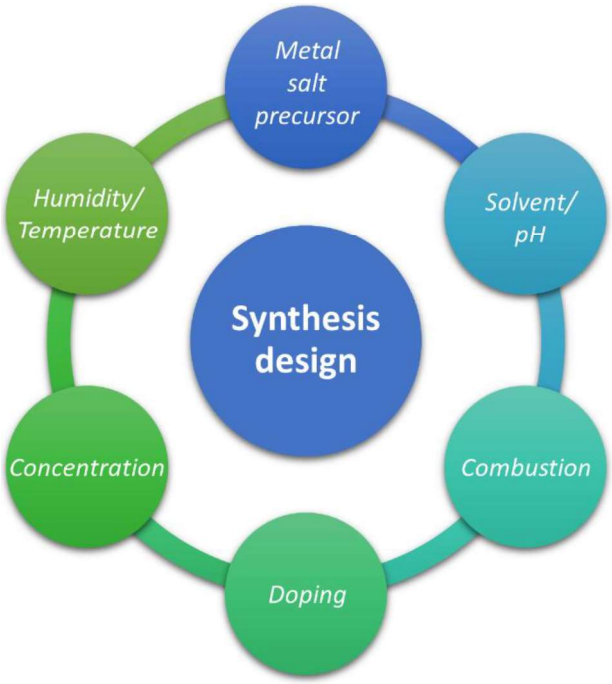

Figure 3.3. Solution synthesis approaches to boost low temperature solution-based oxide TFTs. Copyright © 2021 Elsevier B.V. All rights reserved.

The use of a proper metal salt-based precursor as metal alkoxides, a class of compounds categorised by the metal-oxygen-carbon (M-O-C) bonding system offering a great potential to change the chemical and physical properties.[335] When these metal alkoxides are exposed to an aqueous environment, hydrolysis and condensation reactions occur by nucleophilic substitution and addition mechanisms. This allows the formation of metal-oxygen-metal (M-O-M) at low temperatures (< 250 °C) since these reactions imply a proton transfer from the incoming water molecule to the bound alkoxide group leading to the elimination of the protonated leaving group.[4] Nonetheless, metal alkoxides are quite reactive if non-hydrolysed process is performed, resulting in an uncontrolled and undesirable precipitation in solution. An in-situ hydrolysed process avoids these drawbacks retaining molecular ink dispersion and controlled metal oxide film formation.

Using this method IZO TFTs with high mobility (10 $cm^2/V \cdot s$), reproducibility and stability were produced. This approach proposed by *H. Sirringhaus et al.*[4] is suitable to a large range of amorphous metal oxide compositions being of highly interesting for low-cost flexible TFT applications. Another important factor is how the precursor mass changes with the temperature increment. Among distinct metal salts precursors, acetate, chloride and nitrate to synthetize metal oxides, the nitrate-based solution is the one that affords lower temperature to convert the precursor into metal oxide as shown in Figure 3.4 (a).[93] For the case of acetate and chloride precursors a higher temperature is required to remove all the residual organics, thus reducing the impurities present in the TFTs fundamental layers (dielectric and semiconductor).

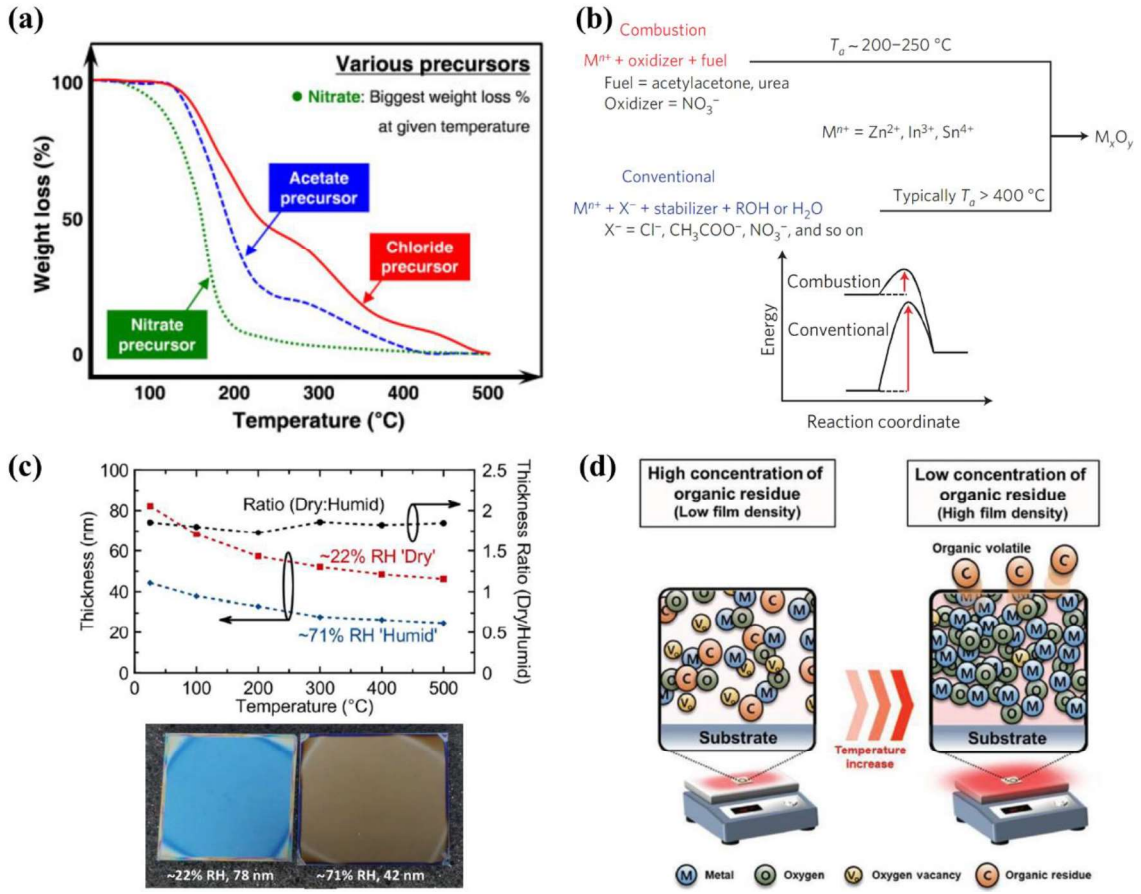

Figure 3.4. (a) Schematic diagram of thermogravimetric analyses of various precursors. Reproduced with permission.[93] Copyright © 2019, IOP Publishing Ltd; (b) Depiction of the two different synthetic approaches; Energetics of combustion synthesis-based processes versus conventional processes. Reproduced with permission.[2] Copyright © 2011, Springer Nature; (c) Thickness comparison of $HafSO_x$ films deposited at ~22% (red) and ~71% RH (blue). A ratio of film thickness (dry: humid) is plotted in black; Pictures of as-deposited $HafSO_x$ thin films deposited at ~22% and ~71% RH. The film thicknesses (determined using XRR) are 78 and 42 nm, respectively. Reproduced with permission. [336] Copyright © 2017, American Chemical Society; (d) Schematic illustration of annealing process for oxidation and

impurity removal of solution-processed oxide semiconductors. Reproduced with permission.[5] Copyright © 2019 WILEY-VCH Verlag GmbH & Co. KGaA, Weinheim.

A self-energy generating combustion chemistry has been developed by *Marks et al.*[2] to decrease even more the annealing temperature in solution-processed metal oxide TFTs as depicted in Figure 3.4 (b). This strategy consists in a redox based combustion synthetic approach, using a fuel (acetylacetone, urea, citric acid) as reducing agent and metal nitrates as oxidizing agent.[2,35]

Through combustion synthesis an exothermic reaction occurs, resulting in a reduction of the external heating required for the film formation; i.e. the removal of organic solvents and film densification. In contrast, the conventional method requires higher external energy to fully form M-O-M lattices, since the oxide formation via metal hydroxide and/or alkoxide precursors conversion is endothermic. Solution-based In_2O_3 thin film transistors processed at 200 °C showed a great performance with a high mobility of 13 $cm^2/V \cdot s$ and low operating voltages using the self-combustion method. Nowadays, low temperature combustion synthesis is applied in all oxide TFTs assembly including semiconductors, dielectrics, and conductors.

A low temperature (200 °C) process of solution-based oxide TFTs can be reached also by doping the metal oxide network as demonstrated by *Bae et al.*[323] In this work, a fluorine dopant was inserted in an indium zinc oxide (IZO) semiconductor network replacing the oxygen lattice, which generate free electrons and subsequently increase the carrier concentration. Therefore, the fluorine doping improved the mobility and stability of low temperature solution-processed oxide TFTs. As an alternative to metal oxide doping, organics can be used to improve the properties of solution-based semiconductors at low temperature. *Facchetti et al.*[288] reported that the use of an insulating polymer, poly(4-vinylphenol) known as PVP, enhanced indium oxide (In_2O_3) semiconductor thin films quality. The presence of hydroxyl groups and the high solubility of this polymer in the semiconductor precursor formulation solution facilitates the coordination with the metal-oxygen lattice. This outcome boosts the semiconductor performance in TFTs, increasing the electron mobility (10 $cm^2/V \cdot s$) and more importantly the resistance to mechanical stress; being compatible with ultra-flexible circuits. Hybrid structures will be essential in the next generation of flexible electronics using low-cost process to up-scale production.

Another key factor is the solvent which constitutes a substantial portion of the oxide precursor solutions around 98 % and 90 % for low and higher concentrations, respectively. So, an imperative impact needs to be considered from the solvent on the thin film's deposition and production process. Following this pathway *Bay et al.*[322] propose a new aqueous route solvent capable of producing In_2O_3 thin films at lower temperatures compared with alcohol route. Even temperatures as low as 100 °C were achieved with vacuum annealing that promote the

condensation reaction by completely removing by-product water molecules. This novel route allows the production of solution-based metal oxide TFTs on any kind of low-cost flexible substrates, like PEN or PET. Also, *Fortunato et al.*[78] noted the dual role of the organic solvent in the formation reaction of zinc tin oxide (ZTO) semiconductor thin films and how it can affect the TFTs performance. Analysing the ZTO precursor solutions through thermal thermogravimetry it could be observed that 2-methoxyethanol (2-ME) acts simultaneously as solvent and fuel. Therefore, when urea is used there is an excess of fuel in the precursor solution resulting in a non-stochiometric reaction during the film formation which leads to a lower stability and reproducibility ZTO TFTs. Certainly, the choice of the right solvent influences the metal oxide precursor solution and strictly needs to be taking into account.

Humidity and temperature over the deposition/production of solution-based oxide thin films are vital parameters in their final properties to have a good performance and reproducibility at high and low temperatures. These parameters are more difficult to control and often they are not mentioned which hinders the reproducibility of the results by other research groups. *Page et al.*[336] reported how important is the relative humidity (RH) during the deposition of metal oxide thin films (AlO_x, LZO and $HafSO_x$). Basically, if a dry (RH ~22 %) or humid (RH ~71 %) environment is adopted while keeping temperature, spin speed, spin acceleration, and solution composition constant, the films thickness decreased from 78 nm to 42 nm, respectively. A thickness ratio (dry/humid) higher than 1.75 can be reached if the spin-deposition humidity is not restricted when preparing the thin films, as shown in Figure 3.4 (c). Afterwards, *Kim et al.*[324] studied the humidity and temperature influence in the formation of solution-based oxide thin films for TFT applications. An improvement in the thin films' quality was noticed for humidity values higher than 30 % for the as deposited aluminum oxide thin films, without the presence of partial cracks. Increasing the humidity to 40 – 50 % and the temperature from 25 °C to 35 °C during the film deposition enhanced dramatically the current density and breakdown field of the dielectric. Therefore, the TFTs produced with humidity lower than 40 % presented a poor performance related with the high leakage current through the insulator. Then, controlled environment should be mandatory to avoid these significant variations, humidity and temperature change can depend on place and even time of year.

The precursor concentration plays a crucial role on oxide thin films formation by spin-coating process. Lu et al.[325] noted that as the concentration increased, the dielectric properties improved (lower current density) of zirconium oxide, however if the concentration value is equal or higher than 0.7 M cracks start to appear. Another relevant point related with concentration is the higher amount of organic residues in low temperature (≤ 150 °C) oxide thin films used in annealing.

Typically, higher temperatures are required to increment the film densification and eliminate remaining organic residues, as depicted in Figure 3.4 (d).

3.2.2. Post-deposition process to form the M-O-M network

Mainly low temperature annealed oxide thin films have higher number of metal-hydroxide bonds then of metal-oxide-metal frameworks, which will affect straight the TFTs operation and stability. Photoactivation processes have been widely used for lowering the annealing temperature by changing different parameters (source type as lamp or laser; wavelength; intensity and time).[329] In 2012, *Park et al.*[3] report a method using deep-ultraviolet (DUV) to photochemically activate sol-gel metal oxide semiconductor thin films. The DUV irradiation from the mercury lamp (184.9 nm (10 %) and 253.7 nm (90 %)) induces photochemical cleavage of alkoxy groups, and activates metal and oxygen atoms to enable M-O-M network formation of the as-spun films at low temperature (unintentional heating up to 150 °C from lamp). This leads to a rapid decrease of carbon and oxygen contents in the first 30 min of exposure, known as condensation. Then, by increasing the time exposure a gradual structural rearrangement and film densification occurs. Similar material and electrical characteristics compared to high temperature annealing were reached adopting this method. This novel route allows the achievement of low temperature solution-based metal oxide semiconductors with high quality being compatible for printed and flexible electronic devices. In 2015 the same group went deeper to understand the physicochemical mechanism of sol-gel oxide films including semiconductors and insulators.[20] A rapid film formation within 5 min via in situ radical-mediated reactions by DUV was demonstrated in Figure 3.5 (a) supporting a fast densification and removal of impurities. Stable and reproducible all-solution metal oxide TFTs were achieved with a high mobility (> 12 $cm^2/V{\cdot}s$).[20] *Alastalo et al.*[21] combined a more energetic UV lamp, far ultraviolet (FUV) irradiation, and low thermal annealing (150 °C - 250 °C) to convert efficiently metal-nitrate-based precursors to metal-oxide semiconductor (IZO and In_2O_3) in a short processing time (< 30 min). The FUV light with the main peak at 160 nm caused an efficient *in situ* hydroxyl radial formation resulting into a continuous M-O-M structure in the film in just 5 min. In_2O_3 TFTs annealed for 15 min at 180 °C reached a high mobility of 3.2 $cm^2/V{\cdot}s$ being relevant for R2R process conditions once a short annealing time was applied.

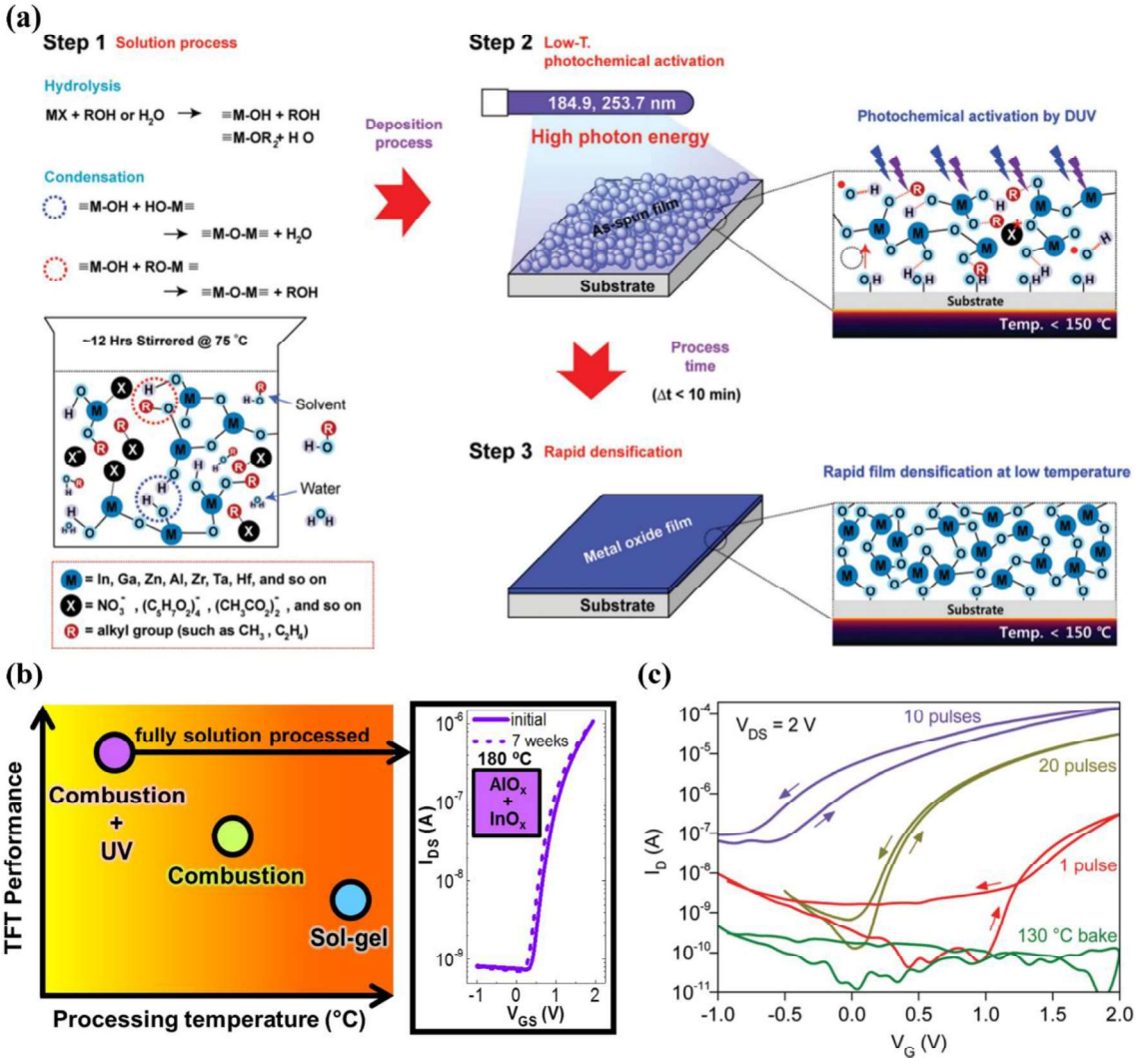

Figure 3.5. (a) Overall schematic illustration of the rapid low-temperature photoactivation of various sol–gel metal oxide films. Reproduced with permission.[20] Copyright © 2015 WILEY-VCH Verlag GmbH & Co. KGaA, Weinheim; (b) Proposed mechanism of the low temperature photoactivation combined with the combustion synthesis of metal oxide thin films for TFT performance. Reproduced with permission.[307] Copyright © 2016, American Chemical Society; (c) Transfer characteristics measured for In_2O_3 TFTs after soft-baking at 130 °C and subsequently exposed to 1, 10 and 20 xenon light pulses with energy density per pulse and duration of 5 J/cm^2 and 500 ms, respectively. Multiple pulse exposure was performed at a fire rate of 1.2 Hz. Reproduced with permission.[337] Copyright © 2017, Royal Society of Chemistry.

Afterwards, *Fortunato el al.*[307] also combined FUV irradiation to produce fully solution based In_2O_3/AlO_x TFTs in a short processing time (15 min) at low temperature of 180 °C. In that work the combination of combustion synthesis and the influence of FUV irradiation to produce aluminum oxide thin films was reported for the first time being relevant to reduce the annealing temperature and stabilize the devices, as observed in Figure 3.5 (b).

Moreover, pulse-light-induced annealing via xenon flash lamps with a wide wavelength (350 - 950 nm) are also used to fast curing and sintering of solution-based metal oxides. This high photon energy process allows a high throughput and a low substrate heating since there is a low heat transfer to the substrate. ZnO TFTs combining a heating stage at 90 °C and 30 pulses from a xenon lamp exhibited the best performance with a mobility of 0.06 $cm^2/V \cdot s$.[338] This approach is compatible with flexible substrates and printing as short-duration and low-temperature annealing were performed. *Anthopoulos et al.*[337] accomplished an ultra-fast processing time of less than 18 s per layer on solution based oxide semiconductors using a high-power xenon flash lamp (200 - 1500 nm). Higher mobilities (36 $cm^2/V \cdot s$) and low voltage operation were achieved with In_2O_3/ZnO heterojunction TFTs. By this method the optical energy, light pulse duration and number of pulses can be changed being ideal for the control of M-O-M thin films formation in TFTs as observed in Figure 3.5 (c). The considerable advantage of this photonic curing is the high temperature reached on the surface of the films without increasing the substrate temperature, which remains close to room temperature. Therefore, this approach has great potential for ultra-fast processing metal oxides over large areas required for printing lines.

Changing the photoactivation source type to a laser irradiation process enables area selectivity and fast film densification which are key factors in printing of solution-based metal oxides. *Koutsogeorgis et al.*[327] validate the use of KrF (UV wavelength of 248 nm) excimer laser to form as-spun solution-processed In_2O_3 thin films dried for 15 min at low temperature (150 °C). The laser annealed In_2O_3 TFTs showed higher mobility (13 $cm^2/V \cdot s$) when compared with the reference device annealed at higher temperature (250 °C). The proposed laser annealing does not rely in controlled atmosphere, which can simplify its scale up and application to the printing industry.

Also, a laser spike annealing (LSA) with near-infrared (NIR) can provide a rapid temperature increase into a specific region in a short processing time reducing the thermal energy on the substrate through a rapid cooldown. *Guo et al.*[339] demonstrate the improvement of solution based IGZO TFTs baked at 200 °C by scanning with a NIR (1064 nm) laser 40 times, as illustrated in Figure 6 (a). However, with this sort of laser is not possible to use single pulses in the ns range as with excimer laser annealing (ELA).

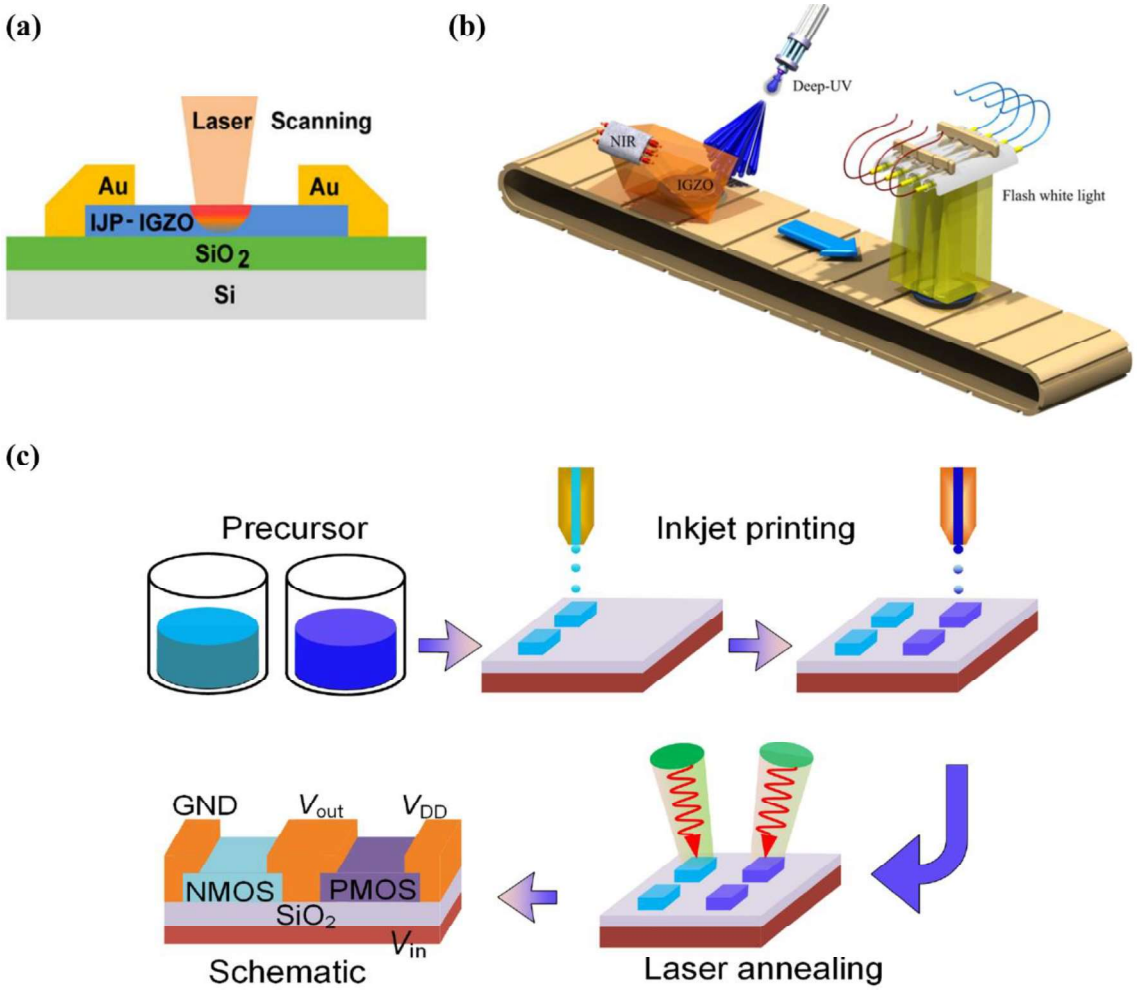

Figure 3.6. (a) Schematic diagram of a laser spike annealing treated IGZO TFTs. Reproduced with permission.[339] Copyright © 2017, The Minerals, Metals & Materials Society; (b) Schematics of the IPL annealing process of IGZO via flash white light combined with NIR and DUV drying. Reproduced with permission.[340] Copyright © 2019, American Chemical Society; (c) Schematic for CMOS inverters via inkjet printing (IJP) and laser annealing (LA).[341] Copyright © 2019, IEEE.

Lately, *Kim et al.*[340] adopt the photoactivation combination of different wavelengths to form solution processed IGZO thin films without any thermal annealing. First, the films were dried with near NIR and DUV light simultaneously, and then annealed with intense pulse light (IPL) as observed in Figure 3.6 (b), accomplishing high mobility and on/off ratio IGZO TFTs.

Recently, Guo *et al.* [341] reported the use of a femtosecond (fs) laser to anneal inkjet printed p-type and n-type metal oxide thin film transistors, as depicted in Figure 3.6 (c). These oxide TFTs were combined to produce CMOS inverters which displayed a gain over 10. The results achieved pave a practical path to produce low-power consumption integrated circuits for large area without additional connection.

In a general overview, the treatment methods with ultraviolet irradiation (DUV and FUV) are more effective as the precursor solutions or xerogels of metal oxides absorb UV light and the photons energy is higher compared to visible and infrared light. Also, in terms of light source, UV lasers will be highly demanded in printing industry to densify the thin films by a selective mode in a short processing time without damaging sensitive substrates.

Other post-treatment processes have been used, as microwave irradiation annealing, rapid thermal annealing, high pressure annealing, atmospheric-pressure plasma, and plasma assisted annealing.[342–347] However, these processes require more confined conditions (chamber, controlled environment, substrate type), which are not suitable for in-line printing industry.

3.3. Solution-processed high-κ oxide dielectrics for TFTs application

Most of research has been focused on solution-based oxide semiconductors, which is considered the "brain" of the TFT, however the dielectric plays a crucial role on the TFT performance being considered its "heart". The gate dielectric controls the conductance of the semiconductor channel by inducing charge carriers at the semiconductor/dielectric and at the same time behaves as electrical insulator to avoid leakage current. Silicon dioxide (SiO_2) has been widely used in modern complementary metal oxide semiconductor (CMOS) technology but the demand of miniaturization and integration to achieve smaller and faster circuits lead to some issues. When SiO_2 thickness is scaled down to 1.2 nm a high tunnel current is caused (Figure 3.7 (a)) forcing a high power dissipation in CMOS logic chips due to the severe gate leakage.[348] In 2001 this problem started to be surpassed by replacing SiO_2 ($\kappa = 3.9$) with a high-κ dielectric, HfO_2, enabling a thicker layer to afford the same capacitance, i.e., the effective oxide thickness (EOT) increases proportionally.[349] Subsequently this suppresses leakage current, since tunneling probability drops exponentially with tunneling distance.[350] Afterwards, high-κ dielectrics have been widely investigated in academic and industrial fields for different applications (memories, energy storage, TFTs, capacitors, etc.).

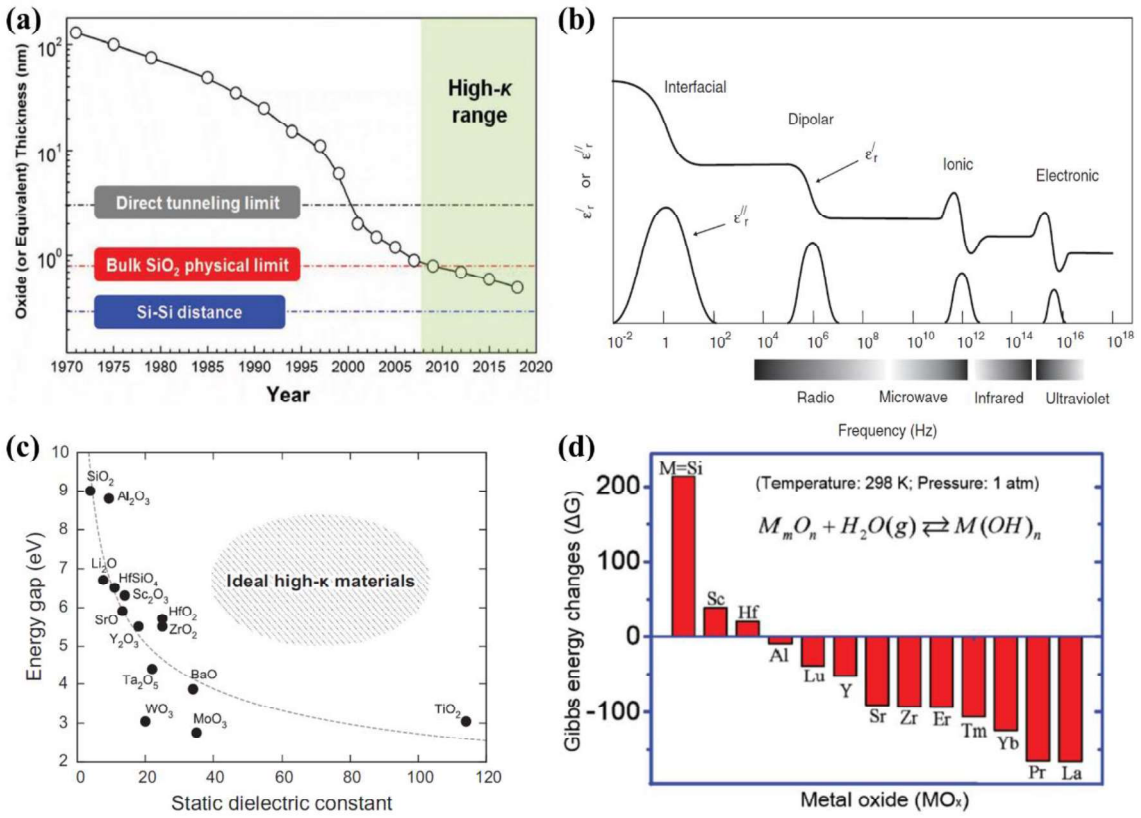

Figure 3.7. (a) The roadmap suggested by the Semiconductor Industry Association (SIA) for gate dielectric thickness scaling. Reproduced with permission.[351] Copyright © 2006 Elsevier B.V.; (b) Frequency dependence of the real, ε_r', and imaginary, ε_r'', parts of the permittivity in the presence of interfacial, orientational, ionic and electronic polarization mechanisms. Reproduced with permission.[352] Copyright © 1969, John Wiley and Sons; (c) The experimental band gap and dielectric constant for well-known oxides. The property region ideal for dielectrics is also shown. Reproduced with permission.[353] Copyright © 2015, Springer Nature; (d) Gibbs energy changes (ΔG) for moisture absorption reactions in high-κ oxides under standard conditions. Reproduced with permission.[354] Copyright © 2010, AIP Publishing.

There are five categories of high-κ dielectrics: ferroelectric polymers, self-assembled monolayers (SAM), electrolyte, organic–inorganic hybrid materials, and inorganic metal oxides.[350] In this review we will explore in more detail the recent developments in solution processed inorganic high-κ dielectrics and their application in TFTs. Their performance has continuously improved with high-κ dielectrics, mainly the field effect mobility (10–100 $cm^2/V^1 \cdot s^1$) and low operating voltage. Solution-based metal high-κ oxide dielectrics (Al_2O_3, ZrO_2, HfO_2, Ta_2O_5, and Y_2O_3 among others) have been widely studied as alternative to replace the conventional SiO_2 dielectric layer.[355] Moreover, an ideal oxide gate dielectric should have certain characteristics as an amorphous structure, a smooth surface (< 1 nm), a large breakdown field, a high dielectric constant, a low leakage current density (< 1 nA/cm^2 at 1 MV/cm) and low interface defect density with the semiconductor.

The dielectrics capacitance can be defined as:

$$C_{ox} = \frac{\varepsilon_0 \kappa A}{d} \tag{3.1}$$

Where ε_0 is the permittivity of free space, κ is the relative dielectric constant, A is the areal capacitance, and d is the thickness of the dielectric layer.

To know if solution-based oxide dielectric is suitable for application as gate insulator in TFTs some requirements need to be fulfilled. First, the dielectric constant or permittivity of the material should be higher than 10 (ideally > 20) to allow larger film thickness while maintaining the areal capacitance. As such, dielectric films with less than 1 nm EOT have a physical thickness above the direct tunnelling limit and low leakage current density. The advantage of high permittivity materials arises from dipole active displacement of metal ions promoted by their *d*-state electrons. The permittivity represents polarizability in response to an applied electric field, and that leads to a charge reorganization which includes interfacial, orientational (or dipolar), ionic and electronic polarization mechanism, as depicted in Figure 3.7 (b). At low frequencies, applying an electric field leads to interfacial polarization due to the accumulation of charges at interfaces within the material, followed by the reorientation of dipoles, named dipolar polarization. Then, at higher frequencies, ionic polarization arises due to the displacement of positive and negative ions, and also electronic polarization due to the displacement of the electron clouds around the nucleus.[352] This is why high-κ materials show lower permittivity at higher frequencies since ionic charges are not able to respond fast enough to the applied AC electric field. Typically, solution-based oxide high-κ dielectrics provide a lower κ compared to theoretical values allocated to the presence of organic residues and unconverted hydroxides (M-OH instead of M-O-M formation).[356] Furthermore, when these dielectrics are applied in TFTs the capacitance at lower frequencies should always be considered to avoid mobility overestimation.

Besides permittivity another relevant parameter is the materials bandgap (E_g) which controls the band offset with adjacent semiconductor. A high bandgap (E_g) is demanded in the dielectric film since it allows the mitigation of parasitic electrical conduction by blocking the charge injection between the dielectric and the electrodes, and reducing the thermal generation of intrinsic free carriers. Most of the high-κ oxide dielectrics display a confined E_g and smaller band offset caused by the *d*-state electrons and high coordination ionic bond. Mainly, a metal oxides` bandgap is ruled by the metal electronegativity which influence the metal oxide bond ionicity disturbing the conduction band.[349,357] To assure an enough band offset (> 1 eV) with the semiconductor the insulators bandgap should be higher than 5 eV. If lower band offset than 1 eV prevail, a thermionic emission of electrons or holes into the dielectric band will arise causing the increase of the leakage current. For this reason, insulators even with κ values higher than 40, like TiO_2, Sc_2O_3, and Nb_2O_5

dielectrics, are not so suitable as gate dielectrics in TFTs due to the lower band offset energy. ZrO_2 and HfO_2 are desirable gate dielectrics with high permittivity (> 20) and a bandgap higher than 5 eV. Nevertheless, there is a typically a compromise between the energy band gap and the static dielectric constant for different gate dielectric metal oxide materials, as shown in Figure 3.7 (c).

Another significant parameter, even more when solution-based processes are performed to produce oxides is moisture absorption. High-κ dielectrics should have a high resistance to moisture absorption which is strongly linked to the change in Gibbs free energy (ΔG) during the reaction.[354] By increasing ΔG the moisture absorption tends to be suppressed, with Sc_2O_3, HfO_2 and Al_2O_3 high-κ dielectrics, being less exposed to that as depicted in Figure 3.7 (d).

Other conditions must be considered when dielectric material is incorporated into a TFT structure mainly, the dielectric/gate electrode and the dielectric/semiconductor thin film interfaces. The dielectric-semiconductor interface is vital, since the charge transport in the TFT occurs near this interface, so some requirements need to be fulfilled: (i) low surface roughness and surface energy between both layers to enhance charge accumulation and minimize charge-trapping sites, leading to stable devices; (ii) high film density to minimize leakage current; (iii) high dielectric constant and low film thickness to allow low power consumption devices; (iv) large band offset (> 1 eV) contributing to a low leakage current, but not so high to facilitate the carrier injection; (v) defective sites minimization, like dangling bonds and interstitial defects, that obstruct effective polarization; (vi) amorphous structure to have limited grain boundaries and subsequently a low surface roughness, low leakage current and high breakdown voltage. Nonetheless, the main issue in oxide dielectrics applied in TFTs is the leakage current and this can be associated to different mechanisms, categorized as electrode-limited conduction and bulk-limited conduction. The electrode-limited conduction mechanisms (Schottky emission, Fowler-Nordheim tunneling, the thermionic field emission) depend on the electrical properties at the electrode-dielectric interface. The bulk limited conduction depends on the dielectric electrical properties and comprise hopping conduction, ionic conduction, Poole-Frenkel (P–F) emission, ohmic conduction, grain boundary limited conduction, and space charge limited conduction.[352]

Considering the requirements stated above for high-κ dielectrics, ZrO_2, HfO_2 and Al_2O_3 show the most promising properties to reach high performance thin film transistors. In the last decade, intensive efforts have been made to produce these high-κ dielectrics from solution-based processes to decrease the associated costs compared to the high-vacuum conventional methods (CVD and PVD), and the processing temperature, as depicted in Figure 3.8. This allows compatibility with flexible substrates and further implementation in large area electronics. Also, can be noticed that from all the reports from 2009 – 2019 (a total of 66) only 15 % used a process

temperature below 200 °C.[350] Therefore, the studies for each high-κ dielectric where the processing temperature is equal or lower than 150 °C being suitable for low cost flexible substrates (PEN, PET and paper) will be described.

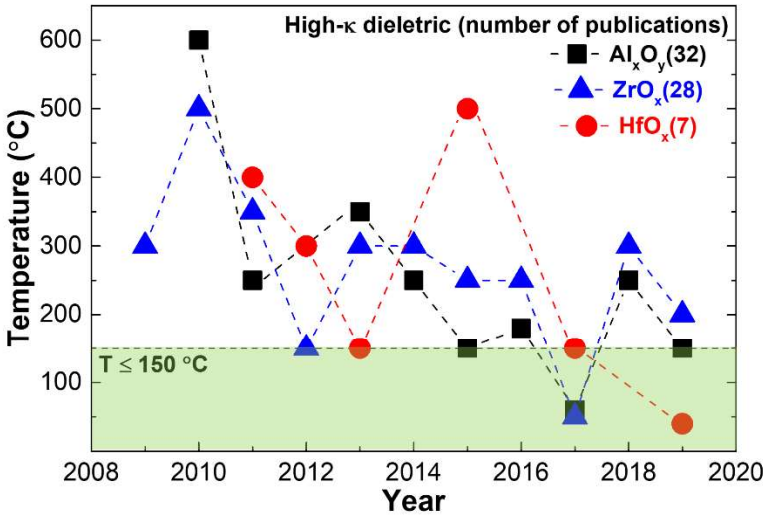

Figure 3.8. Lowest annealing temperature applied in spin coated high-κ binary oxide dielectrics (Al_xO_y, ZrO_x and HfO_x) in the last decade for each year. Copyright © 2021 Elsevier B.V. All rights reserved.

Zirconium dioxide:

In 2012 *Guo et al.*[358] reported the first solution processed ZrO_x via ultraviolet irradiation in zinc oxide TFTs at low temperature (150 °C). The dielectric film had a low surface roughness of 0.18 nm being suitable for a high-quality semiconductor interface. The Al/ZrO_x/Al capacitor exhibits a low leakage current density (10^{-6} A/cm^2), high breakdown voltage (18 MV/cm) and low permittivity of 8.79 at a frequency of 1 kHz. The TFTs showed a low field effect mobility of 0.45 cm^2/Vs, nonetheless this process temperature allows high throughput printing on low-cost or sensitive flexible substrates. In 2017, *Wang et al.*[359] reported a low cost strategy to form solution processed ZrO_2 by ultraviolet ozone (UVO) treatment reaching a maximum temperature of 50 °C. The dielectric reach high-κ dielectric properties, such as permittivity of 13 at 100 Hz, low leakage current (10^{-8} A/cm^2), breakdown higher than 3 MV/cm, and a smooth surface roughness (< 0.54 nm). Also, a fully room-temperature solution processed oxide TFT showed a high carrier mobility of 1.65 cm^2/Vs and a low operation voltage. Nevertheless, one both studies the permittivity values were lower compared to the theoretical value (~25) due to the presence of unconverted hydroxides linked to the low temperature processes and higher porosity of the thin films.

Hafnium oxide:

In 2013, *Baik et al.*[360] reported a method to decompose a hafnium precursor at low temperature (< 200 °C) using an aqueous solution which induces strong hydration of $HfCl_4$ yielding $HfOCl_2$.

This solution-processed high-κ HfO_2 dielectrics is amorphous and present a smooth surface roughness of 0.75 nm. For the lowest temperature (150 °C) the MIM devices showed a capacitance with high dependence of frequency, dielectric constant of ~17 at 20 Hz, leakage current density of 5.7×10^{-6} A/cm^2 at 1 MV/cm and breakdown voltage of 4.4 MV/cm. However, the dielectric constant is higher for the lowest temperature due to the presence of hydroxyl groups (Hf-OH). The ZnO/HfO_2 TFT present a field effect mobility of 1.17 cm^2/Vs but a large leakage current was observed in the devices. To solve some of these issues in 2017 *Fortunato et al.*[92] combined solution combustion synthesis and UV irradiation to produce high-κ dielectrics at low temperature (150 °C). Previously, for a solvent-based (2-methoxyethanol or acetonitrile) solution process a high temperature annealing was needed to process HfO_2 thin films. In that work, a combustion synthesis with a fuel rich condition (ϕ = 1.1) was performed to decrease the temperature required to convert the hafnium oxide precursor from 273 °C to 221 °C using 2-methoxyethanol as solvent. Also, since the HfO_x precursor solution absorbs in the UV region, a DUV lamp was applied to enhance the film condensation and densification at low temperature. The ultrathin HfO_x thin films exhibit a low surface roughness of 0.17 nm an enhanced interface between the dielectric and the semiconductor. The dielectric presents breakdown voltage of 2.7 MV/cm, dielectric constant of 11.7 at 1 kHz and low leakage current density of 2.1×10^{-8} A/cm^2 at 1 MV/cm. The IGZO TFTs with HfO_x as dielectric offer high saturation mobility, low subthreshold slope and operation voltage. Recently, *Ha et al.*[361] reported the use of only UV to cure hafnium oxide precursor thin films with a Hg lamp of 400 W for 3 minutes. These dielectrics show leakage current density of 6.6×10^{-7} A/cm^2 and smooth surface roughness (< 2 nm). The fabricated amorphous oxide TFTs with this method showed the good performance and low operation voltage being suitable for implementation in printing the industry due to the short curing time.

Aluminum oxide:

In 2015, *Park et al.*[20] studied the photochemical activation of distinct sol-gel oxide films (semiconductors and dielectrics) with special attention to aluminum oxide for TFTs application at a maximum temperature of 150 °C. It was noticed that deep ultraviolet irradiation boost the film formation process, such as impurity decomposition, polycondensation and densification in a short period of time (5 min). The photochemical activated aluminum oxide dielectric thin films present low leakage current density of 2×10^{-8} A/cm^2 at 2 MV/cm, high breakdown field (~8 MV/cm) and a low dependence of capacitance with frequency. All solution processed InO_x/AlO_x TFTs with a field effect mobility of 8.33 cm^2/Vs and low subthreshold slope (0.11 V/dec) were achieved allowing further production for large area flexible displays. In 2017, a new strategy to reach ultralow temperature (60 °C) solution based Al_2O_3 dielectric using nanoclusters as precursor

and a spatially controllable photochemical activation via DUV was developed by *Park et al.*[362] This solution processed aluminum oxide exhibits great densification, high breakdown field (> 6 MV/cm), low leakage current density (1×10^{-8} A/cm^2 at 2 MV/cm), dielectric constant of 8.37 and good electrical stability even compared to high-temperature processed dielectric films. The IGZO/(nanocluster-Al_2O_3) TFTs present good average mobility of 5.86 cm^2/Vs and reproducibility. This ultralow temperature dielectric permits the use of low-cost flexible substrates.

Nevertheless, these binary high-κ oxides do not have the best correlation between dielectric constant and the bandgap to be the ideal dielectric for TFTs. Other approaches have been made to simultaneously reach high-κ and large E_g by multicomponent doping (Hf, La, Y, Zn, Mg, Al, Zr, Sr, Na) and multilayers dielectrics. However, these conditions typically require high temperature to form the M-O-M bonding.[350] Few reports have been performed at low temperatures (≤ 150 °C) for both cases and one of the issues is the poor semiconductor-dielectric interface due to high surface energy of the dielectric. *Park et al.*[363] overcome these issues by doping zirconium into the aluminum oxide network. The optimized Zr incorporated (5 %) AlO_x (ZAO) gate dielectric, presented low leakage current density (~10^{-9} A/cm^2 at 1 MV/cm) and high breakdown (> 7 MV/cm). Also, an increase of the dielectric constant was observed with the increment of zirconium doping, from 6.08 (without Zr) to 8.82. The resultant IGZO/ZAO TFTs present a higher mobility and negligible hysteresis compared to pure AlO_x dielectric. In terms of multilayers, *Kim et al.*[328] report a ZrO_2/Al_2O_3-F multilayer dielectric produced at 150 °C assisted by UV exposure. Compared with the single layers of each binary oxide, the leakage current density was improved with the reduction of one order of magnitude to 1.19×10^{-11} A/cm^2 at 1 MV/cm and dielectric constant increase to 12.3 (compared to aluminium oxide). Few years later via the same binary oxides, *Park et al.*[364] invert the bilayer structure to Al_2O_3/ZrO_2 dielectric reaching a high dielectric constant of 8.53 and a low leakage current density (10^{-9} A/cm^2 at 1 MV/cm). This IGZO/(Al_2O_3/ZrO_2) TFTs presented an increase of the field effect mobility and a reduction of the hysteresis by adding zirconium oxide. Also, *Fortunato et al.*[92] studied the effect of high-κ nano multilayer dielectrics with HfO_x and AlO_x combining SCS and UV irradiation at low temperature. The AlO_x/HfO_x bilayer dielectric exhibited a high dielectric constant of 10.4 and the highest breakdown field (4.9 MV/cm) yielding a better interface between the layers. By applying these multilayers in TFTs it was detected that when HfO_x was deposited onto the gate electrode the carrier injection was promoted due to the lower bandgap, which improves the interface (low subthreshold slope) and decreases the off current.

Low temperature solution-based high-κ dielectrics are extremely promising due to the simple, low cost and low voltage operation allowing large-area manufacturing for wearable applications.

To complement that further studies should be done in solution-based high-κ dielectrics to understand how to improve the interface defect density with the semiconductor and between multilayer dielectrics to guarantee stable and reliable TFTs with high performance at low processing temperatures.

3.4. Emerging printing techniques for oxide TFTs

In the last years, several processing techniques have been used to deposit solution-processed oxide TFTs. Typically, solution-based processing techniques, such as spin coating, dip coating, spray coating, bar coating and chemical bath deposition are used to deposit the oxide thin films on the entire substrate.[5] Amongst these, the most adopted technique is the spin-coating due to its simplicity, reproducibility and compatibility with flexible and rigid substrates, as shown in Figure 3.9. However, it is not suitable for large area nor compatible with R2R processing and most of the precursor solution is wasted during the deposition process, remaining only 5 %.

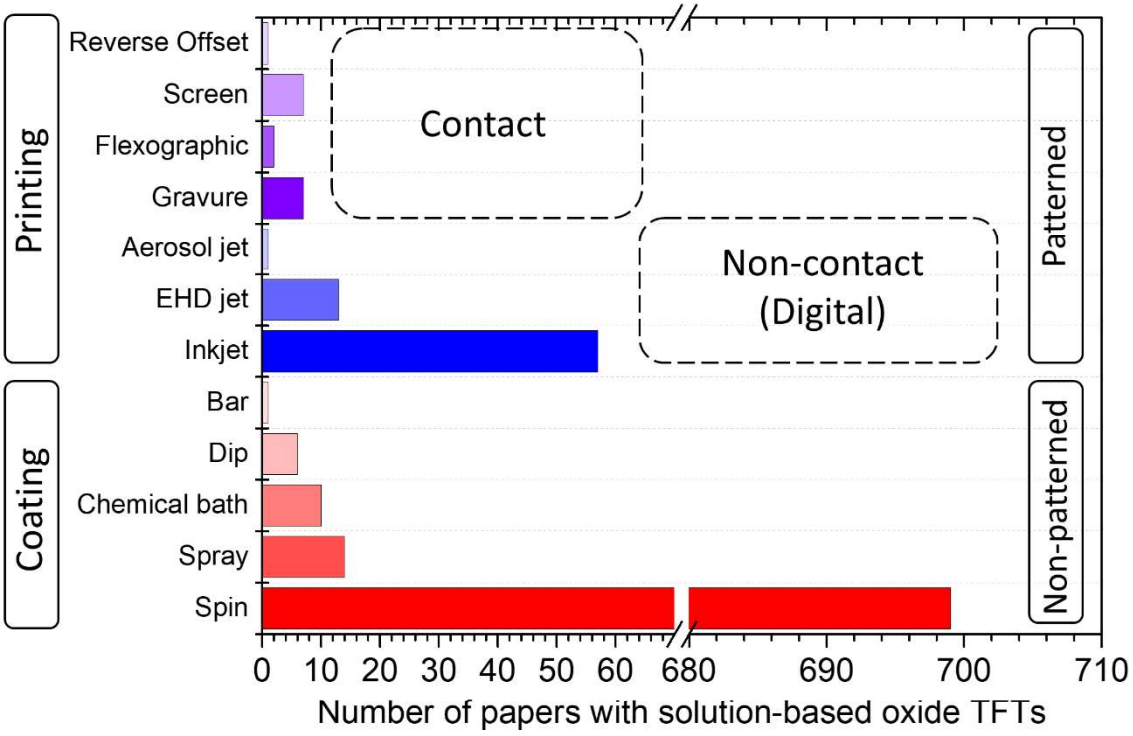

Figure 3.9. The number of publications on the particular processing techniques (coating and printing) in solution-processed oxide TFTs over a decade (2009 – 2019). Copyright © 2021 Elsevier B.V. All rights reserved.

Printing techniques provide scalability, reduction of chemical waste, direct writing of the oxide materials, and higher reproducibility. Nonetheless, before going into more detail in printing processes some critical aspects need to be considered, such as the surface (substrate, printed electrodes and metal oxides) and ink interactions. To measure the surface wettability of the ink the interface between a liquid and solid is studied by contact angle assessment, which depends on the surface tension of the liquid and the surface free energy of the substrate.[365] Namely, if the substrates have a hydrophilic surface subsequently the contact angle is low and the opposite if the substrates are hydrophobic. Consequently, wettability of substrates is enhanced before printing by an O_2 plasma or UV/O_3 treatment to increase surface free energy of the substrate.[366,367] This

surface wettability improvement treatments are highly demanded to control the ink spreading and flow on the substrate, affecting the resolution of printed devices. Another important factor is to maintain ink printability without negatively affecting the electrical performance of the devices which is quite critical in solution-based oxide TFTs.

Printing deposition techniques are divided in two main groups, the contact processes; gravure, screen, flexography and reverse offset) and non-contact processes; inkjet, electrospray and aerosol jet. A brief introduction to the printing techniques and their application to deposit the constituent layers (dielectrics, semiconductors or conductors) of oxide based TFTs will be provided.

Gravure printing is a simple printing process with low ink waste that provides high printing quality (high resolutions patterns) and printing speed, allowing a high-throughput and large area production. In gravure printing, the ink is transferred from carved micro cavities embedded in the printing cylinder, which form the printing pattern as shown in Figure 3.10 (a). Afterwards, the ink is transferred from the printing cylinder to the substrate by matching surface energies. The printing cylinder is partially immersed in an ink bath and before contacting the substrate a doctor blade removes any excess ink and the ink remains only in the cavities.[368] Gravure printing is highly dependent on the pressure applied by the impression roller onto the substrate, ink viscosity and printing speed. The main disadvantage is the high cost of varying the patterns as a new printing cylinder is required. Gravure printing has been widely used in organic thin film transistors (OTFTs) to print all layers. *Kim et al.*[369] reported the first oxide TFTs by gravure printing IGZO semiconductor on glass at 550 °C. The optimized printed layer was achieved with a printing speed of 0.4 m/s and a printing force of 400 N. The printed active layer had a thickness of 45 nm and the resultant TFTs presented a field effect mobility of 0.81 cm^2/Vs. In 2015, *Dörsam et al.*[370] printed IZO layers on Si using ultralow viscosity precursor inks at a printing speed of 0.8 m/s resulting in 10 nm thickness. The IZO TFTs annealed at 425 °C exhibited a small hysteresis and field effect mobility of 9.1 ± 1.4 cm^2/Vs.

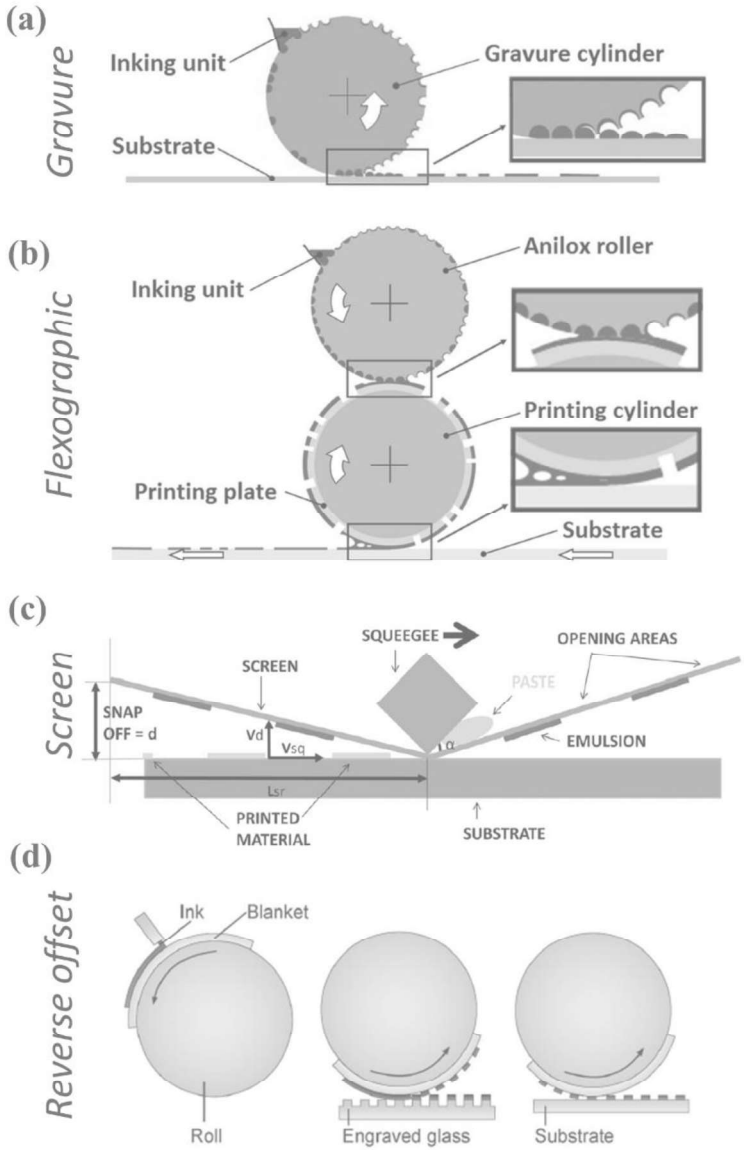

Figure 3.10. Schematic of (a) gravure printing and (b) flexographic printing with the magnified views of the printing nips, where the film separation occurs. Reproduced with permission.[370] Copyright © 2015, IEEE; (c) Schematic of the elements involved in the screen printing mechanism. Reproduced with permission.[371] Copyright © 2015 IOP Publishing Ltd; (d) Schematic illustrations of the reverse-offset printing method: a) inking (left), patterning (middle), and transfer step (right). Reproduced with permission.[372] Copyright © 2015 WILEY-VCH Verlag GmbH & Co. KGaA, Weinheim.

Flexographic printing uses a low-cost and easily tuned soft printing-plate cylinder (made of rubber or photopolymer) with patterned areas in relief protruding the printing plate. This printing process starts with the immersion of an anilox cylinder in an ink reservoir followed by the removal of the excess ink from the non-engraved surface of the anilox. Then, the ink in the engraved cups is transferred to the relief areas in the printing-plate and relocated to the substrate under nip pressure, as shown in Figure 3.10 (b).[373] This technique offers high printing speed and a high

resolution when using nanoporous stamps.[374] In 2015, *Dörsam et al.*[370] printed for the first-time inorganic semiconductors in Si that were applied in TFTs. The IZO thin films annealed at 450 °C revealed a smooth surface roughness (< 1nm) and were printed at 0.8 m/s. Field effect mobility of 2.4 cm^2/Vs was reached and enhanced one year later to 8.1 cm^2/Vs by the same author.[370,375] *Alastalo et al.*[376] reported the first work on metal oxide TFTs where the semiconductor was printed by flexographic printing on flexible substrates. The In_2O_3 semiconductor was printed onto the Al_2O_3 dielectric processed by ALD on a polyimide substrate and annealed at 300 °C. Continuous films with a smooth surface roughness of 0.5 nm were formed using a low viscosity ink (2 cP) and a high printing speed (50 m/min) allowing R2R compatibility. The high performance In_2O_3 TFTs showed a high saturation mobility of 8 cm^2/Vs and turn-on voltage of 0 V, which paves the way for printed circuits on flexible substrates. Recently, *Fortunato et al.*[309] using the same technique printed a highly stable ultra-thin high-κ oxide dielectric at low-temperature annealing (≤ 200 °C) combined with low-wavelength far-ultraviolet (FUV) exposure on flexible substrates. The ink viscosity was higher (28.4 cP) when compared to that of the semiconductor reported by *Alastalo et al.*[376] to reach a thicker layer with only one print and avoid interface issues. In the near future, it is expected that R2R printed metal oxide TFTs and circuits will be achieved on low cost flexible substrates for large area applications.

Screen printing is the simpler and inexpensive method compared to the other contact methods where the process involves a mesh to transfer the inks to the substrate. The ink is pushed through the open areas in the mesh with the help of a squeegee, as depicted in Figure 3.10 (c). This technique requires high viscosity inks resulting in thicker films and low volatility solvents. Screen printing is divided in two main methods, flatbed screen printing and rotary screen printing. However, for large scale processes rotary screen printing is ideal, since it can reach speeds over 100 m/min compared to 0 – 35 m/min for flatbed screen printing.[368] The finest feature size that can be obtained is more limited compared to the other printing techniques. Screen printing have been mostly used to print conductive inks for electrodes in TFTs, where the most common are silver based conductive inks.[377] In 2015, *Fukada et al.*[378] reported screen printed electrodes for oxide TFTs and incorporate it on an active matrix backplane. Recently, a zinc oxide nanoparticle matrix was screen printed to produce electrolyte gate transistors at low processing temperature on paper substrates by *Pereira et al.*[379]

Reverse offset printing (ROP) is an emerging technique that uses low viscosity inks being easier to form a semi-dried film and enables high throughput, high-resolution printing and patterning. The method can be divided in three steps: (i) the ink is coated using capillary slot coater over the entire surface of a silicone blanket of polydimethylsiloxane (PDMS); (ii) then a pattern is defined by pressing the coated blanked softly against an engraved glass (rigid) or metal foil (flexible)

substrate, also called stamp; (iii) to finalize, the ink pattern remaining on the blanket is transferred to the substrate, as shown in Figure 10 (d). Since in reverse offset the ink that remains on the blanket is transferred onto the receiver (final substrate) is considered a subtractive transfer printing. Also, if the stamp pattern is too flat or the nip pressure (between the blanket and the stamp) is too high, undesirable contact of the stamp with the ink can occur resulting in excess ink removal.[380,381] This method has been mostly used to print electrodes and was first reported by *Chung et al.*[382] to deposit silver metal electrodes.[382–385] However, these printed electrodes required higher temperature (> 200 °C) to achieve proper conductivity which is not compatible with low cost flexible substrates. In 2015, *Tokito et al.*[372] reached submicrometric channel lengths (0.6 μm) with reverse offset using silver nanoparticles inks being quite relevant for large-scale device manufacturing. Recently, *Leppäniemi et al.*[386] demonstrated for the first time the printing of In_2O_3 semiconductor using ROP with linewidths down to ≈2 μm. The source and drain electrodes were also printed with ROP and this In_2O_3 printed TFTs on flexible substrates exhibited mobility of 1.4 cm^2/Vs. In general, ROP has multiple advantages compared to conventional printing, as large-area patterning, submicrometric resolution, uniform layer thickness and good edge definition. The patterned features achieve similar dimensions to photolithography without additional subtractive processes (etching or lift-off).

The non-contact printing processes also called digital printing which, rely on images or patterns that are in the digital format. These are electronic design files, the opposite of the contact mode where printing relies on a master or a template that carries the images or patterns and cannot be changed. The digital images can be easily altered, and every printing can be customized. Typical digital printing techniques are electrohydrodynamic (EHD) jet printing, aerosol jet printing and inkjet printing the most used to produce oxide based TFTs, as depicted in Figure 3.11.

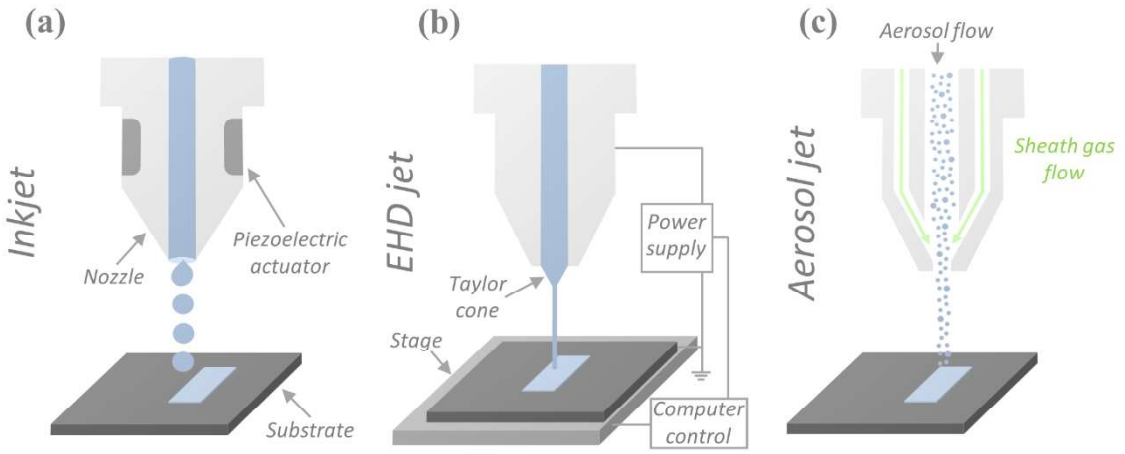

Figure 3.11. Schematic diagrams showing the working principles of (a) piezoelectric drop-on-demand inkjet printing, (b) a jetting mechanism of the electro-hydrodynamic jet printing and (c) an aerosol jet printing system. Copyright © 2021 Elsevier B.V. All rights reserved.

Inkjet printing is widely explored in lab scale research in printed electronics where many parameters (volume, velocity, direction and number of ink droplets as well as the temperature of the ink or substrate) can be controlled in a precise way being one of the most promising alternatives to vacuum processes. Many ink materials can be inkjet-printed, as organic and inorganic, polymers, carbon and metallic materials. The most reliable printing materials are metallic conductive inks, mostly silver (Ag) where good conductivity and chemical stability is achieved. Some critical requirements are demanded for the ink materials to extract the full profit of inkjet, such as low volatility to avoid nozzle clogging, low viscosity, surface tension and if the ink is a colloid or a suspension the particles should have fine size. Inkjet printing deposition depends on the formation of droplets at or near a nozzle aperture and can be divided into two modes of operation, continuous or drop-on-demand (DOD). However, DOD inkjet is the most popular operation method in printed electronics and comprise the ejecting of ink droplets when a pulse voltage is applied. Based on the driving force behind the fluid ejection from the printer head, two main mechanisms exist: the thermal and piezoelectric inkjet propelling. In the thermal printer head an electrical current is applied through a heating element to locally vaporize the ink to form a bubble in the chamber that will cause a pressure increase thus pushing an ink droplet from the nozzle. In the piezoelectric printer head a voltage is applied to the piezoelectric pressure transducer to make bend or change shape which results in the ink jetting from the nozzle, as shown in Figure 3.11 (a).[373] If the nozzle diameter is larger, the printing experience is easier although printing resolution is lower. Since in the piezoelectric inkjet printing the adjustment of the actuation signal is easier, these printing heads present higher durability and higher compatibility with the ink formulation, being preferred for printing functional materials.[387] In 2007, *Chang et al.*[319] reported for the first time the inkjet printing of a metal oxide semiconductor (ZIO) and its

application in TFTs with a mobility of 16 cm^2/Vs. Since then various oxides semiconductors (IZTO, IGO, IGZO, InO_x, ZnO and ZTO), oxide dielectrics (AlO_x and ZrO_x) and transparent conductive oxides (ITO, ATO, FTO and ACO) have been printed but the majority still require high annealing temperatures (> 250 °C). Also, almost all suffer from coffee ring effect. This phenomenon occurs due to the higher evaporation rate on the edge region of the droplet compared to the centre region, resulting in a non-homogeneous film formation which affects the performance of printed TFTs. Then, several ways to minimize this effect were developed: (i) high substrate temperature to evaporate the solvent before the droplets spread completely;[388] (ii) mixture of minor (high boiling point and low surface tension) and major (low boiling point and high surface tension) solvents where the minor solvent addition retards the evaporation at the contact edge, known as Marangoni flow;[389] (iii) increment of the ink viscosity being highly resistant to the outward capillary flow;[390] and (iv) increase of the metal precursor concentration avoiding additional solvents or stabilizers.[339] *Cui et al.*[391] overcame other issues related to spreading of the ink droplets which determines how close two ink droplets can be placed by performing a substrate surface treatment (hydrophobic) and incrementing the ink viscosity to avoid the random movement of the ink droplets. Printed PVP-doped IGZO oxide TFTs were achieved with a small spacing of 50 μm and mobility of 6.2 cm^2/Vs. Also, with inkjet printing it is possible to produce a fully inkjet printed metal oxide TFT as reported by *Subramanian et al.*[382], *Lan et al.*[392] and *Sharma et al.*[393] However, high temperature annealing (> 400 °C) was performed in the processing of each constituent layer to reach these devices. Recently, *Subramanian et al.*[333] reported all inkjet printed layers (source and drain, semiconductor and dielectric) processed at a low temperature of 250 °C with UV irradiation for metal oxide TFTs. However further improvement is required to achieve ≤ 150 °C processing of metal oxide layers to allow compatibility with low cost flexible substrates (PEN, PET and paper). *Ning et al.*[394] printed silver electrodes at a low temperature of 150 °C with a silver salt ink instead of colloidal silver inks, however this can lead to carbon residues in the conductor-semiconductor interface. Then, *Gilliam et al.*[395] improved this the interface while maintaining 150 °C by adding a doped semiconductor interlayer that promotes the electron transport between the inkjet printed silver electrodes and the semiconductor layer. This results in a decrease of the contact resistance improving the charge carrier mobility by two orders of magnitude. In terms of the semiconductor, *Leppäniemi et al.*[65] accomplished inkjet printed In_2O_3 TFTs at low temperature annealing (150 °C) combined with FUV exposure on flexible PEN substrates. To reach lower temperature in a shorter processing time, *Dasgupta et al.*[396] reported high performance inkjet printed In_2O_3 TFTs processed using photonic curing after the films´ drying at 100 °C for 2-3 min. The devices showed a high mobility of 29 cm^2/Vs and low operation voltage which paves the way for printed electronics on flexible substrates. Recently, for high-κ oxide dielectrics *Bolat et al.*[397] investigated the effect of inkjet

printed yttrium oxide on aluminium oxide thin films at low temperature of 150 °C assisted by DUV irradiation and applied in TFTs. The flexible oxide TFTs presented a high current on/off ratio of 10^8 and a mobility of 4.3 cm^2/Vs with a good stability opening the window for large-scale manufacturing.

Electrohydrodynamic (EHD) jet printing technique can solve some of the drawbacks present in both thermal and piezoelectric inkjet printing, such as the limited printing resolution, undesired flow of large ink volume printed in the substrate, nozzle clogging and droplet deviation. This emerging technique enables high-resolution patterns with submicrometric features with a minimal printing feature size of 0.1 μm and a precise line width down to less than 1.5 μm.[398] EHD jet printing uses an electric field to create the ink flow through a fine nozzle (as small as 300 nm in diameter) onto a substrate. The mechanism behind that is electrohydrodynamics, the study of the dynamics of electrically charged fluids. The ink in this technique is pumped through a nozzle by a syringe pump and a strong electrical field is applied between the nozzle and the conductive substrate holder. Then, when the applied electric field overcomes the surface tension, a droplet (considerable smaller than the nozzle diameter) is formed and ejected out to the substrate, as depicted in Figure 3.11 (b).[373] Nonetheless, despite the high resolution, EHD printing present some issues as the non-compatibility with large areas printing due to slower process speed and non-uniform films printability if the inks present low conductivity. In 2012, *Paik et al.*[399] printed a high resolution (1.5 μm) IZO semiconductor with 10 nm thickness by EHD for the first time applied in TFTs. The semiconductor was annealed at 500 °C, and the IZO/HfO_2 TFTs present a high mobility of 32 cm^2/Vs and a low operating voltage. IZO and ZTO semiconductors were printed with the same technique but did not reach such high resolution.[400–402] *Park et al.*[403] printed a high resolution (minimum line width of 2 μm) In_2O_3 semiconductor at low temperature (250 °C) on flexible substrates. The resultant In_2O_3/Al_2O_3 TFTs exhibit a mobility of 5 cm^2/Vs and open the window for wearable electronics using this technique.

Aerosol jet printing starts with the production of an aerosol (colloid of solid particles or liquid droplets in a gas between 1-5 μm in size), where the ink is turned into a dense aerosol ultrasonically or pneumatically in an atomizer. Through the help of a carrier gas a pressure is built-up in the atomizer, which ensures the ejection of aerosolized particles toward a target substrate by aerodynamic focusing. Also, a sheath gas is applied to shield the aerosol particles from the inner walls of the print head nozzles during the high velocity particle stream so the deposition remains focused on the substrate, as shown in Figure 3.11 (c).[398] Aerosol jet printing is more tolerable to different ink materials (wider range of viscosities) and prevents nozzle clogging issues compared to inkjet printing.[373] Also, this technique allows higher resolution features (< 5 μm) and the possibility to eliminate the coffee ring effect formation due to the

formation of very small droplets (0.0001 – 0.0005 pL in volume).[404] This technique presents some challenges but the main issue is the lagging effect when the printing parameters are adjusted since a large amount of atomized liquid droplets are constantly under flow being harder to track compared to a single droplet of inkjet printing. The aerosol jet printing has been mainly used to print polymer dielectrics, source and drain electrodes (TCOs and metals), and semiconductor oxides.[387] In 2013, *Frisbie et al.*[405] reported high performance, aerosol-jet printed ZnO electrolyte gate transistors (EGTs) in flexible substrates. The ZnO EGTs exhibited low operation voltage and subthreshold slope, and were later integrated into complementary circuits.[406] More recently the same group produced In_2O_3 EGTs with a high mobility of 11 cm^2/Vs by aerosol jet printing.[407]

An in-depth comparison between contact and digital printing techniques was made for different printing features (ink viscosity, film thickness, throughput, printing speed, resolution, line width and alignment accuracy), as shown in Table 3.1. As can be observed, non-contact printing techniques have a higher alignment accuracy in general when compared with contact printing techniques. On the other hand, the roll-based techniques (contact mode) exhibit a high throughput (suitable for high-volume large area manufacturing) but are limited by the patterns defined in the metal rollers or plates. Also, using a high printing speed can affect the printing resolution.

The future of printing electronic industry can reside on the combination of both contact and non-contact printing techniques, thus allowing the combination of high resolution and throughput. However, some major challenges still remain in oxides TFTs printing, such as the high annealing temperature required for the semiconductor and dielectric layers, as depicted in Figure 3.12. In a general overview most of the printed oxide TFTs require temperature above 200 °C to achieve metal-oxide thin films. For printed oxide semiconductors (ZnO and In_2O_3), only inkjet (thermal and piezoelectric) and screen printing require temperatures below 200 °C. In terms of printed high-κ oxide dielectrics both, flexographic and inkjet printing allow low temperature processing.

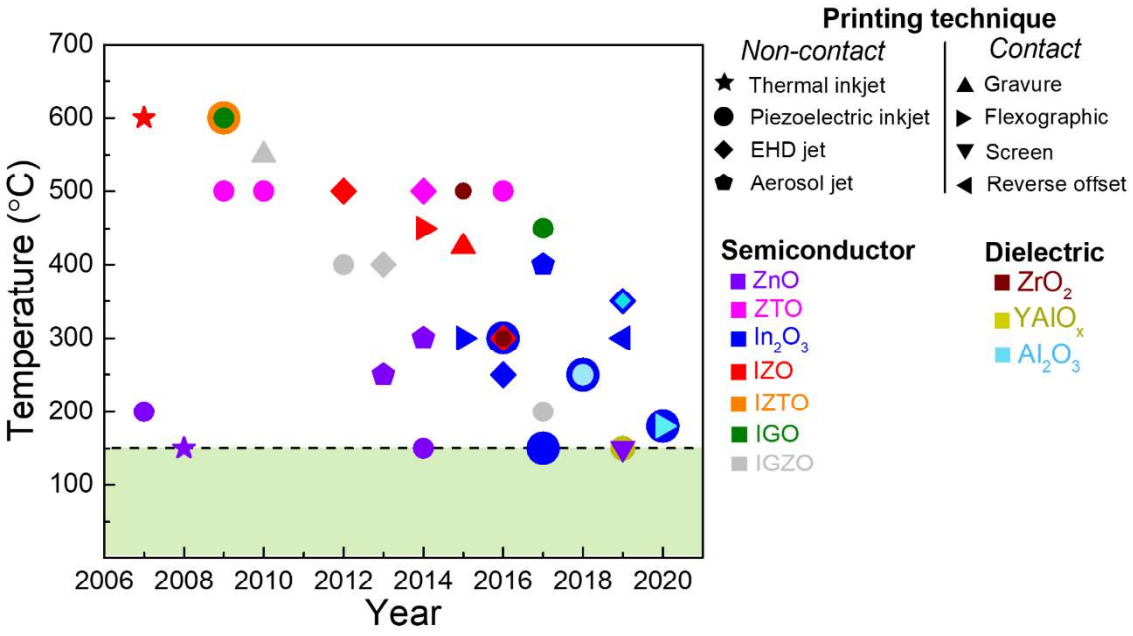

Figure 3.12. Lowest processing temperature required for printed metal oxide semiconductors and dielectrics applied in metal oxide TFTs using different printing methods.[65,286,294,309,319,333,339,366,369,370,375,379,386,390,392,397,399–403,405–418]

An overall trend to decrease the annealing temperature (more evident in the last 3 years) in printed metal oxide TFTs can be observed due to ultraviolet irradiation mentioned in the previous sections. This low temperature condition is crucial to allow implementation of oxide TFTs on flexible substrates and to avoid thermal expansion of the substrates which will affect device quality, as shown in Figure 3.13. The XENOMAX polyimide (PI) flexible substrate is the most suitable as it can withstand higher temperatures, it has a low surface roughness (< 1nm) and a low coefficient of thermal expansion (CTE) of 3 ppm/°C, even lower than glass. However, these PI based substrates are coloured which hinders transparent electronic applications and are much more expensive than PEN or PET which require low annealing temperatures to avoid degradation. For this reason, it is paramount that printed oxides are processed at low temperatures in order to decrease the associated costs in the printing industry and allow large scale production.

Table 3.1. Comparison of characteristic features and ink properties for different contact and non-contact printing techniques.

		Feature						
		Ink viscosity (cP)	*Film thickness* (nm)	*Throughput*[a)] (m^2/s)	*Printing speed* (mm/s)	*Resolution* (μm)	*Line width* (μm)	*Alignment accuracy* (μm)
Contact Printing Techniques	*Screen* [379,419–426]	30 – 12000	1000 – 25000	Medium/High	50 – 100000	30	40	± 10
	Gravure [313,419,426–431]	100 – 12000	10 – 400	High	5 – 1000000	2	35	± 10
	Flexography [374–376,419,426,432]	2 – 500	5 – 50	Medium/High	200 – 500000	1	3	± 10
	Reverse offset [380,384,386,433,434]	1.5 – 70	15 – 400	Medium	0.8 – 200	1	2	1 – 2
Non-contact (Digital) Printing Techniques	*Piezoelectric Inkjet* [419,435–440]	1 – 30	100 – 500	Low/Medium	1.25 – 7000	2	2 – 8	± 2
	EHD jet [402,403,441,442]	1 – 10000	20 -180	Low	0.2 – 8	2	2	± 1
	Aerosol jet [407,443–446]	1 – 1000	30 – 150	Low	0.1 - 10	10	10	1 – 2

[a)] *Low (< 0.01 m^2/s); Medium (0.01 – 1 m^2/s); High (> 1 m^2/s)*

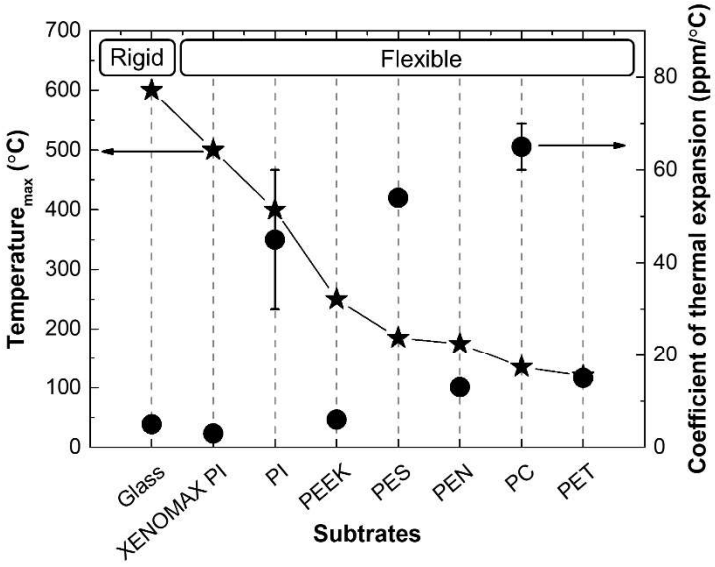

Figure 3.13. Maximum temperature sustained and coefficient of thermal expansion for a rigid substrate (glass) and several flexible substrates. Copyright © 2021 Elsevier B.V. All rights reserved.

Also, beyond the substrate's thermal stability under heat, it should have low moisture and oxygen absorption, low CTE, low shrinkage, and a smooth (< 2 nm of roughness) surface. Most flexible substrates suffer from high surface roughness or, even when the roughness mean square (rms) is low some high aspect ratio features, like spikes are present, for example typical industrial PEN presents a 2.55 nm roughness however several features with height > 50 nm can be observed. This spikes affect the subsequent layers of printed oxide TFTs and the overall performance, although by polishing or applying a specific coating can help overcoming this issue and attain a smother surface.[447] Besides the substrate and the printed oxide layers (semiconductor and dielectric), the printed electrodes also play a crucial role in the device integration. The challenges that need to be surpassed, in electrodes printing include film thickness, surface roughness and annealing temperature. Figure 3.14 shows the annealing temperature and thickness of printed source and drain electrodes in oxide TFTs over the years using different methods. Piezoelectric inkjet printing is the most used technique to print transparent conductive oxides (like ITO, ATO and FTO), however these require high annealing temperatures (≥ 300 °C) to form the M-O-M network. Recently, *Vivek et al.*[418] explored the role of Al doping in cadmium oxide (ACO), increasing the conductivity of ACO electrodes at low temperature (250 °C). Although, the films presented a surface roughness of 18 nm which is expected for printed electrodes and some spikes > 150 nm height were also present. Also, most of the printed electrodes (metallic nanoparticles based and TCOs) require a film thickness ≥ 100 nm to maintain the required conductivity. Then, thicker dielectrics are required to compensate these artifacts (high roughness, coffee ring effect) and ensure reliability of the devices. Therefore, printed underlying gate electrodes are not yet

applied in printed oxide TFTs since the higher roughness of the printed gate affects device reliability and induces defects to the subsequently printed layers.

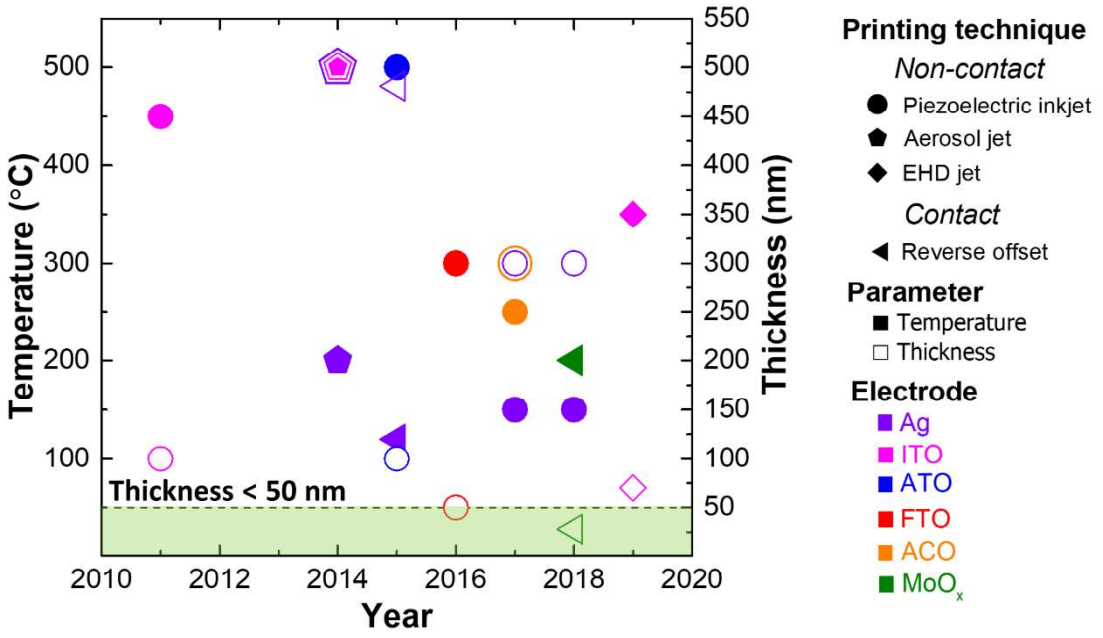

Figure 3.14. Lowest processing temperature and thickness of printed source and drain (S/D) electrodes applied in metal oxide TFTs using different printing methods.[294,366,383,394,395,417,418,448,449] Copyright © 2021 Elsevier B.V. All rights reserved.

Recently, *Kusaka et al.*[383] report the use of reverse offset printing, an emerging technique, to print metal acetylacetone inks to produce conductive source and drain electrodes. The metal inks were dried at 130 °C and then treated by hydrogen plasma for 60 s at 200 °C. The MoO_x printed layers present the highest conductivity among the metal ink materials being selected for S/D electrodes. The breakthrough of using this technique for printed electrodes is related to the low pronunciation of the coffee ring effect (good edge definition) and the smooth surface. The MoO_x S/D electrodes present a low thickness of 28 nm and surface roughness of 0.22 nm. Since these features can be achieved with a good conductivity at relative low temperature the printing of the gate electrode for printed oxide TFTs became a possibility. A printed gate electrode with these characteristics will be ideal to print thin (< 30 nm) high-κ oxide dielectrics and semiconductors on top.

3.5. Current challenges and future trends

The growth of solution processed oxide TFTs over the last decade has been quite demanding to reach higher throughput, lower costs, decrease the thermal budget and less material waste. At the same time the devices should demonstrate similar performance to the standard vacuum based devices, which present high reproducibility and stability over time. However, some gaps/challenges still exist that need to be further investigated to successful applications for printing industry market:

i. The solution synthesis and deposition of the oxide layers are highly dependent on the ambient humidity and temperature. So, a controlled environment is demanded to preserve reproducibility of the process in solution-based oxide TFTs;
ii. The low processing temperature for most of the constituent layers in the TFT is already reachable with the help of UV irradiation. However, at low temperature some layers present lower densification or even in some cases the complete formation of the M-O-M structure is not reached due to the existence of hydroxyl groups which affect the general performance of the devices (aging, stability).
iii. For applications in the printing industry, the printing speed is a key factor to allow a high throughput. Nonetheless, solution processed oxide TFTs require long processing times (> 30 min) when low processing temperatures (≤ 150 °C) are used which is not compatible with in-line printing (≤ 5 min). For this reason, photonic curing (UV flash lamp or excimer laser) start to be implemented since a short processing time (< 3 min) can be applied with the use of highly energetic pulses in the ns range. This allows the film densification improvement at low temperatures without damaging the flexible substrate, opening the window to large scale production. Excimer laser annealing also allows area selectivity being quite relevant to up-scale in printing industry.
iv. Few reports show the electrical characteristics under stress and stability over time (ageing) of solution-based oxide TFTs. These tests are essential to show reliability and further implementation in printed electronics. Stability issues should be investigated properly to clarify the electrical instability mechanism of these devices;
v. Further studies on hybrid materials will be a requirement to implement the solution-based oxides in ultra-flexible devices to improve ductility and prevent cracks which affect the overall performance of the TFTs;
vi. The performance of a TFT fundamentally depends on the quality of the dielectric-semiconductor interface. However, the research on solution-based high-κ dielectrics is quite limited compared to the semiconductor. Further studies should be performed to enhance the TFT operation at low operating voltages.

vii. The surface roughness plays a crucial role in the device performance when the constituent layers are stacked affecting the overall TFT performance. Currently, the most crucial layer is the gate electrode which relies mainly on nanoparticles offering low temperature processability, but present higher surface roughness. Further work should be performed in this layer to allow a good conductivity at low temperature with a smooth surface (< 2 nm) and low thickness of less than 30 nm to grant a good interface with the subsequent oxide layers (semiconductor or dielectric). Also, more sustainable substrates that are biodegradable, malleable, and present a smooth surface should be developed and studied.

viii. Printing technologies have been increasing their applicability to produce oxide thin films and TFTs. Each printing technique technology demonstrates different ink parameters, different resolutions with certain alignment accuracy and in-line printing speeds, as depicted in Figure 3.15. An emerging printing technique, reverse offset, offers high resolution and accuracy even when compared to inkjet, with no coffee ring effect pronunciation. Reverse offset printing of solution-based oxide TFTs, should be further studied to improve printing speed without compromising resolution.

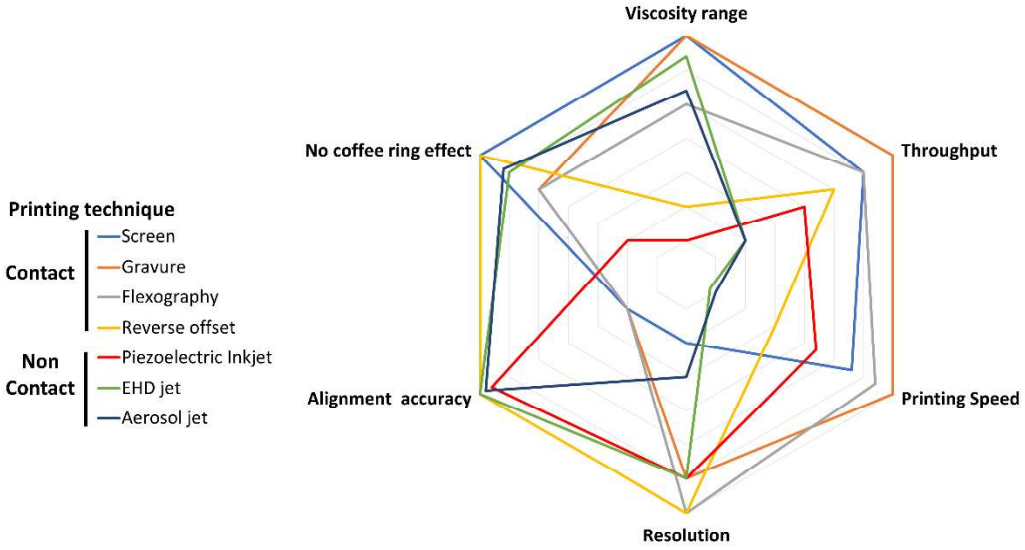

Figure 3.15. Comparison of relevant features for various contact and non-contact printing techniques. Copyright © 2021 Elsevier B.V. All rights reserved.

The outlook of printed metal oxides TFTs is really promising for large-scale manufacturing. We visualize in the next 10 years, the emerging field of printed oxides association to flexible hybrid electronics will boost exponentially the level of industrial research on wearable electronics.

Chapter 4

Solution-based metal oxide thin film transistors

Lately, printed oxide electronics have advanced to meet the challenges in performance and low-temperature solution processability that are required for the dawn of low-cost flexible applications. However, some remaining limitations need to be surpassed. These include the printability of the layers using Roll-to-Roll (R2R) compatible techniques without compromising the device's electronic performance and operational stability. This chapter focuses on recent low temperature approaches as combustion synthesis and irradiation (UV) post annealing treatments which allow their implementation in printable flexible TFTs. First, special attention is given to solution-based high-κ oxide dielectrics produced at low temperature that play a critical role to achieve low power consumption. Next, a significant work is performed to lift printed metal oxide TFTs a step closer to the flexible applications of future electronics. Finally, excimer laser annealing (ELA) is used as a viable option to produce aluminium oxide thin films at low temperature, offering high quality materials at a reduced associated cost and process time.

Keywords: solution combustion synthesis, metal oxides, thin film transistors, low temperature, UV irradiation, printing electronics

The results presented in this chapter are published in:

- ✓ *Emanuel Carlos, Rita Branquinho, Asal Kiazadeh, Jorge Martins, Pedro Barquinha, Rodrigo Martins, Elvira Fortunato. "Boosting Electrical Performance of High-κ Nanomultilayer Dielectrics and Electronic Devices by Combining Solution Combustion Synthesis and UV Irradiation", ACS Applied Materials & Interfaces, 2017;*
- ✓ *Emanuel Carlos, Jaakko Leppäniemi, Asko Sneck, Ari Alastalo, Jonas Deuermeier, Rita Branquinho, Rodrigo Martins, Elvira Fortunato. "Printed, Highly Stable Metal Oxide TFTs with Ultra-Thin High-κ Oxide Dielectric", Advanced Electronic Materials, 2020; (In collaboration with VTT, Finland)*
- ✓ *Emanuel Carlos, Spilios Dellis, Nikolaos Kalfagiannis, Loukas Koutsokeras, Demosthenes C. Koutsogeorgis, Rita Branquinho, Rodrigo Martins, Elvira Fortunato. "Laser induced ultrafast combustion synthesis of solution-based AlO_x for thin film transistors", Journal of Materials Chemistry C, 2020; (In collaboration with Nottingham Trent University, UK)*

4.1. Boosting high-κ dielectrics processed at low temperature

4.1.1. Introduction

Technology has been growing exponentially leading to the necessity of low-cost processes and materials that allow a more sustainable world. For that, printable, flexible, disposable and transparent electronics have been highly explored.[1,8] However, the typical fabrication techniques for oxide films and devices are vacuum-based techniques, like atomic layer deposition, chemical and physical vapor deposition. These techniques require an expensive high vacuum equipment resulting in high production costs.[8] For the production of printed electronics, suitable materials and optimized processes or techniques with low cost manufacturing need to be identified and developed. As a result solution-based thin films have gained a lot of attention due to the low cost, simplicity and good film uniformity in large areas.[450] Spin coating, screen printing, inkjet printing, bar-coating and spray pyrolysis are the mostly used techniques for solution processing oxide semiconductors and gate dielectrics.[78,334,450–452] Actually, choice of suitable functional/active materials that can be printed is essential for the performance of the printed electronic devices. In thin film transistors, the semiconductor layer have been used in organics and inorganics (oxides) with high success at low temperature.[2,3]

The insulator layer plays a crucial role in the devices performance too, by mainly defining the devices stability and operation voltages.[2,3,20,307] Also, the solution process of this layer has been frequently used, either for organics or oxides materials. In the case of organic materials, (Polyvinyl alcohol) PVA or PVP are possible alternatives;[416,453,454] however, these have some setbacks, such as the operation voltage control with the decrease of the thickness, low carrier mobility and instability issues which limit their application.[2,3,307] By using solution based high-κ inorganic dielectrics is possible to enhance the capacitance coupling between the gate dielectric and the channel layer in TFTs. As a result, the subthreshold slope is improved and the operating voltage is reduced leading to low consumption electronic devices.[455,456] Moreover, the use of multilayers allows the insulator to achieve remarkable properties with just one material (e.g. high-κ and band gap).[457,458] The most used inorganic dielectrics are zirconium oxide (ZrO_2), tantalum oxide (Ta_2O_5), aluminum oxide (Al_2O_3), hafnium oxide (HfO_2) and their mixtures.[7,450,457,459,460] The larger capacitance obtained with these allows a higher density of charges induced in the semiconductor, which lead to an easier trap filling. Solution-processed Al_2O_3 and HfO_2 are the most promising candidates, with high dielectric constant, 9 and 25 respectively, and in the case of HfO_2 a lower bandgap (5.8 eV) when compared with Al_2O_3 (8.9 eV).[307,455] Since the bandgap is smaller in the case of HfO_2 the carrier injection is easier than in Al_2O_3.[457,461] However, these materials needed high annealing temperatures, so new methods and techniques have been

developed, like solution combustion synthesis (SCS) and deep ultraviolet (DUV) treatment, to obtain high-quality films at low temperature being compatible with low cost flexible substrates.[2,3] In the case of SCS an oxidizer (nitrates) and a fuel (urea, citric acid) are added to the precursor solution. During the annealing process a exothermic reaction occurs, resulting in a reduction of the external heat required for the film formation; the remove of organic solvents and film densification.[2,7] By using a DUV treatment the films are exposed to high-energy photons which causes the cleavage of alkoxy groups, active metals, and oxygen atoms to simplify M−O−M network formation. After less than 10 min of UV irradiation, the polymeric chains break into smaller fragments, which induces degradation, leading to removal of oxygen, carbon and improving the film densification.[20,307,462] The combination of these methods improves the reliability of the nanoscale film morphology, composition of metal oxides and stability over time. The additional energy provided by the exothermic combustion reaction contributes to enhanced film densification in a short annealing time.

In this work, we report for the first time the combination between the solution combustion synthesis (SCS) and deep ultraviolet (DUV) treatment in HfO_x single and nanomultilayer dielectrics (composed by AlO_x and HfO_x thin films) at low temperature (150 °C) in gallium-indium-zinc oxide (IGZO) TFTs (Table 1). The effects of increasing the number of dielectric layers in the electric performance were investigated using different characterization techniques. Finally, stable and low voltage (HfO_x|HfO_x)/IGZO TFTs have been applied to a diode-connected inverter.

Table 4.1. Literature of developed high-κ solution-based hafnium oxide single layers and multilayers applied in TFTs. Copyright © 2017, American Chemical Society.

Year	TFT (Dielectric/ Semiconductor)	T (°C)	SS (V dec^{-1})	μ_{SAT} (cm^2 V^{-1} s^{-1})	$I_{ON/OFF}$	V_{ON} (V)	V_G range (V)
2012[457]	(HfO_x |AlO_x)/ ZTO	400	0.12	3.8	10^5	0.4	-2–3
	(AlO_x |HfO_x)/ ZTO		0.16	1.2		-0.2	
2012[463]	(HfO_x)/ ZTO	300	0.11	1.1	10^7	0.2	- 5–5
2015[464]	(HfO_x)/ HIZO	500	1.1	3.6	10^4	-0.1	- 5–10
2015[465]	(HfO_x)/ ZnO	380	-	42±1.4	10^7	-0.4	- 1–6
2015[456]	(HfO_x)/ IZO	300	0.72	25.7	10^6	1.5	- 1–5
		200	1.32	6.2	10^3	0.8	
2017[455]	(HfO_x)/ ZTO	350	0.07	13.2	10^8	- 0.1	- 1 –2
This work (2017)	(HfO_x)/ IGZO	150 + UV	0.082±0.002	31.2±1.4	10^5	-0.04±0.05	-1–2
	(HfO_x |HfO_x)/ IGZO		0.066±0.010	43.9±1.1	10^6	0±0.03	-1–2
	(HfO_x |AlO_x)/ IGZO		0.076±0.009	23.6±0.6	10^5	0.01±0.03	-1–2
	(HfO_x|AlO_x|HfO_x) /IGZO		0.101±0.004	37.5±2.2		0.03±0.06	-1–3
	(AlO_x |HfO_x)/ IGZO		0.099±0.019	37.2±1.9		-0.01±0.06	-1–2
	(AlO_x|HfO_x|AlO_x) /IGZO		0.133±0.013	30.5±1.8		-0.09±0.09	-1–3

4.1.2. Experimental details

4.1.2.1. Precursor solution preparation and characterization

Aluminum nitrate nonahydrate ($Al(NO_3)_3 \cdot 9H_2O$, Fluka, 98%) was dissolved in 2-methoxyethanol (2-ME, $C_3H_8O_2$, ACROS Organics, 99%), to yield solution with an Al^{3+} ion concentration of 0.1 M. Urea ($CO(NH_2)_2$, Sigma, 98%) was then added to the prepared solution which was maintained under constant stirring for at least 1 h. The urea to aluminum nitrate molar proportion was 2.5:1, to guarantee the redox stoichiometry of the reaction.[7] Hafnium chloride based precursor ($HfCl_4$, Alfa Aesar, 99.9%) was dissolved in 2-methoxyethanol (2-ME, $C_3H_8O_2$, ACROS Organics, 99%) and maintained under constant stirring for 4 h. Then the oxidizing agent, ammonium nitrate (NH_4NO_3, Roth, 98%) and the fuel, urea was added and stirred at least 2 h for a concentration of 0.1 M. For the ammonium nitrate precursor, the urea molar proportion was 1:(1/3). All precursor solutions were filtrated through 0.20 μm hydrophilic filters before use.

The precursor's solvent evaporation with a rotatory evaporator (Heidolph, model Hei-VAP Value/G3) was done before the thermogravimetry and differential scanning calorimetry (TG-DSC) at 70 °C with a rotation of 50 rpm during 1 h 30 min. Then a thermal characterization of precursors was performed by TG-DSC under air atmosphere up to 500 °C with a 10 °C min^{-1} heating rate in an aluminum crucible using a simultaneous thermal analyzer, Netzsch (TG-DSC - STA 449 F3 Jupiter). The optical properties were obtained using a Perkin Elmer lambda 950 UV/VIS/NIR spectrophotometer by measuring absorbance (A) in the wavelength range of 190 to 400 nm.

4.1.2.2. Dielectric deposition and characterization

Prior to deposition all substrates (silicon wafer and corning glass with an area of 2.5×2.5 cm^2) were cleaned in an ultrasonic bath at 60 °C in acetone for 10 min, then in 2-isopropanol for 10 min and dried under nitrogen (N_2); followed by a 10 min UV/Ozone surface activation step in a PSD-UV Novascan system. Thin films were deposited by spin coating, forming a single layer (AlO_x; HfO_x) and multilayers ($AlO_x|HfO_x$; $AlO_x|HfO_x|AlO_x$; $HfO_x|HfO_x$; $HfO_x|AlO_x$; $HfO_x|AlO_x|HfO_x$) using the AlO_x and HfO_x precursor solutions with a concentration of 0.1 M for 35 s at 2000 rpm (Laurell Technologies). That was followed by an immediate thermo annealing at 150 °C assisted by ultraviolet irradiation (UV) (PSD Pro Heated Series, PSDP-UVT Novascan system; emission wavelengths of 253.7 (90%) and 184.9 nm (10%); area of 20 × 20 cm^2) at a lamp distance of 2 cm (the output energy intensity of the lamp was 75 $mW \cdot cm^{-2}$ at 254 nm) for 30 min each layer in nitrogen ambient, with a gas flow of 240 mbar. The films´ structure was assessed by glancing angle X-ray diffraction (GAXRD) performed by an X'Pert PRO PANalytical powder diffractometer using Cu Kα line radiation (λ = 1.540598 Å) with an angle of incidence of the X-ray beam fixed at 0.9°. The surface morphology was investigated by atomic force microscopy (AFM, Asylum MFP3D) and the film thickness by scanning electron microscopy analysis of a sample cross section prepared by focused ion beam using Ga^+ ions (SEM-FIB, Zeiss Auriga Crossbeam microscope). Fourier Transform Infra-Red (FTIR) spectroscopy characterization of thin films deposited on Si substrates data were recorded using an Attenuated Total Reflectance (ATR) sampling accessory (Smart iTR) equipped with a single bounce diamond crystal on a Thermo Nicolet 6700 Spectrometer. The spectra were acquired with a 45° incident angle in the range of 4500–540 cm^{-1} and with a 4 cm^{-1} resolution.

4.1.2.3. Electronic device fabrication and characterization

Metal–insulator–semiconductor (MIS) capacitors were produced by depositing a single layer, AlO_x or HfO_x, and multilayers onto p-type silicon substrates (1–10 Ω·cm) as described above. Aluminum electrodes (80 nm thick) with an area of 1.96 × 10^{-3} cm^2 were deposited by thermal

evaporation via shadow mask on top of the insulators, with similar but unpatterned electrodes being also deposited on the back of the silicon wafer. Electrical characterization was performed measuring both the capacitance–voltage and capacitance-frequency characteristics in the range of 1 kHz to 1 MHz of frequency using a semiconductor parameter analyser (Keithley 4200SCS) and probe station (Janis ST-500). The TFTs were produced in a staggered bottom-gate, top-contact structure by depositing the single layers or the nanomultilayers onto p-type silicon substrates acting as gate electrodes.

The IGZO semiconductor film (30 nm thick) was sputtered onto the dielectric thin films via shadow mask for all temperatures. The deposition was performed using a commercial IGZO ceramic target (2:1:2 In:Ga:Zn atomic ratio) by rf magnetron sputtering in an Ar+O_2 atmosphere without intentional substrate heating in an AJA 1300-F system.[466]

Finally, source and drain aluminum electrodes (80 nm thick) were deposited by thermal evaporation via shadow mask onto the films. Hereafter the IGZO TFTs were annealed at 150 °C, for 1 h in air. An 80 nm thick aluminum film was also deposited on the back of the silicon wafer.

The current–voltage characteristics of the devices were obtained in double sweep mode in ambient conditions using a semiconductor parameter analyser (Agilent 4155C) attached to a microprobe station (Cascade M150) inside a dark box, at room temperature.

The saturation mobility (μ_{SAT}) was determined from the following equation:

$$I_D = \left(\frac{C_{ox} W \mu_{SAT}}{2L} \right) \left(V_G - V_T \right)^2 \qquad (4.1)$$

where C_{ox} is the gate dielectric capacitance per unit area, the channel length (L) and width (W) are 90 and 1000 μm, V_G is the gate voltage and V_T is the threshold voltage, which was determined in the saturation region by linear fitting of a $I_D^{1/2}$ vs V_G plot. V_T was obtained by the linear extrapolation method, which defines V_T as the gate voltage axis intercept of the tangent of the $I_D^{1/2}$–V_G characteristics at its maximum first derivative (slope) point.

Gate bias stress tests were performed on TFTs with one and two layers of dielectric under air environment by applying a constant gate voltage (0.5 MV·cm^{-1} electric field) for one hour, after which the devices were allowed to recover. Transfer characteristics were measured at fixed time intervals during stress and recovery processes.

To investigate the possibility of solution based TFTs in circuit application, the inverter structure was constructed with two TFTs in different substrates. A semiconductor parameter analyser

(Keysight B1500A) was used for the DC characterization of the inverter. For transient measurements of the inverter, the input waveforms were generated by a function generator (Wavetek 395) and the output signal was acquired by an oscilloscope (ISO-TECH IDS 8062).

4.1.3. Results and discussion

Solution combustion synthesis of nanomaterials has been crucial for the fabrication of high-quality metal oxides at low temperature.[2] In combustion synthesis at certain temperature, a violent redox reaction between an organic fuel, urea, and the oxidizer, ammonium nitrate, occurs, related with the release of massive reaction heat. This local heat results in the increase of local temperature inside the dielectric films, which promotes the precursors conversion into oxides at low temperature.[7] Since 2011, the solution combustion synthesis of AlO_x thin films applied in TFTs has been reported, however for HfO_x only a few results have been succeeded with high performance TFTs requiring high temperatures (Table 4.1).[2,455,467]

The solution combustion synthesis of HfO_2 from hafnium chloride and ammonium nitrate (oxidizer), and urea (reducing agent) can be represented by the combination of ammonium nitrate decomposition reaction (equation 4.2) and urea oxidation reaction (equation 4.3).

$$HfCl_4 + 4NH_4NO_3 \rightarrow HfO_2 + 6H_2O + 4N_2 + 4HCl + 2O_2 \qquad (4.2)$$

$$CO(NH_2)_2 + \left(\frac{3}{2}\right)O_2 \rightarrow 2H_2O + CO_2 + N_2 \qquad (4.3)$$

The overall reaction can thus be written as bellow (equation 4.4):

$$3HfCl_4 + 12NH_4NO_3 + 4CO(NH_2)_2 \rightarrow 3HfO_2 + 16N_2 + 4CO_2 + 26H_2O + 12HCl \qquad (4.4)$$

This is a theoretical reaction equation that neglects possible secondary reactions, although, it allows the calculation of a stoichiometric condition that can be used as a reference.[38] In the oxide formation, the chemistry of the redox reaction is determinant for the thermodynamics, particularly, the nature of the reagents and the fuel/oxidizer (ϕ).[38]

The optimal stoichiometry composition of the redox mixture is obtained for $\phi = 1$, however, in order to achieve lower temperatures in the thin film formation, as shown by TG-DSC analysis (Figure 4.1 (a)), a $\phi = 1.1$ was used. In this composition the redox mixture is under fuel-rich condition, requiring molecular oxygen to fully convert the fuel.[38,39] The oxidizing/reducing characteristics of a mixture can be calculated by the Jain method, which is based on propellant chemistry.[33] In this method carbon and hydrogen are considered as reducing elements with final valences of +4 and +1, respectively; hafnium metal ions are also considered reducing elements

with a final valence of +4. Oxygen and nitrogen are considered oxidizers with their final valences of -2 and 0, respectively. The reducing valence of urea is +6 and the oxidizing valence of ammonium nitrate is −2 as calculated by the Jain method hence (1/3) mol of urea are required per mole of the nitrate precursor (ammonium nitrate) to ensure redox stoichiometry. In this condition, to minimize the generation of cracks and pores in metal oxide films, which can significantly contribute to leakage current in the vertical direction, deep ultraviolet (DUV) treatment was used.[3,20] The condensation and film densification in metal oxides are improved with DUV irradiation in nitrogen environment; however, some ozone (O_3) is also formed, which in this case helps to fully convert the fuel in the combustion reaction at low temperatures.

4.1.3.1. Precursor solutions characterization

Thermal analysis of precursor solutions was performed to investigate the decomposition behaviour of the hafnium oxide precursors with different stoichiometry compositions. Figure 4.1 (a) shows the differential scanning calorimetry (DSC) and thermogravimetry (TG) of the HfO_x up to 350 °C, since above this temperature no further events were observed. The most promising precursor solution with a fuel rich condition, $\phi = 1.1$, exhibits an intense exothermic peak at 221 °C and small peak at 304 °C, which is attributed to the combustion reaction of residual fuel resulting in a mass loss of 40 %. Also, two endothermic peaks were observed at 139 °C and 172 °C, which are related to the solvent evaporation and some residual organics. In the case of the stoichiometry condition, $\phi = 1$, the precursor solution show a smaller exothermic peak at 232 °C and the most intense one at 273 °C, which is higher than the fuel rich condition. Thermal analysis indicates that the minimum temperature required for full degradation is 304 °C. The DSC-TG analysis 2-ME based of AlO_x precursor solutions, has been previously reported by our group[6], and shows an intense exothermic peak at 176 °C corresponding to oxide formation, and a residual endothermic peak at 250 °C attributed to the degradation of residual organics. The difference in combustion reaction temperature of HfO_x and AlO_x is expected as it depends on the specific bonding energy of the ligands with the metal ions in solution which varies from metal to metal, as reported by Epifani et al.[77]

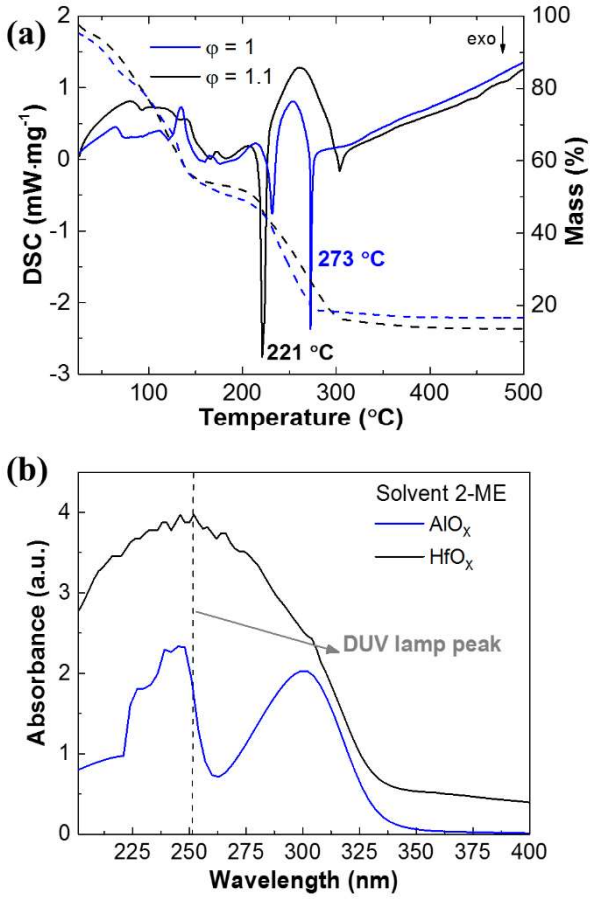

Figure 4.1. (a) TG-DSC analysis of HfO_x precursor solution and (b) absorbance spectra of both, AlO_x and HfO_x, precursor solutions.[92] Copyright © 2017, American Chemical Society.

The absorbance of the precursor solutions in the UV–Vis range was performed to assess the efficiency of irradiation with a DUV lamp with a maximum emission at 254 nm (90 %) to enhance film condensation and densification.[3,20] Figure 4.1 (b) shows that both solutions absorb in that wavelength, being more significant for the hafnium oxide precursor solution. Therefore DUV treatment is expected to contribute to degradation of organic residuals and decreasing the temperature required for the formation of M-O-M.[3]

4.1.3.2. Dielectric thin films characterization

The optical transmission of single and multilayer thin films was measured. Figure 4.2 shows that all films are highly transparent (> 89%) in the visible range. However, with increase of the number of layers and film thickness, total transmittance is slightly decreased. The optical bandgap (E_g), determined via Tauc plot analysis is 4.9 eV for HfO_x thin films, as shown in Figure 4.2. This value is lower than the expected 5.8 eV reported for physical vapour deposition (PVD) techniques.[455,461] HfO_x thin films produced by solution may have some residual chloride species which slow down the dehydroxylation process and increase the amount of oxygen vacancies in the thin film, which

results in a decrease of the bandgap energy due to the increasing of density of states.[455] The bandgap of the other layers was not obtained due to the presence of aluminium oxide, which has a large bandgap (8.9 eV) unable to be measured using Tauc plot analysis.[468]

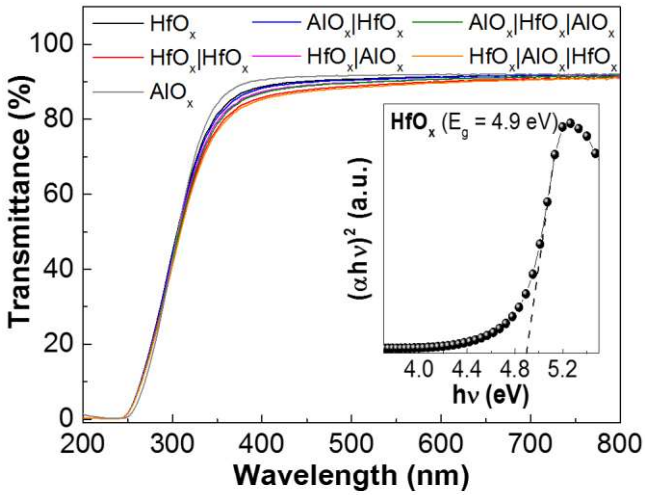

Figure 4.2. Optical transmittances of the single and multilayer dielectric thin films. The inset shows the Tauc plot of HfO_x.[92] Copyright © 2017, American Chemical Society.

The dielectric thin films produced were characterized with ATR-FTIR before and after annealing, as shown in Figure 4.3 (a). All samples show an absorbance peak at 1107 cm^{-1} attributed to the Si-O transversal optic stretching.

Prior to annealing absorption bands related to organic precursors in the film can be observed, namely, a broad band between 3700 and 3000 cm^{-1} and bands at 1630 and 1575 cm^{-1} assigned to O–H stretching vibrations associated with water absorption and OH increase; weak absorption bands between 3090 and 2800 cm^{-1} associated to the C–H stretch and between 1500 and 1300 cm^{-1} with C–H deformation and carbonate .[469] After annealing at 150 °C assisted by DUV treatment, none of these bands were observed confirming the elimination of all residual organics.

The absorption peaks at, 889, 739–748 and 611–601 cm^{-1}, are attributed to the presence of metal oxide (M–O) chemical bonds, Hf–O and Al–O.[469–471] The FTIR analysis of multilayer thin films showed similar results, as depicted in Figure A1 in the Appendix A.

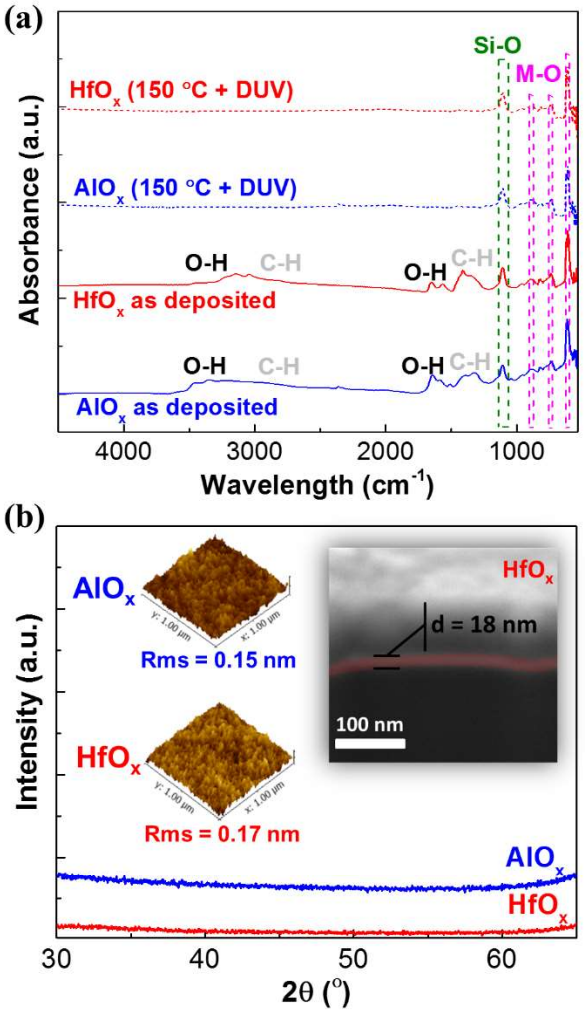

Figure 4.3. (a) FTIR spectra of AlO_x and HfO_x thin films before and after annealing; (b) XRD diffractograms, AFM deflection images (1×1 μm^2) of both dielectric thin films, and high-resolution SEM-FIB cross-section image of HfO_x thin film.[92] Copyright © 2017, American Chemical Society.

The structure of the solution based dielectric thin films was investigated by X-ray diffraction (XRD). The absence of diffraction peaks in Figure 4.3 (b) reveals that amorphous thin films are obtained in the single layer and multilayer samples (see Figure A2 in Appendix A). Amorphous materials have less grain boundaries and are expected to have a small surface roughness, low leakage current and high breakdown voltage.[467]

Atomic force microscopy (AFM) images were used to analyse the surface morphology. The lowest roughness was observed for single layers, AlO_x and HfO_x, 0.15 nm and 0.17 nm, respectively, as depicted in Figure 4.3 (b). Figure A3 in Appendix A shows that all multilayer samples have a smooth surface morphology and a surface roughness bellow 1.2 nm. The surface morphology was not affected by the release of dichloride during the combustion reaction.[455] The

low surface roughness leads to a better interface between the dielectric layer and the IGZO improving the electrical performance.

High resolution SEM-FIB cross-section image of all the dielectric multilayer thin films was performed to measure the films thickness. Single layer HfO_x thin film has a thickness of about 18 nm (Figure 4.3 (b)); multilayer films have a thickness of about 26 nm for $HfO_x|HfO_x$, 28 nm for $HfO_x|AlO_x$, 44 nm for $HfO_x|AlO_x|HfO_x$, 30 nm for $AlO_x|HfO_x$ and 44 nm for $AlO_x|HfO_x|AlO_x$ (see Figure 4.4 and Figure A4 in Appendix A). To demonstrate a better film densification achieved with the combination of UV treatment and combustion synthesis, a study was done with AlO_x for different concentrations showing thinner films when combustion method with UV was used (see Figure A5 in Appendix A). The film densification is more significant for higher concentration due to the higher amount organics to be decomposed, nevertheless the film degradation is relevant regardless the film densification.

4.1.3.3. Dielectric multilayers electrical characterization

The increasing number of high-κ dielectric layers using combustion synthesis and DUV treatment were studied to determine the best dielectric composition and dielectric/semiconductor interface. The electrical characterization of all dielectrics was performed by measuring the capacitance-voltage (C-V), capacitance-frequency (C-f) and breakdown voltage (E) of metal-insulator-semiconductor (MIS) structures, in Figure S6 in the Supporting information.

In order to clarify the dielectrics performance a statistical analysis was done, as depicted in Figure 4.4 and Table A1 in Appendix A. Higher dielectric constants for the multilayer dielectrics with three layers, $AlO_x|HfO_x|AlO_x$ (13.5) and $HfO_x|AlO_x|HfO_x$ (12.5) were obtained, as depicted in Figure 4.4. However, dielectric constant is slightly higher for the $AlO_x|HfO_x|AlO_x$ due to the higher capacitance of the multilayer. In the case of HfO_x was obtained the highest dielectric constant as expected, but when you add a second layer of HfO_x the dielectric constant decreases because the thin film produced have more residual chloride species. This species will slow down the dehydroxylation process and increase the amount of oxygen vacancies in the thin film, which affect the dielectric constant.[455] In the other cases when is added a layer of HfO_x in AlO_x, the dielectric constant increases due to the higher dielectric constant of HfO_x. The breakdown voltage using a single layer of HfO_x was improved from 2.7 $MV \cdot cm^{-1}$ to 3.6 $MV \cdot cm^{-1}$ with a bilayer due to the thickness increase and interface quality. The highest breakdown field of 4.9 $MV \cdot cm^{-1}$ was achieved for the $HfO_x|AlO_x$ multilayer, which was also enhanced when compared with the $AlO_x|HfO_x$ multilayer, 4.3 $MV \cdot cm^{-1}$, meaning a better interface when AlO_x is in the top of HfO_x, as shown in Figure 4.4. HfO_x presents a lower band gap facilitating carrier injection when compared to AlO_x. Also, the fact that HfO_x precursor contains chlorides leads to increased

interface charge defects. Therefore, a higher breakdown voltage is achieved when the AlO_x is deposited over HfO_x. To further improve the $AlO_x|HfO_x$ interface quality a longer annealing could be performed.

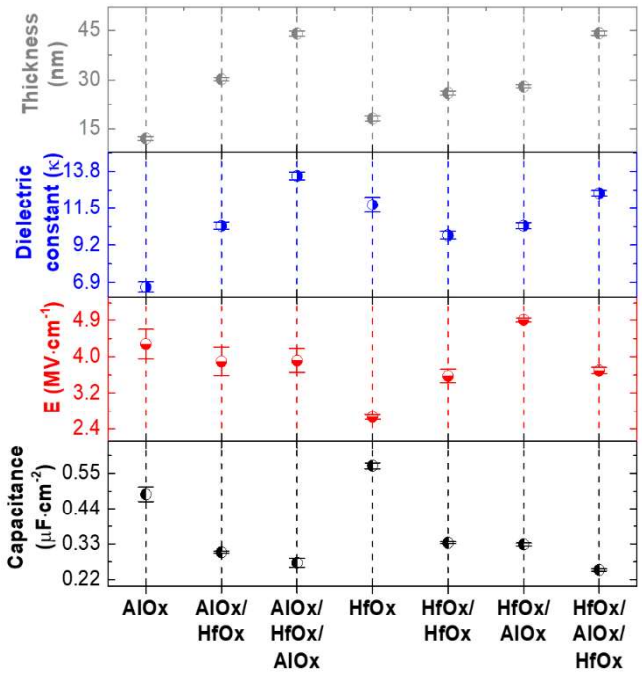

Figure 4.4. Statistical analysis of capacitance measured at 1 kHz, dielectric thickness, breakdown voltage and dielectric constant of all dielectric thin films.[92] Copyright © 2017, American Chemical Society.

By increasing the number of layers, the capacitance decrease showing fairly a constant value over the range of frequencies, as presented in Figure A6 (a) in Appendix A.

Hysteresis starts to increase in the capacitance-voltage characteristics of the MIS structure, with the increase of the number of layers, as shown in Figure A6 (b) in Appendix A. The flat band voltage is changed with respect to the different layer composition and increasing the number of layers. The HfO_x bilayer shows less hysteresis change when compared with a single layer of HfO_x.

Taking into account the properties achieved, the most promising dielectrics were all the ones with more than one layer.

4.1.3.4. Low voltage multilayer TFTs

All the TFTs produced at low temperature (150 °C) demonstrated low voltage operation (maximum 3 V) and exhibited a good electrical performance with low gate leakage current. To our knowledge this is the first time that TFTs with a single layer of HfO_x and multilayers combining AlO_x and HfO_x solution based dielectrics are reported at 150 °C. This was possible by

the combination of thermal annealing with deep-ultraviolet (DUV) irradiation to enhance the intrinsic properties of the films, resulting in more uniform and compact films and by using a slightly fuel-rich solution combustion synthesis (SCS) which decreased the ignition temperature of the exothermic reaction, and hence the M-O-M formation. Typical transfer curves of the TFTs can be observed in Figure 4.5 (a,b) and the output curves in Figure A7 in the Appendix A. Figure 4.5 (b) shows that using HfO_x layer instead of AlO_x in contact with the gate electrode, facilitates carrier injection due to the lower bandgap resulting in an improved interface and lower off current.

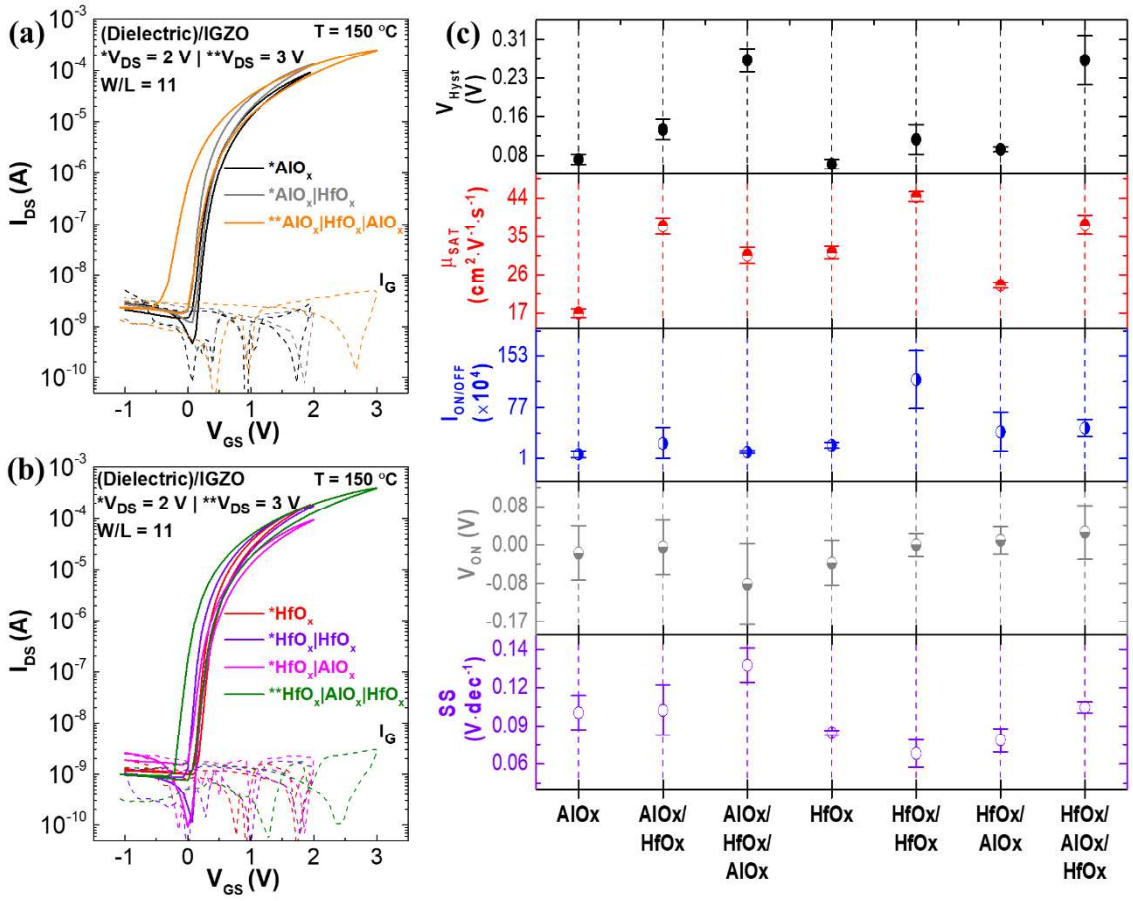

Figure 4.5. (a,b) Typical transfer characteristics of the single and multilayers insulator thin films applied in IGZO TFTs; (c) statistical distributions of device parameters, hysteresis (V_{Hyst}), saturation mobility (μ_{SAT}), current on-off ratio ($I_{ON/OFF}$), turn-on voltage (V_{ON}) and subthreshold slope (SS).[92] Copyright © 2017, American Chemical Society.

To study the uniformity and reproducibility of these devices a set of 15 devices was produced and characterized for all the dielectric thin films, as shown in Figure 4.5 (c). This analysis was assessed through the measurement of the turn-on voltage (V_{ON}), hysteresis (V_{Hyst}), drain current on−off ratio (I_{ON}/I_{OFF}), subthreshold slope (SS), and saturation mobility (μ_{SAT}), which was calculated using the dielectric capacitance measured in MIS devices at a frequency of 1 kHz (see

Table A1 in Appendix A). High mobility which surpassed the state-of-the-art was obtained for all the multilayer dielectric TFTs. The highest mobility, 43.9 ± 1.1 $cm^2 \cdot V^{-1} \cdot s^{-1}$, was achieved for the bilayer of $HfO_x|HfO_x$ based TFTs. The roughness at the $HfO_x|AlO_x$ surface may form interface charge traps, which increase the carrier scattering centres explaining the lower mobility obtained.[456] Other reasons for the high carrier mobility achieved for the solution-based dielectrics IGZO TFTs are the indium content in the IGZO semiconductor and the high areal capacitance of the dielectrics used.[456] In terms of on/off current ratio, most of the devices show 10^5. We note that a ratio of 10^6 is achieved for devices with a bilayer of HfO_x which is high when compared with literature (Table 4.1). The turn-on voltage of most devices was close to 0. The $HfO_x|HfO_x$ multilayer exhibited less variation of turn-on voltage in different devices. The lowest subthreshold slope (SS) value of 0.066 ± 0.01 $V \cdot dec^{-1}$ was obtained for $(HfO_x|HfO_x)$/IGZO TFTs indicating the enhanced quality of dielectric-semiconductor interface.

All devices showed an anti-clockwise hysteresis, as shown in Figure 4.6 (a), due to mobile ions, namely some organic residues or defects in the gate dielectric. This is a consequence of using a low temperature (150 °C) which can be surpassed by performing a longer annealing time with DUV treatment or using higher temperature.

In order to determine how device performance is affected after aging in air environment, TFTs were again characterized after 2 months. The IGZO TFT with the solution-based $AlO_x|HfO_x$ dielectric showed a slight SS degradation, whereas, the SS of $AlO_x|HfO_x|AlO_x$ multilayer device was larger, as shown in Figure A8 and Table A2 in Appendix A. It was also observed the impact of humidity on degraded on/off ratio of aged-devices based on $HfO_x|AlO_x|HfO_x$ multilayer.[307] To improve the quality in the interfaces of layers a longer annealing should be performed and in addition, a device passivation is also suggested.[466] All other devices with one and two dielectrics layers showed good stability over time, with only a slight variation of the electrical parameters. The $(HfO_x|HfO_x)$/IGZO TFTs revealed the best switching behaviour over time, from 0.061 to 0.068 $V \cdot dec^{-1}$, as depicted in Figure 4.6 (a).

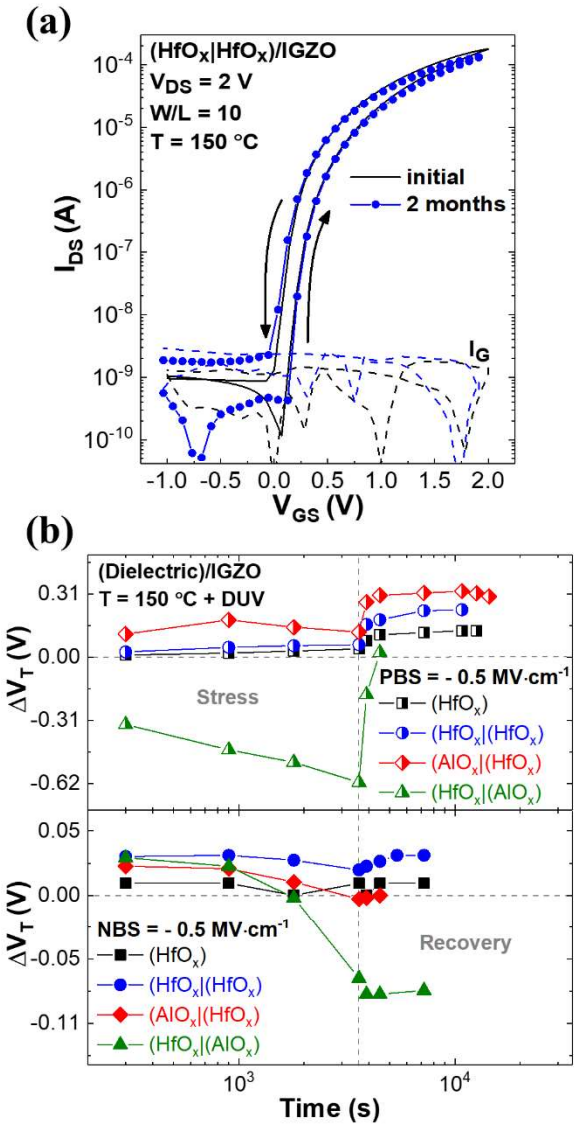

Figure 4.6. (a) Aging effect of ($HfO_x|HfO_x$)/IGZO TFTs after 2 months; (b) Threshold voltage variation (ΔV_T) during a 0.5 MV·cm^{-1} stress in selected dielectrics under PBS and NBS tests for 1 h in air environment.[92] Copyright © 2017, American Chemical Society.

To investigate the devices operational stability, a positive and negative gate bias stress was performed in air environment by applying a constant gate voltage equivalent to electrical field of ± 0.5 MV·cm^{-1} while keeping the source and drain electrodes grounded. The multilayer devices with 3 layers were not examined due to their instability over time, and also the AlO_x single layer did not show an improved performance when compared with literature.[20,307] The other devices were stressed for 1 h, combined with ~ 2 h recovery time in dark condition. Transfer characteristics were obtained in the saturation regime (V_{DS} = 2 V) at selected times during stress and recovery processes, as shown in Figure A9 and A10 in the Appendix A. Figure 4.6 (b) shows the threshold voltage variation (ΔV_T) with time during stress and recovery phases.

By applying a positive gate bias stress (PBS) a maximum V_T shift of - 0.61 V is obtained for the $HfO_x|AlO_x$ multilayer based TFTs. The negative threshold voltage shift under positive gate bias stress of a device employing the AlO_x gate dielectric has been reported in a previous publication, where this phenomenon was related to the release of hydrogen from the dielectric to the semiconductor[7].

The TFTs with $AlO_x|HfO_x$ multilayer, having the HfO_x in contact to the channel show dual shift of threshold voltage (see A8 Appendix A). Simultaneously, two mechanisms contribute for the TFT instability: (i) Negative shift related to the AlO_x layer[7] and (ii) charge trapping into the dielectric and/or at the interface of channel and dielectric (HfO_x) which results in the positive shift of threshold voltage. Interestingly, the electron donating effect happens although the AlO_x layer is not located at the interface to the semiconductor. This means that the hydrogen can easily penetrate into the HfO_x layer.

The TFTs with $HfO_x|AlO_x$ in contact to the channel are recovered in 15 mins whereas, the ones with $AlO_x|HfO_x$ are not fully recovered after 3 h of rest in dark condition. The single and bilayers of HfO_x applied in IGZO TFTs were the ones that presented lower positive V_T shift under PBS. However, after removing the stress, the threshold voltage is still shifting toward the positive direction even more pronounced than when the TFT is under PBS (see Figure A9 in Appendix A). The recovery of the devices to the initial state can be only achieved by a re-annealing process of the TFTs. It is possible that this shows how under PBS compensating acceptor defects are created which persist beyond the stressing. In addition, the residual Cl may be a strong candidate for an extra trap sites in the HfOx layer[455]. Further investigations are required to elucidate the mechanism at the HfO_x/IGZO interface, which leads to the absence of recovery.

The V_T under negative gate bias stress (NBS) for the different conditions showed a small negative shift with negligible degradation of SS, which is frequently reported for n-type semiconductor TFTs (see more detail Figure A10 in Appendix A).[472]

5.1.3.4. Diode-connected inverter

Since the $(HfO_x|HfO_x)$/IGZO thin film transistors revealed the best electrical performance, a good stability and uniformity, we applied them in a basic building block, an inverter. The structure of this circuit was performed using two TFTs, the load and the driver, with the same W/L = 11. The load TFT had the gate short-circuited with the drain in order to work as a resistor. The voltage transfer characteristics (VTC) of the obtained inverter were measured at various supplied voltages (V_{DD}), 1 V, 1.5 V and 2 V, as shown in Figure 4.7 (a). It is noticed that the output high voltage, 1.9 V, is close to the V_{DD}, 2 V, and the output low voltage is 0.3 V, when was supposed to be 0

V. For this configuration the high output value is $V_{DD} - V_{T\,(LOAD)}$ and for the low output value a higher than 0 V is expected, as the load TFT cannot be completely turned OFF. The inverter exhibits a maximum gain ($-\partial V_{OUT}/\partial V_{IN}$) of 1.15 for the different supplied voltages, but due to the use of two identical TFTs the expected value was 1. This difference can be explained by a slight mismatch between the two TFTs, as depicted in Figure A11 in the Appendix A.

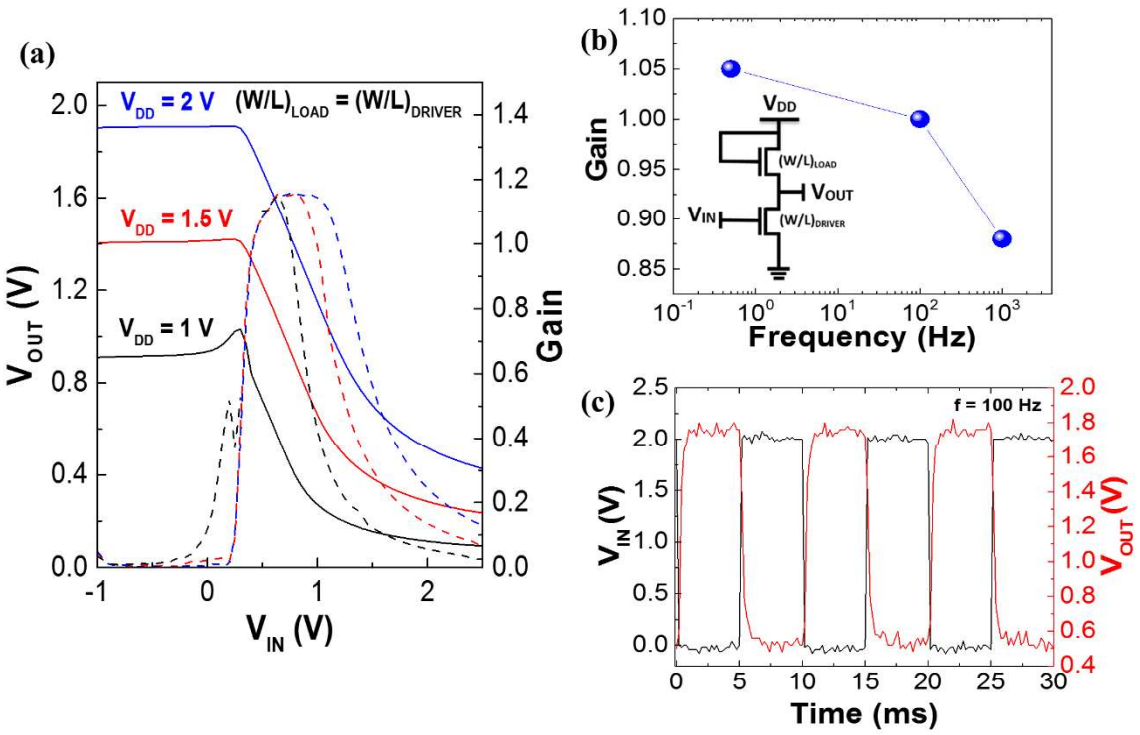

Figure 4.7. (a) The voltage transfer characteristics and signal gain of the diode-connected inverter with (HfO_x|HfO_x)/IGZO TFTs. (b) Voltage gain for different frequencies and (c) a dynamic switching behaviour of the inverter under AC square waves at 100 Hz.[92] Copyright © 2017, American Chemical Society.

To investigate the alternative current (AC) characteristic of the inverter, the dynamic behaviour under AC square wave was measured for different frequencies and the result is shown in Figure 4.7 (b). The device exhibited good inversion properties however, the gain decreased slightly with the increase of the frequency, more precisely to 1 kHz. The gain values are smaller in the dynamic measurements when compared with the values in the static VTC curve because a buffer was not used to provide enough current for full voltage swing, losing some current in the cables. To improve the AC results, some tests of etching should be done to produce structures suitable for these measurements. Figure 4.7 (c) shows that the device can achieve sufficient switching speeds for wearable applications.

4.1.4. Conclusions

In this work, we have demonstrated for the first time the combustion solution synthesis alliance with UV treatment in HfO_x dielectric thin films and multilayer thin films using AlO_x and HfO_x at low temperatures (150 °C) and their implementation in electronic structures. The physical properties of the single layers and multilayers were investigated using a wide range of characterization techniques that revealed smooth surface (< 1.2 nm), high-κ (13.5), high transparency (> 89 %), low leakage currents and high breakdown voltages (> 2.7 $MV \cdot cm^{-1}$). The multilayer MIS devices exhibit an improvement by presenting low capacitance dependence at low frequencies when compared with the single layers. In terms of thin film transistors (TFTs), the (HfO_x|HfO_x)/IGZO TFTs showed the best electrical performance with low voltage operation, low subthreshold slope (0.066 ± 0.01 $V \cdot dec^{-1}$), 0 V turn-on voltage, a high saturation mobility (43.9 ± 1.1 $cm^2 \cdot V^{-1} \cdot s^{-1}$) and current ratio of 10^6. This device also presented good stability over time (2 months) and under positive gate bias stress (PBS) for 1 h, having a maximum threshold voltage variation of 0.06 V. These devices were applied in a diode-connected inverter showing good switching speed at 100 Hz with a maximum gain of 1 at 2 V. Taking in consideration the excellent results achieved in this report, the next step will be the implementation in large area processing techniques.

4.2. Printed and Highly Stable Metal Oxide TFTs

4.2.1. Introduction

New demands and challenges are emerging with the Internet of Things (IoT), which can also be considered as part of the next-generation of electronics.[310] The quick growth of ubiquitous electronics is expected to help revolutionise modern life through applications such as flexible displays, wearables and implantable devices.[473–475] In order to achieve these large-volume markets, novel low-cost solutions in terms of suitable materials and processes are highly desirable. In addition, more and more of the electronics of the future must be free of rigid substrates as well as subtractive processes (traditional physical/chemical vapour depositions (PVD/CVD) and photolithography) which are expensive, cannot be freely scaled to large area and are not sustainable.[350,476] Printing technologies are a promising alternative for the manufacturing of novel flexible and large area electronics.[374,477] However, breakthroughs in printing technologies are crucially needed to reach scalable manufacturing of electronic devices, such as resistors, antennas, capacitors, diodes, batteries and thin film transistors (TFTs).[478–483]

TFTs are essential as switching components for flexible displays, sensor arrays, memories and wearable electronics.[484] Various classes of semiconductor materials have been studied on their suitability to produce flexible TFTs, which include organic semiconductors, metal oxides (ZnO, In_2O_3, InGaZnO, etc.), carbon nanotubes and 2D materials.[334,376,388,418,485,486] Amorphous oxide semiconductors, such as amorphous IGZO, possess several outstanding properties when compared to others. These include their low-temperature-process compatibility using PVD, smooth surfaces, amorphous structures and high electron mobility.[1] Furthermore, high-κ dielectric oxides are the key to limit power consumption in TFTs which influences applications running on battery power or energy scavenging such as IoT sensors or wearables.[92,487] The high cost associated with processing metal-oxide materials using capital-cost-intensive vacuum-deposition methods over large areas on flexible substrates could be reduced by investments in readily-scalable printing methods (PM).[475,488] Generally, printing is a reproductive process and various printable functional materials have been developed and optimized for different printing approaches, including screen, inkjet, gravure, reverse-offset and flexographic printing.[373,386] However, for enabling the flexible printed TFTs to meet the demands of electronics manufacturing industry, the challenges that are reported to be solved separately such as low annealing temperature (e.g. UV-assisted annealing),[5,21,489] high in-line speed (e.g. flexographic printing),[376] high printing resolution (e.g. reverse-offset printing),[386] and low substrate surface roughness (e.g. smooth polyimide)[376] would need to be achieved simultaneously. Furthermore, to boost reproducibility and stability in printed TFTs, a number of printability requirements (smooth

substrates, surface energy, ink formulation, printing resolution) and annealing conditions (low-temperature for oxides using e.g. UV-assisted curing) must be well-controlled.[2,3,374,386,490,491] It has been shown that high quality oxide films can be obtained at low process temperature by using UV irradiation. When the films are exposed to high-energy photons, the cleavage of alkoxy groups into active metals and oxygen atoms occurs to simplify the M–O–M network formation through radical-mediated chemical reactions. Consequently, the thin films' densification is improved.[21,65,307] Even higher efficiency can be achieved by combining solution combustion synthesis (SCS) with UV curing at low temperature as previously reported by our group. This helps to boost the local temperature during annealing through exothermic reactions.[92]

In this work, we report for the first time the printing of ultrathin aluminium oxide (Al_2O_3) using flexographic printing which is a roll-to-roll-compatible and industrially scalable printing method. The viscosity of the Al_2O_3 inks and the printing speed play a crucial role in the printability of the dielectric. The flexographic printing of the Al_2O_3 thin films onto flexible substrates was investigated by assessing the effect of number of layers and annealing process conditions (combined with low-temperature and UV irradiation) on the printing quality. Printed low-voltage solution-based flexible oxide TFTs were pursued by inkjet printing an indium oxide (In_2O_3) semiconductor layer that was annealed at low-temperature using combined UV and thermal annealing.[65] The operational stability under bias-stress, ageing during storage and mechanical bending stress were studied to probe the usability of the printed oxide TFTs in flexible applications.

4.2.2. Experimental details

4.2.2.1. Precursor solution synthesis and characterisation

Aluminum-oxide dielectric precursor ink ($Al(NO_3)_3 \cdot 9H_2O$, Merck, 99.997 %) was dissolved in 2-methoxyethanol (2-ME, $C_3H_8O_2$, ACROS Organics, 99 %). Afterwards urea ($CO(NH_2)_2$, Sigma, 98 %) was added to guarantee the redox stoichiometry of the reaction in a molar proportion of 2.5:1 to aluminum nitrate.[307] The prepared solution was maintained under constant stirring for 12 h at room temperature. Different solute concentrations (0.2; 0.4; 0.8; 1; 1.2; 1.6 M) were tested for their printability. For each concentration, the viscosity was measured using m-VROC viscometer (Rheosense Inc.) at 10 k/s shear rate and RT (23 °C).

Indium-oxide precursor ink ($In(NO_3)_3 \cdot H_2O$, 99.99 % from EpiValence, where x = 2.5) was dissolved in 2-methoxyethanol (anhydrous, 99.8 % Sigma-Aldrich) in inert condition with a concentration of 0.2 M. The solution was stirred overnight at 75 °C to completely dissolve and stabilize the solution and filtered using 0.45 µm pore size polytetrafluoroethylene (PTFE) to obtain the base solution. Then, 10 wt % of ethylene glycol (EG) (anhydrous, 99.8 % Sigma-Aldrich) was added to the solution to improve the printability as reported in our earlier work.[65]

Thermogravimetry and differential scanning calorimetry (TG-DSC) measurement (Netzsch, TG-DSC - STA 449 F3 Jupiter) was performed for the Al_2O_3 ink under air atmosphere up to 500 °C with a 10 °C min^{-1} heating rate in an aluminum crucible. The sample was prepared by drying 10 mL of Al_2O_3 precursor solution in a hotplate at 90 °C with a rotation of 300 rpm during 5 h.

4.2.2.2. Film deposition and characterization

An initial 1 min O_2 plasma treatment (≈200 W, Diener Nano) was performed on the flexible (38 µm thick) Xenomax® polyimide substrate (Toyobo Co. Ltd., Japan) for improving wettability. Then, flexographic printing of the patterned dielectric layer (Al_2O_3) was performed with RK Flexiproof 100 table-top printing machine (see Figure B12 (a), Appendix B). The printing was tested with different printing speeds of 40, 50, 60 $m \cdot min^{-1}$ using anilox rolls with different transfer volumes: 3 $mL \cdot m^{-2}$ (400 lines·cm^{-1}), 4 $mL \cdot m^{-2}$ (320 lines·cm^{-1}), and 5 $mL \cdot m^{-2}$ (200 lines·cm^{-1}). After printing, all the samples were dried at 130 °C in an oven in air for 10 min. All the printing tests and drying of the ink were performed at the laboratories of VTT in controlled ambient conditions where the relative humidity and temperature varied between 36.5–40 % and 21.7–23.6 °C, respectively. Finally, a combined FUV and thermal annealing (180 °C and 200 °C) was performed in dry N_2 glovebox (MBraun MB 200, $H_2O \leq 1$ ppm, $O_2 \leq 0.1$ ppm) for 30 min. A deuterium UV source (Hamamatsu L11798, 160 nm) with MgF_2 window was used as reported in previous work.[21,65,307]

The printing resolution was characterized using optical microscopy. The average thickness (from 6 scan areas) of the printed Al_2O_3 layers were measured using a stylus profilometer (Veeco Dektak 150) after annealing the samples with and without FUV exposure. The surface morphology of selected printed Al_2O_3 layers were investigated by atomic force microscopy (AFM, Asylum MFP3D).

X-Ray Reflectivity (XRR) measurements were performed in a PANalytical X´Pert PRO, using the Cu Kα line. The X-ray generator was operated at 45 kV and 40 mA and the reflected intensity was recorded by a scintillator detector in the range of 0.1 to 3 degrees 2 theta.

X-ray photoelectron spectroscopy (XPS) was measured with a Kratos Axis Supra, using monochromated Al Kα irradiation (1486.6 eV). The procedure was the same as mentioned in a previous report.[279] The quantification of the elemental composition (C 1s, Al 2p, O 1s) was done by dividing the integral peak intensity by the respective relative sensitivity factor (RSF) of the instrument.

4.2.2.3. Printed devices production and characterization

Metal-Insulator-Metal (MIM) structures were prepared on the flexible polyimide substrates mentioned above. First, 40 nm thick Al metal gate lines were evaporated using thermal vacuum evaporation through a metal shadow mask. Then, Al_2O_3 precursor ink with 1.2 M concentration was printed on top of the gate lines with printing direction perpendicular to the gate electrode lines. The printing was optimized for homogeneous layers using a printing speed of 50 $m \cdot min^{-1}$ and anilox rolls with 4 $mL \cdot m^{-2}$ transfer volume (320 $lines \cdot cm^{-1}$). The method to produce the dielectric thin films is described in the section above. Finally, 80 nm thick Al top electrodes were thermally vacuum evaporated using a shadow mask. The area for all of the MIM devices was 198 μm^2. As noted above, the MIM devices were annealed with combined FUV exposure and thermal treatment at low-temperature and reference devices were produced at 300 °C.

Electrical characterization of the MIMs (a set of 18 devices for each condition) were performed using an Alpha-A high performance frequency analyser (Novocontrol Technologies GmbH & Co. KG) to measure the capacitance-frequency (*C–f*) characteristics over a wide range of frequencies (1 Hz to 1 MHz) and a semiconductor analyser (Keithley 4200 SCS) to measure the current-voltage (*I–V*) characteristics.

Thin-film transistor fabrication with $Al/Al_2O_3/In_2O_3/Al$ stack was done using a bottom-gate top-contact structure using the same kind of flexible substrates. First, Al gate lines were evaporated using thermal evaporation in vacuum. The Al_2O_3 precursor ink was printed by flexographic printing in the same conditions as used for the MIM devices. Before the semiconductor was

printed on top of the dielectric, an UV/O_3 (FUSION UV, H+ BULB (13 mm)) surface treatment for 10 min was performed to improve the semiconductor adhesion and allow adequate wetting of the In_2O_3 ink. The semiconductor was printed by inkjet using In_2O_3 precursor ink and Dimatix Materials Printer DMP-2831 (Fujifilm) with the DMCLCP-11610 cartridges of 10 pl droplet volume as reported in our previous work.[65] After printing, the samples were dried at 130 °C on a hot plate in air for 15 min. Then, similarly to the dielectric layer, a combination of low-temperature thermal annealing (varied temperature, 180 – 200 °C, and time, 30 min – 1 h 30 min) on hotplate and FUV exposure was performed. Afterwards, a metal shadow mask having the patterns for source and drain electrodes with a width-to-length-ratio (W/L) of ~12.5 (W = 1000 µm, L = 80 µm) was aligned to the printed semiconductor areas. Al metal contact with 80 nm thickness was deposited through a shadow mask by thermal vacuum evaporation. The devices were post-annealed on a hot plate at 150 °C for 30 min in air to ensure better injection properties.[21] A schematic image of the printed oxide TFT fabrication is shown in Figure 4.8.

Electrical characterization of the TFTs was performed in dark environment using a semiconductor analyser (Keithley 4200 SCS). Back and forth transfer curves were recorded in saturation mode by sweeping the gate voltage (V_G) in 0.08 V steps using a 0.01 s step time while keeping the drain voltage (V_D = 1.5 V) constant. The output curves were recorded by sweeping V_D in 0.5 V steps using a 0.01 s step time while keeping the V_G constant.

The saturation mobility (μ_{SAT}) is calculated from:

$$\mu_{SAT} = \frac{\left(\frac{\partial(\sqrt{I_D})}{\partial V_G}\right)^2}{\frac{1}{2} C_{ox} \frac{W}{L}} \tag{4.2}$$

where I_D is the drain current, C_{ox} the gate capacitance density, and W/L the width to length-ratio of the transistor channel. The subthreshold slope (SS) was calculated as:

$$SS = \left[max\left(\frac{dlog(I_D)}{dV_G}\right)\right]^{-1} \tag{4.3}$$

Positive and negative gate bias stress tests were performed on the TFTs using the semiconductor parameter analyzer (Keysight 4200SCS) and probe station (Janis ST-500) under air environment by applying a constant gate voltage (corresponding to 0.5 and 1 MV·cm^{-1} electric field) for one hour. The transfer characteristics were measured at fixed time intervals during the bias-stress and recovery processes. Also, to test device reliability and stability ageing tests were performed after 5 months of storage. Mechanical bending strain with 5 mm radius was performed for a maximum

of 100 h at 1 bending per second rate using a homemade system (see Figure B12 (b), Appendix B).

4.2.3. Results and Discussion

Flexographic printing is a direct replicate technique in which the printing relies on an elastic master plate containing a relief pattern that carries the ink on its raised area to a flexible substrate under a nip pressure. The anilox cylinder that contains engraved cups of defined shape and size is a key component that controls the transfer of the precise amount of ink to the printing plate.

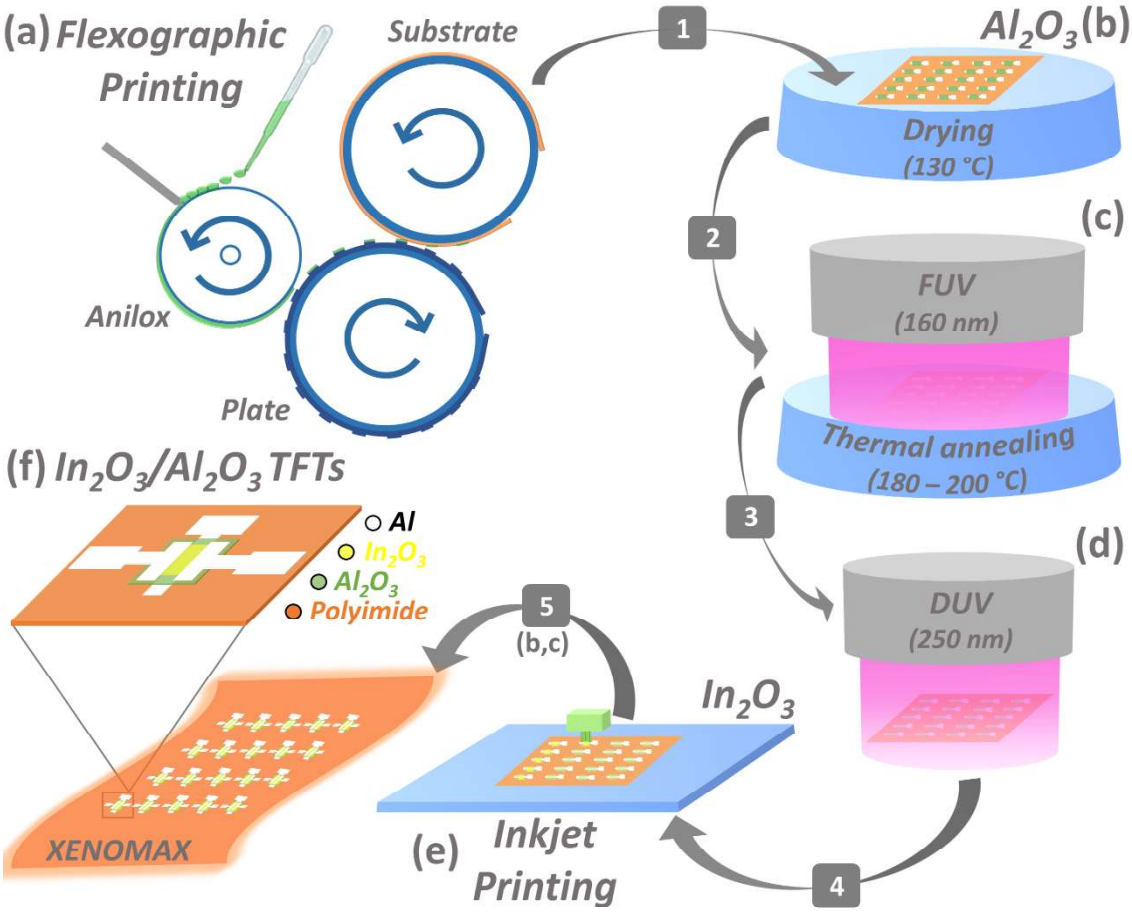

Figure 4.8. Schematic image of printing steps of the TFT production: a) flexographic printing process of the Al_2O_3 dielectric ink on top of the bottom electrode deposited by thermal evaporation; b) drying process on hotplate after printing; c) formation of the Al_2O_3 thin film using thermal annealing combined with FUV; d) surface treatment with deep-ultraviolet (DUV) on the dielectric to improve the semiconductor adhesion and wetting; e) inkjet printing of the In_2O_3 semiconductor ink; f) final devices printed in a flexible substrate after S/D evaporation.[309] Copyright © 2020, Wiley-VCH Verlag GmbH & Co. KGaA, Weinheim.

Figure 4.8 (a) shows the Al_2O_3 ink being transferred to the printing plate and then subsequently to the substrate by contact force. The maximum ink transferred by a surface relief printing plate is usually less than screen printing or gravure printing. This allows a thin printed layer with

relatively sharp edges and smooth surface which is critical for thin film transistors. Other advantages of this technique are the large ink viscosity range (2–500 cP), the high-throughput and the low-cost printing plates.[376,475] First, the pressure in the flexographic printing unit was optimized to assure a good contact of the printing plate cylinder with the anilox and substrate cylinders. To guarantee the formation of continuous films, 1 min O_2 plasma treatment was used for the substrates before the printing. Since highly uniform thin film layers are critical for TFTs, the printing speed and the transfer volume were varied in the range of $40 - 60$ m·min^{-1} and $3 - 5$ mL·m^{-2}, respectively (see Figure B1, Appendix B). The most homogeneous layer was obtained when using a high printing speed (PS) of 50 m·min^{-1}. Using lower or higher PS, the uniformity of the film was lost. In terms of transfer volume of the anilox, 3 and 4 mL·m^{-2} allowed a uniform printing pattern. However, 4 mL·m^{-2} was selected for further tests since with the lower transfer volume the films were thinner, which could compromise the dielectric film properties during TFT fabrication. For 5 mL·m^{-2} using the same printing plate and mask pattern, the pattern edge definition was lost due to excess ink (see Figure B1, Appendix B). After optimization of the printing speed and anilox volume, the film thickness was increased by printing two consecutive layers and by varying the Al_2O_3 ink concentration ($0.4 - 1.6$ M). A reduction in printing quality is observed for two-layer films, as the printed films show a clear coffee ring effect and more defects are visible (see Figure B1, Appendix B). Increasing ink concentration allows high quality uniform dielectric single layers to be achieved until 1.2 M. For the higher concentration of 1.6 M, a non-uniform layer related with the ink spreading starts to appear.

In Figure 4.9 (a), a visual increment of the layer thickness of the printed dielectric patterns can be observed which is proportional to the ink viscosity. However, when a higher ink concentration (1.6 M) with high viscosity (78 cP) was used, a decrease in uniformity was observed which compromises the device performance. Taking that into account, 1.2 M ink concentration was selected for further tests as this concentration allowed a higher film thickness whilst maintaining good uniformity, which is crucial to prevent high leakage and pinholes probability (see Figure B1, Appendix B). Notably, by using combustion synthesis in the ink formulation as shown here, a higher viscosity values can be reached due to a higher solute concentration, when compared with conventional sol-gel as reported earlier by Subramanian *et al.*[333] This can be beneficial for roll-to-roll (R2R) printing of thin oxide films from combustion inks.

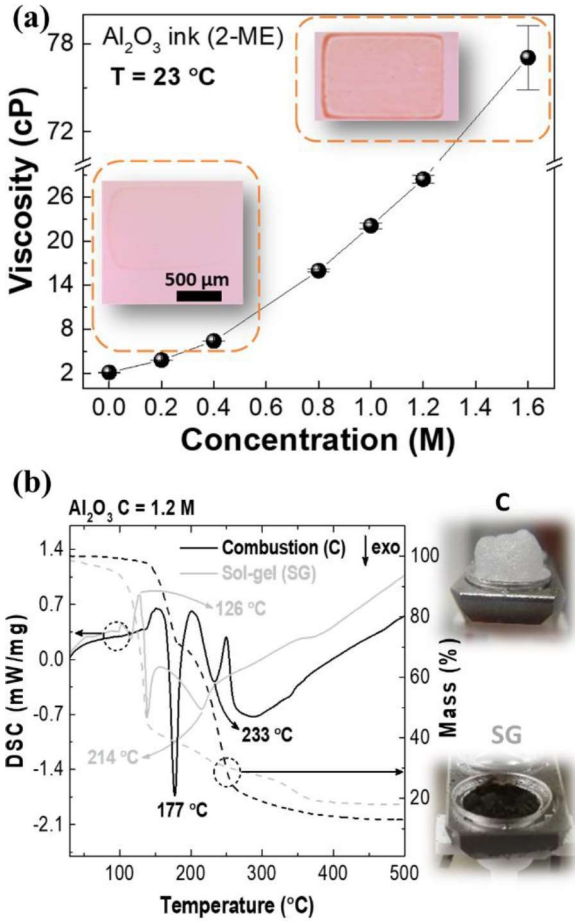

Figure 4.9. a) Viscosity versus concentration for Al_2O_3 precursor inks with the printing image of the lowest and highest volume used; b) TG-DSC analysis of 1.2 M Al_2O_3 precursor sol-gel and combustion xerogel; Samples photograph after TG-DSC showing the typical product in combustion (C) and sol-gel (SG) reaction.[309] Copyright © 2020 WILEY-VCH Verlag GmbH & Co. KGaA, Weinheim.

Thermogravimetry and differential scanning calorimetry (TG-DSC) was performed on the 1.2 M Al_2O_3 sol-gel and combustion xerogel, as depicted in Figure 4.9 (b). For the stochiometric (combustion) xerogel the mass loss in the TG data confirms that the precursor conversion is nearly completed at 250 °C, while the complete degradation of some remaining residual organics occurs at higher temperature yielding a white foam-like powder. However, for the sol-gel xerogel conversion at least 350 °C is needed to achieve degradation of the residual organics and a black powder due to the presence of carbon which inevitably decreases the purity of Al_2O_3. DSC analysis of the combustion xerogel indicates that the conversion of the dried Al_2O_3 xerogel in air shows two main exothermic peaks during the combustion reaction process; an intense exothermic peak at 177 °C with a mass loss of 30 % and a broad exothermic peak at higher temperature around 233 °C with a mass loss of approximately 40 %. For the sol-gel xerogel mass percentage decreases initially 54 % which is related to both the endothermic peak at 126 °C due to solvent

evaporation and the exothermic peak at 139 °C related to the high concentration of nitrates. Also, a small exothermic peak occurs at 213 °C due to remaining residues. It can be noticed that by increasing the concentration exothermic peaks also occur in the sol-gel xerogel decomposition in bulk when compared to lower concentration as previously reported.[35] Also, major differences between the precursor decomposition processes in bulk (as in TG-DSC measurement) and thin film form are to be expected due to the quantity of material involved affecting the gas transport mechanisms.[492] To guarantee higher purity and avoid the presence of carbon in the dielectric thin films the combustion method was selected for integration in MIM and TFTs devices. Since the second peak in the combustion xerogel occurs at a higher temperature (233 °C) than the annealing temperature used to form the dielectric thin films UV treatment was applied. When low-wavelength far UV irradiation (160 nm) is combined with thermal annealing the required process temperature is decreased as the high-energy UV photons enhance the degradation of organic residuals and improve the metal-oxygen-metal (M-O-M) densification through radical mediated reactions.[21,65,307]

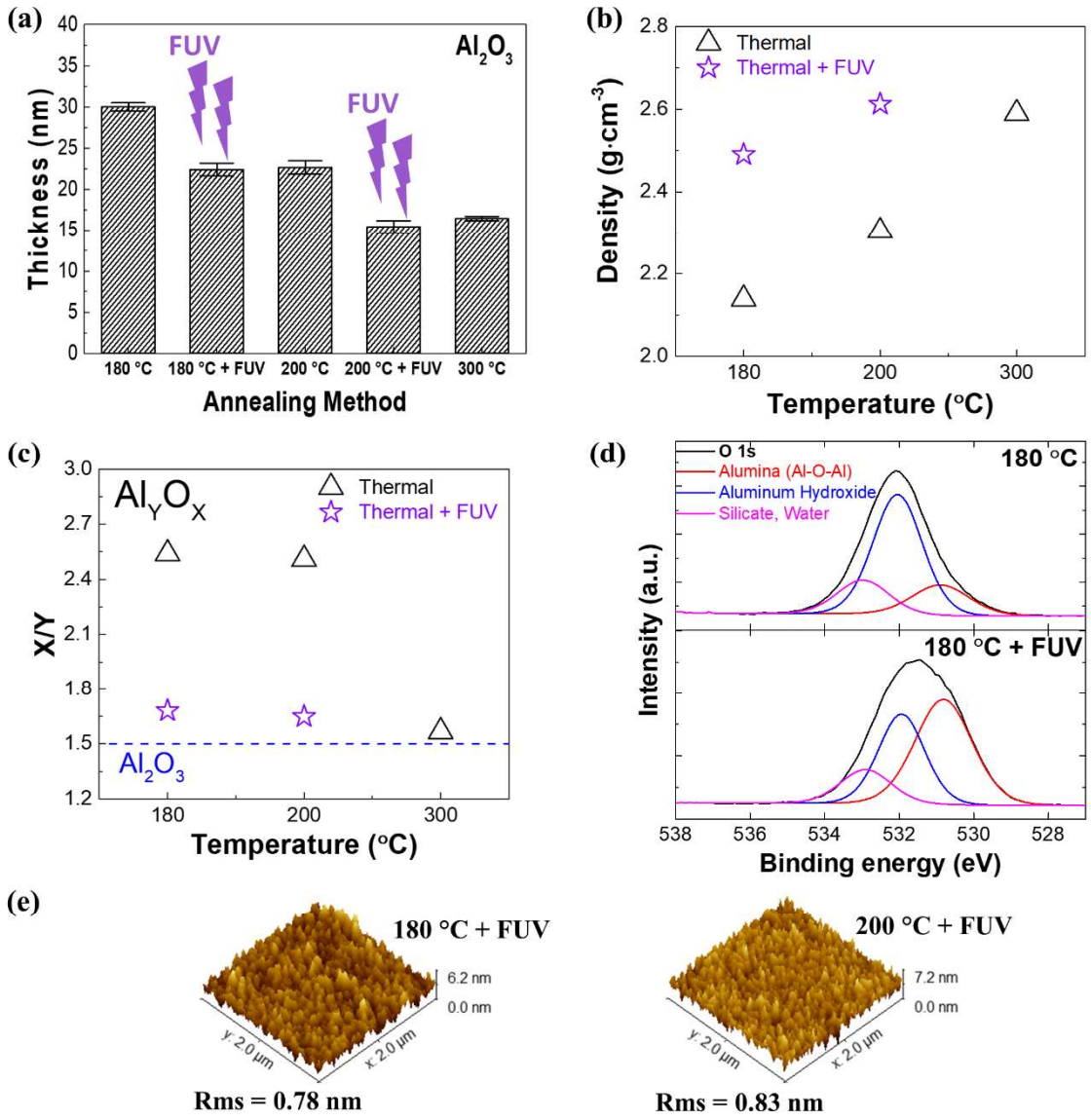

Figure 4.10. a) Statistical analysis of Al_2O_3 dielectric thin film thickness for different annealing conditions; Dielectric thin films' b) density extracted from XRR measurements and c) stoichiometry extracted from XPS analysis; d) Deconvoluted XPS O 1s emission peaks of the aluminum oxide thin films for different annealing conditions with and without FUV at 180 °C; e) AFM images (2 µm × 2 µm) for both conditions combining thermal annealing with FUV irradiation.[309] Copyright © 2020 WILEY-VCH Verlag GmbH & Co. KGaA, Weinheim.

Figure 4.10 (a) depicts the influence of thermal annealing and its combination with FUV irradiation in the printed thin films' thickness. The thickness of the flexographic-printed and thermally annealed Al_2O_3 layers were reduced from 30 nm to 22.4 nm at 180 °C and from 22.7 nm to 15.4 nm at 200 °C when the thermal annealing was assisted by FUV exposure (Table B1 in the Appendix B). The thinnest layer is obtained for the film annealed with FUV at 200 °C, which is lower than the high-temperature reference films annealed at 300 °C. As predicted, a clear

effect of FUV irradiation is noticed in the thin film's densification based on XRR data (Figure B2, see Appendix B), as shown in Figure 4.10 (b). The trends in the total thickness of the films are reflected in the average density, where lower thickness corresponds to higher density. The highest density of 2.6 $g \cdot cm^{-3}$ is obtained for the film annealed with FUV at 200 °C (15.4 nm thick). Metal-oxygen-metal (M–O–M) bonding and the stoichiometry of the printed dielectric films were studied by XPS measurements for samples annealed at different conditions, as depicted in Figure 4.10 (c). The M–O–M bonding is enhanced by the FUV irradiation when compared with the films annealed at low temperature without UV irradiation. In all annealing conditions, the Al 2p peak present a binding energy of 74.1 ± 0.1 eV (Figure B3 in the Appendix B), which corresponds to the formation of the Al_2O_3 phase.[493] However, when using thermal annealing combined with FUV or high temperature annealing at 300 °C, the binding energy is 74.0 eV, whereas for low temperature annealing without UV, the binding energy is slightly shifted to higher energy at 74.2 eV, which indicates that OH- groups remain in the film.[494] This is confirmed by the deconvolution of the O 1s peak (Figure 4.10 (d) and Figure B3 and B4 in the Appendix B), showing for low temperature annealing without UV more adsorbed oxygen (OH-) with a binding energy of 532 eV (Al-OH) than aluminium oxide (Al-O-Al) for which the binding energy is 531 eV.[495,496] Using FUV in the low temperature thermal annealing leads to a 44 % improvement in the fraction of O/Al (1.65) bringing it close to both theoretical stoichiometric value (1.5) and the high temperature sample (1.57). Furthermore, the percentage of the contribution from C 1s in the thin films with just low thermal annealing (≤ 200 °C) were higher (around 10 %) due to the presence of more unconverted precursor (289.3 ± 0.3 eV), as depicted in Figure B5 in the Appendix B. This is in accordance with the TG-DSC results shown in Figure 4.9 (b) which confirms that without concurrent FUV treatment some organic residues remain in the films. Atomic force microscopy (AFM) was performed to analyse the surface morphology of the printed dielectric films annealed with and without the assistance of FUV irradiation. Figure 4.10 (e) shows that the films annealed at 180 °C and 200 °C with FUV irradiation had a low surface roughness of 0.78 nm and 0.83 nm, respectively. All the other conditions without FUV irradiation, also present a roughness below 1 nm (Figure B6 in Appendix B) but the values are slightly larger for the low-temperature annealing without FUV and the high-temperature annealing results in smoothest film with RMS = 0.72 nm. The low surface roughness and the good layer uniformity contribute to a better interface between the dielectric and the semiconductor layers, which is important for TFT applications.

The optimized printed dielectric layer was then applied in MIM devices and their performance and reliability were studied, as shown in Figure 4.11. The FUV-assisted low-temperature annealed printed capacitors were compared to the devices obtained using high-temperature

annealing (300 °C). Figure 4.11 (a) shows that the devices have a stable capacitance value over a wide frequency range (1 Hz - 1 MHz) for the different annealing conditions. The capacitance-frequency (CF) factor, calculated as the ratio between low (1 Hz) and high-frequency capacitance (0.1 MHz), is smaller than 1.2 (Figure B7 (a), see Appendix B), indicating that an increase in the low-frequency capacitance observed with conventional sol-gel route is absent in the printed films.[497] Such effect can be explained by residual hydroxyl groups and proton hopping and can lead to device instability and overestimation of the device mobility. A lower capacitance is observed for the 180 °C assisted by FUV capacitors due to higher thickness. The devices annealed at 180 °C with FUV were tested after 3 weeks and their performance remains stable over the test period (Figure B7 (b), see Appendix B).

To assure that the mobility of the TFTs was not overestimated due to a possible change in the MIMs' capacitance during the annealing of the semiconductor layer, a new batch of printed capacitors was fabricated which were subjected to similar conditions as the printed oxide semiconductor. The capacitance over frequency remained stable after the additional deep UV treatment and longer (1 h) FUV assisted low temperature annealing steps, as shown in Figure 4.11 (a).

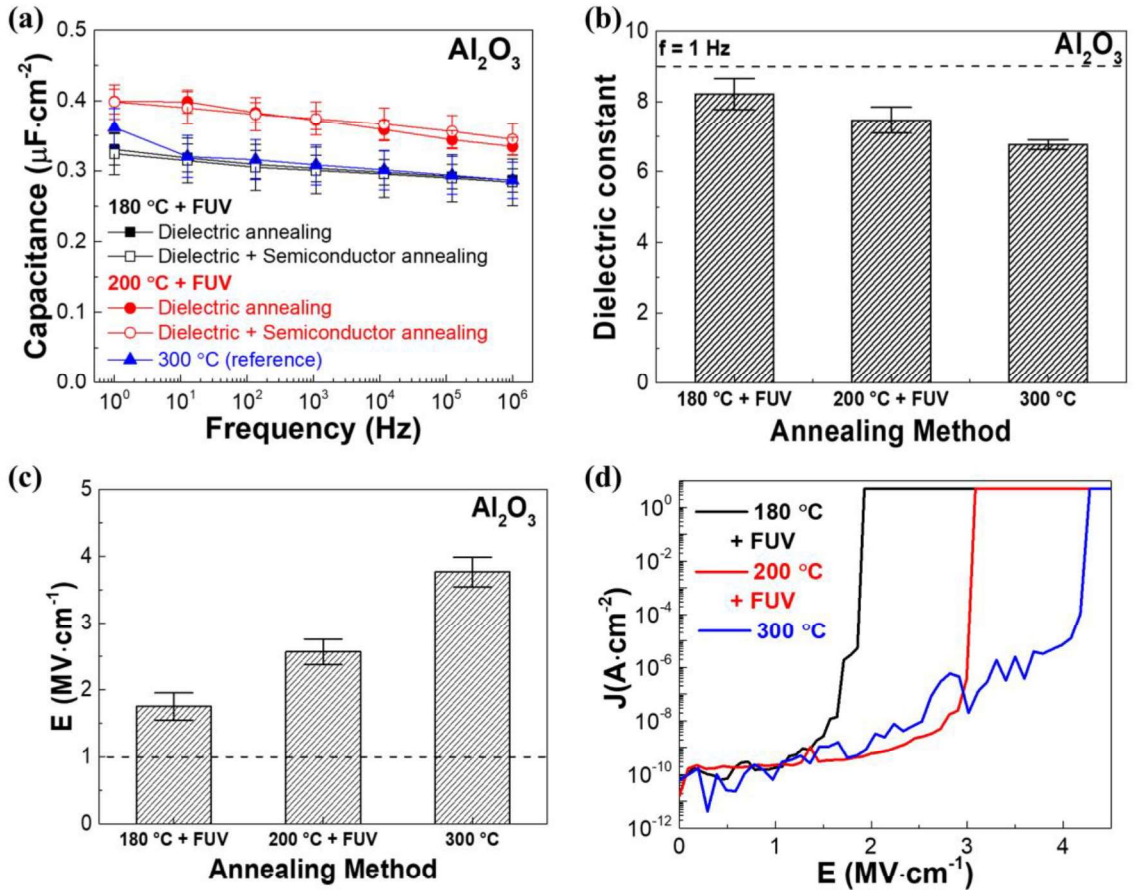

Figure 4.11. Statistical analysis of Al_2O_3 MIM for different annealing conditions: a) capacitance versus frequency characteristics and influence of the semiconductor annealing treatment on the capacitance; b) dielectric constant (capacitance measured at 1 Hz); c) breakdown field and d) typical leakage current density versus the breakdown field curves.[309] Copyright © 2020 WILEY-VCH Verlag GmbH & Co. KGaA, Weinheim.

Figure 4.11 (b) shows the calculated dielectric constant at 1 Hz for different annealing treatments. The theoretical dielectric constant for Al_2O_3 is 9 (as represented by the dashed line) however for solution processed films, it is expected to be lower due to the presence of hydroxyl groups. In literature, the reported[350] dielectric constant values are within the range of 6 –10.4 for solution processed Al_2O_3. In our results, the highest dielectric constant of 8.2 ± 0.4 is obtained for the samples annealed at 180 °C with FUV exposure. The reduction in the value of the dielectric constant observed with the increment of the annealing temperature is related to the decrease of the hydroxyl groups, as observed in the thin films XPS analysis (Figure B4, see Appendix B). Figure 4.11 (c) illustrates the average breakdown field and the inset shows typical leakage current density of the flexible printed capacitors. The breakdown voltage of the capacitors should be at least 1 MV·cm^{-1} for TFT applications in order to withstand a gate voltage of 10 V over a dielectric thickness of 100 nm. Using higher annealing temperature leads to an increment in the breakdown

voltage of the printed capacitors. Low leakage current densities of 10^{-10} A·cm^{-2} were reached for the capacitors annealed with the combination of thermal treatment and FUV exposure, and high thermal annealing at 1 MV·cm^{-1} electric field, as depicted in Figure 4.11 (d).

Printed TFTs that were fabricated with thermal annealing combined with FUV irradiation show excellent performance at low temperature (≤ 200 °C), as depicted in Figure 4.12 (a). The semiconductor layer (In_2O_3) was inkjet-printed on top of the flexography-printed dielectric layer (Al_2O_3) using a nitrate-based semiconductor ink reported earlier.[65] The annealing time of the semiconductor was varied from 30 min to 90 min at both 180 °C and 200 °C annealing temperatures. To investigate the uniformity and reproducibility of these devices, a set of more than 10 devices was produced and characterized for each annealing condition of the semiconductor layer without passivation layer. For flexible integrated circuits (ICs), the TFTs need to achieve (i) a turn-on voltage and a threshold voltage close to 0 V, (ii) current ON-OFF ratio of ≥ 10^6, (iii) subthreshold slope of ≤ 100 mV·dec^{-1} and (iv) saturation mobility of ≥ 1 cm^2·V^{-1}s^{-1}. For ICs a large fluctuation of V_{ON} and V_T would restrain the possibility to integrate thousands of devices onto one functional circuit. Our TFTs exhibit a V_{ON} close to 0 V (0.03 ± 0.08 V) with a small standard deviation up to 1 h annealing time of the In_2O_3 layer for both annealing temperatures (180 °C and 200 °C). After that, a slightly negative shift is observed in V_{ON} for both annealing temperatures. The subthreshold slope (SS) is linked to the quality of the dielectric-semiconductor interface of the TFTs. The SS value varied for different annealing conditions and it increased with annealing time for the devices annealed at 200 °C. However, the lowest SS value of 0.079 ± 0.008 V·dec^{-1} was achieved for the semiconductor annealed for 1 h at 180 °C that is close to the thermionic limit of 60 mV·dec^{-1}. A degradation in SS was observed for longer annealing times at 180 °C. In terms of current ON-OFF ratio that is a key metric for low-power sensors, displays and circuits, acceptable values were achieved even for devices not encapsulated/passivated.

Most of the devices show values of the order of 10^6 with the highest value achieved being 10^7. By increasing the annealing time for both temperatures, the saturation mobility is improved from 1.6 to 2.8 cm^2·V^{-1}s^{-1}, and the hysteresis is reduced from 0.10 to 0.05 V. Notably, a clockwise hysteresis was observed in all of the devices. Typical output characteristics of the printed oxide TFTs can be found in Figure B8 in the Appendix B. In order to study how the device performance is affected after ageing in an air environment, some of the TFTs were characterized after 5 months in dark. Figure 4.12 (b) shows the transfer curve of an In_2O_3/Al_2O_3 TFT for which the shortest annealing time (30 min) and the lowest temperature (180 °C) with FUV irradiation was used for both layers. The device showed only a slight degradation in the ON-OFF current ratio and in the mobility, which could be correlated to the effect of humidity in air on the non-passivated devices.

The most significant changes in ON-OFF current ratio were noticed for the devices annealed for more than 1h (Figure B9, see Appendix B).

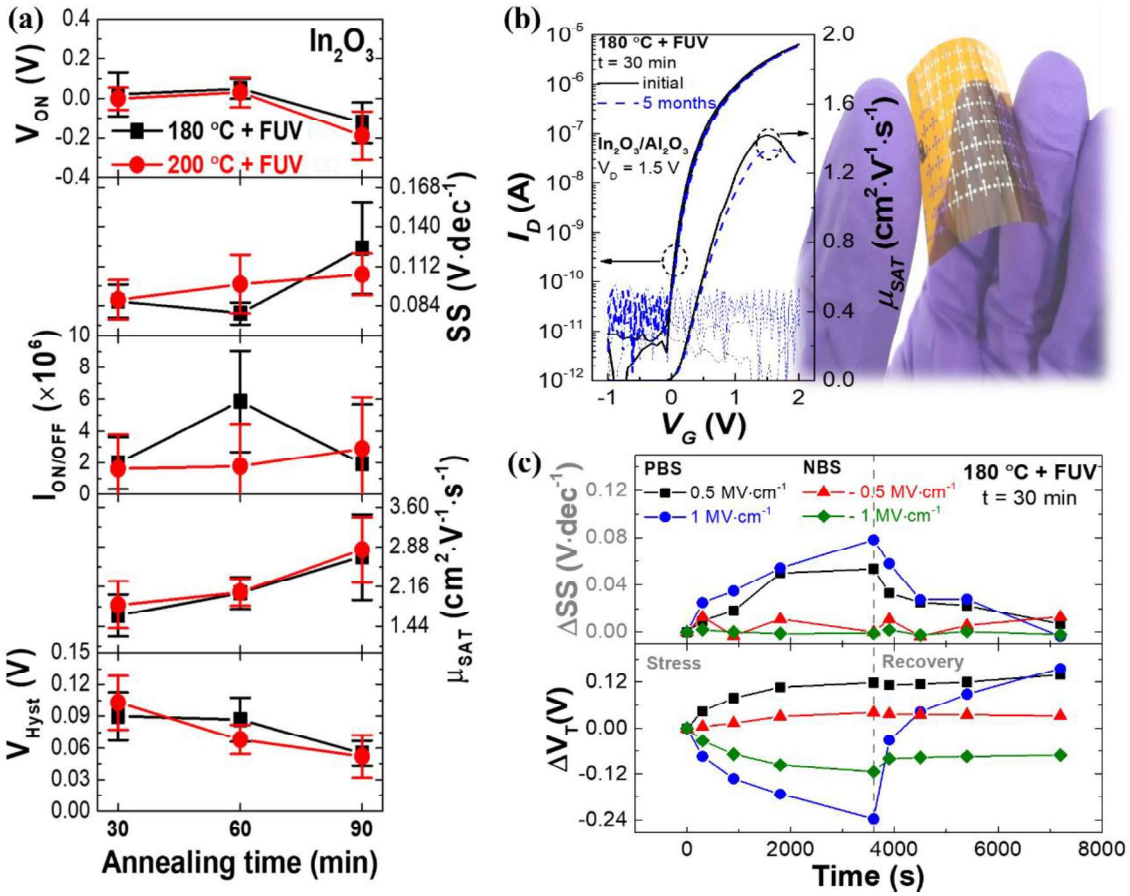

Figure 4.12. (a) Statistical distributions of the In_2O_3 TFT device parameters, turn-on voltage (V_{ON}), subthreshold slope (SS), on-off current ratio ($I_{ON/OFF}$), saturation mobility (μ_{SAT}) and hysteresis (V_{Hyst}) for In_2O_3 with different annealing times; (b) Ageing effect of In_2O_3/Al_2O_3 TFT after 5 months; (c) Subthreshold slope (ΔSS) and threshold voltage variation (ΔV_T), for 0.5 and 1 MV·cm^{-1} stress (for selected device with 180 °C + FUV annealing for 30 min) under PBS and NBS tests for 1 h in air environment.[309] Copyright © 2020 WILEY-VCH Verlag GmbH & Co. KGaA, Weinheim.

We selected the sample annealed at the lowest temperature and for the shortest time (180 °C + FUV, 30 min) to access the behaviour under bias and bending stress as they have been subjected to the mildest annealing conditions and thus could be more prone to instability under bias-stress. The low temperature and short annealing time are also processing-wise beneficial. To explore the viability of our devices in circuit-level applications, a positive (PBS) and negative (NBS) gate bias stress was performed in air environment. The devices were subjected to constant gate voltage corresponding to an electrical field of ± 0.5 and ± 1 MV·cm^{-1} for 1 h followed by a recovery for 1 h in dark conditions. The transfer characteristics in the saturation regime were obtained during stress and recovery processes, as shown in Figure B10 in the Appendix B. Figure 4.12 (c) shows

the change in the subthreshold slope (ΔSS) and threshold voltage (ΔV_T) during the stress and recovery phases. The devices subjected to PBS had a maximum shift of V_T of 0.12 V for 0.5 $MV \cdot cm^{-1}$ and - 0.24 V for 1 $MV \cdot cm^{-1}$. The negative value of ΔV_T using the higher electric field is correlated with the increase in the ΔSS. Also, only a slight saturation mobility degradation of 7.3 % occurs during stress for the highest PBS (1 $MV \cdot cm^{-1}$), as depicted in Figure B10 (e) in the Appendix B. Hereafter, the device shows a fast recovery which is coherent with charge trapping.[307] For NBS, the ΔSS (0.01 $V \cdot dec^{-1}$) and ΔV_T (0.04 V) under - 0.5 $MV \cdot cm^{-1}$ did not show significant changes, but for - 1 $MV \cdot cm^{-1}$ a maximum shift of - 0.11 V was observed in the V_T. In addition to the bias stress, the mechanical stability of the printed flexible oxide TFTs was examined in a bending machine (10, 100, 1000, 10000, 360000 cycles) during 100 h with a bending radius of 5 mm, as depicted in Figure 4.13 and Figure B11 in the Appendix B. The three TFTs that were examined are highlighted in Figure 4.13 (a) by square, circle and triangle symbols. In this case, the electrical current flow and the bending axis were parallel in the devices. The transfer curves show no degradation of the saturation mobility (Figure 4.13 (a) and (b)) and only a slight negative shift of -0.08 V in ΔV_T at 1000 cycles for two of the devices (circle and triangle), as shown in Figure 4.13 (b). When bent for more than 1000 cycles, the devices start to recover to the initial state and, for 360000 cycles, they even surpass the initial values in V_T. This effect can be related to oxygen in air, which can induce doping in the semiconductor causing a positive shift in V_T, since devices are not passivated. However, in general the devices printed on the 38 μm thick flexible substrate are mechanically robust towards bending as both ΔV_T and saturation mobility do not present significant changes. In future work, the devices will be passivated and tested with different bending radius.

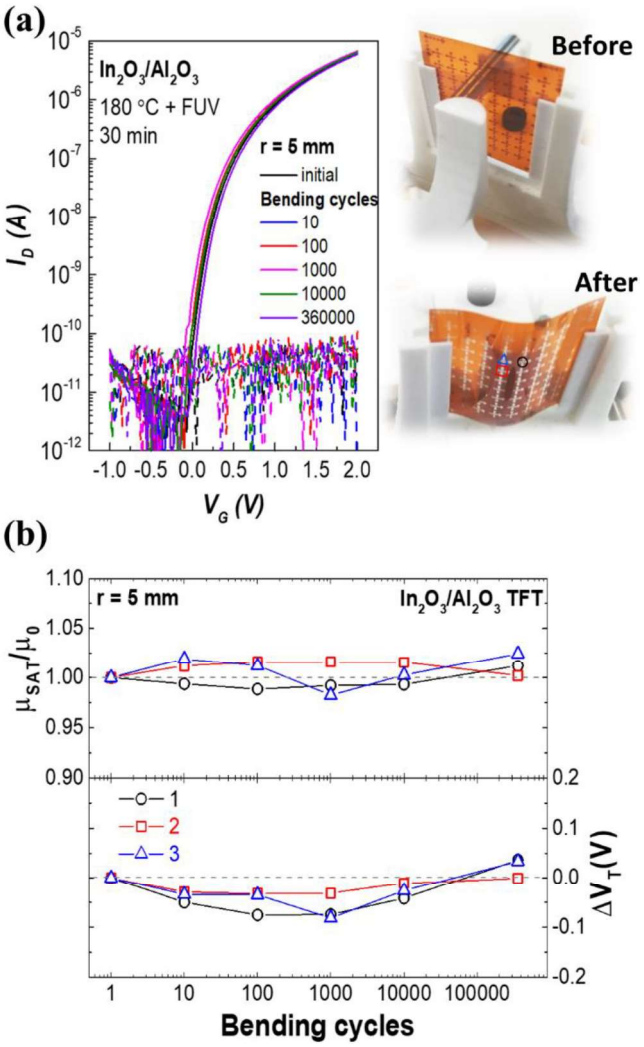

Figure 4.13. (a) Transfer characteristics of a flexible printed In_2O_3/Al_2O_3 TFT on a bending machine with 5 mm radius, with a picture before and after the bending cycle; (b) Bending fatigue test results of the changes in saturation mobility and V_T for three In_2O_3/Al_2O_3 TFTs with 360000 continuous bending/unbending cycles.[309] Copyright © 2020 WILEY-VCH Verlag GmbH & Co. KGaA, Weinheim.

4.2.4. Conclusions

Printed flexible oxide TFTs have challenges that currently limit their implementation in commercial applications. These include limited repeatability and uniformity over large area, high curing temperature, long processing time, high power consumption, large device size, limited long-term stability and limited solutions for encapsulation. In this work, we explored and overcame some of these constraints by using printing techniques that can be applied in industry over large area and with high throughput. The TFTs showed a good electrical performance, reproducibility and both mechanical and operational stability at low processing temperature below 200 °C. The low processing temperature was achieved by using a combination of low-wavelength UV irradiation with thermal annealing and a combustion-synthesis-based ink formulation to lower the required thermal budget. The fabricated devices (50 $m \cdot min^{-1}$ printing speed) on the flexible substrate operate at low voltage ($\leq$ 2 V) with minimal hysteresis thanks to the printed ultra-thin (15 - 25 nm) and smooth ($\leq$ 1 nm) layer of a high-κ dielectric. Under electrical and mechanical stress, the devices showed great stability. Although the devices have large size, the nitrate-based inks used in the flexography- and inkjet-printing could be tuned to novel high-resolution printing methods such as reverse-offset-printing that could lead to printed oxide TFT miniaturization.[386] The electrodes were not printed in this work, since it is not possible yet to print a smooth conductive layer with less than 40 nm thickness, which is crucial for the bottom gate electrode and low-temperature solutions for printable Ohmic S/D contact materials are not readily available. However, the steps taken in this work will allow, in the future, the production of fully-printed oxide TFTs with low operation voltage and, thus, help to reshape the application window for printed flexible electronics like wearables devices or flexible displays.

4.3. Ultrafast curing of solution-based metal oxides

4.3.1. Introduction

Over the last decade, solution-based metal oxide (MO) materials have become excellent candidates for thin film transistors (TFTs), offering conductors, semiconductors and high-κ dielectrics applicable to flexible and large area electronics.[1,4,8,329,450,498] Several processing techniques have been used to fabricate the constituent layers for the TFTs, like inkjet-printing, spray-coating, flexographic printing, screen printing, dip-coating and the most widely utilised spin-coating.[334,376,450,451] These techniques allow to reduce the associated fabrication costs (compared to vacuum technology) and at the same time can provide a high carrier mobility, excellent uniformity and operational stability. The high processing temperatures required to process most semiconductors and dielectric layers has been surpassed with the use of solution combustion synthesis (SCS) and deep-ultraviolet (DUV) photochemical activation. SCS provides additional thermal energy, via an exothermic reaction, resulting in a reduction of the external heating required (both in duration and temperature) for the film formation; i.e. the removal of organic solvents and film densification.[27,92] The DUV concurrent treatment additionally allows for the cleavage of alkoxy groups, active metals, and oxygen atoms to promote the metal-oxide-metal (M−O−M) network formation.[3,362,499,500] Overall, the combinatorial utilisation of SCS and DUV improves condensation and densification of the resultant metal oxide thin filmed, at processing temperatures ≤150 °C.[2,3,20,307,450] However, these methods require long processing times (≥ 30 min) that are not suitable for large-scale roll-to-roll (R2R) processes.[2,3,309] In a R2R processing line, annealing times are restricted by the length of the in-line curing ovens. For example, for a moderate web speed of 1 m/min and a typical oven length of 5 m, the curing time for each processed layer is limited to 5 min.[3,21,501]

Consequently, the industry demands alternative methods that can deliver a rapid annealing process.[502,503] Lately, excimer laser annealing (ELA) has been introduced as a favourable alternative in the fabrication of solution-based MO thin films. This method offers ultrafast processing (in the nanosecond regime), with precise and selective energy delivery , both in depth via critical photon energy absorption as well as spatially (over a well-defined location), [327,504] resulting in a significant improvement of the electronic properties of MO thin films, that can outperform conventional annealing.[327,505] Nevertheless most effort has concentrated in semi-conductive and conductive thin films [326,327,339,503–509], with a notable lack of work on dielectric materials, despite its importance in the robust operation of TFTs.[307] Laser annealing of sol-gel processed HfO_2 has been reported by Teodorescu et al.[510] demonstrating the applicability of XeCl (308 nm) in the densification of amorphous hafnium oxide structure while achieving a high

dielectric constant. However, a double coated layer was required (to eliminate nanoporosity, as well as a very high number of pulses (10000) and a 30 min annealing at 150 °C prior to ELA. Anodization is another promising solution process for the production of high quality dielectric thin films for application in TFTs.[511–515]

The promise of future state-of-the-art electronics (like wearable electronics) can only be enabled by low cost, easy to process, high quality dielectrics, that will allow low power consumption, as well as good mechanical and operational stability.[309,327,501] High-κ dielectric materials such as ZrO_2, HfO_2, Ta_2O_5, SrO_x, $ZrGdO_x$ or Al_2O_3 increase the areal capacitance of the gate dielectric allowing low operation voltage of TFTs.[450,516,517] Among these dielectrics, amorphous Al_2O_3 is one of the most promising due to its characteristic properties such as its high dielectric constant (~9) combined with a large band gap (8.9 eV), low interfacial trap density with semiconductors, high breakdown electric field.[307] At the same time, Al_2O_3 can be obtained from aluminium which is one of the most abundant materials on earth and hence it meets current demands for use of non-critical materials in the life-cycle assessment.[451]

In this work we demonstrate the production of amorphous aluminium oxide (AlO_x) thin films from solution and via a combination of SCS and ELA, and we report the performance of TFTs comprising these thin films. We applied a short drying cycle (15 min or 1 min) at low temperature (≤150 °C) after spin coating of the solution. Subsequently the samples were irradiated with a few pulses (1 to 3) from a KrF (248 nm) excimer laser, varying the laser fluence. The dielectric quality of the AlO_x layers was evaluated via metal insulator semiconductor (MIS) devices, prior to implementing them in low operation voltage TFTs.

4.3.2. Experimental details

4.3.2.1. Precursor solution preparation

Aluminum nitrate nonahydrate ($Al(NO_3)_3 \cdot 9H_2O$, Fluka, 98%) was dissolved in 2-methoxyethanol (2-ME, $C_3H_8O_2$, ACROS Organics, 99%), to yield a solution with an Al^{3+} ion concentration of 0.1 M. Urea ($CO(NH_2)_2$, Sigma, 98%) was then added to the prepared solution was maintained under constant stirring (430 rpm) for at least 1 h after dissolving the precursors. The urea to aluminum nitrate molar proportion was 2.5:1, to guarantee the redox stoichiometry of the reaction.[7] The precursor solution was filtered through a 0.20 μm hydrophilic filter before use.

4.3.2.2. Dielectric deposition, processing and characterization

Prior to deposition all substrates (p-type silicon wafers, of 1-10 Ω·cm, with size of 2.5cm×2.5 cm) were cleaned in an ultrasonic bath at 60 °C in acetone for 10 min, then in 2-isopropanol for 10 min and dried under nitrogen (N_2); followed by a 10 min UV/Ozone surface activation step in

a PSD-UV Novascan system. Thin films were deposited by spin coating a single layer of the AlO_x precursor solution for 35 s at 2000 rpm (Laurell Technologies) followed immediately by a short drying cycle (hot plate annealing) at 150 °C with two different durations, 15 min or 1 min. Then, the photonic processing was performed, on different areas of the sample and with various laser conditions (fluence and number of pulses). The photonic processing station comprises a KrF excimer laser (Lambda Physik 305i, $\lambda = 248$ nm, 25 ns pulse duration) and a beam delivery system that provides the sample with a top hat profile laser spot (3x3 mm^2 in size) with fluence (energy density, mJ/cm^2) uniformity better than 2 % across the area of the laser spot. The photonic processing station is described in detail elsewhere.[518,519] Finally, reference layers thermally annealed on a hotplate for 1h at 300 °C (without any photonic processing) were also fabricated, for comparison.

The films´ structure was assessed by glancing angle X-ray diffraction (GAXRD) performed on an X'Pert PRO PANalytical powder diffractometer using the Cu Kα line radiation ($\lambda = 1.540598$ Å) with an angle of incidence fixed at 0.9°. The surface morphology was investigated by atomic force microscopy (AFM, Asylum MFP3D). Spectroscopic ellipsometry measurements of the thin films deposited on silicon substrates were made over an energy range of 1.5–6.0 eV, at an incident angle of 70°, with a Jobin Yvon Uvisel system, in order to access the films´ thickness.

X-Ray Reflectivity (XRR) measurements were performed in a Rigaku Ultima IV diffractometer equipped with a multilayer X-ray mirror, using the Cu Ka line. The X-ray generator was operated at 40 kV and 40 mA and the reflected intensity was recorded by a scintillator detector in the range of 0.1 to 5 degrees 2 theta.

Fourier Transform Infra-Red (FTIR) spectroscopy characterization of the thin films was performed using an Attenuated Total Reflectance (ATR) sampling accessory (Smart iTR) equipped with a single bounce diamond crystal on a Thermo Nicolet 6700 Spectrometer. The spectra were acquired at a 45° incident angle in the range of 4500–540 cm^{-1} and with a 4 cm^{-1} resolution.

4.3.2.3. Electronic device fabrication and characterization

Two type of devices were fabricated for the evaluation of the quality of the AlO_x thin films produced: Metal-Insulator-Semiconductor (MIS) capacitors and Thin-Film-Transistor (TFTs).

MIS capacitors were produced by depositing an AlO_x single layer onto p-type silicon substrates as described above. Aluminum electrodes with an area of 7.85×10^{-3} cm^2 (dots of 1 mm in diameter 100 nm thickness), were deposited by thermal evaporation via a shadow mask on top of the insulators, with similar but unpatterned aluminium electrodes being also deposited on the back

of the silicon wafer (after removal of the native SiO_2 by scratching with a diamond tip pen). Electrical characterization was performed measuring both the capacitance–voltage and capacitance-frequency characteristics in the range of 1 kHz to 1 MHz, using a semiconductor parameter analyser (Keysight B1500A).

TFTs were produced in a staggered bottom-gate architecture, by depositing the single layer AlO_x onto p-type silicon substrates to act as gate dielectric.

The indium-gallium-zinc oxide (IGZO) semiconductor film (30 nm thick) was sputtered onto the dielectric thin film via a shadow mask. The deposition was performed using a commercial IGZO ceramic target (2:1:2 In:Ga:Zn atomic ratio) by RF magnetron sputtering in an $Ar+O_2$ (14 sccm and 2 sccm respectively) atmosphere and without intentional substrate heating in an AJA 1300-F system.[466]

Finally, source and drain aluminum electrodes (80 nm thick) were deposited by thermal evaporation via a shadow mask, forming TFTs with a channel length (L) of 90 μm and width (W) of 1000 μm, as shown in the inset of Figure 4.19 (a). Thereafter the IGZO TFTs were annealed at 150 °C, for 1 h in air. A back contact of 80 nm thick aluminum film was also deposited on the back of the silicon wafer to improve the ohmic contact.

The current–voltage characteristics of the devices were obtained in double sweep mode in ambient conditions using a semiconductor parameter analyser (Agilent 4155C) attached to a microprobe station (Cascade M150) inside a dark box.

To assess device shelf life stability tests were performed after 1 year of storage in atmospheric conditions. Positive gate bias stress tests were performed on the TFTs using a semiconductor parameter analyzer (Keysight 4200SCS) and probe station (Janis ST-500) under atmospheric conditions by applying a constant gate voltage (corresponding to 0.5 MV/cm electric field) for one hour. The transfer characteristics were measured at fixed time intervals during the bias-stress process.

4.3.3. Results and discussion

The combinatorial methodology (SCS and ELA) implemented in this work, to achieve ultra-rapid high-quality solution-based M-O-M thin film formation, is depicted in Figure 1. At the outset, the metal precursor ($Al(NO_3)_3 \cdot 9H_2O$) is dissolved in 2-methoxyethanol (2-ME) and stirred for more than 12 h at room temperature (20–28 °C), where a ligand exchange reaction occurs from nitrate to hydroxide (Figure 4.14 (a)). Then the as-spun films are subjected to a short drying cycle (15 min or 1 min) at 150 °C (Figure 4.14 (b)). The choice of 150 °C, besides allowing the use of flexible substrates, was also made in order to sit roughly in the middle of the range defined by the boiling point of the solvent utilised (126 °C for 2-ME and hence some solvent removal is achieved), but below the threshold for combustion (180 °C and hence no combustion is initiated).[309]

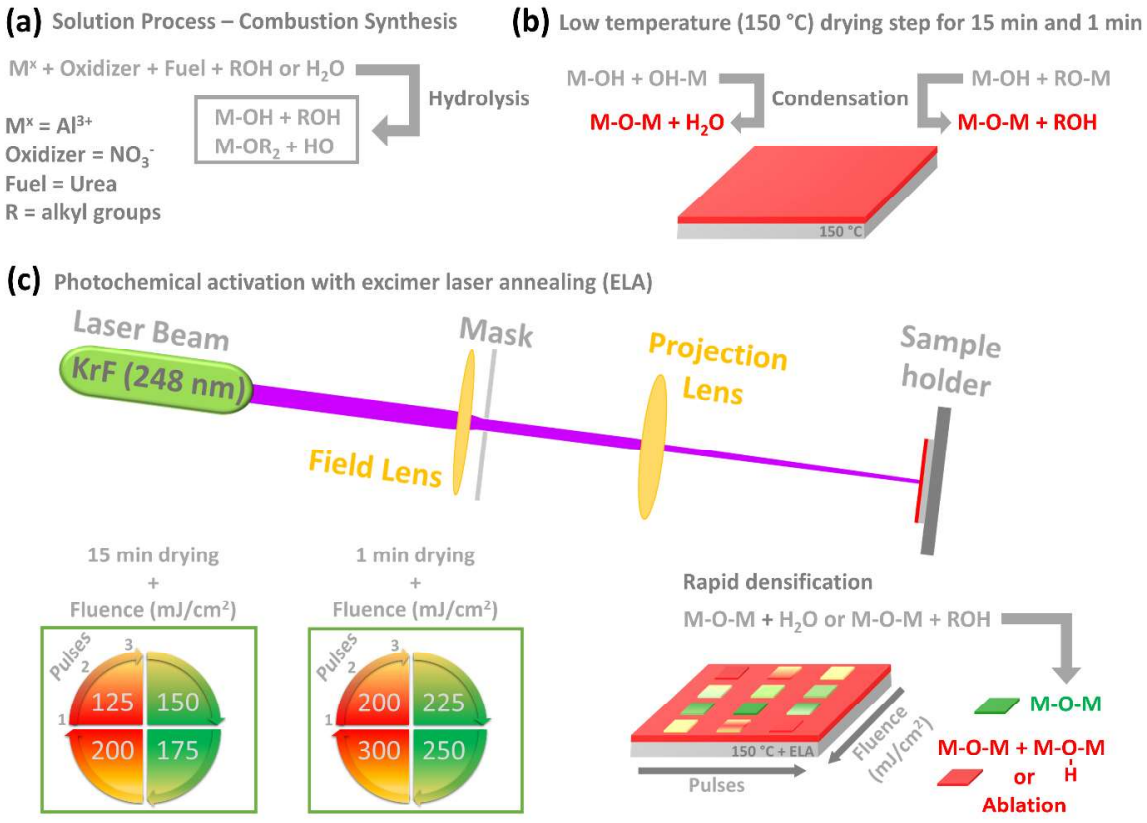

Figure 4.14. Illustration of the SCS and ELA combinatorial approach showing the (a) hydrolysis and (b) condensation mechanism of metal-oxide precursors; (c) Schematic representation of the photonic processing for AlO_x thin films with different fluences and number of pulses, after 15 min or 1 min of hotplate drying at 150 °C immediately after spin coating.[520] Copyright © 2020, Royal Society of Chemistry.

Previous work[92] has revealed that the precursor solution displays an absorption peak well in the vicinity of a KrF excimer laser emission (248 nm). Naturally, this wavelength enables the

photochemical cleavage of alkoxy groups, activating oxygen and metal ions, for the facilitation of the M-O-M network formation.[3] This solid-state chemical reaction is extremely fast and rapidly activates the reaction between the oxidizer (aluminium nitrate) and the fuel (urea). Additionally, the ultra-fast character of ELA enables the utilization of flexible substrates,[521] along with reducing the processing time drastically (as compared to DUV lamp irradiation typically requiring 30 min).[92] In Figure 4.14 (c), the circular schematics depict (in a clockwise manner) the increasing fluence and number of pulses applied on samples of each drying cycle. The coloured coded regions indicate AlO_x thin films obtained at different conditions. The colour intermixing suggests conditions where the photonic processing was either not enough to cause densification or was excessive and caused damage (red regions), and where it was suitable for the formation of AlO_x thin films (green regions).

4.3.3.1. Thin films structural characterization

The degree of densification can be revealed by the critical angle of an X-ray Reflectivity (XRR) measurement. Figure 4.15 (a) shows the XRR curves around the critical angle for 5 characteristic cases: the reference thin film (hotplate treated for 1h at 300 °C), the as spun film after drying at 150 °C for 15 min and for 1 min, as well as the same two dried films photonically processed with one laser pulse at 175 mJ/cm^2 and 250 mJ/cm^2 respectively. By qualitatively comparing the critical angles of the dried films, one can notice that both samples have the same critical angle and thus density, independently of the drying time. The additional photonic processing has resulted in a considerable densification compared to the dried thin films and notably present a similar density to the reference sample (1h at 300 °C). Therefore, it immediately educes that the photonic processing approach can provide AlO_x thin films of similar density to those produced by a long duration higher temperature thermal (hotplate) annealing, but at a considerable fraction of the time and in a macroscopically cold process. The XRR curves were fitted with a three layer model (AlO_x film/SiO_2/Si) using Parrat's formalism.[522] The density extracted for the dried samples was 1.6 ± 0.1 g/cm^3, irrespective of the drying time. On the other hand, the density of the reference film was found to be 2.6 ± 0.1 g/cm^3, which is in agreement to values reported in the literature (~2.53 g/cm^3).[523] The photonically processed samples were found to have densities of 2.4 ± 0.1 g/cm^3 (for the 15 min + 175 mJ/cm^2) and 1.7 ± 0.1 g/cm^3 (for the 1 min + 250 mJ/cm^2) respectively.

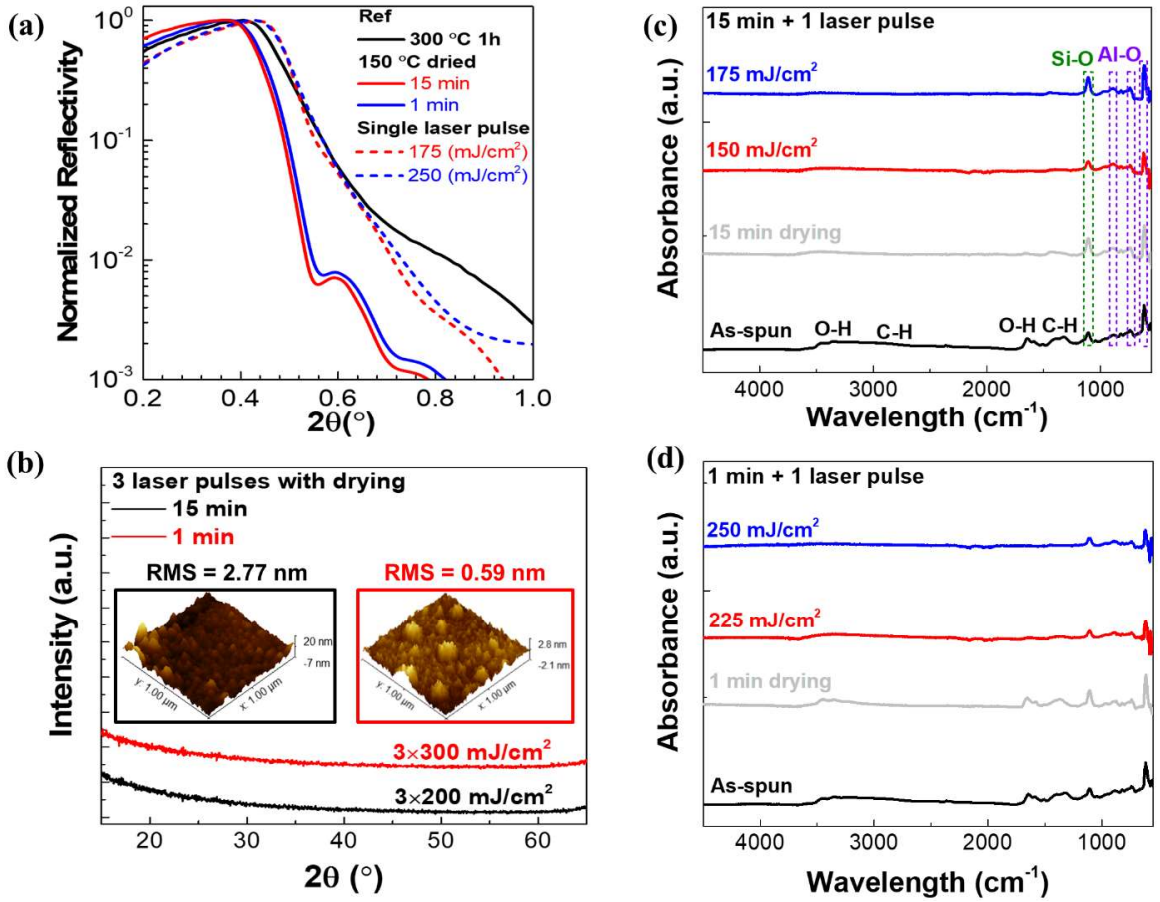

Figure 4.15. (a) XRR measurements of 5 selected samples showing the critical angle, (b) XRD diffractograms and AFM images (1×1 μm²) of two samples dried at 15 min and 1 min, combined with photonic processing at the highest fluence values in each case (200 mJ/cm² and 300 mJ/cm² respectively) and maximum pulses (three pulses), (c) and (d) FTIR spectra of AlO_x thin films before and after single laser pulse photonic processing of the 15 min and 1 min dried (at 150 °C) sample respectively.[520] Copyright © 2020, Royal Society of Chemistry.

The microstructure of the solution-based AlO_x thin films was investigated by glancing angle X-ray diffraction (GAXRD). The absence of any diffraction peaks in Figure 4.15 (b) reveals that the thin films are amorphous, for both drying cycles combined with the photonic processing, even at the highest fluences and number of pulses. The insets in Figure 4.15 (b) are show the films' surface morphology obtained by atomic force microscopy (AFM) measurements for the highest fluences. A surface roughness (≤ 2.8 nm) was observed for both drying cycles combined with photonic processing at the highest fluence and number of pulses. However, the surface morphology was not highly uniform, with some peak to valley values at 27.2 nm and 4.9 nm, for 15 min and 1 min drying cycle, respectively. For lower fluences the surface roughness was below 2 nm which guarantee a more uniform interface between the dielectric and the semiconductor.

In order to evaluate the extent of solvent removal, the AlO_x thin films were characterized by attenuated total reflection Fourier-transform infrared spectroscopy (ATR-FTIR), as shown in Figure 4.15 (c) and (d), for the two drying cycles respectively. All samples show an absorbance peak attributed to Si-O vibration (1107 cm^{-1}), due to the presence of native oxide on the Si wafer. Absorption bands related to O–H stretching vibrations (3700 – 3000 cm^{-1}; 1630 cm^{-1}; 1575 cm^{-1}) associated to water absorption and C–H (3090 – 2800 cm^{-1}; 1500 – 1300 cm^{-1}) due to the organic solvent, can be observed on the as-spun samples (prior to drying) and after both drying cycles at 150 °C (for both 15 or 1 min, prior to ELA). Evidently, the residuals are more prominent after the shorter drying cycle. A subsequent ELA treatment even with a single pulse seems to eliminate the residual solvent, as demonstrated by the diminishing relevant bands in the FTIR spectra, with increasing the laser fluence. For a full set of FTIR spectra for all the samples see Figure C1 and C2 in Appendix C. Finally, the absorption peaks observed at, 889, 739–748 and 611–601 cm^{-1}, are attributed to the presence of Al–O chemical bonds.[471]

4.3.3.2. Dielectric thin film electrical characterization

The electrical performance of the dielectric was evaluated by measuring the capacitance-voltage (C-V), capacitance-frequency (C-f) and breakdown field (E) of metal-insulator-semiconductor (MIS) structures. A summary of these results is shown in Figure 4.16, while the full measurements analytically can be found in Figures C3, C4, C5 and C6, as well as Tables C1 and C2 in the Appendix C. Each MIS device was replicated three times for reproducibility purposes.

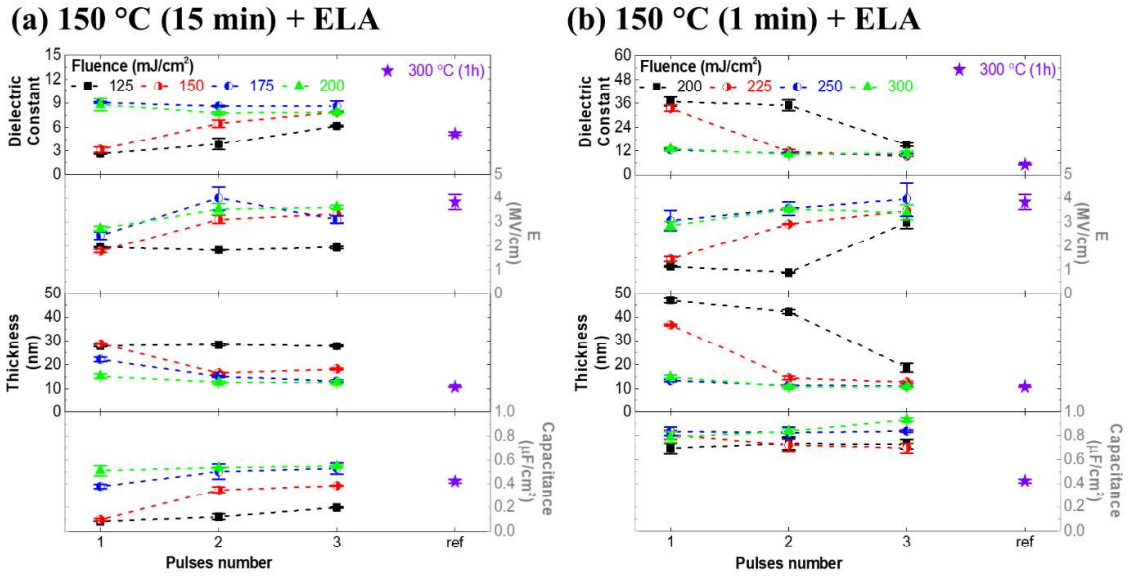

Figure 4.16. Statistical analysis of AlO_x thin films' performance: dielectric constant, breakdown voltage (E), thickness and capacitance measured at 1 kHz, for all fluences and number of pulses applied on films with initial drying of (a) 15 min and (b) 1 min. For comparison the equivalent characteristic of the reference

device (thermally annealed at 300 °C for 1h) is also shown.[520] Copyright © 2020, Royal Society of Chemistry.

The films dried for 15 min (Figure 4.16 (a)), show a considerable improvement of the dielectric constant as the fluence and the number of pulses is increased. For fluences above 150 mJ/cm^2, a dielectric constant of ~9 (calculated at 1 kHz) is achieved, which is typical for Al_2O_3 achieved via PVD techniques.[524] Interestingly, the dielectric constant of the reference MIS device (annealed at 300 °C for 1 h) was surpassed even with the lower fluence of 125 mJ/cm^2 using 3 pulses. These results corroborate the XRR findings, suggesting that ELA enhances condensation and densification of the AlO_x thin film, providing an improved dielectric constant in an ultra-rapid fashion and at lower processing temperatures. Conversely when the drying cycle is shorter (1 min, Figure 4.16 (b)), higher fluences were required in order to achieve reasonable values for the dielectric constant. The unrealistic values (>10) for the dielectric constant achieved at lower fluences are explained by the presence of ionic movement (see Figure C4 in Appendix C).

Another important factor is the durability and stability of the AlO_x dielectric thin films, as expressed by the breakdown voltage. ELA provided films with breakdown voltages up to 4.0 MV/cm, closely matching the breakdown voltage demonstrated by the reference sample (3.8 MV/cm). The breakdown voltage values were found to show a local maximum within the range of fluences investigated, therefore the optimum annealing conditions have been identified.

These are two pulses of 175 mJ/cm^2 and three pulses of 250 mJ/cm^2 for the 15 min and 1 min drying cycles respectively, presenting breakdown voltages of 4.0 ± 0.5 MV/cm and 3.9 ± 0.7 MV/cm, whilst the reference device presented a breakdown voltage of 3.82 ± 0.03 MV/cm. The thickness required in order to calculate the breakdown voltage and the dielectric constant, was determined by UV-VIS ellipsometry, for each device. Besides Figure 4.16, the full results for all devices fabricated can be seen in the Appendix C in Tables C1 and C2 as well as Figures C5 and C6.

The devices' aerial capacitance values at 1 kHz are shown in the bottom panel of Figure 4.16 (a) and (b) for the two drying cycles. The majority of the ELA devices present a higher aerial capacitance than the reference device (0.42 ± 0.02 μF/cm^2). Full C-V characteristic curves at 100 kHz and a summary of aerial capacitance vs frequency is presented in the Appendix C in Figures C3 and C4, respectively. The drying cycles result in a considerable difference in the dispersive character of capacitance, with the shorter drying cycle being more adversely impacted (i.e. more dispersive) potentially due to the probable incomplete conversion and removal of the precursor.

In conclusion, the combination of short drying cycles (15 or 1 min) at relatively low temperatures (150 °C) and ELA delivers in an ultra-fast manner AlO_x thin films with similar or enhanced dielectric properties compared to those achieved via high temperature (300 °C) prolonged (1h) thermal annealing.

4.3.3.3. Low operation voltage IGZO/AlO_x TFTs

Informed by the results presented above (namely the dielectric constant and breakdown voltage) a suitable selection of AlO_x thin films were tested in TFT devices, with IGZO as the semiconductor. A summary of the electrical characteristics of these devices is shown in Figure 4.17 (a) and (b). The full set of the respective transfer curves for each device is shown in Figures C7 and C8 of the Appendix C. Device performance was assessed through the measurement of the hysteresis (V_{Hyst}), turn-on voltage (V_{ON}, the on-set voltage at which the drain current starts to increase), drain current on–off ratio (I_{ON}/I_{OFF}), subthreshold slope (SS), and saturation mobility (μ_{SAT}) which was calculated using the dielectric capacitance measured in AlO_x MIS devices at a frequency of 1 kHz (see Table C3 and C4 in Appendix C).

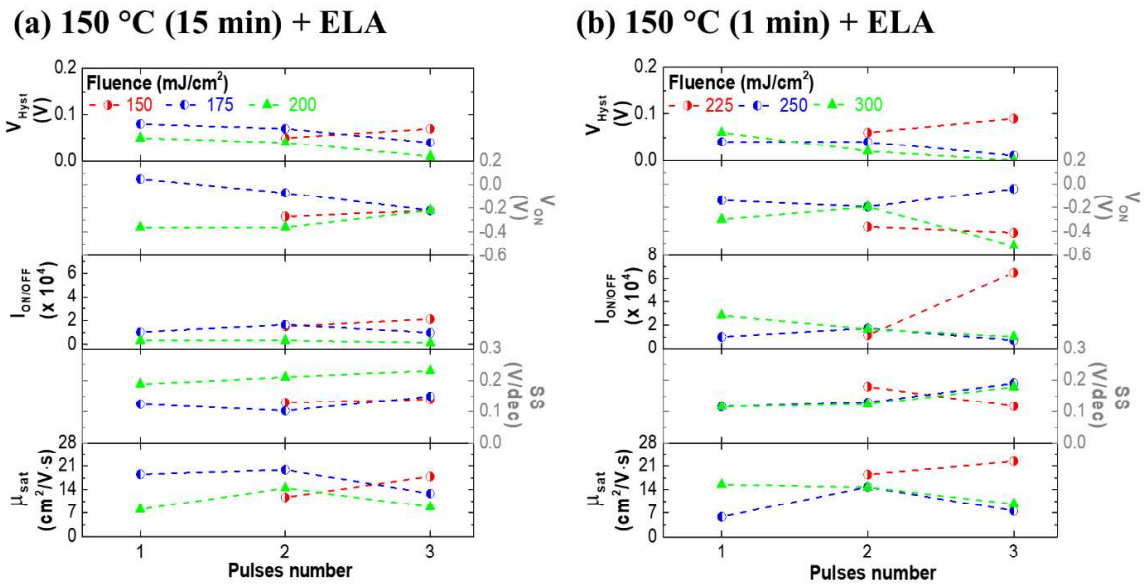

Figure 4.17. TFT parameters: hysteresis (V_{Hyst}), turn-on voltage (V_{ON}), current on-off ratio ($I_{ON/OFF}$), subthreshold slope (SS) and saturation mobility (μ_{SAT}), for the two drying cycles: (a) 15 min and (b) 1 min followed by ELA treatment.[520] Copyright © 2020, Royal Society of Chemistry.

All the devices exhibited an anticlockwise direction and low hysteresis (less than 0.15 V). A moderate hysteresis reduction with the increase of number of pulses and fluence was observed. Equally all of the device presented a current on-off ration of the order of 10^4. In the case of the 15 min drying cycle followed by ELA, the turn-on voltage presents an optimum value (closer to

0 V) at a fluence of 175 mJ/cm^2, whereas higher fluences and number of pulses result in a negative turn-on voltage. Below this optimum fluence some ionic species could remain in the dielectric, whereas above surface damage may occur compromising the quality of the semiconductor-dielectric interface. This is further supported by the deterioration of both the subthreshold slope and the saturation mobility. Surface damage and high density of generated defects is likely at higher fluences, since the solution combustion synthesis (SCS) is an exothermic reaction that occurs in the thin film in an ultra-rapid fashion (due to the ELA pulse lasting only a few nanoseconds). In the case of the 1 min drying cycle followed by ELA, a similar trend was found with an optimum fluence value of 250 mJ/cm^2. The results above are summarised in Figure 4.18 (a) were the best performing ELA devices, for each drying cycle, are presented alongside the reference device (300 °C for 1h).

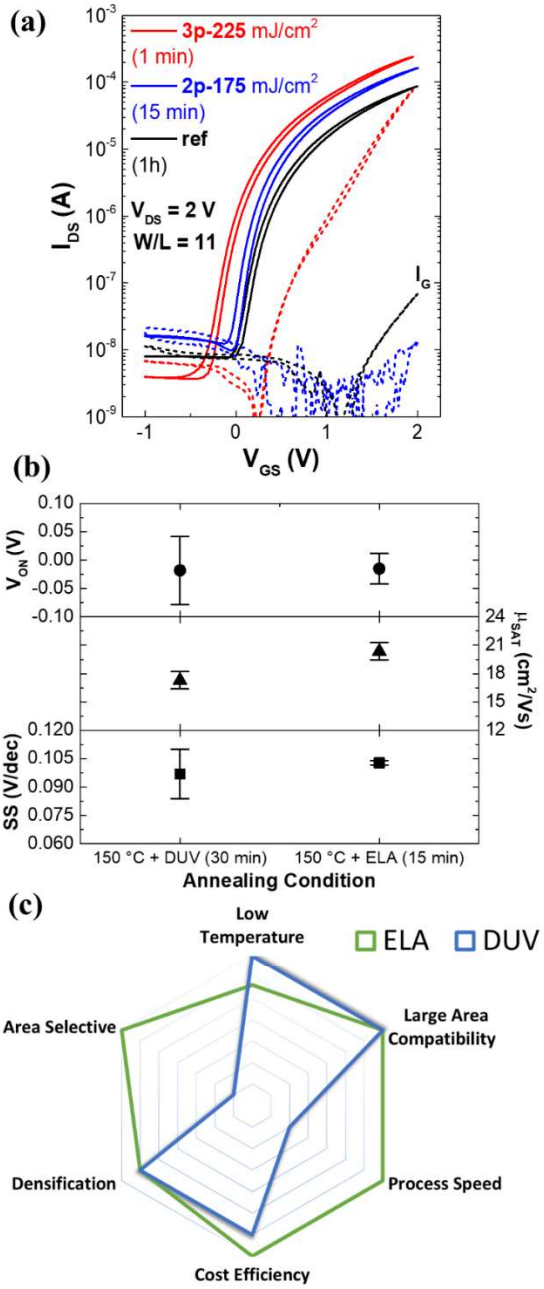

Figure 4.18. (a) Transfer characteristics of IGZO TFT devices fabricated with solution-based aluminium oxide (AlO_x) insulator thin films for different drying times (15 min and 1 min) followed by ELA treatment. The reference device (300 °C for 1h) is also shown for comparison. (b) Summary of TFT device characteristics using deep ultraviolet (DUV) for 30 min (previous report[92]) and this work using the 15 min drying followed by ELA. (c) Comparison of quality characteristics between ELA and DUV treatment for the production of solution-based oxides for the printed electronics industry.[520] Copyright © 2020, Royal Society of Chemistry.

Both drying cycles provide TFTs with comparable or better properties than the reference device, however, the 1 min drying followed by ELA present a higher gate leakage current. Furthermore, we present a comparison of the best performing ELA device (15 min drying cycle and 2x175

mJ/cm^2) to devices with AlO_x fabricated with DUV curing at low temperature[92] (the IGZO layer is identical in both cases). Figure 4.18 (b) shows a statistical analysis revealing that ELA provides solution processed AlO_x dielectric thin films for TFTs with similar electrical characteristics to the DUV devices, but with an improved saturation mobility (see also Table C5 in Appendix C). In general, we can conclude that the combination of ELA treatment with a short drying cycle, immediately after spin coating, can result in AlO_x thin films with quality comparable, if not better, than the standard approach of high temperature thermal annealing (hot plate). The implications of this approach are considerable for the industry of flexible and plastic electronics, as it lends itself to R2R production, for a variety of reasons including: - it enables the use of plastic substrates (maximum processing temperature 150 °C) as it is a macroscopically cold process; - it is rapid enough to allow inline processing while maintaining a reasonable web speed; - it is area selective via laser writing, removing the need for extra fabrication steps for patterning; - it offers oxide thin films of high quality from solution based materials. As such, this approach could provide a significant boost to the printed electronics industry. In comparison to DUV curing (see Figure 4.18 (c)) ELA presents similarly high performance in densification and in large area processability but offers increased overall efficiency through its excellent area selectivity and its massively faster processing time as can be seen in the Appendix C in Table C6. The temperature rise in the metal oxide material is far more extreme with ELA, but at the same time considerably faster, resulting in a completely macroscopically cold process, unlike DUV processing. To investigate the effect of the ambient atmosphere on the IGZO/AlO_x TFTs were performed some ageing and stress measurements as depicted in Figure 4.19.

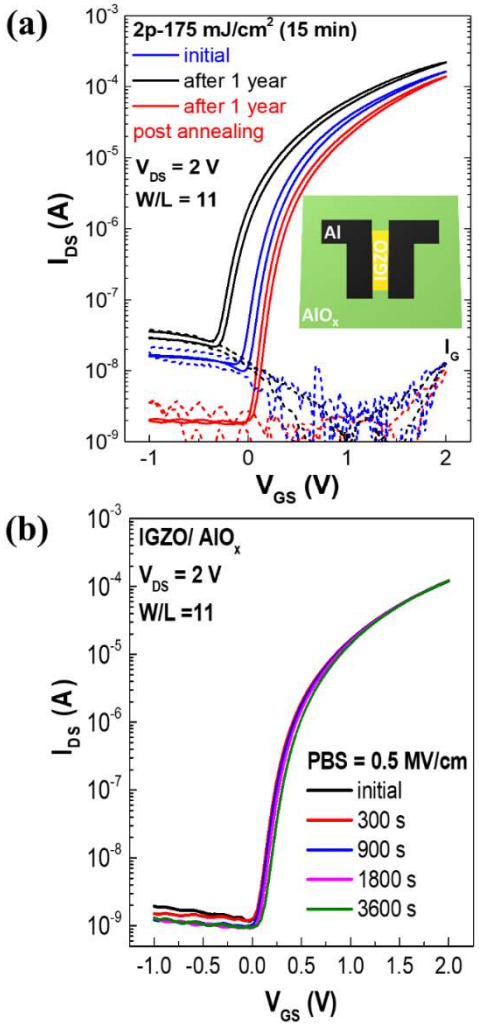

Figure 4.19. Stability tests for the best condition achieved with ELA treatment: (a) Ageing effects of IGZO/AlO_x TFTs after 1 year exposed in air environment without passivation and after a post annealing at 120 °C; inset shows the top view TFT schematic (each electrode had an area of 11.9 × 10^{-3} cm^2); (b) Positive gate-bias stress (PBS) measurements of 0.5 MV/cm on IGZO/AlO_x TFTs for 1 h in air environment.[520] Copyright © 2020, Royal Society of Chemistry.

Figure 4.19 (a) shows transfer characteristics of the same device taken a few days after full fabrication and after 1 year of storage in atmospheric conditions, to determine device ageing. In general, the device performance was preserved, however the turn-on voltage displayed a slight negative shift a year later, most probably associated to surface traps. Also, a small increase of off-current was observed, most probably due to the humidity present in atmospheric environment (which can be surpassed by device passivation).[525,526] To determine the device behaviour after one year but without the influence of surface adsorption of water molecules, a post annealing at 120 °C (30 min) was performed. As expected, the device´s on voltage recovered fully and furthermore the off current was improved by an order of magnitude compared to the initial fabrication.

Following this, the device was subjected to a positive gate-bias stress (PBS) of 0.5 MV/cm for 3600 s as depicted in Figure 4.19 (b). The IGZO/AlO_x TFTs under PBS remained stable showing only a slight threshold voltage shift to a positive value of just 0.02 V, meaning that a reduced quantity of trap sites exists in the dielectric/semiconductor interface. As no deterioration was observed in the subthreshold slope under bias stress, the mechanism present is the charge trapping model.[527] Optimization of production parameters is ongoing, nonetheless these tests already prove the potential of ELA treatment for solution-based oxide TFTs.

4.3.4. Conclusions

In conclusion we have demonstrated the combustion solution synthesis alliance with ELA of AlO_x dielectric thin films at low temperatures in a short drying cycle (15 min or 1 min) and their implementation in TFTs. The AlO_x dielectric films revealed an amorphous nature, low roughness, high-κ (9), low leakage currents (10^{-6} A/cm^2 at 1 MV/cm) and high breakdown voltages ~4 MV/cm. These results indicate that ELA treatment is a viable platform for the fabrication of metal-oxide dielectric thin films at low processing temperatures. Subsequently ELA treatment in combination with combustion synthesis, can be the answer to obtain high performance printed metal oxide TFTs in the R2R industry.

Chapter 5

Solution-based resistive switching memories

Metal oxide resistive switching memories have been a crucial component for the requirements of the Internet of Things (IoT) which demands ultra-low power and high-density devices with new computing principles, exploiting low cost green products and technologies. Most of the reported resistive switching devices use conventional methods (PVD and CVD) which are quite expensive due to their up-scale production. Solution-processing methods have been improved, being now a reliable technology that offers many advantages for resistive random-access memory (RRAM) such as, high versatility, large area uniformity, transparency, low-cost and a simple fabrication of two-terminal structures. Solution-based metal oxide RRAM devices are emergent and promising non-volatile memories for future electronics. In this review, a brief history of non-volatile memories is highlighted as well as the present status of solution-based metal oxide resistive random-access memory (S-RRAM). Then, a focus on describing the solution synthesis parameters of S-RRAMs which induce a massive influence in the overall performance of these devices is discussed. Next, a precise analysis is performed on the metal oxide thin film and electrode interface and the recent advances on S-RRAM that will allow their large-area manufacturing. Finally, the figures of merit and the main challenges in S-RRAMs are discussed and future trends are proposed.

Keywords: solution-based technology, metal oxide thin films, resistive random-access memory (RRAM), memristor, resistive switching.

The literature presented in this chapter is published in:

- ✓ *Emanuel Carlos, Rita Branquinho, Rodrigo Martins, Asal Kiazadeh, Elvira Fortunato. "Recent progress in solution-based metal oxide resistive switching devices", Review, Advanced Materials, 2020.*

5.1. Recent progress in solution-based metal oxide resistive switching devices

5.1.1. Introduction

5.1.1.1. History, emerging resistive switching devices and fundamentals

The increment of wearable electronics connected to the Internet of Things motivates the scale-up of intelligent data store and transmission applications, such as edge computing technologies. For these applications, due to the high velocity required, the volume of data generated and the lower energy consumption, non-von Neumann architectures like RRAM or memristors are highly promising.[528] The incapability to linearly scale power with existing, mostly silicon-based, complementary metal oxide semiconductor (CMOS) technologies lead us to look at new materials and architectures based on resistive switching devices that can be used in edge devices, neuromorphic and quantum computing.[529,530] Resistive switching (RS) devices exploit the RS phenomena to store information. This feature consists in the change of their electrical resistivity between different stable levels when a specific electrical stress is applied.[531] The RS present between two (high resistive state (HRS) and low resistive state (LRS)) or more resistive states allow reaching new types of devices for digital applications that can boost the performance of conventional semiconductor electronic devices.[532] However, before going into more detail, it is vital to step back more than 60 years ago when *Hickmott* observed for the first time the resistive switching phenomena in oxide materials such as, SiO_x, TiO_2, Al_2O_3, Ta_2O_5 and ZrO_2.[533] In 1967, Simmons and Verderber reported the first RS cells based on Au/SiO_2/Al structures (Figure 5.1).[534] Nonetheless, only after 33 years the RS memories research arouse in magnetoresistive films by the group of *Ignatiev*.[535] Two years later, *Zhuang* reported a 64-bit RRAM array using $Pr_{0.7}Ca_{0.3}MnO_3$ via a 500-nm CMOS process.[536] In the following 6 years, notable progress on RS memories was made until 2008 by academic and giant companies like Samsung, Infineon and HP.[537–542] In 2008, *Williams et al.* reported a new concept for the RS devices, the memristor, which makes significant improvement in their use for logic circuits and neural networks.[537] Since then, a large bet has been made by the industry, like SanDisk/Toshiba, IMECAS, Unity and Micron/Sony showing the potential of this technology.[543–546]

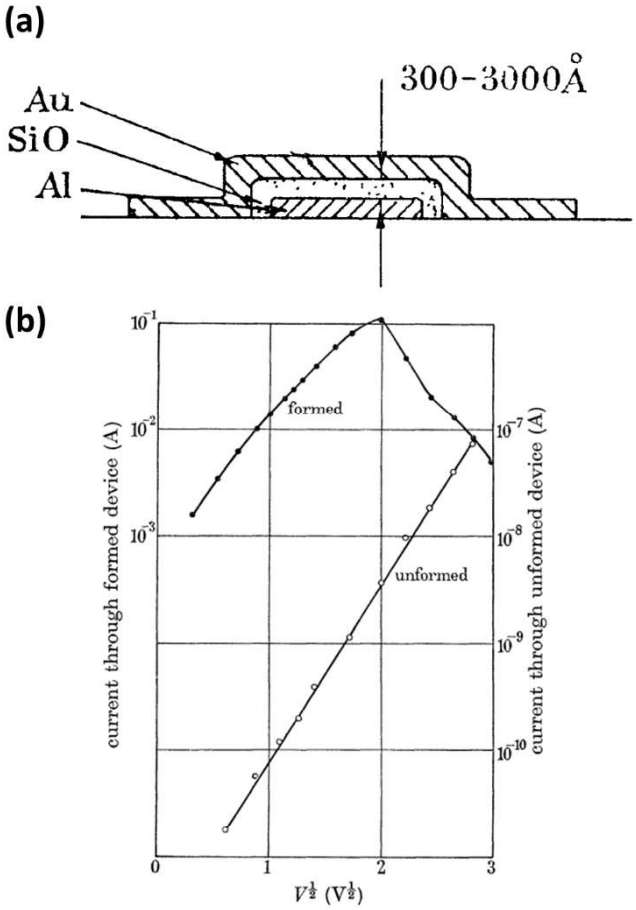

Figure 5.1. a) Sample construction and b) *V–I* characteristics of unformed and formed device. Device no. 1–1: SiO 400 Å thick. Reproduced with permission.[534] Copyright © 1967, Proceedings of the Royal Society of London. Series A, Mathematical and physical sciences.

The current status of the internet of things (IoT) demands physical flexibility, but still must rely on CMOS technology while pushing for enhanced reliability, ultra-low power consumption and ultra large-scale co-integration of antennas, CPUs and non-volatile memories (NVMs), where the RS devices are included.[547] The CMOS circuits and RS devices are in the same package, although in the memory domain the RS technologies have advantages since these require smaller areas and less power consumption for a similar operation.[548,549] The NVMs can store information over long periods of time (> 10 years at 85 °C is the industry standard) and retain information without any power supplied in comparison with volatile memories. Also, NVM technology has the capability for low power consumption, high endurance, high operation speed, small size below 600 nm^2 and high-density capacity.[550] Currently, the most used NVM device is the NAND Flash[551,552] memory, and from the perspective of physics of the emergent NVM devices, three main promising potential technologies are: resistive random-access memory (RRAM), also referred to as ReRAM and memristor,[548,553] magnetoresistive RAM (MRAM),[554,555] and phase change RAM (PCRAM), as depicted in Figure 5.2.[556] Figure 5.3 shows the comparison of the key features of various NVM.

RRAM and PCRAM operate based on the rearrangement of atomic configurations, have significantly larger resistance windows that allow the storage of intermediate resistance states and can even be applied in flexible devices. Going into more detail, spin transfer torque (STT)-MRAM consists of a magnetic tunnel junction structure with two ferromagnetic metal layers, pinned and free, and a thin tunnel oxide that separates them. During the magnetic polarization, the pinned layer acts as a reference while the free layer is free to change during the write operation. To switch the polarization of the free layer voltage, pulses of opposite polarity are applied. Depending on whether the two ferromagnetic polarizations are parallel or antiparallel, the LRS and HRS states are obtained respectively on the device due to the tunnel magnetoresistive effect.[554,555,557]

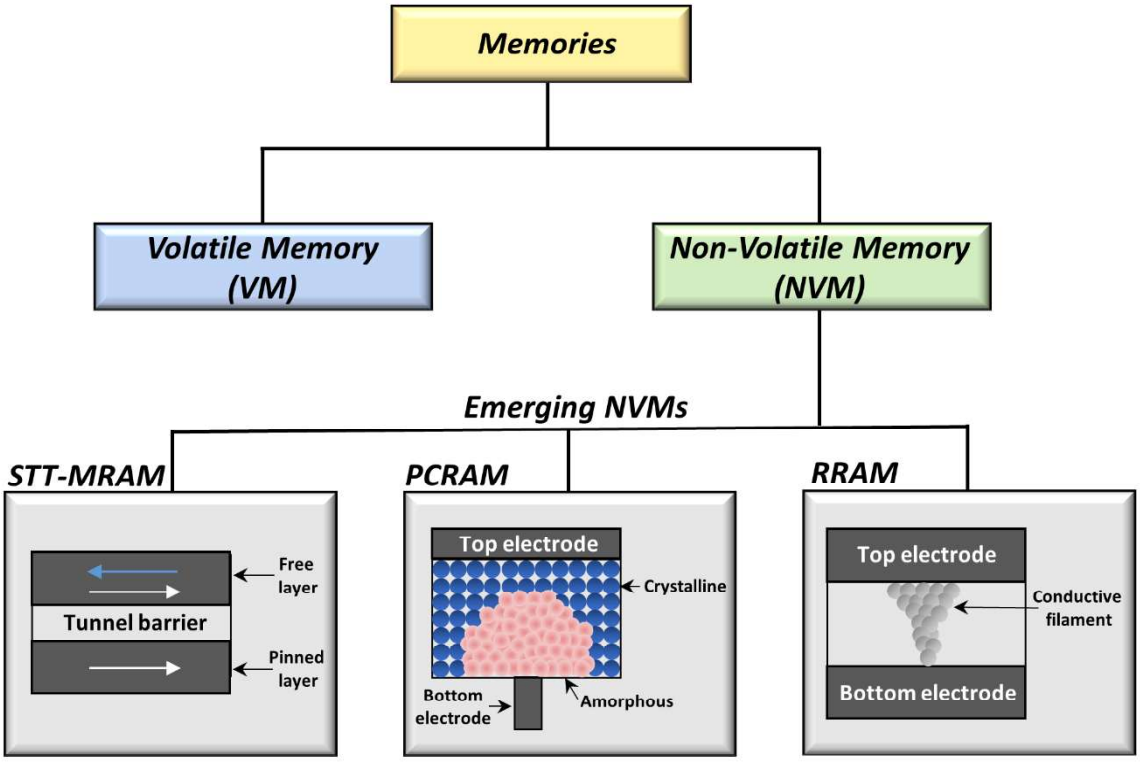

Figure 5.2. Emerging non-volatile resistance-based memory (NVMs) devices: spin transfer torque magnetoresistive RAM (STT-MRAM), phase change RAM (PCRAM) and resistive RAM (RRAM). Copyright © 2020 WILEY-VCH Verlag GmbH & Co. KGaA, Weinheim.

The PCRAM devices are based on specific types of material which suffer a fast and reversible transition from a highly resistive amorphous phase to a highly conductive crystalline phase induced by the joule heating effect (heat sources can be laser or electrical pulses). In this memory, the bottom electrode confines heat and current, which results in a near-hemispherical shape of the amorphous region (HRS state). The LRS state is achieved by crystalizing the amorphous region.[556,558]

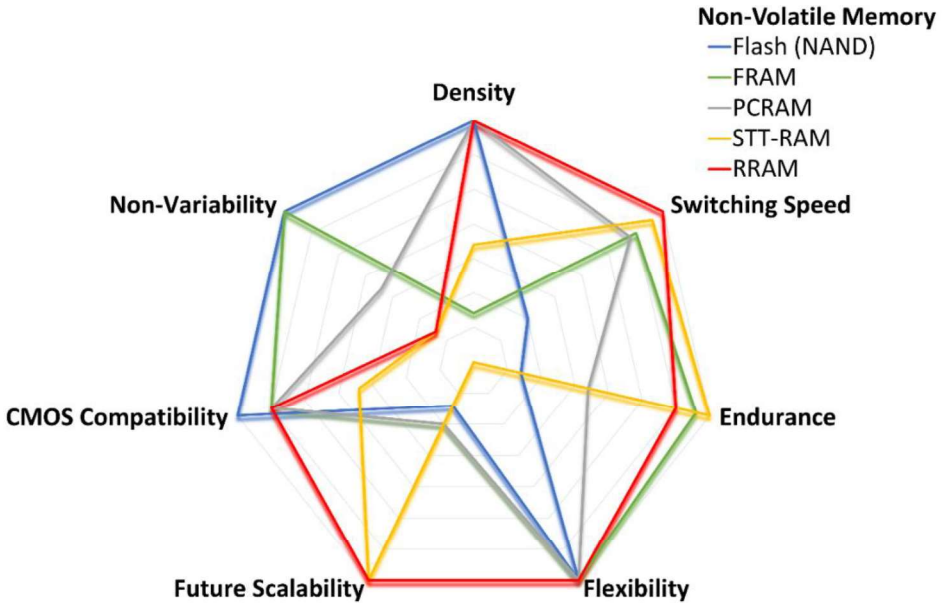

Figure 5.3. Comparison of key features of existing and emerging NVMs.[532,555,559,560] Copyright © 2020 WILEY-VCH Verlag GmbH & Co. KGaA, Weinheim.

RRAM consists of a simple metal–insulator–metal (MIM) cell structure where the material showing the RS capability, active layer, (typically an insulator based on transition metal oxides) is sandwiched between two electrodes. The RS process involves the creation (LRS state) and disruption (HRS state) of conductive filaments (CF)/interface/bulk modulation comprising a localized concentration of defects.[561,562] Typically, these devices involve three main redox based resistive switching mechanisms activated by temperature, electrical voltage or both: (i) the valence change mechanism (VCM) or memory effect based on anion/oxygen-ion motion, (ii) the electrochemical metallization (ECM) mechanism or memory effect based on cation motion and (iii) the thermochemical mechanism or memory effect (TCM) based on cation or anion motion.[562,563] The VCM mechanism is triggered by the migration of oxygen anion species (i.e. motion of the corresponding oxygen vacancies) in the active or resistive switching layer under an external electric field.[563,564] The VCM cells structure commonly uses active metals such as Ta, Hf, Ni, Al and Ti as the ohmic electrode and Pt or Au as the counter electrode material or as another high work function electrode, which is chemically inert (i.e. noble electrode) to guarantee an appropriate Schottky barrier.[562,565] The ECM cell typically uses Ag or Cu as the active electrode due to reversibility of the electrode half-cell reactions and the higher mobility compared to other ions. Thus, the electromigration of metal cations through the resistive switching layer induce a variation on the internal resistance of the device.[566–568] The TCM cell leads to a change of stoichiometry by Joule effect due to a current-induced increase of the temperature.[569] The main distinctive aspect of ECM and VCM is the presence of a bipolar switching behaviour, whereas TCM memories have a unipolar switching behaviour.[562] In the bipolar RS, the set (e.g. transition

from HRS to LRS) and reset (e.g. transition from LRS to HRS) processes need to be triggered by applying stresses of opposed polarity while in the unipolar RS, the set and reset process are applied in the same polarity, as shown in Figure 5.4.[531]

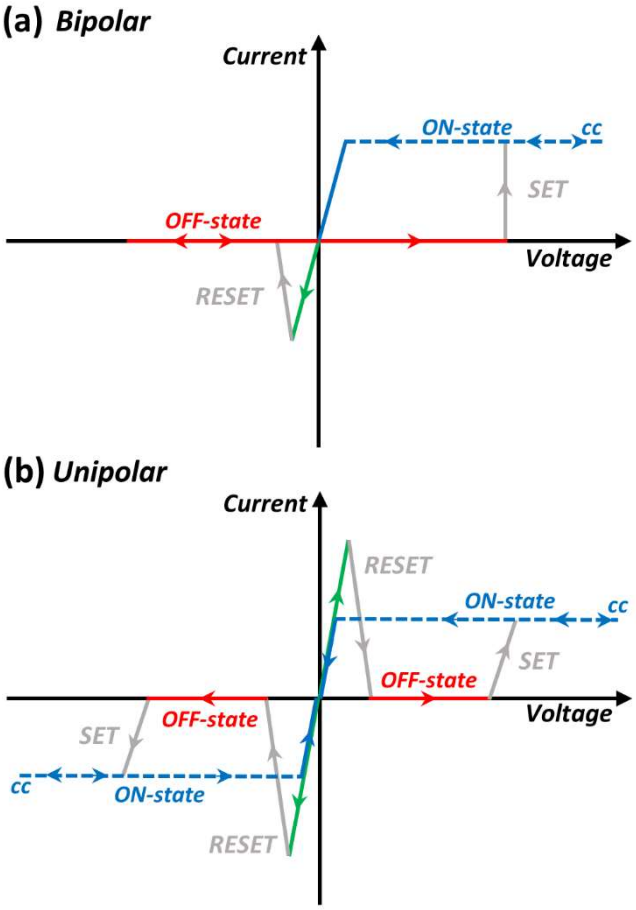

Figure 5.4. a) Unipolar and b) bipolar resistive switching behaviour in RRAM cells. Copyright © 2020 WILEY-VCH Verlag GmbH & Co. KGaA, Weinheim.

The interest in RRAM or also called ReRAM has dramatically increased in the last decade after being associated to the concept of memristor, as shown in Figure 5.5.[537] Certainly, memristors will be the new generation of memories for electronics granting high speed, high scalability, low power consumption, CMOS compatibility and suitability for artificial neural networks.[570]

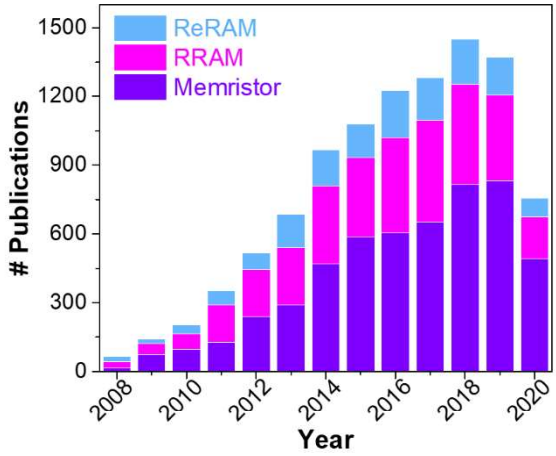

Figure 5.5. Publications on resistive switching devices from 2008 – 2020 (search engine: Web of Science accessed on August 2020; keywords: RRAM; ReRAM; Memristor). Copyright © 2020 WILEY-VCH Verlag GmbH & Co. KGaA, Weinheim.

5.1.1.2. RRAM resistive switching materials

Another crucial point of RRAMs is the type of material used as storage layer between two electrodes which can compromise their operation. These are classified as inorganic (grouped into binary oxides[571–573], ternary and multinary oxides[574,575], nitrides[576,577], chalcogenides[578] and others) and organic materials (e.g. poly(methylmethacrylate) (PMMA), poly(N-vinylcarbazole) (PVK) and polyaniline (PANI))[579–581]. Inorganic materials possess a notable advantage when compared to organic materials: the switching stability. However, organic materials have high mechanical flexibility, simple production methods and lower costs.[582] To achieve most of these features in inorganics, the production methods mainly based on vacuum techniques, like pulsed laser deposition (PLD)[574], magnetron sputtering[571,583,584], thermal oxidation[585], plasma oxidation[586], chemical vapour deposition (CVD)[587] and atomic layer deposition (ALD)[588,589] need to be altered to solution-based processes (e.g. coating and printing techniques)[590,591]. Lately, tremendous effort has been made on solution-based processes to produce oxide one-dimensional (1D) and two-dimensional (2D) nanomaterials for RRAM devices, like metal oxide nanowires and graphene oxide, respectively. These nanomaterials present remarkable properties such as high flexibility, large specific surface area, high transparency and low cost.[550,570,592,593] However, the low production efficiency that compromise their upscale production, as depicted in Figure 5.6, is a considerable issue. In the case of metal oxide thin films, they can be processed in a simple way and without expensive methods on roll-to-roll (R2R) compatible techniques, which decreases the associated cost by 64 %.[1] Also, a huge advantage of oxides, particularly transition metal oxides (TMOs), is that many of them exhibit resistive switching behaviour, as shown in periodic table in Figure 5.7.

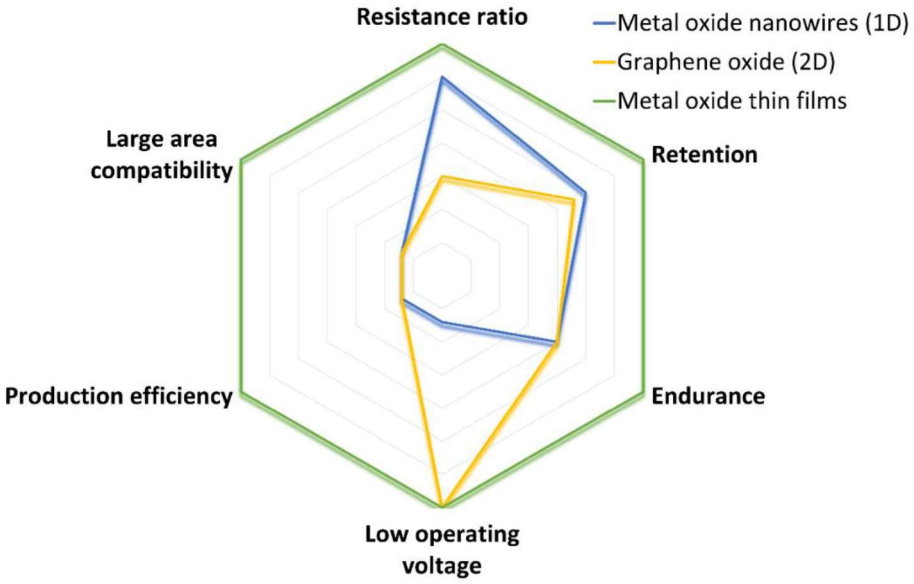

Figure 5.6. Comparison of some key performance indicators of RRAM devices using different oxide materials.[532,550,570,594] Copyright © 2020 WILEY-VCH Verlag GmbH & Co. KGaA, Weinheim.

This opens a new window for the application of solution-based metal oxide RRAM in large scale manufacturing which are highly demanded for wearable applications. Still, some challenges need to be overcome beforehand, as is discussed in this work.

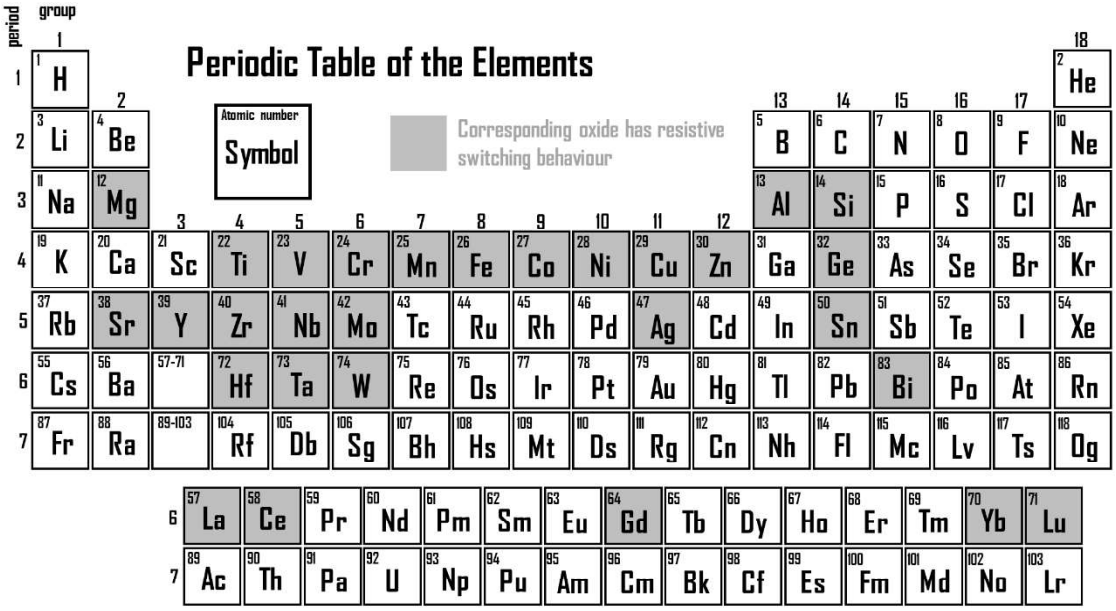

Figure 5.7. Periodic table highlighting elements which demonstrate resistive switching behaviour. Copyright © 2020 WILEY-VCH Verlag GmbH & Co. KGaA, Weinheim.

In this chapter, a detailed analysis is performed in section 5.1.2. regarding the synthesis of solution-based oxide RRAMs (deposition method, molar proportion, doping, concentration,

solvent, ambient condition and annealing method), which severely affect the overall performance of the devices. Then, the interface between the solution-based metal oxide and the diverse electrodes are analysed. In section 5.1.3, the thermal budget requirements for flexible solution-based metal oxide RRAM and their printability are examined. Next, the current status of the figures of merit in solution-based metal oxide RRAM as well as their current challenges are discussed in section 5.1.4. Finally, section 5.1.5 summarizes the main conclusions and future perspectives for resistive memory devices which can have distinct applications depending on the device characteristics. However, the main objective in this chapter was to perform a survey on a new and emerging technology based on solution processes in order to show the potential of these new fabrication methods.

5.1.2. Fundamentals of solution-based metal oxide RRAMs

Solution-based transparent amorphous metal oxides have been widely studied for diverse applications, but mainly in thin film transistors.[5] In 2005, solution-based metal oxide resistive switching devices appear on Ag–SiO_2 nanocomposite thin films deposited by spin-coating.[595] Then, in 2009, one year after the discovery of the memristor devices by Hewlett Packard (HP) researchers[537], a large quantity of publications on solution-based oxide thin films resistive switching devices start to emerge. However, to guarantee enhanced quality of the metal-oxygen-metal (M-O-M) frameworks formation for application in resistive switching devices, solution synthesis parameters should be considered. Parameters such as the synthesis method, molar proportion, doping, metal salt precursor, solvent, film thickness and ambient conditions are crucial for the solution-based RRAM performance, as depicted in Figure 5.8.

5.1.2.1. Effect of the solution synthesis and film formation

Diverse solution synthesis methods (hydrothermal[596–598], anodization[599,600] and sol-gel[601–604]) have been reported for the production of solution-based metal oxide RRAM. However, the most common is the sol-gel method which is subdivided into two main routes: the nanoparticle-based process[605] and the metal-salt sol-gel chemistry[606,607]. The metal salt precursor approach is typically the most suitable and used.

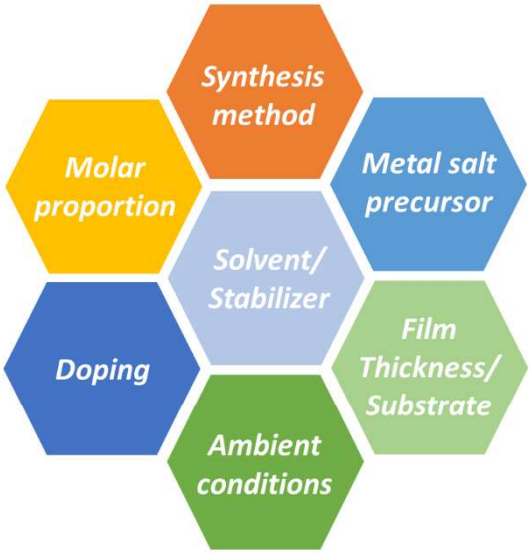

Figure 5.8. Identification of the crucial parameters to enhance solution-based metal oxide thin film RRAMs. Copyright © 2020 WILEY-VCH Verlag GmbH & Co. KGaA, Weinheim.

The sol-gel chemistry method allows the synthesis of materials through a transformation from liquid precursors to a colloidal suspension until a gel is finally obtained (e.g. the network structure).[450,608] This sol-gel chemical reaction starts when the metal salts are dissolved in an alcohol or aqueous solvent. During this process (Figure 5.9 (a)), the metal cations undergo a hydrolysis reaction, leading to metal hydroxides. Afterwards, condensation reactions lead to the formation of oxide frameworks, through an oxolation reaction between metal hydroxides.[608] To complete the formation of the metal oxide thin film, the precursor solution is deposited by a coating or printing technique and exposed to a post-annealing process. Typically, the films are annealed at high temperatures, above 400 °C, to promote the metal-oxygen-metal (M–O–M) structure formation (condensation), the by-products and solvents are removed through their decomposition/evaporation and, finally, the oxide film densification increases.[609–612] In addition to the conventional sol-gel method, there is solution combustion synthesis (SCS), a simple, efficient and versatile method which has been used for a wide range of applications, particularly for thin film transistors (TFTs).[2,7,27,92,302,307,613,614] SCS involves a self-sustained redox reaction initiated by a source of energy between a fuel and an oxidant in the presence of metal cations, requiring less energy to form the metal oxide thin films, as depicted in Figure 5.9 (b) . The fuel is the crucial component present in SCS and is mainly composed by organics containing carbon and hydrogen that facilitate the liberation of heat by the formation of CO_2 and H_2O during the combustion process. The main advantages of this method compared to conventional sol-gel are the low ignition temperature required to trigger the combustion reaction and form the metal oxide lattices, the higher homogeneity and the purity of the thin films.[27] Recently, *Pei et al.* and *Carlos*

et al. reported the use of SCS for the production of oxide-based resistive switching memories.[279,615] In the case of *Pei et al.,* low temperature (250–300 °C) solution-based nickel oxide (NiO) bipolar resistive switching devices with a good retention were achieved via the solution combustion method. As observed, the solution precursors can be converted into oxides at low process temperatures.

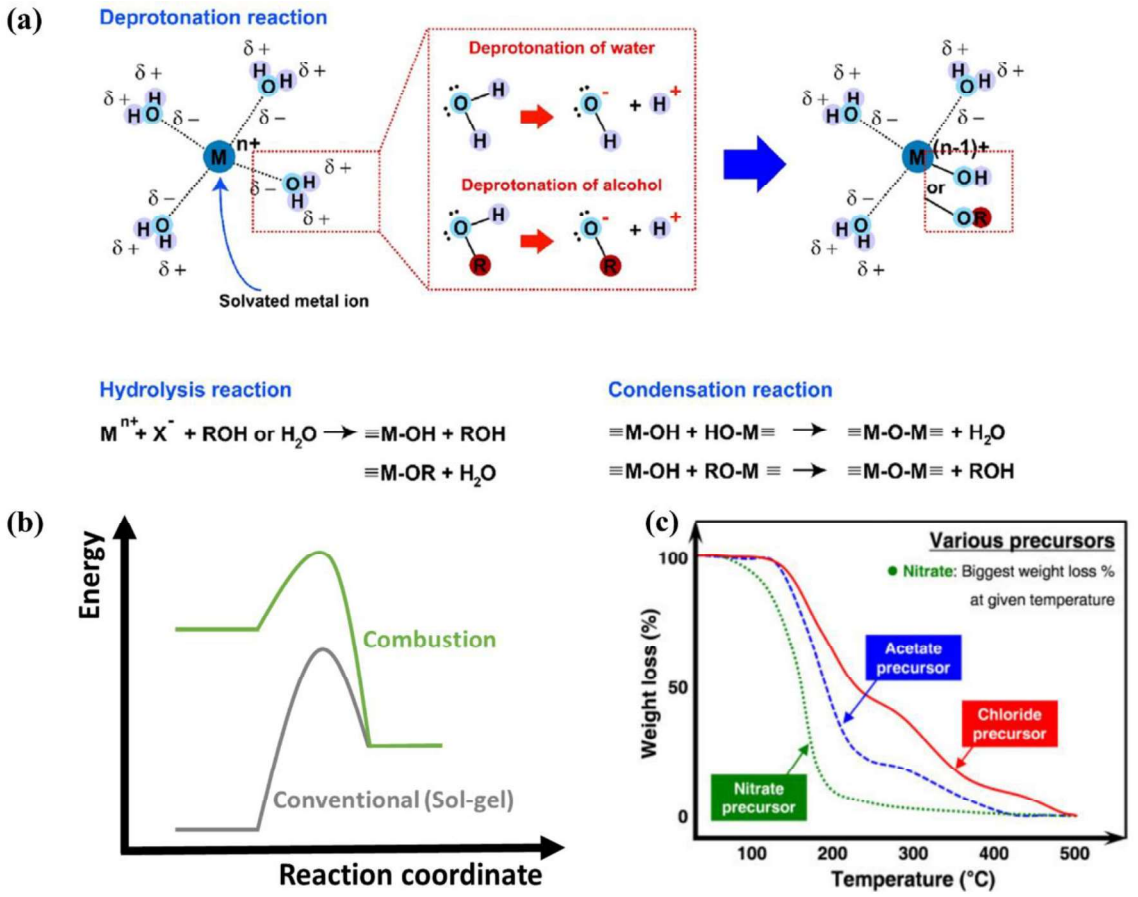

Figure 5.9. a) Sol-gel chemistry in metal oxide materials. A schematic of the reaction between metal ions and water/alcohol molecules to metal hydroxides. After water or alcohol molecules are deprotonated, metal and hydroxide ions are bound to each other by electrostatic interaction. Representative chemical reactions are shown for hydrolysis and condensation. Reproduced with permission.[450] Copyright © 2017 Elsevier B.V. All rights reserved. b) Illustration of the two different synthetic approaches for metal oxides: energetics of combustion synthesis-based processes versus sol-gel conventional process. Copyright © 2020 WILEY-VCH Verlag GmbH & Co. KGaA, Weinheim. c) Schematic diagram of thermogravimetric analyses of various precursors. Reproduced with permission.[83] Copyright © 2014, IOP Publishing Ltd.

Another critical parameter on the synthesis process of resistive switching devices is the metal salt precursors which are subdivided into three counter anions groups[80]; oxidants (hydrated nitrates)[279,597,604,605,616–636], reducers (alkoxides[632,637–640], acetates[597,601,603,604,619,620,624,626,628–633,641–668] and acetylacetonates[606,649,659,669–672]) and neutrals (chlorine-based)[590,596,618,622,625,627,631,634,640,647,673–

[679]. Among these, oxidant counter ions are preferable due to the high oxidizing power (negative charge), greater solubility in water or polar organic solvents and low decomposition temperature, which are related to the electronic interactions between the metal and the nitrate group, as shown in Figure 5.9 (c).[81–83] Their low processing temperature is related to the high volatility of the decomposition by-products, leading to a higher purity in the final product.[27,95] However, only 26 % of the solution-based oxide resistive switching devices use oxidants as metal salt precursors. The remaining 74 % are based on reducer (56 %) and neutral precursors (18%). This may explain why, up until now, a reasonable portion of the resistive switching devices are processed at higher annealing temperatures (≥ 400 °C). Also, the use of neutral precursors, such as chlorine-based, should be avoided due to the release of HCl as a by-product since it is harmful for the operators in the printing lines manufacturing.

All these synthesis processes are based on solution, making the solvent (water or alcohol-based) a key factor in the precursor solution formulation, thin film's deposition and production. It constitutes a substantial portion of the oxide precursor solutions: around 98 % and 90 % for lower and higher concentrations, respectively. The most common solvents in solution-based metal oxide RRAMs are 2-methoxyethanol (2-ME)[279,590,597,604,605,617,619,620,622,624,627,628,630–634,636,642,644,645,648,649,652,654,657,659,665–668,673,674,680–697], ethanol[597,602,603,607,618,623,628,629,635,641,647,650,651,653,660,662,672,677–680,698–712], deionized (DI) water[598,616,631,635,638,663,677,678,702,713], acetic acid[618,636,644–646,649,655,657,659,664,665,667,669,685,691,692,695,714], isopropanol[550,638,640,643,651,681,693,715] amongst others (ethylene glycol[656,716], 2-butoxyethanol[717], acetylacetone[664], acetonitrile[676]). 2-ME, a toxic organic solvent, is the most reported in literature (used in 40 % of publications), thus a large effort has been made to substitute it with a friendly and low-cost solvent such as ethanol, used in 28 % of publications. Moreover, some solvent mixtures (2-ME/acetic acid, 2-ME/isopropanol and ethanol/water) have been reported. Nevertheless, it should be considered that the chosen solvent influences the final properties[718] of the films such as structural, morphological, optical and electrical due to its evaporation rate[719], its interaction with the metal salt precursor, its composition and its chain size.

Another key feature in the solution synthesis is the addition of a stabilizer, i.e. a chelating agent, in the precursor solution, with the most commonly used in solution-based oxide RRAM being monoethanolamine (MEA)[630] and diethanolamine (DEA)[654]. This prevents the precipitation of metal ions and preserves the compositional homogeneity between all the constituents, reinforcing the coordinate bonds.[42]

The active layer film thickness plays a crucial role in the overall performance of solution-based RRAM devices due to the oxygen/anion/cation gradient. The thicker the active layer is, the higher

is the potential field required for electroforming, which can lead to thicker filaments and higher current states. The films´ thickness is mainly controlled by the precursor solution concentration, the number of layers deposited and the deposition technique. *Hsu et al.* reported that a precursor solution concentration (0.03 – 0.1 M) of indium zinc oxide (IZO) affects the RRAM performance.[629] When a low concentration of IZO solution was applied for RRAM devices, a low resistance ratio was observed due to the higher quantity of oxygen vacancy filaments. The increment of the solution concentration and decrease of the spin speed increased film thickness and reduced the oxygen content in the IZO layer, resulting in a higher resistance window, as shown in Figure 5.10 (a). However, if the concentration is too high (≥ 0.7 M), the appearance of cracks is observed at higher annealing temperatures, as well as the presence of a higher amount of organic residues at lower temperatures.

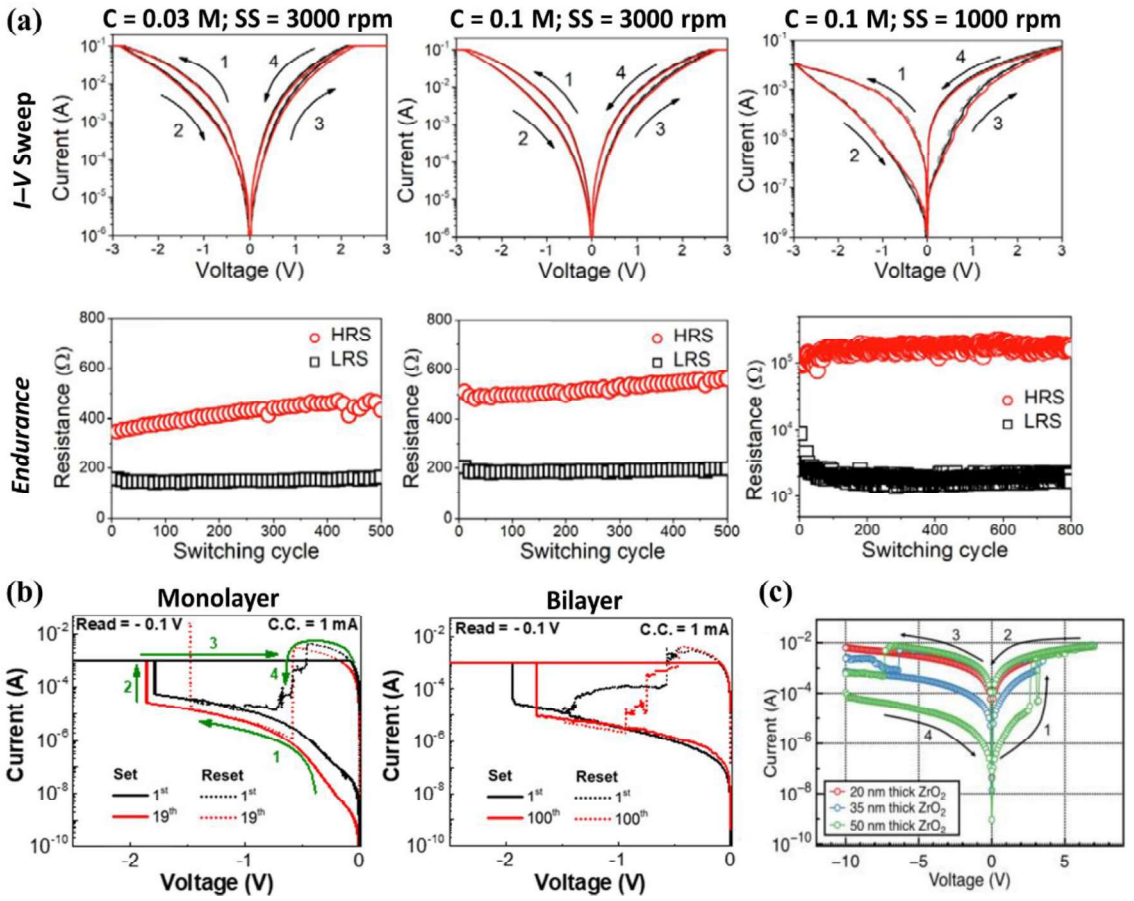

Figure 5.10. Influence of film thickness on the electronic performances of solution-based metal oxide RRAMS: a) *I–V* sweep curves and endurance of IZO RRAMs with different solution precursor concentration (C) and spin speed (SS) deposition; Reproduced with permission.[629] Copyright © 2019 Elsevier B.V. All rights reserved. b) *I–V* characteristic endurance of Al_2O_3 monolayer (30 nm) and bilayer (66 nm) RRAMs; Reproduced with permission.[279] Copyright © c) Representative *I–V* curves obtained from

ZrO_2 RRAM devices, with different film thickness by changing the number of layers. Reproduced with permission.[720] Copyright © 2018, IEEE.

Carlos el al.[279] and *Jang et al.*[720] reported the impact of the film thickness on the device performance by changing the number of layers on Al_2O_3 and ZrO_2 thin films, respectively. Carlos el al. detected that the use of an Al_2O_3 bilayer improved the memory endurance and yield compared to the monolayer, as depicted in Figure 5.10 (b). In the case of *Jang et al.*, the IZO thin films become smoother and the resistance window was improved from ~10 to ~10^3 with the increase of the number of layers, as shown in Figure 5.10 (c).

Besides the active oxide layer film thickness, the substrate also plays a critical role on the S-RRAMs performance. As for other thin film devices a substrates' surface roughness below 2 nm is highly desirable. Rigid substrates, such as silicon wafers, offer a smooth surface although flexible substrates are required to reach large area and low-cost production. However, most flexible substrates suffer from high surface roughness or, even when the root mean square (rms) roughness is low, some high aspect ratio features (spikes) are usually present. These spikes affect the subsequent layers of S-RRAMs and the overall performance, mainly the device variability. This can be overcome by polishing the substrates or depositing a specific coating to attain a smoother surface.[447] The substrate's thermal stability under heat is also highly important when printing flexible S-RRAM devices. Since most of the active layers require high thermal annealing the flexible substrates used must have a low thermal expansion coefficient (CTE) to avoid shrinking which affects devices performance. Some flexible substrates, like XENOMAX polyimide (PI) can resist higher temperatures with a low CTE of 3 ppm/°C however these can be quite expensive. However, in the printing industry low cost subtrates, such as PEN and PET, are typically used which demand low annealing temperatures to prevent degradation. To reach processing temperatures that are compatible with these substrates new curing methods have been used to produce the active layer at lower temperatures, as discussed further in section 5.1.3.

The composition ratio, or molar proportion, highly influences the resistive switching of S-RRAMs by changing the required resistive switching elements, such as oxygen vacancies in the active material for VCM type of mechanisms. Furthermore, the pristine state or initial resistance state of the device can be modified. This generally results in reasonable required electroforming fields or even forming-free processing. *Cho et al.* studied the stoichiometric effects of solution-based amorphous indium–gallium–zinc-oxide (a-IGZO) resistive switching memory devices for different In:Ga:Zn molar proportions.[620] When a higher content of indium is used, the devices exhibit an ohmic behaviour, whereas when the zinc is increased, a rectifying switching behaviour is observed. An increase in Ga content proved to enhance the IGZO RRAM characteristics by

controlling the concentration of oxygen vacancies through strong Ga-O bonding. This results in a decrease of the reset voltage from – 0.9 V to – 0.4 V and in the increment of the resistance window from 0.7×10^1 to 3×10^1.

Recently, *Kim et al.* reported a highly stable solution-based IGZO (1:*x*:1) RRAM by changing the Ga composition ratio from $x = 1$ to 4, keeping the amount of In and Zn fixed.[604] The Ga increment helps to suppress the formation and generation of oxygen deficiencies and consequential mobile electrons in IGZO thin films. However, if the Ga content is above 3, the switching behaviour is unstable from HRS to LRS state. For more stable and reproducible devices, the Ga content was set to 3 as previously reported by *Cho et al.*[620] To improve the devices´ characteristics, a 5 nm thick Ni film was added to the bottom electrode as a local oxygen capturer to attain an oxygen-gradient structure (non-linear). Also, the active cell area was reduced to 10×10 μm^2, reaching highly stable devices with low cycle to cycle variability.[604]

Similarly, doping has been widely used on solution-based metal oxide RRAMs to enhance the metal oxide network and improve the resistive switching behaviour. Diverse dopants such as Mg[721], Mn[722], Mo[646], Ni[605,674], S[709], V[642], Cr[654,705], Cu[643,723], Al[627,634,653,724], Hf[622], Ta[674], Sb[640], Ag[691] and rare earth elements (La, Gd, Dy and Ce)[636,724] have been used to produce doped solution-based metal oxides. In 2012, *Kim et al.* reported the doping of Ni nanoparticles (NPs) embedded in the nickel oxide (NiO) precursor solution for RRAM applications.[605] These NPs enhanced oxygen mobility in the thin films, effectively reduced the insulator thickness and lead to fewer Ni^{2+} vacancies, *i.e.*, stoichiometric variations. Therefore, the amount of Ni^{3+} content (higher ionic bonding energy to oxygen) was reduced leading to devices with lower operation voltages. In the same year, *Kim et al.* studied the influence of rare earth elements (Gd, Dy and Ce) doping in solution-based ZrO_2 thin films.[636] Pristine ZrO_2 RRAMs exhibited a forming free behaviour and an amorphous state, but also a large fluctuation on the HRS state due to a large number of film defects leading to non-controlled branches of different conductive filaments. After doping the ZrO_2 film with Gd and Dy, the HRS current level was increased due to generation of an excessive number of oxygen vacancies. Nevertheless, Ce doping improved crystallization and densification of the ZrO_2 film and probably reduced film defects without increasing the amount of oxygen vacancies, leading to stable endurance characteristics (5×10^3 cycles with low cycle-to-cycle variability). In 2014, *Tang et al.* reported the enhancement of the resistive switching behaviour of ZnO thin films by the doping with Cr (1 % ,2 % ,3 % and 5 %).[654] By increasing the Cr content, the resistance ratio is improved from ~17 to $\sim7\times10^3$, as shown in Figure 5.11 (a). No electroforming process was required for the devices and good retention characteristics ($\geq 10^4$ s) were achieved.

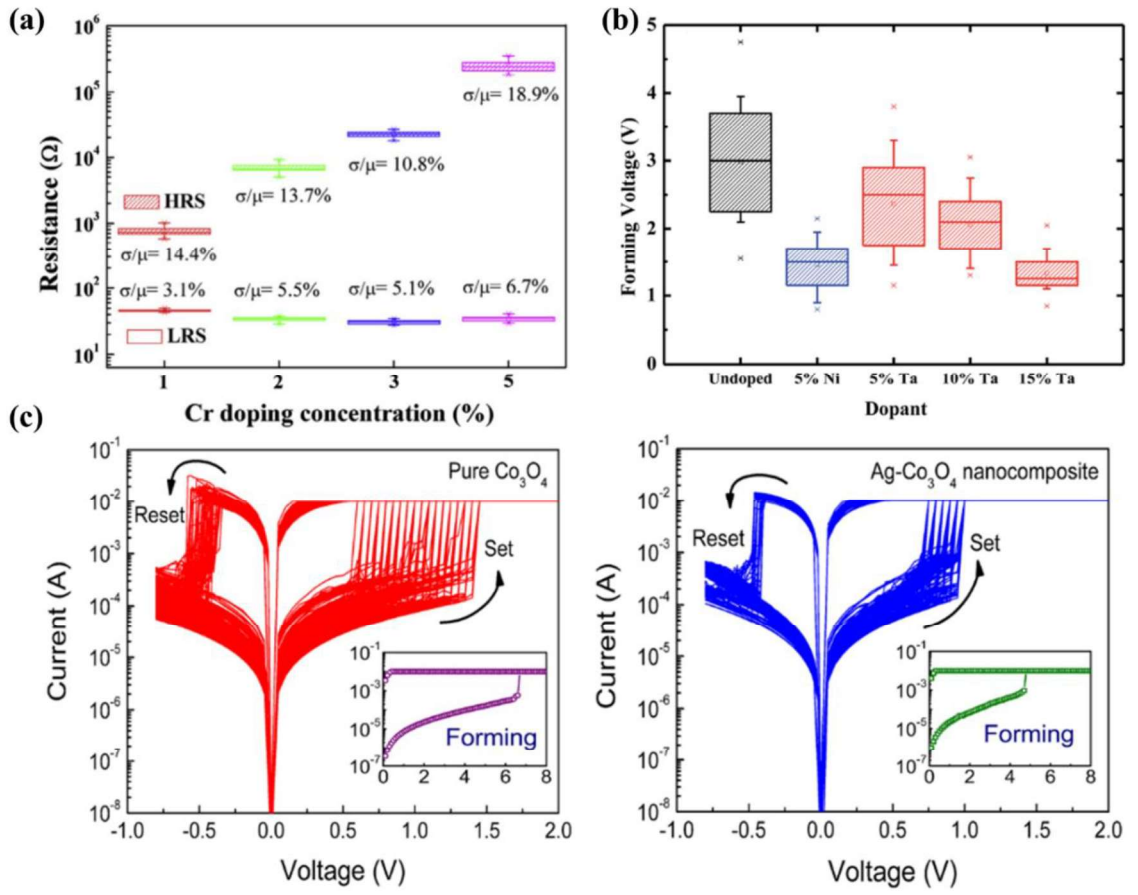

Figure 5.11. Influence of doping on the electronic performances of solution-based metal oxide RRAMs: a) The statistical distributions of the resistance values of LRS and HRS in the Pt/$Zn_{1-x}Cr_xO$/Pt devices; Reproduced with permission.[654] Copyright © 2013 Elsevier B.V. All rights reserved. b) Statistical distribution of forming voltage in undoped and doped HfO_X samples; Reproduced with permission.[674] Copyright © The Royal Society of Chemistry 2016 c) Typical bipolar current–voltage (*I–V*) characteristics (inset figure shows the forming process) of pure Co_3O_4 and Ag-Co_3O_4 devices. Reproduced with permission.[691] Copyright © 2019 WILEY ‐ VCH Verlag GmbH & Co. KGaA, Weinheim.

Kim et al. tested the doping effect of Hf content (2 %, 10 %, 30 % and 100 %) in NiOx thin films for resistive switching devices.[622] For low content doping's of 2 % and 10 % of Hf, a bi-stable unipolar and bipolar resistive switching was achieved, respectively. This main difference is explained by the present mechanism on each device, which in the case of the 2 % Hf:NiO_x devices, the TCM mechanism is dominated. Although for the 10 % Hf:NiO_x, the VCM mechanism is promoted due to the absence of a non-metallic behaviour and the increment of oxygen vacancies centres. They also showed that no resistive switching properties can be obtained with higher doping ratios of Hf (30 % and 100 %) in NiO_x thin films. In 2016, *Lee et al.* investigated the effect of Ni and Ta doping in solution-based HfO_x RRAM devices.[674] Here, the doping concentration increased the initial resistances. As a result, the forming voltage (Figure 5.11 (b)) is reduced due

to the increment of oxygen vacancies concentration in the film. However, the 10 % Ni doping had a more significant effect on the forming process of the devices, resulting in a forming free behaviour, highly desired for further applications. Recently, *Cho et al.* reported the Al doping on solution-based zin tin oxide (ZTO) RRAM devices.[627] Similarly, the increase of Al doping in ZTO thin films resulted in the increment of the resistance window (from 4.9 to 2.9×10^{1}) and increased the forming voltage (from 0.45 V to 1.85 V) since the Al supresses the generation of oxygen vacancies. *Bao et al.* studied the doping of cobalt oxide (Co_3O_4) thin films with Ag to boost the resistive switching parameters.[691] An improvement of the switching characteristics as better stability (i.e. low set and reset voltage variability) and lower forming voltage were observed due to the enhancement of the local electric field and the generation of oxygen vacancies by the addition of Ag, as depicted in Figure 5.11 (c).

There should be a careful attention to ambient conditions such as humidity, temperature, atmosphere and also precursor solution aging and how these affect the performance of S-RRAMs. *Hsu et al.* reported an interesting study on the precursor solution aging of HfO_x over 150 days and their behaviour in resistive switching devices.[680] At least 60 days of aging were required to reach a complete and transparent HfO_x solution, as shown in Figure 5.12 (a). These devices present the most stable resistive switching behaviour (low cycle to cycle variability) with a good endurance. However, when the aging time increases (from 90 to 150 days), the devices show high transition voltages and unstable resistive switching behaviours due to the presence of more defect states.

The effect of humidity during the electrical measurements has been studied in several reports on metal oxide RRAMs produced by vacuum-based techniques.[725,726] This parameter can change the resistive switching behaviour dramatically when the relative humidity is higher than 45 % and lower than 30 %. In S-RRAMs, the relative humidity during the thin films' production should be very well-controlled since it affects the reproducibility of the process. *Page et al.* reported the importance of relative humidity (RH) during the deposition of solution-based metal oxide thin films (AlO_x, LZO and $HafSO_x$).[336] Namely, when a dry (RH ~22 %) or humid (RH ~71 %) environment is implemented while all other parameters (temperature, spin speed and solution composition) remain constant, the films thickness decreased from 78 nm to 42 nm, respectively, as depicted in Figure 5.12 (b). Later, *Kim et al.* studied the relative humidity impact (10 – 50 %) in the formation of solution-based aluminium oxide.[324] An improvement in the thin films quality was noticed for humidity values higher than 30 % without the existence of partial cracks. The current density of the MIM devices improves (from 10^{-1} A/cm^2 to 10^{-4} A/cm^2) by increasing the relative humidity content (40 – 50 %) during the film deposition.

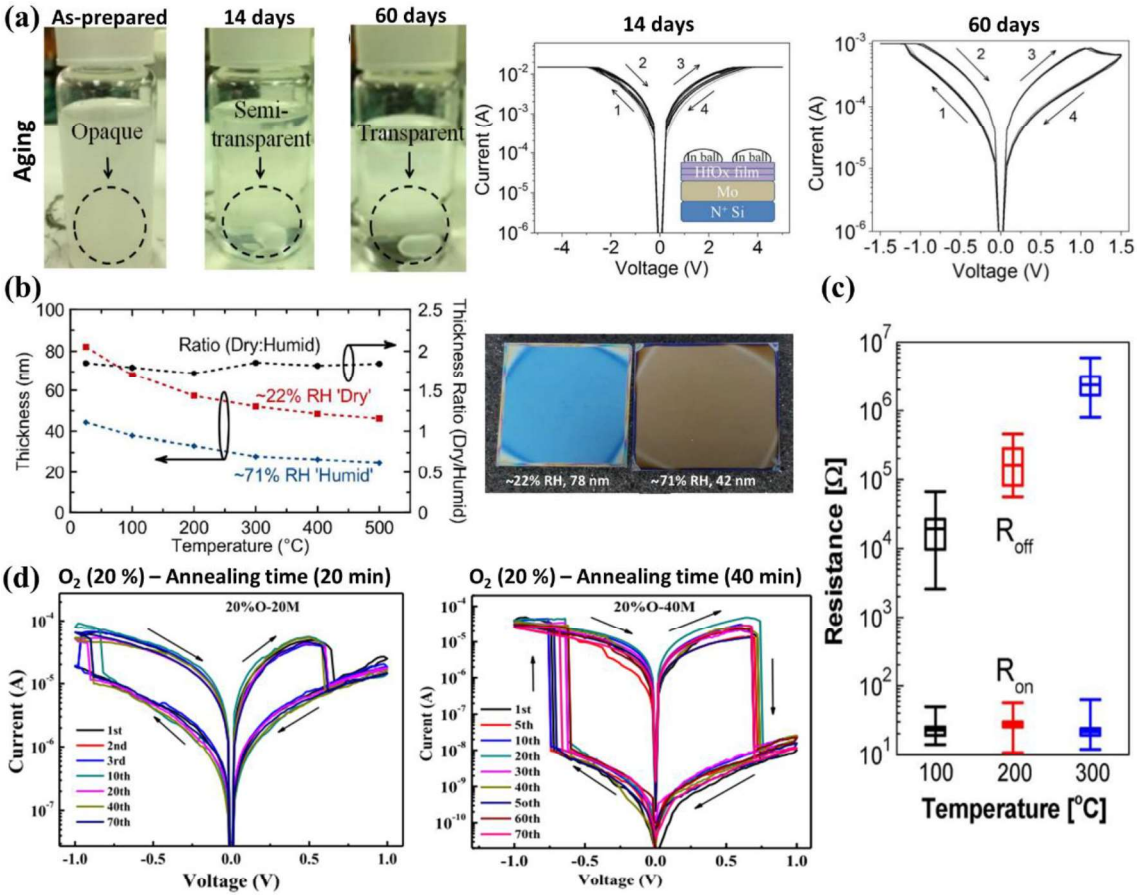

Figure 5.12. Influence of ambient conditions on the electronic performances of solution-based metal oxides: a) Pictures of as-prepared HfO_x sol-gel solution, aged for 14 and 60 days; *I-V* curves of the In/HfO_x/Mo RRAM prepared with the HfO_x solution aged for 14 and 60 days; Reproduced with permission.[680] Copyright © 2016 Elsevier B.V. All rights reserved. b) Thickness comparison of $HafSO_x$ films deposited at ~22 % (red) and ~71 % RH (blue). A ratio of film thickness (dry:humid) is plotted in black; Pictures of as-deposited $HafSO_x$ thin films deposited at ~22 % and ~71 % RH. The film thicknesses (determined using XRR) are 78 and 42 nm, respectively; Reproduced with permission.[336] Copyright © 2017, American Chemical Society c) R_{on} and R_{off} as a function of the annealing temperature for the ZnO films. Each data point was extracted from ten devices after 10^3 trials of cyclic switching; Reproduced with permission.[652] Copyright © 2009, IEEE d) *I-V* characteristics of Au/Cu_xO/ITO devices with different annealing conditions: 20 % O_2 – 20 min and 20 % O_2 – 40 min. Reproduced with permission.[727] Copyright © 2018, American Chemical Society.

The precursor solution temperature[324] during the solution deposition and following annealing temperature[652,712,728,729] are crucial conditions to reach optimal metal oxide thin films and apply them in electronic devices. *Choi et al.* reported the influence of the annealing temperature on ZnO thin films for RRAM devices.[652] Figure 5.12 (c) shows that the resistance ratio was improved with increasing annealing temperature by the increment of HRS state due to improved film densification and the decrease of current paths.

To study the impact of the atmosphere ambient, *Kim et al.* tested different oxygen contents (0 %, 20 %, 40 % and 100 %) and annealing times (20, 40 and 60 min) in an argon ambient to determine how this parameter affects the resistive switching behaviour of solution-based crystalline copper oxide (Cu_xO) thin films.[727] The absence of oxygen leads to a Cu_xO film with high percentage of cationic defects, resulting in a poorer RS performance. Then, through the increment of the oxygen content (from 0 to 20 %) and 40 min annealing time, a transition of CuO to Cu_2O was observed by XRD, resulting in the improvement of the RRAM parameters (Figure 5.12 (d)) such as the resistance window (10^4) and endurance (200 cycles of *I-V* sweeps). As the oxygen content is increased above 40 %, the number of defects is reduced, leading to a degradation on the resistive switching behaviour (i.e. resistance window and endurance). *Bao et al.* reported the annealing atmosphere (air, argon and oxygen) effect on the resistive switching behaviour of spinel Co_3O_4 thin films.[730] A better stability and uniformity (low forming voltage and cycle-to-cycle variability) was achieved for the Pt/Co_3O_4/Pt RRAM devices in a nitrogen atmosphere due to the formation of confined conductive filaments and the suppression of the oxygen vacancies dispersion. Recently, *Ha et al.* studied the annealing influence on solution-based zirconium oxide (ZrO_x) thin films in air and in an oxygen atmosphere.[673] The oxygen-annealing highly improved the quality of the thin films by supressing the oxygen vacancies which enhanced the RRAM characteristics. Comparable results were achieved with high temperature annealing (400 °C) in air to the films annealed at low temperature (200 °C) in a O_2 atmosphere. This enhancement of the M–O bonding states in a controlled environment at low temperature paves the way for flexible RRAM devices.

Various initiation sources such as furnace[727,731] or oven[696,702,732], rapid thermal annealing (RTA)[646,655,714,716,733,734], microwave[634,637,639,735], ultraviolet (UV) photochemical activation (lamp[633,686,710,736] and laser[737]) and hotplate[279,697] have been used for the solution-based metal oxides films´ conversion for RRAM devices. From these, the most common initiation sources are based on conventional thermal annealing (CTA), like furnace/oven and hotplate annealing. The RTA source allows an ultrafast annealing (typically $\leq$ 1 min) of the solution-based metal oxide thin films. However, high temperatures ($\geq$ 500 °C) are still required to form the M–O–M framework. On the other hand, microwave irradiation results in a homogeneous heat distribution with fast reaction kinetics leading to uniform microstructural and textural properties (surface area, grain and crystal uniform size distribution) by controlling the power and exposure time with a very high yield. *Cho et al.* studied the effect of microwave irradiation (MWI) power (600 W to 3000 W) on the resistive switching performance of solution-based AlO_x RRAM.[637] This source of energy was compared with as-deposited (180 °C) and CTA (400 °C) processed RRAMs. Figure 5.13 (a) shows that a relative improvement on the memory window was observed as the MWI power increased compared to deposited and CTA devices. Also, other groups noticed that

multi-level cell (MLC) storage[639] on the RRAMs and their stability[735] can be enhanced using microwave irradiation. However, the main limitation of using this technique is the scale-up to industry of solution-based RRAM devices.

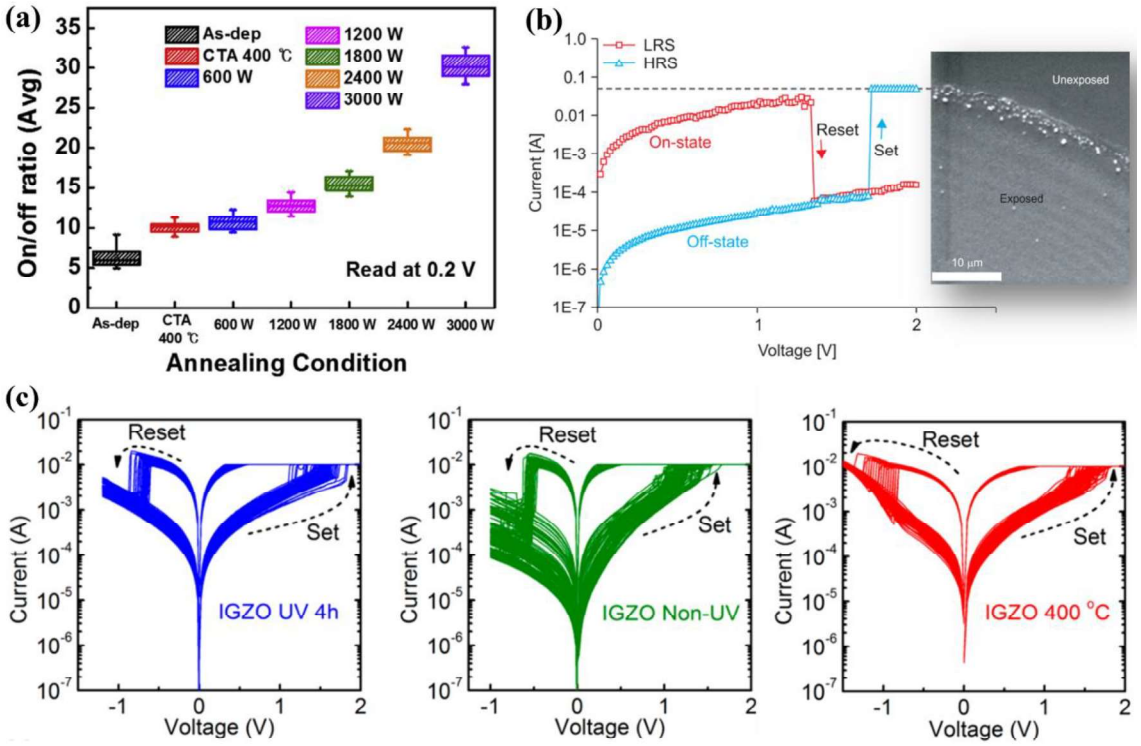

Figure 5.13. a) Average on/off ratio of solution-processed AlO_x ReRAM devices under various heat treatment conditions; Reproduced with permission.[637] Copyright © 2018 Elsevier Ltd. All rights reserved. b) Resistance-switching characteristics of the Pt/NiO/Pt heterostructure (the inset show a SEM image of patterned Ni oxide after KrF excimer laser irradiation, more specifically a high magnification of the edge of a circular pattern); Reproduced with permission.[737] Copyright © 2012 Korean Society of Microscopy. c) Typical $I-V$ characteristics of IGZO RRAMs for UV, Non-UV, and 400 °C thin film conditions. Reproduced with permission.[633] Copyright © 2014, American Chemical Society.

To overcome this issue, UV photochemical techniques have been explored as a viable option due to their compatibility with printed electronic industry, offering high quality materials at a reduced associated cost and process time.[309,614] *Yang et al.* studied the use of a UV-based (KrF, 248 nm) excimer laser annealing to produce solution-based NiO thin films and their application in RRAMs.[737] Specific areas of these films were exposed to the laser irradiation for only 3 min, resulting in the production NiO RRAMs with a resistance window of 10^3, as shown in Figure 5.13 (b). Later, *Bao et al.* reported solution-based IGZO resistive switching devices using UV lamp irradiation to form the IGZO thin films at low temperature.[633] The resulting devices compared to non-UV and high temperature (400°C) annealed devices exhibited stable, reproducible and highly uniform resistive switching properties, as depicted in Figure 5.13 (c). The

exceptional RS properties are attributed to the UV irradiation which reduced the residual organics content and enhanced the formation of M-O bonding and M-OH bonding networks by hydrogen bonding.

The results achieved until now are promising and expected to be of high value for printed and flexible RRAMs.

5.1.2.2. Influence of the electrodes/metal oxide interface

Beyond the active material in solution-based metal oxide RRAM devices, the electrode configuration is highly important in the resistive switching behaviour. Two different electrode configurations are reported in the literature: symmetric and asymmetric.[738]

Symmetric devices are composed by equal metals as bottom and top electrodes. These can be inert metals (e.g., Au[739], TaN[733], Pt[633]) or active and oxidizable metals (e.g., Al[740], ITO[619], Ni[741], Ti[597], Cu[698] and Ag[591]). Table 5.1 shows the reports of symmetric contacts S-RRAMs. We note that when the devices possess both inert electrodes, a limited reservoir of donor-type defects are rearranged randomly during the switching process which can compromise their reliability. However, the device structure can be enhanced by heterojunctions of active materials. *Bao et al.* reported a solution-based heterojunction structure of *p*-NiO/*n*-$Mg_{0.6}Zn_{0.4}O$ to improve the resistive switching properties of symmetric (Pt-Pt) RRAMs.[612] This *p-n* heterojunction highly improved the resistive switching behaviour compared to the single Pt/NiO/Pt and Pt/$Mg_{0.6}Zn_{0.4}O$/Pt devices by reducing the threshold current pulse and reset voltage dispersion. Also, a high resistance ratio of six orders of magnitude was achieved. Another way to improve inert-symmetric solution-based metal oxide RRAMs is the increment of the oxygen deficiency of the resistive oxide layers. *Cho et al.* studied the number of layers influence on high-κ (HfO_x and TaO_x) thin films for RRAM devices.[590] As the number of stack layers increase, the off-state leakage current decreases due to the increment of the active layer thickness which decreases the number of defects present in the film, resulting in a large memory window. However, for more than three HfO_x layers and two TaO_x layers, the set voltage operation increases as well as the probability of a hard breakdown. Both solution-based RRAM devices present excellent thermal stability with great retention and endurance characteristics. In conclusion, if an asymmetric structure (i.e. M (ohmic-type)- O- M (Schottky-type) is not provided by electrode selection, different strategies, as previously mentioned in section 5.1.2 by doping[654] and by the annealing atmosphere[730], are fundamental.

Aluminium electrodes have been used as active metals in symmetric solution-based metal oxide RRAMs due to their low cost and high ductility, allowing good flexibility, high retention and

mechanical endurance.[652,673,740] In the case of (non-inert)-symmetric structures, the Al or Ti electrodes for example, have the tendency to form an interfacial intermediate oxide layer between the active electrode and the oxide layer, which can be beneficial to the RRAM performance.[742] However, for certain active metals such as Al, a thick interfacial layer of oxide (AlO_x) can form on both electrodes, which leads to significant degradation during resistive switching operation by affecting the resistive switching layer´s stoichiometry.[683]

Table 5.1. Symmetric solution-based metal oxide resistive switching memories. (BE: Bottom electrode; TE: Top electrode; $R_{on/off}$: Resistance on/off ratio; n.d.: not defined; T_{max}: maximum temperature; RT: Room temperature; Spin: Spin-coating; Anodic: Anodization; Blade: Blade coating; Drop: Drop casting).

Year	Material	Method	T_{max} [°C]	BE/TE interface	Switching behaviour	$R_{on/off}$	Retention [s]	Endurance [cycles]
2005[595]	$Ag-SiO_2$	Spin	400	Pt/Pt	n.d.	10^6	n.d.	10
2008[743]	MgZnO	Spin	650	Pt/Pt	n.d.	2.5×10^1	n.d.	5×10^1
2009[744]	ZnO	Spin	450	Al/Al	Unipolar	10^2	10^0	n.d.
2009[740]	TiO_2	Spin	150	Al/Al	Bipolar	10^4	1.2×10^6	4×10^3
2009[652]	ZnO	Spin	300	Al/Al	Unipolar	10^5	10^5	10^4
2009[739]	TiO_2	Spin	200	Au/Au	Unipolar	10^2	10^4	3×10^2
2009[745]	Al_yO_x	Anodic	RT	Al/Al	Unipolar	$\sim10^4$	2×10^2	$\sim10^2$
2009[746]	MgZnO	Spin	650	Pt/Pt	n.d.	$>10^9$	n.d.	10
2011[612]	NiO/ MgZnO	Spin	650	Pt/Pt	Bipolar	$\sim10^6$	6×10^4	10^2
2011[721]	ZnMgO	Spin	700	Pt/Pt	Unipolar	$\sim10^3$	n.d.	5×10^1
2011[645]	STO	Spin	700	Pt/Pt	Unipolar	$\sim10^3$	10^5	5×10^1
2011[667]	SZO	Spin	800	Pt/Pt	Unipolar	$\sim10^4$	n.d.	6×10^3
2011[747]	La:ZnO	Spin	550	Pt/Pt	Unipolar	$\sim10^4$	10^6	1.5×10^2
2011[619]	GZO	Spin	500	ITO/ITO	Bipolar	15	n.d.	3.5×10^2
2012[737]	NiO	Spin	RT*	Pt/Pt	Unipolar	$\sim10^3$	n.d.	n.d.
2012[748]	ZnO	Spin	500	Ag/Ag	Bipolar	~10	3.1×10^3	n.d.
2012[749]	IGZO	Spin	370	Al/Al	Bipolar	2.7	n.d.	10^2
2012[750]	TiO_2	n.d./	n.d.	Al/Al	Bipolar	n.d.	n.d.	n.d.
2012[751]	AlO_x	Anodic	RT	Al/Al	Unipolar	$\sim10^4$	n.d.	n.d.

2012[752]	AlO_x	Anodic	RT	Al/Al	Unipolar	~10^5	10^5	10^4
2012[753]	ZnO	Spin	550	Pt/Pt	Unipolar	10^2	10^5	6×10^1
2013[631]	ZnO NRs	Spin	500	Au/Au	Unipolar	10	2×10^4	10^2
2013[733]	$Ag:SiO_2$	Spin	500	TaN/TaN	Bipolar	~10^3	2×10^4	n.d.
2013[591]	ZrO_2	EHD inkjet	150	Ag/Ag	Bipolar	~10	n.d.	1.4×10^2
2014[687]	TiO_x	Drop	90	Al/Al	Bipolar	~10	1.4×10^3	n.d.
2014[633]	IGZO	Spin	130	Pt/Pt	Bipolar & Unipolar	>10	10^4	10^2
2014[666]	ZnO	Spin	450	Pt/Pt	Bipolar	10^0	n.d.	3
2014[642]	ZnVO	Spin	550	Pt/Pt	Bipolar & Unipolar	~10^2 ~10^3	10^4	10^5 10^4
2014[736]	TiO_2	Spin	150	Pt/Pt	Bipolar	~10^2	2×10^3	10^2
2014[654]	ZnCrO	Spin	550	Pt/Pt	Bipolar	7×10^3	4×10^4	5×10^1
2014[754]	$Bi_{12}TiO_{20}$	Spin	600	Pt/Pt	Bipolar	5×10^1	10^4	10^3
2014[755]	$CoFe_2O_4$	Spin	600	Pt/Pt	Bipolar	~10^2	10^4	10^2
2014[756]	La:ZnO	Spin	550	Pt/Pt	Unipolar	~10^4	10^4	10^2
2014[590]	HfO_x / TaO_x	Spin	600	Pt/Pt	Bipolar	8.3×10^2 / 3.5×10^3	10^4	10^2
2015[757]	TiO_2	Spin	400	Pt/Pt	Bipolar	n.d.	n.d.	1.35×10^2
2015[758]	Bi_2O_3	Spin	150	Pt/Pt	Bipolar	>10	10^4	10^2
2016[715]	HfO_x	Drop	80	Al/Al Ti/Ti	Bipolar	9.8	n.d.	n.d.
2016[603]	ZnO	Spin	100	Al/Al	Bipolar	10^4	n.d.	1.5×10^1
2016[759]	Co_3O_4	Spin	600	Pt/Pt	Bipolar & Unipolar	~10^3	10^4	10^2
2016[760]	TiO_2/Ta_2O_5	Spin	400	Pt/Pt	Bipolar	10^3	n.d.	n.d.
2016[653]	Al:ZnO	Spin	400	Pt/Pt	Bipolar	3.5	n.d	10
2016[701]	ZTO NC	EHDA	500	Ag/Ag	Bipolar	~10	8.64×10^4	10^2
2016[761]	TiO_2	Anodic	RT	Ti/Ti	Bipolar	3×10^1	n.d.	n.d.
2017[597]	IGZO NPs	Spin	350	Ti/Ti	Bipolar	>10	10^4	10^2

2017[762]	TiO_2	Spin	400	Pt/Pt	Bipolar	5.5×10^1	n.d.	5×10^2
2017[640]	Sb:SnO_2/ TiO_2	Spin	400	Al/Al	Bipolar	8.3×10^2	n.d.	4×10^1
2017[763]	TiO_2	Spin	550	ITO/ITO	Bipolar	$\sim10^2$	10^4	2×10^2
2017[764]	Pr:ZnO	Spin	700	Pt/Pt	Bipolar & Unipolar	>10	2×10^4	3×10^2
2017[765]	NFC	Spin	750	Pt/Pt	Unipolar	10^3	10^5	5×10^2
2018[766]	NFG	Spin	750	Pt/Pt	Unipolar	10^2	10^5	5×10^2
2018[767]	NiO NC	Imprint	80	Pt/Pt	Unipolar	10^5	n.d.	n.d.
2018[651]	ZnO/ ZrO_2	Spin	300	Al/Al	Bipolar	$\sim10^3$	n.d.	2×10^1
2018[698]	ZnO	Blade	500	Cu/Cu	Bipolar	n.d.	n.d.	n.d.
2019[730]	Co_3O_4	Spin	600	Pt/Pt	Bipolar	$\sim10^2$	10^4	8×10^2
2019[692]	Co_3O_4	Spin	600	Pt/Pt	Bipolar	$\sim10^2$	10^4	3×10^2
2019[768]	$NiFeCrO_4$	Spin	700	Pt/Pt	Bipolar	10^2	10^5	5×10^2
2019[691]	Ag:Co_3O_4	Spin	600	Pt/Pt	Bipolar	$\sim10^2$	2×10^4	1.5×10^3
2019[769]	Bi_2SiO_5	Spin	600	Pt/Pt	Bipolar	10^2	10^4	10^2
2020[673]	ZrO_2	Spin	200	Al/Al	Bipolar	6×10^3	10^4	1.5×10^2
2020[741]	NiO NC	Spin	180	Ni/Ni	Unipolar	$\sim10^3$	n.d.	1.2×10^2
2020[770]	TiO_2	Blade	500	Pt/Pt	Bipolar	n.d.	n.d.	n.d.
2020[700]	ZnO	EHD inkjet	500	Ag/Ag	Bipolar	10^3	n.d.	10^3
2020[685]	YIG	Spin	700	Pt/Pt	Unipolar	10^2	10^4	2×10^2
2020[771]	ZrO_2	EHD inkjet	150	Ag/Ag	Bipolar	n.d.	n.d.	n.d.

Asymmetrical devices are composed by two different electrodes and can have inert-inert (e.g., Pt-Au[772]), inert-active (e.g., Pt-Al[605], Pt-Ti[773], Au-Al[709], Pt-Ag[611], Au-Ag[671], TaN-Cu[734]) or (non-inert)-active (e.g., Cu-Al[689], Cu-Ag[711], Ti-Cu, W-Al[774], LNO-Al[664], FTO-Ti[598], FTO-Al[713], ATO-Cu[658], ITO-Ag[704], ITO-Al[663], ITO-Ti[606]) electrode structures. Figure 5.14 shows the reported metal oxide S-RRAMs with different configurations, symmetric and asymmetric structures.

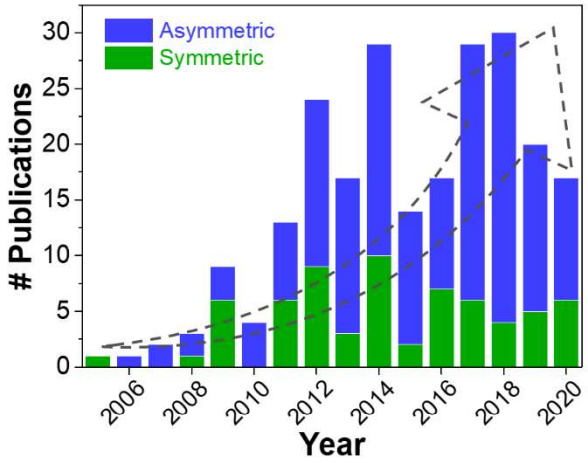

Figure 5.14. The number of the symmetric and asymmetric solution-processed metal oxide RRAM papers published from 2005 to 2020, based on "Google Scholar" search engine accessed on June 2020. The "Google Scholar" was chosen since a wide range of available materials including world-wide patents databases, research databases university databases (for theses), and other published papers on the web. To have a better perception, different keyword names considering the terms for solution-based metal oxide thin film resistive switching devices were used, such as RRAM, resistive RAM, ReRAM, memristor, memristive, resistive switching and resistive memory. Also, diverse keyworks for the solution-based process were searched, such as solution-based, solution-processed, anodized, sol-gel and combustion.

The performance of S-RRAM devices in the presence of asymmetrical structures has been greatly improved and studied over the years by applying asymmetrical vacancy profiles of substoichiometric metal oxide films compared to symmetric structures (Figure 5.14). *Wang et al.* studied the influence of multilayer solution-based barium titanate (BTO) thin films and different asymmetrical structures using various electrodes such as Al, ITO, Au, and Pt for RRAM devices.[657] The resistance window of these memories show an increment with the decrease of the metal work function, being the highest for Glass/ITO/BTO/Al devices, maximum 10^6, as can be observed in Figure 5.15. The low work function (4.1 – 4.3 eV) of electrodes, like Ti and Al represents a pronounced tendency to oxidation which results in an oxygen getter effect and increases the conductivity of the oxide material at the interface with the low work function electrode. Hence, a low work function or an oxidizable metal can increase the oxygen vacancy concentration at the interface of an active oxide layer, typically leading to higher on/off ratios.[775] Later, using the same electrode structure, *Wang et al.*, *Rhee et al.* reported solution-based NiO resistive switching devices with a good resistance window (>10^3), high retention time (10^5 s) and higher endurance (10^5) characteristics.[697]

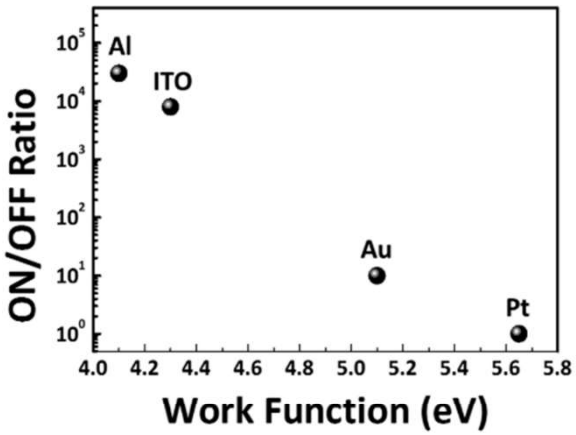

Figure 5.15. Resistance on/off ratio as a function of metal work function for Al, ITO, Au, and Pt as top electrodes. Reproduced with permission.[657] Copyright © 2014, IEEE.

Table 5.2 shows asymmetric solution-based metal oxide resistive switching memories reported in the literature. Generally, for inert-symmetric and inert-inert-asymmetric structures, a non-controlled high electroforming voltage (or also called soft breakdown) is required before reaching stable resistive switching performance on the oxygen deficient metal oxide thin films.[776]

To control the electroforming voltage, or even eliminate it, a low work function electrode or capping layer with a high oxygen-getter like activity is selected, with Ti, Al, Ta and Hf being preferred for inert-active-asymmetric structures.[565,636,777,778] When the chemical reactive metal, also called oxygen exchange layer (OEL), is in contact with the metal oxide resistive switching layer, ion transfer occurs instantly across the interface due to the difference in the free energy of metal oxide formation of the two systems. The interfacial ion transfer is highly important, specifically the extraction of oxygen ions from the resistive switching layer during the process of electroforming, which is vital for a stable operation of RRAM devices.[779–781]

Table 5.2. Asymmetric solution-based metal oxide resistive switching memories. (BE: Bottom electrode; TE: Top electrode; $R_{on/off}$: Resistance on/off ratio; n.d.: not defined; T_{max}: maximum temperature; RT: Room temperature; Spin: Spin-coating; Anodic: Anodization; Blade: Blade coating; Drop: Drop casting; Hydro: Hydrothermal; Dip: Dip coating; Electrodep.: Electrodeposition).

Year	Material	Method	T_{max} [°C]	BE/TE interface	Switching behaviour	$R_{on/off}$	Retention [s]	Endurance [cycles]
2006[664]	SZO	Spin	200	LNO/Al	Bipolar	10^3	1.3×10^4	n.d.
2007[609]	SZO	Spin	500	LNO/Al	Bipolar	10^4	n.d.	n.d.
2007[646]	Mo–$SrZrO_3$	Spin	400	LNO/Al	Bipolar	10^2	$\sim10^4$	10^3
2008[610]	LCMO	Spin	750	FTO/Au	Bipolar	>10	2×10^4	10^2
2008[655]	SZO/Cr/SZO	Spin	600	LNO/Al	Bipolar	$\sim10^5$	n.d.	5×10^1
2009[782]	LMCO	Spin	750	FTO/Au	Bipolar	2.7	4×10^4	10^4
2009[783]	BTO	Spin	700	LNO/Pt	Unipolar	10^4	2×10^6	10^2
2009[611]	TiO_2	Spin	450	Pt/Ag	Unipolar	10^5	10^4	$\sim8\times10^1$
2010[599]	TiO_2	Anodic	n.d.	Ti/Ag	Bipolar	n.d.	n.d.	n.d.
2010[784]	ZnO NCs	Spin	RT	ITO/Al	Bipolar	$\sim10^5$	n.d.	n.d.
2010[706]	TiO_2	Dip	500	ATO/Cu	Bipolar	n.d.	n.d.	n.d.
2010[699]	TiO_2	Spin	250	W/Pt	Bipolar	>10	10^5	3×10^2
2011[683]	TiO_x	Spin	n.d.	Al/IAI	Bipolar	$\sim10^3$	10^4	5×10^1
2011[658]	CuO	Dip	300	ATO/Cu	Bipolar	n.d.	n.d.	n.d.
2011[713]	WO_x	Dip	400	FTO/Al	Bipolar	$>10^4$	1.2×10^4	10^2
2011[602]	TiO_2	Spin	250	W/Pt	Bipolar	>10	10^5	3×10^2
2011[785]	GeO_2	Spin	700	ITO/Pt	Bipolar	10	n.d.	n.d.
2011[786]	SiO_2	Dip	500	ATO/Cu	Unipolar	$\sim10^2$	n.d.	3×10^1
2011[684]	TiO_x	Spin	150	W/Al	Bipolar	$\sim10^3$	n.d.	10^3
2012[774]	TiO_x	Spin	150	W/Al	Bipolar	$\sim10^3$	n.d.	1.2×10^3
2012[787]	Nb_2O_5	Anodic	RT	Nb/Au	Unipolar	4×10^2	3×10^6	4×10^1
2012[788]	Nb_2O_5 / ZrO_2	Anodic	RT	Nb/Au / Zr/Au	Unipolar	8×10^2 / $> 10^2$	n.d.	3.5×10^1 / 9

	Ta_2O_5			Ta/Au		$> 10^2$		3×10^1
2012[711]	TiO_2	EHD inkjet	350	Cu/Ag	Bipolar	10^2	n.d.	n.d.
2012[753]	ZnO	Spin	550	Pt/Ag	Bipolar	10^2	10^5	6×10^1
2012[636]	Ce-ZrO_2	Spin	400	Pt/Al	Bipolar	10^2	n.d.	5×10^3
2012[663]	NiO_x	Spin	500	ITO/Al	Bipolar	$\sim10^4$	5.4×10^4	10
2012[601]	CuO_x	Dip	300	ATO/Pt	Unipolar	$\sim10^3$	n.d.	n.d.
2012[708]	ZrO_2	EHD inkjet	120	ITO/Ag	Bipolar	$>10^5$	n.d.	10^2
2012[789]	BTO	Spin	n.d.	ITO/Al	Bipolar	$\sim10^2$	n.d.	n.d.
2012[605]	Ni NPs :NiO	Spin	500	Pt/Al	Unipolar	$\sim10^5$	10^4	10^2
2012[717]	TiO_x	Spin	200	ITO/Al	Bipolar	$\sim10^3$	3×10^3	10^4
2012[790]	HfO_2	Spin	500	ITO/Ag	Bipolar	<10	n.d.	n.d.
2012[709]	GeO_2:S	Spin	120	Au/Al	Unipolar	10^7	10^4	10^3
2013[676]	ZTO	Spin	500	Pt/Al	Bipolar	10^3	10^4	5.4×10^1
2013[707]	ZnO	EHD inkjet	500	Cu/Ag	Bipolar	10^3	n.d.	5×10^2
2013[791]	Bi_2O_3	Electrod.	65	Au/Pt	Unipolar	10^6	5×10^4	10^2
2013[792]	CuO/AgO	Inkjet	320	Cu/Ag	Bipolar	~10	n.d.	4×10^1
2013[704]	ZrO_2 NPs	EHDA	135	ITO/Ag	Bipolar	10	10^6	n.d.
2013[594]	Nb_2O_5	Spin	620	Pt/Ag	Unipolar	$\sim10^8$	10^5	10^2
2013[793]	Co:In_2O_3	ECD	85	FTO/Au	Bipolar	$\sim10^2$	$\sim4.75\times10^3$	8×10^3
2013[695]	STS	Spin	700	Pt/TiN	Bipolar	~6	10^4	5×10^2
2013[697]	NiO	Spin	475	ITO/Al	Bipolar	$>10^3$	10^4	10^5
2013[598]	TiO_2	Hydro	200	FTO/Ti	Bipolar	$\sim10^4$	5×10^3	10^5
2013[794]	TiO_2	Spin	350	Pt/Ag	Bipolar	~10	n.d.	3×10^3
2013[682]	MgZnO	Spin	400	ITO/Ag	Bipolar	$\sim10^2$	n.d.	6.5×10^2
2013[795]	$ZrTiO_4$	Spin	600	ITO/Pt	Bipolar	10^2	n.d.	n.d.
2013[796]	ZnO	Electrod.	RT	Pt/Ag	Bipolar	>10	n.d.	3×10^1
2014[702]	TiO_2 NP	Inkjet	180	C/Ag	Bipolar	$\sim10^3$	3×10^4	10^3
2014[734]	ZrO_x	Spin	500	TaN/Cu	Unipolar	$\sim10^4$	10^4	5
2014[797]	TiO_x	Spin	600	Pt/Ti	Unipolar	>10	n.d.	n.d.
2014[728]	TiO_2	Spin	250	ITO/Pt	Bipolar	n.d.	n.d.	3

2014[798]	TiO_x	Spin	250	ITO/Pt	Bipolar	2.29	n.d.	n.d.
2014[657]	BTO	Spin	100	ITO/Al	Bipolar	10^6	10^5	10^2
2014[722]	SnO_2:Mn	Spin	560	FTO/Al	Bipolar	10^3	2.75×10^3	3
2014[799]	TiO_2	Spin	650	p-Si/Pt	Bipolar	10	10^3	10^2
2014[712]	ZrO_2	Dip	300	ATO/Cu	Bipolar	10^4	n.d.	3×10^1
2014[618]	ZrO_2	Spin	500	FTO/ITO	Bipolar	>10	10^3	10^2
2014[723]	Cu:NiO	Spin	600	ITO/GaIn	Bipolar	~10^2	n.d.	10
2014[670]	MNO	Spin	500	ITO/Al	Bipolar	>10	4×10^4	10^2
2014[724]	La:ZrO_2 Al:ZrO_2	Spin	500	FTO/ITO	Bipolar	~10	4×10^3 3×10^3	10^2
2014[756]	La:ZnO	Spin	550	Pt/Ag	Bipolar	~10^4	10^4	10^2
2014[800]	$ZnMn_2O_4$	Spin	650	p-Si/Ag	Bipolar	10^2	10^5	10^2
2014[801]	BFO	Spin	600	ITO/Pt	Bipolar	~10	n.d.	10^2
2014[622]	Hf:NiO_X	Spin	450	Pt/Al	Bipolar & Unipolar	~10^3 ~10^5	n.d.	n.d.
2014[620]	IGZO	Spin	300	Pt/Ti	Bipolar	3×10^1	10^4	9×10^1
2014[773]	Hf:AlO_x HfO_x	Spin	600	Pt/Ti	Bipolar	2.9×10^1	5×10^4	10^2
2015[802]	GZO	Spin	500	p^+Si/Al	Bipolar	10^2	n.d.	10^2
2015[803]	Cu_2O	Eletrodep.	n.d.	Au/ Au-Pd	Unipolar	10^4	8×10^4	1.7×10^2
2015[632]	ZnO	Spin	80	ITO/Ag	Bipolar	6×10^1	4×10^3	1.2×10^2
2015[804]	ZrO_2	EHDA	135	ITO/Ag	Bipolar	n.d.	n.d.	n.d.
2015[660]	ZnO	Spin	400	Pt/Ag	Bipolar	n.d.	n.d.	10
2015[731]	TiO_x	Spin	600	Pt/Ti	Bipolar	3×10^1	10^4	2.5×10^2
2015[805]	ZnO/ TiO_2	Spin	450	ITO/Pt	Bipolar	2.07	n.d.	n.d.
2015[806]	ZnO	Spin	350	ITO/Au	Bipolar	1.3	n.d.	n.d.
2015[807]	STO	Spin	750	Pt/Ni	Bipolar	n.d.	n.d.	n.d.
2015[808]	ZnO	Spin	300	ITO/Pt	Bipolar	1.7	n.d.	n.d.
2015[809]	VO_2	n.d.	600	SiO_2/Au	Bipolar	n.d.	n.d.	n.d.

2015[810]	STN	Spin	100	ITO/Al	Bipolar	10^6	10^5	5×10^1
2016[674]	HfO_x Ni–HfO_x Ta–HfO_x	Spin	300	Pt/Al	Bipolar	~10^2	n.d.	n.d.
2016[811]	AlO_x	Dip	n.d.	Al/Hg	Bipolar	~10^3	n.d.	10^2
2016[641]	ZnO	Spin	400	Pt/Al	Bipolar	n.d.	n.d.	n.d.
2016[659]	$MgTiNiO_x$	Spin	100	ITO/Al	Bipolar	10^6	2×10^5	1.1×10^2
2016[689]	TiO_2	Drop	RT	Cu/Al	Bipolar	>10^2	n.d.	1.5×10^1
2016[812]	$ZnSnO_3$	EHD inkjet	130	ITO/Ag	Bipolar	>10	1.2×10^4	2×10^2
2016[630]	ZnO	Spin	350	ITO/Pt	Bipolar	1.74	n.d.	n.d.
2016[813]	NiO	Spin	250	Al/Ag	Unipolar	~10^4	n.d.	2×10^1
2016[814]	TiO_2	Anodic	250	Ti/Pt	Bipolar	n.d	n.d	n.d
2017[671]	ZrO_2	Spin	500	Au/Ag	Bipolar	~10^2	10^5	10^4
2017[649]	STN	Spin	100	ITO/Al	Bipolar	10^5	10^5	1.4×10^2
2017[606]	ZrO_2	Spin	500	ITO/Ti	Bipolar	7×10^1	10^4	10^2
2017[710]	ZrO_2	Dip	150	ITO/Pt	Bipolar	10^5	10^4	6×10^2
2017[732]	HfO_2 NPs	Inkjet	240	Au/Ag	Bipolar	10^3	n.d.	1.28×10^2
2017[597]	IGZO NPs	Spin	200	Ti/Ag	Bipolar	>10	10^4	10^2
2017[679]	SnO_x	Spin	120	ITO/W	Bipolar	10^3	n.d.	5×10^2
2017[678]	HfO_x	Spin	100	Mo/In	Bipolar	~10	n.d.	2×10^2
2017[693]	MgZnO/ $ZnMn_2O_4$	Spin	650	p^+-Si/Ag	Bipolar	10^4	10^6	10^3
2017[815]	CuO	SILAR	80	SS/Al	Bipolar	n.d.	n.d.	n.d.
2017[816]	WO_3	Drop	450	FTO/Ag	Bipolar	n.d.	n.d.	10^4
2017[625]	AZTO	Spin	120	n^+-Si/In	Bipolar	~10^3	10^3	5×10^2
2017[817]	FeSTO	Spin	700	ITO/Au	Unipolar	~10^5	10^4	5×10^1
2017[648]	ZnO	Spin	500	p^+-Si/Al	Bipolar	~10^4	n.d.	n.d.
2017[680]	HfO_x	Spin	100	Mo/In	Bipolar	2.71	n.d.	5×10^2
2017[818]	CFO	Spin	400	FTO/Al	Bipolar	~10^3	10^4	2×10^2
2017[665]	STN	n.d.	100	Pt/Al	Bipolar	10^5	10^5	4×10^1
2017[686]	TiO_2	Dip	150	ITO/Pt	Bipolar	10^3	10^4	6×10^2

2017[656]	NiO/ZnO	Spin	150	ITO/GaIn	Bipolar	10^3	n.d.	10^3
2017[681]	LZMO/ MZO	Spin	600	p^+-Si/Ag	Bipolar	10^6	2×10^6	10^3
2017[705]	Cr:STO	Drop	80	FTO/Au	Bipolar	n.d.	n.d.	10
2017[735]	AlO_x	Spin	600	Pt/Ti	Bipolar	> 24	10^4	10^3
2018[607]	SnO_2	Spin	200	FTO/Au	Bipolar	n.d.	n.d.	2×10^2
2018[634]	AZTO	Spin	250	Pt/Ti	Bipolar	>17	10^4	10^3
2018[639]	AlO_X	Spin	565	Pt/Ti	Bipolar	4.3×10^2	10^4	10^2
2018[647]	ZTO	Spin	300	n^+Si/In	Bipolar	3×10^2	n.d.	10^3
2018[727]	CuO NPs	Spin	300	ITO/Au	Bipolar	10^4	10^4	2×10^2
2018[819]	NiO	Spin	200	Pt/Ag	Bipolar	10^5	10^4	8×10^1
2018[279]	Al_2O_3	Spin	500	Pt/Ti	Unipolar	$\sim10^5$	10^5	10^2
				ITO/IZO		10^4	10^4	n.d.
2018[596]	HfO_2 NPs	Blade	n.d.	Pt/Pt-Ir	Bipolar	10^5	n.d.	5×10^1
2018[675]	TiO_2	Anodic	RT	Ti/Cu	Bipolar	8×10^1	n.d.	n.d.
2018[637]	AlO_x	Spin	347	Pt/Ti	Bipolar	10	10^4	10^3
2018[820]	BFO	Spin	450	FTO/Ag	Bipolar	4.5×10^1	10^4	10^3
2018[720]	ZrO_2	Spin	500	ITO/Ag	Bipolar	$\sim10^3$	10^4	4×10^2
2018[626]	NiO/CeO_2	Spin	400	ITO/GaIn	Bipolar	$\sim10^3$	n.d.	10^2
2018[615]	NiO	Spin	350	Pt/Ag	Bipolar	>10	10^4	10^2
2018[644]	STO	Spin	650	ITO/Au	Unipolar	10^3	10^4	n.d.
2018[821]	Al-In-O/ InO_x	Spin	180	Pt/Ag	Bipolar	$>10^2$	10^4	5×10^2
2018[662]	Cu_xO	Spin	400	n^+Si/In	Bipolar	4×10^1	n.d.	10^4
2018[672]	ZrO_x	Spin	400	n^+Si/In	Bipolar	$\sim10^3$	10^4	5×10^2
2018[643]	Cu:ZnO	Spin	450	ITO/Al	Bipolar	$\sim10^3$	10^6	n.d.
2018[772]	$ZnFe_2O_4$	Spin	700	Pt/Au	Bipolar & Unipolar	$\sim10^2$	10^4	2.5×10^2
2018[688]	$ZnMn_2O_4$	Spin	650	p^+Si/Ag	Bipolar & Unipolar	10^2	n.d.	10^2

2018[822]	MgZnO	Spin	600	p-Si/Ag	Bipolar	~10^3	10^5	10^2
2018[823]	TiO_2	Anodic	RT	Ti/Cu	Bipolar	n.d.	n.d.	n.d.
2018[824]	TiO_2	Anodic	RT	Ti/Ag	Bipolar	2.7×10^1	n.d.	1.6×10^1
2018[628]	IGZO	Spin	150	ITO/Pt	Bipolar	~10^3	10^4	10^4
2018[825]	ZnO	SILAR	300	FTO/Ag	Bipolar	10^3	10^3	10^4
2019[627]	AZTO	Spin	250	Pt/Ti	Bipolar	5×10^1	10^4	10^2
2019[621]	AlO_x	Spin	RT	ITO/Ag	Unipolar	~10^3	10^4	10^2
2019[616]	AlO_x	Spin	250	Pt/TiN	Bipolar	3.5×10^1	10^3	10^2
2019[617]	MgO	Spin	250	W/Mg	Bipolar	10^5	10^4	1.4×10^2
2019[629]	IZO	Spin	300	n^+Si/In	Bipolar	~10^2	n.d.	5×10^2
2019[624]	NiO/Al_2O_3	Spin	450	FTO/Ag	Bipolar	~10^3	10^4	9×10^1
2019[729]	AlO_x	Spin	250	Pt/Ni	Bipolar	~10^4	10^4	1.5×10^2
2019[635]	AlO_x	Spin	200	Pt/TiN	Bipolar	1.8×10^2	10^4	3×10^2
2019[661]	Cu_xO	Spin	200	n^+Si/Al	Bipolar	10^4	2×10^4	10^4
2019[716]	STO	Spin	400	FTO/Au	Bipolar	10^2	n.d.	10^2
2019[826]	ZnO	Spin	120	ITO/ PEDOT:PSS	Bipolar	5.3×10^2	2.592×10^6	3×10^2
2019[638]	HfO_2	Spin	500	p^{++}Si/Cu	Bipolar	10^4	1.8×10^4	5×10^1
2019[827]	TiO_2/ CuPc	Spin	120	ITO/Al	Bipolar	10^4	2×10^4	n.d.
2019[828]	In_2O_3/Ag NPs/In_2O_3	Spin	400	p-Si/Al	Bipolar	n.d.	n.d.	1.5×10^2
2019[829]	HfO_2	Rotary	700	Pt/Au	Bipolar	~10^2	n.d.	10^2
2020[604]	IGZO	Spin	250	Ni/Pt	Unipolar	~10^2	10^4	2.5×10^2
2020[830]	TiO_x	Spin/Drop	RT	Cu/Pt	Bipolar	3.9	4.5×10^1	6×10^1
2020[623]	AlO_x	Spin	250	ITO/Ag	Bipolar	~10^3	10^4	5×10^2
2020[600]	TaO_x	Anodic	RT	Ta/Pt	Bipolar	8×10^1	n.d.	n.d.
2020[690]	IZO	Spin	400	TiO_2/Al	Bipolar	n.d.	2×10^3	n.d.
2020[650]	ZnO-rGO	Dip	RT	FTO/Al	Bipolar	4×10^1	n.d.	10^2

2020[669]	HfO_2	Spin	300	ZnO/Au	Bipolar	n.d.	n.d.	n.d.
2020[831]	$Ce_{0.9}Y_{0.1}O_2$ /TiO_2	Spin	600	Pt/Au	Bipolar	2.8×10^3	n.d.	n.d.
2020[832]	Ti_6O	Anodic	RT	Ti/Al	Bipolar	~10	n.d.	n.d.
2020[833]	HCO	Drop	80	FTO/Ag	Bipolar	~10	2.6×10^6	2×10^4
2020[834]	CoO	Blade	500	FTO/Al	Bipolar	~10	5×10^3	10^3

Mainly the (inert-active)-asymmetric and (non-inert-active)-asymmetric structures present a valence change mechanism (VCM) due to oxygen exchange reactions at the electrode-metal oxide interfaces and oxygen-vacancy migration into the metal oxide.[622] Around 74 % of the reported solution-based metal oxide RRAMs are based on VCM and only 26 % are based on electrochemical mechanism (ECM).

The VCM mechanism present in solution-based metal oxide RRAMs is preferred for edge computing technologies due to their high endurance, low variability, high retention, low operating voltage and high scalability potential.

Typically, when the active electrode materials are Ag and Cu, the RS occurs by ECM due to the reversibility of the electrode half-cell reactions and the higher mobility of Ag^+ and Cu^{z+} compared to other ions.[562,568] Several studies using these active electrodes have been reported in solution-based metal oxide RRAMs.[594,638,734,819] *Cho et al.* studied the resistive switching behaviour on solution-based niobium pentoxide (Nb_2O_5) thin films.[594] The resultant Pt/Nb_2O_5/Ag devices presented a unipolar switching, low operating voltage, fast switching speed (100 ns) and ultrahigh resistance window, $\geq 10^8$. In 2014, *Lin et al.* reported a forming-free TaN/ZrO_x/Cu RRAMs devices due to the formation and rupture of Cu conductive filaments. Also, since the ZrO_x thin films have a porous structure the Cu ion fast migration into the switching layer is favoured.[734] *Pei et al.* reported a multistate data storage in ECM cells with solution-based NiO thin films as the resistive switching layer and Ag as the active electrode.[819] These devices showed a high resistance ratio (10^5) and retention characteristics for the different level states. Lately, *Mohammad et al.* produced solution-based HfO_2 thin films and then incorporated in $p^{++}Si/HfO_2$/Cu resistive switching devices.[638] These exhibited an electroforming-free and bipolar resistive switching behaviour and also a low variability, large resistance window (10^4) and suitable endurance end retention characteristics for radiation sensing. When exposed to gamma-rays radiation, the device shows a clear shift towards lower log(R_{on}) values (conductive filaments are formed more strongly during the exposure) and recover to the initial state after the radiation is removed. However, all

the previously mentioned solution-based metal oxides ECM cells present a low endurance (≤ 100 cycles) which is a setback.

5.1.3. Low temperature solution-based metal oxide RRAMs

Usually, the most commonly adopted technique to deposit solution-based metal oxide thin films to produce S-RRAM devices (~74 % of the reports) is spin coating due to its reproducibility and simplicity, as observed in Figure 5.16 (a). Nonetheless, to reach large-scale production a change needs to be made from coating to printing techniques (only 6 % of the reports) which presents additional challenges, including low processing temperature, whilst maintaining device performance.

5.1.3.1. Low temperature solution-based metal oxide RRAMs

Most of the reported S-RRAM devices, about 65 % are produced using a high thermal annealing process (> 200 °C) as observed in Figure 16 (b), which is not compatible with roll-to-roll (R2R) printing techniques. To achieve printable S-RRAM devices, the elimination of the metal-hydroxyl (M-OH) bonds in the thin film's arrangement must occur at low processing temperatures while assuring devices' reproducibility and stability. Ultraviolet (UV) photoactivation processes (lamp or laser) can assure that by the use of a low thermal budget to reach high quality metal oxide thin films and compatibility with inline R2R manufacturing.[633,737,758]

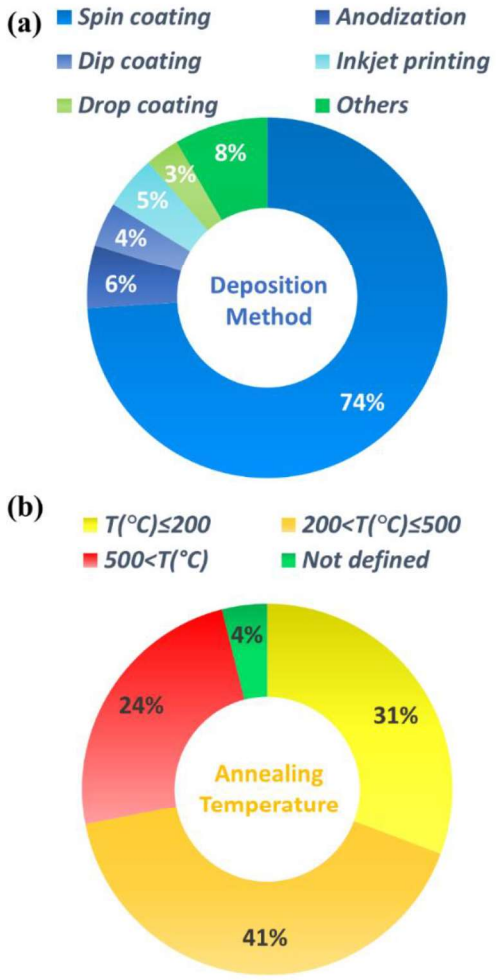

Figure 5.16. Statistical percentage of the a) deposition techniques and b) annealing temperatures reported in solution-based metal oxide RRAMs. Copyright © 2020 WILEY-VCH Verlag GmbH & Co. KGaA, Weinheim.

The use of UV irradiation induces photochemical cleavage of alkoxy groups, and activates metal and oxygen atoms to enable M-O-M network formation of the as-deposited films at low temperature, as shown in Figure 5.17.[3,20] During the exposure there is a rapid decrease of carbon and oxygen contents and by increasing the exposure time a gradual structural rearrangement and film densification occur. By adopting this method, electrical characteristics similar to high temperature annealed films were reached in solution-based IGZO RRAMs as demonstrated earlier in Figure 5.13 (c). Also in that year, the same author reported the influence of UV irradiation treatment in TiO_2 thin films deposited by spin-coating method.[736] The resultant devices present low variability (set and reset voltages), stable resistance window and long retention time, similarly to the high annealing temperature (600 °C) devices.

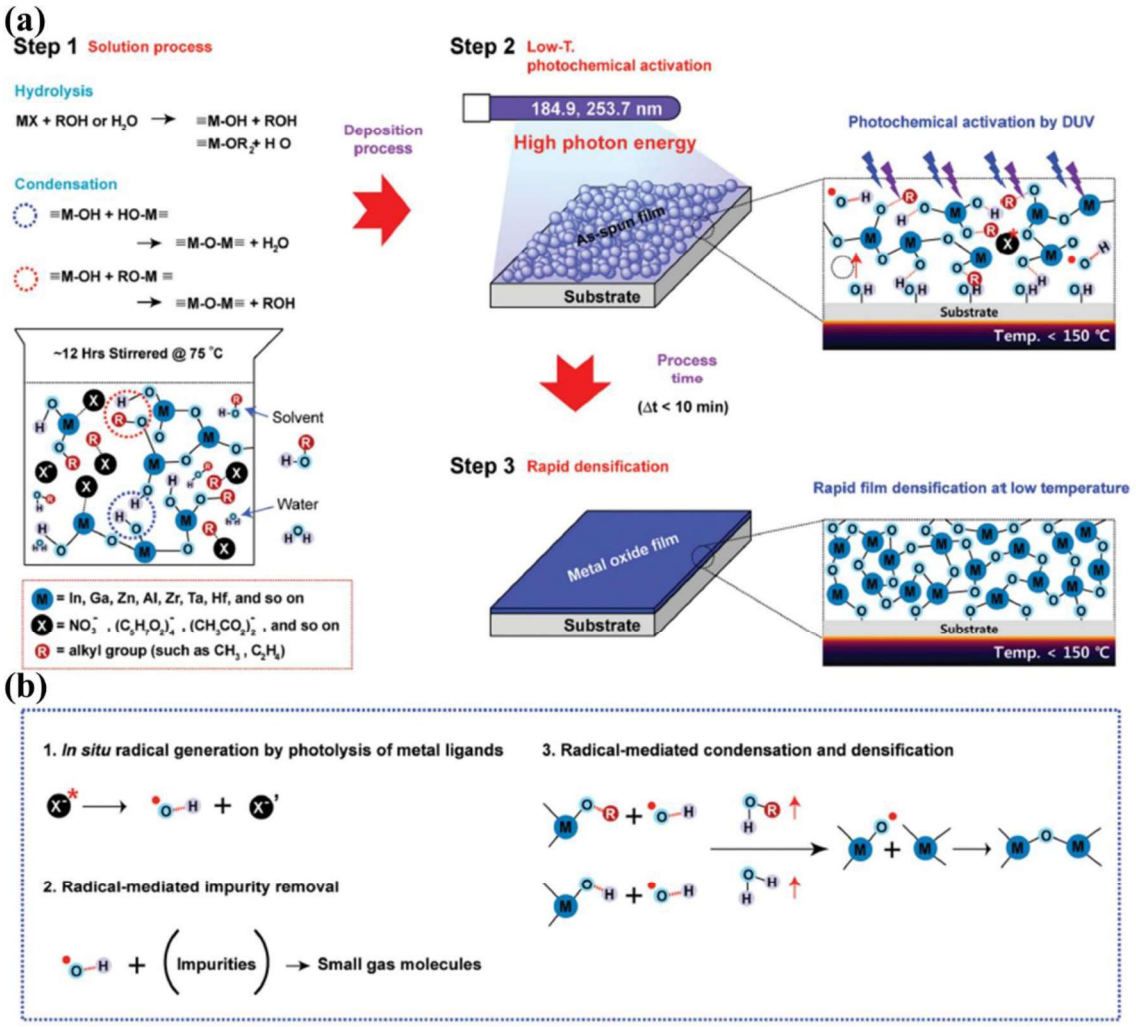

Figure 5.17. Photoactivation of sol–gel metal oxide materials and the proposed mechanism. a) Overall schematic illustration of the rapid low-temperature photoactivation of various sol–gel metal oxide films b) Proposed physicochemical mechanism of the rapid low-temperature photoactivation process via photochemical activation (direct photodecomposition of impurities, in situ radical formation, enhancement of rapid condensation and densification). Reproduced with permission.[20] Copyright © 2015 WILEY ‐ VCH Verlag GmbH & Co. KGaA, Weinheim.

This innovative route allows the achievement of low temperature solution-based metal oxide thin films with high quality that are compatible with large-area manufacturing and flexible systems.

5.1.3.1. Flexible S-RRAMs

The potential of UV irradiation for the production of flexible S-RRAM devices was studied by *Wang et al.* on spin coated manganese doped ZnO thin films.[632] The resultant ITO/ZnO/Ag devices showed stable resistive switching behaviour, even in flexible substrates, showing only a decrease of 10 % on the resistance ratio. Other resistive switching materials such as TiO_2 and ZrO_2 were subjected to the same post-treatment and used as resistive switching layers in flexible

substrates based on PET/ITO.[686,710] Both devices presented good retention and endurance characteristics even after being bent 1000 times, which is quite promising for further flexible applications.

Another advantage related to solution-based metal oxide thin films processed at low temperature is the presence of an amorphous oxide which is highly desirable for flexible S-RRAMs, since electronic performance does not depend on the degree of films´ disorder and the materials have ultra-smooth surfaces for supressing interface traps and scattering centres.[1,283]

The high demand of low-cost and sustainable processes has led to the increase of flexible electronics research using solution-processes. Reports[652,739,740] related with solution-based metal oxide RRAMs on flexible substrates were first published in 2009 and have been increasing fairly in the last decade (Table 5.3). *Choi et al.* reported outstanding results with solution-based ZnO thin films for memory applications in flexible substrates.[652] The ZnO solution-based RRAMs exhibited high resistance window, high endurance, high retention time and a fast programming ($\leq$ 50 ns), even after bending 10^5 times (Figure 5.18 (a)). These results pave the way for low-cost flexible memory devices. *Jeon et al.* reported solution-based TiO_2 RRAM devices formed on ITO/PES substrates without showing significant changes in both resistance states after 100 bending cycles.[684] The same research group reported a different structure Al/TiO_x/IAI on PES substrate (thermally stable up to 85 °C) with good retention characteristics (Figure 5.18 (b)).[683]

Table 5.3. Flexible solution-based metal oxide RRAMs. (BE: Bottom electrode; TE: Top electrode; $R_{on/off}$: Resistance on/off ratio; n.d.: not defined; T_{max}: maximum temperature; RT: Room temperature). Copyright © 2020 WILEY-VCH Verlag GmbH & Co. KGaA, Weinheim.

Year	Material/Substrate	Printed	T_{max} [°C]	BE/TE interface	$R_{on/off}$	Retention [s]	Endurance [cycles]	Bending times
2009[739]	TiO_2/PES	No	200	Au/Au	10^2	10^4	n.d	3×10^2
2009[652]	ZnO/PES	No	100	Al/Al	~10^3	10^5	10^4	10^5
2009[740]	TiO_2/n.d.	No	RT	Al/Al	10^4	1.2×10^6	n.d	4×10^3
2011[684]	TiO_x/PES	No	150	ITO/Al	~10^2	10^5	10^3	10^2
2011[683]	TiO_x/PES	No	150	IAI/Al	10^3	10^4	5×10^2	4×10^3
2012[835]	TiO_2/PES	Yes	150	Ag/Ag	10^3	n.d.	10^2	5×10^2
2012[836]	ZrO_2/PI	Yes	n.d.	ITO/Ag Ag/Ag	>10 10^2	n.d.	n.d.	n.d. 10^2
2012[709]	GeO_2:S/PES	No	120	Au/Al	10^7	10^4	n.d.	10^3
2013[591]	ZrO_2/PI	Yes	150	Ag/Ag	10^2	n.d.	1.4×10^2	5×10^2

2013[704]	ZrO_2/PET	Yes	135	ITO/Ag	>10	10^6	5×10^1	n.d.
2013[792]	(CuO/AgO)/PI	Yes	320	Cu/Ag	10	n.d.	4×10^1	n.d.
2014[702]	TiO_2/Paper	Yes	180	C/Ag	10^3	3×10^4	10^3	10^3
2015[632]	ZnO/PET	No	80	ITO/Ag	>10	4×10^3	1.1×10^2	2.4×10^3
2015[694]	TiO_2/n.d.	No	RT	Al/Al	n.d.	n.d.	n.d.	n.d.
2015[804]	ZrO_2	Yes	135	ITO/Ag	n.d.	n.d.	n.d.	n.d.
2016[813]	NiO/Al foil	No	250	Al/Ag	$>10^3$	n.d.	2×10^1	n.d.
2016[668]	NiO/Al foil	No	250	Al/Ag	$>10^2$	3×10^4	3.8×10^1	5×10^2
2016[603]	ZnO/PI	No	100	Al/Al	10^4	n.d.	1.5×10^1	n.d.
2016[837]	STN/PET	No	100	ITO/Al	10^5	n.d.	n.d.	1.4×10^1
2016[696]	TiO_x/PET	Yes	150	Ag/Ag	$>10^2$	n.d.	n.d.	n.d.
2016[812]	$ZnSnO_3$/PET	Yes	130	ITO/Ag	3×10^2	1.2×10^4	2×10^2	n.d.
2017[649]	STN/PET	No	100	ITO/Al	10^5	10^4	n.d.	1.4×10^1
2017[656]	(NiO/ZnO)/PET	No	150	ITO/GaIn	>10	n.d.	2×10^1	10^3
2017[838]	SOG/PEN	Yes	200	Ag/ PEDOT:PSS	10^4	1.6×10^4	10^3	n.d.
2017[710]	ZrO_2/PET	No	150	ITO/Pt	$\sim10^5$	10^4	6×10^2	10^3
2017[686]	TiO_2/PET	No	150	ITO/Pt	10^3	10^4	6×10^2	10^3
2018[821]	(Al-In-O/InO_x)/ Ni tape	No	180	Ni/Ag	$>10^2$	10^4	2.5×10^2	5×10^2
2019[829]	HfO_2/Mica	No	700	Pt/Au	$\sim5\times10^1$	n.d.	10^2	n.d.
2019[826]	ZnO/PET	No	120	ITO/ PEDOT:PSS	$>10^2$	2.6×10^6	5×10^2	n.d.
2019[617]	MgO/PDMS	No	250	W/Mg	10^5	10^4	1.4×10^2	n.d.
2020[741]	NiO/PI	No	180	Ni/Ni	$>10^2$	n.d.	1.2×10^2	1.2×10^2
2020[669]	HfO_2/Mica	No	650	ZnO/Au	n.d.	n.d.	n.d.	n.d.
2020[673]	ZrO_2/PI	No	200	Al/Al	10^4	$\sim10^4$	1.5×10^2	1.5×10^2

In 2012, *Choi et al.* reported a fully printed Ag/TiO_2/Ag RRAM on a PES substrate using electrohydrodynamic (EHD) printing technique.[835] The devices presented an acceptable resistance window and remain stable even after being subjected to 500 bending tests. These printed devices cured at low temperature (150 °C) prove the potential scale-up of solution-based metal oxides to flexible electronic applications. Two years later, *He et al.* reported all-printed C/TiO_2/Ag RRAM devices on paper using two printing techniques, inkjet and screen printing.[702] These devices were processed at a maximum temperature of 180 °C and revealed excellent electrical characteristics such as, a good resistance window (10^3), relevant endurance (10^3 cycles), considerable retention (3×10^4 s at 85 °C) and great operation under extreme bending conditions (radius = 10 mm) for 1000 times (Figure 5.18 (c)). These paper-based RRAM devices were also attached to different object surfaces showing a stable switching behaviour. The main advantages of all-printed paper RRAM are their biocompatibility, facile disposal (Figure 5.18 (d)) and large-area manufacturing suitability, which is highly demanded for internet of things (IoT) applications decreasing the associated costs.

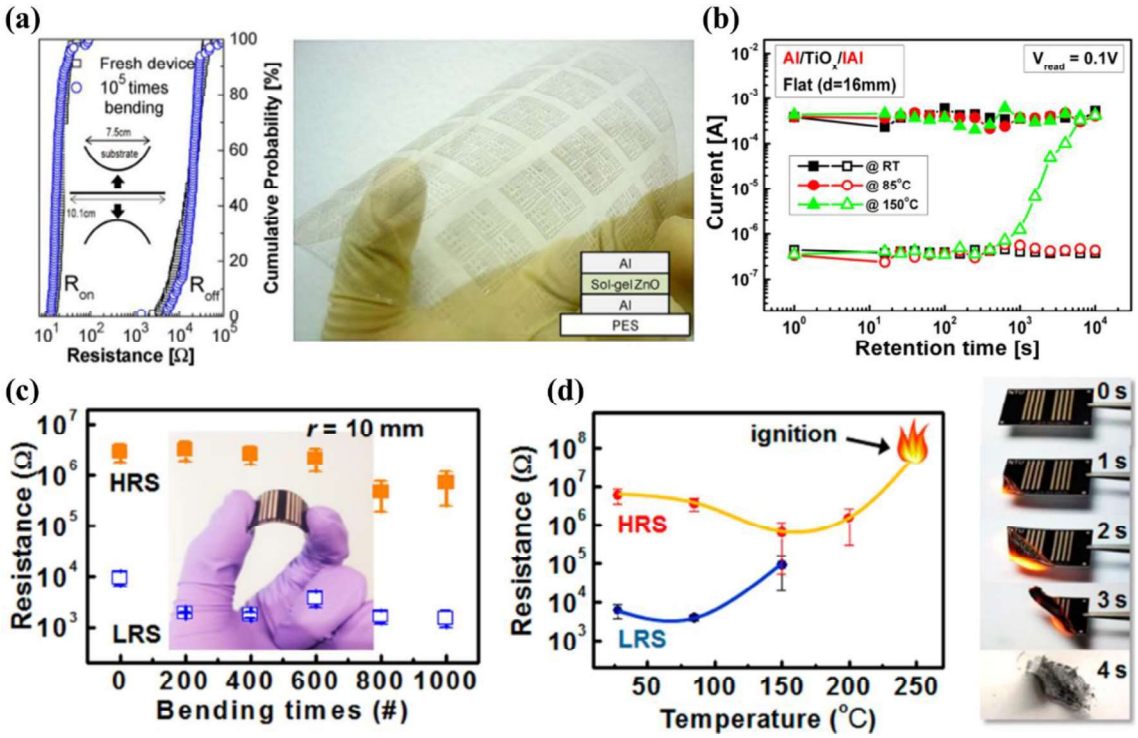

Figure 5.18. a) Cumulative probabilities of R_{on} and R_{off} values after 10^5 trials of cyclic bending of the PES substrate and photograph of the flexible solution-based ZnO RRAM; Reproduced with permission.[652] Copyright © 2009, IEEE b) Retention characteristics at various temperature ranges from 25 to 150 °C for the IAI device under mechanically flat condition. Each resistance state was extracted at a reading bias of 0.1 V; Reproduced with permission.[683] Copyright © AIP Publishing. All-printed RRAM: c) on/off distribution as a function of bending time with a bending radius of ~10 mm; d) Thermal test and security

demonstration. Variation of resistive switching states as a function of environmental temperature. Sequence of pictures showing the ignition process of the paper memory at 250 °C within 4s, leading to permanent data removal. Reproduced with permission.[702] Copyright © 2014, American Chemical Society.

Later, *Takei et al.* implemented solution-based nickel oxide (NiO) resistive switching memory devices with a good retention (10^4 s) in a flexible tactile touch sensor.[668] Figure 5.19 (a) and (b) display the cross-sectional and equivalent circuit schematics of the device operation to set NiO RRAM device on the OFF (before touch, original state – HRS – low current) and ON state (after touch – LRS – high current), respectively (Figure 5.19 (c)). Fundamentally, the memorized touch information is monitored by reading the current flow through the NiO RRAM integrated in the tactile device. When a zero voltage is applied the device is reset to the OFF state. This work demonstrates the potential of solution-based metal oxide flexible RRAMs for flexible device platforms highly requested for wearable technologies.

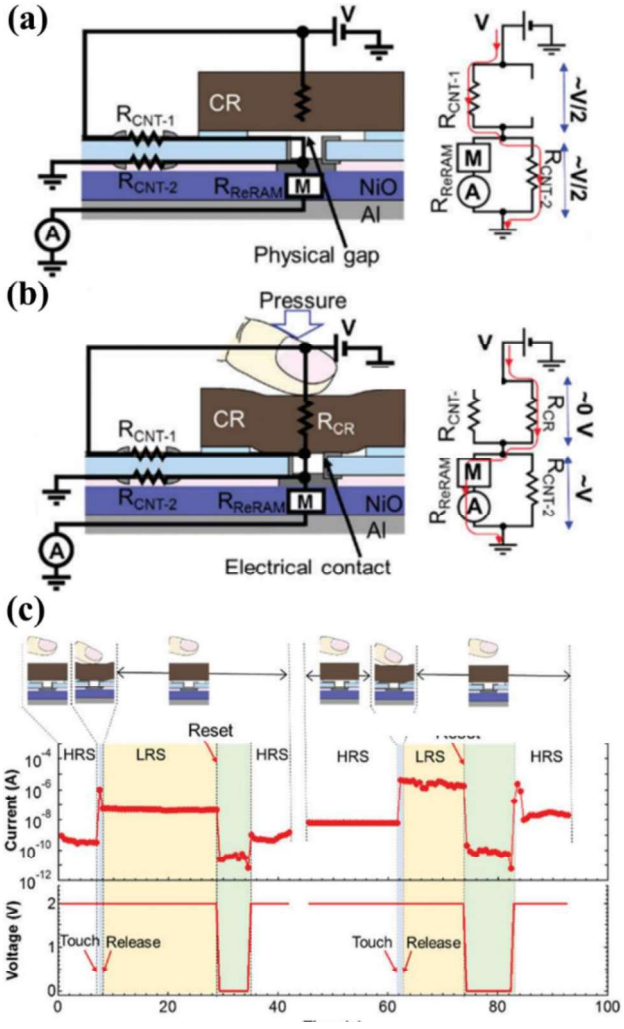

Figure 5.19. Cross-sectional images and equivalent circuits for the operation mechanism of the tactile touch memory device a) before a touch and b) after a touch; c) Real-time tactile touch memory demonstration by

applying a touch, SET voltage, and RESET voltage. Reproduced with permission.[668] Copyright © The Royal Society of Chemistry 2016.

Further work on printed materials is highly demanded to provide scalability (R2R compatibility), reduction of chemical waste, direct writing of the oxide materials (i.e. patterning without lithography processes), and higher reproducibility. Thus, in the future a substantial effort should be done on solution-based metal oxides processed at low temperature in low cost flexible substrates (i.e. Paper, PET, PEN, PES) to afford their implementation and scale-up for R2R-based techniques.

5.1.4. Figures of merit and current challenges of S-RRAM

5.1.4.1. Applied methods and figures of merit

Generally, to validate the resistive switching phenomenon, the first characteristic is DC current sweep showing pinched hysteresis of the set and reset process. The way the electrical characteristics are collected is fundamental to maintain an accurate interpretation of the data. Besides that, other required criteria for RRAM should be evaluated for a certain application such as state retention, endurance, switching speed, power consumption, scalability, multilevel cell (MLC) and sneak paths.

More specifically, in S-RRAM devices the cycle-to-cycle and device-to-device variability are crucial parameters to be also investigated and reported. Recently Lanza *et al.* recommended methodologies and a complete checklist to study a resistive switching device.[532] The consistency of the applied methods and figures of merit of solution processed RRAMs were evaluated considering Lanza *et al* work.[532]

Data retention is the evaluation of non-volatility of various resistance states of the device. A long data retention of 10 years is desired for RRAM devices. To be more precise and correct on the prediction, retention tests should be performed at higher temperatures (>80 °C) to observe possible failures.[839,840] Long retention tests ($\geq 10^5$ s) collected at ≥ 85 °C have been reported for solution-based metal oxide RRAMs.[279,657,659,684,783] *Wang et al.* reported ITO/MgTiNiO_x/Al S-RRAM devices with long retention data at 85 °C (Figure 5.20).[659] These results show the capability of S-RRAM devices to project trends retention up to 10 years as achieved in devices produced by vacuum-based techniques. It is notable that retention time mostly concerns the application of devices for memories.

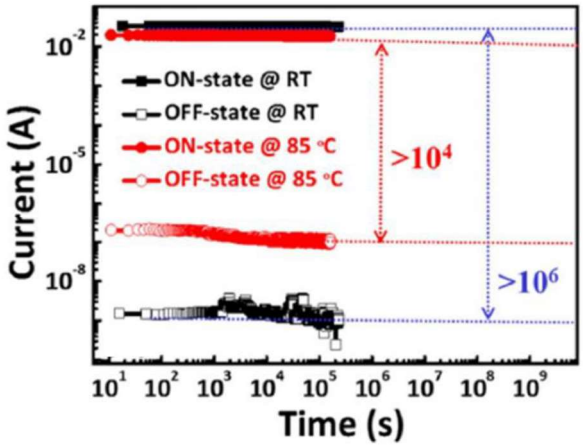

Figure 5.20. Retention characteristics of the solution-based $MgTiNiO_x$ RRAM at RT and 85 °C. Reproduced with permission.[659] Copyright © 2016, IEEE.

In resistive switching devices the endurance is defined by the number of times it can be switched between two or more resistive states and simultaneously maintain a sufficient resistance ratio (> 5) between them.[532,550] The lifetime of these devices can be, in certain cases, as low as 10^4 cycles which is not applicable for systems which are required to frequently alter the resistance states.[841]

In solution-based metal oxide RRAM device an endurance of 10^5 cycles was already achieved however further investigation should be performed in this figure of merit.[642,697] Nonetheless, the most common method to measure the endurance characteristics in S-RRAMs is the *I–V* sweep, as depicted in Figure 5.21 (a). This method is highly reliable (Figure 5.21 (b)) but can induce undesired stress. Hence, 1000 DC sweeps can be equivalent to 10^6 set and reset pulses (current-visible and current-blind pulse voltage stress (PVS)[532]) as an average performance of endurance measurements. The current-visible PVS allows millions of cycles in few minutes since the pulse widths can be of the order of microseconds, being much faster than the *I–V* sweeps (Figure 5.21 (c)). The current-blind PVS can be distinguished easily due to the spacing of the data points during the endurance characteristic collection, as shown in Figure 5.21 (d). However, this method is not recommended and cannot verify that 100 % of the applied pulses really induced state transitions in each cycle.[532] This method is only applicable for mature technologies at the industrial scale.

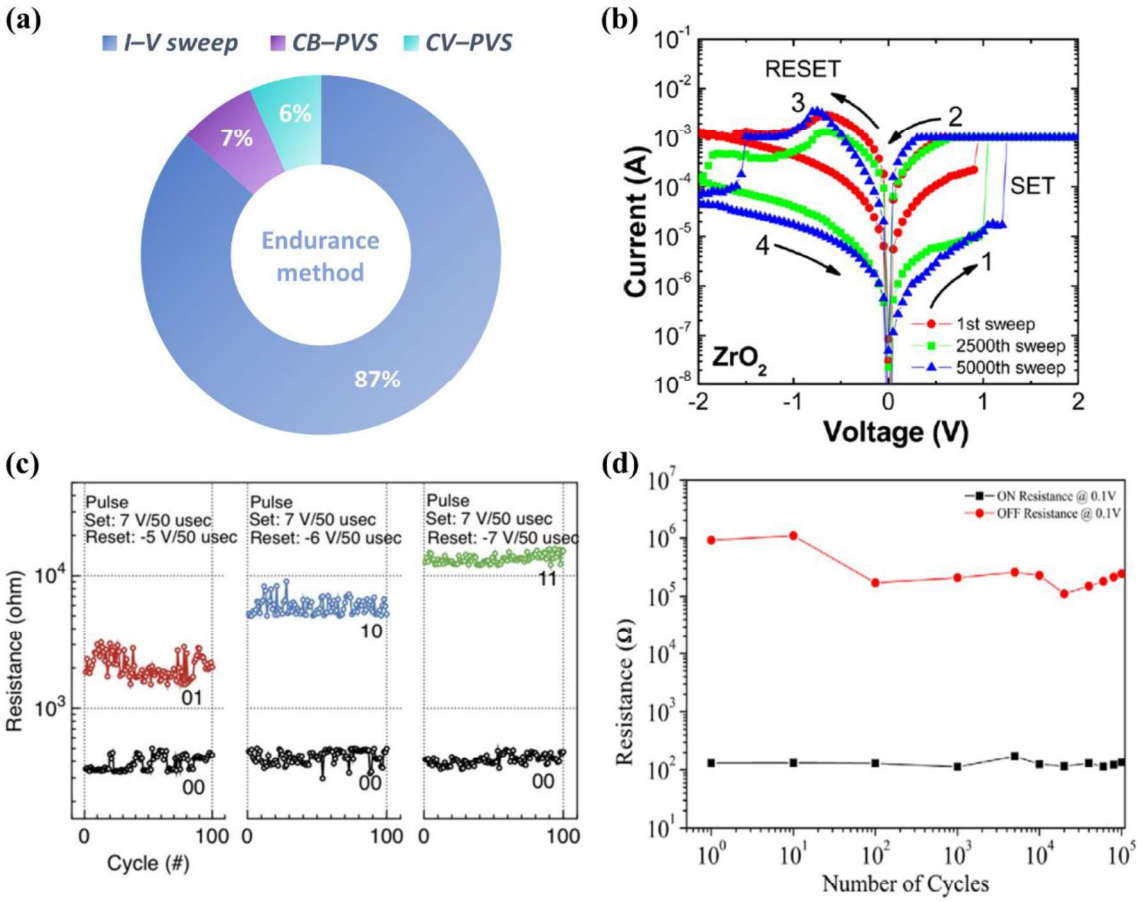

Figure 5.21. a) Statistical percentage of the endurance methods reported in solution-based metal oxide RRAMs; Copyright © 2020 WILEY-VCH Verlag GmbH & Co. KGaA, Weinheim. b) Bipolar resistive switching *I-V* characteristics of the ZrO_2 RRAM devices; Reproduced with permission.[636] Copyright © AIP Publishing c) Multi-level programming characteristics by CV-PVS: endurance characteristics of ITO/ZrO_2/Ti/Au memory; Reproduced with permission.[606] Copyright © 2017 Elsevier B.V. All rights reserved. d) Endurance characteristics of the ITO/NiO/Al memory device for 100 000 cycles of switching operations by CB-PVS. Reproduced with permission.[697] Copyright © 2013 IOP Publishing Ltd.

It is noteworthy that some RRAM fundamentals can be less demanding for some applications, such as wearables sensors, where such high endurance is not required.

The device switching speed plays a crucial role on the power consumption and performance of resistive switching circuits. In the literature a wide range of device speeds, from nanosecond (5 – 100 ns) to microseconds (1 – 100 µs), can be typically observed for solution-based metal oxide RRAMs.[594,609,611,623,642,648,714,722,774,838] *Cho et al.* studied the pulse width (ns to µs) influence on the SET and RESET of solution-based TiO_2 RRAM devices.[611] The resistance ratio on the devices tend to increase slightly for lower pulse voltage duration (from 100 ns to 100 µs), as depicted in Figure 5.22. Also, these resistive switching properties were maintained for 1 year, clearly demonstrating their stability.

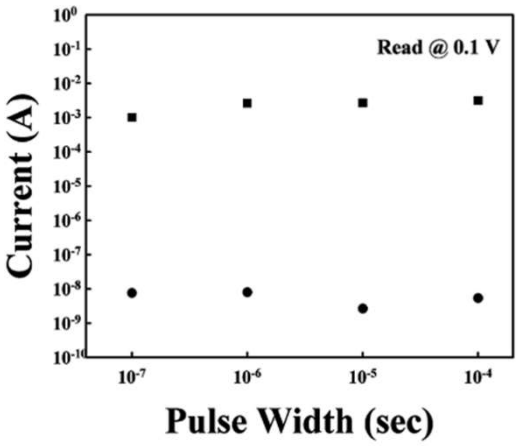

Figure 5.22. The current measurement of sol-gel TiO_2 device with different pulse widths (100 ns, 1 μs, 10 μs, and 100 μs) for the SET process at 4 V and the RESET process at 1 V. Reproduced with permission.[611] Copyright © 2009, American Chemical Society.

Unlike for vacuum-based metal oxide RRAM devices,[842] sub-nanosecond speed (picoseconds range) has not yet been reached for S-RRAM devices. Nevertheless, the results achieved until now are quite promising to reach ultra-fast speed using similar measurement methodologies and structures to avoid parasitic effects.

A low operating voltage, typically less than 1 V, is a fundamental condition on non-volatile memory technologies.[550] Typically, most of the reported solution-based metal oxide RRAM devices (around 92 %) require more than 1 V operating voltage, as shown in Figure 5.23. Nevertheless, already some reports use operating voltage bellow 1 V, opening the path for solution-based processes.[690,711,816,830] For example, *Chu et al.* reported an interesting study of solution-based WO_3 resistive switching devices with low operating voltage (0.8 V), synaptic plasticity and learning behaviour, being highly promising for neuromorphic computing systems.[816] Higher operating voltages as selector-less devices with strong non-linear characteristics is also not discarded for bio-inspiring computation applications.[843]

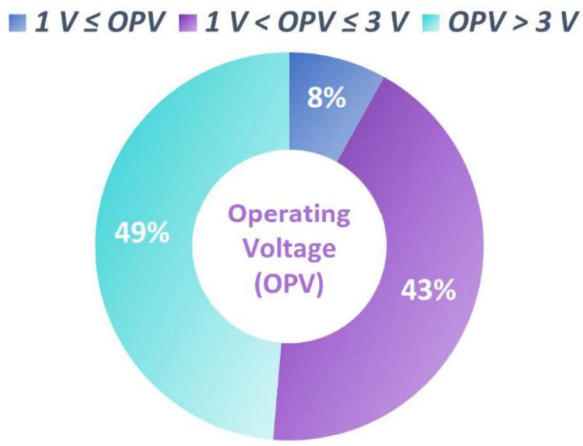

Figure 5.23. Statistical percentage of the operating voltage (OPV) reported in solution-based metal oxide RRAMs. Copyright © 2020 WILEY-VCH Verlag GmbH & Co. KGaA, Weinheim.

The stability of more complex systems, like information storage using resistive switching devices really depend on the device-to-device (spatial) and cycle-to-cycle (temporal) variation of the electrical characteristics such as, set voltage, reset voltage and various resistance states. As in vacuum-based metal oxides, the solution-based RRAM the device-to-device variability can be reduced by decreasing device size, as depicted in Figure 5.24 (a).[684] On the other hand, the cycle-to-cycle variability of each solution-based metal oxide RRAM device is highly dependent on the production process (mainly the annealing method (Figure 5.24 (b)), doping (Figure 5.24 (c)) and ambient conditions (Figure 5.24 (d))),[691,730,736] since is an intrinsic characteristic of the device (resistive switching layer and their interface properties). Consideration of all these parameters ensures that the S-RRAM variability can be controlled and diminished.

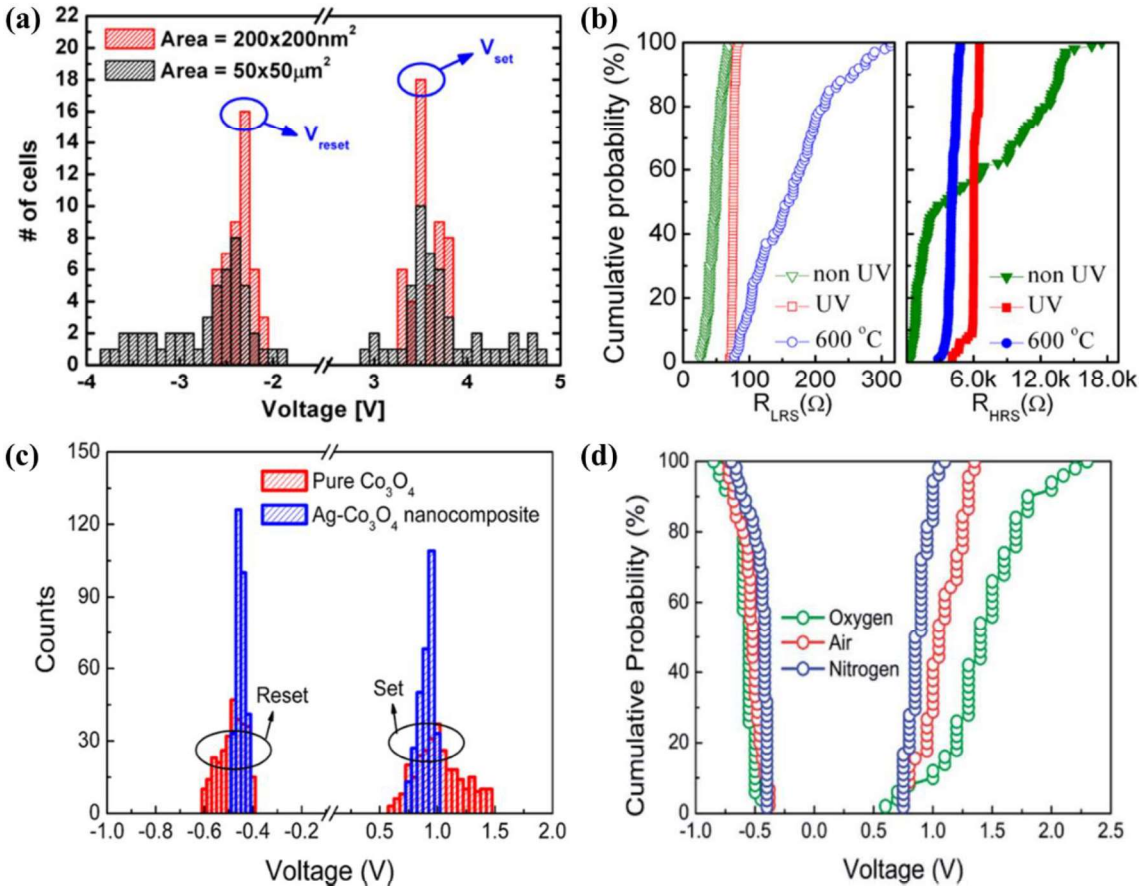

Figure 5.24. Variability on S-RRAM devices: a) Uniformity comparison between devices with 50×50 μm² and 200×200 nm² active area. Set/reset voltages are measured in each 50 fresh devices; Reproduced with permission.[684] Copyright © 2011 Elsevier B.V. All rights reserved. b) Distribution of the resistance variation in HRS and LRS read at 0.2 V during the 100 successive cycles of the TiO_2 non-UV films, UV-films, and 600 °C-films; Reproduced with permission.[736] Copyright © 2014 Elsevier B.V. All rights reserved. c) Statistical distribution of Set and Reset voltages of pure pure Co_3O_4 and Ag-Co_3O_4 devices; Reproduced with permission.[691] Copyright © 2019 WILEY-VCH Verlag GmbH & Co. KGaA, Weinheim d) Statistical distribution of the set and reset voltages of Co_3O_4 thin films in different annealing atmosphere. Reproduced with permission.[730] Copyright © The Royal Society of Chemistry 2019.

Typically, large areas are used in most of solution-based metal oxide resistive switching devices (around 65 %), as shown in Figure 5.25 (a). However, a decrease on device size (nanometres range) is demanded to reduce variability. This requires device patterning by photolithography with sizes ≤ 3 μm² which is quite challenging to achieve in most research institutes and universities. *Jeon et al.* investigated the area dependence of solution-based TiO_x RRAM devices down to the nano-scale (200 × 200 nm²).[684,774] By reducing the area from 50×50 μm² to 200 × 200 nm², resistive switching properties are more uniform and stable due to the decrease of the extrinsic defects (i.e. suppress multi-filament generation).[684,774] For solution-based ZrO_2 RRAM devices, *Jang et al.* observed that as the device size increases the resistance ratio decreases due to the

increment of the leakage current.[720] This is related with the formation of conductive filaments where the resistive switching is a stochastic process taking place at the weakest locations of the sample, with probability being higher for larger devices. Also, a vast portion (33 %) of the reported S-RRAM devices do not provide device area details (Figure 5.25 (a)) which compromises their analysis.

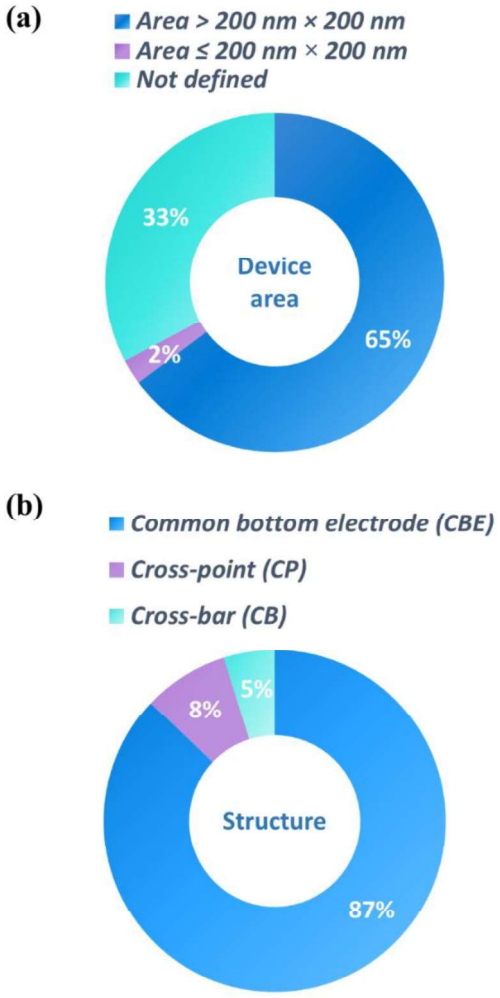

Figure 5.25. Statistical percentage of the a) device area and b) structure reported in solution-based metal oxide RRAMs. Copyright © 2020 WILEY-VCH Verlag GmbH & Co. KGaA, Weinheim.

Another important feature that influences the device variability is related to the device configuration. It can be based on a common bottom electrode (CBE) or on cross structures (individual, a cross-point (CP) or matrix, a cross-bar (CB)). The most common structure reported in the literature for solution-based metal oxide RRAMs is CBE, around 87 % (Figure 5.25 (b)), however this method should be avoided since normally large electrodes are used inducing device variability. Also, another disadvantage is the mechanical stress made by the probing tip on the top electrode of the CBE structure which can change the resistive switching characteristics. Cross

structures avoid that issue however only 13 % of the reports adopted these structures (Figure 5.25 (b)). *Choi et al.* reported one of the smallest feature size (3×3 μm^2) of ZnO S-RRAM devices using conventional lithography based on a cross-bar structure.[652] A clear improvement of HRS and LRS on the standard deviation was achieved. Recently, *Kim et al.* observed a tremendous difference on Pt/Ni/IGZO/Pt S-RRAM devices stability by changing a cross-point structure from 200 × 200 μm^2 to 10 × 10 μm^2 by conventional lithography.[604] In the smallest device size a narrow distribution of the set and reset voltage was reached due to the controlled number of conductive filaments formed and their stable reversibility.

Multilevel cell (MLC) RRAMs have a significant potential allowing the achievement of more than two resistive states, highly required for information processing technologies. Several reports with MLC operation have been performed on solution-based metal oxide RRAM devices up to three to eight level states.[279,606,610,634,639,697] *Cho et al.* reported solution-based AZTO RRAM devices treated by microwave irradiation (MWI) that exhibit multistage storage characteristics with 3 bit/cell (i.e. 2^3 states).[634] These devices revealed a stable endurance and retention characteristics (85 °C), as depicted in Figure 5.26 (a) and (b), respectively. The results achieved with S-RRAM devices show great potential for high-density non-volatile multilevel memory applications.

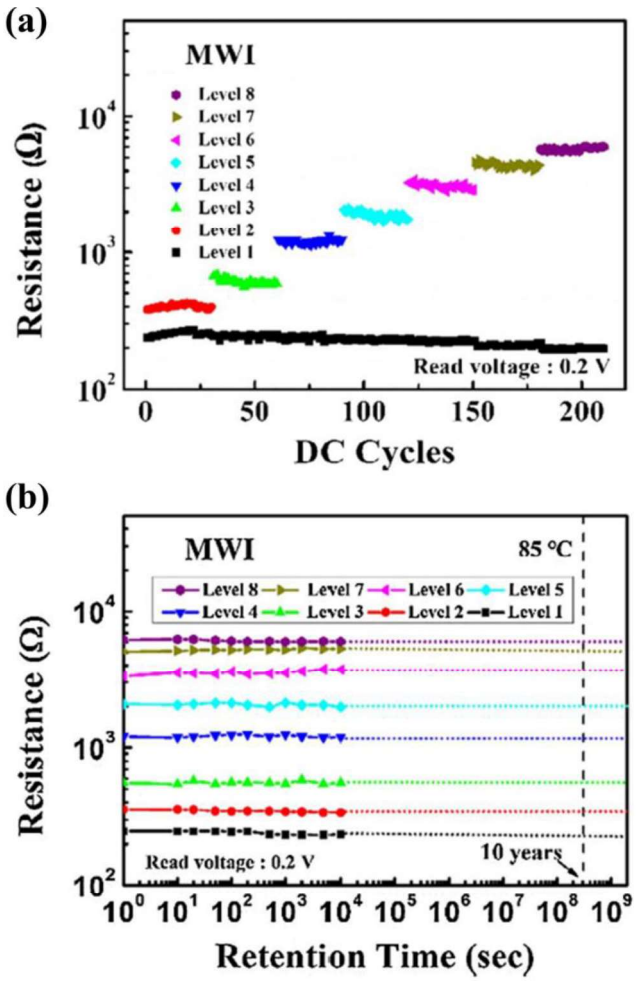

Figure 5.26. a) Modulation of HRS resistance by varying reset stop voltages for microwave irradiation (MWI)-treated AZTO RRAMs; b) Retention characteristics for different reset stop voltages measured from MWI-treated AZTO RRAMs at high temperature (85 °C). Reproduced with permission.[634] Copyright © 2017 Elsevier Ltd. All rights reserved.

Before the application of the individual RRAM devices in more complex systems and circuits some strategies should be performed to reduce the effect of sneak path. Some possible approaches to overcome it were performed in solution-based metal oxide RRAM devices.[665,699,826,831,844] *Wang et al.* demonstrated the integration of one solution-based Ni/TiO_2/Ti diode and one Al/Strontium Titanate Nickelate (STN)/Pt RRAM device (1D1R) to supress undesired sneak current in a cross-point array.[665] These devices present reproducible and uniform switching with self-rectifying behaviour in low-resistance state, being suitable for the production of high-density integrated solution-based metal oxide NVM for various applications. However, adding diodes to the array increases the delay of the system due to capacitive loads and diode threshold voltages which decrease the output swing.[845] Recently, *Bae et al.* developed an asymmetric function with Schottky diode based RRAM device based on solution-processed ZnO/PEDOT:PSS

heterojunction to reduce the sneak current issue.[826] The respective ITO/ZnO(n-type)/PEDOT:PSS(p-type)/Ag device can open a new door for stable and flexible memory devices for high-density crossbar arrays.

5.1.4.2. Applied methods and figures of merit

To finalize this review on solution-based metal oxide RRAM devices the current status and challenges of relevant features namely, solution synthesis, fabrication technique, thin film properties, device structure, scalability, retention, endurance, HRR/LRS ratio, operating voltage, device speed and maturity of technology are summarized in Table 5.4.

Table 5.4. Current status and challenges of relevant parameters of solution-based metal oxide RRAMs. Copyright © 2020 WILEY-VCH Verlag GmbH & Co. KGaA, Weinheim.

Parameter	Current status	Challenge/Recommendation
Solution synthesis	▪ Sol-gel synthesis is the most common method ▪ The choice of the right molar proportion and doping highly improve the performance of the devices	▪ Use nitrate-based precursors ▪ Use green-solvents ▪ Combustion synthesis recommended to decrease the temperature required
Fabrication technique	▪ Spin-coating is the most common method (around 74 % of the reports)	▪ Use printing techniques in flexible substrates to allow devices scale-up
Thin films deposition and annealing	▪ Most studies do not report the relative humidity during deposition	▪ Relative humidity (%) must be reported for accurate analysis ▪ Nitrogen ambient recommended ▪ Post-treatment curing recommended to reach lower temperatures
Variability	▪ Just 9 % of the papers report the yield ▪ Most studies do not report the device-to-device and cycle-to-cycle dispersion (set and reset voltage; HRS and LRS state)	▪ Yield must be reported for accurate analysis ▪ At least 10 devices should be measured ▪ Recommend the device-to-device and cycle-to-cycle variability assessment
Device structure	▪ Common bottom electrode is the most common structure	▪ Cross structures recommended to avoid extra mechanical stress on the device ▪ Devices with asymmetric structures recommended

Scalability	▪ Typically, large areas ≥ 100 μm^2 are used	▪ Nanometre and sub-nanometre areas recommended by using nanoimprint lithography
Retention	▪ > 10 years @ 85 °C ▪ 45 % of studies do not report retention tests and only 4 % have retention of 10^6 s	▪ Recommended retention tests (≥ 10^4s) at temperatures above 80 °C
Endurance	▪ 10^6 cycles ▪ 24 % do not report endurance tests and only 6 % have endurance ≥ 10^4 cycles ▪ *I–V* sweep is the most common method, 87 % of reports	▪ ≥ 10^{12} cycles recommended ▪ Current-visible pulse voltage stress recommended to enhance endurance ▪ Bending tests for the flexible devices
HRS/LRS ratio	▪ Up to 10^8 ratio ▪ 44 % of studies show ratio > 10^2 and only 4 % show resistance ratio ≥ 10^6	▪ Resistance ratio will depend of the application
Operating Voltage	▪ Only 8 % of devices have an operating voltage ≤ 1 V	▪ Operating voltages ≤ 1 V recommended
Device speed	▪ Down to 5 ns per transition ▪ Most of the studies do not report the devices switching speed	▪ Range of ms to ps depending on the application
Maturity of technology	▪ Solution-based metal oxide RRAM devices have a long way to go since it is a recent approach field compared to vacuum-based devices	▪ Measurement of parasitic capacitances associated to connections and to the device structure ▪ Heterojunctions and 1D1R memory device recommended help to reduce the sneak path ▪ Design and integration of devices at circuit level for various applications ▪ Simulation at device and circuit level

Concerning solution synthesis, combustion methods are recommended in order to reduce the thermal processing required for the film formation. Regarding the fabrication process, printing techniques are suggested to be further investigated since large-scale manufacturing processes

using sustainable approaches are highly demanded. In fact, power-efficient IoT systems by using S-RRAMs combined with mass produced printed electronics result in extremely low-cost operation and fabrication.

A comprehensive set of studies on thin film deposition considering the impact of all parameters which affect the reproducibility of devices is essential. This means that the chemical processing-related issues should be investigated, then possible solutions to control the fabrication should be assessed. Particularly for S-RRAM devices, the following fabrication parameters should be addressed to facilitate their upscale for the printing industry: number of layers (to minimize defects and enhance film densification); processing ambient conditions, mainly the relative humidity (strongly affects ink viscosity and solvent evaporation rate which influences the active layer film thickness); post-treatment curing processes.

In addition, uniform resistive switching properties are greatly dependent on the size of devices. For S-RRAMs the most used structure relies on a common bottom electrode which induces a higher mechanical stress and enhances device-to-device and cycle-to-cycle measurements variability. Thus, patterned devices with cross point structure are preferred and fully printed S-RRAMs are desired to avoid more costly and complex processes, like lithography. However, the printed electrodes processed at low temperature (compatible with low cost flexible substrates) are typically based on nanoparticle inks such as Ag which, to achieve low resistance, require a high film thickness and present high surface roughness. The bottom electrode roughness is the most critical challenge since it can promote variability and damage the subsequent active layer of the S-RRAMs leading to low endurance that eventually causes device short circuit. Recently, an emerging contact printing technique, reverse offset printing, accomplished highly conductive MoO_x printed electrodes based on metal inks. These electrodes reached significant conductivity at a low film thickness (28 nm) with a smooth surface (roughness of 0.22 nm) that can be used in the future to boost the overall performance of fully printed S-RRAMs.[383]

There are also general parameters for tuning the RS performance, which are applicable to both physical (vacuum-based) and chemical fabrication methods. These include; energy band alignments at interfaces, chemical interface reactions and the doping profile of the RS material. Since these challenges are not exclusive to solution-processed devices, the reader is referred to the excellent existing reviews and book chapters on these topics.[846,847]

Regarding the applications of S-RRAM, most studies report the properties of resistive switching to seek non-volatile memory applications where the key parameters are fast switching speed (like SRAM), large on/off ratio with a reasonable state retention for MLC storage (like flash). It is

notable that different applications can be targeted based on device characteristics. As an example, retention loss which mimics the dynamics of biological memory is beneficial for artificial neural network applications.[848] Furthermore, a large on/off ratio is not a main concern for some neuromorphic applications.[843] However, low endurance is a limitation for computation and in memory logics which require frequent alteration of the resistance states. Recently, other applications such as hardware security systems based on intrinsic randomness of resistance properties of memristor devices and cycle-to-cycle variations were reported.[849] Here, printed electronics open up new applications for memristor technology in biometric identification smart cards.

5.1.4. Conclusions

In this review, the fundamental parameters to control the synthesis (method, metal salt precursor, solvent, stabilizer, doping and molar proportion) and formation (film thickness, environmental conditions and initiation source) of solution-based metal oxide thin films (i.e. active resistive switching layer) to enhance S-RRAM devices are covered. Of all these characteristics the most critical are the synthesis and deposition methodology, and the controlled ambient conditions (temperature, humidity and atmosphere) which play a key role on the reproducibility of the devices by different research institutes. Also crucial for REDOX-based S-RRAM devices is an asymmetrical structure composed of chemically Schottky and ohmic-type interfaces by engineering the switching material or contacts.

Certainly, S-RRAM devices processed at low temperature are improved with UV irradiation exposition by reducing the residual organics and enhancing the formation of M-O-M networks. This post-treatment is highly demanded and promising especially for flexible S-RRAMs and their compatibility with R2R printing techniques.

To complement the study of S-RRAM devices the figures of merit and applied methods were analysed as well as the current challenges of this field. Variability, scalability and device structure require special attention, being the most challenging features, which directly influence the devices' figures of merit: retention, endurance, resistance window and device speed. Although S-RRAM devices are not yet a matured technology, it is quite promising in consumer electronics market for future IoT applications with large area manufacturing potential using low-cost and sustainable electronic devices.

Chapter 6

From spin to print resistive switching devices

Lately resistive switching memories (RRAM) have been attracting a lot of attention due to their possibilities of fast operation, high density, lower power consumption, simple fabrication process and scalability. However, most of these RRAM are produced by conventional methods and nowadays the industry demands more simplicity typically associated with low-cost manufacturing. First, an insight of a relevant production parameter, the number of layers deposited by spin-coating of aluminum oxide thin films is explored. Then, to provide a more viable process inkjet printing was applied to produce resistive switching (RS) devices at low temperature by the combination of thermal annealing (150 °C) and deep ultraviolet (DUV) treatment.

Keywords: solution-based, metal oxide thin films, solution combustion synthesis, resistive switching, inkjet printing, low temperature

The results presented in this chapter are published in:

- ✓ *Emanuel Carlos, Asal Kiazadeh, Jonas Deuermeier, Rita Branquinho, Rodrigo Martins, Elvira Fortunato. "Critical role of a double-layer configuration in solution-based unipolar resistive switching memories", Nanotechnology IOP, 2018;*
- ✓ *Emanuel Carlos, Jonas Deuermeier, Rita Branquinho, Cristina Gaspar, Rodrigo Martins, Asal Kiazadeh and Elvira Fortunato, "Design and synthesis of low temperature printed metal oxide memristors", Journal of Materials Chemistry, 2021.*

6.1. Critical role of a double-layer configuration

6.1.1. Introduction

New materials and device concepts have been studied in the semiconductor industry to surpass various technological limitations.[850–852] Due to their high density and low fabrication costs, the most prominent, non-volatile memories (NVM) today are flash memory devices.[563,850,853] Nevertheless, these suffer from low endurance, low write speed, and high voltage requirements for write operations. In addition, the increasing density of flash is expected to run into physical limits, which is not compatible with the Internet of Things (IoT).[563] Taking that into account, a huge demand for fast, small and power efficient memories has grown.[563,850,854,855] Resistive random access memory (ReRAM) has attracted a renewed interest due to many advantages, including high switching speed, low power consumption and high density with a simple structure.[854–856] A ReRAM memory cell is a metal-insulator-metal (MIM) structure composed of a resistive switch medium, such as metal oxides, which could be easily integrated with existing CMOS technology.[563,857] Moreover, the high density mass storage could be supported by multi-level cell (MLC) operations in ReRAMs.[13,639,858] The resistive switching phenomenon has been observed in a wide variety of insulator oxides, such as Ta_2O_5, TiO_2, HfO_2, ZrO_2 and Al_2O_3.[541,588,859–864] The resistive switching in these materials occurs after an electroforming process known as dielectric soft breakdown. Once defects reach a critical density, a template of ReRAM device is obtained. Partial rupture/formation of the conducting filament (CF) results in different resistance states.

Among these materials, Al_2O_3 is the most abundant (noncritical raw material) and has promising resistive switching properties, as well as good breakdown field and good thermal stability.[92,862] Aluminum oxide has been widely reported for use in resistive switching devices with various memory structures fabricated via different techniques such as ALD, thermal oxidation and sputtering.[862,865–874] According to the literature these structures with Al_2O_3 show unipolar and bipolar properties depending on the processing conditions.[858,862,867,870,875] Using a unipolar ReRAM array, the selector circuit structure could potentially be simplified with the integration of a diode and a unipolar ReRAM. Due to good scaling potential and ease of fabrication, applying a passive component is preferred.[855,876] It is widely accepted that the switching mechanism is the consequence of oxygen vacancies and oxygen ion formation in the Al_2O_3 thin film.[870,872,874,877–880] Nevertheless, the conduction mechanism could change according to the resistance states.[858]

Lately, solution-based memories have gained a lot of attention due to their low cost manufacturing, simplicity, comparable performance to those of high vacuum techniques, and good film uniformity in large areas.[8,92,740] Inkjet printing, dip-coating and spin coating are the

techniques most used for solution processing oxide semiconductors and insulators in memory applications.[597,732,740,811] However, only a few reports have been done on solution-based aluminum oxide memories, as depicted in Table 6.1.[639,811,865] Since 2011, combustion synthesis has been used to improve thin film transistor performance, however, until now it has not been applied to memory production.[2] In this synthesis an oxidizer (nitrates) and a fuel (urea, citric acid) are added to the precursor solution. During the annealing process an exothermic reaction occurs, resulting in a reduction of the external heat required for the film formation; the removal of organic solvents and film densification lead to high-quality films.[2,92]

In this work, we report for the first-time solution-based unipolar aluminum oxide memories and study the influence of subsequent depositions using combustion synthesis (SCS) on the device performance. The ReRAM bilayer devices show unipolar resistive switching behaviour with good endurance and retention time of up to 10^5 s at 85 °C in vacuum, which surpass the state-of-the-art. Since transparent devices have attracted a lot of research interest in portable and consumer electronics such as flat panel displays, touch panels, optical sensors and smart windows, Al_2O_3 films with the optimized layer structure were stacked between transparent conductive oxide (TCOs) electrodes.

Table 6.1. Performance comparison of solution-based aluminum oxide ReRAM. Copyright © 2018, IOP Publishing.

Year	BE[a]	TE[b]	*d* (nm)	SB[c]	CC[d] (mA)	Set (V)	Reset (V)	$R_{ON/OFF}$	Retention (s)	Endurance
2016 [811]	Al	Hg	90	Bipolar	n.a.	10.8	12.4	10^3	n.a.	100/100
2017 [865]	Ti/ Pt	Ti	n.a.	Bipolar	10	0.9	-1.5	10^2	10^4	150/150
2017 [639]	Ti/ Pt	Ti	n.a.	Bipolar	10	1.1	- 1.8	10^3	10^4	100/100
This Work (2018)	Ti/ Pt	Ti/ Au	66	Unipolar	1	- 2.2	- 0.6	10^5	10^5	100/100

[a]Bottom electrode, [b]Top electrode, [c]Switching behavior, [d]Current compliance, *d*: Al_2O_3 film thickness, n.a. – not available

6.1.2. Experimental details

6.1.2.1. Precursor solution development

Aluminum nitrate nonahydrate ($Al(NO_3)_3 \cdot 9H_2O$, Fluka, 98%) was dissolved in 2-methoxyethanol (2-ME, $C_3H_8O_2$, ACROS Organics, 99%), to yield a solution with an Al^{3+} ion concentration of 0.2 M. The fuel (Urea, Sigma, 98%) was then added to the solution and maintained under constant stirring for 24 h. The urea to aluminum nitrate molar proportion was 2.5:1 in order to guarantee the redox stoichiometry of the reaction. The precursor solution was filtrated before use.

6.1.2.2. Film deposition and characterization

Prior to deposition, all substrates were cleaned as mentioned in a previous report.[92] Thin films were deposited by spin coating for 35 s at 2000 rpm (Laurell Technologies), forming a single (30 nm) and a bilayer (66 nm) of aluminum oxide. Each deposition was followed by an immediate annealing at 500 °C on a hotplate for 30 min in air. Before the second layer deposition a 10 min UV/Ozone surface treatment was performed.

Optical properties were obtained using a Perkin Elmer lambda 950 UV/VIS/NIR spectrophotometer by measuring transmittance (T) in the wavelength range of 190 nm to 800 nm.

The film structure was assessed by glancing angle X-ray diffraction (GAXRD) performed by an X'Pert PRO PANalytical powder diffractometer using Cu Kα line radiation (λ = 1.540598 Å) with an angle of incidence of the X-ray beam fixed at 0.9°. Fourier Transform Infra-Red (FTIR) spectroscopy data of thin films deposited on Si substrates were recorded using an Attenuated Total Reflectance (ATR) sampling accessory (Smart iTR) equipped with a single bounce diamond crystal on a Thermo Nicolet 6700 Spectrometer. The spectra's were acquired as reported in a previous article.[92]

X-ray photoelectron spectroscopy (XPS) was measured with a Kratos Axis Supra, using monochromated Al Kα irradiation (1486.6 eV). The detail spectra were acquired under an emission angle of 90° with a pass energy of 5 eV, resulting in an energy resolution better than 0.45 eV. The quantification of the elemental composition was done by dividing the integral peak intensity by the respective relative sensitivity factor (RSF) of the instrument.[493]

6.1.2.3. Memory fabrication and characterization

Metal-insulator-metal (MIM) structures were fabricated on glass substrates (1737, Corning) as shown in Figure 6.1 (a). The bottom electrode, a Ti/Pt bilayer of 20 nm and 50 nm was first deposited on the substrate by e-beam evaporation (homemade apparatus). Then aluminum oxide films were deposited as described above. After that, a multilayer of Ti/Au, 6 nm and 60 nm, respectively, was deposited by e-beam evaporation as the top electrode.

For the transparent memories commercial glass/ITO was used as the bottom electrode, followed by the spin-coating of an aluminum layer as previously described. To finalize the device, a 100 nm film of amorphous indium zinc oxide (IZO) was deposited as top electrode by RF magnetron sputtering from an IZO target at room temperature.[881]

An array of top electrodes with an area of 1.96×10^{-3} cm^2 was deposited through a shadow mask. Each top electrode represents an individual device. The electrode size observed by optical microscopy can be found in the Supporting Information (Figure S1).

The film thickness was obtained by scanning electron microscopy analysis of the sample´s cross section prepared by focused ion beam using Ga^+ ions (SEM-FIB, Zeiss Auriga Crossbeam microscope).

The quasi-static I-V characteristics of the devices were measured using Keithley 4200 SCS semiconductor analyser connected to the Janis ST-500 probe station. The bias was applied to the top electrode. The temperature analysis of memories was measured under vacuum, using a Lakeshore model 336 temperature controller with liquid nitrogen used as the refrigerant.

6.1.3. Results and discussion

Solution combustion synthesis (SCS) has been crucial to the boosting of precursor conversion into metal oxides.[2] This method has been applied to optimize the performance of TFT constituent layers and will now be applied for the first time to solution-based memories.

Figure 6.1 (a) shows the schematic of the memories produced with a monolayer or bilayer of aluminum oxide using metals (Ti/Au and Ti/Pt) and transparent conductive oxides (ITO and IZO) as electrodes.

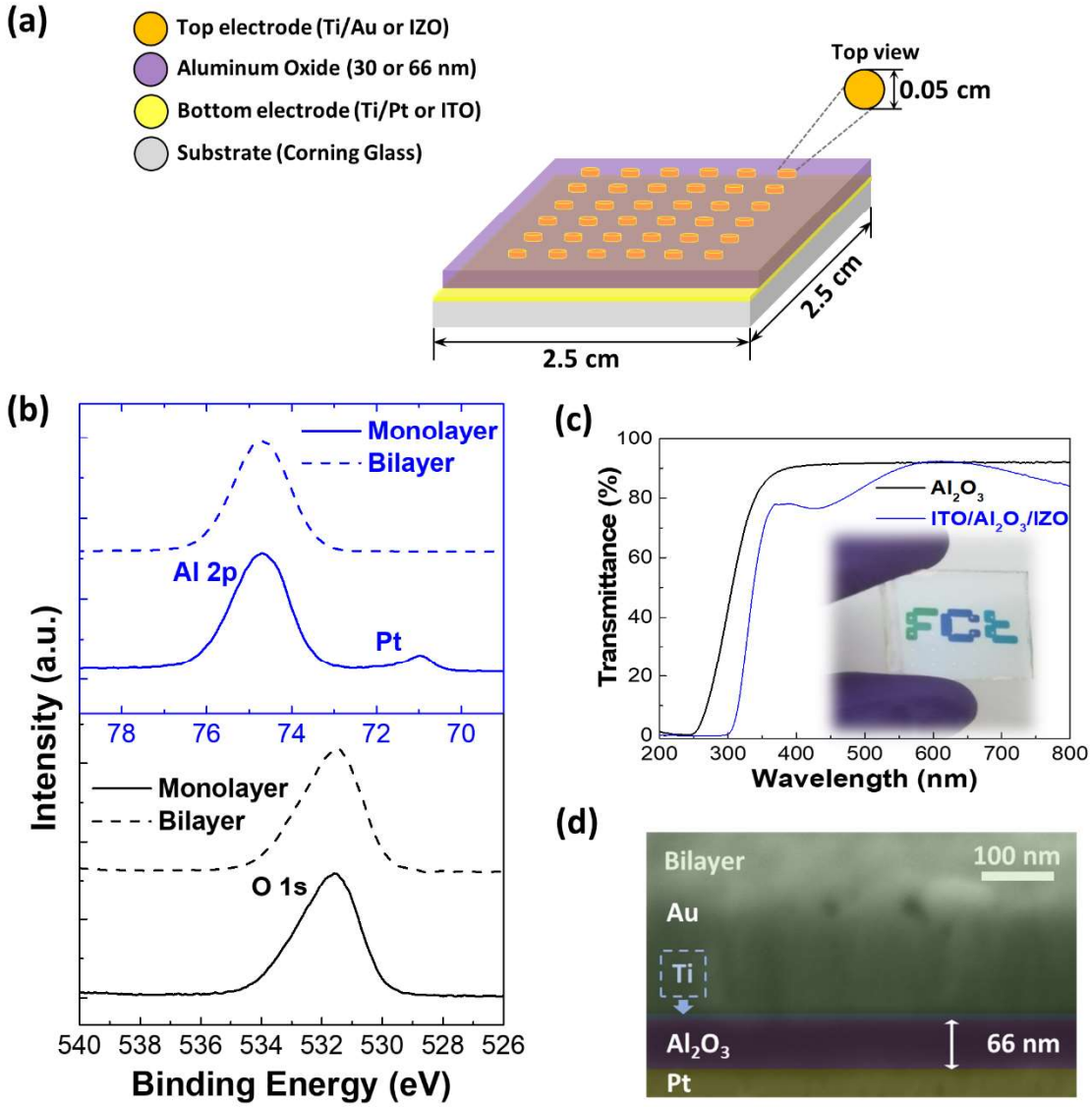

Figure 6.1. (a) Schematic of memory structure; (b) XPS of Al 2p and O 1s emissions of solution-processed Al_2O_3 films with one and two layers; (c) Optical transmittance of aluminum oxide bilayer on glass and of ITO/Al_2O_3/IZO; (d) High-resolution SEM-FIB cross-section image of the bilayer (66 nm) Al_2O_3 thin film.[279] Copyright © 2018, IOP Publishing.

To further investigate the aluminum oxide and the effect of the subsequent depositions, XPS measurements were performed. The Al 2p and O 1s emissions are shown in Figure 6.1 (b). The Al 2p binding energy is found at 74.7 eV in the monolayer and the bilayer. Since this result is similar to values from literature in which charge referencing to C 1s was used, it can be concluded that our measurements did not suffer from artefacts due to charge accumulation.[493]

A peak of metallic platinum (Pt 4f) at 71 eV is observed in the monolayer and not in the bilayer. This means that Pt intermixes with Al_2O_3 during the film formation in the first layer. By using

angle-resolved XPS it can be shown that with increased surface sensitivity the Pt signal disappears, therefore the estimated depth from the surface up to which no platinum is present is approximately 5 nm (Figure D2 in the Appendix D). Besides the platinum signal in the monolayer sample, the surface contains oxygen and aluminum as the main components, and a small percentage of carbon for all samples. Due to the convolution of the Pt $4f_{5/2}$ p and Al 2p peak, the Al 2s emission was used to calculate the O/Al ratio (spectra not shown here). After the first and second deposition, the O/Al ratio is approximately the same, 1.29 and 1.27, respectively.

In order to study the thin film´s transparency, the optical transmittance of the Al_2O_3 bilayer (66 nm) and the full transparent memory (ITO/Al_2O_3/IZO) were measured, showing 91% and 80% of transmittance respectively, as depicted in Figure 6.1 (c).

The produced Al_2O_3 thin films were also characterized with ATR-FTIR before and after annealing at 500 °C in order to monitor organic residues removal, as shown in Figure D3 in the Appendix D.

The structure of solution-based aluminum oxide thin films was investigated by X-ray diffraction (XRD), as shown in Figure D4 in the Appendix D. The absence of diffraction peaks reveals that amorphous thin films are obtained for the aluminum oxide even upon annealing at 500 °C. Since the thin films are amorphous, they have no grain boundaries, low leakage current, and low surface roughness, thus improving device performance. High resolution SEM-FIB cross-section images of the memories (Ti/Pt/Al_2O_3/Ti/Au) were performed to measure the film´s thickness. The single-layer Al_2O_3 thin film has a thickness of about 30 nm (Figure D5 in the Appendix D) and the double-layer thin films have a thickness of about 66 nm, as depicted in Figure 6.1 (d). Note that there is a considerable difference between the Al_2O_3 thickness from the SEM cross-section and the Pt found up to 5 nm below the surface. This is most likely due to the intermixing of the two materials at the interface and the limited resolution of the SEM.

The *I-V* curves of Ti/Pt/Al_2O_3/Ti/Au devices exhibit unipolar resistive switching under a current compliance (CC) of 1 mA for the different thicknesses as depicted in Figure 6.2 (a,d). For both conditions 36 devices were measured. A low forming voltage at the negative side (~ - 2 V) equivalent to the set voltage is required. These *I–V* characteristics were measured under consecutive DC voltage sweeps and the voltage was controlled through the Au top electrode.

In the case of the single layer Al_2O_3, the memory showed a stable and uniform switching behavior (Figure 6.2 (a)), however after 19 cycles it was not possible to switch the memory on (Figure 6.2 (b)), showing low endurance. The device presented a good retention of up to 10^5 s in air, with an $R_{ON/OFF}$ ratio of 10^5 with a small degradation in the end. Figure 6.2 (c) shows the set and reset

voltage, which had a small deviation of (– 2.1 ± 0.4) V and (– 0.7 ± 0.2) V respectively, that could be explained by the unpatterned Al_2O_3. Most of the working devices were in the outer limits of the substrate, reducing the yield to 30 %. The memories that were not working, showed a short-circuit like behavior. This outcome is explained by the diffusion of Pt up to 5 nm below the Al_2O_3 thin film surface, which results in an ultrathin layer of intact Al_2O_3 in the memory without any Pt diffusion. Note that both XPS and SEM-FIB cross-sections where obtain from the center of the sample area.

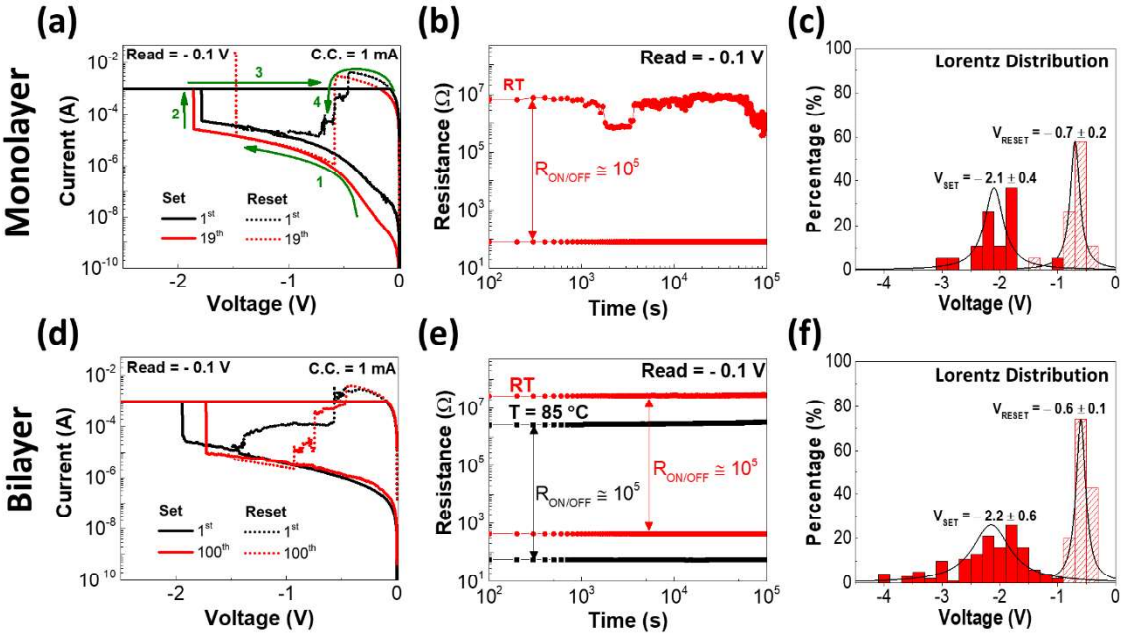

Figure 6.2. Ti/Pt/Al_2O_3/Ti/Au electrical characterization of both memory conditions, monolayer (30 nm) and bilayer (66 nm): (a,d) *I-V* characteristic endurance, (b,e) retention time characteristics and, (c,f) set and reset voltage average.[279] Copyright © 2018, IOP Publishing.

Figure 6.2 (d) shows the bilayer Al_2O_3 memory which revealed better endurance when compared with the monolayer, reaching 100 cycles (Figure D6 (a) in the Appendix D). The resistance states uniformity measured in 100 cycles is shown in Figure D6 (b) of the Appendix D.

Taking that into account, retention tests were also performed at 85 °C in vacuum to verify the reliability of the devices. For both temperatures a good retention of 10^5 s with $R_{ON/OFF}$ ratio of 10^5 was achieved, showing no significant degradation of HRS and LRS; this indicates that the device could maintain these properties for 10 years, as depicted in Figure 6.2 (e). In terms of set and reset voltage, this device also showed a small deviation of (– 2.2 ± 0.6) V and (– 0.6 ± 0.1) V, respectively, as shown in Figure 6.2 (f). The yield as compared to the monolayer memories was also improved, for the first time achieving 100 % for these particular device types.

Note that an ultrathin layer of oxidized titanium at the interface of Al_2O_3 and Ti contact is formed due to the oxygen-getter property of titanium. This layer leads to a chemically reactive contact which reduces the Al_2O_3 and creates a high concentration of oxygen vacancies at the Al_2O_3 interface with the top contact. This increases the local conductivity close to the top aluminum oxide interface.[851] This is in line with the *I-V* characteristics of the pristine state, which show a rectifying behaviour (Figure D7 in the Appendix D). A higher electron barrier is observed at the Pt/Al_2O_3 contact compared to the Al_2O_3/Ti/Au contact. Thus, a preferential negative electroforming at lower voltages can maintain the self-selecting resistive switching scheme.

A multi-level cell (MLC) operation can be obtained in the bilayer Al_2O_3 memories during the reset process. Figure 6.3 (a) shows an example of *I-V* characteristics during the set and reset, and Figure 6.3 (b) the results of a retention test for distinct two-resistance states at room temperature. This was performed in order to verify the reliability of the multi-level operation. To obtain MLC characteristics the reset process was adjusted in two different reset voltages. Once the device is programmed in one state, either level 1 (-0.5 V) or level 2 (-0.9 V), a good retention time of 10^4 s is obtained. Higher voltage amplitudes accelerate local joule heating of the CF.[882] Thus, the MLC operation is due to a thermal-assisted electric field rupture model of the conducting filament.

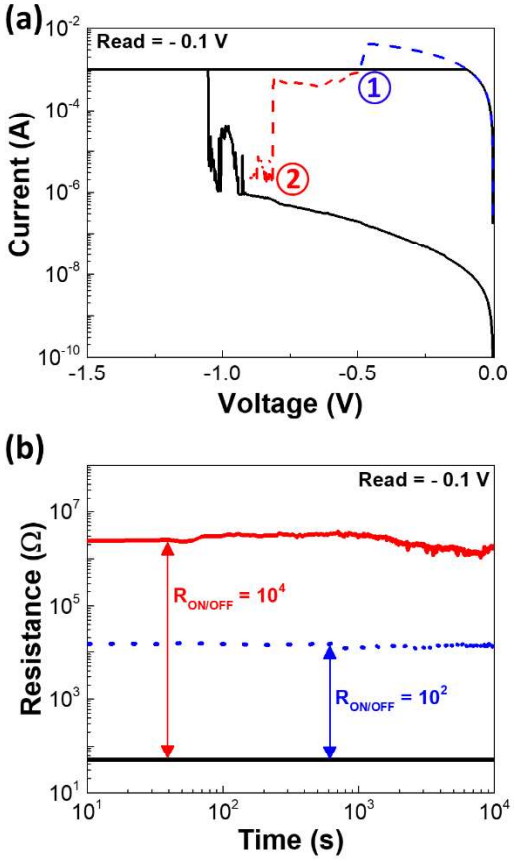

Figure 6.3. (a) Typical *I-V* memory characteristics showing set and the reset with multi-level cell (MLC) operation; (b) Multi-level retention characteristics for different reset voltages.[279] Copyright © 2018, IOP Publishing.

The fitting of typical *I-V* characteristics in a log-log scale is shown in Figure 6.4 (a). The space-charge-limited conduction (SCLC) mechanism following ohmic conduction in the low voltage region, square law (from 0.7 V to 1.05 V) and steep increase region for voltages > 1.1 V were observed at the off-state. The on-state shows ohmic behaviour (slope of 1), indicating the presence of highly conductive paths. The results are in agreement with other reports on Al_2O_3 memories.[865,872,873]

At the low resistance state (on-state), temperature dependency is very weak with an activation energy (E_a) of 0.005 eV while the intermediate resistance state shows slight thermal activation (E_a= 0.069 eV), as observed in Figure 6.4 (b). The trend of resistance versus temperature reveals a degenerated semiconducting-like phase as the nature of the CFs.

Based on the above presented results, the proposed mechanism of these unipolar or thermochemical resistive switching devices is the following: A filamentary thermal breakdown of the oxide increases the local doping between the top Ti contact (oxygen-poor region) and the bottom electrode (oxygen-rich region). The electroforming is an irreversible process, and the CFs are never completely ruptured during set/reset operation. Thus, the set process always occurs at the lower voltages. In the reset process different stop voltages result in the partial thermal rupture (nano-scale antifuse process) of the CFs into variable sizes, which is then associated with the different resistance states. The interrelated effects of ohmic and SCLC conduction mechanism probably alter the activation energy of the intermediate state.

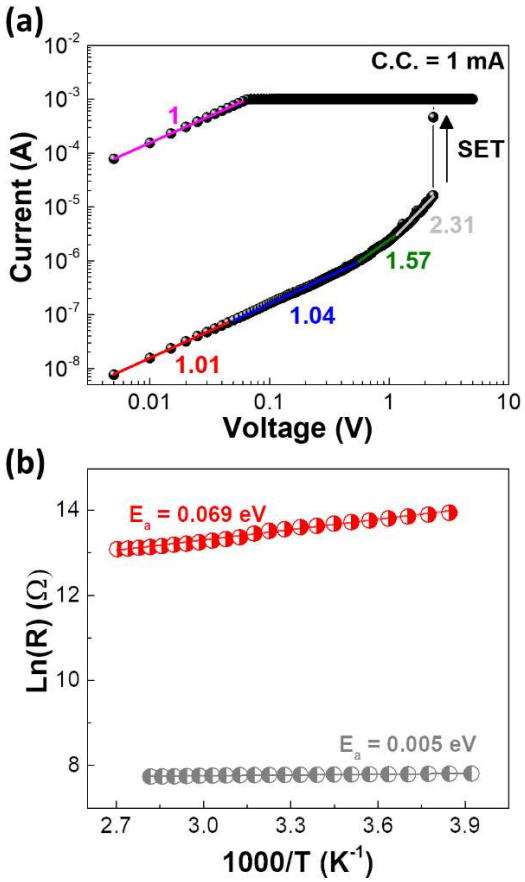

Figure 6.4. (a) I-V characteristics of Ti/Pt/Al_2O_3/Ti/Au device plotted in log–log scale, showing a space–charge–limited conduction mechanism; (b) Temperature analysis of the memory in different resistance states.[279] Copyright © 2018, IOP Publishing.

A fully transparent bilayer Al_2O_3 ReRAM was produced by replacing metallic electrodes with transparent conducting oxides (TCOs), ITO as bottom and IZO as top electrode. Figure 6.5 (a) represents the typical I-V curve of transparent unipolar memory writing and erasing. The set occurs when a negative bias voltage (0 V to - 6 V) is applied; an abrupt increase in the current was observed at - 4.2 V, achieving the LRS. A compliance (CC) of 1 mA was established to prevent device breakdown. To reset the memory a negative bias voltage (0 V to - 4.5 V) was applied without CC, and the memory reverted to the HRS at - 4 V due to the joule effect. Figure 6.5 (b) shows the retention of the ITO/Al_2O_3/IZO memory. The device revealed a reliable retention of up to 10^4 s with a $R_{ON/OFF}$ ratio of 10^4 without deterioration. Table D1 in the Appendix D depict other oxide transparent memories, and this is the first report of aluminum oxide obtained via a solution-based method for such devices.

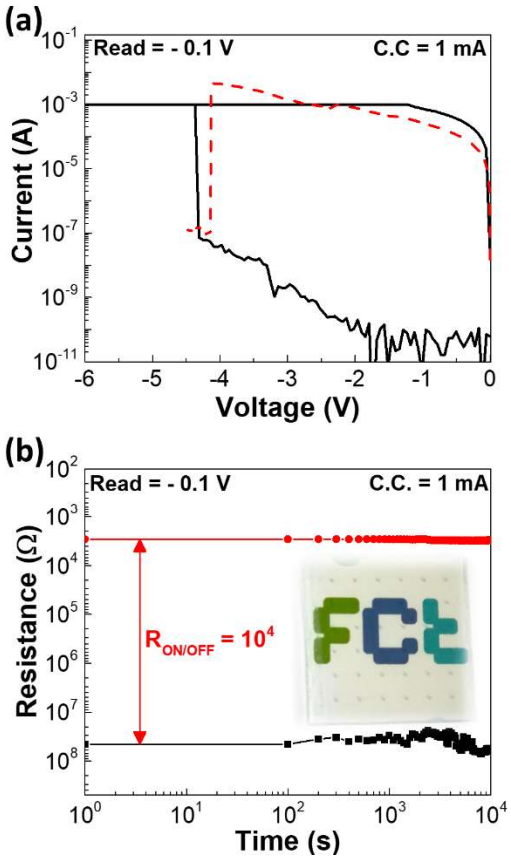

Figure 6.5. (a) Typical I-V characteristic and (b) retention of the transparent memory (ITO/Al_2O_3/IZO) with the respective photo.[279] Copyright © 2018, IOP Publishing.

Although their performance is not as good as that of non-transparent memories, these results clearly demonstrate the feasibility of a cost-effective System-On-Panel approach for transparent electronics.

6.1.4. Conclusions

In this work, we demonstrate for the first time the use of solution combustion synthesis (SCS) in the production of aluminum oxide memories. The physical properties of the aluminum oxide layers were investigated using a wide range of characterization techniques that revealed high transparency (> 90 %) and the elimination of all residual organics. The Al_2O_3 memories were improved with by a dual stage deposition process, which limits the Pt diffusion into the aluminum oxide. These ReRAM devices showed a unipolar resistive switching behaviour with good endurance (100 cycles), retention time up to 10^5 s at 85 °C, and a yield of 100 %. Also, a multilevel cell operation (MLC) was achieved by application of different reset voltages. Temperature analysis of various resistance states reveals a filamentary nature based on different doping levels of the oxygen vacancies.

Furthermore, a fully transparent device using ITO/Al_2O_3/IZO showing good memory performance was successfully produced, which paves the way for cost effective System-On-Panel technology in transparent electronics.

6.2. Printed metal oxide resistive switching devices

6.2.1. Introduction

Printed electronics has been acquiring a substantial attention in microelectronics due to its cheap and simple processes, suitable for large scale manufacturing. Printed electronic devices such as thin film transistors, capacitors, fuel cells, batteries and memories are key components for the expansion of the Internet of Things (IoT).[5,309,333,702,883,884] For these applications memory devices, particularly non-volatile memories (NVM) like resistive random-access memories (RRAM) using memristors offer the required high-density, ultra-low power and high velocity.[885] Typically, in these resistive switching (RS) devices the active layer is based on transition metal oxides and is sandwiched between two electrodes.[532] The RS behavior involves the formation and disruption of conductive filaments as well as the interface/bulk modulation comprising a localized concentration of defects.[561,562] Also, these devices can have different applications (artificial neural network, neuromorphic, computation, memory logics and hardware security) which are defined by their electrical characteristics.[843,848,849,886] However, most RS devices use expensive production and time-consuming techniques such as PVD (i.e. sputtering) and CVD (i.e. atomic layer deposition).[887–890] Coating (spin-coating, dip-coating and drop-coating) methods have been widely used to produce RS devices at low production costs although subtractive processes (i.e. lithography) are required to pattern them.[689,697,706,891] Printing techniques have the potential to overcome that step and attain large scale production.[475] Inkjet printing, a non-contact technique, has been the mostly exploited to produce solution-based metal oxide RS devices.[591,732] However, typically the active layer requires high annealing temperatures (≥ 300 °C) for the formation of the metal-oxygen-metal (M-O-M) networks without impurities (i.e. hydroxides and carbon) which is not compatible with low-cost flexible substrates (i.e. PEN, PET or cellulose).[279,713] To overcome this issue, different methodologies such as solution combustion synthesis (SCS) and ultraviolet irradiation have been applied in solution-based RS devices.[615,633] Compared to the conventional sol-gel process, SCS allows a higher homogeneity and purity of the thin films and a low ignition temperature is required to start the combustion reaction and form the metal oxide.[27] *Pei et al.* reported solution-based nickel oxide bipolar RRAMs processed at low temperature (250 °C) with good endurance (10^2) and retention (10^4 s) using the solution combustion method.[615] UV treatments by laser or lamp irradiation require even lower annealing temperatures (≤ 150 °C) for the formation and densification of metal oxides.[92,614] Also, these UV photochemical techniques have compatibility with the printed electronic industry by reducing the associated cost and manufacturing time. *Bao et al.* studied the effect of deep ultraviolet (DUV) irradiation lamp on IGZO, Bi_2O_3 and TiO_2 thin films at low temperature.[633,736,758] These devices exhibited a stable and highly uniform resistive switching behavior even compared with high temperature conditions

(400 °C). *Yang et al.* reported a fast curing of only 3 min to produce solution-based NiO RRAMs using UV excimer laser annealing.[737] Besides the low temperature production and processing time factors, the sustainability of the materials is a critical parameter to upscale to the industry. Solution-based aluminum oxide (Al_2O_3) is a promising and abundant material for resistive switching devices.[534] Different solution-based methods have been used to produce Al_2O_3 RS devices such as anodization, dip-coating and spin-coating (Table E1 in the Appendix E).[279,745,811] However, their processing by printing techniques at low temperature is required to decrease the associated cost and allow application in large area manufacturing. Inkjet printing is the most explored printing technique at lab scale research in printed electronics since many parameters (velocity, direction, temperature of the ink and substrate, among others) can be controlled in a precise way as well as their versatility once it is based on a digital process not requiring a master template.[477]

In this work, we report for the first-time inkjet printed SCS-based aluminum oxide resistive switching devices processed at low temperature (150 °C) by combining DUV irradiation and thermal treatment. These devices show a bipolar resistive switching behavior with a good current-voltage (I-V) sweep endurance, a high retention time of up to 10^5 s and multi-level cell (MLC) operation. The results achieved are suitable for low-cost substrates which paves the way for large area manufacturing.

6.2.2. Experimental details

6.2.2.1. Ink preparation

Aluminum-oxide dielectric precursor ink ($Al(NO_3)_3 \cdot 9H_2O$, Merck, 99.997 %) was dissolved in 2-methoxyethanol (2-ME, $C_3H_8O_2$, ACROS Organics, 99 %) to obtain a solute concentration of 0.2 M and obtain ultrathin films. Afterwards urea ($CO(NH_2)_2$, Sigma, 98 %) was added to guarantee the redox stoichiometry of the reaction in a molar proportion of 2.5:1 to aluminum nitrate.[307] The prepared solution was maintained under constant stirring for 12 h at room temperature to stabilize the solution and filtered using 0.45 µm pore size polytetrafluoroethylene (PTFE) to obtain the base solution. A commercially available silver (Ag) nanoparticle colloidal ink (Sicrys™ I50T-13) from PV Nano Cell company was used in this work. The metallic nanoparticle-based ink contains around 50 wt % Ag nanoparticles in a polar solvent, with a particle diameter of around 70–115 nm.

The viscosity test was performed using a Cap01 spindle on the BROOKFIELD Cap 2000+ viscometer. The aluminium precursor ink was maintained at 30˚C and the characterization was done using 500 rotations per minute (rpm) in order to guarantee an optimal correlation factor.

6.2.2.2. Film deposition and characterization

An initial 15 min UV/ozone surface activation step was made on commercial glass/indium-tin-oxide (ITO) substrates to improve wettability. The thin films of aluminum oxide were deposited by inkjet printing at 1000 dpi with 1 nozzle at 30 °C using a piezoelectric multi nozzle printing head from Dimatix (DMCLCP-16110) with 10 pL cartridges in a PiXDRO LP50 inkjet printer. The printing was tested with different printing speeds of 100 and 150 mm/sec using a tailored waveform to print square shapes (1000×1000 μm^2). Then, the printed patterns of the dielectric precursor solution were dried at 130 °C in a hotplate in air for 10 min. Afterwards, a combined low power DUV treatment (lamp with an output energy intensity of 75 mW/cm^2 at 254 nm) and thermal annealing (150 °C) was performed in a nitrogen environment for 90 min.

While printing and drying the ink, ambient conditions were controlled where the relative humidity and temperature varied between 51–57 % and 23.3–24.6 °C, respectively.

Optical characterization of the inkjet printed patterns was performed using an optical microscope Olympus BX51 equipped with an Olympus SC30 camera to visually check the printing quality of the patterns.

The surface morphology of the printed AlO_x layer was investigated by atomic force microscopy (AFM, Asylum MFP3D). The AlO_x thin film structure was assessed by glancing angle X-ray diffraction (GAXRD) performed by an X'Pert PRO PANalytical powder diffractometer using Cu Kα line radiation (λ = 1.540598 Å) with an angle of incidence of the X-ray beam fixed at 0.5 °. Scanning electron microscopy (SEM) analysis was performed to achieve the AlO_x film thickness of a sample cross section prepared by focused ion beam using Ga^+ ions (SEM-FIB, Zeiss Auriga Crossbeam microscope).

X-ray photoelectron spectroscopy (XPS) using monochromated Al Kα irradiation (1486.6 eV) was measured with a Kratos Axis Supra). The procedure was the same as mentioned in a previous report.[279] The quantification of the elemental composition (Al 2p, O 1s) was performed by dividing the integral peak intensity by the respective relative sensitivity factor (RSF) of the instrument.

6.2.2.3. Printed devices production and characterization

Solution-based RRAMs were fabricated on the commercial glass/ITO substrates. Then, AlO_x precursor ink was printed on top of ITO using an optimized printing speed of 150 $mm \cdot s^{-1}$. Production of AlO_x thin films is described in section 6.2.2.2. Following a 15 min UV/ozone surface activation step, performed prior to printing the top Ag electrode. The silver was printed as two subsequent layers on top of the AlO_x layer by inkjet printing in a square shape (250×250

µm^2) with 1000 dpi with 1 nozzle at 30 °C using a tailored waveform. Afterwards, the printed Ag ink was hotplate sintered in air at 150 °C for 45 min. The complete printed device was observed by optical microscopy (Figure E1 in the Appendix E).

The quasi-static I-V characteristics of the printed devices were measured using Keithley 4200 SCS semiconductor analyzer connected to a Janis ST-500 probe station. The bias was applied to the top electrode (Ag) while maintaining the bottom electrode (ITO) connected to ground. The temperature analysis of the resistive switching devices was measured under vacuum, from 300 K to 400 K using a Lakeshore model 336 temperature controller. A schematic representation of the printed aluminium oxide RRAM production main steps is shown in Figure 6.6.

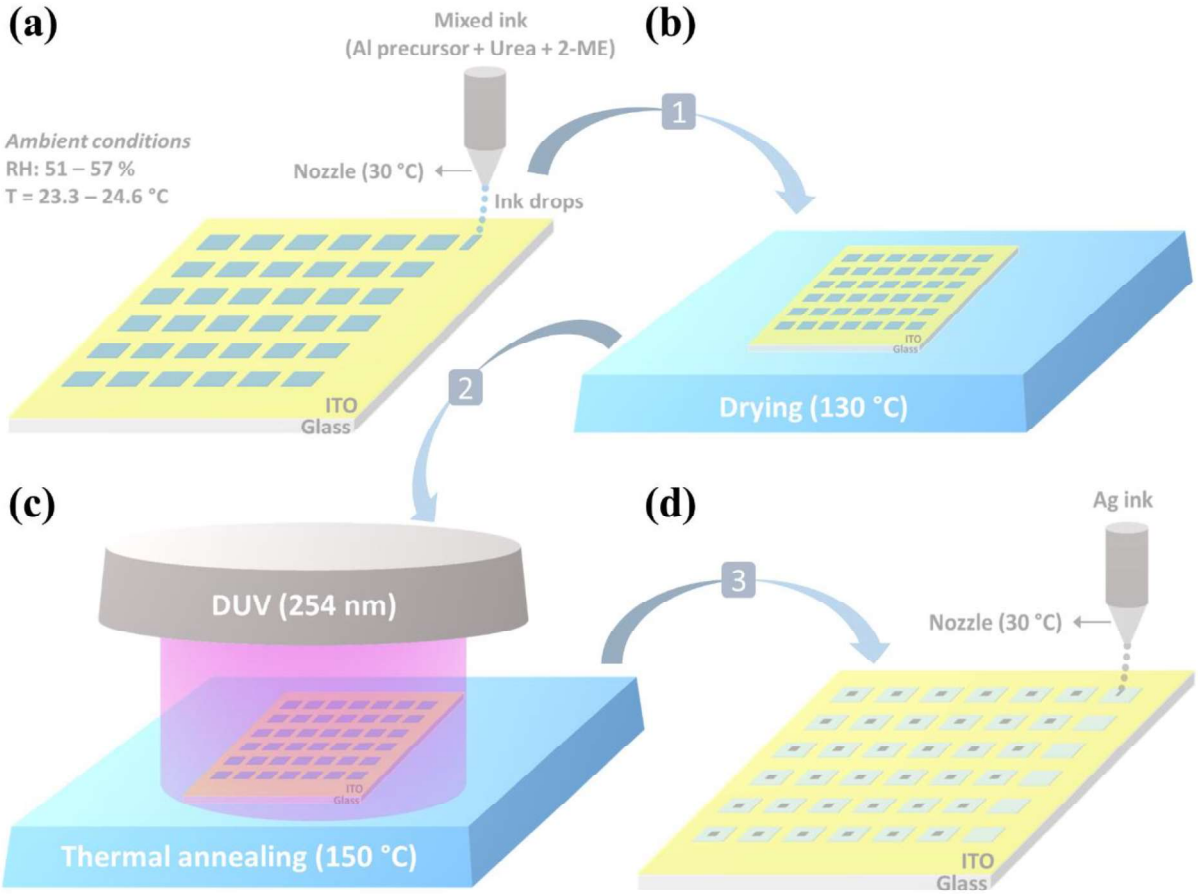

Figure 6.6. Schematic representation of the main printing steps of the metal oxide RRAM production: a) inkjet printing process of the AlO_x ink on top of the ITO bottom electrode; b) drying process on hotplate after printing; c) formation of the AlO_x thin film using thermal annealing combined with DUV irradiation; d) inkjet printing of the Ag nanoparticle ink. Copyright © 2021, Royal Society of Chemistry.

6.2.3. Results and discussion

Printing techniques reduce the amount of chemical waste, because of a direct writing of the materials without the need for subtractive processes, thus promoting their scalability.[475] Inkjet printing is a non-contact printing process which relies on patterns that are in the digital format being easily changed and is widely used to print RS devices. Since 2012, a few solution-based metal oxide RS devices have been printed by inkjet, however, these suffer from low electronic performance due to the annealing treatment method (Table E2 in the Appendix E). Most of these consist solely on thermal annealing, where a high quantity of residual organics could remain when a low temperature is applied, affecting their overall performance. The combination of a low annealing temperature with DUV irradiation improves the metal oxide thin films condensation and densification by the decomposition of alkoxy groups.[309] Following this methodology, printed aluminium oxide (AlO_x) RS memories were produced.

Firstly, the precursor ink viscosity was measured to examine if it could be printed by inkjet since low viscosities are typically required (1 – 30 cP). To guarantee the best correlation, the ink viscosity test was performed at 30 °C, the same temperature as applied in the nozzle to print the AlO_x thin films. A viscosity of 2.1 cP was achieved, which is compatible with the printing technique. However, to guarantee a uniform printability in inkjet printing, the inverse Ohnesorge (Z) number must obey a specific range ($1 < Z < 10$).[892] Once the Z value of AlO_x ink was 4.85, a decent printing performance can be achieved (see more details in Table E3 in the Appendix E).

Afterwards, the printed AlO_x thin films were examined by X-ray diffraction (XRD) as depicted in Figure 6.7 (a). The absence of diffraction peaks confirmed these films to be amorphous. Also, a small surface roughness of 1.53 nm was measured by atomic force microscopy (AFM), which is in accordance with amorphous films due to the absence of grain boundaries, which is desirable for future applications on flexible substrates. To improve the printing quality of the films, different printing speeds were tested. For a lower printing speed (100 mm/sec), the films present a higher coffee ring effect and less uniformity (Figure E1 in the Appendix E) compared with films printed at 150 mm/sec, which show a more homogeneous layer (inset of Figure 6.7 (a)). Figure 6.7 (b) shows a high-resolution SEM-FIB cross section image of the RS device to determine the film thickness of the printed AlO_x thin films, which is 31.5 ± 1.4 nm. X-ray photoelectron spectroscopy (XPS) was performed to determine the stoichiometry and the presence of organic groups in the printed films. Figure 6.7 (c) displays the Al 2p emission peak with a binding energy of 74.2 eV, which indicates the formation of Al_2O_3, but it is slightly shifted to a higher energy due to the presence of –OH groups that prevail in the film.[309,493,494] However, when analysing the deconvoluted O 1s peak in Figure 6.7 (d), it is found that –OH groups play a role on the

composition of the films. After all, the percentage of aluminum hydroxide (Al–OH) at 531.8 eV is similar to the aluminum oxide (Al–O–Al) at 530.7 eV. Furthermore, the elemental ratio of O/Al was found to be 2.1 due to the presence of adsorbed oxygen (–OH).[309] Note, that the presence of –OH groups facilitates the formation and rupture of anion vacancy filaments which can stabilize the device performance.[621,893]

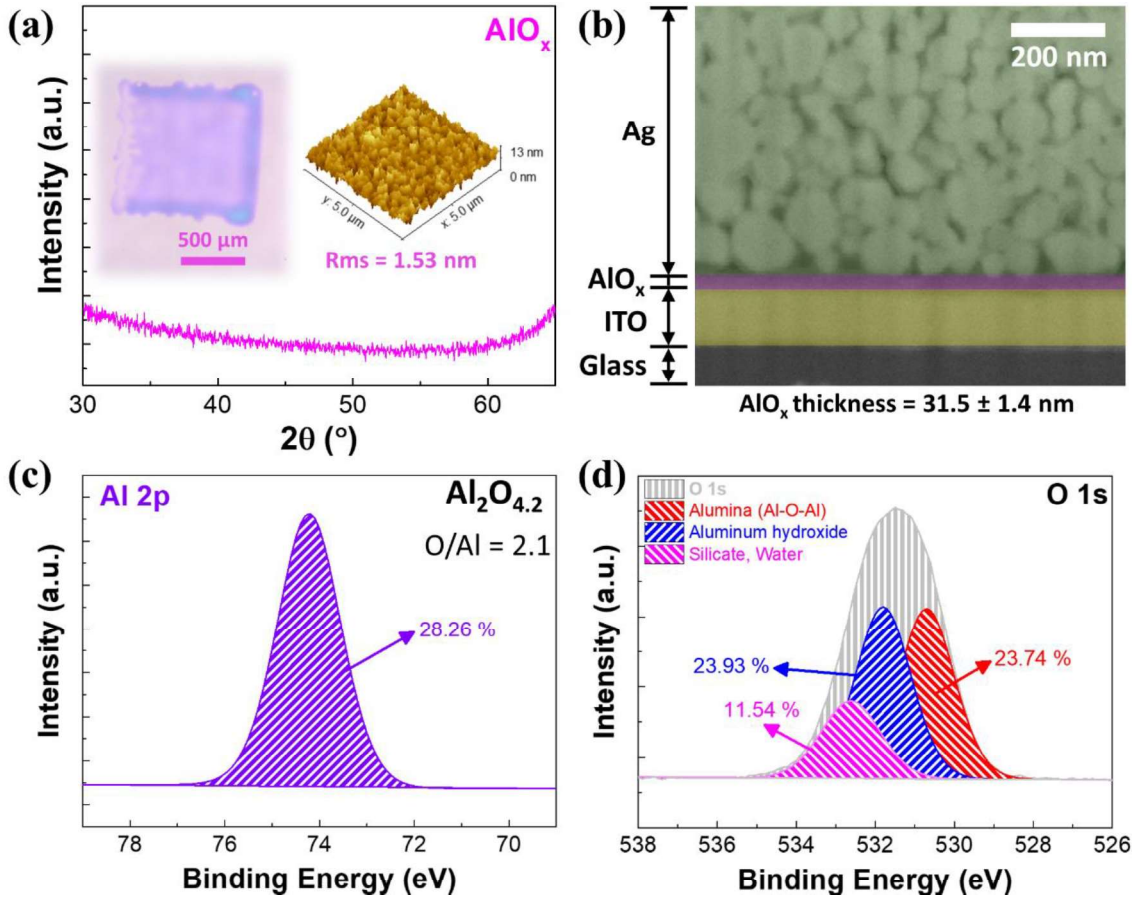

Figure 6.7. (a) XRD diffractogram, printed image and AFM image (5×5 µm^2) of aluminium oxide (AlO_x) thin films processed at low temperature (150 °C) assisted by deep-ultraviolet (DUV) irradiation; (b) High-resolution SEM-FIB cross-section image of the complete resistive switching device. XPS of (c) Al 2p and (d) deconvoluted O 1s emission peaks of the printed AlO_x thin films. Copyright © 2021, Royal Society of Chemistry.

To study the switching properties and related mechanism of solution-based ITO/AlO_x/Ag RS devices, a sequence of electrical experiments was executed. Two different methods were used to perform an electroforming process: i) application of DC voltage sweep and ii) constant voltage stress. In all devices the voltage was applied to the top Ag electrode (TE). The device has a preferential electroforming (i.e. at lower voltages) under positive voltage bias sweep. Attempts to form the device by application of negative voltage sweep were also made. Not only higher voltages are required but also the low resistance state does not reset back to the high resistance

state (see Figure E2 (a) and (b) in the Appendix E). Hence, the breakdown under negative voltage bias is not referred to as electroforming.

Various constant voltage stress methods were also applied to obtain the forming time for positive voltage polarity and breakdown time for negative voltage polarity. Figure 6.8 shows the forming/breakdown time of ITO/AlO_x/Ag RS devices, plotted as a function of the bias voltage under a constant voltage application. Generally, larger delay times are observed for lower voltages at both polarities. However, higher voltage amplitudes (> - 2 V) are required at constant negative voltage stress compared with the positive voltage stress (forming time of 4.8×10^2 s at + 0.55 V). In addition, for negative voltage stress, mainly a breakdown rather than memory properties is observed. This shows that a positive bias at the top electrode clearly favours the formation of the conductive filaments in the resistive switching devices compared to a negative bias. Corresponding current evolution with respect to time is shown in Figure E2 (c) and (d) in the Appendix E.

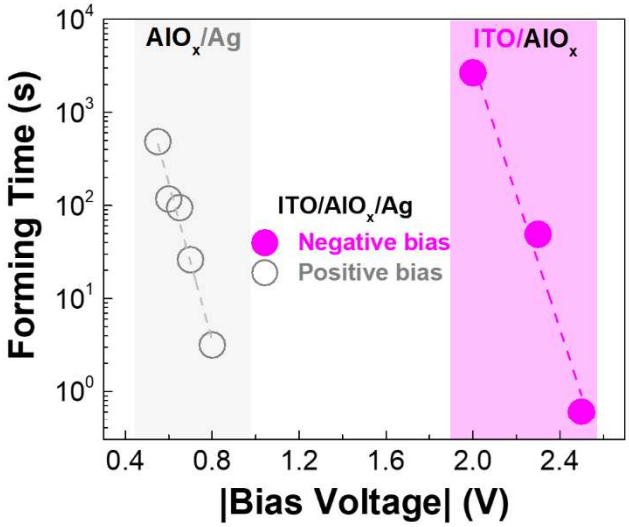

Figure 6.8. Forming/breakdown time of ITO/AlO_x/Ag cells, plotted as a function of the bias voltage under a constant voltage application. The open circles and closed circles are the results for the application of positive (grey) and negative bias (pink) to the Ag top electrode, respectively. Copyright © 2021, Royal Society of Chemistry.

Figure 6.9 (a) shows a good endurance by DC sweeps over 100 cycles and a low device cycle-to-cycle variability in the resistance states (high resistance state (HRS) and low resistance state (LRS)) and in the operating voltages (set and reset) as shown in Figure E3 in the Appendix E. Typically, when DC sweeps are performed instead of pulsed measurements, the number of cycles is lower due to the additional DC bias stress of the devices.[532] To test the reliability of these devices a long retention was recorded up to 10^5 s in air, as depicted in Figure 6.9 (b). An LRS/HRS ratio of 4×10^1 (maximum value achieved of 2.5×10^2 for other device) was observed during that

retention time. Also, the devices showed a high device-to-device reproducibility with a yield of 95 % (19 out of 20 working), as shown in Figure E4 in the Appendix E. These devices present some variability on the LRS/HRS ratio, as well as set and reset voltages, which can be reduced by application of cross-point (CP) structures in future work. However, to produce fully printed resistive switching devices using CP structures, new materials for the bottom electrode should be developed.[891] Generally, the conductive ink used to produce the bottom electrode is based on nanoparticles presenting a high surface roughness which can short or affect the endurance of these devices. Also, the electric field strength is changed in different locations of the device due to the nature of electrode material based on Ag nanoparticles. A smaller electrode area can reduce the impact of electric field variation.

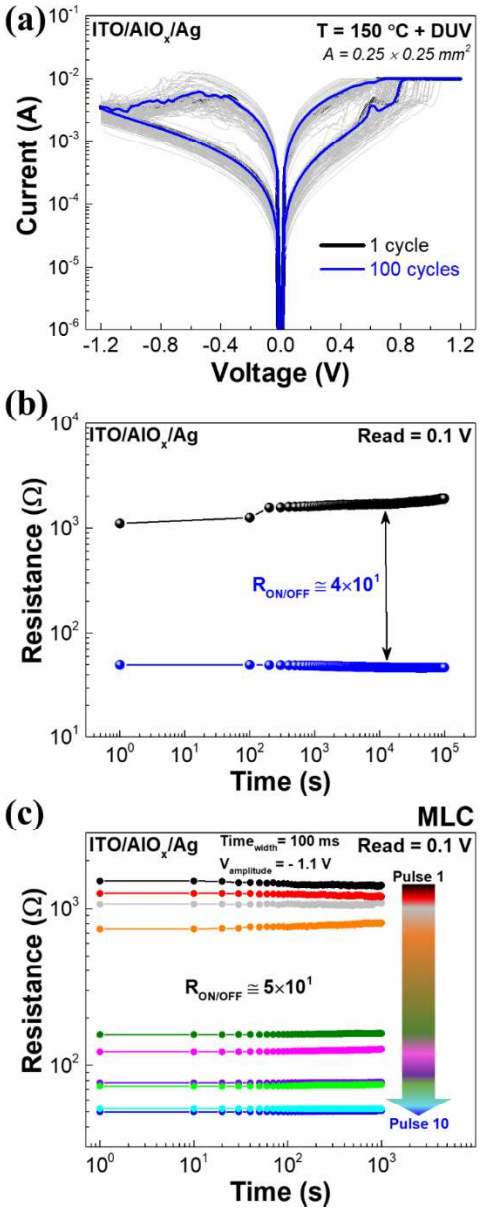

Figure 6.9. Electrical characteristics of the glass/ITO/AlO_x/Ag printed resistive switching (RS) devices. (a) *I–V* sweeps endurance showing a bipolar RS behaviour during 100 cycles; (b) *I–t* curves, collected using a read voltage of 0.1 V, showing the retention of the LRS and HRS; (c) Multilevel cell retention characteristics to reach the HRS through the appliance of 10 pulses. Copyright © 2021, Royal Society of Chemistry.

Multilevel cell (MLC) operation is highly desired for RS devices applied to information processing technologies since more than two resistive states can be reached. Figure 6.9 (c) shows the multistage storage characteristic on the reset side by the application of a current visible pulse voltage stress (CV-PVS) with a voltage amplitude of -1.1 V and a time width of 100 ms. Typically, to have a multilevel cell storage, the minimum window of resistance ratio should be ≥ 2.[894] These devices present at least 4 distinct level states that can be clearly distinguished with stable endurance for 10^3 s.

Cycle-to-cycle and device-to-device variations are intrinsic properties of memristor devices. These variations are useful for security applications.[849] Here, the devices are fabricated at low temperatures using printing techniques in order to be eventually implemented on plastic or paper substrates. By relying on the intrinsic variability of the printed devices, potential applications such as low-cost and secure identification and authentication of commercial goods are targeted.

To understand the mechanism behind the formation of the filament, some specific experiments were performed. Based on the space-charge-limited-conduction mechanism, the device (Figure 6.10 (a)) shows an Ohmic conduction in the low voltage region (< 0.25 V) and for a voltage higher than 0.25 V, the slope highly increases up to 3.67, which indicates the Child´s law conduction dominance.[697] After the set, the LRS presents an Ohmic nature (slope of 1.02), proving the existence of highly conductive paths. To clarify the conductive filament's nature/composition, the trend between resistance and temperature was studied.

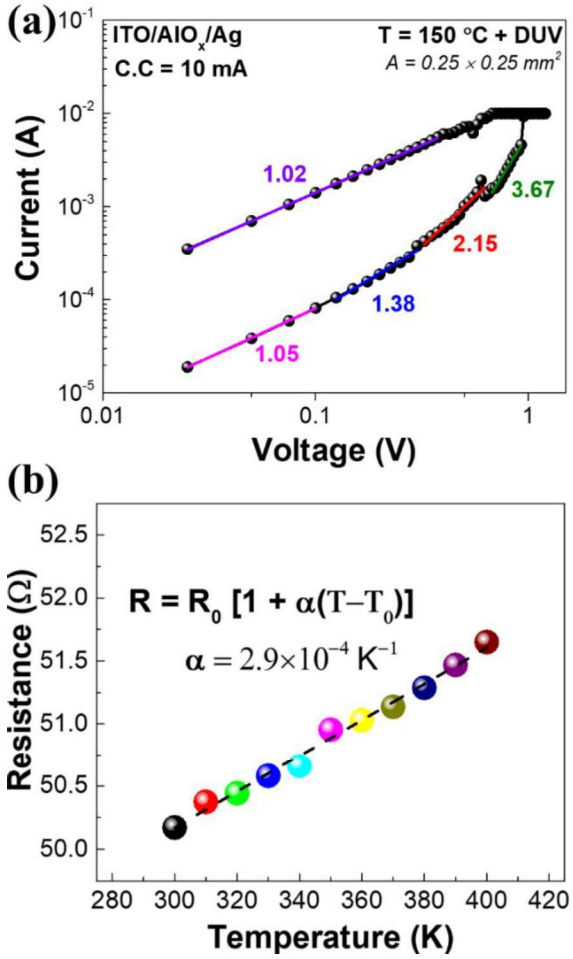

Figure 6.10. (a) I-V curve of ITO/AlO_x/Ag device plotted in log–log scale, showing a space–charge–limited conduction mechanism; (b) Temperature analysis of the RS device in the low resistance state (LRS). Copyright © 2021, Royal Society of Chemistry.

In the case of the LRS, a temperature dependence of the resistance is observed (Figure 6.10 (b)), which could be associated to a metallic conduction mechanism. The α is the temperature coefficient of resistance (TCR) and R_0 is the resistance at the initial temperature, typically room temperature. The positive TCR achieved for ITO/AlO_x/Ag RS devices on the LRS proves the metallic nature of the conducting filaments. However, the TCR value is 2.9×10^{-4} K^{-1}, one order of magnitude lower than the TCR of bulk Ag metal (3.8×10^{-3} K^{-1}).[895] A low TCR (3×10^{-4} K^{-1}) similar to the results achieved here was reported for printed nanoparticle-based Ag films which are processed at low temperature (≤ 150 °C).[896] Thus, the TCR value of the conducting filaments is comparable with nanostructured silver, which is related to the spatial confinement in the filament. The current-temperature dependency was also studied after breakdown with application of a negative voltage bias. Almost no temperature dependency was observed (Figure E5 in the Appendix E) excluding the metallic filament formation on this polarity.[897]

Also, the presence of –OH groups and moisture were shown in the XPS data, indicating their contribution to the resistive switching characteristics. The existence of –OH groups are essential for the electrochemical metallization (ECM) process.[898] It is notable that these groups can act as counter charges/reactions[899] to maintain the charge neutrality in cation-based charge transportation devices. Thus, eliminating moisture or –OH groups is not favourable, but controlling to attain a balanced concentration results in stable and reliable RS characteristic. To confirm this and to see if moisture is affecting the resistive switching behaviour, measurements of the devices under air and vacuum conditions were performed. A significant difference was observed on the required set voltage of the device. When the device operates in air, it is exposed to humidity reducing the set voltage in comparison with the device operated in vacuum, as depicted in Figure E6 in the Appendix E, which corroborates with reports in literature.[898,900]

6.2.4. Conclusions

The printing of metal oxide memristors has an enormous potential due to the advantage of using mask-less patterning which is highly desirable for mass production. For now, some key challenges prevail in their manufacturing such as, uniformity over large area, long processing times, large device size and high thermal budget. In this work, some of these issues were surpassed by the production of low voltage inkjet printed AlO_x memristors with high yield at low temperature (150 °C) using the combination of DUV irradiation (low power) and thermal treatment. This printing method is quite promising since high printing resolution (up to 2 μm)[435] and accuracy can be reached, which are requirements for scalability. In the near future, fully printed metal oxide memristors using low-cost and sustainable materials may be used in IoT applications with diverse features, from MLC storage to hardware security.

Chapter 7

Conclusions and future perspectives

The research work presented in this dissertation was divided into two main areas: the first objective was to investigate the combustion synthesis in solution-based metal oxides, mostly focusing on high-κ dielectric thin films regarding low temperature processes, their printability and short annealing time for their application in thin film transistors; the second objective was to study the implementation of the previous synthesis to develop solution-processed metal oxide resistive switching memories, due to their promising features such as, energy efficiency, non-volatility and process compatibility with standard complementary metal-oxide-semiconductor (CMOS) technology.

In this chapter are presented general conclusions of the work developed during this dissertation as well as the future perspectives considering the results achieved and the current state-of-the-art.

7.1. Main conclusions

Solution combustion synthesis (SCS) proved to be a suitable method for the development of metal oxide nanostructures and thin films. However, it is of extremely important to consider certain parameters such as, fuel to oxidizer ratio, fuel type, metal cation precursor, pH, ambient atmosphere and initiation type to reduce the processing temperature. These parameters determine the final metal oxide morphologies and respective applications, being in our case fundamental for the achievement of reliable metal oxide TFTs. Nevertheless, a combination between SCS and a post-treatment, such as UV irradiation should be made to boost their performance at low temperature. That alliance was demonstrated in this dissertation for the first time to develop HfO_x dielectric thin films and multilayer thin films using AlO_x and HfO_x at low temperatures (150 °C). The resultant thin films were applied in MIS structures showing a good performance (low leakage current and high breakdown voltage) which enable their application in IGZO TFTs. These devices had a low voltage operation (≤ 2 V), a low subthreshold slope (0.066 ± 0.01 $V \cdot dec^{-1}$), a high saturation mobility (43.9 ± 1.1 $cm^2 \cdot V^{-1} \cdot s^{-1}$) and a good stability over time (2 months) under atmospheric conditions.

After reaching solution-based high-κ dielectrics processed at low temperature, the next step was their implementation in large area processing techniques. So, a versatile printing technique, flexographic printing was used to print (50 $m \cdot min^{-1}$ printing speed) ultrathin Al_2O_3 thin films with high quality and uniformity followed by a post-deposition with a low-wavelength UV irradiation combined with a hotplate annealing at low processing temperatures (≤ 200 °C). The dielectric presents a dielectric constant of 8.2 ± 0.4 and low leakage current densities of 10^{-10} $A \cdot cm^{-2}$ at 1 $MV \cdot cm^{-1}$ electric field. Subsequently, this dielectric was implemented in inkjet printed In_2O_3 TFTs leading to low voltage devices with great stability under ageing, stress and even after a mechanical stress for 100 h which corresponds to 3.6×10^5 bending cycles. However, another challenge remains, the long processing time (≥ 30 min) for each layer which is not compatible with the printing industry, since in printing lines less than 5 min curing time is required. To overcome this limitation of solution-based metal oxide TFTs an ultrafast curing was induced by excimer laser annealing (ELA) after a short drying cycle (15 min or 1 min) at low temperature (150 °C) to produce AlO_x dielectric thin films. These films showed a smooth surface, high-κ, low leakage currents and high breakdown voltages ~4 $MV \cdot cm^{-1}$. Then, this dielectric was applied in IGZO thin film transistors showing a good performance which indicates that ELA treatment is a viable platform for the fabrication of metal-oxide thin films in a short processing time being quite relevant for the R2R industry.

Solution-based resistive switching memories have high potential and a lot of advantages such as, high switching speed, simple structure, high density, and low power consumption. Taking that into account, performed the production of solution-based aluminium oxide memories using combustion synthesis was performed in this dissertation. Different number of layers were deposited to guarantee the optimal condition and avoid the Pt diffusion into the aluminum oxide. The Al_2O_3 bilayer memories showed a unipolar resistive switching behaviour with a good retention time up to 10^5 s at 85 °C, a good endurance (100 cycles) and a yield of 100 % compared to the one-layer devices. These devices also showed a multilevel cell operation (MLC) which are highly important for logic operations and the Al_2O_3 was implemented in a fully transparent device paving the way for transparent electronics. To go even further, printed combustion-based aluminium oxide (AlO_x) RS devices were produced via inkjet printing at low temperature by the combination of thermal annealing (150 °C) and deep ultraviolet (DUV) irradiation treatment. The attained results help to understand the electrical characteristics of printed metal oxide RS devices processed at low temperature and prove their potential for high-density non-volatile multilevel memory applications.

7.2. Future perspectives

Printed flexible electronics have great potential to enhance the quality of life in our society, not just in terms of sustainability (greener materials) due to the process manufacturing (lower cost) used, but most importantly the comfort offered to the population. In the last years, the demand of printed resourceful materials for technology has increased exponentially and I believe in near future it will become a reality from the market to the consumers. It is expected a growing interest of 21.5 % from 2020 to 2025 as depicted in Figure 7.1.

Figure 7.1. Global printed electronics market trends from 2020 to 2025 (https://www.marketsandmarkets.com/Market-Reports/printed-electronics-market-197.html consulted on the 22/10/2020).

However, most of the manufactures are not aware of the advantages of printed electronics. The biggest key market players in this field for now are Samsung, LG, PARC, Agfa-Gevaert and Molex. And you may ask, why they are not fully integrating printed electronics in their manufacturing process? The answer is simple, manufacture innovation is highly demanded to fulfil the requirements and reach viable devices that undergo the same kind of rigorous verification, validation, and testing to compete with the ones present in the market. For that to happen some key challenges need to be surpassed and demonstrated in printed metal oxides:

- ***The ink development:***
  - Inks that are stable for more than 6 months in ambient conditions. For this solution combustion synthesis (SCS) can be a good method to assure a good stoichiometry and reliable ink. The synthesis design is a fundamental issue.

- The use of greener solvents and solvents that can be decomposed at low temperatures (low boiling point) being compatible with low-cost substrates such as paper, PET and PEN to suit in-line R2R processing.
- Viscosity and evaporation rate control to apply in diverse printing techniques due to the printing speed associated.

❖ ***Ambient conditions on the manufacturing***

- Relative humidity and temperature parameters control should me mandatory to avoid instabilities (thickness and water content influence) in the films produced which will affect the devices performance and reproducibility.

❖ ***Surface roughness***

- The surface roughness of the substrates should be quite smooth to avoid defects and short circuits between the layers affecting the devices performance. Also, the surface roughness of printed electrodes remains a considerable challenge when applied in oxide thin film transistors and memories.

❖ ***Low temperature processing of all oxide-based devices***

- Solution-processed transparent conductive oxides (TCOs) continue to require higher temperature to make them conductive. Only a few reports show TCOs processed at low temperature with a good conductivity. It is demanded a deeper study to reach high conductivity with a low thermal budget, high power lamps and lasers could be a possibility to reach these conditions.
- In terms of semiconductors and dielectrics thin films the low temperature was achieved already and now the next focus is to form these films in a short processing time being compatible with R2R.

❖ ***Printing speed for large-area manufacturing***

- Most of the techniques to print metal oxides rely on non-contact printing, mostly inkjet printing, however this technique has a low printing speed which is not compatible with in-line R2R. So, a huge demand is now on contact printing techniques such as screen printing, gravure printing and flexographic printing that can accomplish high printing speeds being ideal for the printing industry. However, the inks also need to be transformed to the film state in a short processing time. That is possible by using photonic curing which already exist in the printing lines in industry.

❖ ***Resolution***

- More effort should be put in manufacture innovation, for now the resolution reached by printing techniques (1 μm) is quite limited.

- ***Variability***
  - Printed devices remain with some device to device and sample to sample variation which is not desirable and acceptable to implement in products. Also, ageing and stress tests should be performed.
  - Other aspects that highly influence the device variability are the ambient conditions and the printing alignment accuracy that must be controlled.
- ***Connection between research institutes and companies***
  - Even today there is still a gap between research and companies about their up-scale issues. This is also related with the maturity of printed electronics technology.

Appendix A

The Appendix A contains relevant data related to the production of high-κ dielectrics thin films from solution combustion synthesis combined with ultraviolet (UV) treatment and their application in TFTs mentioned in section 4.1. Figure A1 and A2 show XRD diffractograms and the FTIR spectra of multilayer dielectric thin films, respectively. Figure A3 depicts AFM surface morphology of multilayer dielectric thin films. Figure A4 show the SEM-FIB cross-section image of multilayer dielectric thin films to determine films thickness. Figure A5 depicts the influence of the fuel in AlO_x thin films thickness for different concentrations assisted by UV treatment. Figure A6 show the capacitance–frequency, capacitance–voltage and current density (J) characteristics of Al/p-type Si/(Dielectric)/Al MIS capacitors with single and multilayer dielectric thin films. Table A1 show the summary of dielectric properties obtained for the capacitors. Figure A7 depicts the typical output curves of all dielectric's conditions applied in TFTs. Figure A8 and Table A2 shows the electrical characteristics obtained for the different dielectric's conditions applied in IGZO TFTs after 2 months in air environment. Figure A9 and A10 show the transfer curves after stress and recovery measurements of the dielectric bilayers applied in IGZO TFTs. Figure A11 depicted the transfer curves of TFTs used in the diode-connected inverter.

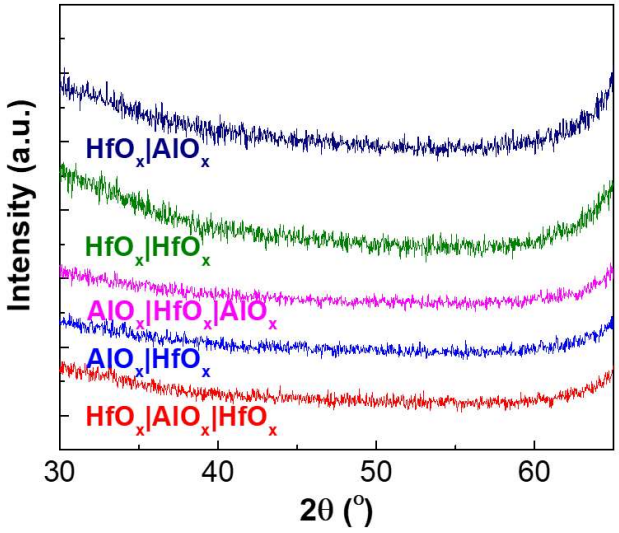

Figure A1. XRD diffractograms of multilayer dielectric thin films annealed at 150 °C with DUV treatment.

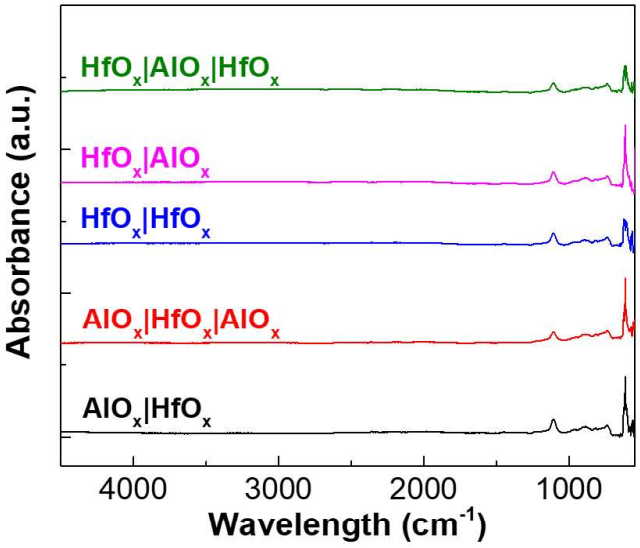

Figure A2. FTIR spectra of multilayer dielectric thin films annealed at 150 °C with DUV treatment.

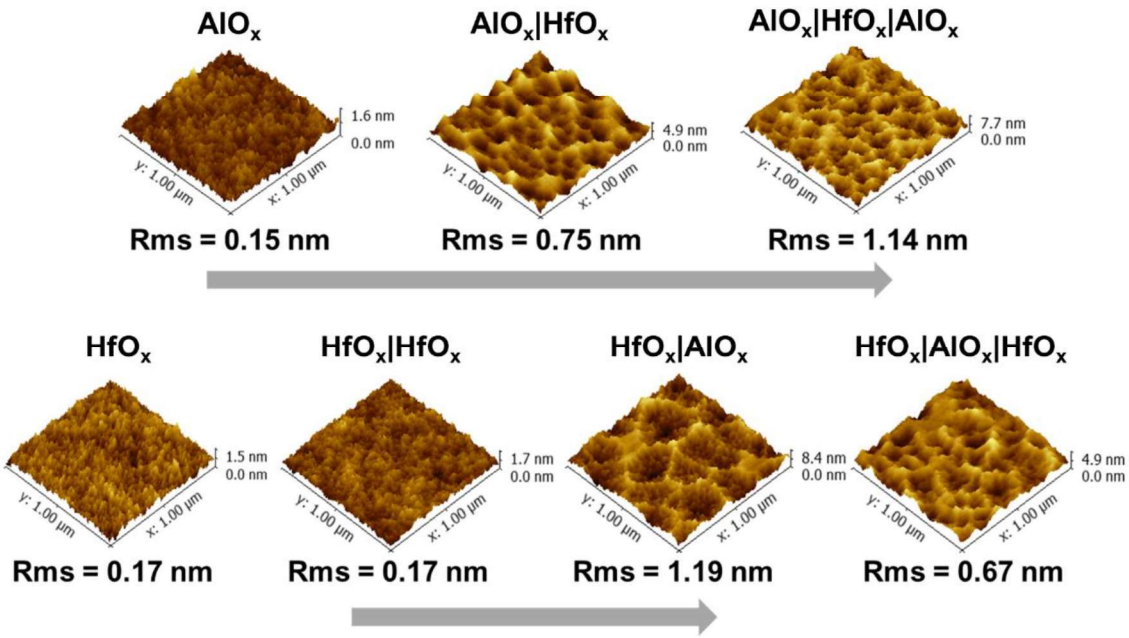

Figure A3. Morphological characterization of all dielectric thin films annealed at 150 °C with DUV treatment.

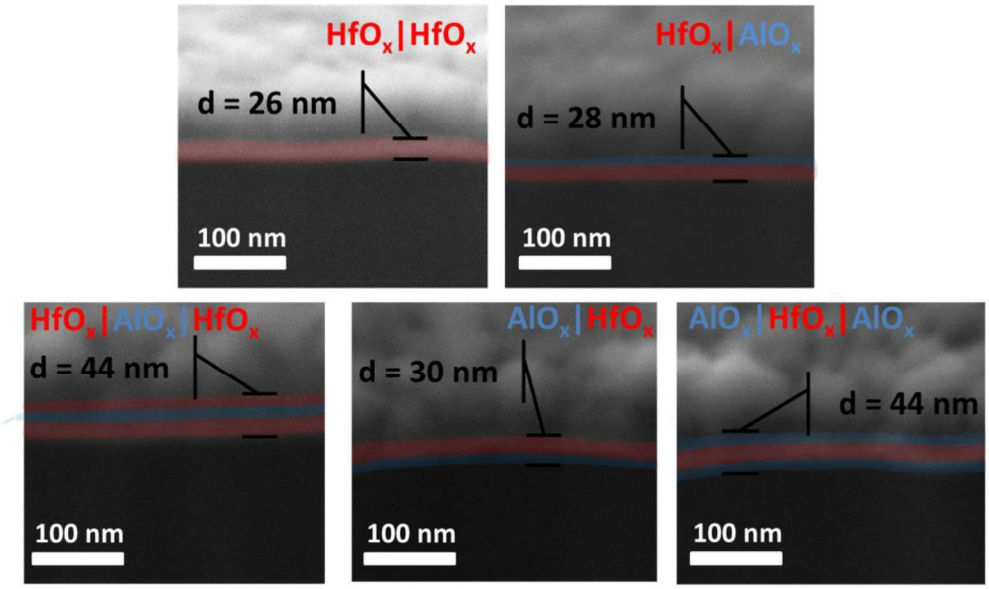

Figure A4. High resolution SEM-FIB cross-section images of multilayer dielectric thin films.

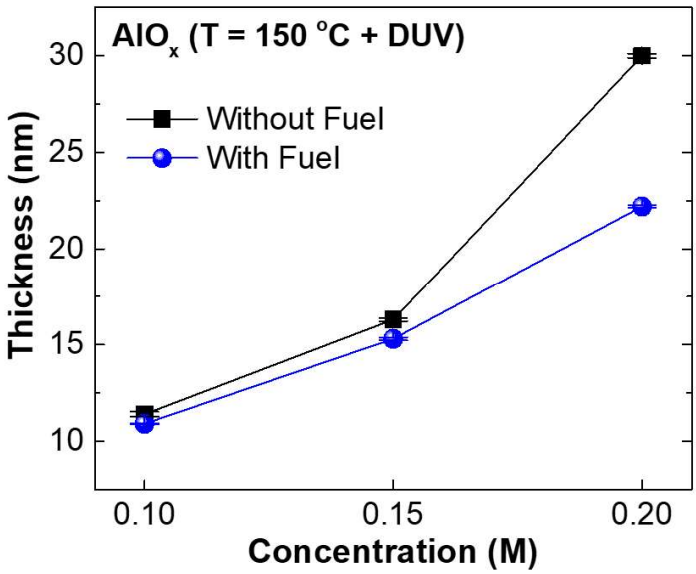

Figure A5. Influence of the fuel in AlO_x thin films thickness for different concentrations assisted by UV treatment.

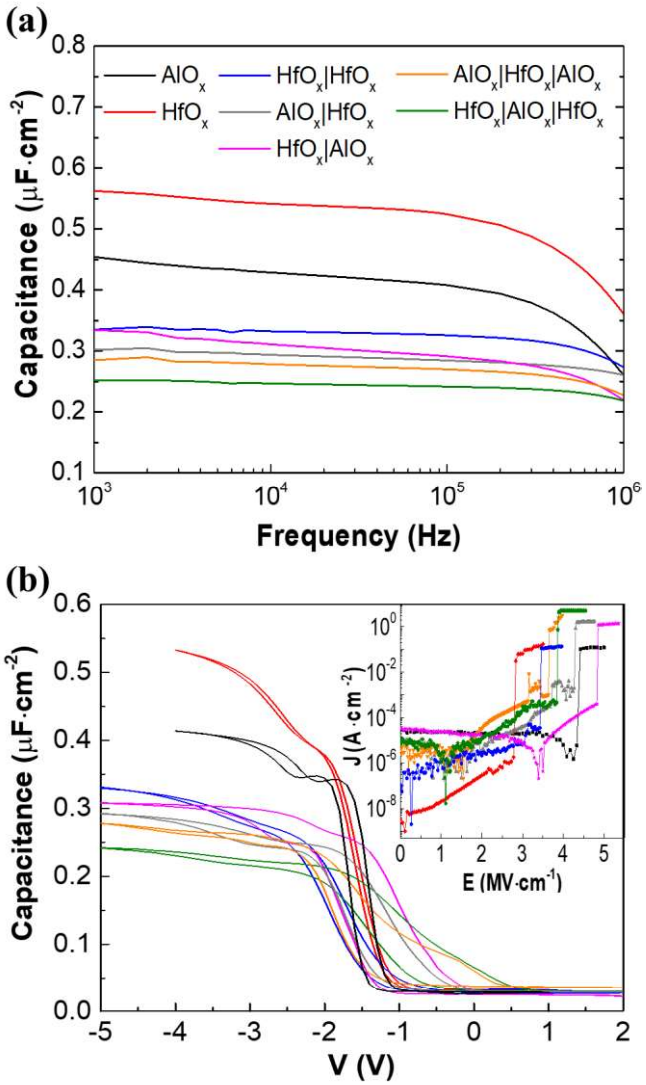

Figure A6. (a) Capacitance–frequency, (b) Capacitance–voltage and current density (J) characteristics of Al/p-type Si/(Dielectric)/Al MIS capacitors with single and multilayer dielectric thin films.

Table A1. Summary of dielectric properties obtained for the devices depicted in Figure 4.4.

Dielectric	Capacitance ($\mu F \cdot cm^{-2}$)	E ($MV \cdot cm^{-1}$)	Dielectric constant (κ)	Thickness (nm)
AlO_x	4.86 ± 0.22	4.33 ± 0.33	6.61 ± 0.32	12.04 ± 0.59
AlO_x|HfO_x	3.04 ± 0.03	3.95 ± 0.32	10.38 ± 0.21	30.22 ± 0.58
AlO_x|HfO_x|AlO_x	2.72 ± 0.14	3.97 ± 0.26	13.52 ± 0.24	43.99 ± 0.78
HfO_x	5.74 ± 0.09	2.70 ± 0.05	11.71 ± 0.48	18.05 ± 0.74
HfO_x|HfO_x	3.33 ± 0.03	3.62 ± 0.15	9.80 ± 0.25	26.06 ± 0.63
HfO_x|AlO_x	3.28 ± 0.04	4.87 ± 0.05	10.39 ± 0.18	28.02 ± 0.49
HfO_x|AlO_x|HfO_x	2.50 ± 0.03	3.75 ± 0.07	12.45 ± 0.17	44.06 ± 0.60

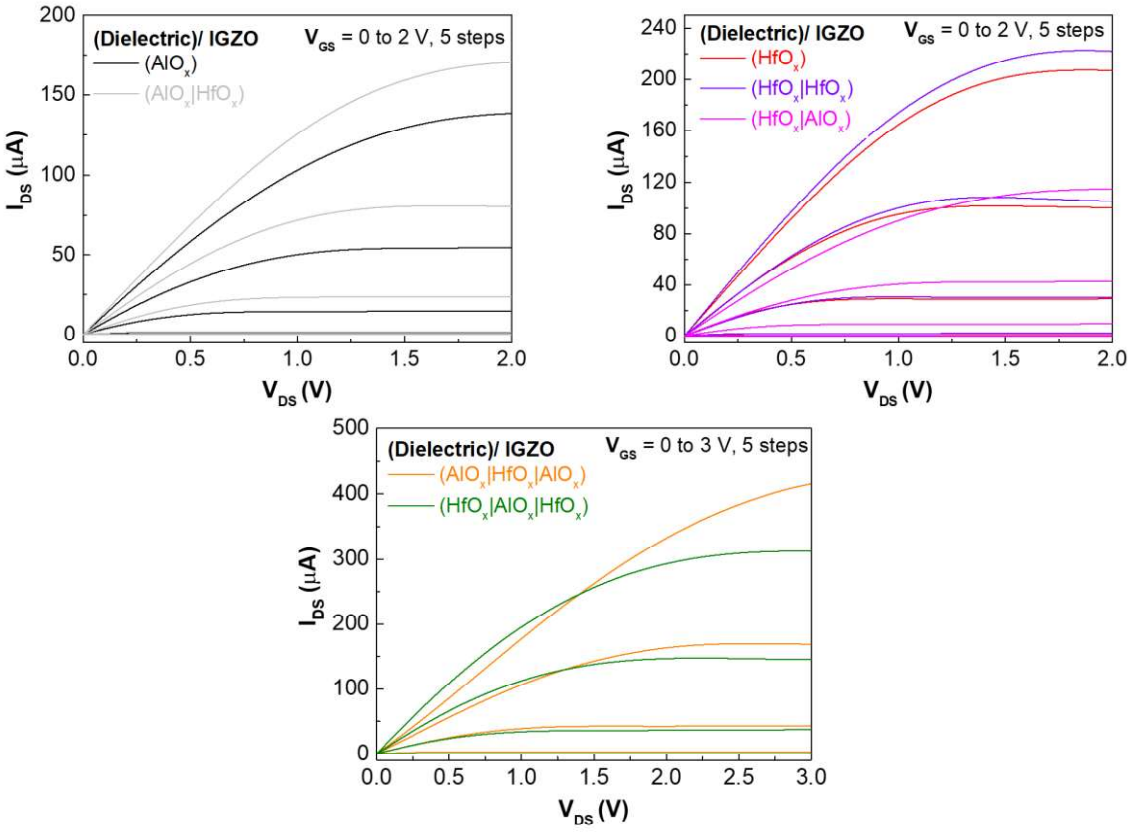

Figure A7. Output curves of all dielectric's conditions applied in thin film transistors.

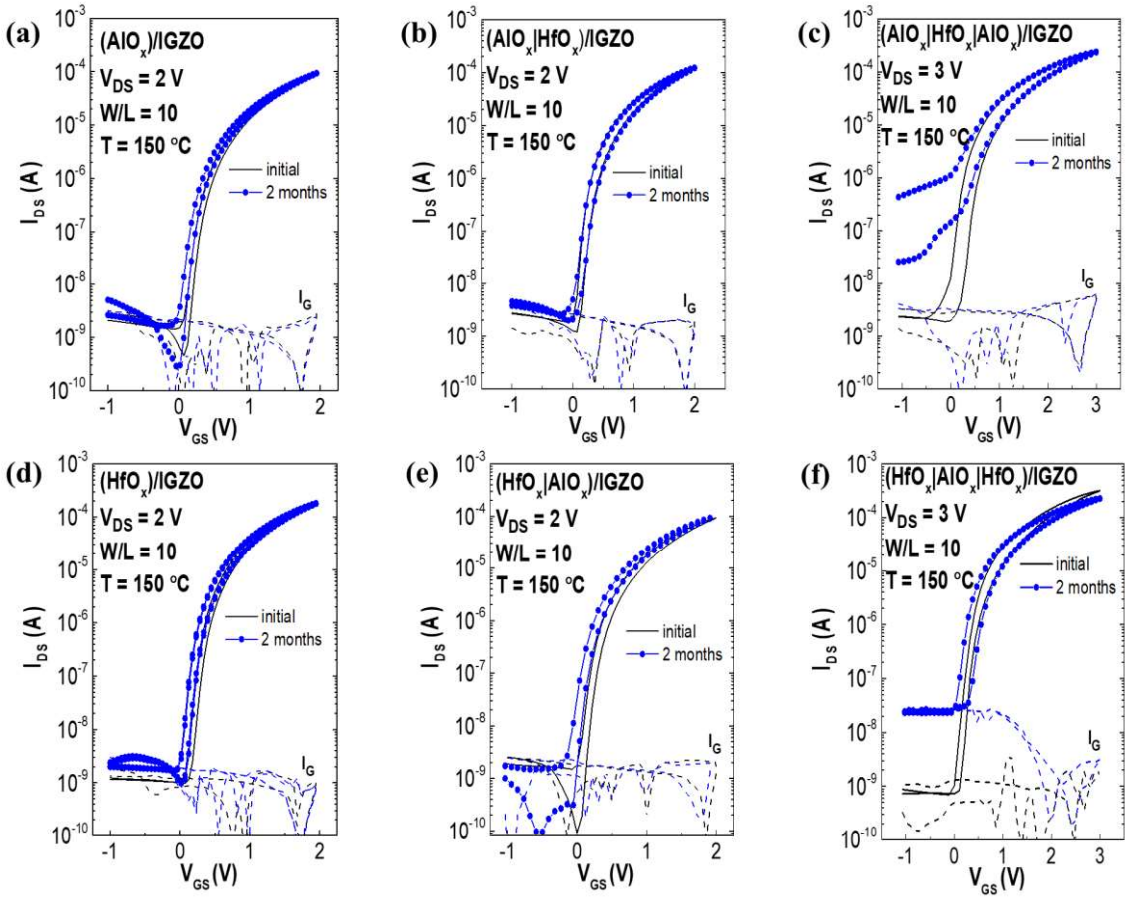

Figure A8. Aging effects of IGZO TFTs over 2 months using different solution-based dielectrics: (a) (AlO_x), (b) ($AlO_x|HfO_x$), (c) ($AlO_x|HfO_x|AlO_x$), (d) (HfO_x), (e) ($HfO_x|AlO_x$) and (f) ($HfO_x|AlO_x|HfO_x$).

Table A2. Electrical characteristics obtained for the devices depicted in Figure A8.

Insulator	Measure	SS ($V \cdot dec^{-1}$)	μ_{SAT} ($cm^2 \cdot V^{-1} \cdot s^{-1}$)	$I_{ON/OFF}$	V_{ON} (V)	V_{Hyst} (V)
(HfO_x)	Initial	0.079	30.18	1.90×10^5	0.02	0.07
	2 months	0.081	25.44	1.85×10^5	0.02	0.09
(HfO_x|HfO_x)	Initial	0.061	43.94	1.52×10^6	0.07	0.12
	2 months	0.068	35.8	3.03×10^5	0.12	0.14
(HfO_x|AlO_x)	Initial	0.069	22.22	1.02×10^6	0	0.09
	2 months	0.081	21.76	2.98×10^5	-0.05	0.1
(HfO_x|AlO_x|HfO_x)	Initial	0.101	43.06	4.40×10^5	0	0.105
	2 months	0.17	26.4	1.00×10^4	0.11	0.28
(AlO_x)	Initial	0.077	17.66	2.00×10^5	0.07	0.08
	2 months	0.074	16.18	3.26×10^5	-0.04	0.09
(AlO_x|HfO_x)	Initial	0.086	34.41	1.11×10^5	0.07	0.1
	2 months	0.11	34.01	6.00×10^4	-0.07	0.13
(AlO_x|HfO_x|AlO_x)	Initial	0.134	32.5	1.38×10^5	-0.108	0.27
	2 months	0.336	30.09	1.00×10^4	-1.18	1.87

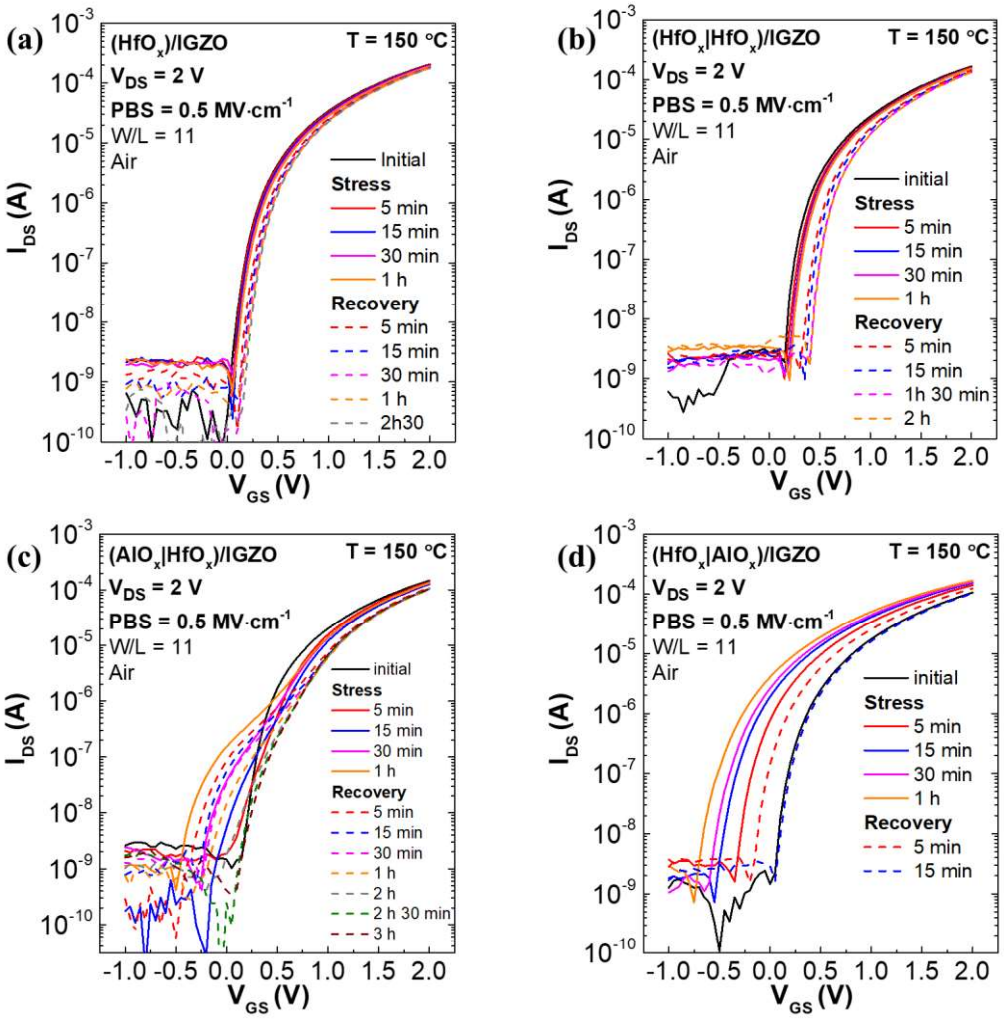

Figure A9. Positive gate-bias stress (PBS) measurements of IGZO TFTs with different dielectric conditions: (a) (HfO_x), (b) ($HfO_x|HfO_x$), (c) ($AlO_x|HfO_x$) and (d) ($HfO_x|AlO_x$).

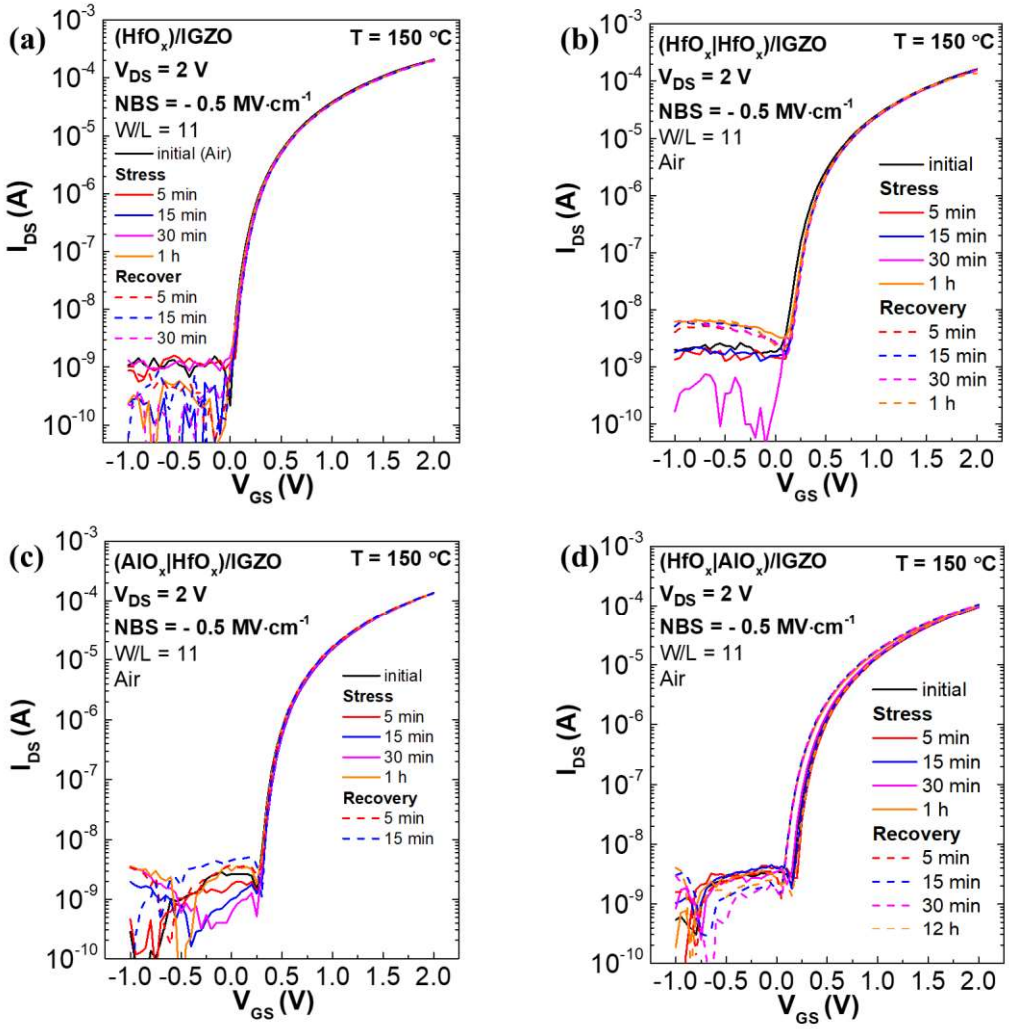

Figure A10. Negative gate-bias stress (NBS) measurements of IGZO TFTs with different dielectric conditions: (a) (HfO_x), (b) ($HfO_x|HfO_x$), (c) ($AlO_x|HfO_x$) and (d) ($HfO_x|AlO_x$).

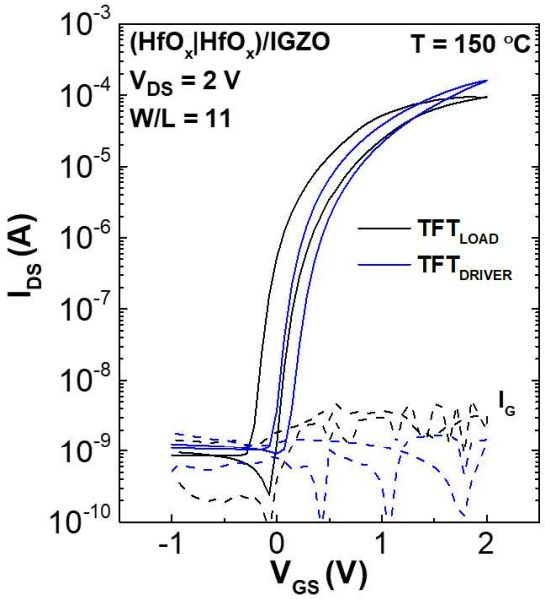

Figure A11. Transfer curves of the TFTs, load and driver, used in the diode-connected inverter.

Appendix B

The Appendix B contains the data of section 4.2 related to the production and characterization of flexographic printed aluminum oxide (Al_2O_3) dielectric thin films and their application in indium oxide (In_2O_3) thin film transistors (TFTs). Figure B1 depicts the flexographic printing patterns after drying using different printing parameters (surface treatment, number of layers, solution concentration, anilox volume and printing speed). Table B1 show the thickness of the printed aluminum oxide thin films using different annealing conditions. Figure B2 shows the X-ray reflectivity (XRR) measurements of Al_2O_3 thin films produced with different annealing conditions. Figure B3, B4 and B5 depict the X-ray photoelectron spectroscopy (XPS) emission from Al 2p, O 1s and C 1s peaks from the printed Al_2O_3 thin films. Figure B6 shows the AFM deflection images for the different thermal annealing conditions used in the dielectric. Figure B7 depicts the capacitance–frequency (CF) factor and aging characteristics of $Al/Al_2O_3/Al$ MIM capacitors for different annealing conditions. Figure B8 shows typical output curves of two test TFT devices annealed at different temperatures. Figure B9 depicts the transfer curves of the printed In_2O_3 TFTs initially and after 5-month storage in air (dark environment). Figure B10 shows the device behaviour after positive and negative gate bias stress, their recovery and saturation mobility behaviour under stress. Figure B11 depicts the TFT transfer curves after mechanical bending stress. Figure B12 shows photographs (a) after the dielectric ink printing and (b) of the homemade bending machine used.

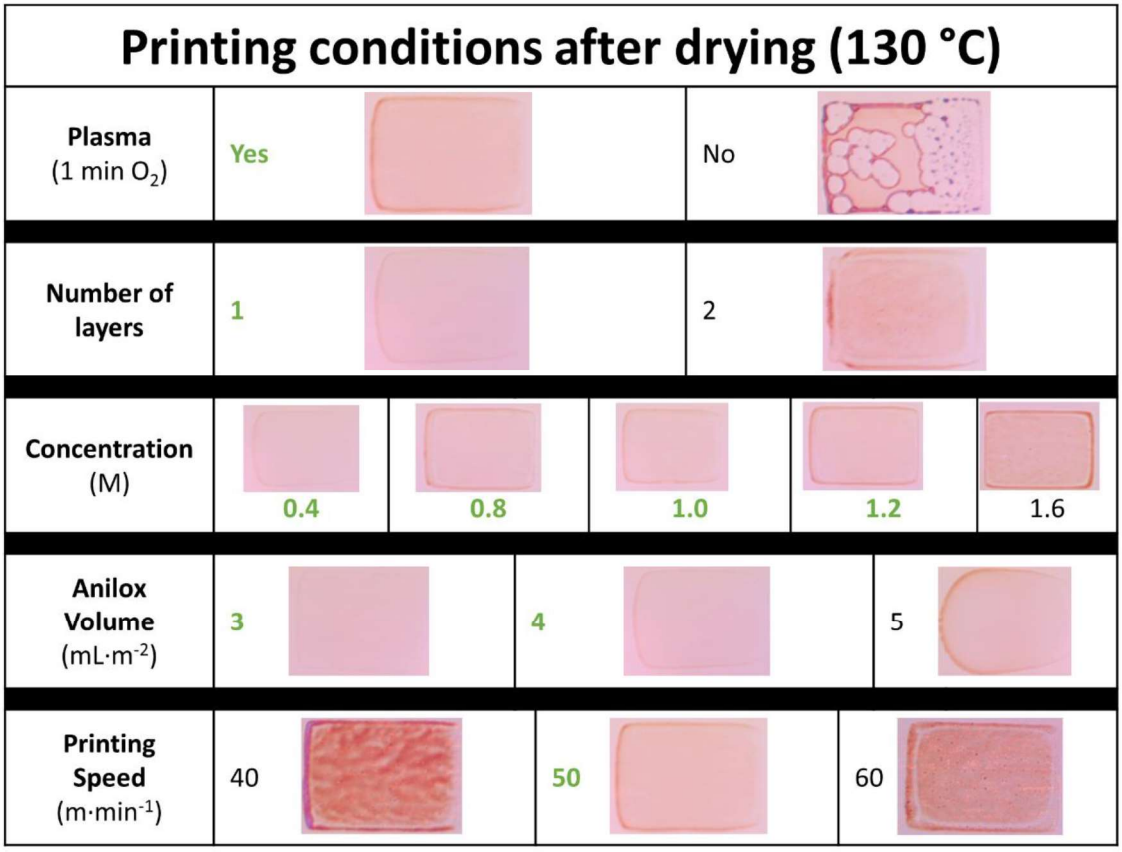

Figure B1. Flexographic printing patterns of Al_2O_3 after a thermal drying at 130 °C using different printing parameters: surface treatment with plasma; number of layers; ink concentration; the anilox volume; printing speed. Numbers with green colour reflect optimal conditions.

Table B1. Al_2O_3 dielectric thickness thin films for the different annealing conditions.

Condition	180 °C	180 °C + FUV	200 °C	200 °C + FUV	300 °C
Thickness (nm)	30 ± 0.5	22.4 ± 0.8	22.7 ± 0.8	15.4 ± 0.8	16.5 ± 0.3

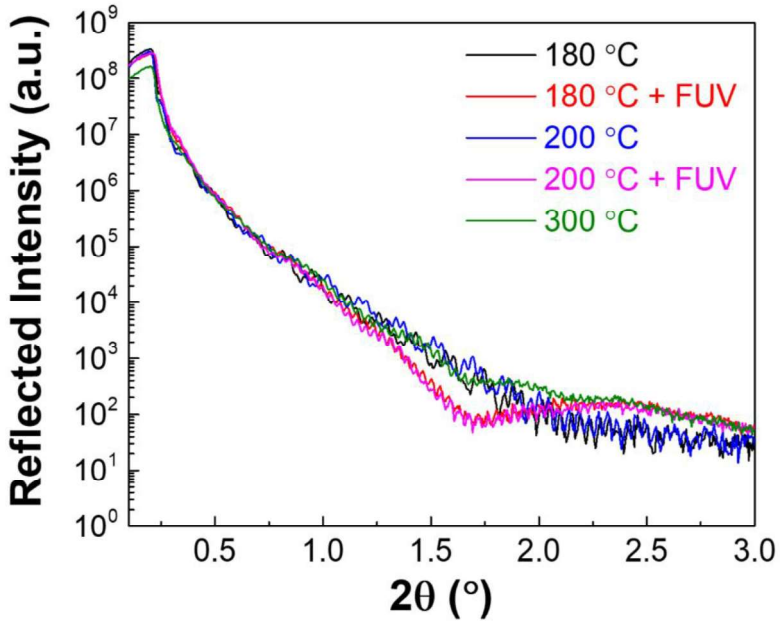

Figure B2. XRR measurements of the Al_2O_3 thin films thermal annealed with and without FUV irradiation.

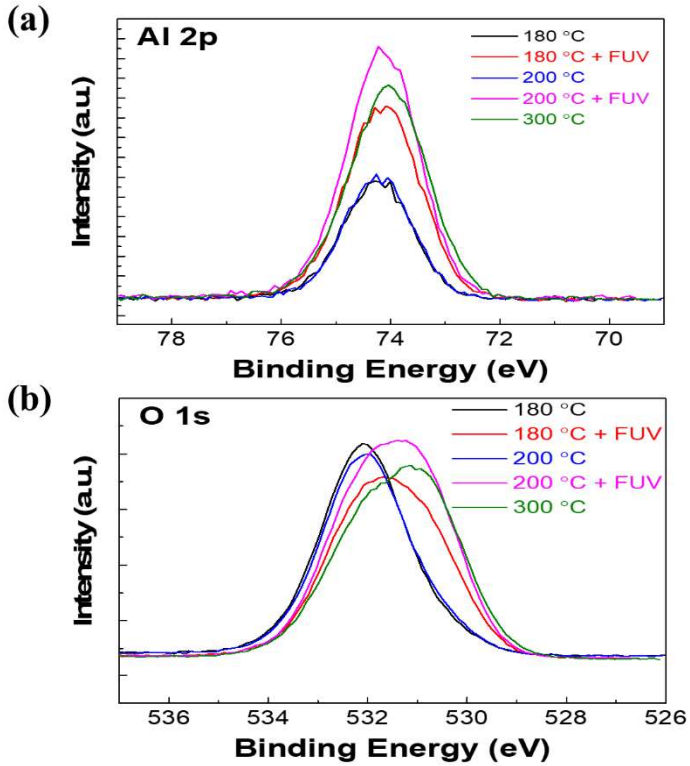

Figure B3. XPS of (a) Al 2p and (b) O 1s emission peaks of the printed aluminum oxide thin films.

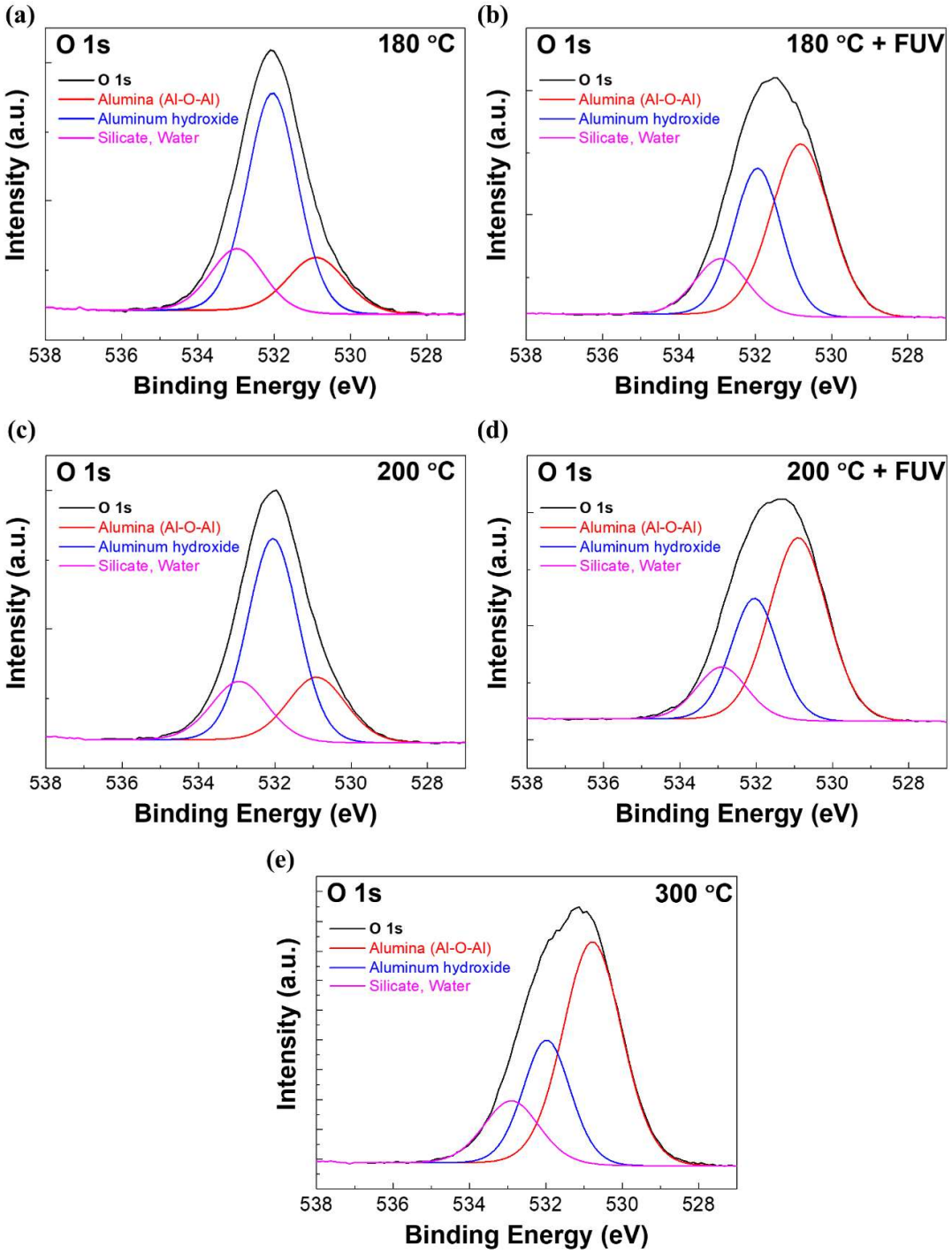

Figure B4. Deconvoluted XPS O 1s emission peaks of the printed aluminum oxide thin films for different annealing conditions: (a) 180 °C, (b) 180 °C + FUV, (c) 200 °C, (d) 200 °C + FUV and (e) 300 °C.

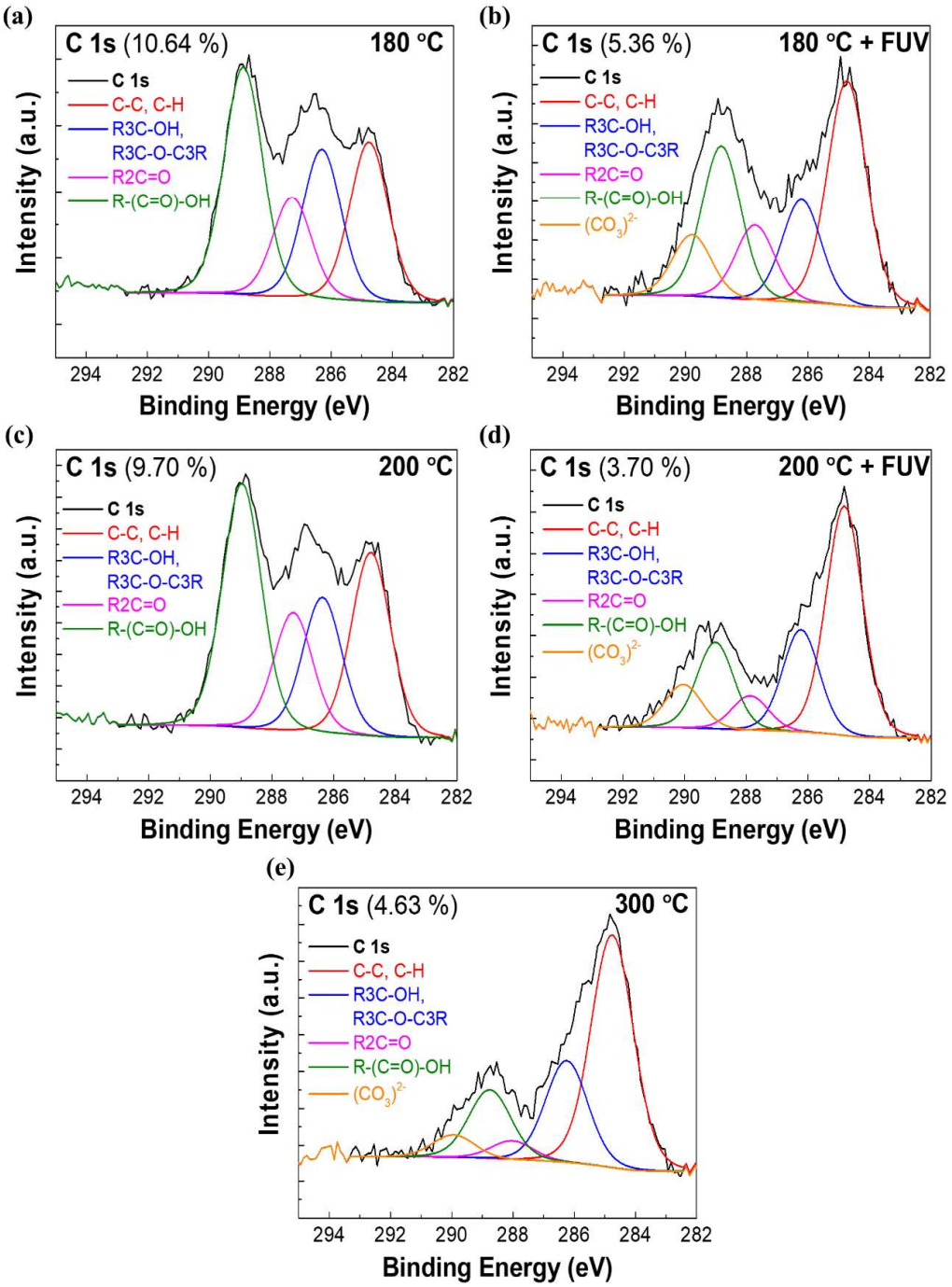

Figure B5. Deconvoluted XPS C 1s emission peaks of the printed aluminum oxide thin films for the different annealing conditions: (a) 180 °C, (b) 180 °C + FUV, (c) 200 °C, (d) 200 °C + FUV and (e) 300 °C.

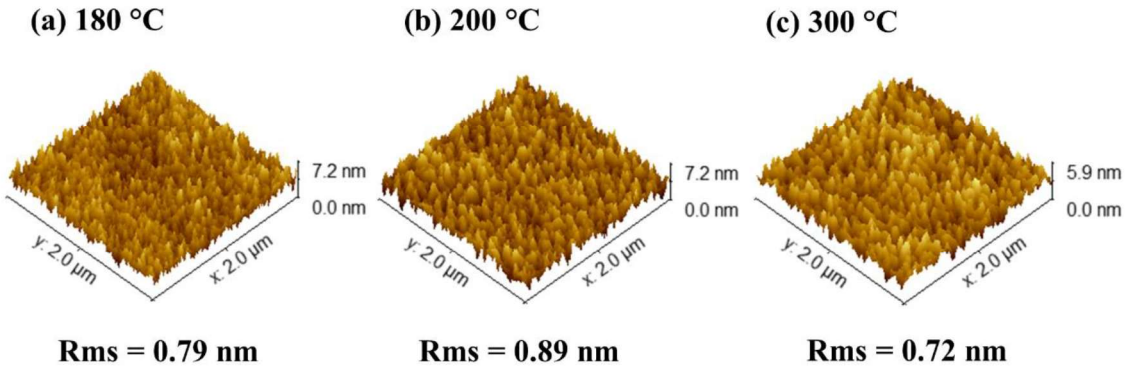

Figure B6. AFM deflection images (2 µm × 2 µm) of the printed aluminum oxide thin films for different annealing temperatures: (a) 180 °C, (b) 200 °C and (c) 300 °C.

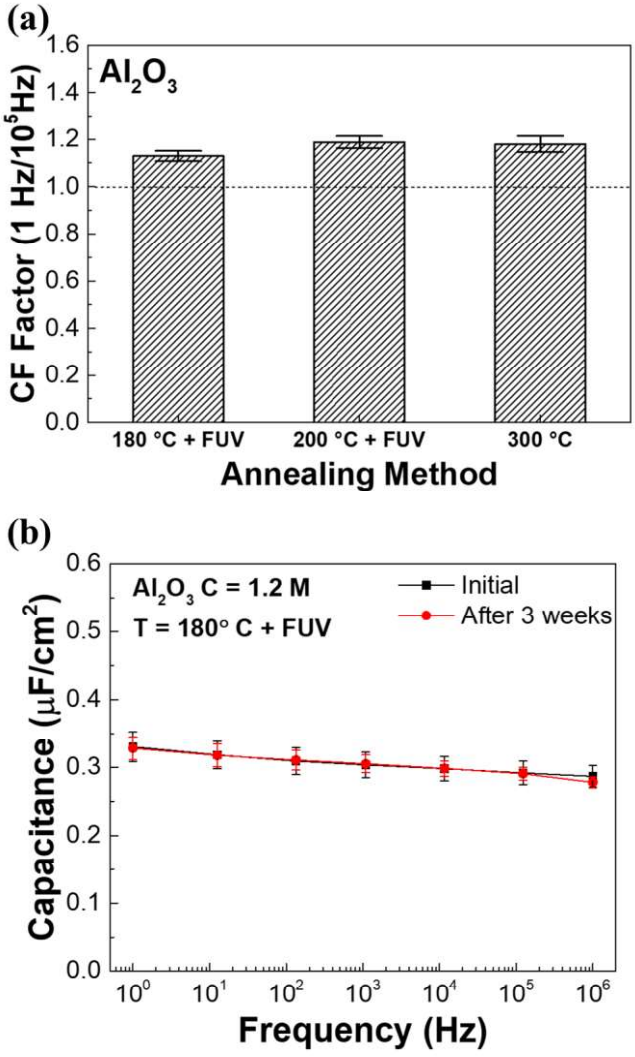

Figure B7. (a) Capacitance-frequency (CF) factor for the different annealing conditions applied in the MIM devices; (b) Ageing of the dielectric annealed at 180 °C assisted by FUV irradiation after 3 weeks of storage in air environment.

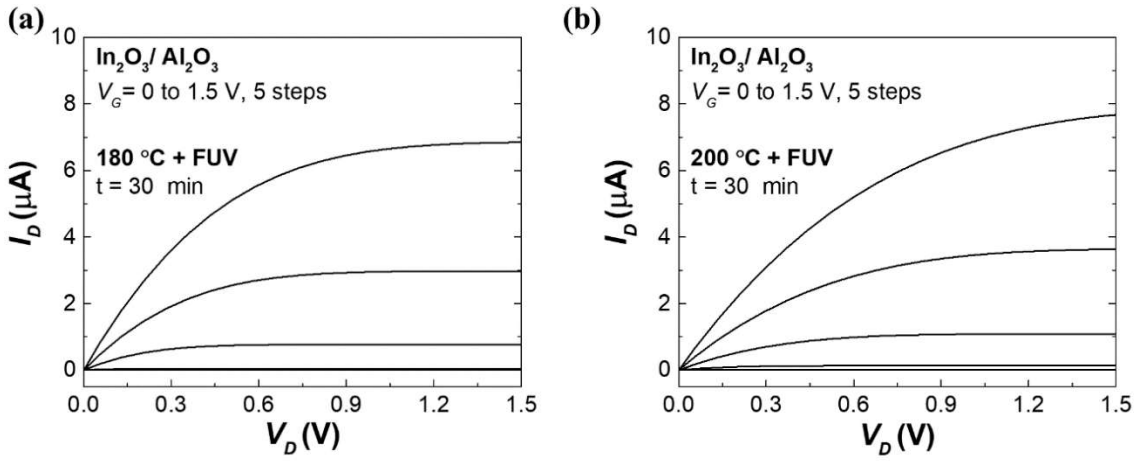

Figure B8. Typical output curves of the In_2O_3 TFTs with the combination of thermal annealing and FUV irradiation for 30 min at (a) 180 °C and (b) 200 °C.

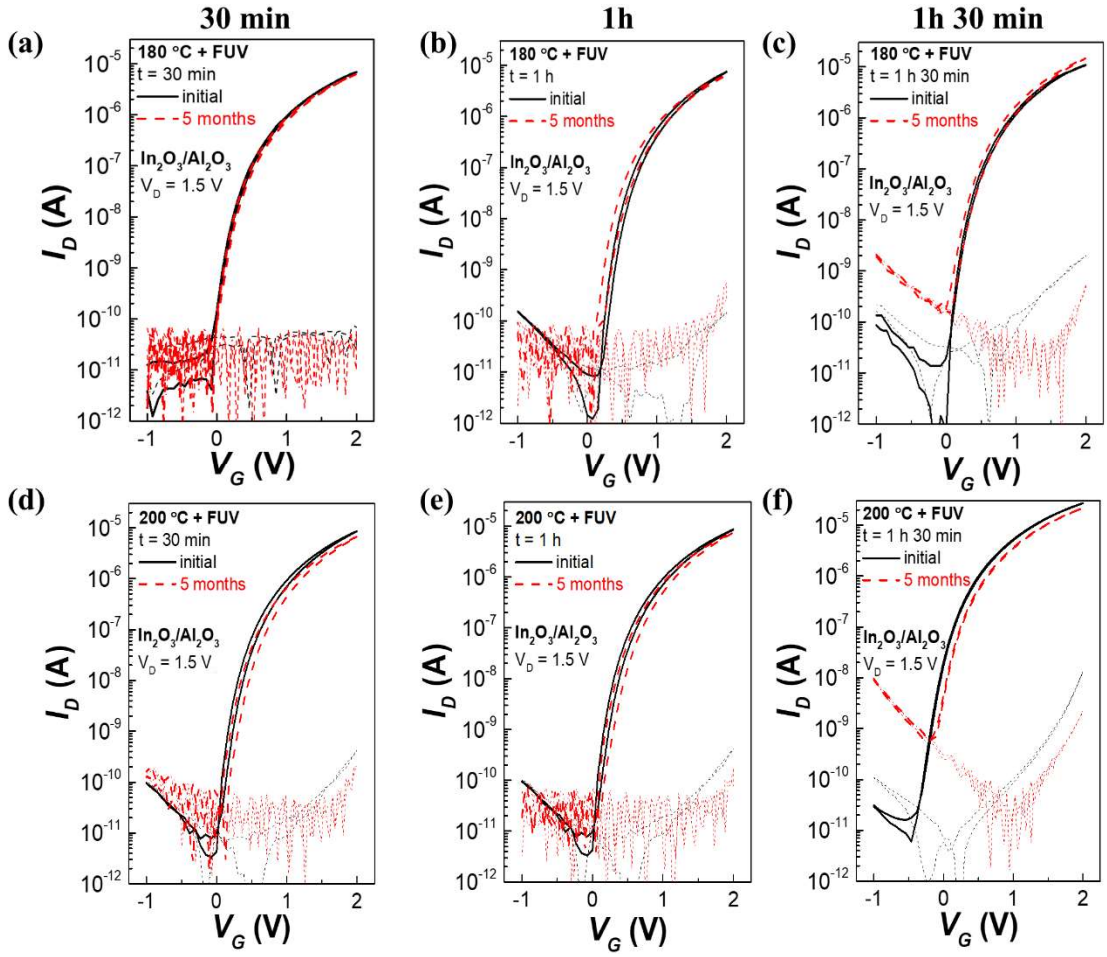

Figure B9. Aging effect on the performance of the In_2O_3/Al_2O_3 TFTs after 5 months storage for different annealing conditions (180 °C + FUV and 200 °C + FUV) for the printed semiconductor for (a,d) 30 min, (b,e) 1h and (c,f) 1h 30 min annealing time.

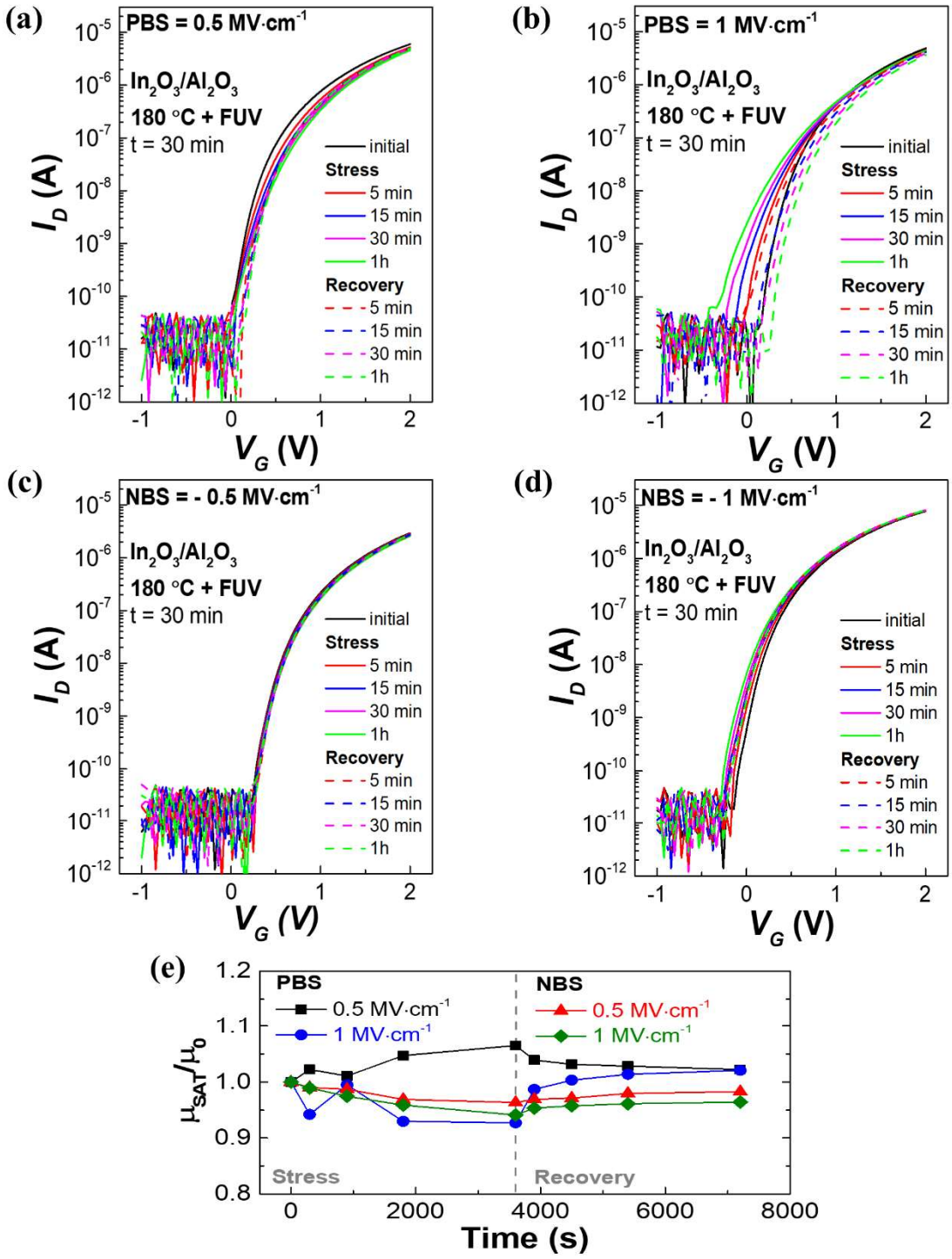

Figure B10. (a,b) Positive (PBS) and (c,d) negative (NBS) gate-bias stress measurements of In_2O_3 TFTs using different electric field: 0.5 and 1 MV·cm^{-1}. (e) Saturation mobility change for 0.5 and 1 MV·cm^{-1}

stress (for selected device with 180 °C + FUV annealing for 30 min) under PBS and NBS tests for 1 h in air environment.

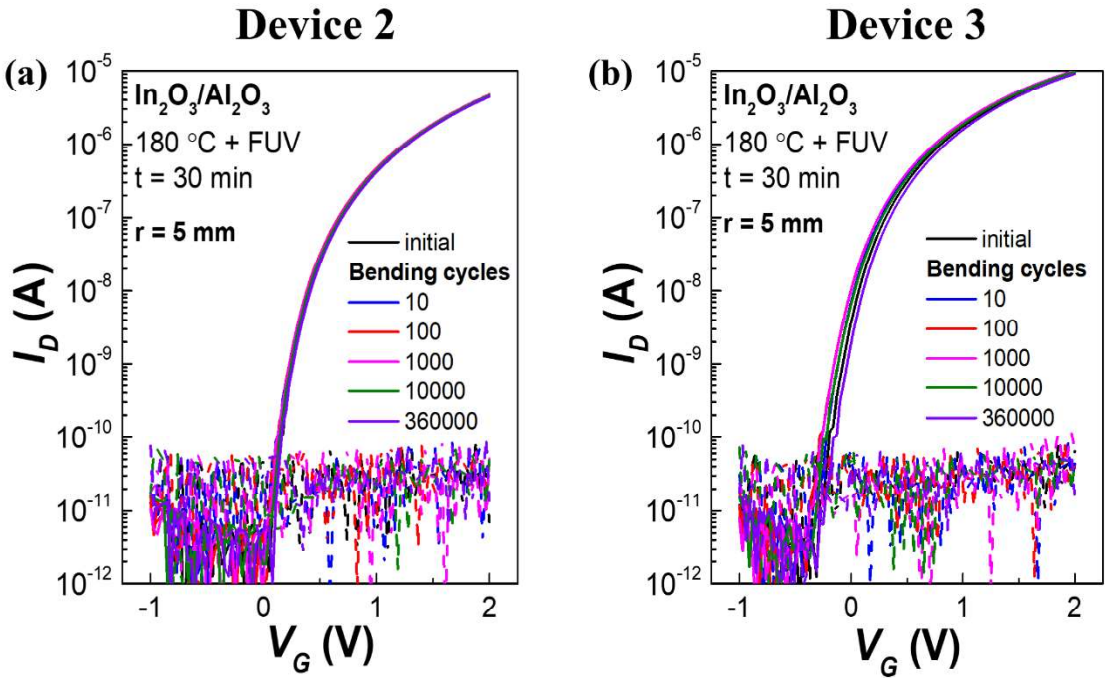

Figure B11. Transfer characteristics of In_2O_3 TFTs under repeated bending cycles, to 5 mm bending radius that was applied along the channel length: (a) device 2 and (b) 3.

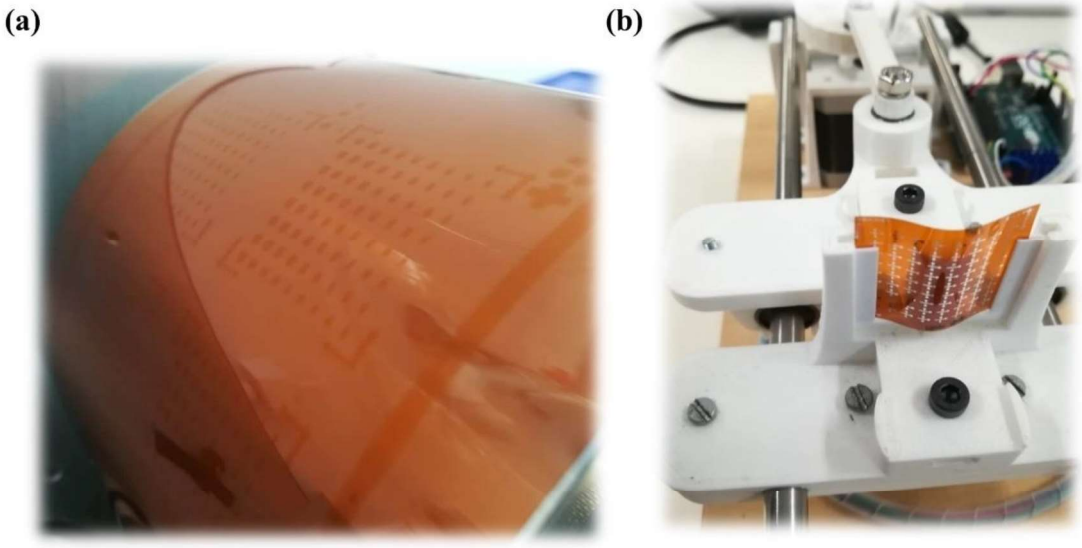

Figure B12. Photographs (a) after the dielectric printing in the flexographic machine and (b) of our homemade bending system.

Appendix C

The Appendix C contains the full data sets of section 4.3 related to the production of AlO_x dielectric thin films from solution, by excimer laser annealing (ELA) treatment inducing combustion synthesis, and their application in thin film transistors (TFTs). Table C1 and C2 shows the statistical parameters of dielectric properties obtained from MIS devices. Figure C1 and C2 depicts FTIR spectra for all ELA conditions and for both drying durations, 15 min and 1 min, respectively. Figure C3, C4 and C5-C6 show the capacitance–voltage, capacitance–frequency and breakdown voltage (E) characteristics of Al/p-type Si/(AlO_x)/Al MIS capacitors for both drying durations. Tables C3 and C4 depicts the electrical characteristics summary obtained from IGZO TFTs comprising the sol-gel AlO_x fabricated by all the different ELA treatments, while Figures C7 and C8 show the transfer curves of the same IGZO TFTs devices. Finally, Figure C9 depicts the typical output curves of two test TFT devices and the reference. Table C5 shows the statistical TFT parameters from a previous report using deep ultraviolet (DUV) curing for 30 min[92], alongside those of the optimum devices produced in this work (using 15 min drying cycle followed by ELA). Table C6 depicts relevant low temperature solution-based AlO_x layers processed by different curing methods applied in TFTs reported previously in the literature

Table C1. Statistical parameters of dielectric properties obtained for the MIS devices dried for 15 min and then treated by ELA. These are all graphically depicted in Figure 4.16 (a) in the main paper. The reference device (300 °C for 1h) is also shown for comparison.

Fluence (mJ/cm^2)	**Number of pulses**	**Capacitance** ($\mu F/cm^2$)	**Thickness** (nm)	**E** (MV/cm)	**Dielectric constant**
125	1	0.08 ± 0.01	27.9 ± 0.4	1.94 ± 0.01	2.62 ± 0.01
	2	0.12 ± 0.02	28.3 ± 0.5	1.82 ± 0.02	3.8 ± 0.8
	3	0.20 ± 0.01	27.7 ± 0.4	1.93 ± 0.05	6.2 ± 0.1
150	1	0.10 ± 0.01	28.7 ± 0.3	1.78 ± 0.01	3.1 ± 0.4
	2	0.35 ± 0.02	16.5 ± 0.3	3.10 ± 0.02	6.5 ± 0.4
	3	0.38 ± 0.01	18.2 ± 0.4	3.3 ± 0.3	7.9 ± 0.1
175	1	0.38 ± 0.02	22.1 ± 0.9	2.4 ± 0.2	9.1 ± 0.1
	2	0.50 ± 0.06	15.2 ± 0.4	4.0 ± 0.5	8.6 ± 0.1
	3	0.53 ± 0.05	13.2 ± 0.3	3.1 ± 0.1	8.6 ± 0.7
200	1	0.51 ± 0.04	15.2 ± 0.9	2.72 ± 0.09	8.8 ± 0.7
	2	0.54 ± 0.01	12.7 ± 0.6	3.5 ± 0.2	7.8 ± 0.2
	3	0.55 ± 0.01	12.8 ± 0.6	3.61 ± 0.06	7.9 ± 0.1
Reference (300 °C, 1h)	0	0.42 ± 0.02	10.9 ± 0.1	3.82 ± 0.03	5.2 ± 0.2

Table C2. Statistical parameters of dielectric properties obtained for the MIS devices dried for 1 min and then treated by ELA. These are all graphically depicted in Figure 4.16 (b) in the main paper. The reference device (300 °C for 1h) is also shown for comparison.

Fluence (mJ/cm^2)	**Number of pulses**	**Capacitance** ($\mu F/cm^2$)	**Thickness** (nm)	**E** (MV/cm)	**Dielectric constant**
200	1	0.69 ± 0.04	47.1 ± 0.9	1.15 ± 0.02	37 ± 2
	2	0.74 ± 0.05	42.3 ± 0.8	0.89 ± 0.03	35 ± 3
	3	0.73 ± 0.04	18.6 ± 1.8	3.0 ± 0.2	15.3 ± 0.9
225	1	0.81 ± 0.04	36.8 ± 0.4	1.5 ± 0.1	33 ± 1
	2	0.72 ± 0.05	14.4 ± 0.7	2.9 ± 0.1	11.7 ± 0.8
	3	0.70 ± 0.04	12.7 ± 0.5	3.5 ± 0.2	9.4 ± 0.1
250	1	0.84 ± 0.03	13.4 ± 0.5	3.1 ± 0.4	12.7 ± 0.5
	2	0.83 ± 0.05	11.4 ± 0.3	3.6 ± 0.3	10.6 ± 0.6
	3	0.84 ± 0.01	11.1 ± 0.4	3.9 ± 0.7	10.2 ± 0.5
300	1	0.79 ± 0.05	14.9 ± 0.7	2.9 ± 0.2	13.2 ± 0.8
	2	0.84 ± 0.02	10.9 ± 0.5	3.5 ± 0.1	10.3 ± 0.2
	3	0.93 ± 0.01	11.0 ± 0.5	3.4 ± 0.3	11 ± 1
Reference (300 °C, 1h)	0	0.42 ± 0.02	10.9 ± 0.1	3.82 ± 0.03	5.2 ± 0.2

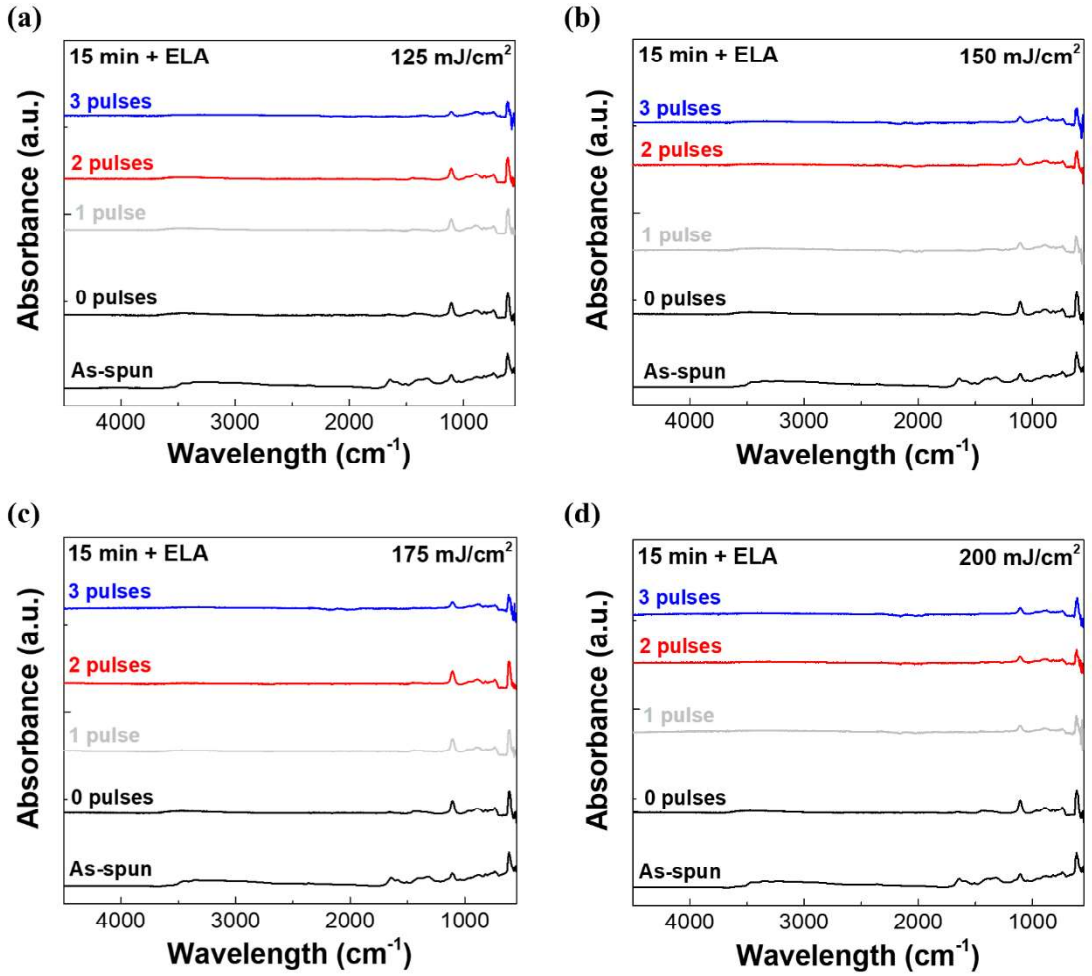

Figure C1. FTIR spectra of AlO_x thin films with 15 min of drying and ELA treatment using different fluences and pulses: (a) 125 mJ/cm^2; (b) 150 mJ/cm^2; (c) 175 mJ/cm^2; (d) 200 mJ/cm^2.

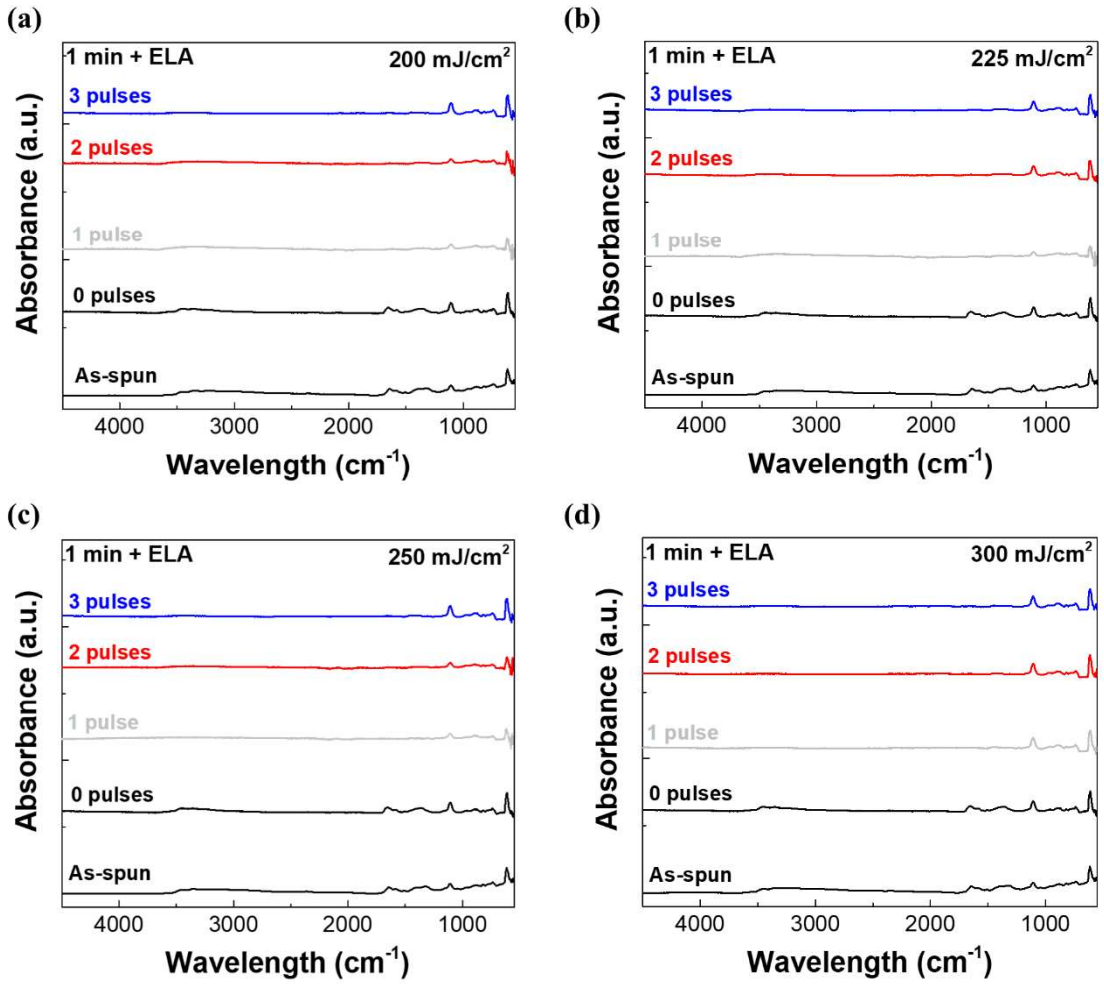

Figure C2. FTIR spectra of AlO_x thin films with 1 min of drying and ELA treatment using different fluences and pulses: (a) 200 mJ/cm^2; (b) 225 mJ/cm^2; (c) 250 mJ/cm^2; (d) 300 mJ/cm^2.

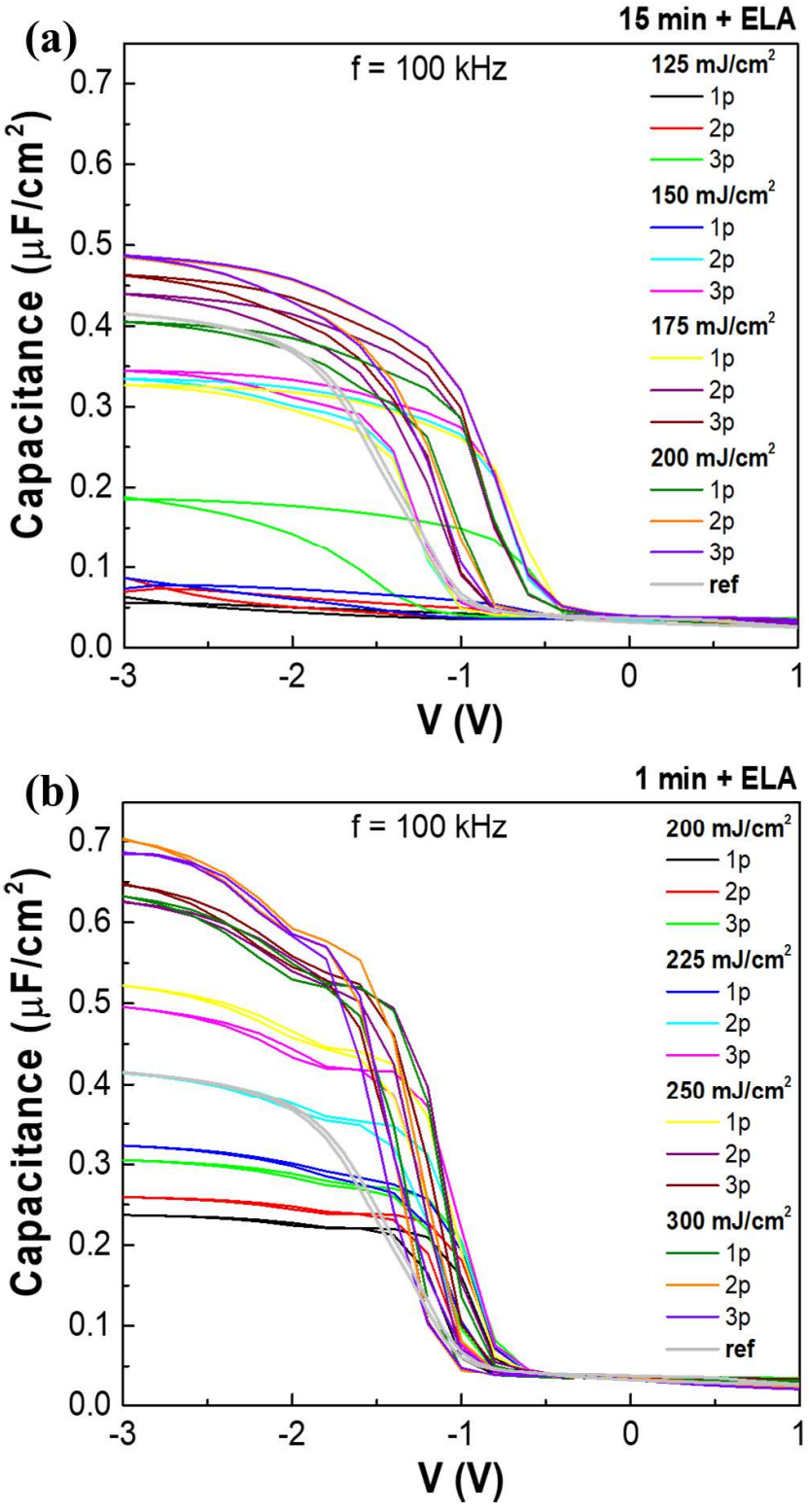

Figure C3. Typical capacitance–voltage characteristics at 100 kHz of solution-based AlO_x MIS capacitors dried at 150 °C for (a) 15 min and (b) 1 min followed by ELA treatment for different fluences and pulses. The reference device (300 °C for 1h) is also shown for comparison.

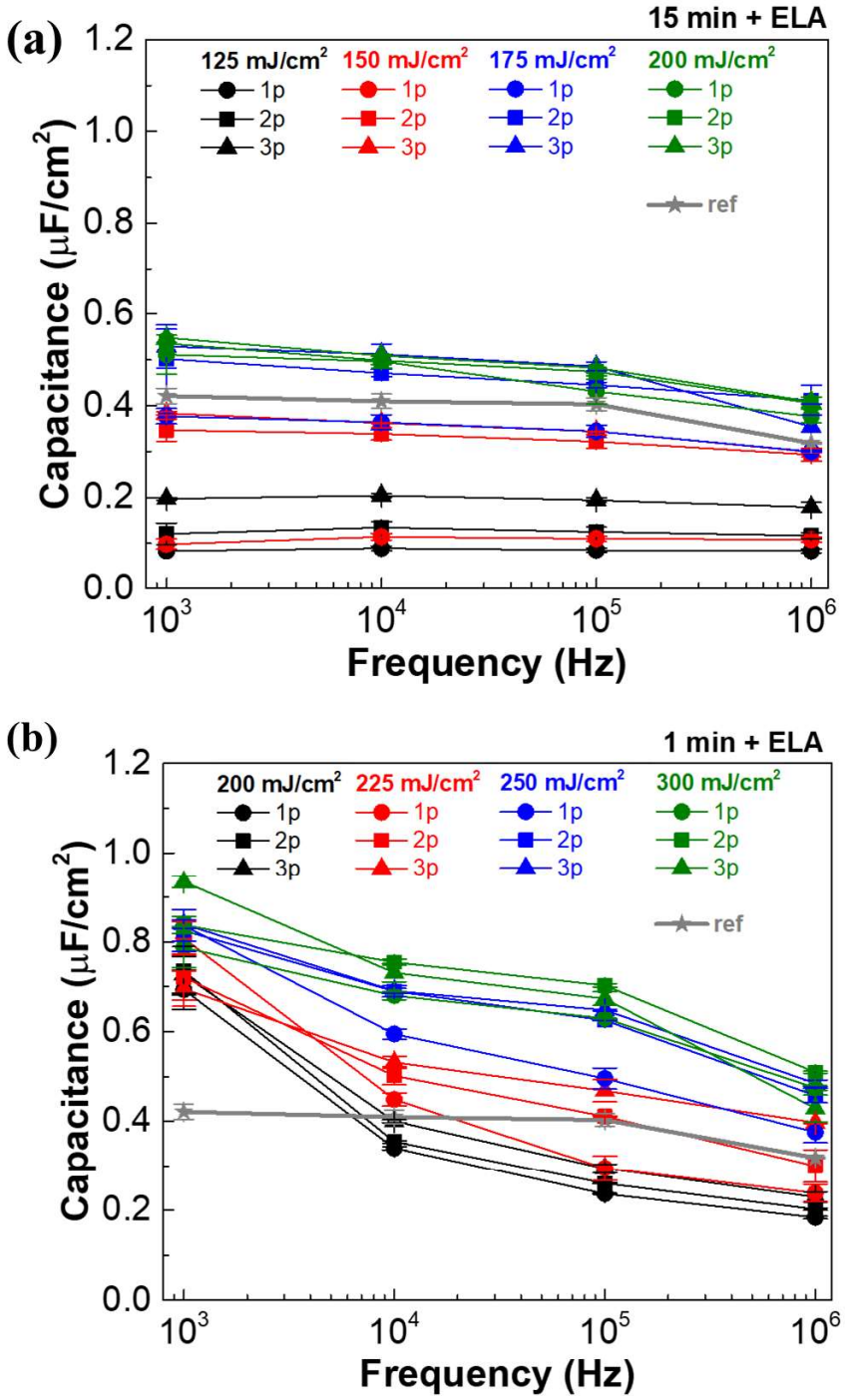

Figure C4. Typical capacitance–frequency characteristics of solution-based AlO_x MIS capacitors dried at 150 °C for (a) 15 min and (b) 1 min followed by ELA treatment for different fluences and pulses. The reference device (300 °C for 1h) is also shown for comparison.

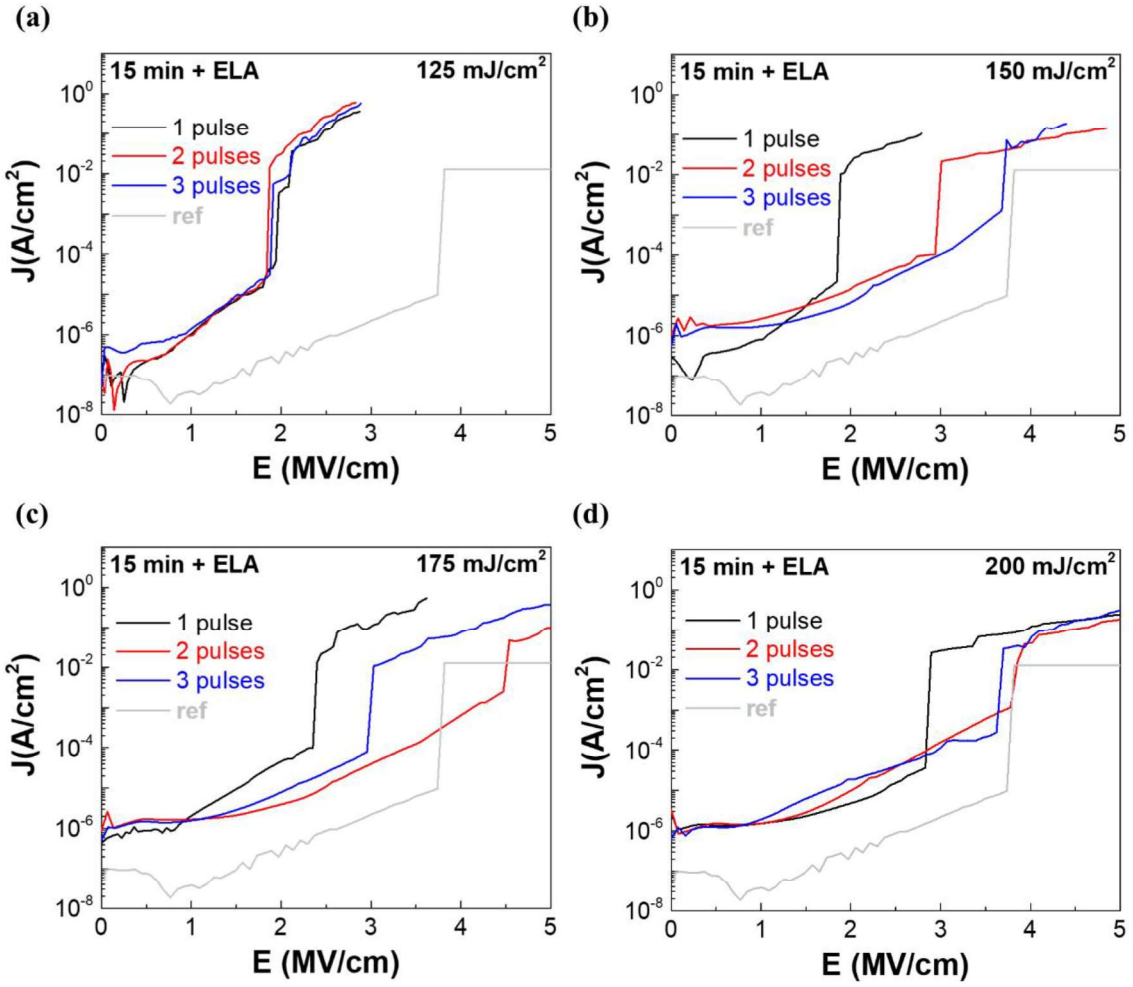

Figure C5. Typical current density (J) and breakdown field (E) characteristics of solution-based AlO_x MIS capacitors with 15 min of drying and ELA treatment using different fluences and pulses: (a) 125 mJ/cm^2; (b) 150 mJ/cm^2; (c) 175 mJ/cm^2; (d) 200 mJ/cm^2. The reference device (300 °C for 1h) is also shown for comparison.

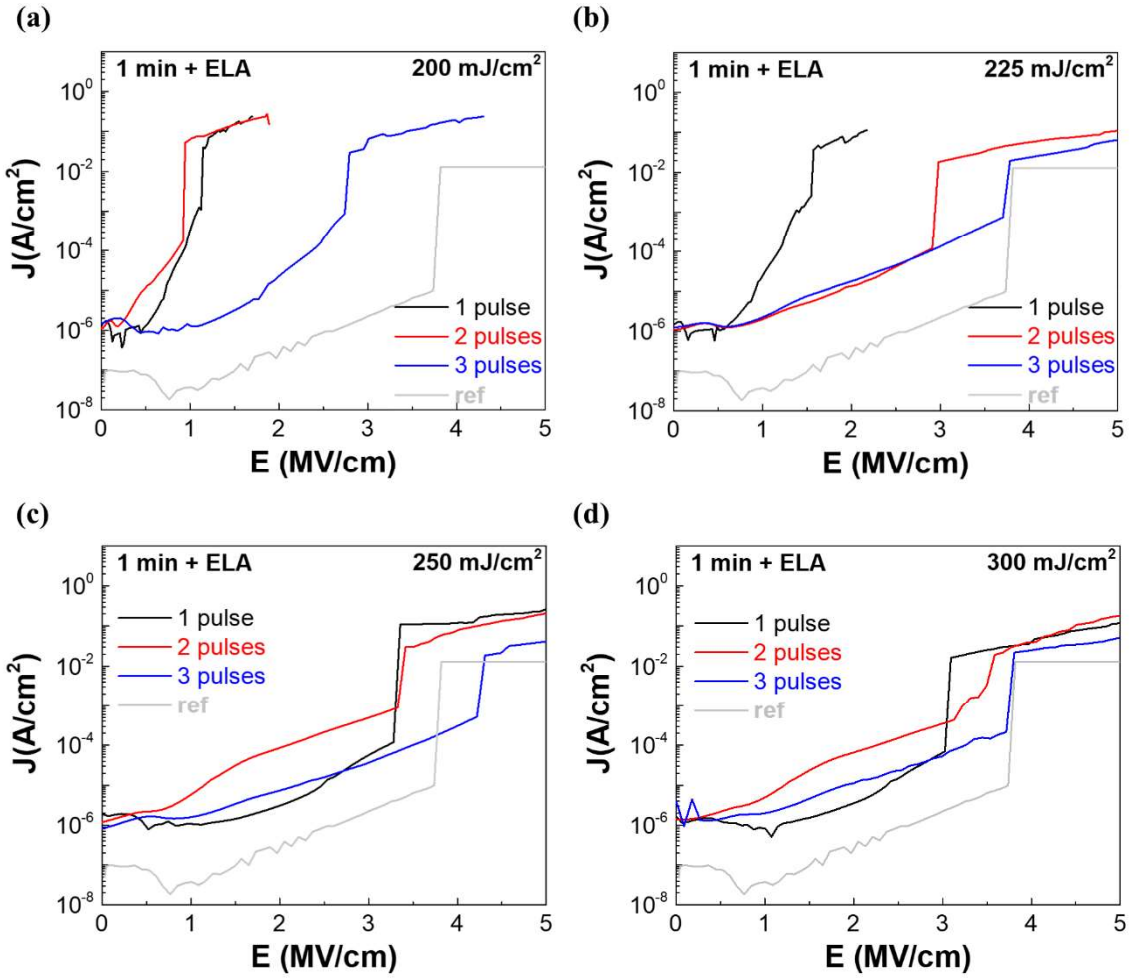

Figure C6. Typical current density (J) and breakdown field (E) characteristics of solution-based AlO_x MIS capacitors with 1 min of drying and ELA treatment using different fluences and pulses: (a) 200 mJ/cm^2; (b) 225 mJ/cm^2; (c) 250 mJ/cm^2; (d) 300 mJ/cm^2. The reference device (300 °C for 1h) is also shown for comparison.

Table C3. Parameters of TFTs obtained for the devices with 15 min of drying followed by ELA. These are all graphically depicted in Figure 4.17 (a) in the main paper. The reference device (300 °C for 1h) is also shown for comparison.

Fluence (mJ/cm^2)	**Number of pulses**	μ_{SAT} ($cm^2/V \cdot s$)	**SS** (V/dec)	$I_{ON/OFF}$	V_{ON} (V)	V_{Hyst} (V)
150	2	11.7	0.13	1.5×10^4	-0.27	0.05
	3	17.9	0.14	2.1×10^4	-0.22	0.07
175	1	18.6	0.13	1.0×10^4	0.05	0.08
	2	20.0	0.10	1.6×10^4	- 0.07	0.07
	3	12.8	0.15	9.7×10^3	- 0.22	0.04
200	1	8.0	0.19	3.1×10^3	- 0.36	0.05
	2	14.5	0.21	3.2×10^3	- 0.36	0.04
	3	8.71	0.23	1.4×10^3	- 0.22	0.01
Reference (300 °C, 1h)	0	13.7	0.13	1.1×10^4	- 0.07	0.06

Table C4. Parameters of TFTs obtained for the devices with 1 min of drying followed by ELA. These are all graphically depicted in Figure 4.17 (b) in the main paper. The reference device (300 °C for 1h) is also shown for comparison.

Fluence (mJ/cm^2)	**Number of pulses**	μ_{SAT} ($cm^2/V \cdot s$)	**SS** (V/dec)	$I_{ON/OFF}$	V_{ON} (V)	V_{Hyst} (V)
225	2	18.4	0.18	1.2×10^4	- 0.36	0.06
	3	22.4	0.12	6.5×10^4	- 0.41	0.09
250	1	5.8	0.12	1.0×10^4	- 0.14	0.04
	2	14.8	0.13	1.7×10^4	- 0.20	0.04
	3	7.6	0.19	7.2×10^3	- 0.04	0.01
300	1	15.5	0.12	2.8×10^4	- 0.30	0.06
	2	14.7	0.12	1.7×10^4	- 0.20	0.02
	3	9.7	0.18	1.0×10^4	- 0.50	0
Reference (300 °C, 1h)	0	13.7	0.13	1.1×10^4	- 0.07	0.06

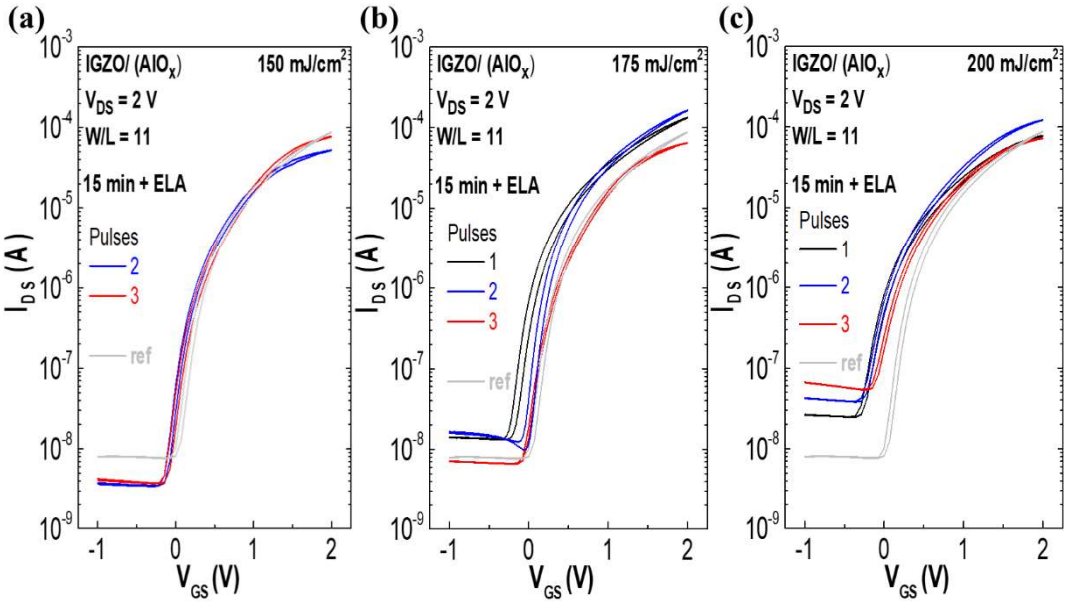

Figure C7. Transfer curves of IGZO TFTs with 15 min of drying followed by ELA treatment using different fluences and pulses: (a) 150 mJ/cm^2; (b) 175 mJ/cm^2; (c) 200 mJ/cm^2. The reference device (300 °C for 1h) is also shown for comparison.

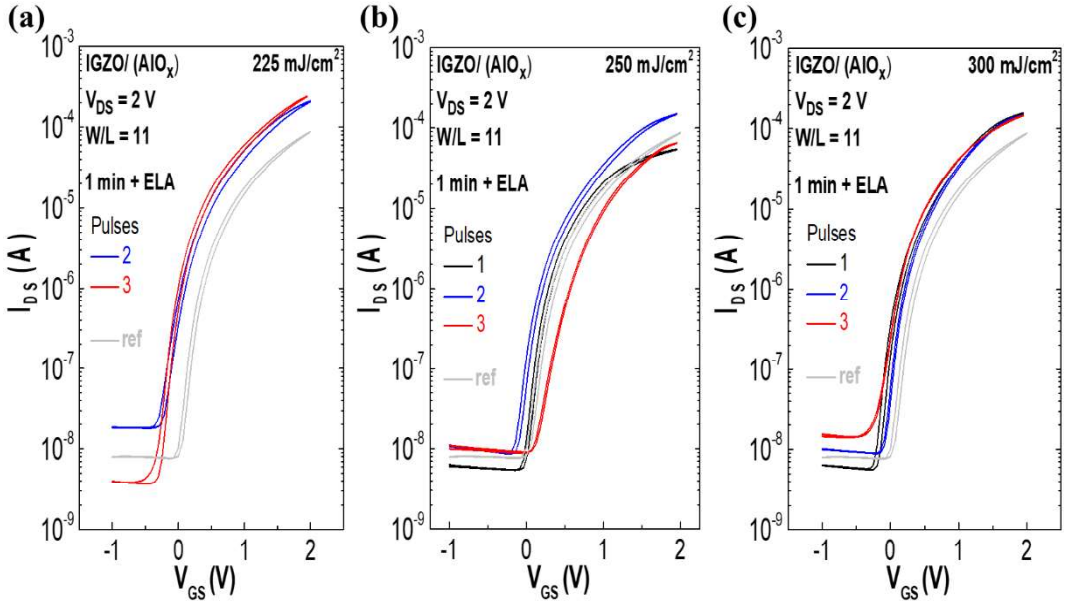

Figure C8. Transfer curves of IGZO TFTs with 1 min of drying followed by ELA treatment using different fluences and pulses: (a) 225 mJ/cm^2; (b) 250 mJ/cm^2; (c) 300 mJ/cm^2. The reference device (300 °C for 1h) is also shown for comparison.

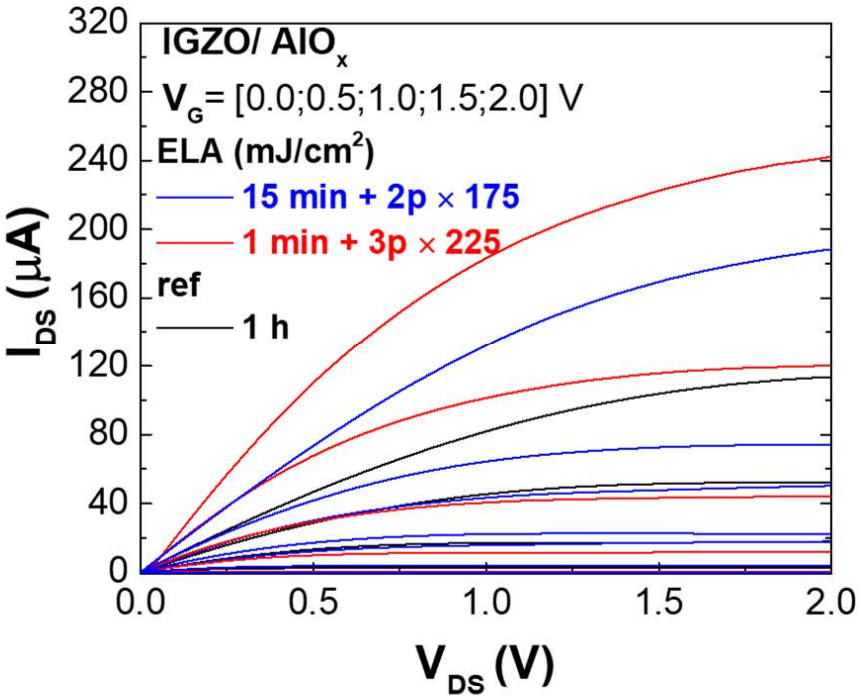

Figure C9. Typical output curves of IGZO/AlO_x TFTs.

Table C5. Statistics of TFT parameters in a previous report[92] using deep ultraviolet (DUV) for 30 min and this work using the 15 min drying followed by ELA. These are all graphically depicted in Figure 4.18 (b) in the main paper.

Condition	V_{ON} (V)	μ_{SAT} ($cm^2/V \cdot s$)	**SS** (V/dec)
150 °C + **DUV (30 min)**	-0.02 ± 0.06	17.3 ± 0.9	0.09 ± 0.01
150 °C + **ELA (15 min)**	-0.015 ± 0.027	20.4 ± 0.9	0.103 ± 0.001

Table C6. Literature of relevant low temperature (≤ 150 °C) solution-based AlO_x layers processed by different curing methods applied in TFTs.

Year	**Irradiation source (wavelength)**	**Irradiation time (pre-annealing time)**	**T** (°C)	μ_{SAT} ($cm^2\ V^{-1}\ s^{-1}$)	**Selectivity**
2015[20]	Deep-ultraviolet lamp (254 nm)	30 min (–)	150	8.33	No
2016[307]	Far ultraviolet lamp (160 nm)	30 min (–)	150	14.10	No
2017[92]	Deep-ultraviolet lamp (254 nm)	30 min (–)	150	17.3	No
2017[362]	Deep-ultraviolet lamp (254 nm)	120 min (–)	60	5.9	No
2019[901]	Deep-ultraviolet lamp (254 nm)	120 min (–)	150	~ 6	No
Present study	Excimer laser (248 nm)	2 s (15 min)	150	20.0	Yes
		3 s (1 min)		22.4	Yes

Appendix D

The Appendix D contains relevant data of section 6.1 related to the material and electrical characterization of the memories. Figure D1 shows the optical microscope images of the different electrodes used as top contact. Figure D2 contains data related to XPS analysis with angle-resolved in a single-layer of aluminum oxide. Figure D3 depict the FTIR spectra of Al_2O_3 thin films before and after annealing. Figure D4 and D5, show the XRD diffractograms of the aluminum oxide thin films and a high-resolution SEM-FIB cross-section image of the single layer Al_2O_3 thin film, respectively. Figure D6 (a) and (b) depict the DC endurance characteristics during 100 cycles and the cumulative probability of the resistance states in the bilayer aluminum oxide memory, respectively. Figure D7 shows the bilayer memories´ *I-V* in the pristine state and the respective forming for both sides, negative and positive. Table D1 show a comparison of current oxide transparent memories with ours.

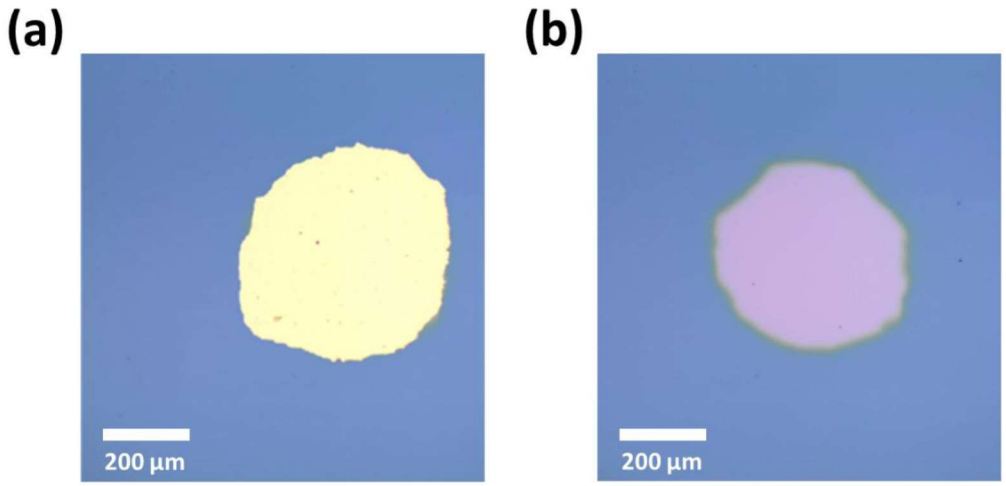

Figure D1. Optical microscope images of the diferent top electrodes used in the devices, (a) Au and (b) IZO.

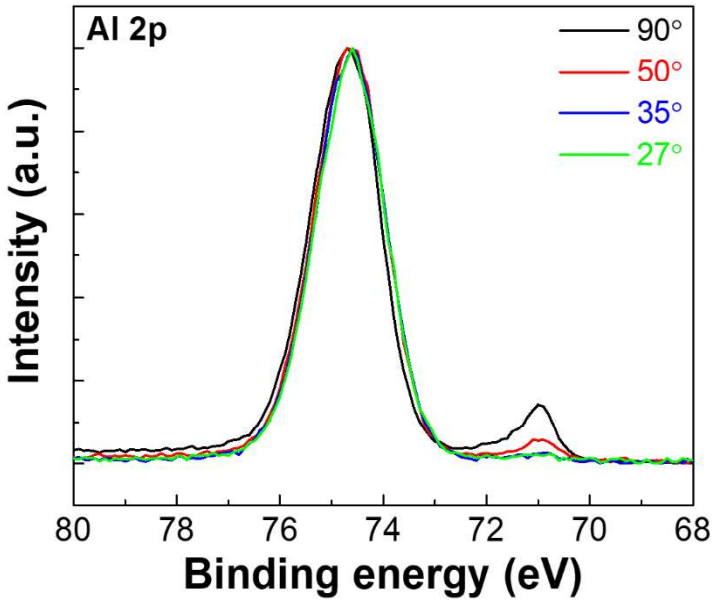

Figure D2. XPS spectra with angle-resolved for different angles in a single layer of Al_2O_3.

The information depth d (the thickness from the surface where 95% of the photoelectrons come from) in the dependence on the emission angle θ and the inelastic mean free path of electrons λ can be estimated with the equation $d = 3\lambda \sin\theta$. The value of λ at a kinetic energy of 1.4 keV is 2.7 nm.[902] The angle-resolved spectra in Figure S2 still show the platinum signal at 50°, which corresponds to an information depth of 6.2 nm. At an emission angle of 35° and below, corresponding to an information depth of 4.6 nm and smaller, the platinum signal is not detectable

anymore. Hence, it is concluded, that platinum diffuses into the aluminum oxide layer up to approximately 5 nm below the surface.

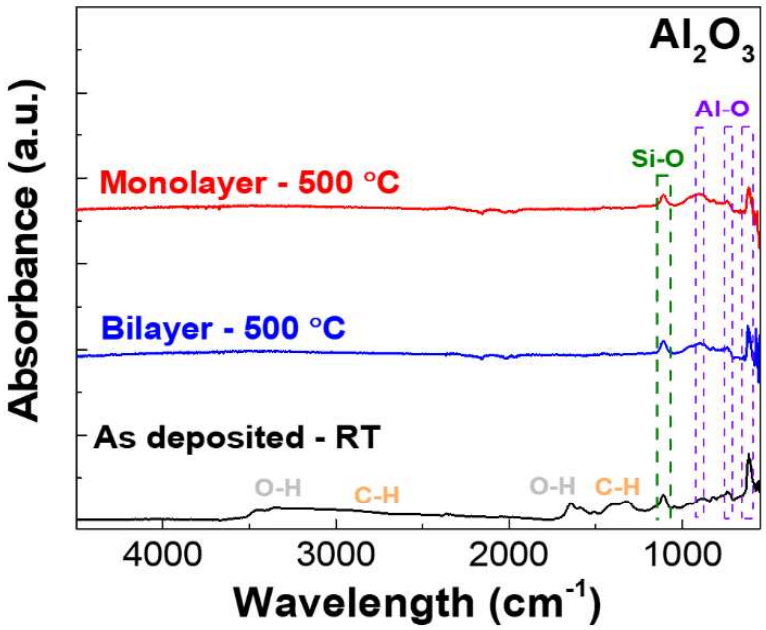

Figure D3. FTIR spectra of Al_2O_3 thin films before and after annealing.

All samples show an absorbance peak at 1107 cm^{-1} attributed to Si-O vibration due to the native SiO_2 formed on the Si substrate's surface.

Before annealing absorption bands related to organic precursors in the film can be observed OH stretching vibrations due to water content and absorption; also weak absorption bands associated to the C–H bonds were observed as depicted in Figure S3.[92,469] After annealing the films at 500 °C with monolayer (30 nm) and bilayer (66 nm) of aluminum oxide, none of these bands were observed confirming the elimination of all residual organics.

The absorption peaks observed at, 889, 739–748 and 611–601 cm^{-1}, are attributed to the presence of Al–O chemical bonds.[471]

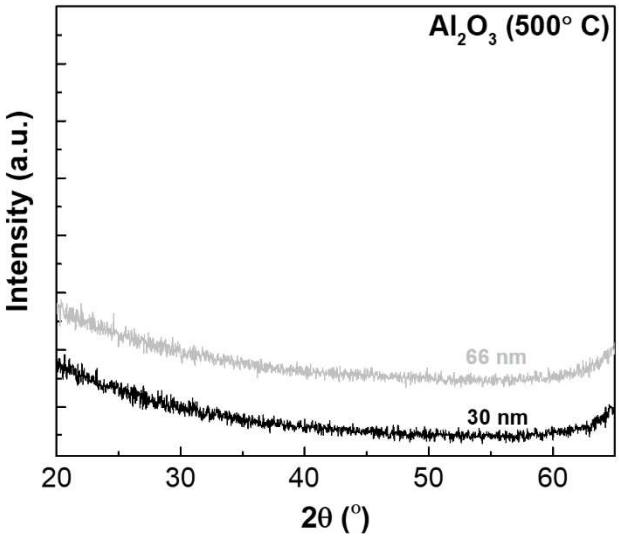

Figure D4. XRD diffractograms of aluminum oxide thin films with different thicknesses.

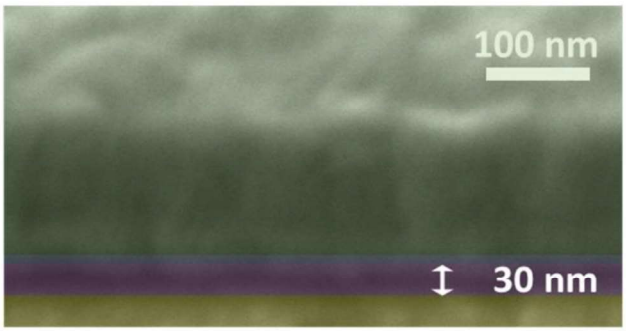

Figure D5. High-resolution SEM-FIB cross-section image of Al_2O_3 monolayer device.

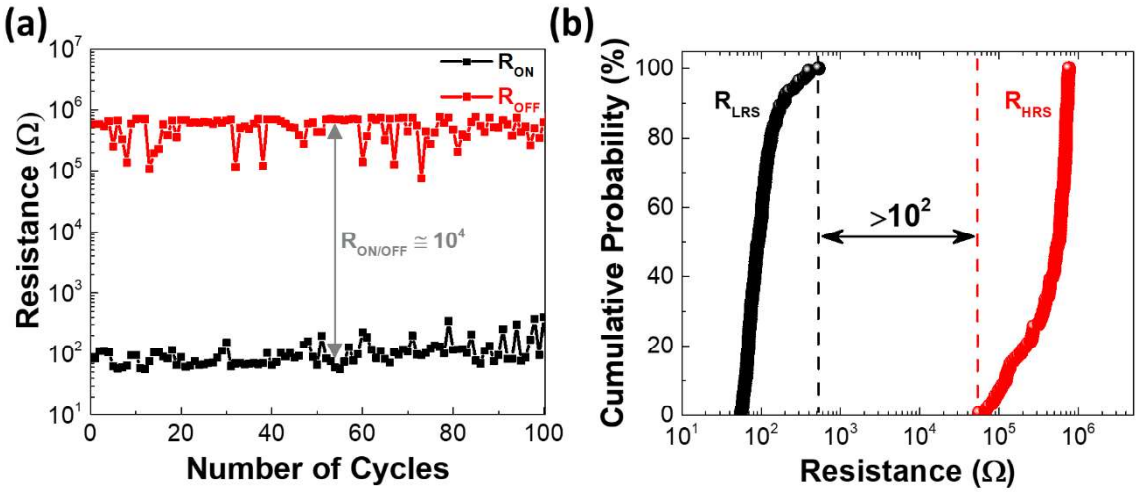

Figure D6. (a) DC endurance characteristics of the bilayer memory for 100 cycles and (b) respective cumulative probability of the resistance states.

The cumulative probabilities of the resistance in the low resistance state (R_{LRS}) and high resistance state (R_{HRS}) were studied based on 100 successive switching cycles of the bilayer memory. The LRS and HRS show an average value of ~10^2 Ω and ~5×10^5 Ω respectively. This corresponds to an average memory window of ~5×10^3, guaranteeing a minimum window of >10^2.

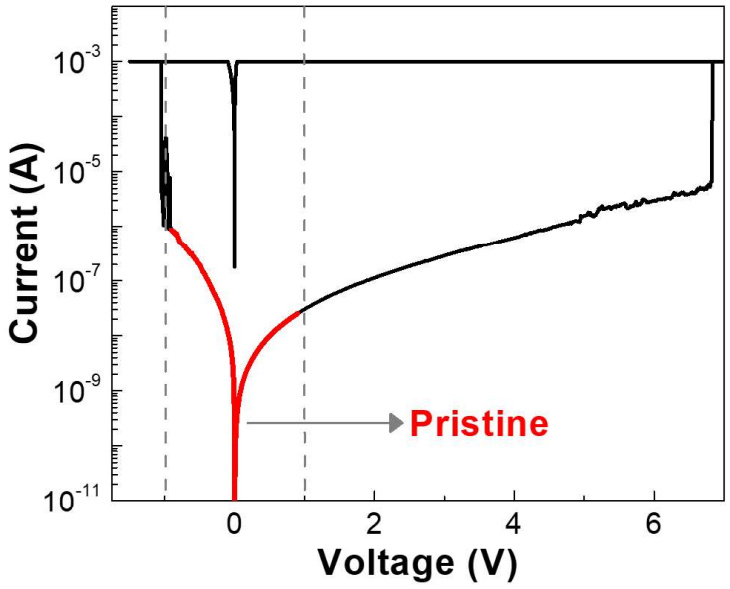

Figure D7. Bilayer memories *I-V* in the pristine state and the respective forming for both sides, negative and positive.

Table D1. Performance comparison of transparent oxide ReRAMs using different production methods.

Year	BE[a]	TE[b]	Method/ Active layer	SB[c]	T[d] (%)	Set (V)	Reset (V)	$R_{ON/OFF}$	Retention (s)	Endurance
2008 [903]	ITO	ITO	MOCVD/ **ZnO**	Unipolar	81	2.6	1.8	10^2	10^5	10^2
2009 [904]	ITO/ Ag/ ITO	ITO	RF Sputtering/ **ZnO**	Unipolar	80	1.5	0.6	~ 50	10^5	2×10^2
2010 [905]	ITO	ITO	RF Sputtering/ **IGZO**	Bipolar	80	- 1	3.5	10^2	10^4	10^2
2011 [619]	ITO	ITO	Spin-coating/ **GZO**	Bipolar	86.5	5	- 6	15	n.a.	3×10^2
2012 [906]	GZO	GZO	MOCVD/ **GZO**	Bipolar	90	10	-12	10^2	n.a.	n.a.
2012 [907]	ITO	G	E-BEAM/ **SiO_x**	Unipolar	90	4	13	10^4	10^5	3×10^2
2014 [908]	ITO	ITO	RF Sputtering/ **HfO_x**	Bipolar	80	0.5	- 2.3	45	10^6	$\sim 5 \times 10^7$
2014 [909]	STO	ITO	PLD/ **LAO**	Bipolar	76	- 1.3	5	10^2	4×10^4	2×10^3
2016 [910]	IZO	IZO	RF Sputtering/ **AlO_x**	Bipolar	80	- 2.8	3.2	10^3	10^5	10^3
2016 [874]	IZO	IZO	ALD/ **TiO_x**	Bipolar	83	5	- 6	8	10^5	10^3
2016 [911]	ITO	ITO	(ALD/ RF Sputtering) **AlON/ZrO_2**	Bipolar	80	2.1	- 4	10	10^4	10^4
2017 [912]	ZnS/ Ag/ ZnS/ Ti	Mg O/ ZnS/ Ag/ ZnS	ALD/ **Al_2O_3**	Bipolar	73	0.6	- 0.3	10^6	10^4	1.5×10^2
This Work 2018	ITO	IZO	Spin-coating/ **Al_2O_3**	Unipolar	80	- 4.2	- 4	10^4	10^4	n.a.

[a]Bottom electrode, [b]Top electrode, [c]Switching behavior, [d]Transmittance, n.a. – not available

Appendix E

The Appendix E comprises the data related to the production and characterization of printed aluminum oxide (AlO_x) resistive switching (RS) devices. Table E1 contains the literature of solution-based AlO_x resistive switching memories. Figure E1 shows the optical microscope images of a complete printed device and the printing of AlO_x thin films using different printing speeds. Table E2 depicts the literature of inkjet printed metal oxide resistive switching memories. Table E3 shows the aluminium oxide ink parameters using 2-methoxyethanol as solvent to calculate the inverse Ohnesorge (Z) number. Figure E2 shows two methods to perform the electroforming process. Figure E3 depicts ITO/AlO_x/Ag device cycle-to-cycle variability. Figure E4 shows the device-to-device variability. Figure E5 depicts the temperature analysis of the devices after breakdown in the negative polarity. Figure E6 shows the resistive switching behaviour of a device under different environment conditions.

Table E1. Solution-based aluminium oxide resistive switching memories. (BE: Bottom electrode; TE: Top electrode; $R_{on/off}$: Resistance on/off ratio; n.d.: not defined; T_{max}: maximum temperature; RT: Room temperature; UV: Ultraviolet; TA: Thermal Annealing; Spin: Spin-coating; Dip: Dip-coating).

Year	Material/ Substrate	Deposition method	Annealing method	T_{max} [°C]	BE/TE interface	$R_{on/off}$	Retention [s]	Endurance [cycles]
2009[745]	Al_yO_x	Anodic	n.d.	RT	Al/Al	~10^4	2×10^2	~10^2
2012[751]	AlO_x	Anodic	n.d.	RT	Al/Al	~10^4	n.d.	n.d.
2012[752]	AlO_x	Anodic	n.d.	RT	Al/Al	~10^5	10^5	10^4
2016[811]	AlO_x	Dip	n.d.	n.d.	Al/Hg	~10^3	n.d.	10^2
2017[735]	AlO_x	Spin	TA	600	Pt/Ti	> 24	10^4	10^3
			Microwave	180		> 20	10^4	10^3
2018[639]	AlO_X	Spin	Microwave	565	Pt/Ti	4.3×10^2	10^4	10^2
2018[279]	Al_2O_3	Spin	TA	500	Pt/Ti	~10^5	10^5	10^2
2018[637]	AlO_x	Spin	Microwave	347	Pt/Ti	10	10^4	10^3
2019[621]	AlO_x	Spin	UV	RT	ITO/Ag	~10^3	10^4	10^2
2019[616]	AlO_x	Spin	TA	250	Pt/TiN	3.5×10^1	10^3	10^2
2019[729]	AlO_x	Spin	TA	250	Pt/Ni	~10^4	10^4	1.5×10^2
2019[635]	AlO_x	Spin	TA	200	Pt/TiN	1.8×10^2	10^4	3×10^2
2020[623]	AlO_x	Spin	TA	250	ITO/Ag	~10^3	10^4	5×10^2
This Work	**AlO_x**	**Inkjet**	**UV + TA**	**150**	**ITO/Ag**	**> 10**	**10^5**	**10^2**

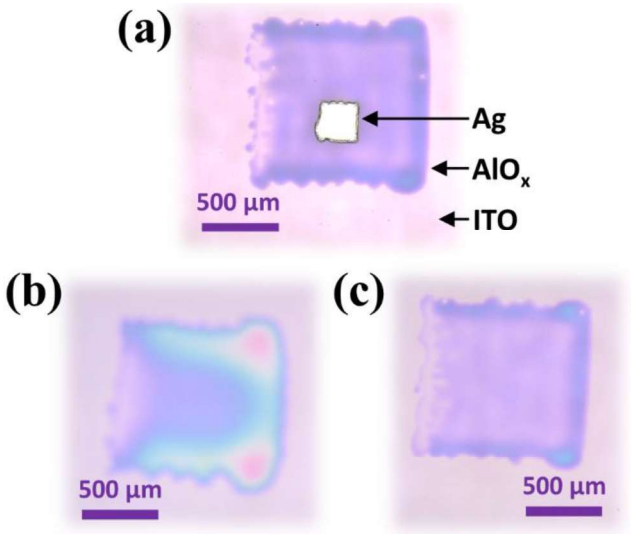

Figure E1. (a) Complete image of the printed resistive switching device acquired by optical microscopy. Influence of the printing speed on the aluminum oxide (AlO_x) layer: (b) 100 mm/sec and (c) 150 mm/sec.

Table E2. Inkjet printed solution-based metal oxide resistive switching memories. (BE: Bottom electrode; TE: Top electrode; $R_{on/off}$: Resistance on/off ratio; n.d.: not defined; T_{max}: maximum temperature; RT: Room temperature; UV: Ultraviolet; TA: Thermal Annealing).

Year	Material/ Substrate	Inkjet type	Annealing method	T_{max} [°C]	BE/TE interface	$R_{on/off}$	Retention [s]	Endurance [cycles]
2012[711]	TiO_2/Si	EHD	TA	450	Cu/Ag	10^2	n.d.	n.d.
2012[708]	ZrO_2/Glass	EHD	TA	120	ITO/Ag	$>10^5$	n.d.	10^2
2012[835]	TiO_2/PES	EHD	TA	150	Ag/Ag	10^3	n.d.	10^2
2012[836]	ZrO_2/PI	EHD	n.d.	n.d.	ITO/Ag Ag/Ag	>10 10^2	n.d.	n.d.
2013[707]	ZnO/Si	EHD	TA	500	Cu/Ag	10^3	n.d.	5×10^2
2013[591]	ZrO_2/PI	EHD	TA	150	Ag/Ag	10^2	n.d.	1.4×10^2
2013[704]	ZrO_2/PET	EHD	TA	135	ITO/Ag	>10	10^6	5×10^1
2013[792]	(CuO/AgO)/PI	Piezo	TA	320	Cu/Ag	10	n.d.	4×10^1
2014[702]	TiO_2/Paper	Piezo	TA	180	C/Ag	10^3	3×10^4	10^3
2015[804]	ZrO_2/PET	EHD	TA	135	ITO/Ag	n.d.	n.d.	n.d.
2016[696]	TiO_x/PET	Piezo	TA	150	Ag/Ag	$>10^2$	n.d.	n.d.
2016[812]	$ZnSnO_3$/PET	EHD	TA	130	ITO/Ag	3×10^2	1.2×10^4	2×10^2
2017[732]	HfO_2/Si	Piezo	TA	240	Au/Ag	10^3	n.d.	1.28×10^2
2020[700]	ZnO/Glass	EHD	TA	500	Ag/Ag	10^3	n.d.	10^3
This work	**AlO_x/Glass**	**Piezo**	**UV + TA**	**150**	**ITO**	**>10**	**10^5**	**10^2**

To guarantee a good printing the Reynolds (equation E1) and Weber (equation E2) numbers should be considered, allowing us to calculate the inverse Ohnesorge (Z) number (equation E3) an essential parameter for inkjet printing.[892] If $1 < Z < 10$, printing is successful; $Z < 1$, represents the lower limit, limited by viscosity (highly viscous fluid is formed), not suitable for inkjet printing. If $Z > 10$, satellite droplets form resulting in a bad printing quality. The Z number of our aluminium oxide ink was 4.85 being ideal value to use in inkjet printing and assure a uniform printability.

Table E3. Aluminium oxide ink parameters using 2-methoxyethanol as solvent.

Ink parameters	**Density (ρ)**	**Length (*L*)**	**Dynamic viscosity (η)**	**Surface tension (y)**
	985 Kg/m^3	*0.00005 m*	2.1 mPa.s	3.8 mN/m

$$\mathrm{Re} = \rho v \frac{L}{\eta} \text{ (equation E1)}$$

$$\mathrm{We} = \rho v^2 \frac{L}{y} \text{ (equation E2)}$$

$$\mathrm{Z} = \frac{We^{\frac{1}{2}}}{Re} = \frac{\eta}{\sqrt{y\rho L}} \qquad 1 < Z(\,4.85) < 10 \quad (equation\ E3)$$

where ρ, *v*, *L*, η, y are density, fluid speed, length, dynamic viscosity, and surface tension respectively.

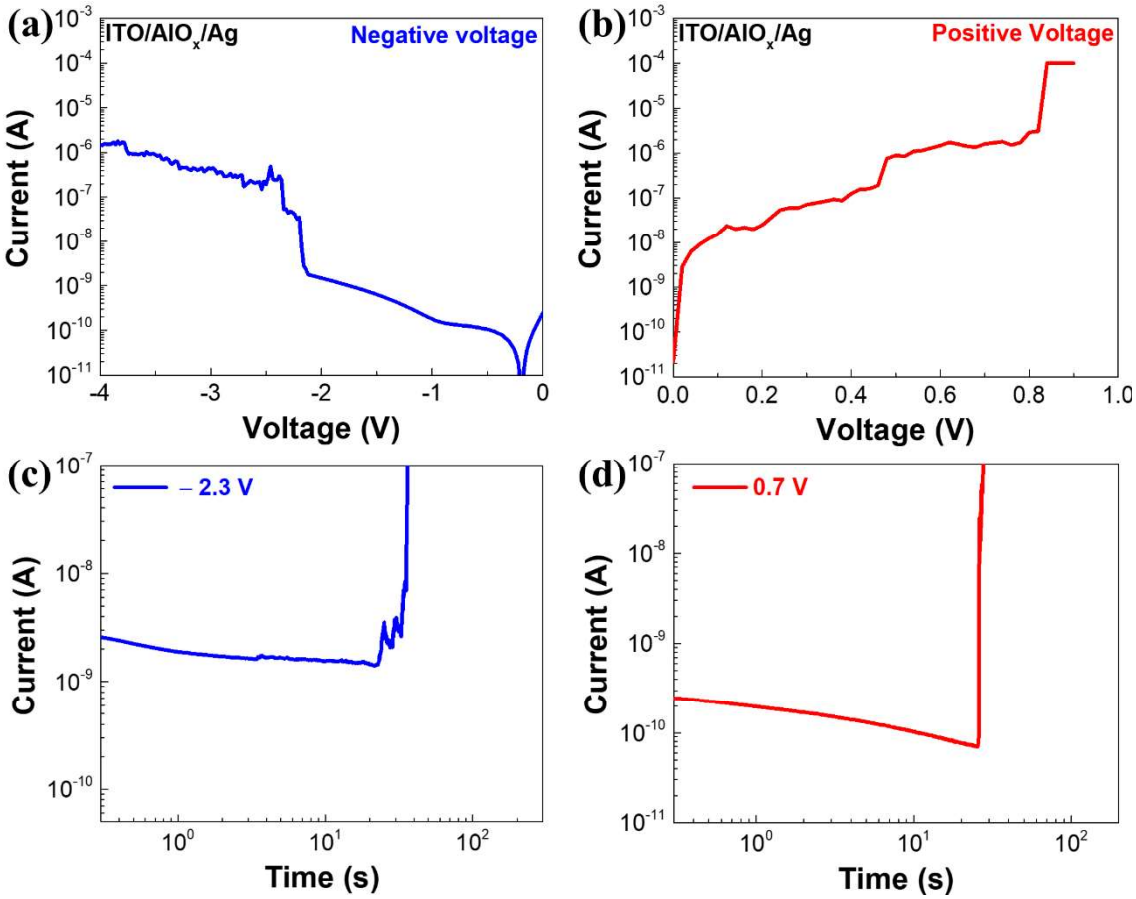

Figure E2. Two different methods to perform an electroforming on the devices: (a,b) DC voltage sweep and (c,d) forming time of constant voltage stress for both negative and positive voltage polarities.

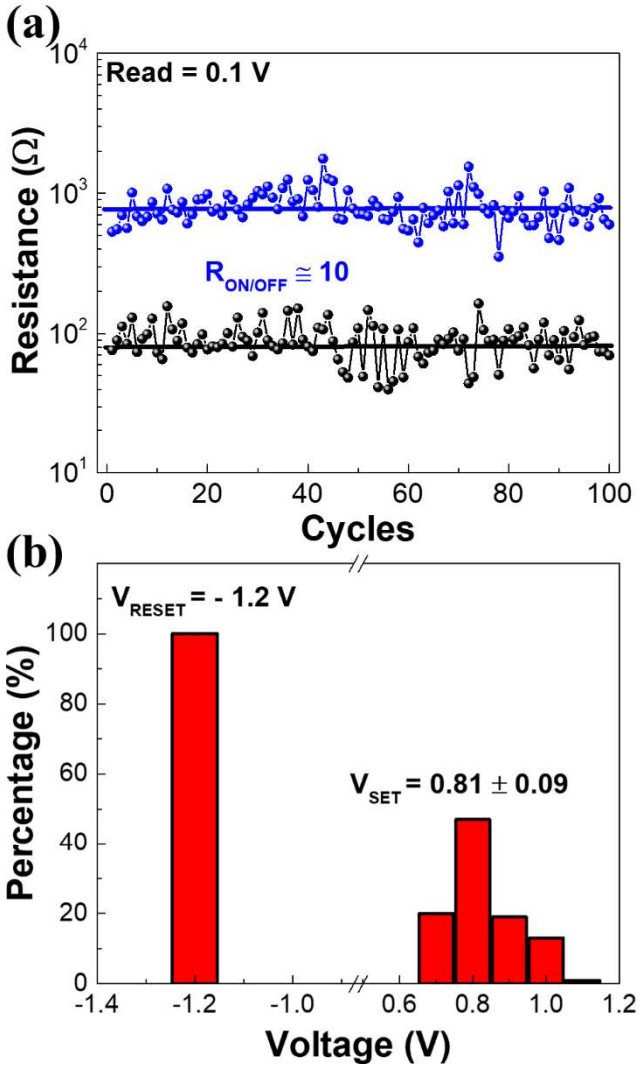

Figure E3. ITO/AlO_x/Ag device cycle-to-cycle variability: (a) resistance states (high resistance state (HRS) and low resistance state (LRS) variation) and (b) operating voltages (set and reset).

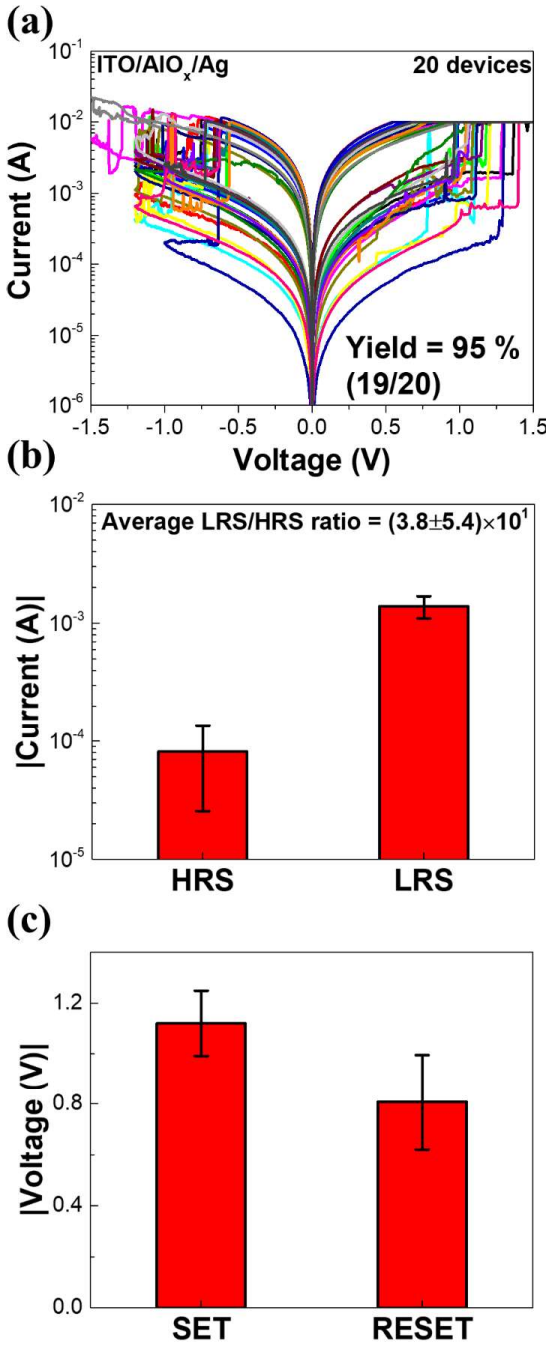

Figure E4. ITO/AlO_x/Ag device-to-device variability: (a) I-V sweep uniformity comparison to see the yield, (b) high resistance state (HRS) and low resistance state (LRS) variation, (c) SET and Reset variation for 20 devices.

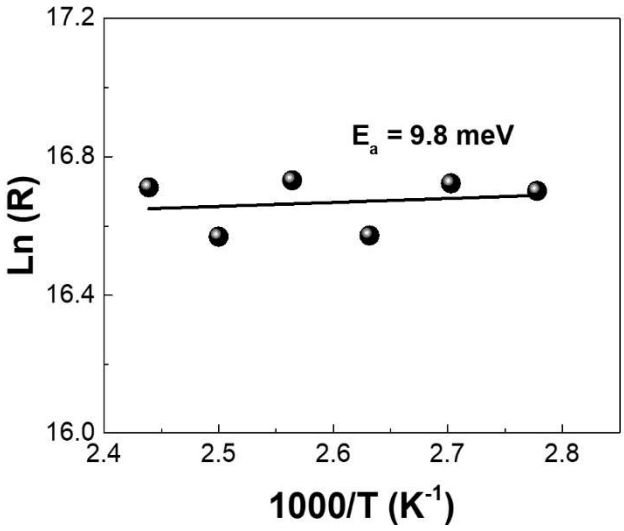

Figure E5. Temperature analysis of the memristor electroformed in the negative polarity.

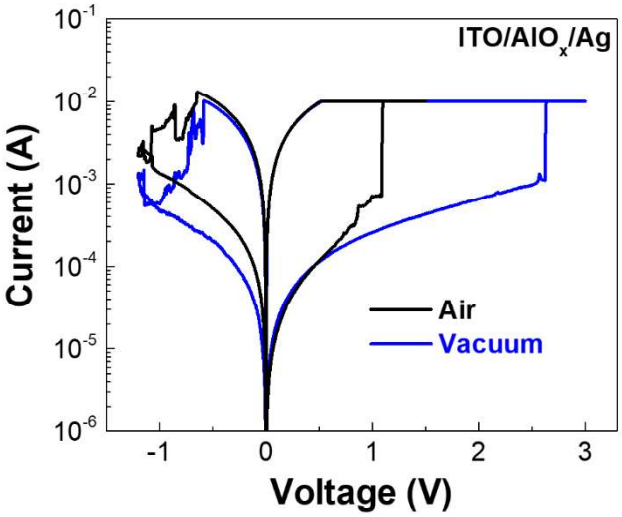

Figure E6. Resistive switching behaviour of a ITO/AlO_x/Ag device under air and vacuum conditions.

References

(1) Fortunato, E.; Barquinha, P.; Martins, R. Oxide Semiconductor Thin-Film Transistors: A Review of Recent Advances. *Adv. Mater.* **2012**, *24* (22), 2945–2986.

(2) Kim, M.-G.; Kanatzidis, M. G.; Facchetti, A.; Marks, T. J. Low-Temperature Fabrication of High-Performance Metal Oxide Thin-Film Electronics via Combustion Processing. *Nat. Mater.* **2011**, *10* (5), 382–388.

(3) Kim, Y.-H.; Heo, J.-S.; Kim, T.-H.; Park, S.; Yoon, M.-H.; Kim, J.; Oh, M. S.; Yi, G.-R.; Noh, Y.-Y.; Park, S. K. Flexible Metal-Oxide Devices Made by Room-Temperature Photochemical Activation of Sol–Gel Films. *Nature* **2012**, *489* (7414), 128–132.

(4) Banger, K. K.; Yamashita, Y.; Mori, K.; Peterson, R. L.; Leedham, T.; Rickard, J.; Sirringhaus, H. Low-Temperature, High-Performance Solution-Processed Metal Oxide Thin-Film Transistors Formed by a 'Sol–Gel on Chip' Process. *Nat. Mater.* **2011**, *10* (1), 45–50.

(5) Park, J. W.; Kang, B. H.; Kim, H. J. A Review of Low-Temperature Solution-Processed Metal Oxide Thin-Film Transistors for Flexible Electronics. *Adv. Funct. Mater.* **2020**, *30* (20), 1904632.

(6) Branquinho, R.; Salgueiro, D.; Santa, A.; Kiazadeh, A.; Barquinha, P.; Pereira, L.; Martins, R.; Fortunato, E. Towards Environmental Friendly Solution-Based ZTO/AlO x TFTs. *Semicond. Sci. Technol.* **2015**, *30* (2), 024007.

(7) Branquinho, R.; Salgueiro, D.; Santos, L.; Barquinha, P.; Pereira, L.; Martins, R.; Fortunato, E. Aqueous Combustion Synthesis of Aluminum Oxide Thin Films and Application as Gate Dielectric in GZTO Solution-Based TFTs. *ACS Appl. Mater. Interfaces* **2014**, *6* (22), 19592–19599.

(8) Lorenz, M.; Ramachandra Rao, M. S. S.; Venkatesan, T.; Fortunato, E.; Barquinha, P.; Branquinho, R.; Salgueiro, D.; Martins, R.; Carlos, E.; Liu, A.; Shan, F. K. K.; Grundmann, M.; Boschker, H.; Mukherjee, J.; Priyadarshini, M.; Dasgupta, N.; Rogers, D. J. J.; Teherani, F. H. H.; Sandana, E. V. V; Bove, P.; Rietwyk, K.; Zaban, A.; Veziridis, A.; Weidenkaff, A.; Muralidhar, M.; Murakami, M.; Abel, S.; Fompeyrine, J.; Zuniga-Perez, J.; Ramesh, R.; Spaldin, N. A. A.; Ostanin, S.; Borisov, V.; Mertig, I.; Lazenka, V.; Srinivasan, G.; Prellier, W.; Uchida, M.; Kawasaki, M.; Pentcheva, R.; Gegenwart, P.; Miletto Granozio, F.; Fontcuberta, J.; Pryds, N. The 2016 Oxide Electronic Materials and Oxide Interfaces Roadmap. *J. Phys. D. Appl. Phys.* **2016**, *49* (43), 433001.

(9) Han, S. Y.; Herman, G. S.; Chang, C. H. Low-Temperature, High-Performance, Solution-Processed Indium Oxide Thin-Film Transistors. *J. Am. Chem. Soc.* **2011**, *133* (14), 5166–5169.

(10) Pasquarelli, R. M.; Ginley, D. S.; O'Hayre, R. Solution Processing of Transparent Conductors: From Flask to Film. *Chem. Soc. Rev.* **2011**, *40* (11), 5406.

(11) Kaltenbrunner, M.; Sekitani, T.; Reeder, J.; Yokota, T.; Kuribara, K.; Tokuhara, T.; Drack, M.; Schwödiauer, R.; Graz, I.; Bauer-Gogonea, S.; Bauer, S.; Someya, T. An Ultra-Lightweight Design for Imperceptible Plastic Electronics. *Nature* **2013**, *499* (7459), 458–463.

(12) Bahubalindruni, P. G.; Tavares, V. G.; Barquinha, P.; Duarte, C.; De Oliveira, P. G.; Martins, R.; Fortunato, E. Transparent Current Mirrors with A-GIZO TFTs: Neural Modeling, Simulation and Fabrication. *IEEE/OSA J. Disp. Technol.* **2013**, *9* (12), 1001–1006.

(13) Chang, M.-F.; Lin, K.-F.; Chuang, C.-H.; Huang, L.-Y.; Chien, T.-F.; Sheu, S.-S.; Su, K.-

L.; Lee, H.-Y.; Chen, F. T.; Lien, C.-H.; Chen, P.-C.; Chiou, L.-Y.; Ku, T.-K.; Tsai, M.-J.; Kao, M.-J. Circuit Design Challenges and Trends in Read Sensing Schemes for Resistive-Type Emerging Nonvolatile Memory. In *2012 IEEE 11th International Conference on Solid-State and Integrated Circuit Technology*; IEEE, 2012; pp 1–4.

(14) Sharath, S. U.; Bertaud, T.; Kurian, J.; Hildebrandt, E.; Walczyk, C.; Calka, P.; Zaumseil, P.; Sowinska, M.; Walczyk, D.; Gloskovskii, A.; Schroeder, T.; Alff, L. Towards Forming-Free Resistive Switching in Oxygen Engineered HfO<inf>2-X</Inf>. *Appl. Phys. Lett.* **2014**, *104* (6).

(15) Rocha, P. R. F.; Kiazadeh, A.; De Leeuw, D. M.; Meskers, S. C. J.; Verbakel, F.; Taylor, D. M.; Gomes, H. L. The Role of Internal Structure in the Anomalous Switching Dynamics of Metal-Oxide/Polymer Resistive Random Access Memories. *J. Appl. Phys.* **2013**, *113* (13).

(16) Sun, Y.; Rogers, J. A. Inorganic Semiconductors for Flexible Electronics. *Adv. Mater.* **2007**, *19* (15), 1897–1916.

(17) MacDonald, W. A. Engineered Films for Display Technologies. *J. Mater. Chem.* **2004**, *14* (1), 4.

(18) Nomura, K.; Ohta, H.; Takagi, A.; Kamiya, T.; Hirano, M.; Hosono, H.; Kenji Nomura1;Hiromichi Ohta1;Akihiro Takagi2;Toshio Kamiya1 2,3, 2;Masahiro Hirano1;& Hideo Hosono1. Room-Temperature Fabrication of Transparent Flexible Thin-Film Transistors Using Amorphous Oxide Semiconductors. *Nature* **2004**, *432* (7016), 488–492.

(19) Nomura, K.; Ohta, H.; Ueda, K.; Kamiya, T.; Hirano, M.; Hosono, H. Thin-Film Transistor Fabricated in Single-Crystalline Transparent Oxide Semiconductor. *Science* **2003**, *300* (5623), 1269–1272.

(20) Park, S. K.; Kim, K.-H. H. K. T. K. H. K.-T.; Jo, J.-W. W.; Sung, S.; Kim, K.-H. H. K. T. K. H. K.-T.; Lee, W.-J. J.; Kim, J.; Kim, H. J.; Yi, G.-R. R.; Kim, Y.-H. H.; Yoon, M.-H. H.; Park, S. K. In-Depth Studies on Rapid Photochemical Activation of Various Sol-Gel Metal Oxide Films for Flexible Transparent Electronics. *Adv. Funct. Mater.* **2015**, *25* (19), 2807–2815.

(21) Leppäniemi, J.; Ojanperä, K.; Kololuoma, T.; Huttunen, O.-H.; Dahl, J.; Tuominen, M.; Laukkanen, P.; Majumdar, H.; Alastalo, A. Rapid Low-Temperature Processing of Metal-Oxide Thin Film Transistors with Combined Far Ultraviolet and Thermal Annealing. *Appl. Phys. Lett.* **2014**, *105* (11), 113514.

(22) BP statistical review of world energy https://www.bp.com/en/global/corporate/energy-economics/statistical-review-of-world-energy/primary-energy.html.

(23) *Combustion Synthesis: Novel Routes to Novel Materials*; Lackner, M., Ed.; BENTHAM SCIENCE PUBLISHERS, 2012; Vol. 53.

(24) Dmitrienko, M. A.; Legros, J. C.; Strizhak, P. A. Experimental Evaluation of Main Emissions during Coal Processing Waste Combustion. *Environ. Pollut.* **2018**, *233*, 299–305.

(25) Merzhanov, A. G. The Chemistry of Self-Propagating High-Temperature Synthesis. *J. Mater. Chem.* **2004**, *14* (12), 1779.

(26) Chick, L. A.; Pederson, L. R.; Maupin, G. D.; Bates, J. L.; Thomas, L. E.; Exarhos, G. J. Glycine-Nitrate Combustion Synthesis of Oxide Ceramic Powders. *Mater. Lett.* **1990**, *10* (1–2), 6–12.

(27) Carlos, E.; Martins, R.; Fortunato, E.; Branquinho, R. Solution Combustion Synthesis: Towards a Sustainable Approach for Metal Oxides. *Chem. – A Eur. J.* **2020**, *26* (42),

chem.202000678.

(28) Pechini, M. P. Method of Preparing Lead and Alkaline Earth Titanates and Niobates and Coating Method Using the Same to Form a Capacitor. US3330697A, 1967.

(29) Patil, K. C.; Hegde, M. S.; Rattan, T.; Aruna, S. T. Solution Combustion Synthesis of Oxide Materials. In *Chemistry of Nanocrystalline Oxide Materials*; WORLD SCIENTIFIC, 2008; pp 42–60.

(30) Wooldridge, M. S. Gas-Phase Combustion Synthesis of Particles. *Prog. Energy Combust. Sci.* **1998**, *24* (1), 63–87.

(31) Brezinsky, K. Gas-Phase Combustion Synthesis of Materials. *Symp. Combust.* **1996**, *26* (2), 1805–1816.

(32) Ravichandran, K.; Praseetha, P. K.; Arun, T.; Gobalakrishnan, S. Synthesis of Nanocomposites. In *Synthesis of Inorganic Nanomaterials*; Elsevier, 2018; pp 141–168.

(33) Jain, S. R.; Adiga, K. C.; Pai Verneker, V. R. A New Approach to Thermochemical Calculations of Condensed Fuel-Oxidizer Mixtures. *Combust. Flame* **1981**, *40*, 71–79.

(34) Kingsley, J. J.; Patil, K. C. A Novel Combustion Process for the Synthesis of Fine Particle α-Alumina and Related Oxide Materials. *Mater. Lett.* **1988**, *6* (11–12), 427–432.

(35) Branquinho, R.; Santa, A.; Carlos, E.; Salgueiro, D.; Barquinha, P.; Martins, R.; Fortunato, E. Solution Combustion Synthesis: Applications in Oxide Electronics. In *Developments in Combustion Technology*; Konstantinos G. Kyprianidis and Jan Skvaril, Ed.; InTech, 2016; Vol. i, p 13.

(36) Evecan, D.; Kaplan, Ş. S.; Sönmez, M. Ş.; Yıldırım, S.; Okutan, M.; Deligöz, H.; Zayim, E. Smart Glass Electrochromic Device Fabrication of Uniform Tungsten Oxide Films from Its Powder Synthesized by Solution Combustion Method. *Microelectron. Eng.* **2019**, *215* (May), 110989.

(37) Zheng, D.; Wang, G.; Huang, W.; Wang, B.; Ke, W.; Logsdon, J. L.; Wang, H.; Wang, Z.; Zhu, W.; Yu, J.; Wasielewski, M. R.; Kanatzidis, M. G.; Marks, T. J.; Facchetti, A. Combustion Synthesized Zinc Oxide Electron-Transport Layers for Efficient and Stable Perovskite Solar Cells. *Adv. Funct. Mater.* **2019**, *29* (16), 1900265.

(38) González-Cortés, S. L.; Imbert, F. E. Fundamentals, Properties and Applications of Solid Catalysts Prepared by Solution Combustion Synthesis (SCS). *Appl. Catal. A Gen.* **2013**, *452*, 117–131.

(39) González-Cortés, S. L.; Imbert, F. E.; Shao, Z.; Zhou, W.; Zhu, Z. Advanced Synthesis of Materials for Intermediate-Temperature Solid Oxide Fuel Cells. *Appl. Catal. A Gen.* **2013**, *452* (4), 117–131.

(40) Danks, A. E.; Hall, S. R.; Schnepp, Z. The Evolution of 'Sol–Gel' Chemistry as a Technique for Materials Synthesis. *Mater. Horizons* **2016**, *3* (2), 91–112.

(41) Birol, H.; Renato Rambo, C.; Guiotoku, M.; Hotza, D. Preparation of Ceramic Nanoparticlesvia Cellulose-Assisted Glycine Nitrate Process: A Review. *RSC Adv.* **2013**, *3* (9), 2873–2884.

(42) Eivazihollagh, A.; Svanedal, I.; Edlund, H.; Norgren, M. On Chelating Surfactants: Molecular Perspectives and Application Prospects. *J. Mol. Liq.* **2019**, *278*, 688–705.

(43) Deganello, F. Nanomaterials for Environmental and Energy Applications Prepared by Solution Combustion Based-Methodologies: Role of the Fuel. *Mater. Today Proc.* **2017**, *4* (4), 5507–5516.

(44) Fathi, H.; Masoudpanah, S. M.; Alamolhoda, S.; Parnianfar, H. Effect of Fuel Type on the

Microstructure and Magnetic Properties of Solution Combusted Fe3O4 Powders. *Ceram. Int.* **2017**, *43* (10), 7448–7453.

(45) Podbolotov, K. B.; Khort, A. A.; Tarasov, A. B.; Trusov, G. V.; Roslyakov, S. I.; Mukasyan, A. S. Solution Combustion Synthesis of Copper Nanopowders: The Fuel Effect. *Combust. Sci. Technol.* **2017**, *189* (11), 1878–1890.

(46) Khort, A.; Podbolotov, K.; Serrano-García, R.; Gun'ko, Y. K. One-Step Solution Combustion Synthesis of Pure Ni Nanopowders with Enhanced Coercivity: The Fuel Effect. *J. Solid State Chem.* **2017**, *253* (March), 270–276.

(47) Deganello, F.; Tyagi, A. K. Solution Combustion Synthesis, Energy and Environment: Best Parameters for Better Materials. *Prog. Cryst. Growth Charact. Mater.* **2018**, *64* (2), 23–61.

(48) Erri, P.; Pranda, P.; Varma, A. Oxidizer−Fuel Interactions in Aqueous Combustion Synthesis. 1. Iron(III) Nitrate−Model Fuels. *Ind. Eng. Chem. Res.* **2004**, *43* (12), 3092–3096.

(49) Azadmanjiri, J.; Seyyed Ebrahimi, S. A. The Effects of PH and Citric Acid Concentration on the Characteristics of Nanocrystalline NiFe2O4 Powder Synthesized by a Sol-Gel Autocombustion Method. *Phys. Met. Metallogr.* **2006**, *102* (S1), S21–S23.

(50) Tsay, J.; Fang, T. Effects of Molar Ratio of Citric Acid to Cations and of PH Value on the Formation and Thermal-Decomposition Behavior of Barium Titanium Citrate. *J. Am. Ceram. Soc.* **2004**, *82* (6), 1409–1415.

(51) Vaqueiro, P.; López-Quintela, M. A. Influence of Complexing Agents and PH on Yttrium−Iron Garnet Synthesized by the Sol−Gel Method. *Chem. Mater.* **1997**, *9* (12), 2836–2841.

(52) Pavithra, N. S.; Lingaraju, K.; Raghu, G. K.; Nagaraju, G. Citrus Maxima (Pomelo) Juice Mediated Eco-Friendly Synthesis of ZnO Nanoparticles: Applications to Photocatalytic, Electrochemical Sensor and Antibacterial Activities. *Spectrochim. Acta Part A Mol. Biomol. Spectrosc.* **2017**, *185*, 11–19.

(53) Yu, X.; An, X. Enhanced Magnetic and Optical Properties of Pure and (Mn, Sr) Doped BiFeO3 Nanocrystals. *Solid State Commun.* **2009**, *149* (17–18), 711–714.

(54) Gaidamavičienė, G.; Abakevičienė, B.; Žalga, A. Oxalic Acid Assisted Synthesis of the Gadolinium-Doped Ceria Oxide-Ion Conductor as Electrolyte for the Solid Oxide Fuel Cells. *Chem. Pap.* **2019**, *73* (4), 891–899.

(55) Jian, X. M.; Wenren, H. Q.; Huang, S.; Shi, S. J.; Wang, X. L.; Gu, C. D.; Tu, J. P. Oxalic Acid-Assisted Combustion Synthesized LiVO3 Cathode Material for Lithium Ion Batteries. *J. Power Sources* **2014**, *246*, 417–422.

(56) Nassar, M. Y.; Mohamed, T. Y.; Ahmed, I. S.; Samir, I. MgO Nanostructure via a Sol-Gel Combustion Synthesis Method Using Different Fuels: An Efficient Nano-Adsorbent for the Removal of Some Anionic Textile Dyes. *J. Mol. Liq.* **2017**, *225*, 730–740.

(57) Amaral, F.; Valente, M.; Costa, L. C. Synthesis and Characterization of Calcium Copper Titanate Obtained by Ethylenediaminetetraacetic Acid Gel Combustion. *Mater. Chem. Phys.* **2010**, *124* (1), 580–586.

(58) ten Donkelaar, S. F. P.; Ruhl, R.; Veldhuis, S. A.; Nijmeijer, A.; Winnubst, L.; Bouwmeester, H. J. M. Auto-Combustion Synthesis of Perovskite-Type Oxides SrTi1−xFexO3−δ. *Ceram. Int.* **2015**, *41* (10), 13709–13715.

(59) Gardey Merino, M. C.; Lascalea, G. E.; Sánchez, L. M.; Vázquez, P. G.; Cabanillas, E. D.; Lamas, D. G. Nanostructured Aluminium Oxide Powders Obtained by Aspartic Acid–

Nitrate Gel-Combustion Routes. *J. Alloys Compd.* **2010**, *495* (2), 578–582.

(60) Merino, M. C. G.; RominaArreche; Lassa, M. S.; Lascalea, G. E.; Estrella, A.; Rodriguez, M. E. Combustion Synthesis of Co-Cu-Mn Oxides Deploying Different Fuels. *Matéria (Rio Janeiro)* **2015**, *20* (3), 779–786.

(61) Merino, M. C. G.; Palermo, M.; Belda, R.; Rapp, M. E. F. de; Lascalea, G. E.; Vázquez, P. G. Combustion Synthesis of Co3O4 Nanoparticles: Fuel Ratio Effect on the Physical Properties of the Resulting Powders. *Procedia Mater. Sci.* **2012**, *1*, 588–593.

(62) Mukherjee, S. T.; Bedekar, V.; Patra, A.; Sastry, P. U.; Tyagi, A. K. Study of Agglomeration Behavior of Combustion-Synthesized Nano-Crystalline Ceria Using New Fuels. *J. Alloys Compd.* **2008**, *466* (1–2), 493–497.

(63) Park, K.; Heo, M. H.; Kim, K. Y.; Dhoble, S. J.; Kim, Y.; Kim, J. Y. Synthesized By Solution Combustion Method. *Powder Technol.* **2013**, *237* (3), 102–106.

(64) Vijaya Bhasker Reddy, P.; Ramesh, B.; Gopal Reddy, C. Electrical Conductivity and Dielectric Properties of Zinc Substituted Lithium Ferrites Prepared by Sol–Gel Method. *Phys. B Condens. Matter* **2010**, *405* (7), 1852–1856.

(65) Leppäniemi, J.; Eiroma, K.; Majumdar, H.; Alastalo, A. Far-UV Annealed Inkjet-Printed In 2 O 3 Semiconductor Layers for Thin-Film Transistors on a Flexible Polyethylene Naphthalate Substrate. *ACS Appl. Mater. Interfaces* **2017**, *9* (10), 8774–8782.

(66) Wang, B.; Zeng, L.; Huang, W.; Melkonyan, F. S.; Sheets, W. C.; Chi, L.; Bedzyk, M. J.; Marks, T. J.; Facchetti, A. Carbohydrate-Assisted Combustion Synthesis To Realize High-Performance Oxide Transistors. *J. Am. Chem. Soc.* **2016**, *138* (22), 7067–7074.

(67) Wang, B.; Leonardi, M. J.; Huang, W.; Chen, Y.; Zeng, L.; Eckstein, B. J.; Marks, T. J.; Facchetti, A. Marked Cofuel Tuning of Combustion Synthesis Pathways for Metal Oxide Semiconductor Films. *Adv. Electron. Mater.* **2019**, *5* (10), 1900540.

(68) Huang, T.; Zhao, C.; Qiu, Z.; Luo, J.; Hu, Z. Hierarchical Porous ZnMn 2 O 4 Synthesized by the Sucrose-Assisted Combustion Method for High-Rate Supercapacitors. *Ionics (Kiel).* **2017**, *23* (1), 139–146.

(69) Ajamein, H.; Haghighi, M.; Alaei, S. The Role of Various Fuels on Microwave-Enhanced Combustion Synthesis of CuO/ZnO/Al2O3 Nanocatalyst Used in Hydrogen Production via Methanol Steam Reforming. *Energy Convers. Manag.* **2017**, *137*, 61–73.

(70) Zhang, J.; Guo, Q.; Liu, Y.; Cheng, Y. Preparation and Characterization of Fe 2 O 3 /Al 2 O 3 Using the Solution Combustion Approach for Chemical Looping Combustion. *Ind. Eng. Chem. Res.* **2012**, *51* (39), 12773–12781.

(71) Kang, W.; Varma, A. Hydrogen Generation from Hydrous Hydrazine over Ni/CeO2 Catalysts Prepared by Solution Combustion Synthesis. *Appl. Catal. B Environ.* **2018**, *220* (April 2017), 409–416.

(72) Gilabert, J.; Palacios, M. D.; Sanz, V.; Mestre, S. Fuel Effect on Solution Combustion Synthesis of Co(Cr,Al) 2 O 4 Pigments. *Boletín la Soc. Española Cerámica y Vidr.* **2017**, *56* (5), 215–225.

(73) GarcÍa, R.; Hirata, G. A.; McKittrick, J. New Combustion Synthesis Technique for the Production of (In x Ga 1− x) 2 O 3 Powders: Hydrazine/Metal Nitrate Method. *J. Mater. Res.* **2001**, *16* (4), 1059–1065.

(74) TAKEDA, T.; KATO, K.; KIKKAWA, S. Gel Combustion Synthesis of Rare Earth Aluminate Using Glycine or Urea. *J. Ceram. Soc. Japan* **2007**, *115* (1346), 588–591.

(75) Zhuravlev, V. D.; Bamburov, V. G.; Beketov, A. R.; Perelyaeva, L. A.; Baklanova, I. V.;

Sivtsova, O. V.; Vasil'ev, V. G.; Vladimirova, E. V.; Shevchenko, V. G.; Grigorov, I. G. Solution Combustion Synthesis of α-Al2O3 Using Urea. *Ceram. Int.* **2013**, *39* (2), 1379–1384.

(76) Chandradass, J.; Balasubramanian, M.; Bae, D. sik; Kim, K. H. Effect of Different Fuels on the Alumina-Ceria Composite Powders Synthesized by Sol-Gel Auto Combustion Method. *J. Alloys Compd.* **2009**, *479* (1–2), 363–367.

(77) Epifani, M.; Melissano, E.; Pace, G.; Schioppa, M. Precursors for the Combustion Synthesis of Metal Oxides from the Sol–Gel Processing of Metal Complexes. *J. Eur. Ceram. Soc.* **2007**, *27* (1), 115–123.

(78) Salgueiro, D.; Kiazadeh, A.; Branquinho, R.; Santos, L.; Barquinha, P.; Martins, R.; Fortunato, E. Solution Based Zinc Tin Oxide TFTs: The Dual Role of the Organic Solvent. *J. Phys. D. Appl. Phys.* **2017**, *50* (6), 065106.

(79) Lyagaeva, J.; Danilov, N.; Korona, D.; Farlenkov, A.; Medvedev, D.; Demin, A.; Animitsa, I.; Tsiakaras, P. Improved Ceramic and Electrical Properties of CaZrO 3 -Based Proton-Conducting Materials Prepared by a New Convenient Combustion Synthesis Method. *Ceram. Int.* **2017**, *43* (9), 7184–7192.

(80) Banerjee, S.; Kumar, A.; Sujatha Devi, P. Preparation of Nanoparticles of Oxides by the Citrate–Nitrate Process. *J. Therm. Anal. Calorim.* **2011**, *104* (3), 859–867.

(81) Deganello, F.; Marcì, G.; Deganello, G. Citrate–Nitrate Auto-Combustion Synthesis of Perovskite-Type Nanopowders: A Systematic Approach. *J. Eur. Ceram. Soc.* **2009**, *29* (3), 439–450.

(82) Chourashiya, M. G.; Urakawa, A. Solution Combustion Synthesis of Highly Dispersible and Dispersed Iridium Oxide as an Anode Catalyst in PEM Water Electrolysis. *J. Mater. Chem. A* **2017**, *5* (10), 4774–4778.

(83) Kim, S. J.; Yoon, S.; Kim, H. J. Review of Solution-Processed Oxide Thin-Film Transistors. *Jpn. J. Appl. Phys.* **2014**, *53* (2S), 02BA02.

(84) Vijayadarshan, P.; Mohan, T.; Viswanath, J.; Venugopal, K. J.; Rao, N. V; Gupta, A.; Venkataraman, A. Large Scale Synthesis of Nickel Oxide (Nio) by Self Propagated Combustion Reaction. *Mater. Sci. Res. India* **2017**, *14* (1), 37–42.

(85) Ortega-San-Martín, L.; Vidal, K.; Roldán-Pozo, B.; Coello, Y.; Larrañaga, A.; Arriortua, M. I. Synthesis Method Dependence of the Lattice Effects in Ln 0.5 M 0.5 FeO 3 Perovskites (Ln = La and (Nd or Gd); M = Ba and (Ca or Sr)). *Mater. Res. Express* **2016**, *3* (5), 056302.

(86) Nair, S. R.; Purohit, R. D.; Sinha, P. K.; Tyagi, A. K. Sr-Doped LaCoO3 through Acetate–Nitrate Combustion: Effect of Extra Oxidant NH4NO3. *J. Alloys Compd.* **2009**, *477* (1–2), 644–647.

(87) Pourgolmohammad, B.; Masoudpanah, S. M.; Aboutalebi, M. R. Synthesis of CoFe 2 O 4 Powders with High Surface Area by Solution Combustion Method: Effect of Fuel Content and Cobalt Precursor. *Ceram. Int.* **2017**, *43* (4), 3797–3803.

(88) Deshpande, K.; Mukasyan, A.; Varma, A. Direct Synthesis of Iron Oxide Nanopowders by the Combustion Approach: Reaction Mechanism and Properties. *Chem. Mater.* **2004**, *16* (24), 4896–4904.

(89) Manukyan, K. V.; Chen, Y.-S. S.; Rouvimov, S.; Li, P.; Li, X.; Dong, S.; Liu, X.; Furdyna, J. K.; Orlov, A.; Bernstein, G. H.; Porod, W.; Roslyakov, S.; Mukasyan, A. S. Ultrasmall α-Fe2O3 Superparamagnetic Nanoparticles with High Magnetization Prepared by Template-Assisted Combustion Process. *J. Phys. Chem. C* **2014**, *118* (29), 16264–16271.

(90) Burgos-Montes, O.; Moreno, R.; Colomer, M. T. T.; Fariñas, J. C. C. Influence of Combustion Aids on Suspension Combustion Synthesis of Mullite Powders. *J. Eur. Ceram. Soc.* **2006**, *26* (15), 3365–3372.

(91) Fraigi, L. B.; Lamas, D. G.; Walsöe de Reca, N. E. Comparison between Two Combustion Routes for the Synthesis of Nanocrystalline SnO2 Powders. *Mater. Lett.* **2001**, *47* (4–5), 262–266.

(92) Carlos, E.; Branquinho, R.; Kiazadeh, A.; Martins, J.; Barquinha, P.; Martins, R.; Fortunato, E. Boosting Electrical Performance of High-κ Nanomultilayer Dielectrics and Electronic Devices by Combining Solution Combustion Synthesis and UV Irradiation. *ACS Appl. Mater. Interfaces* **2017**, *9* (46), 40428–40437.

(93) Chen, R.; Lan, L. Solution-Processed Metal-Oxide Thin-Film Transistors: A Review of Recent Developments. *Nanotechnology* **2019**, *30* (31), 312001.

(94) Yuvaraj, S.; Fan-Yuan, L.; Tsong-Huei, C.; Chuin-Tih, Y. Thermal Decomposition of Metal Nitrates in Air and Hydrogen Environments. *J. Phys. Chem. B* **2003**, *107* (4), 1044–1047.

(95) Lim, K.-H.; Lee, J.; Huh, J.-E.; Park, J.; Lee, J.-H.; Lee, S.-E.; Kim, Y. S. A Systematic Study on Effects of Precursors and Solvents for Optimization of Solution-Processed Oxide Semiconductor Thin-Film Transistors. *J. Mater. Chem. C* **2017**, *5* (31), 7768–7776.

(96) Addison, C. C.; Logan, N. Anhydrous Metal Nitrates. In *Advances in Inorganic Chemistry and Radiochemistry*; 1964; Vol. 6, pp 71–142.

(97) L'vov, B. V. The Physical Approach to the Interpretation of the Kinetics and Mechanisms of Thermal Decomposition of Solids: The State of the Art. *Thermochim. Acta* **2001**, *373* (2), 97–124.

(98) Rayner-canham, G. *Descriptive Inorganic Chemistry*; Elsevier, 2016.

(99) Cochran, E. A.; Woods, K. N.; Johnson, D. W.; Page, C. J.; Boettcher, S. W. Unique Chemistries of Metal-Nitrate Precursors to Form Metal-Oxide Thin Films from Solution: Materials for Electronic and Energy Applications. *J. Mater. Chem. A* **2019**, *7* (42), 24124–24149.

(100) Cochran, E. A.; Park, D.-H.; Kast, M. G.; Enman, L. J.; Perkins, C. K.; Mansergh, R. H.; Keszler, D. A.; Johnson, D. W.; Boettcher, S. W. Role of Combustion Chemistry in Low-Temperature Deposition of Metal Oxide Thin Films from Solution. *Chem. Mater.* **2017**, *29* (21), 9480–9488.

(101) Rudolph, W. W.; Irmer, G. Hydration and Ion Pair Formation in Common Aqueous La(<scp>iii</Scp>) Salt Solutions – a Raman Scattering and DFT Study. *Dalt. Trans.* **2015**, *44* (1), 295–305.

(102) Rudolph, W. W.; Irmer, G. Hydration and Ion Pair Formation in Aqueous Y 3+ –Salt Solutions. *Dalt. Trans.* **2015**, *44* (42), 18492–18505.

(103) Rudolph, W. W.; Mason, R.; Pye, C. C. Aluminium(III) Hydration in Aqueous Solution. A Raman Spectroscopic Investigation and an Ab Initio Molecular Orbital Study of Aluminium(III) Water Clusters. *Phys. Chem. Chem. Phys.* **2000**, *2* (22), 5030–5040.

(104) Rudolph, W. W.; Fischer, D.; Tomney, M. R.; Pye, C. C. Indium(<scp>iii</Scp>) Hydration in Aqueous Solutions of Perchlorate, Nitrate and Sulfate. Raman and Infrared Spectroscopic Studies and Ab-Initio Molecular Orbital Calculations of Indium(<scp>iii</Scp>)–Water Clusters. *Phys. Chem. Chem. Phys.* **2004**, *6* (22), 5145–5155.

(105) Marcus, Y. Thermodynamics of Solvation of Ions. Part 5.—Gibbs Free Energy of Hydration at 298.15 K. *J. Chem. Soc., Faraday Trans.* **1991**, *87* (18), 2995–2999.

(106) Richens, D. *The Chemistry of Aqua Ions: Synthesis, Structure and Reactivity: A Tour Through the Periodic Table of the Elements*; Wiley, 1997.

(107) Varma, A.; Mukasyan, A. S.; Rogachev, A. S.; Manukyan, K. V. Solution Combustion Synthesis of Nanoscale Materials. *Chem. Rev.* **2016**, *116* (23), 14493–14586.

(108) Pine, T.; Lu, X.; Mumm, D. R.; Samuelsen, G. S.; Brouwer, J. Emission of Pollutants from Glycine–Nitrate Combustion Synthesis Processes. *J. Am. Ceram. Soc.* **2007**, *90* (12), 071019062949002-???

(109) Jorgensen, C. K. *Inorganic Complexes*; Academic Press: London, 1963.

(110) Livage, J. Sol–Gel Synthesis of Heterogeneous Catalysts from Aqueous Solutions. *Catal. Today* **1998**, *41* (1–3), 3–19.

(111) Henry, M.; Jolivet, J. P.; Livage, J. Aqueous Chemistry of Metal Cations: Hydrolysis, Condensation and Complexation. In *Chemistry, Spectroscopy and Applications of Sol-Gel Glasses*; Springer-Verlag: Berlin/Heidelberg, 2006; pp 153–206.

(112) Pourgolmohammad, B.; Masoudpanah, S. M.; Aboutalebi, M. R. Effect of Starting Solution Acidity on the Characteristics of CoFe 2 O 4 Powders Prepared by Solution Combustion Synthesis. *J. Magn. Magn. Mater.* **2017**, *424*, 352–358.

(113) Junliang, L.; Wei, Z.; Cuijing, G.; Yanwei, Z. Synthesis and Magnetic Properties of Quasi-Single Domain M-Type Barium Hexaferrite Powders via Sol–Gel Auto-Combustion: Effects of PH and the Ratio of Citric Acid to Metal Ions (CA/M). *J. Alloys Compd.* **2009**, *479* (1–2), 863–869.

(114) Pathak, L. .; Singh, T. .; Das, S.; Verma, A. .; Ramachandrarao, P. Effect of PH on the Combustion Synthesis of Nano-Crystalline Alumina Powder. *Mater. Lett.* **2002**, *57* (2), 380–385.

(115) Yu, L.; Cao, S.; Liu, Y.; Wang, J.; Jing, C.; Zhang, J. Thermal and Structural Analysis on the Nanocrystalline NiCuZn Ferrite Synthesis in Different Atmospheres. *J. Magn. Magn. Mater.* **2006**, *301* (1), 100–106.

(116) Fragnaud, P.; Nagarajan, R.; Schleich, D. M.; Vujic, D. Thin-Film Cathodes for Secondary Lithium Batteries. *J. Power Sources* **1995**, *54* (2), 362–366.

(117) Pathak, T. K.; Kumar, A.; Swart, C. W.; Swart, H. C.; Kroon, R. E. Effect of Fuel Content on Luminescence and Antibacterial Properties of Zinc Oxide Nanocrystalline Powders Synthesized by the Combustion Method. *RSC Adv.* **2016**, *6* (100), 97770–97782.

(118) Sutka, A.; Mezinskis, G. Sol-Gel Auto-Combustion Synthesis of Spinel-Type Ferrite Nanomaterials. *Front. Mater. Sci.* **2012**, *6* (2), 128–141.

(119) Deganello, F.; Tummino, M. L.; Calabrese, C.; Testa, M. L.; Avetta, P.; Fabbri, D.; Prevot, A. B.; Montoneri, E.; Magnacca, G. A New, Sustainable LaFeO 3 Material Prepared from Biowaste-Sourced Soluble Substances. *New J. Chem.* **2015**, *39* (2), 877–885.

(120) Ghose, R.; Hwang, H. T.; Varma, A. Oxidative Coupling of Methane Using Catalysts Synthesized by Solution Combustion Method. *Appl. Catal. A Gen.* **2013**, *452*, 147–154.

(121) Sertkol, M.; Köseoğlu, Y.; Baykal, A.; Kavas, H.; Toprak, M. S. Synthesis and Magnetic Characterization of Zn0.7Ni0.3Fe2O4 Nanoparticles via Microwave-Assisted Combustion Route. *J. Magn. Magn. Mater.* **2010**, *322* (7), 866–871.

(122) Muhammed Ali, S. A.; Anwar, M.; Somalu, M. R.; Muchtar, A. Enhancement of the Interfacial Polarization Resistance of La 0.6 Sr 0.4 Co 0.2 Fe 0.8 O 3-δ Cathode by Microwave-Assisted Combustion Method. *Ceram. Int.* **2017**, *43* (5), 4647–4654.

(123) Radpour, M.; Masoudpanah, S. M.; Alamolhoda, S. Microwave-Assisted Solution

Combustion Synthesis of Fe3O4 Powders. *Ceram. Int.* **2017**, *43* (17), 14756–14762.

(124) G., R.; R., S.; K., S. Microwave Combustion Method: Effect of Starch, Urea and Glycine as Processing Fuels in the Co 3 O 4 Nanostructures. *Opt. - Int. J. Light Electron Opt.* **2018**, *153*, 73–80.

(125) Cheng, B.; Zhang, Z.; Liu, H.; Han, Z.; Xiao, Y.; Lei, S. Power- and Energy-Dependent Photoluminescence of Eu3+ Incorporated and Segregated ZnO Polycrystalline Nanobelts Synthesized by a Facile Combustion Method Followed by Heat Treatment. *J. Mater. Chem.* **2010**, *20* (36), 7821.

(126) Cheng, B.; Zhang, Z.; Han, Z.; Xiao, Y.; Lei, S. SrAl 2 O 4 :Eu 2+ ,Dy 3+ Nanobelts: Synthesis by Combustion and Properties of Long-Persistent Phosphorescence. *J. Mater. Res.* **2011**, *26* (17), 2311–2315.

(127) Dhiman, P.; Kumar, A.; Singh, M. Solution Combustion Preparation Of Fe2O3- Nano-Flakes: Synthesis And Characterization. *Adv. Mater. Lett.* **2012**, *3* (4), 330–333.

(128) Vijayakumar, S.; Nagamuthu, S.; Muralidharan, G. Supercapacitor Studies on NiO Nanoflakes Synthesized Through a Microwave Route. *ACS Appl. Mater. Interfaces* **2013**, *5* (6), 2188–2196.

(129) Ko¨seoğlu, Y.; Celaleddin Durmaz, Y.; Yilgin, R. Rapid Synthesis and Room Temperature Ferromagnetism of Ni Doped ZnO DMS Nanoflakes. *Ceram. Int.* **2014**, *40* (7), 10685–10691.

(130) Umar, A.; Kumar, R.; Akhtar, M. S.; Kumar, G.; Kim, S. H. Growth and Properties of Well-Crystalline Cerium Oxide (CeO2) Nanoflakes for Environmental and Sensor Applications. *J. Colloid Interface Sci.* **2015**, *454*, 61–68.

(131) Murugan, K.; Samidoss, C. M.; Theerthagiri, J.; Panneerselvam, C.; Madhavan, J.; Rajasekar, A.; Canale, A.; Benelli, G. Solution Combustion Synthesis of Hierarchically Structured V 2 O 5 Nanoflakes: Efficacy Against Plasmodium Falciparum, Plasmodium Berghei and the Malaria Vector Anopheles Stephensi. *J. Clust. Sci.* **2017**, *28* (4), 2337–2348.

(132) Arun Kumar, N. B.; Mahendra, B.; Sirajudeeen, J.; Anil Kumar, M. R.; Nagaswarupa, H. P.; Ravi Kumar, C. R.; Umesh, B. Green Mediated Synthesis of MgO Nano-Flakes and Its Electro-Chemical Applications. *Mater. Today Proc.* **2018**, *5* (10), 22275–22282.

(133) Goel, S.; Tomar, A. K.; Sharma, R. K.; Singh, G. Highly Pseudocapacitive NiO Nanoflakes through Surfactant-Free Facile Microwave-Assisted Route. *ACS Appl. Energy Mater.* **2018**, *1* (4), 1540–1548.

(134) Umadevi, M.; Jegatha Christy, A. Synthesis, Characterization and Photocatalytic Activity of CuO Nanoflowers. *Spectrochim. Acta Part A Mol. Biomol. Spectrosc.* **2013**, *109*, 133–137.

(135) Kumar, A. R.; Kumar, R.; Chakra, C. S.; Rao, K. V. Silver Doped Manganese -Zinc – Ferrite Nano Flowers for Biomedical Applications. *Int J Emerg. Technol Adv Eng* **2014**, *5* (June), 2250–2459.

(136) Mousavi, S. F.; Davar, F.; Loghman-Estarki, M. R. Controllable Synthesis of ZnO Nanoflowers by the Modified Sol–Gel Method. *J. Mater. Sci. Mater. Electron.* **2016**, *27* (12), 12985–12995.

(137) Karthik, K.; Pradeeswari, K.; Mohan Kumar, R.; Murugesan, R. Microwave-Assisted V 2 O 5 Nanoflowers for Efficient Lithium-Ion Battery. *Mater. Res. Innov.* **2019**, *00* (00), 1–5.

(138) Wang, X.; Qin, M.; Fang, F.; Jia, B.; Wu, H.; Qu, X.; Volinsky, A. A. Solution

Combustion Synthesis of Nanostructured Iron Oxides with Controllable Morphology, Composition and Electrochemical Performance. *Ceram. Int.* **2018**, *44* (4), 4237–4247.

(139) Huang, M.; Qin, M.; Chen, P.; Jia, B.; Chen, Z.; Li, R.; Liu, Z.; Qu, X. Facile Preparation of Network-like Porous Hematite (α-Fe 2 O 3) Nanosheets via a Novel Combustion-Based Route. *Ceram. Int.* **2016**, *42* (8), 10380–10388.

(140) Senthilkumar, B.; Selvan, R. K.; Vasylechko, L.; Minakshi, M. Synthesis, Crystal Structure and Pseudocapacitor Electrode Properties of γ-Bi2MoO6 Nanoplates. *Solid State Sci.* **2014**, *35*, 18–27.

(141) Jiang, D.; Wang, H.; Li, G.; Li, G.; Lan, X.; Abib, M. H.; Zhang, Z.; Jiang, Y. Self-Combustion Synthesis and Ion Diffusion Performance of NaV 6 O 15 Nanoplates as Cathode Materials for Sodium-Ion Batteries. *J. Electrochem. Soc.* **2015**, *162* (4), A697–A703.

(142) Kumari, K. Magnetic and Dielectric Properties of Fe 3 BO 6 Nanoplates Prepared through Self-Combustion Method. *J. Adv. Dielectr.* **2017**, *07* (06), 1750043.

(143) Kumari, K. Structural, Vibrational and Surface Analysis of Fe 3 BO 6 Nanoplates Synthesized by Combustion Method. *J. Mol. Struct.* **2018**, *1165*, 293–298.

(144) Christy, A. J.; Nehru, L. C.; Umadevi, M. A Novel Combustion Method to Prepare CuO Nanorods and Its Antimicrobial and Photocatalytic Activities. *Powder Technol.* **2013**, *235* (3), 783–786.

(145) Dejene, F. B.; Kebede, M. A.; Redi-Abshiro, M.; Kgarebe, B. V. Structural and Photoluminescence Properties of Dy3+ Co-Doped and Eu2+ Activated MAl2O4 (M=Ba,Ca,Sr) Nanophosphors. *Opt. Mater. (Amst).* **2013**, *35* (11), 1927–1931.

(146) Chen, W.; Liu, M.; Lin, Y.; Liu, Y.; Yu, L.; Li, T.; Hong, J. A Novel Synthesis Route to Sn1−xRExO2−x/2 Nanorods via Microwave-Induced Salt-Assisted Solution Combustion Process. *Ceram. Int.* **2013**, *39* (7), 7545–7549.

(147) Nagabhushana, G. P.; Chandrappa, G. T. Facile Solution Combustion Synthesis of Monoclinic VO2: A Unique and Versatile Approach. *J. Mater. Chem. A* **2013**, *1* (38), 11539.

(148) Vidya, S.; Solomon, S.; Thomas, J. K. Synthesis and Characterisation of MoO3 and WO3 Nanorods for Low Temperature Co-Fired Ceramic and Optical Applications. *J. Mater. Sci. Mater. Electron.* **2015**, *26* (5), 3243–3255.

(149) Prakash, N. G.; Dhananjaya, M.; Narayana, A. L.; Shaik, D. P.; Rosaiah, P.; Hussain, O. M. High Performance One Dimensional α-MoO3 Nanorods for Supercapacitor Applications. *Ceram. Int.* **2018**, *44* (8), 9967–9975.

(150) Tao, X.; Wang, X.; Li, X. Nanomechanical Characterization of One-Step Combustion-Synthesized Al 4 B 2 O 9 and Al 18 B 4 O 33 Nanowires. *Nano Lett.* **2007**, *7* (10), 3172–3176.

(151) Al-Hazmi, F.; Alnowaiser, F.; Al-Ghamdi, A. A.; Al-Ghamdi, A. A.; Aly, M. M.; Al-Tuwirqi, R. M.; El-Tantawy, F. A New Large – Scale Synthesis of Magnesium Oxide Nanowires: Structural and Antibacterial Properties. *Superlattices Microstruct.* **2012**, *52* (2), 200–209.

(152) Wen, W.; Yao, J.-C.; Jiang, C.-C.; Wu, J.-M. Solution-Combustion Synthesis of Nanomaterials for Lithium Storage. *Int. J. Self-Propagating High-Temperature Synth.* **2017**, *26* (3), 187–198.

(153) Albohani, S.; Minakshi Sundaram, M.; Laird, D. W. Egg Shell Membrane Template Stabilises Formation of β-NiMoO4 Nanowires and Enhances Hybrid Supercapacitor

Behaviour. *Mater. Lett.* **2019**, *236*, 64–68.

(154) Chen, P.; Qin, M.; Liu, Y.; Jia, B.; Cao, Z.; Wan, Q.; Qu, X. Superior Optical Properties of Fe 3+ –W 18 O 49 Nanoparticles Prepared by Solution Combustion Synthesis. *New J. Chem.* **2015**, *39* (2), 1196–1201.

(155) Dasgupta, N. P.; Sun, J.; Liu, C.; Brittman, S.; Andrews, S. C.; Lim, J.; Gao, H.; Yan, R.; Yang, P. 25th Anniversary Article: Semiconductor Nanowires - Synthesis, Characterization, and Applications. *Adv. Mater.* **2014**, *26* (14), 2137–2184.

(156) Mangalaraja, R. V.; Mouzon, J.; Hedström, P.; Kero, I.; Ramam, K. V. S.; Camurri, C. P.; Odén, M. Combustion Synthesis of Y2O3 and Yb–Y2O3. *J. Mater. Process. Technol.* **2008**, *208* (1–3), 415–422.

(157) Jung, C.-H.; Kim, Y.-K.; Han, Y.-M.; Lee, S.-J. Effects of Fuel to Synthesis of CaTiO 3 by Solution Combustion Synthesis for High-Level Nuclear Waste Ceramics. *J. Nanosci. Nanotechnol.* **2016**, *16* (2), 1676–1679.

(158) Laishram, K.; Mann, R.; Malhan, N. A Novel Microwave Combustion Approach for Single Step Synthesis of α-Al2O3 Nanopowders. *Ceram. Int.* **2012**, *38* (2), 1703–1706.

(159) Khimich, N. N.; Poddenezhnyi, E. N.; Boiko, A. A.; Zdravkov, A. V.; Ugolkov, V. L.; Koptelova, L. A.; Grishkova, E. I.; Dobrodei, A. O. Synthesis of Nanopowders of Yttrium Aluminum Garnet Doped by Cerium(III). *Glas. Phys. Chem.* **2009**, *35* (5), 504–510.

(160) Lubis, S.; Sheilatina; Murisna. Synthesis, Characterization and Photocatalytic Activity of α-Fe 2 O 3 /Bentonite Composite Prepared by Mechanical Milling. *J. Phys. Conf. Ser.* **2018**, *1116* (4), 042016.

(161) Reddy, A. J.; Kokila, M. K.; Nagabhushana, H.; Chakradhar, R. P. S.; Shivakumara, C.; Rao, J. L.; Nagabhushana, B. M. Structural, Optical and EPR Studies on ZnO:Cu Nanopowders Prepared via Low Temperature Solution Combustion Synthesis. *J. Alloys Compd.* **2011**, *509* (17), 5349–5355.

(162) Chandradass, J.; Kim, K. H. Mixture of Fuels Approach for the Solution Combustion Synthesis of LaAlO3 Nanopowders. *Adv. Powder Technol.* **2010**, *21* (2), 100–105.

(163) Shi, S.; Yang, Y.; Guo, P.; Wang, J.; Geng, L.; Fu, L. Improved Morphology and Optimized Luminescence of Eu3+-Doped La2Ce2O7 Composite Nanopowders by Surfactant-Assisted Solution Combustion Synthesis. *J. Lumin.* **2019**, *206*, 91–96.

(164) Madhusudhana, H. C.; Shobhadevi, S. N.; Nagabhushana, B. M.; Murugendrappa, M. V.; Hari Krishna, R.; Nagabhushana, H. A Comparable Study of Structural, Dielectric and Humidity Sensing Properties of Solution Combustion Synthesized ZrO2 and ZrTiO4 Nano Powders. *J. Nanosci. Technol.* **2018**, *4* (1), 314–316.

(165) Li, F.; Zhao, Y.; Liu, Y.; Hao, Y.; Liu, R.; Zhao, D. Solution Combustion Synthesis and Visible Light-Induced Photocatalytic Activity of Mixed Amorphous and Crystalline MgAl2O4 Nanopowders. *Chem. Eng. J.* **2011**, *173* (3), 750–759.

(166) Chen, W.; Li, F.; Yu, J.; Liu, L. A Facile and Novel Route to High Surface Area Ceria-Based Nanopowders by Salt-Assisted Solution Combustion Synthesis. *Mater. Sci. Eng. B* **2006**, *133* (1–3), 151–156.

(167) Nagabhushana, B. M.; Chakradhar, R. P. S.; Ramesh, K. P.; Prasad, V.; Shivakumara, C.; Chandrappa, G. T. Effect of Fuel on the Formation Structure, Transport and Magnetic Properties of LaMnO 3+ δ Nanopowders. *Philos. Mag.* **2010**, *90* (15), 2009–2025.

(168) Aali, H.; Azizi, N.; Baygi, N. J.; Kermani, F.; Mashreghi, M.; Youssefi, A.; Mollazadeh, S.; Khaki, J. V.; Nasiri, H. High Antibacterial and Photocatalytic Activity of Solution Combustion Synthesized Ni0.5Zn0.5Fe2O4 Nanoparticles: Effect of Fuel to Oxidizer

Ratio and Complex Fuels. *Ceram. Int.* **2019**, *45* (15), 19127–19140.

(169) Gu, S.; Qin, M.; Zhang, H.; Ma, J. Fabrication of La2O3 Uniformly Doped Mo Nanopowders by Solution Combustion Synthesis Followed by Reduction under Hydrogen. *Materials (Basel).* **2018**, *11* (12), 2385.

(170) Ahmad, M.; Ahmed, E.; Zhang, Y.; Khalid, N. R.; Xu, J.; Ullah, M.; Hong, Z. Preparation of Highly Efficient Al-Doped ZnO Photocatalyst by Combustion Synthesis. *Curr. Appl. Phys.* **2013**, *13* (4), 697–704.

(171) Yang, J.; Li, X.; Zhou, J.; Tang, Y.; Zhang, Y.; Li, Y. Factors Controlling Pure-Phase Magnetic BiFeO3 Powders Synthesized by Solution Combustion Synthesis. *J. Alloys Compd.* **2011**, *509* (37), 9271–9277.

(172) Wu, H.; Qin, M.; Cao, Z.; Li, X.; Jia, B.; Chen, P.; Huang, M.; Qu, X. Direct Synthesis of Vanadium Oxide Nanopowders by the Combustion Approach. *Chem. Phys. Lett.* **2018**, *706*, 7–13.

(173) Nguyen, T.-S.; Postole, G.; Loridant, S.; Bosselet, F.; Burel, L.; Aouine, M.; Massin, L.; Gélin, P.; Morfin, F.; Piccolo, L. Ultrastable Iridium–Ceria Nanopowders Synthesized in One Step by Solution Combustion for Catalytic Hydrogen Production. *J. Mater. Chem. A* **2014**, *2* (46), 19822–19832.

(174) Ianoş, R.; Tăculescu, A.; Păcurariu, C.; Lazău, I. Solution Combustion Synthesis and Characterization of Magnetite, Fe 3 O 4 , Nanopowders. *J. Am. Ceram. Soc.* **2012**, *95* (7), 2236–2240.

(175) Suresh, D.; Udayabhanu; Nethravathi, P. C.; Lingaraju, K.; Rajanaika, H.; Sharma, S. C.; Nagabhushana, H. EGCG Assisted Green Synthesis of ZnO Nanopowders: Photodegradative, Antimicrobial and Antioxidant Activities. *Spectrochim. Acta Part A Mol. Biomol. Spectrosc.* **2015**, *136* (PC), 1467–1474.

(176) Azam, A.; Jawad, A.; Ahmed, A. S.; Chaman, M.; Naqvi, A. H. Structural, Optical and Transport Properties of Al3+ Doped BiFeO3 Nanopowder Synthesized by Solution Combustion Method. *J. Alloys Compd.* **2011**, *509* (6), 2909–2913.

(177) Kumar, A.; Wolf, E. E.; Mukasyan, A. S. Solution Combustion Synthesis of Metal Nanopowders: Copper and Copper/Nickel Alloys. *AIChE J.* **2011**, *57* (12), 3473–3479.

(178) Reddy, A. J.; Kokila, M. K.; Nagabhushana, H.; Rao, J. L.; Shivakumara, C.; Nagabhushana, B. M.; Chakradhar, R. P. S. Combustion Synthesis, Characterization and Raman Studies of ZnO Nanopowders. *Spectrochim. Acta Part A Mol. Biomol. Spectrosc.* **2011**, *81* (1), 53–58.

(179) Chandradass, J.; Kim, K. H. Synthesis and Characterization of LaAlO3 Nanopowders by Emulsion Combustion Method. *J. Alloys Compd.* **2009**, *481* (1–2), L31–L34.

(180) Ravichandran, A. T.; Catherine Siriya Pushpa, K.; Ravichandran, K.; Karthika, K.; Nagabhushana, B. M.; Mantha, S.; Swaminathan, K. Effect of Al Doping on the Structural and Optical Properties of ZrO 2 Nanopowders Synthesized Using Solution Combustion Method. *Superlattices Microstruct.* **2014**, *75*, 533–542.

(181) Laishram, K.; Mann, R.; Malhan, N. Single Step Synthesis of Yttrium Aluminum Garnet (Y3Al5O12) Nanopowders by Mixed Fuel Solution Combustion Approach. *Ceram. Int.* **2011**, *37* (8), 3743–3746.

(182) Golsheikh, M. M.; Arabi, A. M.; Afarani, M. S. Microwave Assisted Combustion Synthesis of Photolumiescent ZnAl 2 O 4 :Eu Nano Powders. *Mater. Res. Express* **2019**, *6* (12), 125052.

(183) Ramakrishna, G.; Nagabhushana, H.; Sunitha, D. V.; Prashantha, S. C.; Sharma, S. C.;

Nagabhushana, B. M. Effect of Different Fuels on Structural, Photo and Thermo Luminescence Properties of Solution Combustion Prepared Y2SiO5 Nanopowders. *Spectrochim. Acta Part A Mol. Biomol. Spectrosc.* **2014**, *127*, 177–184.

(184) Chen, W.; Li, F.; Yu, J.; Li, Y. Novel Salt-Assisted Combustion Synthesis of High Surface Area Ceria Nanopowders by An Ethylene Glycol-Nitrate Combustion Process. *J. Rare Earths* **2006**, *24* (4), 434–439.

(185) Kumar, A.; Wolf, E. E.; Mukasyan, A. S. Solution Combustion Synthesis of Metal Nanopowders: Nickel-Reaction Pathways. *AIChE J.* **2011**, *57* (8), 2207–2214.

(186) Krsmanović, R.; Antić, Ž.; Bártová, B.; Dramićanin, M. D. Characterization of Rare-Earth Doped Lu2O3 Nanopowders Prepared with Polymer Complex Solution Synthesis. *J. Alloys Compd.* **2010**, *505* (1), 224–228.

(187) Lascalea, G. .; Lamas, D. .; Pérez, L.; Cabanillas, E. .; Walsöe de Reca, N. . Synthesis of ZrO2–15 Mol% CeO2 Nanopowders by a PH-Controlled Nitrate–Glycine Process. *Mater. Lett.* **2004**, *58* (20), 2456–2460.

(188) Vasei, H. V.; Masoudpanah, S. M.; Adeli, M.; Aboutalebi, M. R. Solution Combustion Synthesis of ZnO Powders Using CTAB as Fuel. *Ceram. Int.* **2018**, *44* (7), 7741–7745.

(189) Chandradass, J.; Kim, M. H.; Bae, D.-S. Influence of Citric Acid to Aluminium Nitrate Molar Ratio on the Combustion Synthesis of Alumina–Zirconia Nanopowders. *J. Alloys Compd.* **2009**, *470* (1–2), L9–L12.

(190) Yıldız, Ö.; Soydan, A. M.; Ata, A.; Tunaboylu, B.; Akın, D.; İpcizade, E. F. Properties of Ceria Based Novel Anode Nanopowders Synthesized by Glycine-Nitrate Process. *Acta Phys. Pol. A* **2013**, *123* (2), 432–435.

(191) Shi, S.; He, L.; Geng, L.; Jiang, L.; Wang, S.; Zhang, J.; Zhou, J. Solution Combustion Synthesis and Enhanced Luminescence of Eu3+-Activated Y2Ce2O7 Phosphor Nanopowders. *Ceram. Int.* **2015**, *41* (9), 11960–11965.

(192) Zampiva, R. Y. S.; Bergmann, C. P.; Alves, A. K.; Giorgini, L. Solution Combustion Synthesis of Mo-Fe/MgO: Influence of the Fuel Composition on the Production of Doped Catalyst Nanopowder. *IOP Conf. Ser. Mater. Sci. Eng.* **2019**, *659*, 012078.

(193) Kang, W.; Ozgur, D. O.; Varma, A. Solution Combustion Synthesis of High Surface Area CeO 2 Nanopowders for Catalytic Applications: Reaction Mechanism and Properties. *ACS Appl. Nano Mater.* **2018**, *1* (2), 675–685.

(194) Tarwal, N. L.; Jadhav, P. R.; Vanalakar, S. A.; Kalagi, S. S.; Pawar, R. C.; Shaikh, J. S.; Mali, S. S.; Dalavi, D. S.; Shinde, P. S.; Patil, P. S. Photoluminescence of Zinc Oxide Nanopowder Synthesized by a Combustion Method. *Powder Technol.* **2011**, *208* (1), 185–188.

(195) Gupta, B.; Pujar, P.; Mal, S. S.; Gupta, D.; Mandal, S. Retention of High Dielectric Constant Sodium Beta Alumina via Solution Combustion: Role of Aluminum Ions Complexation with Fuel. *Ceram. Int.* **2018**, *44* (2), 1500–1511.

(196) Sclar, H.; Kovacheva, D.; Zhecheva, E.; Stoyanova, R.; Lavi, R.; Kimmel, G.; Grinblat, J.; Girshevitz, O.; Amalraj, F.; Haik, O.; Zinigrad, E.; Markovsky, B.; Aurbach, D. On the Performance of LiNi[Sub 1/3]Mn[Sub 1/3]Co[Sub 1/3]O[Sub 2] Nanoparticles as a Cathode Material for Lithium-Ion Batteries. *J. Electrochem. Soc.* **2009**, *156* (11), A938.

(197) Raza, M. A.; Rahman, I. Z.; Beloshapkin, S. Synthesis of Nanoparticles of La0.75Sr0.25Cr0.5Mn0.5O3−δ (LSCM) Perovskite by Solution Combustion Method for Solid Oxide Fuel Cell Application. *J. Alloys Compd.* **2009**, *485* (1–2), 593–597.

(198) Zhang, Z.; Wang, W.; Shang, M.; Yin, W. Low-Temperature Combustion Synthesis of

Bi2WO6 Nanoparticles as a Visible-Light-Driven Photocatalyst. *J. Hazard. Mater.* **2010**, *177* (1–3), 1013–1018.

(199) Karami, H.; Taala, F. Synthesis, Characterization and Application of Li3Fe2(PO4)3 Nanoparticles as Cathode of Lithium-Ion Rechargeable Batteries. *J. Power Sources* **2011**, *196* (15), 6400–6411.

(200) Lathika Devi, S. K.; Sudarsana Kumar, K.; Balakrishnan, A. Rapid Synthesis of Pure and Narrowly Distributed Eu Doped ZnO Nanoparticles by Solution Combustion Method. *Mater. Lett.* **2011**, *65* (1), 35–37.

(201) Sharma, P.; Lotey, G. S.; Singh, S.; Verma, N. K. Solution-Combustion: The Versatile Route to Synthesize Silver Nanoparticles. *J. Nanoparticle Res.* **2011**, *13* (6), 2553–2561.

(202) Wen, W.; Wu, J.-M.; Tu, J.-P. A Novel Solution Combustion Synthesis of Cobalt Oxide Nanoparticles as Negative-Electrode Materials for Lithium Ion Batteries. *J. Alloys Compd.* **2012**, *513*, 592–596.

(203) Jegatha Christy, A.; Umadevi, M. Novel Combustion Method to Prepare Octahedral NiO Nanoparticles and Its Photocatalytic Activity. *Mater. Res. Bull.* **2013**, *48* (10), 4248–4254.

(204) Saad, A. A.; Khan, W.; Dhiman, P.; Naqvi, A. H.; Singh, M. Structural, Optical and Magnetic Properties of Perovskite (La 1-x Sr x)(Fe 1-x Ni x)O 3 , (x = 0.0, 0.1 & 0. 2) Nanoparticles. *Electron. Mater. Lett.* **2013**, *9* (1), 77–81.

(205) Jahagirdar, A. A.; Dhananjaya, N.; Monika, D. L.; Kesavulu, C. R.; Nagabhushana, H.; Sharma, S. C.; Nagabhushana, B. M.; Shivakumara, C.; Rao, J. L.; Chakradhar, R. P. S. Structural, EPR, Optical and Magnetic Properties of α-Fe 2O3 Nanoparticles. *Spectrochim. Acta - Part A Mol. Biomol. Spectrosc.* **2013**, *104*, 512–518.

(206) Jung, C.-H.; Jalota, S.; Bhaduri, S. B. Quantitative Effects of Fuel on the Synthesis of Ni/NiO Particles Using a Microwave-Induced Solution Combustion Synthesis in Air Atmosphere. *Mater. Lett.* **2005**, *59* (19–20), 2426–2432.

(207) Ragupathi, C.; Vijaya, J. J.; Kennedy, L. J. Synthesis, Characterization of Nickel Aluminate Nanoparticles by Microwave Combustion Method and Their Catalytic Properties. *Mater. Sci. Eng. B* **2014**, *184* (1), 18–25.

(208) Mukherjee, S.; Sudarsan, V.; Sastry, P. U.; Patra, A. K.; Tyagi, A. K. Morphology and Luminescence Characteristics of Combustion Synthesized Y2O3: (Eu, Dy, Tb) Nanoparticles with Various Amino-Acid Fuels. *J. Lumin.* **2014**, *145*, 318–323.

(209) Chanu, T. I.; Muthukumar, T.; Manoharan, P. T. Fuel Mediated Solution Combustion Synthesis of ZnO Supported Gold Clusters and Nanoparticles and Their Catalytic Activity and in Vitro Cytotoxicity. *Phys. Chem. Chem. Phys.* **2014**, *16* (43), 23686–23698.

(210) Ayeshamariam, A.; Kashif, M.; Bououdina, M.; Hashim, U.; Jayachandran, M.; Ali, M. E. Morphological, Structural, and Gas-Sensing Characterization of Tin-Doped Indium Oxide Nanoparticles. *Ceram. Int.* **2014**, *40* (1), 1321–1328.

(211) Deng, J.; Kang, L.; Bai, G.; Li, Y.; Li, P.; Liu, X.; Yang, Y.; Gao, F.; Liang, W. Solution Combustion Synthesis of Cobalt Oxides (Co3O4 and Co3O4/CoO) Nanoparticles as Supercapacitor Electrode Materials. *Electrochim. Acta* **2014**, *132*, 127–135.

(212) Schwung, S.; Rogov, A.; Clarke, G.; Joulaud, C.; Magouroux, T.; Staedler, D.; Passemard, S.; Jüstel, T.; Badie, L.; Galez, C.; Wolf, J. P.; Volkov, Y.; Prina-Mello, A.; Gerber-Lemaire, S.; Rytz, D.; Mugnier, Y.; Bonacina, L.; Le Dantec, R. Nonlinear Optical and Magnetic Properties of BiFeO 3 Harmonic Nanoparticles. *J. Appl. Phys.* **2014**, *116* (11), 114306.

(213) Ianoş, R.; Tăculescu (Moacă), E.-A.; Păcurariu, C.; Niznansky, D. γ-Fe 2 O 3

Nanoparticles Prepared by Combustion Synthesis, Followed by Chemical Oxidation of Residual Carbon with H 2 O 2. *Mater. Chem. Phys.* **2014**, *148* (3), 705–711.

(214) Gupta, S. K.; Kadam, R. M.; Natarajan, V.; Godbole, S. V. Nanoparticles of Sr0.995Gd0.005ZrO3-Gel-Combustion Synthesis, Characterization, Fluorescence and EPR Spectroscopy. *Mater. Sci. Eng. B* **2014**, *183* (1), 6–11.

(215) Thomas, A.; Janáky, C.; Samu, G. F.; Huda, M. N.; Sarker, P.; Liu, J. P.; van Nguyen, V.; Wang, E. H.; Schug, K. A.; Rajeshwar, K. Time- and Energy-Efficient Solution Combustion Synthesis of Binary Metal Tungstate Nanoparticles with Enhanced Photocatalytic Activity. *ChemSusChem* **2015**, *8* (10), 1652–1663.

(216) Zhu, C.; Sheng, N.; Akiyama, T. MnO Nanoparticles Embedded in a Carbon Matrix for a High Performance Li Ion Battery Anode. *RSC Adv.* **2015**, *5* (27), 21066–21073.

(217) Cannas, C.; Musinu, A.; Peddis, D.; Piccaluga, G. Synthesis and Characterization of CoFe 2 O 4 Nanoparticles Dispersed in a Silica Matrix by a Sol−Gel Autocombustion Method. *Chem. Mater.* **2006**, *18* (16), 3835–3842.

(218) Sharma, J. K.; Akhtar, M. S.; Ameen, S.; Srivastava, P.; Singh, G. Green Synthesis of CuO Nanoparticles with Leaf Extract of Calotropis Gigantea and Its Dye-Sensitized Solar Cells Applications. *J. Alloys Compd.* **2015**, *632*, 321–325.

(219) Suresh, D.; Shobharani, R. M.; Nethravathi, P. C.; Pavan Kumar, M. A.; Nagabhushana, H.; Sharma, S. C. Artocarpus Gomezianus Aided Green Synthesis of ZnO Nanoparticles: Luminescence, Photocatalytic and Antioxidant Properties. *Spectrochim. Acta Part A Mol. Biomol. Spectrosc.* **2015**, *141*, 128–134.

(220) Kamińska, I.; Fronc, K.; Sikora, B.; Mouawad, M.; Siemiarczuk, A.; Szewczyk, M.; Sobczak, K.; Wojciechowski, T.; Zaleszczyk, W.; Minikayev, R.; Paszkowicz, W.; Stępień, P.; Dziawa, P.; Ciszak, K.; Piątkowski, D.; Maćkowski, S.; Kaliszewski, M.; Włodarski, M.; Młyńczak, J.; Kopczyński, K.; Łapiński, M.; Elbaum, D. Upconverting/Magnetic: Gd 2 O 3 :(Er 3+ ,Yb 3+ ,Zn 2+) Nanoparticles for Biological Applications: Effect of Zn 2+ Doping. *RSC Adv.* **2015**, *5* (95), 78361–78373.

(221) Vignesh, R. H.; Sankar, K. V.; Amaresh, S.; Lee, Y. S.; Selvan, R. K. Synthesis and Characterization of MnFe2O4 Nanoparticles for Impedometric Ammonia Gas Sensor. *Sensors Actuators B Chem.* **2015**, *220*, 50–58.

(222) Anilkumar, M. R.; Nagaswarupa, H. P.; Nagabhushana, H.; Sharma, S. C.; Vidya, Y. S.; Anantharaju, K. S.; Prashantha, S. C.; Shivakuamra, C.; Gurushantha, K. Bio-Inspired Route for the Synthesis of Spherical Shaped MgO:Fe3+ Nanoparticles: Structural, Photoluminescence and Photocatalytic Investigation. *Spectrochim. Acta Part A Mol. Biomol. Spectrosc.* **2015**, *149*, 703–713.

(223) Udayabhanu; Nethravathi, P. C.; Pavan Kumar, M. A.; Suresh, D.; Lingaraju, K.; Rajanaika, H.; Nagabhushana, H.; Sharma, S. . Tinospora Cordifolia Mediated Facile Green Synthesis of Cupric Oxide Nanoparticles and Their Photocatalytic, Antioxidant and Antibacterial Properties. *Mater. Sci. Semicond. Process.* **2015**, *33*, 81–88.

(224) Shikha, P.; Kang, T. S.; Randhawa, B. S. Effect of Different Synthetic Routes on the Structural, Morphological and Magnetic Properties of Ce Doped LaFeO3 Nanoparticles. *J. Alloys Compd.* **2015**, *625*, 336–345.

(225) Suresh, D.; Nethravathi, P. C.; Udayabhanu; Rajanaika, H.; Nagabhushana, H.; Sharma, S. C. Green Synthesis of Multifunctional Zinc Oxide (ZnO) Nanoparticles Using Cassia Fistula Plant Extract and Their Photodegradative, Antioxidant and Antibacterial Activities. *Mater. Sci. Semicond. Process.* **2015**, *31*, 446–454.

(226) Chavan, A. U.; Kim, J.-H.; Im, H.-N.; Song, S.-J. Role of Different Oxide to Fuel Ratios

in Solution Combustion Synthesis of SnO2 Nanoparticles. *J. Korean Ceram. Soc.* **2016**, *53* (1), 122–127.

(227) Javadi, S.; Masoudpanah, S. M.; Zakeri, A. Conventional versus Microwave Combustion Synthesis of CoFe2O4 Nanoparticles. *J. Sol-Gel Sci. Technol.* **2016**, *79* (1), 176–183.

(228) Xiao, Q.; Si, Z.; Yu, Z.; Qiu, G. Sol–Gel Auto-Combustion Synthesis of Samarium-Doped TiO2 Nanoparticles and Their Photocatalytic Activity under Visible Light Irradiation. *Mater. Sci. Eng. B* **2007**, *137* (1–3), 189–194.

(229) Chen, M.; Chen, D.; Liao, Y.; Zhong, X.; Li, W.; Zhang, Y. Layered Lithium-Rich Oxide Nanoparticles Doped with Spinel Phase: Acidic Sucrose-Assistant Synthesis and Excellent Performance as Cathode of Lithium Ion Battery. *ACS Appl. Mater. Interfaces* **2016**, *8* (7), 4575–4584.

(230) Kormányos, A.; Thomas, A.; Huda, M. N.; Sarker, P.; Liu, J. P.; Poudyal, N.; Janáky, C.; Rajeshwar, K. Solution Combustion Synthesis, Characterization, and Photoelectrochemistry of CuNb 2 O 6 and ZnNb 2 O 6 Nanoparticles. *J. Phys. Chem. C* **2016**, *120* (29), 16024–16034.

(231) Bhange, P. D.; Awate, S. V.; Gholap, R. S.; Gokavi, G. S.; Bhange, D. S. Photocatalytic Degradation of Methylene Blue on Sn-Doped Titania Nanoparticles Synthesized by Solution Combustion Route. *Mater. Res. Bull.* **2016**, *76*, 264–272.

(232) Huang, M.; Qin, M.; Cao, Z.; Jia, B.; Chen, P.; Wu, H.; Wang, X.; Wan, Q.; Qu, X. Magnetic Iron Nanoparticles Prepared by Solution Combustion Synthesis and Hydrogen Reduction. *Chem. Phys. Lett.* **2016**, *657*, 33–38.

(233) Angadi, V. J.; Rudraswamy, B.; Sadhana, K.; Praveena, K. Structural and Magnetic Properties of Manganese Zinc Ferrite Nanoparticles Prepared by Solution Combustion Method Using Mixture of Fuels. *J. Magn. Magn. Mater.* **2016**, *409*, 111–115.

(234) Prashanth, K. .; Mahesh, S. .; Nanda Prakash, M. .; Munirathnamma, L. M.; Ningaraju, S.; Ravikumar, H. B.; Somashekar, R. .; Nagabhushana, B. . Solution Combustion Synthesis of Cr2O3 Nanoparticles and Derived PVA/Cr2O3 Nanocomposites-Positron Annihilation Spectroscopic Study. *Mater. Today Proc.* **2016**, *3* (10), 3646–3651.

(235) Gopala Krishna, P.; Paduvarahalli Ananthaswamy, P.; Gadewar, M.; Bora, U.; Bhangi Mutta, N. In Vitro Antibacterial And Anticancer Studies Of ZnO Nanoparticles Prepared By Sugar Fueled Combustion Synthesis. *Adv. Mater. Lett.* **2016**, *08* (01), 24–29.

(236) Nagaraju, G.; Shivaraju, G. C.; Banuprakash, G.; Rangappa, D. Photocatalytic Activity of ZnO Nanoparticles: Synthesis via Solution Combustion Method. *Mater. Today Proc.* **2017**, *4* (11), 11700–11705.

(237) D. Syamala Bai; Kumar, V. R.; Suvarna, R. P. Synthesis and Characterization of Zinc Oxide Nanoparticles by Solution Combustion Method: DC Conductivity Studies. *Indian J. Adv. Chem. Sci.* **2017**, 1–14.

(238) Naderi, P.; Masoudpanah, S. M.; Alamolhoda, S. Magnetic Properties of Li0.5Fe2.5O4 Nanoparticles Synthesized by Solution Combustion Method. *Appl. Phys. A* **2017**, *123* (11), 702.

(239) Krsmanović, R.; Morozov, V. A.; Lebedev, O. I.; Polizzi, S.; Speghini, A.; Bettinelli, M.; Tendeloo, G. Van. Structural and Luminescence Investigation on Gadolinium Gallium Garnet Nanocrystalline Powders Prepared by Solution Combustion Synthesis. *Nanotechnology* **2007**, *18* (32), 325604.

(240) Samu, G. F.; Veres, Á.; Endrődi, B.; Varga, E.; Rajeshwar, K.; Janáky, C. Bandgap-Engineered Quaternary M x Bi 2−x Ti 2 O 7 (M: Fe, Mn) Semiconductor Nanoparticles:

Solution Combustion Synthesis, Characterization, and Photocatalysis. *Appl. Catal. B Environ.* **2017**, *208*, 148–160.

(241) Pourgolmohammad, B.; Masoudpanah, S. M.; Aboutalebi, M. R. Effects of the Fuel Type and Fuel Content on the Specific Surface Area and Magnetic Properties of Solution Combusted CoFe 2 O 4 Nanoparticles. *Ceram. Int.* **2017**, *43* (11), 8262–8268.

(242) Wang, X.; Qin, M.; Fang, F.; Jia, B.; Wu, H.; Qu, X.; Volinsky, A. A. Effect of Glycine on One-Step Solution Combustion Synthesis of Magnetite Nanoparticles. *J. Alloys Compd.* **2017**, *719*, 288–295.

(243) Rasouli, S.; Arabi, A.-M.; Naeimi, A.; Hashemi, S.-M. Microwave-Assisted Combustion Synthesis of ZnO:Eu Nanoparticles: Effect of Fuel Types. *J. Fluoresc.* **2018**, *28* (1), 167–172.

(244) Prashanth, G. K.; Prashanth, P. A.; Nagabhushana, B. M.; Ananda, S.; Krishnaiah, G. M.; Nagendra, H. G.; Sathyananda, H. M.; Rajendra Singh, C.; Yogisha, S.; Anand, S.; Tejabhiram, Y. Comparison of Anticancer Activity of Biocompatible ZnO Nanoparticles Prepared by Solution Combustion Synthesis Using Aqueous Leaf Extracts of Abutilon Indicum, Melia Azedarach and Indigofera Tinctoria as Biofuels. *Artif. Cells, Nanomedicine, Biotechnol.* **2018**, *46* (5), 968–979.

(245) Zarezadeh Mehrizi, M.; Ahmadi, S.; Beygi, R.; Asadi, M. Fabrication of Cerium Oxide Nanoparticles by Solution Combustion Synthesis and Their Cytotoxicity Evaluation. *Russ. J. Non-Ferrous Met.* **2018**, *59* (1), 111–116.

(246) Pathan, A. A.; Desai, K. R.; Vajapara, S.; Bhasin, C. P. Conditional Optimization of Solution Combustion Synthesis for Pioneered La≪Sub≫2≪/Sub≫O≪Sub≫3≪ /Sub≫ Nanostructures to Application as Future CMOS and NVMS Generations. *Adv. Nanoparticles* **2018**, *07* (01), 28–35.

(247) Harish, B. M.; Avinash, B. S.; Chaturmukha, V. S.; Jayanna, H. S.; Suresh, S.; Naveen, C. S.; Lamani, A. R. Synthesis and Dc Electrical Conductivity of Cr-Doped CeO2 Nanoparticles by Solution Combustion Method. In *AIP Conference Proceedings*; 2018; Vol. 1942, p 050037.

(248) Jain, M.; Manju; Singh, K.; Kumar, A.; Sharma, J.; Chae, K. H.; Vij, A.; Thakur, A. Single Step Synthesis and Characterization of ZnAl2O4 Nanoparticles. In *AIP Conference Proceedings*; 2018; Vol. 1953, p 030068.

(249) Lesbayev, A. B.; Smagulova, G. T.; Kim, S.; Prikhod'ko, N. G.; Manakov, S. M.; Guseinov, N.; Mansurov, Z. A. Solution-Combustion Synthesis and Characterization of Fe3O4 Nanoparticles. *Int. J. Self-Propagating High-Temperature Synth.* **2018**, *27* (3), 195–197.

(250) Qiu, Z.; Zhou, Y.; Lü, M.; Zhang, A.; Ma, Q. Combustion Synthesis of Long-Persistent Luminescent MAl2O4: Eu2+, R3+ (M=Sr, Ba, Ca, R=Dy, Nd and La) Nanoparticles and Luminescence Mechanism Research. *Acta Mater.* **2007**, *55* (8), 2615–2620.

(251) Ravichandran, A. T.; Srinivas, J.; Karthick, R.; Manikandan, A.; Baykal, A. Facile Combustion Synthesis, Structural, Morphological, Optical and Antibacterial Studies of Bi 1−x Al x FeO 3 ($0.0 \leq x \leq 0.15$) Nanoparticles. *Ceram. Int.* **2018**, *44* (11), 13247–13252.

(252) Xu, C.; Manukyan, K. V.; Adams, R. A.; Pol, V. G.; Chen, P.; Varma, A. One-Step Solution Combustion Synthesis of CuO/Cu2O/C Anode for Long Cycle Life Li-Ion Batteries. *Carbon N. Y.* **2019**, *142*, 51–59.

(253) Shashankaa, R.; Kamacıa, Y.; Taşb, R.; Ceylan, Y.; Bülbüld; Savaş, A.; Uzune, O.; Karaoglanli, A. C. Antimicrobial Investigation of CuO and ZnO Nanoparticles Prepared

by a Rapid Combustion Method. *Phys. Chem. Res.* **2019**, *7* (4), 799–812.

(254) Vivekanandhan, S. Combustion Process Using Plant-Based Fuels for the Synthesis of Metal- Oxide Nanostructures. *ChemistrySelect* **2019**, *4* (27), 8026–8042.

(255) Patil, S.; Dasari, H. P. Effect of Fuel and Solvent on Soot Oxidation Activity of Ceria Nanoparticles Synthesized by Solution Combustion Method. *Mater. Sci. Energy Technol.* **2019**, *2* (3), 485–489.

(256) Shaat, S. K. K.; Musleh, H.; Zayed, H.; Tamous, H.; Issa, A.; Shurrab, N.; Asad, J.; Mousa, A.; Abu-Shawish, M.; AlDahoudi, N. Solution Combustion-Derived ZnO Nanoparticles for Photoanode of Solar Cells. *Mater. Sci. Eng. B* **2019**, *241* (February), 75–81.

(257) K. Pathak, T.; Swart, H. C. Structural and Luminescence Properties of ZnO Nanoparticles Synthesized by Mixture of Fuel Approach in Solution Combustion Method. In *Zinc Oxide Based Nano Materials and Devices*; IntechOpen, 2019; Vol. i, p 13.

(258) Wang, H.; Han, W.; Li, X.; Liu, B.; Tang, H.; Li, Y. Solution Combustion Synthesis of Cr2O3 Nanoparticles and the Catalytic Performance for Dehydrofluorination of 1,1,1,3,3-Pentafluoropropane to 1,3,3,3-Tetrafluoropropene. *Molecules* **2019**, *24* (2), 361.

(259) Aliasghari, H.; Arabi, A. M.; Haratizadeh, H. A Novel Approach for Solution Combustion Synthesis of Tungsten Oxide Nanoparticles for Photocatalytic and Electrochromic Applications. *Ceram. Int.* **2020**, *46* (1), 403–414.

(260) Tahmasebi, K.; Paydar, M. H. The Effect of Starch Addition on Solution Combustion Synthesis of Al2O3–ZrO2 Nanocomposite Powder Using Urea as Fuel. *Mater. Chem. Phys.* **2008**, *109* (1), 156–163.

(261) Rao, K. V.; Sunandana, C. S. Structure and Microstructure of Combustion Synthesized MgO Nanoparticles and Nanocrystalline MgO Thin Films Synthesized by Solution Growth Route. *J. Mater. Sci.* **2008**, *43* (1), 146–154.

(262) Yu, J.; Duan, L. B.; Wang, Y. C.; Rao, G. H. Influence of Fuel-to-Oxidizer Ratio on the Magnetic Properties of Fe-Doped In2O3 Nanoparticles Synthesized by Solution Combustion Method. *J. Solid State Chem.* **2009**, *182* (6), 1563–1569.

(263) Papadas, I. T.; Ioakeimidis, A.; Armatas, G. S.; Choulis, S. A. Low-Temperature Combustion Synthesis of a Spinel NiCo 2 O 4 Hole Transport Layer for Perovskite Photovoltaics. *Adv. Sci.* **2018**, *5* (5), 1701029.

(264) Halperin, W. P. Quantum Size Effects in Metal Particles. *Rev. Mod. Phys.* **1986**, *58* (3), 533–606.

(265) Reddy, C. V.; Babu, B.; Shim, J. Synthesis of Cr-Doped SnO2 Quantum Dots and Its Enhanced Photocatalytic Activity. *Mater. Sci. Eng. B* **2017**, *223*, 131–142.

(266) Babu, B.; Kadam, A. N.; Ravikumar, R. V. S. S. N.; Byon, C. Enhanced Visible Light Photocatalytic Activity of Cu-Doped SnO2quantum Dots by Solution Combustion Synthesis. *J. Alloys Compd.* **2017**, *703*, 330–336.

(267) Nag, P.; Das, P. P.; Roy, A.; Devi, P. S. Iron Antimonate Quantum Dots Exhibiting Tunable Visible Light Emission. *New J. Chem.* **2017**, *41* (4), 1436–1446.

(268) Thirumala Rao, G.; Babu, B.; Ravikumar, R. V. S. S. N.; Shim, J.; Venkata Reddy, C. Structural and Optical Properties of Fe-Doped SnO2 Quantum Dots. *Mater. Res. Express* **2017**, *4* (12).

(269) Leelavathi, A.; Mukherjee, B.; Nethravathi, C.; Kundu, S.; Dhivya, M.; Ravishankar, N.; Madras, G. Highly Photoactive Heterostructures of PbO Quantum Dots on TiO2. *RSC Adv.* **2013**, *3* (43), 20970–20977.

(270) Mädler, L.; Stark, W. J.; Pratsinis, S. E. Rapid Synthesis of Stable ZnO Quantum Dots. *J. Appl. Phys.* **2002**, *92* (11), 6537–6540.

(271) Epifani, M.; Capone, S.; Rella, R.; Siciliano, P.; Vasanelli, L.; Faglia, G.; Nelli, P.; Sberveglieri, G. In2O3 Thin Films Obtained through a Chemical Complexation Based Sol-Gel Process and Their Application as Gas Sensor Devices. *J. Sol-Gel Sci. Technol.* **2003**, *26* (1–3), 741–744.

(272) Yao, C.; Xu, X.; Wang, J.; Shi, L.; Li, L. Low-Temperature, Solution-Processed Hole Selective Layers for Polymer Solar Cells. *ACS Appl. Mater. Interfaces* **2013**, *5* (3), 1100–1107.

(273) Bai, S.; Cao, M.; Jin, Y.; Dai, X.; Liang, X.; Ye, Z.; Li, M.; Cheng, J.; Xiao, X.; Wu, Z.; Xia, Z.; Sun, B.; Wang, E.; Mo, Y.; Gao, F.; Zhang, F. Low-Temperature Combustion-Synthesized Nickel Oxide Thin Films as Hole-Transport Interlayers for Solution-Processed Optoelectronic Devices. *Adv. Energy Mater.* **2014**, *4* (6), 1301460.

(274) Jung, J. W.; Chueh, C.-C.; Jen, A. K. Y. A Low-Temperature, Solution-Processable, Cu-Doped Nickel Oxide Hole-Transporting Layer via the Combustion Method for High-Performance Thin-Film Perovskite Solar Cells. *Adv. Mater.* **2015**, *27* (47), 7874–7880.

(275) Kang, Y. H.; Jang, K.-S.; Lee, C.; Cho, S. Y. Facile Preparation of Highly Conductive Metal Oxides by Self-Combustion for Solution-Processed Thermoelectric Generators. *ACS Appl. Mater. Interfaces* **2016**, *8* (8), 5216–5223.

(276) Wang, Y.; Xu, M.; Li, J.; Ma, J.; Wang, X.; Wei, Z.; Chu, X.; Fang, X.; Jin, F. Sol-Combustion Synthesis of Al-Doped ZnO Transparent Conductive Film at Low Temperature. *Surf. Coatings Technol.* **2017**, *330* (September), 255–259.

(277) Ullah, S.; Branquinho, R.; Santa, A.; De Matteis, F.; Martins, R.; Davoli, I.; Gonçalves, G.; Fortunato, E. Boosting Highly Transparent and Conducting Indium Zinc Oxide Thin Films through Solution Combustion Synthesis: Influence of Rapid Thermal Annealing. *Semicond. Sci. Technol.* **2018**, *33* (10), 105004.

(278) Wang, J.; Daunis, T. B.; Cheng, L.; Zhang, B.; Kim, J.; Hsu, J. W. P. Combustion Synthesis of P-Type Transparent Conducting CuCrO 2+ x and Cu:CrO x Thin Films at 180 °C. *ACS Appl. Mater. Interfaces* **2018**, *10* (4), 3732–3738.

(279) Carlos, E.; Kiazadeh, A.; Deuermeier, J.; Branquinho, R.; Martins, R.; Fortunato, E. Critical Role of a Double-Layer Configuration in Solution-Based Unipolar Resistive Switching Memories. *Nanotechnology* **2018**, *29* (34), 345206.

(280) Qin, Y.; Song, J.; Qiu, Q.; Liu, Y.; Zhao, Y.; Zhu, L.; Qiang, Y. High-Quality NiO Thin Film by Low-Temperature Spray Combustion Method for Perovskite Solar Cells. *J. Alloys Compd.* **2019**, *810*, 151970.

(281) Pujar, P.; Vardhan, R. V.; Gupta, D.; Mandal, S. A Balancing between Super Transparency and Conductivity of Solution Combustion Derived Titanium Doped Indium Oxide: Effect of Charge Carrier Density and Mobility. *Thin Solid Films* **2018**, *660* (September 2017), 267–275.

(282) Salian, A.; Pujar, P.; Mandal, S. Facile in Situ Formation of High Conductive Ag and Cu x O y Composite Films: A Role of Aqueous Spray Combustion. *J. Mater. Sci. Mater. Electron.* **2019**, *30* (3), 2888–2897.

(283) Hosono, H.; Kikuchi, N.; Ueda, N.; Kawazoe, H. Working Hypothesis to Explore Novel Wide Band Gap Electrically Conducting Amorphous Oxides and Examples. *J. Non. Cryst. Solids* **1996**, *198–200* (PART 1), 165–169.

(284) Hennek, J. W.; Smith, J.; Yan, A.; Kim, M.; Zhao, W.; Dravid, V. P.; Facchetti, A.; Marks,

T. J. Oxygen "Getter" Effects on Microstructure and Carrier Transport in Low Temperature Combustion-Processed a-InXZnO (X = Ga, Sc, Y, La) Transistors. *J. Am. Chem. Soc.* **2013**, *135* (29), 10729–10741.

(285) Yu, X.; Zhou, N.; Smith, J.; Lin, H.; Stallings, K.; Yu, J.; Marks, T. J.; Facchetti, A. Synergistic Approach to High-Performance Oxide Thin Film Transistors Using a Bilayer Channel Architecture. *ACS Appl. Mater. Interfaces* **2013**, *5* (16), 7983–7988.

(286) Everaerts, K.; Zeng, L.; Hennek, J. W.; Camacho, D. I.; Jariwala, D.; Bedzyk, M. J.; Hersam, M. C.; Marks, T. J. Printed Indium Gallium Zinc Oxide Transistors. Self-Assembled Nanodielectric Effects on Low-Temperature Combustion Growth and Carrier Mobility. *ACS Appl. Mater. Interfaces* **2013**, *5* (22), 11884–11893.

(287) Bae, E. J.; Kang, Y. H.; Han, M.; Lee, C.; Cho, S. Y. Soluble Oxide Gate Dielectrics Prepared Using the Self-Combustion Reaction for High-Performance Thin-Film Transistors. *J. Mater. Chem. C* **2014**, *2* (28), 5695–5703.

(288) Yu, X.; Zeng, L.; Zhou, N.; Guo, P.; Shi, F.; Buchholz, D. B.; Ma, Q.; Yu, J.; Dravid, V. P.; Chang, R. P. H.; Bedzyk, M.; Marks, T. J.; Facchetti, A. Ultra-Flexible, "Invisible" Thin-Film Transistors Enabled by Amorphous Metal Oxide/Polymer Channel Layer Blends. *Adv. Mater.* **2015**, *27* (14), 2390–2399.

(289) Yu, X.; Smith, J.; Zhou, N.; Zeng, L.; Guo, P.; Xia, Y.; Alvarez, A.; Aghion, S.; Lin, H.; Yu, J.; Chang, R. P. H.; Bedzyk, M. J.; Ferragut, R.; Marks, T. J.; Facchetti, A. Spray-Combustion Synthesis: Efficient Solution Route to High-Performance Oxide Transistors. *Proc. Natl. Acad. Sci.* **2015**, *112* (11), 3217–3222.

(290) Chen, Y.; Wang, B.; Huang, W.; Zhang, X.; Wang, G.; Leonardi, M. J.; Huang, Y.; Lu, Z.; Marks, T. J.; Facchetti, A. Nitroacetylacetone as a Cofuel for the Combustion Synthesis of High-Performance Indium–Gallium–Zinc Oxide Transistors. *Chem. Mater.* **2018**, *30* (10), 3323–3329.

(291) Wang, B.; Guo, P.; Zeng, L.; Yu, X.; Sil, A.; Huang, W.; Leonardi, M. J.; Zhang, X.; Wang, G.; Lu, S.; Chen, Z.; Bedzyk, M. J.; Schaller, R. D.; Marks, T. J.; Facchetti, A. Expeditious, Scalable Solution Growth of Metal Oxide Films by Combustion Blade Coating for Flexible Electronics. *Proc. Natl. Acad. Sci.* **2019**, 201901492.

(292) Liu, A.; Zhu, H.; Guo, Z.; Meng, Y.; Liu, G.; Fortunato, E.; Martins, R.; Shan, F. Solution Combustion Synthesis: Low-Temperature Processing for p-Type Cu:NiO Thin Films for Transparent Electronics. *Adv. Mater.* **2017**, *29* (34), 1701599.

(293) Wang, Z.; Xu, G.; Zhao, Z.; Cai, L.; Wu, Q.; Cheng, P.; Zhao, Y.; Xue, J.; Wang, R.; Liu, C.; Yang, Y. Cluster Size Control toward High Performance Solution Processed InGaZnO Thin Film Transistors. *ACS Appl. Electron. Mater.* **2019**, acsaelm.9b00653.

(294) Liang, Y.; Yong, J.; Yu, Y.; Nirmalathas, A.; Ganesan, K.; Evans, R.; Nasr, B.; Skafidas, E. Direct Electrohydrodynamic Patterning of High-Performance All Metal Oxide Thin-Film Electronics. *ACS Nano* **2019**, *13* (12), 13957–13964.

(295) Hennek, J. W.; Kim, M.-G.; Kanatzidis, M. G.; Facchetti, A.; Marks, T. J. Exploratory Combustion Synthesis: Amorphous Indium Yttrium Oxide for Thin-Film Transistors. *J. Am. Chem. Soc.* **2012**, *134* (23), 9593–9596.

(296) Rim, Y. S.; Lim, H. S.; Kim, H. J. Low-Temperature Metal-Oxide Thin-Film Transistors Formed by Directly Photopatternable and Combustible Solution Synthesis. *ACS Appl. Mater. Interfaces* **2013**, *5* (9), 3565–3571.

(297) Baeg, K.-J.; Kim, M.-G.; Song, C. K.; Yu, X.; Facchetti, A.; Marks, T. J. Charge-Trap Flash-Memory Oxide Transistors Enabled by Copper-Zirconia Composites. *Adv. Mater.* **2014**, *26* (42), 7170–7177.

(298) Wang, H.; Xu, W.; Zhou, S.; Xie, F.; Xiao, Y.; Ye, L.; Chen, J.; Xu, J. Oxygen Plasma Assisted High Performance Solution-Processed Al 2 O x Gate Insulator for Combustion-Processed InGaZnO x Thin Film Transistors. *J. Appl. Phys.* **2015**, *117* (3), 035703.

(299) Tue, P. T.; Inoue, S.; Takamura, Y.; Shimoda, T. Combustion Synthesized Indium-Tin-Oxide (ITO) Thin Film for Source/Drain Electrodes in All Solution-Processed Oxide Thin-Film Transistors. *Appl. Phys. A* **2016**, *122* (6), 623.

(300) Wang, B.; Yu, X.; Guo, P.; Huang, W.; Zeng, L.; Zhou, N.; Chi, L.; Bedzyk, M. J.; Chang, R. P. H.; Marks, T. J.; Facchetti, A. Solution-Processed All-Oxide Transparent High-Performance Transistors Fabricated by Spray-Combustion Synthesis. *Adv. Electron. Mater.* **2016**, *2* (4), 1500427.

(301) Pujar, P.; Gandla, S.; Singh, M.; Gupta, B.; Tarafder, K.; Gupta, D.; Noh, Y. Y.; Mandal, S. Development of Low Temperature Stoichiometric Solution Combustion Derived Transparent Conductive Ternary Zinc Tin Co-Doped Indium Oxide Electrodes. *RSC Adv.* **2017**, *7* (76), 48253–48262.

(302) Moreira, M.; Carlos, E.; Dias, C.; Deuermeier, J.; Pereira, M.; Barquinha, P.; Branquinho, R.; Martins, R.; Fortunato, E.; Carlos; Dias; Deuermeier; Pereira; Barquinha; Branquinho; Martins; Fortunato. Tailoring IGZO Composition for Enhanced Fully Solution-Based Thin Film Transistors. *Nanomaterials* **2019**, *9* (9), 1273.

(303) Pujar, P.; Gupta, D.; Mandal, S. High-Performance Low Voltage Operation of Indium Zinc Tin Oxide Thin Film Transistors Using Chemically Derived Sodium β-Alumina Dielectric. *J. Mater. Sci. Mater. Electron.* **2019**, *30* (10), 9097–9105.

(304) Clark, T.; Ruiz, J. D.; Fan, H.; Brinker, C. J.; Swanson, B. I.; Parikh, A. N. A New Application of UV−Ozone Treatment in the Preparation of Substrate-Supported, Mesoporous Thin Films. *Chem. Mater.* **2000**, *12* (12), 3879–3884.

(305) Imai, H.; Tominaga, A.; Hirashima, H.; Toki, M.; Asakuma, N. Ultraviolet-Reduced Reduction and Crystallization of Indium Oxide Films. *J. Appl. Phys.* **1999**, *85* (1), 203–207.

(306) Van de Leest, R. E. UV Photo-Annealing of Thin Sol-Gel Films. *Appl. Surf. Sci.* **1995**, *86* (1–4), 278–285.

(307) Carlos, E.; Branquinho, R.; Kiazadeh, A.; Barquinha, P.; Martins, R.; Fortunato, E. UV-Mediated Photochemical Treatment for Low-Temperature Oxide-Based Thin-Film Transistors. *ACS Appl. Mater. Interfaces* **2016**, *8* (45), 31100–31108.

(308) Yang, J.; Wang, B.; Zhang, Y.; Ding, X.; Zhang, J. Low-Temperature Combustion Synthesis and UV Treatment Processed p-Type Li:NiO x Active Semiconductors for High-Performance Electronics. *J. Mater. Chem. C* **2018**, *6* (46), 12584–12591.

(309) Carlos, E.; Leppäniemi, J.; Sneck, A.; Alastalo, A.; Deuermeier, J.; Branquinho, R.; Martins, R.; Fortunato, E. Printed, Highly Stable Metal Oxide Thin-Film Transistors with Ultra-Thin High-κ Oxide Dielectric. *Adv. Electron. Mater.* **2020**, *6* (3), 1901071.

(310) Capra, M.; Peloso, R.; Masera, G.; Roch, M. R.; Martina, M. Edge Computing: A Survey On the Hardware Requirements in the Internet of Things World. *Futur. Internet* **2019**, *11* (4), 100.

(311) Madakam, S.; Ramaswamy, R.; Tripathi, S. Internet of Things (IoT): A Literature Review. *J. Comput. Commun.* **2015**, *03* (05), 164–173.

(312) Rockelé, M.; Pham, D. V.; Steiger, J.; Botnaras, S.; Weber, D.; Vanfleteren, J.; Sterken, T.; Cuypers, D.; Steudel, S.; Myny, K.; Schols, S.; Van Der Putten, B.; Genoe, J.; Heremans, P. Low-Temperature and Low-Voltage, Solution-Processed Metal Oxide n-

TFTs and Flexible Circuitry on Large-Area Polyimide Foil. *Proc. Int. Disp. Work.* **2011**, *2* (December), 1267–1270.

(313) Moonen, P. F.; Yakimets, I.; Huskens, J. Fabrication of Transistors on Flexible Substrates: From Mass-Printing to High-Resolution Alternative Lithography Strategies. *Adv. Mater.* **2012**, *24* (41), 5526–5541.

(314) Petti, L.; M??nzenrieder, N.; Vogt, C.; Faber, H.; B??the, L.; Cantarella, G.; Bottacchi, F.; Anthopoulos, T. D.; Tr??ster, G.; Münzenrieder, N.; Vogt, C.; Faber, H.; Büthe, L.; Cantarella, G.; Bottacchi, F.; Anthopoulos, T. D.; Tröster, G. Metal Oxide Semiconductor Thin-Film Transistors for Flexible Electronics. *Appl. Phys. Rev.* **2016**, *3* (2), 021303.

(315) Huang, Y.-Y.; Chiang, S.-C.; Chen, Y.-H.; Wu, D.-C.; Tseng, K.-H.; Lin, Y.-H.; Chang, H.-M.; Huang, Y.-Y.; Pham, D.-V.; Su, K.-H.; Marinkovic, M.; Weber, D.; Merkulov, A.; Anselmann, R. 12-3: A 5.5 Inch FFS-LCD Driven by Soluble -Metal-Oxide and Implementation in Production Line through BCE TFT Structure. *SID Symp. Dig. Tech. Pap.* **2018**, *49* (1), 125–127.

(316) Lim, J. H.; Shim, J. H.; Choi, J. H.; Joo, J.; Park, K.; Jeon, H.; Moon, M. R.; Jung, D.; Kim, H.; Lee, H. J. Solution-Processed InGaZnO-Based Thin Film Transistors for Printed Electronics Applications. *Appl. Phys. Lett.* **2009**, *95* (1), 2009–2011.

(317) Chang, Y.-J.; Lee, D.-H.; Herman, G. S.; Chang, C.-H. High-Performance, Spin-Coated Zinc Tin Oxide Thin-Film Transistors. *Electrochem. Solid-State Lett.* **2007**, *10* (5), H135.

(318) Ong, B. S.; Li, C.; Li, Y.; Wu, Y.; Loutfy, R. Stable, Solution-Processed, High-Mobility ZnO Thin-Film Transistors. *J. Am. Chem. Soc.* **2007**, *129* (10), 2750–2751.

(319) Lee, D.-H.; Chang, Y.-J.; Herman, G. S.; Chang, C.-H. A General Route to Printable High-Mobility Transparent Amorphous Oxide Semiconductors. *Adv. Mater.* **2007**, *19* (6), 843–847.

(320) Kim, H. S.; Byrne, P. D.; Facchetti, A.; Marks, T. J. High Performance Solution-Processed Indium Oxide Thin-Film Transistors. *J. Am. Chem. Soc.* **2008**, *130* (38), 12580–12581.

(321) Heo, S. J.; Yoon, D. H.; Jung, T. S.; Kim, H. J. Recent Advances in Low-Temperature Solution-Processed Oxide Backplanes. *J. Inf. Disp.* **2013**, *14* (2), 79–87.

(322) Hwan Hwang, Y.; Seo, J.-S.; Moon Yun, J.; Park, H.; Yang, S.; Ko Park, S.-H.; Bae, B.-S. An 'Aqueous Route' for the Fabrication of Low-Temperature-Processable Oxide Flexible Transparent Thin-Film Transistors on Plastic Substrates. *NPG Asia Mater.* **2013**, *5* (4), e45.

(323) Seo, J.-S.; Jeon, J.-H.; Hwang, Y. H.; Park, H.; Ryu, M.; Park, S.-H. K.; Bae, B.-S. Solution-Processed Flexible Fluorine-Doped Indium Zinc Oxide Thin-Film Transistors Fabricated on Plastic Film at Low Temperature. *Sci. Rep.* **2013**, *3* (1), 2085.

(324) Huh, J.-E.; Park, J.; Lee, J.; Lee, S.-E.; Lee, J.; Lim, K.-H.; Kim, Y. S. Effects of Process Variables on Aqueous-Based AlOx Insulators for High-Performance Solution-Processed Oxide Thin-Film Transistors. *J. Ind. Eng. Chem.* **2018**, *68*, 117–123.

(325) Cai, W.; Zhu, Z.; Wei, J.; Fang, Z.; Ning, H.; Zheng, Z.; Zhou, S.; Yao, R.; Peng, J.; Lu, X. A Simple Method for High-Performance, Solution-Processed, Amorphous ZrO2 Gate Insulator TFT with a High Concentration Precursor. *Materials (Basel).* **2017**, *10* (8), 972.

(326) Nakajima, T.; Shinoda, K.; Tsuchiya, T. UV-Assisted Nucleation and Growth of Oxide Films from Chemical Solutions. *Chem. Soc. Rev.* **2014**, *43* (7), 2027–2041.

(327) Dellis, S.; Isakov, I.; Kalfagiannis, N.; Anthopoulos, T. D.; Koutsogeorgis, D. C.; Tetzner, K.; Anthopoulos, T. D.; Koutsogeorgis, D. C. Rapid Laser-Induced Photochemical Conversion of Sol–Gel Precursors to In 2 O 3 Layers and Their Application in Thin-Film

Transistors. *J. Mater. Chem. C* **2017**, *5* (15), 2–6.

(328) Hwang, J.; Lee, K.; Jeong, Y.; Lee, Y. U.; Pearson, C.; Petty, M. C.; Kim, H. UV-Assisted Low Temperature Oxide Dielectric Films for TFT Applications. *Adv. Mater. Interfaces* **2014**, *1* (8), 1400206.

(329) Yarali, E.; Koutsiaki, C.; Faber, H.; Tetzner, K.; Yengel, E.; Patsalas, P.; Kalfagiannis, N.; Koutsogeorgis, D. C.; Anthopoulos, T. D. Recent Progress in Photonic Processing of Metal-Oxide Transistors. *Adv. Funct. Mater.* **2019**, *1906022*, 1906022.

(330) Khan, S.; Lorenzelli, L.; Dahiya, R. S. Technologies for Printing Sensors and Electronics over Large Flexible Substrates: A Review. *IEEE Sens. J.* **2015**, *15* (6), 3164–3185.

(331) Vicente, A.; Águas, H.; Mateus, T.; Araújo, A.; Lyubchyk, A.; Siitonen, S.; Fortunato, E.; Martins, R. Solar Cells for Self-Sustainable Intelligent Packaging. *J. Mater. Chem. A* **2015**, *3* (25), 13226–13236.

(332) Ponce Ortiz, R.; Facchetti, A.; Marks, T. J.; Ortiz, R. P.; Facchetti, A.; Marks, T. J. High-k Organic, Inorganic, and Hybrid Dielectrics for Low-Voltage Organic Field-Effect Transistors. *Chem. Rev.* **2010**, *110* (1), 205–239.

(333) Scheideler, W. J.; McPhail, M. W.; Kumar, R.; Smith, J.; Subramanian, V. Scalable, High-Performance Printed InO x Transistors Enabled by Ultraviolet-Annealed Printed High- k AlO x Gate Dielectrics. *ACS Appl. Mater. Interfaces* **2018**, *10* (43), 37277–37286.

(334) Lee, W.-J.; Park, W.-T.; Park, S.; Sung, S.; Noh, Y.-Y.; Yoon, M.-H. Large-Scale Precise Printing of Ultrathin Sol-Gel Oxide Dielectrics for Directly Patterned Solution-Processed Metal Oxide Transistor Arrays. *Adv. Mater.* **2015**, *27* (34), 5043–5048.

(335) Bradley, D. C. Metal Alkoxides. In *Journal of Organometallic Chemistry*; 2007; Vol. 170, pp 303–361.

(336) Plassmeyer, P. N.; Mitchson, G.; Woods, K. N.; Johnson, D. C.; Page, C. J. Impact of Relative Humidity during Spin-Deposition of Metal Oxide Thin Films from Aqueous Solution Precursors. *Chem. Mater.* **2017**, *29* (7), 2921–2926.

(337) Tetzner, K.; Lin, Y.-H.; Regoutz, A.; Seitkhan, A.; Payne, D. J.; Anthopoulos, T. D. Sub-Second Photonic Processing of Solution-Deposited Single Layer and Heterojunction Metal Oxide Thin-Film Transistors Using a High-Power Xenon Flash Lamp. *J. Mater. Chem. C* **2017**, *5* (45), 11724–11732.

(338) Kim, D. W.; Park, J.; Hwang, J.; Kim, H. D.; Ryu, J. H.; Lee, K. B.; Baek, K. H.; Do, L.-M.; Choi, J. S. Rapid Curing of Solution-Processed Zinc Oxide Films by Pulse-Light Annealing for Thin-Film Transistor Applications. *Electron. Mater. Lett.* **2015**, *11* (1), 82–87.

(339) Huang, H.; Hu, H.; Zhu, J.; Guo, T. Inkjet-Printed In-Ga-Zn Oxide Thin-Film Transistors with Laser Spike Annealing. *J. Electron. Mater.* **2017**, *46* (7), 4497–4502.

(340) Moon, C.-J.; Kim, H.-S. Intense Pulsed Light Annealing Process of Indium–Gallium–Zinc–Oxide Semiconductors via Flash White Light Combined with Deep-UV and Near-Infrared Drying for High-Performance Thin-Film Transistors. *ACS Appl. Mater. Interfaces* **2019**, *11* (14), 13380–13388.

(341) Chen, C.; Yang, Q.; Chen, G.; Chen, H.; Guo, T. Solution-Processed Oxide Complementary Inverter via Laser Annealing and Inkjet Printing. *IEEE Trans. Electron Devices* **2019**, *66* (11), 4888–4893.

(342) Kwak, H.; Yang, J.; Kang, J.; Eom, T.-Y.; Kim, H.; Lee, H.-J.; Kang, C. Employment of Rapid Thermal Annealing for Solution-Processed InGaZnO Thin Film Transistors. *J. Mater. Sci. Mater. Electron.* **2018**, *29* (10), 8660–8665.

(343) Park, J.; Huh, J.-E.; Lee, S.-E.; Lee, J.; Lee, W. H.; Lim, K.-H.; Kim, Y. S. Effective Atmospheric-Pressure Plasma Treatment toward High-Performance Solution-Processed Oxide Thin-Film Transistors. *ACS Appl. Mater. Interfaces* **2018**, *10* (36), 30581–30586.

(344) Cho, W.-J.; Ahn, M.-J.; Jo, K.-W. Performance Enhancement of Solution-Derived Zinc-Tin-Oxide Thin Film Transistors by Low-Temperature Microwave Irradiation. *Phys. status solidi* **2017**, *214* (12), 1700350.

(345) Jeong, Y.; Pearson, C.; Lee, Y. U.; Ahn, K.; Cho, C.-R.; Hwang, J.; Kim, H.; Do, L.-M.; Petty, M. C. Effects of Hydrogen Plasma Treatment on the Electrical Behavior of Solution-Processed ZnO Transistors. *J. Appl. Phys.* **2014**, *116* (7), 074509.

(346) Song, K.; Young Koo, C.; Jun, T.; Lee, D.; Jeong, Y.; Moon, J. Low-Temperature Soluble InZnO Thin Film Transistors by Microwave Annealing. *J. Cryst. Growth* **2011**, *326* (1), 23–27.

(347) Rim, Y. S.; Jeong, W. H.; Kim, D. L.; Lim, H. S.; Kim, K. M.; Kim, H. J. Simultaneous Modification of Pyrolysis and Densification for Low-Temperature Solution-Processed Flexible Oxide Thin-Film Transistors. *J. Mater. Chem.* **2012**, *22* (25), 12491.

(348) Hirose, M.; Koh, M.; Mizubayashi, W.; Murakami, H.; Shibahara, K.; Miyazaki, S. Fundamental Limit of Gate Oxide Thickness Scaling in Advanced MOSFETs. *Semicond. Sci. Technol.* **2000**, *15* (5), 485–490.

(349) Iwong, H. *Nano-Cmos Gate Dielectric Engineering*; CRC Press, 2017.

(350) Liu, A.; Zhu, H.; Sun, H.; Xu, Y.; Noh, Y.-Y. Solution Processed Metal Oxide High-κ Dielectrics for Emerging Transistors and Circuits. *Adv. Mater.* **2018**, *30* (33), 1706364.

(351) Wong, H.; Iwai, H. On the Scaling Issues and High-κ Replacement of Ultrathin Gate Dielectrics for Nanoscale MOS Transistors. *Microelectron. Eng.* **2006**, *83* (10), 1867–1904.

(352) Petty, M. C. *Molecular Electronics*; Wiley Series in Materials for Electronic and Optoelectronic Applications; John Wiley & Sons, Ltd: Chichester, UK, 2007.

(353) Yim, K.; Yong, Y.; Lee, J.; Lee, K.; Nahm, H.-H.; Yoo, J.; Lee, C.; Seong Hwang, C.; Han, S. Novel High-κ Dielectrics for next-Generation Electronic Devices Screened by Automated Ab Initio Calculations. *NPG Asia Mater.* **2015**, *7* (6), e190–e190.

(354) Zhao, Y.; Kita, K.; Toriumi, A. Thermodynamic Analysis of Moisture Absorption Phenomena in High-Permittivity Oxides as Gate Dielectrics of Advanced Complementary-Metal-Oxide-Semiconductor Devices. *Appl. Phys. Lett.* **2010**, *96* (24), 242901.

(355) Houssa, M.; Heyns, M. M. *High k Gate Dielectrics*; Houssa, M., Ed.; CRC Press, 2003.

(356) Song, K.; Yang, W.; Jung, Y.; Jeong, S.; Moon, J. A Solution-Processed Yttrium Oxide Gate Insulator for High-Performance All-Solution-Processed Fully Transparent Thin Film Transistors. *J. Mater. Chem.* **2012**, *22* (39), 21265.

(357) Phillips, J. C. Dielectric Definition of Electronegativity. *Phys. Rev. Lett.* **1968**, *20* (11), 550–553.

(358) Xu, X.; Cui, Q.; Jin, Y.; Guo, X. Low-Voltage Zinc Oxide Thin-Film Transistors with Solution-Processed Channel and Dielectric Layers below 150 °C. *Appl. Phys. Lett.* **2012**, *101* (22), 222114.

(359) Dong, X.; Xia, G.; Zhang, Q.; Li, L.; Gong, H.; Bi, J.; Wang, S. Room-Temperature UV-Ozone Assisted Solution Process for Zirconium Oxide Films with High Dielectric Properties. *Ceram. Int.* **2017**, *43* (17), 15205–15213.

(360) Yoo, Y. B.; Park, J. H.; Lee, K. H.; Lee, H. W.; Song, K. M.; Lee, S. J.; Baik, H. K. Solution-Processed High-k HfO2 Gate Dielectric Processed under Softening Temperature of Polymer Substrates. *J. Mater. Chem. C* **2013**, *1* (8), 1651.

(361) Byun, H.-R.; Ha, Y.-G. UV-Cured Hafnium Oxide-Based Gate Dielectrics for Low-Voltage Organic and Amorphous Oxide Thin-Film Transistors. *J. Nanosci. Nanotechnol.* **2019**, *19* (7), 4249–4253.

(362) Jo, J.-W.; Kim, Y.-H.; Park, J.; Heo, J. S.; Hwang, S.; Lee, W.-J.; Yoon, M.-H.; Kim, M.-G.; Park, S. K. Ultralow-Temperature Solution-Processed Aluminum Oxide Dielectrics via Local Structure Control of Nanoclusters. *ACS Appl. Mater. Interfaces* **2017**, *9* (40), 35114–35124.

(363) Jo, J.-W.; Kim, J.; Kim, K.-T.; Kang, J.-G.; Kim, M.-G.; Kim, K.-H.; Ko, H.; Kim, Y.-H.; Park, S. K. Highly Stable and Imperceptible Electronics Utilizing Photoactivated Heterogeneous Sol-Gel Metal-Oxide Dielectrics and Semiconductors. *Adv. Mater.* **2015**, *27* (7), 1182–1188.

(364) Jo, J.-W.; Kim, K.-H.; Kim, J.; Ban, S. G.; Kim, Y.-H.; Park, S. K. High-Mobility and Hysteresis-Free Flexible Oxide Thin-Film Transistors and Circuits by Using Bilayer Sol–Gel Gate Dielectrics. *ACS Appl. Mater. Interfaces* **2018**, *10* (3), 2679–2687.

(365) Dey, T.; Naughton, D. Cleaning and Anti-Reflective (AR) Hydrophobic Coating of Glass Surface: A Review from Materials Science Perspective. *J. Sol-Gel Sci. Technol.* **2016**, *77* (1), 1–27.

(366) Jang, J.; Kang, H.; Chakravarthula, H. C. N.; Subramanian, V. Fully Inkjet-Printed Transparent Oxide Thin Film Transistors Using a Fugitive Wettability Switch. *Adv. Electron. Mater.* **2015**, *1* (7), 1500086.

(367) Wei, J.; Fang, Z.; Peng, J.; Cai, W.; Zhu, Z.; Yao, R.; Zhou, S.; Yuan, W.; Lu, K.; Ning, H. High-Performance Spin-Coated Aluminum Oxide Dielectric Fabricated by a Simple Oxygen Plasma-Treatment Process. *J. Phys. D. Appl. Phys.* **2018**, *51* (36).

(368) Roth, B.; Søndergaard, R. R.; Krebs, F. C. *Roll-to-Roll Printing and Coating Techniques for Manufacturing Large-Area Flexible Organic Electronics*; Elsevier Ltd, 2014.

(369) Choi, Y.; Kim, G. H.; Jeong, W. H.; Kim, H. J.; Chin, B. D.; Yu, J.-W. Characteristics of Gravure Printed InGaZnO Thin Films as an Active Channel Layer in Thin Film Transistors. *Thin Solid Films* **2010**, *518* (22), 6249–6252.

(370) Spiehl, D.; Haming, M.; Sauer, H. M.; Bonrad, K.; Dorsam, E. Engineering of Flexo- and Gravure-Printed Indium–Zinc-Oxide Semiconductor Layers for High-Performance Thin-Film Transistors. *IEEE Trans. Electron Devices* **2015**, *62* (9), 2871–2877.

(371) Mariani, P.; Vesce, L.; Di Carlo, A. The Role of Printing Techniques for Large-Area Dye Sensitized Solar Cells. *Semicond. Sci. Technol.* **2015**, *30* (10), 104003.

(372) Fukuda, K.; Yoshimura, Y.; Okamoto, T.; Takeda, Y.; Kumaki, D.; Katayama, Y.; Tokito, S. Reverse-Offset Printing Optimized for Scalable Organic Thin-Film Transistors with Submicrometer Channel Lengths. *Adv. Electron. Mater.* **2015**, *1* (8), 1–6.

(373) Lin, J. Printing Processes and Equipments. In *Printed Electronics*; John Wiley & Sons Singapore Pte. Ltd: Singapore, 2016; pp 106–144.

(374) Kim, S.; Sojoudi, H.; Zhao, H.; Mariappan, D.; McKinley, G. H.; Gleason, K. K.; Hart, A. J. Ultrathin High-Resolution Flexographic Printing Using Nanoporous Stamps. *Sci. Adv.* **2016**, *2* (12), e1601660.

(375) Dilfer, S.; Hoffmann, R. C.; Dörsam, E. Characteristics of Flexographic Printed Indium-Zinc-Oxide Thin Films as an Active Semiconductor Layer in Thin Film Field-Effect

Transistors. *Appl. Surf. Sci.* **2014**, *320*, 634–642.

(376) Leppäniemi, J.; Huttunen, O.-H. H.; Majumdar, H.; Alastalo, A. Flexography-Printed In 2 O 3 Semiconductor Layers for High-Mobility Thin-Film Transistors on Flexible Plastic Substrate. *Adv. Mater.* **2015**, *27* (44), 7168–7175.

(377) Pujar, G. M. P.; Gupta, B.; Gupta, D.; Mandal, S. Low - Temperature Reducible Particle - Free Screen - Printable Silver Ink for the Fabrication of High Conductive Electrodes. *J. Mater. Sci. Mater. Electron.* **2019**, No. 0123456789.

(378) Fukada, K.; Maeda, Y.; Liu, X. Y.; Matoba, A.; Takagi, S.; Inoue, S.; Shimoda, T. 33.5: Fabrication of an All-Screen Printed Oxide Semiconductor Thin Film Transistor Active-Matrix Backplane. *SID Symp. Dig. Tech. Pap.* **2015**, *46* (1), 490–493.

(379) Carvalho, J.; Dubceac, V.; Grey, P.; Cunha, I.; Fortunato, E.; Martins, R.; Clausner, A.; Zschech, E.; Pereira, L. Fully Printed Zinc Oxide Electrolyte-Gated Transistors on Paper. *Nanomaterials* **2019**, *9* (2), 169.

(380) Sneck, A.; Mäkelä, T.; Alastalo, A. Reverse-Offset for Roll-to-Roll High-Resolution Printing. *Flex. Print. Electron.* **2018**, *3* (1), 014001.

(381) Fukuda, K.; Someya, T. Recent Progress in the Development of Printed Thin-Film Transistors and Circuits with High-Resolution Printing Technology. *Adv. Mater.* **2017**, *29* (25), 1602736.

(382) Moon, T.-H.; Nam, S.-H.; Kim, N.-K.; Kook, Y.-H.; Jung, Y.-K.; Chang, Y.-G.; Yoo, S.-S.; Kim, C.-D.; Kang, I.; Chung, I.-J. P-185L: Late-News Poster: Direct Patterning of Metal Electrodes ForTFT-LCD Fabrication. *SID Symp. Dig. Tech. Pap.* **2009**, *40* (1), 1348.

(383) Kusaka, Y.; Shirakawa, N.; Ogura, S.; Leppäniemi, J.; Sneck, A.; Alastalo, A.; Ushijima, H.; Fukuda, N. Reverse Offset Printing of Semidried Metal Acetylacetonate Layers and Its Application to a Solution-Processed IGZO TFT Fabrication. *ACS Appl. Mater. Interfaces* **2018**, *10* (29), 24339–24343.

(384) Han, Y. H.; Won, J. Y.; Yoo, H. S.; Kim, J. H.; Choi, R.; Jeong, J. K. High Performance Metal Oxide Field-Effect Transistors with a Reverse Offset Printed Cu Source/Drain Electrode. *ACS Appl. Mater. Interfaces* **2016**, *8* (2), 1156–1163.

(385) Yang, Y. S.; Park, J. H.; You, I. K.; Hong, S. H.; Yun, H. G.; Kang, Y. H.; Lee, C.; Cho, S. Y. Electrical Characteristics of InZnO3 Transistors Fabricated by Reverse Offset Printing. *J. Ceram. Process. Res.* **2015**, *16* (2), 276–279.

(386) Leppäniemi, J.; Sneck, A.; Kusaka, Y.; Fukuda, N.; Alastalo, A. Reverse-Offset Printing of Metal-Nitrate-Based Metal Oxide Semiconductor Ink for Flexible TFTs. *Adv. Electron. Mater.* **2019**, *5* (8), 1900272.

(387) Shao, F.; Wan, Q. Recent Progress on Jet Printing of Oxide-Based Thin Film Transistors. *J. Phys. D. Appl. Phys.* **2019**, *52* (14).

(388) Lee, J. S.; Kwack, Y.-J.; Choi, W.-S. Inkjet-Printed In 2 O 3 Thin-Film Transistor below 200 °C. *ACS Appl. Mater. Interfaces* **2013**, *5* (22), 11578–11583.

(389) Lim, J. A.; Lee, W. H.; Lee, H. S.; Lee, J. H.; Park, Y. D.; Cho, K. Self-Organization of Ink-Jet-Printed Triisopropylsilylethynyl Pentacene via Evaporation-Induced Flows in a Drying Droplet. *Adv. Funct. Mater.* **2008**, *18* (2), 229–234.

(390) Sun, D.; Chen, C.; Zhang, J.; Wu, X.; Chen, H.; Guo, T. High Performance Inkjet-Printed Metal Oxide Thin Film Transistors via Addition of Insulating Polymer with Proper Molecular Weight. *Appl. Phys. Lett.* **2018**, *112* (1), 012102.

(391) Wu, S.; Zhang, Q.; Chen, Z.; Mo, L.; Shao, S.; Cui, Z. Inkjet Printing of Oxide Thin Film Transistor Arrays with Small Spacing with Polymer-Doped Metal Nitrate Aqueous Ink. *J. Mater. Chem. C* **2017**, *5* (30), 7495–7503.

(392) Li, Y.; Lan, L.; Sun, S.; Lin, Z.; Gao, P.; Song, W.; Song, E.; Zhang, P.; Peng, J. All Inkjet-Printed Metal-Oxide Thin-Film Transistor Array with Good Stability and Uniformity Using Surface-Energy Patterns. *ACS Appl. Mater. Interfaces* **2017**, *9* (9), 8194–8200.

(393) Sharma, B. K.; Stoesser, A.; Mondal, S. K.; Garlapati, S. K.; Fawey, M. H.; Chakravadhanula, V. S. K.; Kruk, R.; Hahn, H.; Dasgupta, S. High-Performance All-Printed Amorphous Oxide FETs and Logics with Electronically Compatible Electrode/Channel Interface. *ACS Appl. Mater. Interfaces* **2018**, *10* (26), 22408–22418.

(394) Yang, C.; Fang, Z.; Ning, H.; Tao, R.; Chen, J.; Zhou, Y.; Zheng, Z.; Yao, R.; Wang, L.; Peng, J.; Song, Y. Amorphous InGaZnO Thin Film Transistor Fabricated with Printed Silver Salt Ink Source/Drain Electrodes. *Appl. Sci.* **2017**, *7* (8), 844.

(395) Gillan, L.; Leppäniemi, J.; Eiroma, K.; Majumdar, H.; Alastalo, A. High Performance Solution Processed Oxide Thin-Film Transistors with Inkjet Printed Ag Source–Drain Electrodes. *J. Mater. Chem. C* **2018**, *6* (13), 3220–3225.

(396) Garlapati, S. K.; Marques, G. C.; Gebauer, J. S.; Dehm, S.; Bruns, M.; Winterer, M.; Tahoori, M. B.; Aghassi-Hagmann, J.; Hahn, H.; Dasgupta, S. High Performance Printed Oxide Field-Effect Transistors Processed Using Photonic Curing. *Nanotechnology* **2018**, *29* (23).

(397) Bolat, S.; Fuchs, P.; Knobelspies, S.; Temel, O.; Sevilla, G. T.; Gilshtein, E.; Andres, C.; Shorubalko, I.; Liu, Y.; Tröster, G.; Tiwari, A. N.; Romanyuk, Y. E. Inkjet-Printed and Deep-UV-Annealed YAlO x Dielectrics for High-Performance IGZO Thin-Film Transistors on Flexible Substrates. *Adv. Electron. Mater.* **2019**, *1800843*, 1–9.

(398) Garlapati, S. K.; Divya, M.; Breitung, B.; Kruk, R.; Hahn, H.; Dasgupta, S. Printed Electronics Based on Inorganic Semiconductors: From Processes and Materials to Devices. *Adv. Mater.* **2018**, *30* (40), 1707600.

(399) Lee, S.; Kim, J.; Choi, J.; Park, H.; Ha, J.; Kim, Y.; Rogers, J. A.; Paik, U. Patterned Oxide Semiconductor by Electrohydrodynamic Jet Printing for Transparent Thin Film Transistors. *Appl. Phys. Lett.* **2012**, *100* (10), 102108.

(400) Kwack, Y. J.; Choi, W. S. Patterning and Passivation Effects of Zinc-Tin-Oxide Thin-Film Transistors Using an Electrohydrodynamic Jet Printer. *Mater. Res. Bull.* **2019**, *114* (March), 170–176.

(401) Kwack, Y. J.; Choi, W. S. Electrohydrodynamic Jet Printed Indium-Zinc-Oxide Thin-Film Transistors. *J. Disp. Technol.* **2016**, *12* (1), 3–7.

(402) Lee, Y. G.; Choi, W. S. Electrohydrodynamic Jet-Printed Zinc-Tin Oxide TFTs and Their Bias Stability. *ACS Appl. Mater. Interfaces* **2014**, *6* (14), 11167–11172.

(403) Kim, S.-Y. S.-Y. Y.; Kim, K.; Hwang, Y. H.; Park, J.-U. J.-U. U.; Jang, J.; Nam, Y.; Kang, Y.; Kim, M.; Park, H. J.; Lee, Z.; Choi, J.; Kim, Y.; Jeong, S.; Bae, B.-S. B.-S. S.; Park, J.-U. J.-U. U. High-Resolution Electrohydrodynamic Inkjet Printing of Stretchable Metal Oxide Semiconductor Transistors with High Performance. *Nanoscale* **2016**, *8* (39), 17113–17121.

(404) Liu, R.; Ding, H.; Lin, J.; Shen, F.; Cui, Z.; Zhang, T. Fabrication of Platinum-Decorated Single-Walled Carbon Nanotube Based Hydrogen Sensors by Aerosol Jet Printing. *Nanotechnology* **2012**, *23* (50), 505301.

(405) Hong, K.; Kim, S. H.; Lee, K. H.; Frisbie, C. D. Printed, Sub-2V ZnO Electrolyte Gated

Transistors and Inverters on Plastic. *Adv. Mater.* **2013**, *25* (25), 3413–3418.

(406) Hong, K.; Kim, Y. H.; Kim, S. H.; Xie, W.; Xu, W. D.; Kim, C. H.; Frisbie, C. D. Aerosol Jet Printed, Sub-2 v Complementary Circuits Constructed from P-and N-Type Electrolyte Gated Transistors. *Adv. Mater.* **2014**, *26* (41), 7032–7037.

(407) Xie, W.; Zhang, X.; Leighton, C.; Frisbie, C. D. 2D Insulator–Metal Transition in Aerosol-Jet-Printed Electrolyte-Gated Indium Oxide Thin Film Transistors. *Adv. Electron. Mater.* **2017**, *3* (3), 1–6.

(408) Meyers, S. T.; Anderson, J. T.; Hung, C. M.; Thompson, J.; Wager, J. F.; Keszler, D. A. Aqueous Inorganic Inks for Low-Temperature Fabrication of ZnO TFTs. *J. Am. Chem. Soc.* **2008**, *130* (51), 17603–17609.

(409) Han, S.; Lee, D.; Herman, G. S.; Chang, C. Inkjet-Printed High Mobility Transparent–Oxide Semiconductors. *J. Disp. Technol.* **2009**, *5* (12), 520–524.

(410) Lee, D. H.; Han, S. Y.; Herman, G. S.; Chang, C. H. Inkjet Printed High-Mobility Indium Zinc Tin Oxide Thin Film Transistors. *J. Mater. Chem.* **2009**, *19* (20), 3135–3137.

(411) Kim, D.; Jeong, Y.; Song, K.; Park, S. K.; Cao, G.; Moon, J. Inkjet-Printed Zinc Tin Oxide Thin-Film Transistor. *Langmuir* **2009**, *25* (18), 11149–11154.

(412) Yong-Hoon Kim; Kwang-Ho Kim; Min Suk Oh; Hyun Jae Kim; Jeong In Han; Min-Koo Han; Sung Kyu Park. Ink-Jet-Printed Zinc-Tin-Oxide Thin-Film Transistors and Circuits With Rapid Thermal Annealing Process. *IEEE Electron Device Lett.* **2010**, *31* (8), 836–838.

(413) Hennek, J. W.; Xia, Y.; Everaerts, K.; Hersam, M. C.; Facchetti, A.; Marks, T. J. Reduced Contact Resistance in Inkjet Printed High-Performance Amorphous Indium Gallium Zinc Oxide Transistors. *ACS Appl. Mater. Interfaces* **2012**, *4* (3), 1614–1619.

(414) Jeong, S.; Lee, J. Y.; Lee, S. S.; Seo, Y. H.; Kim, S. Y.; Park, J. U.; Ryu, B. H.; Yang, W.; Moon, J.; Choi, Y. Metal Salt-Derived In-Ga-Zn-O Semiconductors Incorporating Formamide as a Novel Co-Solvent for Producing Solution-Processed, Electrohydrodynamic-Jet Printed, High Performance Oxide Transistors. *J. Mater. Chem. C* **2013**, *1* (27), 4236–4243.

(415) Meyer, S.; Pham, D. V.; Merkulov, S.; Weber, D.; Merkulov, A.; Benson, N.; Schmechel, R. Soluble Metal Oxo Alkoxide Inks with Advanced Rheological Properties for Inkjet-Printed Thin-Film Transistors. *ACS Appl. Mater. Interfaces* **2017**, *9* (3), 2625–2633.

(416) Li, Y.; Lan, L.; Xiao, P.; Sun, S.; Lin, Z.; Song, W.; Song, E.; Gao, P.; Wu, W.; Peng, J. Coffee-Ring Defined Short Channels for Inkjet-Printed Metal Oxide Thin-Film Transistors. *ACS Appl. Mater. Interfaces* **2016**, *8* (30), 19643–19648.

(417) Zeumault, A.; Ma, S.; Holbery, J. Fully Inkjet-Printed Metal-Oxide Thin-Film Transistors on Plastic. *Phys. status solidi* **2016**, *213* (8), 2189–2195.

(418) Scheideler, W. J.; Kumar, R.; Zeumault, A. R.; Subramanian, V. Low-Temperature-Processed Printed Metal Oxide Transistors Based on Pure Aqueous Inks. *Adv. Funct. Mater.* **2017**, *27* (14), 1606062.

(419) Hoth, C. N.; Schilinsky, P.; Choulis, S. a; Balasubramanian, S.; Brabec, C. J. *Applications of Organic and Printed Electronics*; 2013.

(420) Tang, A.; Liu, Y.; Wang, Q.; Chen, R.; Liu, W.; Fang, Z.; Wang, L. A New Photoelectric Ink Based on Nanocellulose/CdS Quantum Dots for Screen-Printing. *Carbohydr. Polym.* **2016**, *148*, 29–35.

(421) Joseph, A. M.; Nagendra, B.; Bhoje Gowd, E.; Surendran, K. P. Screen-Printable

Electronic Ink of Ultrathin Boron Nitride Nanosheets. *ACS Omega* **2016**, *1* (6), 1220–1228.

(422) Liang, J.; Chen, J. Z.; Zhang, Q.; Kuang, Y.; Zhang, X. A Novel XY-Theta Alignment Stage for Screen Printing and Its Accuracy Analysis. *2012 IEEE Int. Conf. Mechatronics Autom. ICMA 2012* **2012**, 1352–1357.

(423) Arapov, K.; Rubingh, E.; Abbel, R.; Laven, J.; De With, G.; Friedrich, H. Conductive Screen Printing Inks by Gelation of Graphene Dispersions. *Adv. Funct. Mater.* **2016**, *26* (4), 586–593.

(424) Cao, X.; Chen, H.; Gu, X.; Liu, B.; Wang, W.; Cao, Y.; Wu, F.; Zhou, C. Screen Printing as a Scalable and Low-Cost Approach for Rigid and Flexible Thin-Film Transistors Using Separated Carbon Nanotubes. *ACS Nano* **2014**, *8* (12), 12769–12776.

(425) Overgaard, M. H.; Kühnel, M.; Hvidsten, R.; Petersen, S. V.; Vosch, T.; Nørgaard, K.; Laursen, B. W. Highly Conductive Semitransparent Graphene Circuits Screen-Printed from Water-Based Graphene Oxide Ink. *Adv. Mater. Technol.* **2017**, *2* (7), 1–7.

(426) Tobjörk, D.; Österbacka, R. Paper Electronics. *Adv. Mater.* **2011**, *23* (17), 1935–1961.

(427) Grau, G.; Kitsomboonloha, R.; Subramanian, V. Fabrication of a High-Resolution Roll for Gravure Printing of 2μm Features. *Org. Field-Effect Transistors XIV; Org. Sensors Bioelectron. VIII* **2015**, *9568*, 95680M.

(428) Grau, G.; Cen, J.; Kang, H.; Kitsomboonloha, R.; Scheideler, W. J.; Subramanian, V. Gravure-Printed Electronics: Recent Progress in Tooling Development, Understanding of Printing Physics, and Realization of Printed Devices. *Flex. Print. Electron.* **2016**, *1* (2), 1–23.

(429) Koutsioukis, A.; Georgakilas, V.; Belessi, V.; Zboril, R. Highly Conductive Water-Based Polymer/Graphene Nanocomposites for Printed Electronics. *Chem. - A Eur. J.* **2017**, *23* (34), 8268–8274.

(430) Nguyen, H. A. D.; Shin, K.; Lee, C. Multi-Response Optimization of R2R Gravure Printing Using Orthogonal Array and Principal Component Analysis as a Weighting Factor. *Int. J. Adv. Manuf. Technol.* **2017**, *90* (9–12), 3595–3606.

(431) Thiburce, Q.; Campbell, A. J. Low-Voltage Polyelectrolyte-Gated Polymer Field-Effect Transistors Gravure Printed at High Speed on Flexible Plastic Substrates. *Adv. Electron. Mater.* **2016**, 1600421.

(432) Lorenz, A.; Senne, A.; Rohde, J.; Kroh, S.; Wittenberg, M.; Krüger, K.; Clement, F.; Biro, D. Evaluation of Flexographic Printing Technology for Multi-Busbar Solar Cells. *Energy Procedia* **2015**, *67*, 126–137.

(433) Kusaka, Y.; Kanazawa, S.; Koutake, M.; Ushijima, H. Pattern Size Tolerance of Reverse Offset Printing: A Proximity Deformation Effect Related to Local PDMS Slipping. *J. Micromechanics Microengineering* **2017**, *27* (10).

(434) Cho, Y. T.; Jeong, Y.; Kim, Y. J.; Kwon, S.; Lee, S. H.; Kim, K. Y.; Kang, D.; Lee, T. M. Printing Speed and Quality Enhancement by Controlling the Surface Energy of Cliché in Reverse Offset Printing. *Appl. Sci.* **2017**, *7* (12).

(435) Bromberg, V.; Ma, S.; Singler, T. J. High-Resolution Inkjet Printing of Electrically Conducting Lines of Silver Nanoparticles by Edge-Enhanced Twin-Line Deposition. *Appl. Phys. Lett.* **2013**, *102* (21), 1–5.

(436) Moya, A.; Gabriel, G.; Villa, R.; Javier del Campo, F. Inkjet-Printed Electrochemical Sensors. *Curr. Opin. Electrochem.* **2017**, *3* (1), 29–39.

(437) Bruner, S.; Xu, D.; Phillips, C. 54.3: Drop Landing Accuracy Improvements in Inkjet Printed OLED Displays. *SID Symp. Dig. Tech. Pap.* **2007**, *38* (1), 1611–1612.

(438) Homenick, C. M.; James, R.; Lopinski, G. P.; Dunford, J.; Sun, J.; Park, H.; Jung, Y.; Cho, G.; Malenfant, P. R. L. Fully Printed and Encapsulated SWCNT-Based Thin Film Transistors via a Combination of R2R Gravure and Inkjet Printing. *ACS Appl. Mater. Interfaces* **2016**, *8* (41), 27900–27910.

(439) Kwon, H. J.; Chung, S.; Jang, J.; Grigoropoulos, C. P. Laser Direct Writing and Inkjet Printing for a Sub-2 Mm Channel Length MoS2 Transistor with High-Resolution Electrodes. *Nanotechnology* **2016**, *27* (40).

(440) Perelaer, J.; De Gans, B. J.; Schubert, U. S. Ink-Jet Printing and Microwave Sintering of Conductive Silver Tracks. *Adv. Mater.* **2006**, *18* (16), 2101–2104.

(441) Yin, Z.; Huang, Y.; Duan, Y.; Zhang, H. *Electrohydrodynamic Direct-Writing for Flexible Electronic Manufacturing*; 2018.

(442) Yudistira, H. T.; Tenggara, A. P.; Oh, S. S.; Nguyen, V.; Choi, M.; Choi, C. G.; Byun, D. High-Resolution Electrohydrodynamic Jet Printing for the Direct Fabrication of 3D Multilayer Terahertz Metamaterial of High Refractive Index. *J. Micromechanics Microengineering* **2015**, *25* (4).

(443) Li, H.; Tang, Y.; Guo, W.; Liu, H.; Zhou, L.; Smolinski, N. Polyfluorinated Electrolyte for Fully Printed Carbon Nanotube Electronics. *Adv. Funct. Mater.* **2016**, *26* (38), 6914–6920.

(444) Khan, S.; Nguyen, T. P.; Thiery, L.; Vairac, P.; Briand, D. Aerosol Jet Printing of Miniaturized, Low Power Flexible Micro-Hotplates. *Proceedings* **2017**, *1* (10), 316.

(445) Salary, R.; Lombardi, J. P.; Samie Tootooni, M.; Donovan, R.; Rao, P. K.; Borgesen, P.; Poliks, M. D. Computational Fluid Dynamics Modeling and Online Monitoring of Aerosol Jet Printing Process. *J. Manuf. Sci. Eng. Trans. ASME* **2017**, *139* (2).

(446) Smith, M.; Choi, Y. S.; Boughey, C.; Kar-Narayan, S. Controlling and Assessing the Quality of Aerosol Jet Printed Features for Large Area and Flexible Electronics. *Flex. Print. Electron.* **2017**, *2* (1).

(447) Caironi, M.; Noh, Y.-Y. *Large Area and Flexible Electronics*; Caironi, M., Noh, Y.-Y., Eds.; Wiley-VCH Verlag GmbH & Co. KGaA: Weinheim, Germany, 2015; Vol. 66.

(448) Olziersky, A.; Vilà, A.; Morante, J. R. Multicomponent Oxide Thin-Film Transistors Fabricated by a Double-Layer Inkjet Printing Process. *Thin Solid Films* **2011**, *520* (4), 1334–1340.

(449) Hong, K.; Kim, S. H.; Mahajan, A.; Frisbie, C. D. Aerosol Jet Printed P- and n-Type Electrolyte-Gated Transistors with a Variety of Electrode Materials: Exploring Practical Routes to Printed Electronics. *ACS Appl. Mater. Interfaces* **2014**, *6* (21), 18704–18711.

(450) Park, S.; Kim, C.-H.; Lee, W.-J.; Sung, S.; Yoon, M.-H. Sol-Gel Metal Oxide Dielectrics for All-Solution-Processed Electronics. *Mater. Sci. Eng. R Reports* **2017**, *114*, 1–22.

(451) Glynn, C.; O'Dwyer, C. Solution Processable Metal Oxide Thin Film Deposition and Material Growth for Electronic and Photonic Devices. *Adv. Mater. Interfaces* **2017**, *4* (2), 1600610.

(452) Nayak, P. K.; Busani, T.; Elamurugu, E.; Barquinha, P.; Martins, R.; Hong, Y.; Fortunato, E. Zinc Concentration Dependence Study of Solution Processed Amorphous Indium Gallium Zinc Oxide Thin Film Transistors Using High-k Dielectric. *Appl. Phys. Lett.* **2010**, *97* (18), 1–4.

(453) Dey, A.; Kalita, A.; Iyer, P. K. High-Performance n - Channel Organic Thin-Film Transistor Based on Naphthalene Diimide. **2014**.

(454) Kim, S. J.; Jang, M.; Yang, H. Y.; Cho, J.; Lim, H. S.; Yang, H.; Lim, J. A. Instantaneous Pulsed-Light Cross-Linking of a Polymer Gate Dielectric for Flexible Organic Thin-Film Transistors. *ACS Appl. Mater. Interfaces* **2017**, *9* (13), 11721–11731.

(455) Liu, A.; Guo, Z.; Liu, G.; Zhu, C.; Zhu, H.; Shin, B.; Fortunato, E.; Martins, R.; Shan, F. Redox Chloride Elimination Reaction: Facile Solution Route for Indium-Free, Low-Voltage, and High-Performance Transistors. *Adv. Electron. Mater.* **2017**, *201600513*, 1600513.

(456) Zhang, F.; Liu, G.; Liu, A.; Shin, B.; Shan, F. Solution-Processed Hafnium Oxide Dielectric Thin Films for Thin-Film Transistors Applications. *Ceram. Int.* **2015**, *41* (10), 13218–13223.

(457) Kim, Y. G.; Avis, C.; Jang, J. Low Voltage Driven, Stable Solution-Processed Zinc-Tin-Oxide TFT with HfOy and AlOx Stack Gate Dielectric. *ECS Solid State Lett.* **2012**, *1* (2), Q23–Q25.

(458) Park, J. H.; Lee, S. J.; Lee, T. Il; Kim, J. H.; Kim, C.-H.; Chae, G. S.; Ham, M.-H.; Baik, H. K.; Myoung, J.-M. All-Solution-Processed, Transparent Thin-Film Transistors Based on Metal Oxides and Single-Walled Carbon Nanotubes. *J. Mater. Chem. C* **2013**, *1* (9), 1840–1845.

(459) Han, S. W.; Park, J. H.; Yoo, Y. B.; Lee, K. H.; Kim, K. H.; Baik, H. K. Solution-Processed Laminated ZrO2/Al2O3 Dielectric for Low-Voltage Indium Zinc Oxide Thin-Film Transistors. *J. Sol-Gel Sci. Technol.* **2017**, *81* (2), 570–575.

(460) Liu, A.; Liu, G. X.; Zhu, H. H.; Xu, F.; Fortunato, E.; Martins, R.; Shan, F. K. Fully Solution-Processed Low-Voltage Aqueous In 2 O 3 Thin-Film Transistors Using an Ultrathin ZrO x Dielectric. *ACS Appl. Mater. Interfaces* **2014**, *6* (20), 17364–17369.

(461) Pereira, L.; Barquinha, P.; Fortunato, E.; Martins, R. Influence of the Oxygen/Argon Ratio on the Properties of Sputtered Hafnium Oxide. *Mater. Sci. Eng. B* **2005**, *118* (1–3), 210–213.

(462) Wang, H.; Sun, T.; Xu, W.; Xie, F.; Ye, L.; Xiao, Y.; Wang, Y.; Chen, J.; Xu, J. Low-Temperature Facile Solution-Processed Gate Dielectric for Combustion Derived Oxide Thin Film Transistors. *RSC Adv.* **2014**, *4* (97), 54729–54739.

(463) Avis, C.; Kim, Y. G.; Jang, J. Solution Processed Hafnium Oxide as a Gate Insulator for Low-Voltage Oxide Thin-Film Transistors. *J. Mater. Chem.* **2012**, *22* (34), 17415.

(464) Gao, Y. N.; Xu, Y. L.; Lu, J. G.; Zhang, J. H.; Li, X. F. Solution Processable Amorphous Hafnium Silicate Dielectrics and Their Application in Oxide Thin Film Transistors. *J. Mater. Chem. C* **2015**, *3* (43), 11497–11504.

(465) Esro, M.; Vourlias, G.; Somerton, C.; Milne, W. I.; Adamopoulos, G. High-Mobility ZnO Thin Film Transistors Based on Solution-Processed Hafnium Oxide Gate Dielectrics. *Adv. Funct. Mater.* **2015**, *25* (1), 134–141.

(466) Kiazadeh, A.; Gomes, H. L.; Barquinha, P.; Martins, J.; Rovisco, A.; Pinto, J. V.; Martins, R.; Fortunato, E. Improving Positive and Negative Bias Illumination Stress Stability in Parylene Passivated IGZO Transistors. *Appl. Phys. Lett.* **2016**, *109* (5), 051606.

(467) Weng, J.; Chen, W.; Xia, W.; Zhang, J.; Jiang, Y.; Zhu, G. Low-Temperature Solution-Based Fabrication of High-k HfO2 Dielectric Thin Films via Combustion Process. *J. Sol-Gel Sci. Technol.* **2016**, 1–7.

(468) Faber, H.; Lin, Y.; Thomas, S. R.; Zhao, K.; Pliatsikas, N.; McLachlan, M. A.; Amassian,

A.; Patsalas, P. A.; Anthopoulos, T. D. Indium Oxide Thin-Film Transistors Processed at Low Temperature via Ultrasonic Spray Pyrolysis. *ACS Appl. Mater. Interfaces* **2015**, *7* (1), 782–790.

(469) Neumayer, D. A.; Cartier, E. Materials Characterization of ZrO2–SiO2 and HfO2–SiO2 Binary Oxides Deposited by Chemical Solution Deposition. *J. Appl. Phys.* **2001**, *90* (4), 1801–1808.

(470) Toledano-Luque, M.; San Andrés, E.; Olea, J.; del Prado, A.; Mártil, I.; Bohne, W.; Röhrich, J.; Strub, E. Hafnium Oxide Thin Films Deposited by High Pressure Reactive Sputtering in Atmosphere Formed with Different Ar/O2 Ratios. *Mater. Sci. Semicond. Process.* **2006**, *9* (6), 1020–1024.

(471) Reyes, J. M.; Perez Ramos, B. M.; Islas, C. Z.; Arriaga, W. C.; Quintero, P. R.; Jacome, a. T. Chemical and Morphological Characteristics of ALD Al2O3 Thin-Film Surfaces after Immersion in PH Buffer Solutions. *J. Electrochem. Soc.* **2013**, *160* (10), B201–B206.

(472) Chang, Y.-H.; Yu, M.-J.; Lin, R.-P.; Hsu, C.-P.; Hou, T.-H. Abnormal Positive Bias Stress Instability of In–Ga–Zn–O Thin-Film Transistors with Low-Temperature Al2O3 Gate Dielectric. *Appl. Phys. Lett.* **2016**, *108* (3), 033502.

(473) Chung, S.; Cho, K.; Lee, T. Recent Progress in Inkjet-Printed Thin-Film Transistors. *Adv. Sci.* **2019**, *6* (6), 1801445.

(474) Drotlef, D. M.; Amjadi, M.; Yunusa, M.; Sitti, M. Bioinspired Composite Microfibers for Skin Adhesion and Signal Amplification of Wearable Sensors. *Adv. Mater.* **2017**, *29* (28), 1–8.

(475) Wu, W. Inorganic Nanomaterials for Printed Electronics: A Review. *Nanoscale* **2017**, *9* (22), 7342–7372.

(476) Sowade, E.; Ramon, E.; Mitra, K. Y.; Martínez-Domingo, C.; Pedró, M.; Pallarès, J.; Loffredo, F.; Villani, F.; Gomes, H. L.; Terés, L.; Baumann, R. R. All-Inkjet-Printed Thin-Film Transistors: Manufacturing Process Reliability by Root Cause Analysis. *Sci. Rep.* **2016**, *6* (1), 33490.

(477) Gao, M.; Li, L.; Song, Y. Inkjet Printing Wearable Electronic Devices. *J. Mater. Chem. C* **2017**, *5* (12), 2971–2993.

(478) Bidoki, S. M.; Nouri, J.; Heidari, A. A. Inkjet Deposited Circuit Components. *J. Micromechanics Microengineering* **2010**, *20* (5), 055023.

(479) Zhu, H.; Narakathu, B. B.; Fang, Z.; Tausif Aijazi, A.; Joyce, M.; Atashbar, M.; Hu, L. A Gravure Printed Antenna on Shape-Stable Transparent Nanopaper. *Nanoscale* **2014**, *6* (15), 9110.

(480) Sternkiker, C.; Sowade, E.; Mitra, K. Y.; Zichner, R.; Baumann, R. R. Upscaling of the Inkjet Printing Process for the Manufacturing of Passive Electronic Devices. *IEEE Trans. Electron Devices* **2016**, *63* (1), 426–431.

(481) Lilja, K. E.; Majumdar, H. S.; Pettersson, F. S.; Österbacka, R.; Joutsenoja, T. Enhanced Performance of Printed Organic Diodes Using a Thin Interfacial Barrier Layer. *ACS Appl. Mater. Interfaces* **2011**, *3* (1), 7–10.

(482) Sowade, E.; Mitra, K. Y.; Ramon, E.; Martinez-Domingo, C.; Villani, F.; Loffredo, F.; Gomes, H. L.; Baumann, R. R. Up-Scaling of the Manufacturing of All-Inkjet-Printed Organic Thin-Film Transistors: Device Performance and Manufacturing Yield of Transistor Arrays. *Org. Electron.* **2016**, *30*, 237–246.

(483) Madej, E.; Espig, M.; Baumann, R. R.; Schuhmann, W.; La Mantia, F. Optimization of Primary Printed Batteries Based on Zn/MnO2. *J. Power Sources* **2014**, *261*, 356–362.

(484) Li, X.; Hasan, M. M.; Jeon, J.; Jang, J. 5-4: Stretchable Oxide TFTs for Wearable Electronics. *SID Symp. Dig. Tech. Pap.* **2017**, *48* (1), 42–45.

(485) Pierre, A.; Sadeghi, M.; Payne, M. M.; Facchetti, A.; Anthony, J. E.; Arias, A. C. All-Printed Flexible Organic Transistors Enabled by Surface Tension-Guided Blade Coating. *Adv. Mater.* **2014**, *26* (32), 5722–5727.

(486) Scheideler, W.; Subramanian, V. Printed Flexible and Transparent Electronics: Enhancing Low-Temperature Processed Metal Oxides with 0D and 1D Nanomaterials. *Nanotechnology* **2019**, *30* (27), 272001.

(487) Zeumault, A.; Subramanian, V. Mobility Enhancement in Solution-Processed Transparent Conductive Oxide TFTs Due to Electron Donation from Traps in High- k Gate Dielectrics. *Adv. Funct. Mater.* **2016**, *26* (6), 955–963.

(488) Zhu, H.; Shin, E.; Liu, A.; Ji, D.; Xu, Y.; Noh, Y. Printable Semiconductors for Backplane TFTs of Flexible OLED Displays. *Adv. Funct. Mater.* **2019**, 1904588.

(489) Pietrikova, A.; Lukacs, P.; Jakubeczyova, D.; Ballokova, B.; Potencki, J.; Tomaszewski, G.; Pekarek, J.; Prikrylova, K.; Fides, M. Surface Analysis of Polymeric Substrates Used for Inkjet Printing Technology. *Circuit World* **2016**, *42* (1), 9–16.

(490) MacDonald, W. A.; Looney, M. K.; MacKerron, D.; Eveson, R.; Adam, R.; Hashimoto, K.; Rakos, K. Latest Advances in Substrates for Flexible Electronics. *J. Soc. Inf. Disp.* **2007**, *15* (12), 1075.

(491) Matsuhisa, N.; Kaltenbrunner, M.; Yokota, T.; Jinno, H.; Kuribara, K.; Sekitani, T.; Someya, T. Printable Elastic Conductors with a High Conductivity for Electronic Textile Applications. *Nat. Commun.* **2015**, *6* (1), 7461.

(492) Sanchez-Rodriguez, D.; Farjas, J.; Roura, P.; Ricart, S.; Mestres, N.; Obradors, X.; Puig, T. Thermal Analysis for Low Temperature Synthesis of Oxide Thin Films from Chemical Solutions. *J. Phys. Chem. C* **2013**, *117* (39), 20133–20138.

(493) Moulder, J. F.; Stickle, W. F.; Sobol, P. E.; Bomben, K. D. *Handbook of X-Ray Photoelectron Spectroscopy*; Perkin-Elmer Corporation: Minnesota, 1992.

(494) Yang, C.-S.; Kim, J.-S.; Choi, J.-W.; Kwon, M.-H.; Kim, Y.-J.; Choi, J.-G.; Kim, G.-T. XPS Study of Aluminum Oxides Deposited on PET Thin Film XPS Study of Aluminum Oxides Deposited on PET Thin Film. *J. Ind. Eng. Chem.* **2000**, *6* (3), 149–156.

(495) Watts, J. F. High Resolution XPS of Organic Polymers: The Scienta ESCA 300 Database. G. Beamson and D. Briggs. 280pp., £65. John Wiley & Sons, Chichester, ISBN 0471 935921, (1992). *Surf. Interface Anal.* **1993**, *20* (3), 267–267.

(496) Nayak, P. K.; Caraveo-Frescas, J. A.; Wang, Z.; Hedhili, M. N.; Wang, Q. X.; Alshareef, H. N. Thin Film Complementary Metal Oxide Semiconductor (CMOS) Device Using a Single-Step Deposition of the Channel Layer. *Sci. Rep.* **2015**, *4* (1), 4672.

(497) Banger, K.; Warwick, C.; Lang, J.; Broch, K.; Halpert, J. E.; Socratous, J.; Brown, A.; Leedham, T.; Sirringhaus, H. Identification of Dipole Disorder in Low Temperature Solution Processed Oxides: Its Utility and Suppression for Transparent High Performance Solution-Processed Hybrid Electronics. *Chem. Sci.* **2016**, *7* (10), 6337–6346.

(498) Coll, M.; Fontcuberta, J.; Althammer, M.; Bibes, M.; Boschker, H.; Calleja, A.; Cheng, G.; Cuoco, M.; Dittmann, R.; Dkhil, B.; El Baggari, I.; Fanciulli, M.; Fina, I.; Fortunato, E.; Frontera, C.; Fujita, S.; Garcia, V.; Goennenwein, S. T. B.; Granqvist, C.-G.; Grollier, J.; Gross, R.; Hagfeldt, A.; Herranz, G.; Hono, K.; Houwman, E.; Huijben, M.; Kalaboukhov, A.; Keeble, D. J.; Koster, G.; Kourkoutis, L. F.; Levy, J.; Lira-Cantu, M.; MacManus-Driscoll, J. L.; Mannhart, J.; Martins, R.; Menzel, S.; Mikolajick, T.; Napari,

M.; Nguyen, M. D.; Niklasson, G.; Paillard, C.; Panigrahi, S.; Rijnders, G.; Sánchez, F.; Sanchis, P.; Sanna, S.; Schlom, D. G.; Schroeder, U.; Shen, K. M.; Siemon, A.; Spreitzer, M.; Sukegawa, H.; Tamayo, R.; van den Brink, J.; Pryds, N.; Granozio, F. M. Towards Oxide Electronics: A Roadmap. *Appl. Surf. Sci.* **2019**, *482* (July), 1–93.

(499) Chae, D.; Kim, J.; Shin, J.; Lee, W. H.; Ko, S. A Low-Temperature and Short-Annealing Process for Metal Oxide Thin Film Transistors Using Deep Ultraviolet Light for Roll-to-Roll Processing. *Curr. Appl. Phys.* **2019**, *19* (8), 954–960.

(500) Bretos, I.; Jiménez, R.; Ricote, J.; Calzada, M. L. Low-Temperature Crystallization of Solution-Derived Metal Oxide Thin Films Assisted by Chemical Processes. *Chem. Soc. Rev.* **2018**, *47* (2), 291–308.

(501) Chang, J. S.; Facchetti, A. F.; Reuss, R. A Circuits and Systems Perspective of Organic/Printed Electronics: Review, Challenges, and Contemporary and Emerging Design Approaches. *IEEE J. Emerg. Sel. Top. Circuits Syst.* **2017**, *7* (1), 7–26.

(502) Garlapati, S. K.; Gebauer, J. S.; Dehm, S.; Bruns, M.; Winterer, M.; Hahn, H.; Dasgupta, S. Room-Temperature Processing of Printed Oxide FETs Using Ultraviolet Photonic Curing. *Adv. Electron. Mater.* **2017**, *3* (9), 1–6.

(503) Yang, Y.-H.; Yang, S. S.; Chou, K.-S. Characteristic Enhancement of Solution-Processed In-Ga-Zn Oxide Thin-Film Transistors by Laser Annealing. *IEEE Electron Device Lett.* **2010**, *31* (9), 969–971.

(504) Tsay, C. Y.; Huang, T. T. Improvement of Physical Properties of IGZO Thin Films Prepared by Excimer Laser Annealing of Sol-Gel Derived Precursor Films. *Mater. Chem. Phys.* **2013**, *140* (1), 365–372.

(505) Chen, C.; Chen, G.; Yang, H.; Zhang, G.; Hu, D.; Chen, H.; Guo, T. Solution-Processed Metal Oxide Arrays Using Femtosecond Laser Ablation and Annealing for Thin-Film Transistors. *J. Mater. Chem. C* **2017**, *5* (36), 9273–9280.

(506) Yang, Y.-H.; Yang, S. S.; Chou, K.-S. Performance Improvements of IGZO and ZnO Thin-Film Transistors by Laser-Irradiation Treatment. *J. Soc. Inf. Disp.* **2011**, *19* (3), 247.

(507) Lee, J.; Song, S.; Cho, S.; Song, M.; Kim, Y.; Kwon, J.; Han, M. Excimer Laser Annealed Low Temperature Solution-Processed Oxide Thin Film Transistors. *IEE* **2012**, 135–138.

(508) Nian, Q.; Callahan, M.; Saei, M.; Look, D.; Efstathiadis, H.; Bailey, J.; Cheng, G. J. Large Scale Laser Crystallization of Solution-Based Alumina-Doped Zinc Oxide (AZO) Nanoinks for Highly Transparent Conductive Electrode. *Sci. Rep.* **2015**, *5* (January), 1–12.

(509) Chen, C. N.; Huang, J. J. Effects of Excimer Laser Annealing on Low-Temperature Solution Based Indium-Zinc-Oxide Thin Film Transistor Fabrication. *J. Appl. Res. Technol.* **2015**, *13* (2), 170–176.

(510) Teodorescu, V. S.; Maraloiu, A. V.; Blanchin, M.-G.; Yamada, T.; Sandu, C. S.; Delaporte, P.; Zaharescu, M. Structure and Dielectric Properties of Low Fluence Excimer Laser Annealing of Sol-Gel HfO<inf>2</Inf> Thin Films Deposited on Si Wafer. In *CAS 2013 (International Semiconductor Conference)*; IEEE, 2013; Vol. 1, pp 77–80.

(511) Lan, L.; Peng, J. High-Performance Indiumgalliumzinc Oxide Thin-Film Transistors Based on Anodic Aluminum Oxide. *IEEE Trans. Electron Devices* **2011**, *58* (5), 1452–1455.

(512) Cai, W.; Park, S.; Zhang, J.; Wilson, J.; Li, Y.; Xin, Q.; Majewski, L.; Song, A. One-Volt IGZO Thin-Film Transistors with Ultra-Thin, Solution-Processed AlxOy Gate Dielectric. *IEEE Electron Device Lett.* **2018**, *39* (3), 375–378.

(513) Gomes, T. C.; Kumar, D.; Fugikawa-Santos, L.; Alves, N.; Kettle, J. Optimization of the Anodization Processing for Aluminum Oxide Gate Dielectrics in ZnO Thin Film Transistors by Multivariate Analysis. *ACS Comb. Sci.* **2019**, *21* (5), 370–379.

(514) Sagar, S.; Mohammadian, N.; Park, S.; Majewski, L. A.; Das, B. C. Ultra-Thin Anodized Aluminium Dielectric Films: The Effect of Citric Acid Concentration and Low-Voltage Electronic Applications. *Nanotechnology* **2020**.

(515) Xie, L.; Shao, Y.; Xiao, X.; Zhang, L.; Bi, X.; Zhang, S. Fabrication of Indium-Tin-Oxide Thin-Film Transistor Using Anodization. In *2014 21st International Workshop on Active-Matrix Flatpanel Displays and Devices (AM-FPD)*; IEEE, 2014; Vol. 1, pp 101–103.

(516) Fan, C.; Liu, A.; Meng, Y.; Guo, Z.; Liu, G.; Shan, F. Solution-Processed SrO x -Gated Oxide Thin-Film Transistors and Inverters. *IEEE Trans. Electron Devices* **2017**, *64* (10), 4137–4143.

(517) Zhu, L.; He, G.; Li, W.; Yang, B.; Fortunato, E.; Martins, R. Nontoxic, Eco-Friendly Fully Water-Induced Ternary Zr-Gd-O Dielectric for High-Performance Transistors and Unipolar Inverters. *Adv. Electron. Mater.* **2018**, *4* (5), 1800100.

(518) Kalfagiannis, N.; Siozios, A.; Bellas, D. V.; Toliopoulos, D.; Bowen, L.; Pliatsikas, N.; Cranton, W. M.; Kosmidis, C.; Koutsogeorgis, D. C.; Lidorikis, E.; Patsalas, P. Selective Modification of Nanoparticle Arrays by Laser-Induced Self Assembly (MONA-LISA): Putting Control into Bottom-up Plasmonic Nanostructuring. *Nanoscale* **2016**, *8* (15), 8236–8244.

(519) Kalfagiannis, N.; Koutsogeorgis, D. C.; Lidorikis, E.; Patsalas, P. Laser Annealing as a Platform for Plasmonic Nanostructuring. In *Nanoplasmonics - Fundamentals and Applications*; InTech, 2017; Vol. i, p 13.

(520) Carlos, E.; Dellis, S.; Kalfagiannis, N.; Koutsokeras, L.; Koutsogeorgis, D. C.; Branquinho, R.; Martins, R.; Fortunato, E. Laser Induced Ultrafast Combustion Synthesis of Solution-Based AlO x for Thin Film Transistors. *J. Mater. Chem. C* **2020**, *8* (18), 6176–6184.

(521) Siozios, A.; Kalfagiannis, N.; Bellas, D. V.; Bazioti, C.; Dimitrakopulos, G. P.; Vourlias, G.; Cranton, W. M.; Lidorikis, E.; Koutsogeorgis, D. C.; Patsalas, P. Sub-Surface Laser Nanostructuring in Stratified Metal/Dielectric Media: A Versatile Platform towards Flexible, Durable and Large-Scale Plasmonic Writing. *Nanotechnology* **2015**, *26* (15), 155301.

(522) Parratt, L. G. Surface Studies of Solids by Total Reflection of X-Rays. *Phys. Rev.* **1954**, *95* (2), 359–369.

(523) Smith, S. W.; Wang, W.; Keszler, D. A.; Conley, J. F. Solution Based Prompt Inorganic Condensation and Atomic Layer Deposition of Al $_2$ O $_3$ Films: A Side-by-Side Comparison. *J. Vac. Sci. Technol. A Vacuum, Surfaces, Film.* **2014**, *32* (4), 041501.

(524) Acharya, J.; Wilt, J.; Liu, B.; Wu, J. Probing the Dielectric Properties of Ultrathin Al/Al 2 O 3 /Al Trilayers Fabricated Using in Situ Sputtering and Atomic Layer Deposition. *ACS Appl. Mater. Interfaces* **2018**, *10* (3), 3112–3120.

(525) Park, J. S.; Jeong, J. K.; Chung, H. J.; Mo, Y. G.; Kim, H. D. Electronic Transport Properties of Amorphous Indium-Gallium-Zinc Oxide Semiconductor upon Exposure to Water. *Appl. Phys. Lett.* **2008**, *92* (7), 90–93.

(526) Cho, S. W.; Kim, D. E.; Kim, K. S.; Jung, S. H.; Cho, H. K. Towards Environmentally Stable Solution-Processed Oxide Thin-Film Transistors: A Rare-Metal-Free Oxide-Based Semiconductor/Insulator Heterostructure and Chemically Stable Multi-Stacking. *J. Mater. Chem. C* **2017**, *5* (40), 10498–10508.

(527) Chen, T.-C.; Chang, T.-C.; Hsieh, T.-Y.; Lu, W.-S.; Jian, F.-Y.; Tsai, C.-T.; Huang, S.-Y.; Lin, C.-S. Investigating the Degradation Behavior Caused by Charge Trapping Effect under DC and AC Gate-Bias Stress for InGaZnO Thin Film Transistor. *Appl. Phys. Lett.* **2011**, *99* (2), 022104.

(528) Satyanarayanan, M. The Emergence of Edge Computing. *Computer (Long. Beach. Calif).* **2017**, *50* (1), 30–39.

(529) Passian, A.; Imam, N. Nanosystems, Edge Computing, and the Next Generation Computing Systems. *Sensors* **2019**, *19* (18), 4048.

(530) Ghoneim, M.; Hussain, M. Review on Physically Flexible Nonvolatile Memory for Internet of Everything Electronics. *Electronics* **2015**, *4* (3), 424–479.

(531) Ielmini, D.; Waser, R. *Resistive Switching: From Fundamentals of Nanoionic Redox Processes to Memristive Device Applications*; Ielmini, D., Waser, R., Eds.; Wiley-VCH: Weinheim, Germany, 2016.

(532) Lanza, M.; Wong, H.-S. P.; Pop, E.; Ielmini, D.; Strukov, D.; Regan, B. C.; Larcher, L.; Villena, M. A.; Yang, J. J.; Goux, L.; Belmonte, A.; Yang, Y.; Puglisi, F. M.; Kang, J.; Magyari-Köpe, B.; Yalon, E.; Kenyon, A.; Buckwell, M.; Mehonic, A.; Shluger, A.; Li, H.; Hou, T.-H.; Hudec, B.; Akinwande, D.; Ge, R.; Ambrogio, S.; Roldan, J. B.; Miranda, E.; Suñe, J.; Pey, K. L.; Wu, X.; Raghavan, N.; Wu, E.; Lu, W. D.; Navarro, G.; Zhang, W.; Wu, H.; Li, R.; Holleitner, A.; Wurstbauer, U.; Lemme, M. C.; Liu, M.; Long, S.; Liu, Q.; Lv, H.; Padovani, A.; Pavan, P.; Valov, I.; Jing, X.; Han, T.; Zhu, K.; Chen, S.; Hui, F.; Shi, Y. Recommended Methods to Study Resistive Switching Devices. *Adv. Electron. Mater.* **2019**, *5* (1), 1800143.

(533) Hickmott, T. W. Low-Frequency Negative Resistance in Thin Anodic Oxide Films. *J. Appl. Phys.* **1962**, *33* (9), 2669–2682.

(534) Simmons, J. G.; Verderber, R. R. New Conduction and Reversible Memory Phenomena in Thin Insulating Films. *Proc. R. Soc. London. Ser. A. Math. Phys. Sci.* **1967**, *301* (1464), 77–102.

(535) Liu, S. Q.; Wu, N. J.; Ignatiev, A. Electric-Pulse-Induced Reversible Resistance Change Effect in Magnetoresistive Films. *Appl. Phys. Lett.* **2000**, *76* (19), 2749–2751.

(536) Zhuang, W. W.; Pan, W.; Ulrich, B. D.; Lee, J. J.; Stecker, L.; Burmaster, A.; Evans, D. R.; Hsu, S. T.; Tajiri, M.; Shimaoka, A.; Inoue, K.; Naka, T.; Awaya, N.; Sakiyama, A.; Wang, Y.; Liu, S. Q.; Wu, N. J.; Ignatiev, A. Novel Colossal Magnetoresistive Thin Film Nonvolatile Resistance Random Access Memory (RRAM). In *Digest. International Electron Devices Meeting,*; IEEE, 2002; pp 193–196.

(537) Strukov, D. B.; Snider, G. S.; Stewart, D. R.; Williams, R. S. The Missing Memristor Found. *Nature* **2008**, *453* (7191), 80–83.

(538) Lee, M.-J.; Park, Y.; Kang, B.; Ahn, S.; Lee, C.; Kim, K.; Xianyu, W.; Stefanovich, G.; Lee, J.-H.; Chung, S.; Kim, Y.; Lee, C.; Park, J.-B.; Baek, I.; Yoo, I. 2-Stack 1D-1R Cross-Point Structure with Oxide Diodes as Switch Elements for High Density Resistance RAM Applications. In *2007 IEEE International Electron Devices Meeting*; IEEE, 2007; pp 771–774.

(539) Baek, I. G.; Kim, D. C.; Lee, M. J.; Kim, H.-J.; Yim, E. K.; Lee, M. S.; Lee, J. E.; Ahn, S. E.; Seo, S.; Lee, J. H.; Park, J. C.; Cha, Y. K.; Park, S. O.; Kim, H. S.; Yoo, I. K.; Chung, U.; Moon, J. T.; Ryu, B. I. Multi-Layer Cross-Point Binary Oxide Resistive Memory (OxRRAM) for Post-NAND Storage Application. In *IEEE InternationalElectron Devices Meeting, 2005. IEDM Technical Digest.*; IEEE, 2005; Vol. 00, pp 750–753.

(540) Seo, S.; Lee, M. J.; Seo, D. H.; Jeoung, E. J.; Suh, D.-S.; Joung, Y. S.; Yoo, I. K.; Hwang,

I. R.; Kim, S. H.; Byun, I. S.; Kim, J.-S.; Choi, J. S.; Park, B. H. Reproducible Resistance Switching in Polycrystalline NiO Films. *Appl. Phys. Lett.* **2004**, *85* (23), 5655–5657.

(541) Baek, I. G.; Lee, M. S.; Sco, S.; Lee, M. J.; Seo, D. H.; Suh, D.-S.; Park, J. C.; Park, S. O.; Kim, H. S.; Yoo, I. K.; Chung, U.; Moon, J. T. Highly Scalable Non-Volatile Resistive Memory Using Simple Binary Oxide Driven by Asymmetric Unipolar Voltage Pulses. In *IEDM Technical Digest. IEEE International Electron Devices Meeting, 2004.*; IEEE, 2004; pp 587–590.

(542) Kund, M.; Beitel, G.; Pinnow, C.-U.; Rohr, T.; Schumann, J.; Symanczyk, R.; Ufert, K.; Muller, G. Conductive Bridging RAM (CBRAM): An Emerging Non-Volatile Memory Technology Scalable to Sub 20nm. In *IEEE InternationalElectron Devices Meeting, 2005. IEDM Technical Digest.*; IEEE, 2005; Vol. 2005, pp 754–757.

(543) Fackenthal, R.; Kitagawa, M.; Otsuka, W.; Prall, K.; Mills, D.; Tsutsui, K.; Javanifard, J.; Tedrow, K.; Tsushima, T.; Shibahara, Y.; Hush, G. 19.7 A 16Gb ReRAM with 200MB/s Write and 1GB/s Read in 27nm Technology. In *2014 IEEE International Solid-State Circuits Conference Digest of Technical Papers (ISSCC)*; IEEE, 2014; pp 338–339.

(544) Tz-Yi Liu; Tian Hong Yan; Scheuerlein, R.; Yingchang Chen; Lee, J. K.; Balakrishnan, G.; Yee, G.; Zhang, H.; Yap, A.; Ouyang, J.; Sasaki, T.; Addepalli, S.; Al-Shamma, A.; Chin-Yu Chen; Gupta, M.; Hilton, G.; Joshi, S.; Kathuria, A.; Lai, V.; Masiwal, D.; Matsumoto, M.; Nigam, A.; Pai, A.; Pakhale, J.; Chang Hua Siau; Xiaoxia Wu; Yin, R.; Liping Peng; Jang Yong Kang; Huynh, S.; Huijuan Wang; Nagel, N.; Tanaka, Y.; Higashitani, M.; Minvielle, T.; Gorla, C.; Tsukamoto, T.; Yamaguchi, T.; Okajima, M.; Okamura, T.; Takase, S.; Hara, T.; Inoue, H.; Fasoli, L.; Mofidi, M.; Shrivastava, R.; Quader, K. A 130.7mm^2 2-Layer 32Gb ReRAM Memory Device in 24nm Technology. In *2013 IEEE International Solid-State Circuits Conference Digest of Technical Papers*; IEEE, 2013; pp 210–211.

(545) Chevallier, C. J.; Siau, C. H.; Lim, S. F.; Namala, S. R.; Matsuoka, M.; Bateman, B. L.; Rinerson, D. A 0.13µm 64Mb Multi-Layered Conductive Metal-Oxide Memory. In *2010 IEEE International Solid-State Circuits Conference - (ISSCC)*; IEEE, 2010; pp 260–261.

(546) Luo, Q.; Xu, X.; Liu, H.; Lv, H.; Gong, T.; Long, S.; Liu, Q.; Sun, H.; Banerjee, W.; Li, L.; Gao, J.; Lu, N.; Liu, M. Super Non-Linear RRAM with Ultra-Low Power for 3D Vertical Nano-Crossbar Arrays. *Nanoscale* **2016**, *8* (34), 15629–15636.

(547) Martins, R.; Nathan, A.; Barros, R.; Pereira, L.; Barquinha, P.; Correia, N.; Costa, R.; Ahnood, A.; Ferreira, I.; Fortunato, E. Complementary Metal Oxide Semiconductor Technology With and On Paper. *Adv. Mater.* **2011**, *23* (39), 4491–4496.

(548) Jo, S. H.; Chang, T.; Ebong, I.; Bhadviya, B. B.; Mazumder, P.; Lu, W. Nanoscale Memristor Device as Synapse in Neuromorphic Systems. *Nano Lett.* **2010**, *10* (4), 1297–1301.

(549) Kim, K.-H.; Gaba, S.; Wheeler, D.; Cruz-Albrecht, J. M.; Hussain, T.; Srinivasa, N.; Lu, W. A Functional Hybrid Memristor Crossbar-Array/CMOS System for Data Storage and Neuromorphic Applications. *Nano Lett.* **2012**, *12* (1), 389–395.

(550) Hui, F.; Grustan-Gutierrez, E.; Long, S.; Liu, Q.; Ott, A. K.; Ferrari, A. C.; Lanza, M. Graphene and Related Materials for Resistive Random Access Memories. *Adv. Electron. Mater.* **2017**, *3* (8), 1600195.

(551) Sako, M.; Watanabe, Y.; Nakajima, T.; Sato, J.; Muraoka, K.; Fujiu, M.; Kono, F.; Nakagawa, M.; Masuda, M.; Kato, K.; Terada, Y.; Shimizu, Y.; Honma, M.; Imamoto, A.; Araya, T.; Konno, H.; Okanaga, T.; Fujimura, T.; Wang, X.; Muramoto, M.; Kamoshida, M.; Kohno, M.; Suzuki, Y.; Hashiguchi, T.; Kobayashi, T.; Yamaoka, M.; Yamashita, R.

A Low Power 64 Gb MLC NAND-Flash Memory in 15 Nm CMOS Technology. *IEEE J. Solid-State Circuits* **2016**, *51* (1), 196–203.

(552) Yoon Kim; Il Han Park; Seongjae Cho; Jang-Gn Yun; Jung Hoon Lee; Doo-Hyun Kim; Gil Sung Lee; Se-Hwan Park; Dong Hua Lee; Won Bo Sim; Wandong Kim; Hyungcheol Shin; Jong-Duk Lee; Byung-Gook Park. A Vertical 4-Bit SONOS Flash Memory and a Unique 3-D Vertical nor Array Structure. *IEEE Trans. Nanotechnol.* **2010**, *9* (1), 70–77.

(553) Govoreanu, B.; Kar, G. S.; Chen, Y.-Y.; Paraschiv, V.; Kubicek, S.; Fantini, A.; Radu, I. P.; Goux, L.; Clima, S.; Degraeve, R.; Jossart, N.; Richard, O.; Vandeweyer, T.; Seo, K.; Hendrickx, P.; Pourtois, G.; Bender, H.; Altimime, L.; Wouters, D. J.; Kittl, J. A.; Jurczak, M. 10×10nm2 Hf/HfOx Crossbar Resistive RAM with Excellent Performance, Reliability and Low-Energy Operation. In *2011 International Electron Devices Meeting*; IEEE, 2011; pp 31.6.1-31.6.4.

(554) Gupta, M. K.; Hasan, M. Robust High Speed Ternary Magnetic Content Addressable Memory. *IEEE Trans. Electron Devices* **2015**, *62* (4), 1163–1169.

(555) Kent, A. D.; Worledge, D. C. A New Spin on Magnetic Memories. *Nat. Nanotechnol.* **2015**, *10* (3), 187–191.

(556) Burr, G. W.; BrightSky, M. J.; Sebastian, A.; Cheng, H.; Wu, J.; Kim, S.; Sosa, N. E.; Papandreou, N.; Lung, H.; Pozidis, H.; Eleftheriou, E.; Lam, C. H. Recent Progress in Phase-Change <?Pub _newline ?> Memory Technology. *IEEE J. Emerg. Sel. Top. Circuits Syst.* **2016**, *6* (2), 146–162.

(557) Khvalkovskiy, A. V.; Apalkov, D.; Watts, S.; Chepulskii, R.; Beach, R. S.; Ong, A.; Tang, X.; Driskill-Smith, A.; Butler, W. H.; Visscher, P. B.; Lottis, D.; Chen, E.; Nikitin, V.; Krounbi, M. Basic Principles of STT-MRAM Cell Operation in Memory Arrays. *J. Phys. D. Appl. Phys.* **2013**, *46* (13), 139601.

(558) Lencer, D.; Salinga, M.; Wuttig, M. Design Rules for Phase-Change Materials in Data Storage Applications. *Adv. Mater.* **2011**, *23* (18), 2030–2058.

(559) Gupta, V.; Kapur, S.; Saurabh, S.; Grover, A. Resistive Random Access Memory: A Review of Device Challenges. *IETE Tech. Rev.* **2020**, *37* (4), 377–390.

(560) Choi, H.-S.; Park, Y. J.; Lee, J.-H.; Kim, Y. 3-D Synapse Array Architecture Based on Charge-Trap Flash Memory for Neuromorphic Application. *Electronics* **2019**, *9* (1), 57.

(561) Lanza, M. A Review on Resistive Switching in High-k Dielectrics: A Nanoscale Point of View Using Conductive Atomic Force Microscope. *Materials (Basel).* **2014**, *7* (3), 2155–2182.

(562) Valov, I. Redox-Based Resistive Switching Memories (ReRAMs): Electrochemical Systems at the Atomic Scale. *ChemElectroChem* **2014**, *1* (1), 26–36.

(563) Waser, R.; Dittmann, R.; Staikov, G.; Szot, K. Redox-Based Resistive Switching Memories - Nanoionic Mechanisms, Prospects, and Challenges. *Adv. Mater.* **2009**, *21* (25–26), 2632–2663.

(564) Lübben, M.; Karakolis, P.; Ioannou-Sougleridis, V.; Normand, P.; Dimitrakis, P.; Valov, I. Graphene-Modified Interface Controls Transition from VCM to ECM Switching Modes in Ta/TaO x Based Memristive Devices. *Adv. Mater.* **2015**, *27* (40), 6202–6207.

(565) Kindsmüller, A.; Meledin, A.; Mayer, J.; Waser, R.; Wouters, D. J. On the Role of the Metal Oxide/Reactive Electrode Interface during the Forming Procedure of Valence Change ReRAM Devices. *Nanoscale* **2019**, *11* (39), 18201–18208.

(566) Valov, I.; Kozicki, M. N. Cation-Based Resistance Change Memory. *J. Phys. D. Appl. Phys.* **2013**, *46* (7), 074005.

(567) Goux, L.; Valov, I. Electrochemical Processes and Device Improvement in Conductive Bridge RAM Cells. *Phys. status solidi* **2016**, *213* (2), 274–288.

(568) Valov, I.; Waser, R.; Jameson, J. R.; Kozicki, M. N. Electrochemical Metallization Memories—Fundamentals, Applications, Prospects. *Nanotechnology* **2011**, *22* (28), 289502.

(569) Ielmini, D.; Bruchhaus, R.; Waser, R. Thermochemical Resistive Switching: Materials, Mechanisms, and Scaling Projections. *Phase Transitions* **2011**, *84* (7), 570–602.

(570) Milano, G.; Porro, S.; Valov, I.; Ricciardi, C. Recent Developments and Perspectives for Memristive Devices Based on Metal Oxide Nanowires. *Adv. Electron. Mater.* **2019**, *5* (9), 1800909.

(571) Chen, C.; Song, C.; Yang, J.; Zeng, F.; Pan, F. Oxygen Migration Induced Resistive Switching Effect and Its Thermal Stability in W/TaO x /Pt Structure. *Appl. Phys. Lett.* **2012**, *100* (25), 253509.

(572) Song, S. J.; Seok, J. Y.; Yoon, J. H.; Kim, K. M.; Kim, G. H.; Lee, M. H.; Hwang, C. S. Real-Time Identification of the Evolution of Conducting Nano-Filaments in TiO2 Thin Film ReRAM. *Sci. Rep.* **2013**, *3* (1), 3443.

(573) Kim, K. M.; Choi, B. J.; Song, S. J.; Kim, G. H.; Hwang, C. S. Filamentary Resistive Switching Localized at Cathode Interface in NiO Thin Films. *J. Electrochem. Soc.* **2009**, *156* (12), G213.

(574) Yan, Z.; Guo, Y.; Zhang, G.; Liu, J.-M. High-Performance Programmable Memory Devices Based on Co-Doped BaTiO3. *Adv. Mater.* **2011**, *23* (11), 1351–1355.

(575) Liu, X.; Biju, K. P.; Bourim, E. M.; Park, S.; Lee, W.; Shin, J.; Hwang, H. Low Programming Voltage Resistive Switching in Reactive Metal/Polycrystalline Pr0.7Ca0.3MnO3 Devices. *Solid State Commun.* **2010**, *150* (45–46), 2231–2235.

(576) Kim, H.-D.; An, H.-M.; Hong, S. M.; Kim, T. G. Forming-Free SiN-Based Resistive Switching Memory Prepared by RF Sputtering. *Phys. status solidi* **2013**, *210* (9), n/a-n/a.

(577) Chen, C.; Yang, Y. C.; Zeng, F.; Pan, F. Bipolar Resistive Switching in Cu/AlN/Pt Nonvolatile Memory Device. *Appl. Phys. Lett.* **2010**, *97* (8), 083502.

(578) Sakamoto, T.; Sunamura, H.; Kawaura, H.; Hasegawa, T.; Nakayama, T.; Aono, M. Nanometer-Scale Switches Using Copper Sulfide. *Appl. Phys. Lett.* **2003**, *82* (18), 3032–3034.

(579) Lai, P. Y.; Chen, J.-S. Ultrahigh on/off -Current Ratio for Resistive Memory Devices With Poly(N-Vinylcarbazole)/Poly(3, 4-Ethylenedioxythiophene)–Poly(Styrenesulfonate) Stacking Bilayer. *IEEE Electron Device Lett.* **2011**, *32* (3), 387–389.

(580) Kondo, T.; Lee, S. M.; Malicki, M.; Domercq, B.; Marder, S. R.; Kippelen, B. A Nonvolatile Organic Memory Device Using ITO Surfaces Modified by Ag-Nanodots. *Adv. Funct. Mater.* **2008**, *18* (7), 1112–1118.

(581) Goswami, S.; Nandy, S.; Banerjee, A. N.; Kiazadeh, A.; Dillip, G. R.; Pinto, J. V.; Joo, S. W.; Martins, R.; Fortunato, E. "Electro-Typing" on a Carbon-Nanoparticles-Filled Polymeric Film Using Conducting Atomic Force Microscopy. *Adv. Mater.* **2017**, *29* (47), 1703079.

(582) Cai, Y.; Tan, J.; YeFan, L.; Lin, M.; Huang, R. A Flexible Organic Resistance Memory Device for Wearable Biomedical Applications. *Nanotechnology* **2016**, *27* (27), 275206.

(583) Chen, G.; Song, C.; Pan, F. Improved Resistive Switching Stability of Pt/ZnO/CoO x /ZnO/Pt Structure for Nonvolatile Memory Devices. *Rare Met.* **2013**, *32* (6), 544–549.

(584) Casa Branca, N.; Deuermeier, J.; Martins, J.; Carlos, E.; Pereira, M.; Martins, R.; Fortunato, E.; Kiazadeh, A. 2D Resistive Switching Based on Amorphous Zinc–Tin Oxide Schottky Diodes. *Adv. Electron. Mater.* **2020**, *6* (2), 1900958.

(585) An Chen; Haddad, S.; Yi-Ching Wu; Tzu-Ning Fang; Zhida Lan; Avanzino, S.; Pangrle, S.; Buynoski, M.; Rathor, M.; Wei Cai; Tripsas, N.; Bill, C.; Van Buskirk, M.; Taguchi, M. Non-Volatile Resistive Switching for Advanced Memory Applications. In *IEEE InternationalElectron Devices Meeting, 2005. IEDM Technical Digest.*; IEEE, 2005; Vol. 00, pp 746–749.

(586) Tang, G. S.; Zeng, F.; Chen, C.; Gao, S.; Fu, H. D.; Song, C.; Wang, G. Y.; Pan, F. Resistive Switching Behaviour of a Tantalum Oxide Nanolayer Fabricated by Plasma Oxidation. *Phys. status solidi - Rapid Res. Lett.* **2013**, *7* (4), 282–284.

(587) Smithe, K. K. H.; Suryavanshi, S. V.; Muñoz Rojo, M.; Tedjarati, A. D.; Pop, E. Low Variability in Synthetic Monolayer MoS 2 Devices. *ACS Nano* **2017**, *11* (8), 8456–8463.

(588) Choi, B. J.; Jeong, D. S.; Kim, S. K.; Rohde, C.; Choi, S.; Oh, J. H.; Kim, H. J.; Hwang, C. S.; Szot, K.; Waser, R.; Reichenberg, B.; Tiedke, S. Resistive Switching Mechanism of TiO2 Thin Films Grown by Atomic-Layer Deposition. *J. Appl. Phys.* **2005**, *98* (3), 033715.

(589) Deuermeier, J.; Kiazadeh, A.; Klein, A.; Martins, R.; Fortunato, E. Multi-Level Cell Properties of a Bilayer Cu2O/Al2O3 Resistive Switching Device. *Nanomaterials* **2019**, *9* (2), 289.

(590) Jang, K. H.; Oh, S. M.; An, H. M.; Cho, W. J. Solution-Processed High-k Thin Films as a Resistive Switching for ReRAM Applications. *Curr. Appl. Phys.* **2014**, *14* (3), 462–466.

(591) Awais, M. N.; Kim, H. C.; Doh, Y. H.; Choi, K. H. ZrO2 Flexible Printed Resistive (Memristive) Switch through Electrohydrodynamic Printing Process. *Thin Solid Films* **2013**, *536*, 308–312.

(592) Tan, C.; Liu, Z.; Huang, W.; Zhang, H. Non-Volatile Resistive Memory Devices Based on Solution-Processed Ultrathin Two-Dimensional Nanomaterials. *Chem. Soc. Rev.* **2015**, *44* (9), 2615–2628.

(593) Rovisco, A.; Branquinho, R.; Martins, J.; Oliveira, M. J.; Nunes, D.; Fortunato, E.; Martins, R.; Barquinha, P. Seed-Layer Free Zinc Tin Oxide Tailored Nanostructures for Nanoelectronic Applications: Effect of Chemical Parameters. *ACS Appl. Nano Mater.* **2018**, *1* (8), 3986–3997.

(594) Baek, H.; Lee, C.; Choi, J.; Cho, J. Nonvolatile Memory Devices Prepared from Sol-Gel Derived Niobium Pentoxide Films. *Langmuir* **2013**, *29* (1), 380–386.

(595) Sarkar, D. K.; Cloutier, F.; El Khakani, M. A. Electrical Switching in Sol–Gel Derived Ag–SiO2 Nanocomposite Thin Films. *J. Appl. Phys.* **2005**, *97* (8), 084302.

(596) Wang, J.; Choudhary, S.; De Roo, J.; De Keukeleere, K.; Van Driessche, I.; Crosby, A. J.; Nonnenmann, S. S. How Ligands Affect Resistive Switching in Solution-Processed HfO2 Nanoparticle Assemblies. *ACS Appl. Mater. Interfaces* **2018**, *10* (5), 4824–4830.

(597) Rosa, J.; Kiazadeh, A.; Santos, L.; Deuermeier, J.; Martins, R.; Gomes, H. L.; Fortunato, E. Memristors Using Solution-Based IGZO Nanoparticles. *ACS Omega* **2017**, *2* (11), 8366–8372.

(598) Senthilkumar, V.; Kathalingam, A.; Kannan, V.; Senthil, K.; Rhee, J. K. Reproducible Resistive Switching in Hydrothermal Processed TiO2 Nanorod Film for Non-Volatile Memory Applications. *Sensors Actuators, A Phys.* **2013**, *194*, 135–139.

(599) Miller, K.; Nalwa, K. S.; Bergerud, A.; Neihart, N. M.; Chaudhary, S. Memristive Behavior in Thin Anodic Titania. *IEEE Electron Device Lett.* **2010**, *31* (7), 737–739.

(600) Sophocleous, M.; Mohammadian, N.; Majewski, L. A.; Georgiou, J. Solution-Processed , Low Voltage Tantalum-Based Memristive Switches. *Mater. Lett.* **2020**, *269*, 127676.

(601) Li, Y.; Zhao, G.; Shi, F. Unipolar Resistive Switching Behavior Study in CuxO Thin Films at Different Annealing Temperatures. *Adv. Mater. Res.* **2012**, *586*, 24–29.

(602) Biju, K. P.; Liu, X.; Shin, J.; Kim, I.; Jung, S.; Siddik, M.; Lee, J.; Ignatiev, A.; Hwang, H. Highly Asymmetric Bipolar Resistive Switching in Solution-Processed Pt/TiO2/W Devices for Cross-Point Application. *Curr. Appl. Phys.* **2011**, *11* (4 SUPPL.), S102–S106.

(603) You, H. C.; Lin, G. K. Solution-Processed ZnO Thin Films for Low Voltage and Low Temperature Application in Flexible Resistive Random Access Memory. *Thin Solid Films* **2016**, *616*, 728–732.

(604) Lee, D.; Chun, M. C.; Ko, H.; Kang, B. S.; Kim, J. Highly Stable, Solution-Processed Quaternary Oxide Thin Film-Based Resistive Switching Random Access Memory Devices via Global and Local Stoichiometric Manipulation Strategy. *Nanotechnology* **2020**, *31* (24), 245202.

(605) Yoon, D. H.; Kim, S. J.; Jung, J.; Lim, H. S.; Kim, H. J. Low-Voltage Driving Solution-Processed Nickel Oxide Based Unipolar Resistive Switching Memory with Ni Nanoparticles. *J. Mater. Chem.* **2012**, *22* (34), 17568.

(606) Jang, J.; Subramanian, V. Effect of Electrode Material on Resistive Switching Memory Behavior of Solution-Processed Resistive Switches: Realization of Robust Multi-Level Cells. *Thin Solid Films* **2017**, *625*, 87–92.

(607) Pan, Y.; Wan, T.; Du, H.; Qu, B.; Wang, D.; Ha, T. J.; Chu, D. Mimicking Synaptic Plasticity and Learning Behaviours in Solution Processed SnO2 Memristor. *J. Alloys Compd.* **2018**, *757*, 496–503.

(608) Brinker, C. J.; Scherer, G. W. *Sol-Gel Science The Physics and Chemistry of Sol-Gel Processing*; Academic Press, 1990.

(609) Liu, C. Y.; Tseng, T. Y. Resistance Switching Properties of Sol-Gel Derived SrZrO3 Based Memory Thin Films. *J. Phys. D. Appl. Phys.* **2007**, *40* (7), 2157–2161.

(610) Zhang, T.; Su, Z.; Chen, H.; Ding, L.; Zhang, W. Resistance Switching Properties of Sol-Gel Derived La0.67Ca0.33MnO3 Thin Films on F-Doped SnO2 Conducting Glass. *Appl. Phys. Lett.* **2008**, *93* (17), 172104.

(611) Lee, C.; Kim, I.; Choi, W.; Shin, H.; Cho, J. Resistive Switching Memory Devices Composed of Binary Transition Metal Oxides Using Sol-Gel Chemistry. *Langmuir* **2009**, *25* (8), 4274–4278.

(612) Chen, X.; Zhou, H.; Wu, G.; Bao, D. Colossal Resistive Switching Behavior and Its Physical Mechanism of Pt/p-NiO/n-Mg0.6Zn0.4O/Pt Thin Films. *Appl. Phys. A Mater. Sci. Process.* **2011**, *104* (1), 477–481.

(613) Branquinho, R.; Salgueiro, D.; Santa, A.; Kiazadeh, A.; Barquinha, P.; Pereira, L.; Martins, R.; Fortunato, E. Towards Environmental Friendly Solution-Based ZTO/AlO $_x$ TFTs. *Semicond. Sci. Technol.* **2015**, *30* (2), 024007.

(614) Carlos, E.; Dellis, S.; Kalfagiannis, N.; Koutsokeras, L.; Koutsogeorgis, D. C.; Branquinho, R.; Martins, R.; Fortunato, E. Laser Induced Ultrafast Combustion Synthesis of Solution-Based AlO x for Thin Film Transistors. *J. Mater. Chem. C* **2020**, *8* (18), 6176–6184.

(615) Li, Y.; Chu, J.; Duan, W.; Cai, G.; Fan, X.; Wang, X.; Wang, G.; Pei, Y. Analog and Digital Bipolar Resistive Switching in Solution-Combustion-Processed NiO Memristor. *ACS Appl. Mater. Interfaces* **2018**, *10* (29), 24598–24606.

(616) Qi, Y. F.; Shen, Z. J.; Zhao, C.; Mitrovic, I. Z.; Xu, W. Y.; Lim, E. G.; Yang, L.; He, J. H.; Luo, T.; Huang, Y. B.; Zhao, C. Z. Resistive Switching Behavior of Solution-Processed AlOx and GO Based RRAM at Low Temperature. *Solid. State. Electron.* **2020**, *168*, 107735.

(617) Song, F.; Wang, H.; Sun, J.; Dang, B.; Gao, H.; Yang, M.; Ma, X.; Hao, Y. Solution-Processed Physically Transient Resistive Memory Based on Magnesium Oxide. *IEEE Electron Device Lett.* **2019**, *40* (2), 193–195.

(618) Wang, Y.; Chen, B.; Liu, D.; Gao, B.; Liu, L.; Liu, X.; Kang, J. Solution Processed Resistive Random Access Memory Devices for Transparent Solid-State Circuit Systems. *MRS Proc.* **2014**, *1633* (3), 105–110.

(619) Kim, A.; Song, K.; Kim, Y.; Moon, J. All Solution-Processed, Fully Transparent Resistive Memory Devices. *ACS Appl. Mater. Interfaces* **2011**, *3* (11), 4525–4530.

(620) Hwang, Y. H.; Hwang, I.; Cho, W. J. Composition-Ratio Influence on Resistive Switching Behavior of Solution-Processed InGaZnO-Based Thin-Film. *J. Nanosci. Nanotechnol.* **2014**, *14* (11), 8196–8200.

(621) Duan, W. All-Room-Temperature Processed High Flexibility Resistive Switching Memory by Ultraviolet-Radioactive Induction. *Mater. Res. Express* **2019**, *6* (11), 115923.

(622) Yoon, D. H.; Kim, S. J.; Jung, J.; Heo, S. J.; Kim, H. J. Effect of Hf Incorporation in Solution-Processed NiOx Based Resistive Random Access Memory. *Appl. Phys. Lett.* **2014**, *104* (9), 1–6.

(623) Qi, Y.; Shen, Z.; Zhao, C.; Zhao, C. Z. Effect of Electrode Area on Resistive Switching Behavior in Translucent Solution-Processed AlOx Based Memory Device. *J. Alloys Compd.* **2020**, *822*, 153603.

(624) Wang, X. L.; Wen, C.; Liu, Y.; Chen, T. P.; Zhang, H. Y.; Zhao, Y.; Liu, Z. Uniform and Electroforming-Free Resistive Memory Devices Based on Solution-Processed Triple-Layered NiO/Al2O3 Thin Films. *Appl. Phys. A* **2019**, *125* (9), 666.

(625) Hsu, C. C.; Chen, Y. T.; Tsao, C. C. Resistive Random Access Memories Fabricated by Using Solution-Processed AlZnSnO Semiconductor Films and Indium Ball Electrodes. *J. Alloys Compd.* **2017**, *696*, 697–700.

(626) Li, J.-C.; Cui, H.-P.; Hou, X.-Y. Effect of P-n Interface on Resistive Switching of NiO/CeO2 Thin Films. *J. Alloys Compd.* **2018**, *752*, 247–252.

(627) Kim, T.-W.; Cho, W.-J. Effects of Al Addition on Resistive-Switching Characteristics of Solution Processed Zn–Sn–O ReRAMs. *J. Nanosci. Nanotechnol.* **2019**, *19* (10), 6099–6105.

(628) Li, L.; Chen, Y.; Qu, W.; He, Y.; Yang, H.; Li, N.; Song, Y.; Shen, Y. Resistive Switching IGZO Micro-Arrays Realized through UV Assisted Photochemical Solution Method. *J. Sol-Gel Sci. Technol.* **2018**, *88* (3), 601–608.

(629) Hsu, C. C.; Tsao, C. C.; Chen, Y. H.; Zhang, X. Z. Bipolar Resistive Switching Characteristics of a Sol-Gel InZnO Oxide Semiconductor. *Phys. B Condens. Matter* **2019**, *561* (January), 64–69.

(630) Shaari, N. A. A.; Sauki, N. S. M.; Herman, S. H. Effect of Annealing Time on Memristive Behavior of Sol-Gel Spincoated ZnO-Based Memristive Device. In *AIP Conference Proceedings*; 2016; Vol. 1774, p 050018.

(631) Park, S.; Lee, J. H.; Kim, H. D.; Hong, S. M.; An, H. M.; Kim, T. G. Resistive Switching Characteristics of Sol-Gel Based ZnO Nanorods Fabricated on Flexible Substrates. *Phys. Status Solidi - Rapid Res. Lett.* **2013**, *7* (7), 493–496.

(632) Wu, X.; Xu, Z.; Yu, Z.; Zhang, T.; Zhao, F.; Sun, T.; Ma, Z.; Li, Z.; Wang, S. Resistive Switching Behavior of Photochemical Activation Solution-Processed Thin Films at Low Temperatures for Flexible Memristor Applications. *J. Phys. D. Appl. Phys.* **2015**, *48* (11), 115101.

(633) Hu, W.; Zou, L.; Chen, X.; Qin, N.; Li, S.; Bao, D. Highly Uniform Resistive Switching Properties of Amorphous InGaZnO Thin Films Prepared by a Low Temperature Photochemical Solution Deposition Method. *ACS Appl. Mater. Interfaces* **2014**, *6* (7), 5012–5017.

(634) Kim, T. W.; Baek, I. J.; Cho, W. J. Resistive Switching Characteristics of Solution-Processed Al–Zn–Sn–O Films Annealed by Microwave Irradiation. *Solid. State. Electron.* **2018**, *140* (xxxx), 122–128.

(635) Qi, Y.; Zhao, C.; Zhao, C. Z.; Xu, W.; Shen, Z.; He, J.; Zhao, T.; Fang, Y.; Liu, Q.; Yi, R.; Yang, L. Enhanced Resistive Switching Performance of Aluminum Oxide Dielectric with a Low Temperature Solution-Processed Method. *Solid. State. Electron.* **2019**, *158* (May), 28–36.

(636) Soo Lee, M.; Choi, S.; An, C.-H.; Kim, H. Resistive Switching Characteristics of Solution-Deposited Gd, Dy, and Ce-Doped ZrO 2 Films. *Appl. Phys. Lett.* **2012**, *100* (14), 143504.

(637) Kang, M.-S.; Cho, W.-J. Effect of Microwave Irradiation Power on Resistive Switching Performance in Solution-Processed Aluminum Oxide Resistive Memory. *J. Phys. Chem. Solids* **2018**, *123* (May), 52–58.

(638) Abdul Hadi, S.; Humood, K. M.; Abi Jaoude, M.; Abunahla, H.; Shehhi, H. F. Al; Mohammad, B. Bipolar Cu/HfO2/P++ Si Memristors by Sol-Gel Spin Coating Method and Their Application to Environmental Sensing. *Sci. Rep.* **2019**, *9* (1), 1–15.

(639) Kim, S.-T.; Cho, W.-J. Improvement of Multi-Level Resistive Switching Characteristics in Solution-Processed AlO x -Based Non-Volatile Resistive Memory Using Microwave Irradiation. *Semicond. Sci. Technol.* **2018**, *33* (1), 015009.

(640) Boratto, M. H.; Ramos, R. A.; Congiu, M.; Graeff, C. F. O.; Scalvi, L. V. A. Memristive Behavior of the SnO2/TiO2 Interface Deposited by Sol–Gel. *Appl. Surf. Sci.* **2017**, *410*, 278–281.

(641) Ayana, D. G.; Ceccato, R.; Collini, C.; Lorenzelli, L.; Prusakova, V.; Dirè, S. Sol-Gel Derived Oriented Multilayer ZnO Thin Films with Memristive Response. *Thin Solid Films* **2016**, *615*, 427–436.

(642) Xu, D.; Xiong, Y.; Tang, M.; Zeng, B. Coexistence of the Bipolar and Unipolar Resistive Switching Behaviors in Vanadium Doped ZnO Films. *J. Alloys Compd.* **2014**, *584*, 269–272.

(643) Boppidi, P. K. R.; Raj, P. M. P.; Challagulla, S.; Gollu, S. R.; Roy, S.; Banerjee, S.; Kundu, S. Unveiling the Dual Role of Chemically Synthesized Copper Doped Zinc Oxide for Resistive Switching Applications. *J. Appl. Phys.* **2018**, *124* (21), 214901.

(644) Thakre, A.; Kumar, A. Unipolar Resistive Switching in Sol-Gel Synthesized Strontium Titanate Thin Films. *Vacuum* **2018**, *151*, 182–184.

(645) Tang, M. H.; Wang, Z. P.; Li, J. C.; Zeng, Z. Q.; Xu, X. L.; Wang, G. Y.; Zhang, L. B.; Xiao, Y. G.; Yang, S. B.; Jiang, B.; He, J. Bipolar and Unipolar Resistive Switching Behaviors of Sol–Gel-Derived SrTiO 3 Thin Films with Different Compliance Currents. *Semicond. Sci. Technol.* **2011**, *26* (7), 075019.

(646) Lin, C. Y.; Lin, C. C.; Huang, C. H.; Lin, C. H.; Tseng, T. Y. Resistive Switching Properties of Sol-Gel Derived Mo-Doped SrZrO3 Thin Films. *Surf. Coatings Technol.*

2007, *202* (4–7), 1319–1322.

(647) Hsu, C.-C.; Chen, Y.-T.; Chuang, P.-Y.; Lin, Y.-S. Abnormal Volatile Memory Characteristic in Normal Nonvolatile ZnSnO Resistive Switching Memory. *IEEE Trans. Electron Devices* **2018**, *65* (7), 2812–2819.

(648) Hu, C.; Wang, Q.; Bai, S.; Xu, M.; He, D.; Lyu, D.; Qi, J. The Effect of Oxygen Vacancy on Switching Mechanism of ZnO Resistive Switching Memory. *Appl. Phys. Lett.* **2017**, *110* (7), 1–5.

(649) Lee, K. J.; Chang, Y. C.; Lee, C. J.; Wang, L. W.; Chou, D. W.; Chiang, T. K.; Wang, Y. H. Effects of Ni in Strontium Titanate Nickelate Thin Films for Flexible Nonvolatile Memory Applications. *IEEE Trans. Electron Devices* **2017**, *64* (5), 2001–2007.

(650) Cardarilli, G. C.; Khanal, G. M.; Nunzio, L. Di; Re, M.; Fazzolari, R.; Kumar, R. Memristive and Memory Impedance Behavior in a Photo-Annealed ZnO–RGO Thin-Film Device. *Electron.* **2020**, *9* (2), 1–14.

(651) Jian, W.-Y.; You, H.-C.; Wu, C.-Y. Resistive Switching Mechanism of ZnO/ZrO 2 - Stacked Resistive Random Access Memory Device Annealed at 300 °C by Sol–Gel Method with Forming-Free Operation. *Jpn. J. Appl. Phys.* **2018**, *57* (1), 011501.

(652) Kim, S.; Moon, H.; Gupta, D.; Yoo, S.; Choi, Y.-K. Resistive Switching Characteristics of Sol–Gel Zinc Oxide Films for Flexible Memory Applications. *IEEE Trans. Electron Devices* **2009**, *56* (4), 696–699.

(653) Ayana, D. G.; Prusakova, V.; Collini, C.; Nardi, M. V.; Tatti, R.; Bortolotti, M.; Lorenzelli, L.; Chiappini, A.; Chiasera, A.; Ferrari, M.; Lunelli, L.; Dirè, S. Sol-Gel Synthesis and Characterization of Undoped and Al-Doped ZnO Thin Films for Memristive Application. *AIP Adv.* **2016**, *6* (11), 111306.

(654) Xu, D. L.; Xiong, Y.; Tang, M. H.; Zeng, B. W.; Li, J. Q.; Liu, L.; Li, L. Q.; Yan, S. A.; Tang, Z. H. Bipolar Resistive Switching Behaviors in Cr-Doped ZnO Films. *Microelectron. Eng.* **2014**, *116*, 22–25.

(655) Lin, C.-Y.; Lin, M.-H.; Wu, M.-C.; Lin, C.-H.; Tseng, T.-Y. Improvement of Resistive Switching Characteristics in <formula Formulatype="inline"><tex Notation="TeX">$\hbox{SrZrO}_{3}$ </Tex></Formula> Thin Films With Embedded Cr Layer. *Ieee Electron Device Lett.* **2008**, *29* (10), 1108–1111.

(656) Yuan, H. L.; Li, J. C. Effect of Bending on Resistive Switching of NiO/ZnO Nanocomposite Thin Films. *J. Alloys Compd.* **2017**, *709*, 752–759.

(657) Chang, Y. C.; Xue, R. Y.; Wang, Y. H. Multilayered Barium Titanate Thin Films by Sol-Gel Method for Nonvolatile Memory Application. *IEEE Trans. Electron Devices* **2014**, *61* (12), 4090–4097.

(658) Li, Y.; Zhao, G.; Su, J.; Shen, E.; Ren, Y. Top Electrode Effects on Resistive Switching Behavior in CuO Thin Films. *Appl. Phys. A Mater. Sci. Process.* **2011**, *104* (4), 1069–1073.

(659) Chang, Y. C.; Lee, K. J.; Lee, C. J.; Wang, L. W.; Wang, Y. H. Bipolar Resistive Switching Behavior in Sol-Gel MgTiNiOx Memory Device. *IEEE J. Electron Devices Soc.* **2016**, *4* (5), 321–327.

(660) Ayana, D. G.; Prusakova, V.; Ceccato, R.; Dire, S. Structural Characterization of Sol-Gel ZnO Thin Films on Different Substrates for Memristive Application. In *2015 XVIII AISEM Annual Conference*; IEEE: Trento, Italia, 2015; pp 1–4.

(661) Hsu, C. C.; Tsai, J. E.; Lin, Y. S. A Write-Once-Read-Many-Times Memory Based on a Sol-Gel Derived Copper Oxide Semiconductor. *Phys. B Condens. Matter* **2019**, *562*

(March), 20–25.

(662) Hsu, C. C.; Chuang, P. Y.; Tsai, J. E.; Chen, Y. H. A Study of Negative Resistance Effect of CuxO RRAM Fabricated by Using a Sol-Gel Method. *Proc. - 2018 7th Int. Symp. Next-Generation Electron. ISNE 2018* **2018**, No. Isne, 1–2.

(663) Chiang, K. K.; Chen, J. S.; Wu, J. J. Aluminum Electrode Modulated Bipolar Resistive Switching of Al/Fuel-Assisted NiO x/ITO Memory Devices Modeled with a Dual-Oxygen-Reservoir Structure. *ACS Appl. Mater. Interfaces* **2012**, *4* (8), 4237–4245.

(664) Liu, C. Y.; Chuang, C. C.; Chen, J. S.; Wang, A.; Jang, W. Y.; Young, J. C.; Chiu, K. Y.; Tseng, T. Y. Memory Effect of Sol-Gel Derived V-Doped SrZrO3 Thin Films. *Thin Solid Films* **2006**, *494* (1–2), 287–290.

(665) Lee, K. J.; Chang, Y. C.; Lee, C. J.; Wang, Y. H. Bipolar and Rewritable Switching of One Diode–One Resistor Nonvolatile Strontium Titanate Nickelate Memory Devices. *Vacuum* **2017**, *140*, 35–41.

(666) Bakar, R. A.; Nazmi, M. N.; Harun, A.; Kamarozaman, N. S.; Shaari, N. A. A.; Kasim, S. M. M.; Herman, S. H. Switching Behavior of Lateral-Structured Zinc Oxide-Based Memristive Device. *IEEE Int. Conf. Semicond. Electron. Proceedings, ICSE* **2014**, 448–451.

(667) Wu, J.; Wen, Z.; Wu, D.; Zhai, H.; Li, A. Current-Voltage Characteristics of Sol-Gel Derived SrZrO3 Thin Films for Resistive Memory Applications. *J. Alloys Compd.* **2011**, *509* (5), 2050–2053.

(668) Kanao, K.; Arie, T.; Akita, S.; Takei, K. An All-Solution-Processed Tactile Memory Flexible Device Integrated with a NiO ReRAM. *J. Mater. Chem. C* **2016**, *4* (39), 9261–9265.

(669) Tang, Z.-X.; Tang, W.-W.; Tang, X.-G.; Liu, Q.-X.; Jiang, Y.-P.; Li, W.-H.; Tang, Z.-H.; Guo, X.-B.; Tang, Z.-F. Analog-Type Resistive Switching Behavior of Au/HfO2/ZnO Memristor Fabricated on Flexible Mica Substrate. *Phys. E Low-dimensional Syst. Nanostructures* **2020**, *120*, 114047.

(670) Ho, Y.-D.; Chen, K.-R.; Huang, C.-L. Resistive Switching Behaviors of Sol-Gel-Derived MgNb 2 O 6 Thin Films on ITO/Glass Substrate . *J. Am. Ceram. Soc.* **2014**, *97* (11), 3544–3548.

(671) Smith, J.; Chung, S.; Jang, J.; Biaou, C.; Subramanian, V. Solution-Processed Complementary Resistive Switching Arrays for Associative Memory. *IEEE Trans. Electron Devices* **2017**, *64* (10), 4310–4316.

(672) Hsu, C. C.; Wang, T. C.; Tsao, C. C. Forming-Free Sol-Gel ZrOx Resistive Switching Memory. *J. Alloys Compd.* **2018**, *769*, 65–70.

(673) Park, S. J.; Yu, B. S.; Jeon, J. Y.; Kang, B. C.; Ha, T. J. Sol-Gel Based Zirconium Dioxide Dielectrics by Oxygen-Annealing at Low Temperature for Highly Stable and Robust Flexible Resistive Random Access Memory. *J. Alloys Compd.* **2020**, *825*, 154086.

(674) Akbari, M.; Lee, J. S. Control of Resistive Switching Behaviors of Solution-Processed HfOX-Based Resistive Switching Memory Devices by n-Type Doping. *RSC Adv.* **2016**, *6* (26), 21917–21921.

(675) Aglieri, V.; Zaffora, A.; Lullo, G.; Santamaria, M.; Di Franco, F.; Lo Cicero, U.; Mosca, M.; Macaluso, R. Resistive Switching in Microscale Anodic Titanium Dioxide-Based Memristors. *Superlattices Microstruct.* **2018**, *113*, 135–142.

(676) Murali, S.; Rajachidambaram, J. S.; Han, S.-Y.; Chang, C.-H.; Herman, G. S.; Conley, J. F. Resistive Switching in Zinc–Tin-Oxide. *Solid. State. Electron.* **2013**, *79*, 248–252.

(677) Du, H.; Wan, T.; Qu, B.; Cao, F.; Lin, Q.; Chen, N.; Lin, X.; Chu, D. Engineering Silver Nanowire Networks: From Transparent Electrodes to Resistive Switching Devices. *ACS Appl. Mater. Interfaces* **2017**, *9* (24), 20762–20770.

(678) Hsu, C. C.; Sun, J. K.; Tsao, C. C.; Chuang, P. Y. Effects of Gibbs Free Energy of Interfacial Metal Oxide on Resistive Switching Characteristics of Solution-Processed HfOx Films. *Phys. B Condens. Matter* **2017**, *519* (May), 21–25.

(679) Hsu, C. C.; Chuang, P. Y.; Chen, Y. T. Resistive Switching Characteristic of Low-Temperature Top-Electrode-Free Tin-Oxide Memristor. *IEEE Trans. Electron Devices* **2017**, *64* (9), 3951–3954.

(680) Hsu, C. C.; Sun, J. K.; Tsao, C. C.; Chen, Y. T. Effects of Sol Aging on Resistive Switching Behaviors of HfOx Resistive Memories. *Phys. B Condens. Matter* **2017**, *508* (November 2016), 98–103.

(681) Wang, H.; Chen, Q.; Xu, J.; Zhang, X.; Yan, S. Bipolar Resistive Switching Behaviour in $$\mathrm{Mn}_{0.03}\mathrm{Zn}_{0.97}{\hbox {O/Amorphous}}$$ Mn 0.03 Zn 0.97 O/Amorphous $$\mathrm{La}_{0.7}\mathrm{Zn}_{0.3}\mathrm{MnO}_{3}$$ La 0.7 Zn 0.3 MnO 3 Heterostructure Films. *Bull. Mater. Sci.* **2017**, *40* (6), 1285–1289.

(682) Wang, H.; Gao, S. M.; Xu, J. W.; Yang, L.; Qiu, W. Effects of Mg-Doping on Resistance Switching Property of MgxZn1-XO Thin Films Prepared by Sol-Gel Method. *Adv. Mater. Res.* **2013**, *750–752*, 1034–1037.

(683) Jung, S.; Kong, J.; Song, S.; Lee, K.; Lee, T.; Hwang, H.; Jeon, S. Flexible Resistive Random Access Memory Using Solution-Processed TiO x with Al Top Electrode on Ag Layer-Inserted Indium-Zinc-Tin-Oxide-Coated Polyethersulfone Substrate. *Appl. Phys. Lett.* **2011**, *99* (14), 142110.

(684) Jung, S.; Kong, J.; Song, S.; Lee, K.; Lee, T.; Hwang, H.; Jeon, S. Resistive Switching Characteristics of Solution-Processed TiOx for next-Generation Non-Volatile Memory Application; Transparency, Flexibility, and Nano-Scale Memory Feasibility. *Microelectron. Eng.* **2011**, *88* (7), 1143–1147.

(685) Yao, C.; Hao, A.; Thatikonda, S. K.; Huang, W.; Qin, N.; Bao, D. Realization of Resistive and Magnetization Switching in Sol-Gel Derived Yttrium Iron Garnet Thin Films. *Thin Solid Films* **2020**, *699*, 137889.

(686) Chen, Y.; Li, L.; Yin, X.; Yerramilli, A.; Shen, Y.; Song, Y.; Bian, W.; Li, N.; Zhao, Z.; Qu, W.; Theodore, N. D.; Alford, T. L. Resistive Switching Characteristics of Flexible TiO2 Thin Film Fabricated by Deep Ultraviolet Photochemical Solution Method. *IEEE Electron Device Lett.* **2017**, *38* (11), 1528–1531.

(687) Gale, E.; Mayne, R.; Adamatzky, A.; De Lacy Costello, B. Drop-Coated Titanium Dioxide Memristors. *Mater. Chem. Phys.* **2014**, *143* (2), 524–529.

(688) Zhang, Y.; Wang, H.; Xu, J.; Li, Z.; Yang, L. Coexistence of Bipolar and Unipolar Resistive Switching Behavior in Ag/ZnMn2O4/P+-Si Device. *J. Wuhan Univ. Technol. Sci. Ed.* **2018**, *33* (6), 1433–1436.

(689) Abunahla, H.; Jaoude, M. A.; O'Kelly, C. J.; Mohammad, B. Sol-Gel/Drop-Coated Micro-Thick TiO2 Memristors for γ-Ray Sensing. *Mater. Chem. Phys.* **2016**, *184*, 72–81.

(690) Shan, F.; Guo, H.-B.; Kim, H.-S.; Lee, J.-Y.; Sun, H.-Z.; Gon Choi, S.; Koh, J.-H.; Kim, S.-J. Enhanced Electrical Performance of Structurally Engineered Memristor Devices with Multi-Stacked Indium Zinc Oxide Films. *Phys. status solidi* **2020**, *23* (30), 1900967.

(691) Yao, C.; Ismail, M.; Hao, A.; Kumar, T. S.; Huang, W.; Qin, N.; Bao, D. Sol–Gel-Derived Spinel Ag-Co3O4 Nanocomposite Thin Films for Resistive and Magnetization Switching

Applications. *Phys. Status Solidi - Rapid Res. Lett.* **2019**, *13* (9), 1–6.

(692) Yao, C.; Hu, W.; Ismail, M.; Thatikonda, S. K.; Hao, A.; He, S.; Qin, N.; Huang, W.; Bao, D. Coexistence of Resistive Switching and Magnetism Modulation in Sol-Gel Derived Nanocrystalline Spinel Co3O4 Thin Films. *Curr. Appl. Phys.* **2019**, *19* (11), 1286–1295.

(693) Wei, C.; Wang, H.; Xu, J.; Zhang, Y.; Zhang, X.; Yang, L. Resistive Switching Behavior of Ag/Mg0.2Zn0.8O/ZnMn2O4/P+-Si Heterostructure Devices for Nonvolatile Memory Applications. *J. Wuhan Univ. Technol. Mater. Sci. Ed.* **2017**, *32* (1), 29–32.

(694) Gale, E.; Pearson, D.; Kitson, S.; Adamatzky, A.; De Lacy Costello, B. The Effect of Changing Electrode Metal on Solution-Processed Flexible Titanium Dioxide Memristors. *Mater. Chem. Phys.* **2015**, *162*, 20–30.

(695) Zhou, Q.; Zhai, J. Electrode-Dependent Resistive Switching Characteristics of Sr(Ti,Sn)O 3 Thin Films. In *2012 International Workshop on Information Storage and Ninth International Symposium on Optical Storage*; Gan, F., Song, Z., Eds.; Society of Photo-Optical Instrumentation Engineers (SPIE): Shanghai, China, 2013; Vol. 8782, p 87820E.

(696) Vilmi, P.; Nelo, M.; Voutilainen, J. V.; Palosaari, J.; Pörhönen, J.; Tuukkanen, S.; Jantunen, H.; Juuti, J.; Fabritius, T. Fully Printed Memristors for a Self-Sustainable Recorder of Mechanical Energy. *Flex. Print. Electron.* **2016**, *1* (2), 1–8.

(697) Kannan, V.; Senthilkumar, V.; Rhee, J. K. Multi-Level Conduction in NiO Resistive Memory Device Prepared by Solution Route. *J. Phys. D. Appl. Phys.* **2013**, *46* (9), 095301.

(698) Barnes, B. K.; Das, K. S. Resistance Switching and Memristive Hysteresis in Visible-Light-Activated Adsorbed ZnO Thin Films. *Sci. Rep.* **2018**, *8* (1), 1–10.

(699) Biju, K. P.; Liu, X.; Bourim, E. M.; Kim, I.; Jung, S.; Siddik, M.; Lee, J.; Hwang, H. Asymmetric Bipolar Resistive Switching in Solution-Processed Pt/TiO 2 /W Devices. *J. Phys. D. Appl. Phys.* **2010**, *43* (49), 495104.

(700) Rafique, A. F.; Haji Zaini, J.; Bin Esa, M. Z.; Nauman, M. M. Printed Memory Devices Using Electrohydrodynamic Deposition Technique. *Appl. Phys. A* **2020**, *126* (2), 134.

(701) Siddiqui, G. U. D.; Ali, J.; Doh, Y. H.; Choi, K. H. Fabrication of Zinc Stannate Based All-Printed Resistive Switching Device. *Mater. Lett.* **2016**, *166*, 311–316.

(702) Lien, D. H.; Kao, Z. K.; Huang, T. H.; Liao, Y. C.; Lee, S. C.; He, J. H. All-Printed Paper Memory. *ACS Nano* **2014**, *8* (8), 7613–7619.

(703) Li, Y.; Sivan, M.; Niu, J. X.; Veluri, H.; Zamburg, E.; Leong, J.; Chand, U.; Samanta, S.; Wang, X.; Feng, X.; Zhao, Y.; Thean, A. V. Y. Aerosol Jet Printed WSe2 Based RRAM on Kapton Suitable for Flexible Monolithic Memory Integration. *FLEPS 2019 - IEEE Int. Conf. Flex. Printable Sensors Syst. Proc.* **2019**, No. c, 4–6.

(704) Awais, M. N.; Muhammad, N. M.; Navaneethan, D.; Kim, H. C.; Jo, J.; Choi, K. H. Fabrication of ZrO2 Layer through Electrohydrodynamic Atomization for the Printed Resistive Switch (Memristor). *Microelectron. Eng.* **2013**, *103*, 167–172.

(705) Wan, T.; Qu, B.; Du, H.; Lin, X.; Guan, P.; Lin, Q.; Chen, N.; Teck Tan, T.; Hang, T.; Chu, D. Tunable Resistance Switching in Solution Processed Chromium-Doped Strontium Titanate Nanoparticles Films. *J. Colloid Interface Sci.* **2017**, *494*, 178–184.

(706) Li, Y.; Zhao, G.; Zhou, X.; Pan, L.; Ren, Y. Resistive Switching Behavior in Amorphous and Crystalline TiO2 Thin Films by Sol-Gel Process. *J. Sol-Gel Sci. Technol.* **2010**, *56* (1), 61–65.

(707) Muhammad, N. M.; Duraisamy, N.; Rahman, K.; Dang, H. W.; Jo, J.; Choi, K. H. Fabrication of Printed Memory Device Having Zinc-Oxide Active Nano-Layer and

Investigation of Resistive Switching. *Curr. Appl. Phys.* **2013**, *13* (1), 90–96.

(708) Choi, K. H.; Awais, M. N. Versatile Resistive Switching (Memristive) Behavior in an ITO/ZrO2/Ag Sandwich Fabricated Using Electrohydrodynamic Printing. *J. Korean Phys. Soc.* **2012**, *61* (1), 119–123.

(709) Chung, I.; Cho, K.; Yun, J.; Kim, S. Flexible Resistive Switching Memory Devices Composed of Solution-Processed GeO 2:S Films. *Microelectron. Eng.* **2012**, *97*, 122–125.

(710) Li, L.; Chen, Y.; Yin, X.; Song, Y.; Li, N.; Niu, J.; Wu, H.; Qu, W. Ultraviolet-Assisted Direct Patterning and Low-Temperature Formation of Flexible ZrO 2 Resistive Switching Arrays on PET/ITO Substrates. *Nanotechnology* **2017**, *28* (48), 485707.

(711) Duraisamy, N.; Muhammad, N. M.; Kim, H.-C.; Jo, J.-D.; Choi, K.-H. Fabrication of TiO2 Thin Film Memristor Device Using Electrohydrodynamic Inkjet Printing. *Thin Solid Films* **2012**, *520* (15), 5070–5074.

(712) Li, Y.; Zhao, G.; Su, J.; Shen, E.; Ren, Y. Temperature Influence and Reset Voltage Study of Bipolar Resistive Switching Behaviour in ZrO2 Thin Films. *Bull. Mater. Sci.* **2014**, *37* (3), 455–460.

(713) Wu, W. T.; Wu, J. J.; Chen, J. S. Resistive Switching Behavior and Multiple Transmittance States in Solution-Processed Tungsten Oxide. *ACS Appl. Mater. Interfaces* **2011**, *3* (7), 2616–2621.

(714) Zhang, F.; Zhuang, W.-W.; Evans, D. R.; Hsu Sheng, T. High Temperature Annealing of Spin Coated Pr1-XCaxMnO3 Thim Film for RRAM Application, 2004.

(715) Abunahla, H.; Jaoude, M. A.; Omar, I. A.; Mohammad, B.; Al-Qutayri, M. Resistive Switching in Sol-Gel Derived Microscale Memristors. In *2016 IEEE 59th International Midwest Symposium on Circuits and Systems (MWSCAS)*; IEEE, 2016; Vol. 0, pp 1–4.

(716) Tang, H.; Tang, X. G.; Jiang, Y. P.; Liu, Q. X.; Li, W. H.; Luo, L. Bipolar Resistive Switching Characteristics of Amorphous SrTiO3 Thin Films Prepared by the Sol-Gel Process. *J. Asian Ceram. Soc.* **2019**, *7* (3), 298–305.

(717) Senthilkumar, V.; Kathalingam, A.; Kannan, V.; Rhee, J. K. Observation of Multi-Conductance State in Solution Processed Al/a-TiO 2/ITO Memory Device. *Microelectron. Eng.* **2012**, *98*, 97–101.

(718) Kumar, K. D. A.; Valanarasu, S.; Kathalingam, A.; Ganesh, V.; Shkir, M.; AlFaify, S. Effect of Solvents on Sol–Gel Spin-Coated Nanostructured Al-Doped ZnO Thin Films: A Film for Key Optoelectronic Applications. *Appl. Phys. A* **2017**, *123* (12), 801.

(719) Winer, I.; Shter, G. E.; Mann-Lahav, M.; Grader, G. S. Effect of Solvents and Stabilizers on Sol–Gel Deposition of Ga-Doped Zinc Oxide TCO Films. *J. Mater. Res.* **2011**, *26* (10), 1309–1315.

(720) Lee, S.; Kim, T.; Jang, B.; Lee, W. Y.; Song, K. C.; Kim, H. S.; Do, G. Y.; Hwang, S. B.; Chung, S.; Jang, J. Impact of Device Area and Film Thickness on Performance of Sol-Gel Processed ZrO2 RRAM. *IEEE Electron Device Lett.* **2018**, *39* (5), 668–671.

(721) Cheng, H. C.; Chen, S. W.; Wu, J. M. Resistive Switching Behavior of (Zn1-XMgx)O Films Prepared by Sol-Gel Processes. *Thin Solid Films* **2011**, *519* (18), 6155–6159.

(722) Wu, X.; Xu, Z.; Zhao, F.; Xu, X.; Liu, B.; Sun, T.; Liu, S.; Zhao, W.; Ma, Z. Transparent Bipolar Resistive Switching Memory Devices Based on Mn Doped SnO2 Films. *J. Alloys Compd.* **2014**, *602*, 175–179.

(723) Li, J. C.; Hou, X. Y.; Cao, Q. Effect of Cu Doping on the Resistive Switching of NiO Thin Films. *J. Appl. Phys.* **2014**, *115* (16), 1–6.

(724) Wang, Y. R.; Chen, B.; Gao, B.; Liu, L. F.; Kang, J. F. La/Al-Doped ZrO2 Thin-Film Resistive Random Access Memory Devices by Sol-Gel Method for Transparent Solid-State Circuit Systems. In *Extended Abstracts of the 2014 International Conference on Solid State Devices and Materials*; The Japan Society of Applied Physics, 2014; pp 76–77.

(725) Mannequin, C.; Tsuruoka, T.; Hasegawa, T.; Aono, M. Composition of Thin Ta 2 O 5 Films Deposited by Different Methods and the Effect of Humidity on Their Resistive Switching Behavior. *Jpn. J. Appl. Phys.* **2016**, *55* (6S1), 06GG08.

(726) Messerschmitt, F.; Kubicek, M.; Rupp, J. L. M. M. How Does Moisture Affect the Physical Property of Memristance for Anionic-Electronic Resistive Switching Memories? *Adv. Funct. Mater.* **2015**, *25* (32), 5117–5125.

(727) Rehman, S.; Hur, J. H.; Kim, D. K. Resistive Switching in Solution-Processed Copper Oxide (Cu XO) by Stoichiometry Tuning. *J. Phys. Chem. C* **2018**, *122* (20), 11076–11085.

(728) Kamarozaman, N. S.; Mohamed Soder, M. F.; Musa, M. Z.; Bakar, R. A.; Abdullah, W. F. H.; Herman, S. H.; Rusop, M. Effect of Post-Deposition Annealing Process on the Resistive Switching Behaviour of TiO2 Thin Films by Sol-Gel Method. *Adv. Mater. Res.* **2014**, *925*, 125–129.

(729) Shen, Z.; Qi, Y.; Mitrovic, I.; Zhao, C.; Hall, S.; Yang, L.; Luo, T.; Huang, Y.; Zhao, C. Effect of Annealing Temperature for Ni/AlOx/Pt RRAM Devices Fabricated with Solution-Based Dielectric. *Micromachines* **2019**, *10* (7), 446.

(730) Yao, C.; Ismail, M.; Hao, A.; Thatikonda, S. K.; Huang, W.; Qin, N.; Bao, D. Annealing Atmosphere Effect on the Resistive Switching and Magnetic Properties of Spinel Co3O4 Thin Films Prepared by a Sol-Gel Technique. *RSC Adv.* **2019**, *9* (22), 12615–12625.

(731) Kim, J. H.; Nam, K. H.; Cho, W. J.; Chung, H. B. Rectifying Characteristics and Bipolar Resistance Switching Behaviors in Sol-Gel Processed TiOx Thin Film. *Jpn. J. Appl. Phys.* **2015**, *54* (4), 4–9.

(732) Vescio, G.; Crespo-Yepes, A.; Alonso, D.; Claramunt, S.; Porti, M.; Rodriguez, R.; Cornet, A.; Cirera, A.; Nafria, M.; Aymerich, X. Inkjet Printed HfO 2 -Based ReRAMs: First Demonstration and Performance Characterization. *IEEE Electron Device Lett.* **2017**, *38* (4), 457–460.

(733) Hsiao, Y.-P.; Yang, W.-L.; Lin, Y.-H.; Yang, Y.-C.; Hsu, C.-C.; Peng, C.-L.; Liao, C.-H.; Chin, F.-T.; Liu, S.-H.; Chang, Y.-M.; Lin, L.-M. Adjustable Switching Voltage Via Sol-Gel Derived and Ag In Situ Doped SiO2 Thin Films for ReRAM. *ECS Trans.* **2013**, *53* (3), 223–228.

(734) Chin, F. T.; Lin, Y. H.; Hsiao, Y. P.; Yang, W. L. Forming-Free ZrOx-Based Electrochemical Metallization ReRAM by Sol-Gel Technique. *Proc. - 2014 Int. Symp. Comput. Consum. Control. IS3C 2014* **2014**, 474–477.

(735) Baek, I.-J.; Cho, W.-J. Investigating Resistive Switching Characteristics in Solution-Processed Aluminum Oxide Layer by Low Thermal Budget Microwave Irradiation. *J. Nanosci. Nanotechnol.* **2017**, *17* (10), 7760–7765.

(736) Zou, L.; Hu, W.; Xie, W.; Chen, R.; Qin, N.; Li, B.; Bao, D. Excellent Resistive Switching Property and Physical Mechanism of Amorphous TiO2 Thin Films Fabricated by a Low-Temperature Photochemical Solution Deposition Method. *Appl. Surf. Sci.* **2014**, *311*, 697–702.

(737) Kim, H.-K.; Bae, J.-H.; Kim, T.-H.; Song, K.-W.; Yang, C.-W. Synthesis and Characterization of a Pt/NiO/Pt Heterostructure for Resistance Random Access Memory. *Appl. Microsc.* **2012**, *42* (4), 207–211.

(738) Xiao, W.; Song, W.; Feng, Y. P.; Gao, D.; Zhu, Y.; Ding, J. Electrode-Controlled Confinement of Conductive Filaments in a Nanocolumn Embedded Symmetric–Asymmetric RRAM Structure. *J. Mater. Chem. C* **2020**, *8* (5), 1577–1582.

(739) Yun, J.; Cho, K.; Park, B.; Park, B. H.; Kim, S. Resistance Switching Memory Devices Constructed on Plastic with Solution-Processed Titanium Oxide. *J. Mater. Chem.* **2009**, *19* (14), 2082–2085.

(740) Gergel-Hackett, N.; Hamadani, B.; Dunlap, B.; Suehle, J.; Richter, C.; Hacker, C.; Gundlach, D. A Flexible Solution-Processed Memristor. *IEEE Electron Device Lett.* **2009**, *30* (7), 706–708.

(741) Yun, H. W.; Woo, H. K.; Oh, S. J.; Hong, S. H. Flexible NiO Nanocrystal-Based Resistive Memory Device Fabricated by Low-Temperature Solution-Process. *Curr. Appl. Phys.* **2020**, *20* (2), 288–292.

(742) Chen, C.; Gao, S.; Zeng, F.; Tang, G. S.; Li, S. Z.; Song, C.; Fu, H. D.; Pan, F. Migration of Interfacial Oxygen Ions Modulated Resistive Switching in Oxide-Based Memory Devices. *J. Appl. Phys.* **2013**, *114* (1), 014502.

(743) Chen, X.; Wu, G.; Bao, D. Resistive Switching Behavior of Pt/Mg0.2Zn0.8O/Pt Devices for Nonvolatile Memory Applications. *Appl. Phys. Lett.* **2008**, *93* (9), 093501.

(744) Deshpande, S.; Nair, V. V. Resistive Switching of Al/Sol-Gel ZnO/Al Devices for Resistive Random Access Memory Applications. In *2009 International Conference on Advances in Computing, Control, and Telecommunication Technologies*; IEEE, 2009; pp 471–473.

(745) Zhu, W.; Chen, T. P.; Liu, Z.; Yang, M.; Liu, Y.; Fung, S. Resistive Switching in Aluminum/Anodized Aluminum Film Structure without Forming Process. *J. Appl. Phys.* **2009**, *106* (9), 093706.

(746) Chen, X.; Wu, G.; Jiang, P.; Liu, W.; Bao, D. Colossal Resistance Switching Effect in Pt/Spinel -MgZnO/Pt Devices for Nonvolatile Memory Applications. *Appl. Phys. Lett.* **2009**, *94* (3), 033501.

(747) Tang, M. H.; Zeng, Z. Q.; Li, J. C.; Wang, Z. P.; Xu, X. L.; Wang, G. Y.; Zhang, L. B.; Yang, S. B.; Xiao, Y. G.; Jiang, B. Resistive Switching Behavior of La-Doped ZnO Films for Nonvolatile Memory Applications. *Solid. State. Electron.* **2011**, *63* (1), 100–104.

(748) Choi, K. H.; Mustafa, M.; Rahman, K.; Jeong, B. K.; Doh, Y. H. Cost-Effective Fabrication of Memristive Devices with ZnO Thin Film Using Printed Electronics Technologies. *Appl. Phys. A Mater. Sci. Process.* **2012**, *106* (1), 165–170.

(749) Kim, M.-S.; Hwan Hwang, Y.; Kim, S.; Guo, Z.; Moon, D.-I.; Choi, J.-M.; Seol, M.-L.; Bae, B.-S.; Choi, Y.-K. Effects of the Oxygen Vacancy Concentration in InGaZnO-Based Resistance Random Access Memory. *Appl. Phys. Lett.* **2012**, *101* (24), 243503.

(750) Gale, E.; de Lacy Costello, B.; Adamatzky, A. Filamentary Extension of the Mem-Con Theory of Memristance and Its Application to Titanium Dioxide Sol-Gel Memristors. In *2012 IEEE International Conference on Electronics Design, Systems and Applications (ICEDSA)*; IEEE, 2012; pp 86–91.

(751) Zhu, W.; Chen, T. P.; Liu, Y.; Fung, S. Conduction Mechanisms at Low- and High-Resistance States in Aluminum/Anodic Aluminum Oxide/Aluminum Thin Film Structure. *J. Appl. Phys.* **2012**, *112* (6), 063706.

(752) Zhu, W.; Chen, T. P.; Yang, M.; Liu, Y.; Fung, S. Resistive Switching Behavior of Partially Anodized Aluminum Thin Film at Elevated Temperatures. *IEEE Trans. Electron Devices* **2012**, *59* (9), 2363–2367.

(753) Tang, M. H.; Jiang, B.; Xiao, Y. G.; Zeng, Z. Q.; Wang, Z. P.; Li, J. C.; He, J. Top Electrode-Dependent Resistance Switching Behaviors of ZnO Thin Films Deposited on Pt/Ti/SiO2/Si Substrate. *Microelectron. Eng.* **2012**, *93*, 35–38.

(754) Chen, R.; Hu, W.; Zou, L.; Xie, W.; Li, B.; Bao, D. Multilevel Resistive Switching Effect in Sillenite Structure Bi 12 TiO 20 Thin Films. *Appl. Phys. Lett.* **2014**, *104* (24), 242111.

(755) Hu, W.; Zou, L.; Chen, R.; Xie, W.; Chen, X.; Qin, N.; Li, S.; Yang, G.; Bao, D. Resistive Switching Properties and Physical Mechanism of Cobalt Ferrite Thin Films. *Appl. Phys. Lett.* **2014**, *104* (14), 143502.

(756) Xu, D.; Xiong, Y.; Tang, M.; Zeng, B. Top Electrode-Dependent Resistance Switching Behaviors of Lanthanum-Doped ZnO Film Memory Devices. *Appl. Phys. A* **2014**, *114* (4), 1377–1381.

(757) Prusakova, V.; Dire, S.; Collini, C.; Pasquardini, L.; Vanzetti, L.; Resta, G.; Pederzolli, C.; Lorenzelli, L. Optimisation and Memristive Response of Sol-Gel Derived TiO<inf>2</Inf> Thin Films. In *2015 XVIII AISEM Annual Conference*; IEEE: Trento, Italia, 2015; pp 1–4.

(758) Chen, R.; Hu, W.; Zou, L.; Li, B.; Bao, D. Highly Uniform Resistive Switching Effect in Amorphous Bi2O3 Thin Films Fabricated by a Low-Temperature Photochemical Solution Deposition Method. *Appl. Phys. A* **2015**, *120* (1), 379–384.

(759) Hu, W.; Zou, L.; Lin, X.; Gao, C.; Guo, Y.; Bao, D. Unipolar Resistive Switching Effect and Mechanism of Solution-Processed Spinel Co3O4 Thin Films. *Mater. Des.* **2016**, *103*, 230–235.

(760) Prusakova, V.; Collini, C.; Lunelli, L.; Vanzetti, L.; Chiappini, A.; Lorenzelli, L.; Pederzolli, C.; Chiasera, A.; Ferrari, M.; Dirè, S. Towards Low Voltage Resistive Switch in Sol-Gel Derived TiO2/Ta2O5 Stack Thin Films. *Mater. Des.* **2016**, *105*, 359–365.

(761) Diamanti, M. V.; Pisoni, R.; Cologni, A.; Brenna, A.; Corinto, F.; Pedeferri, M. Anodic Oxidation as a Means to Produce Memristive Films. *J. Appl. Biomater. Funct. Mater.* **2016**, *14* (3), 0–0.

(762) Prusakova, V.; Collini, C.; Nardi, M.; Tatti, R.; Lunelli, L.; Vanzetti, L.; Lorenzelli, L.; Baldi, G.; Chiappini, A.; Chiasera, A.; Ristic, D.; Verucchi, R.; Bortolotti, M.; Dirè, S. The Development of Sol-Gel Derived TiO2 Thin Films and Corresponding Memristor Architectures. *RSC Adv.* **2017**, *7* (3), 1654–1663.

(763) Zou, L.; Hu, W.; Xie, W.; Bao, D. Uniform Resistive Switching Properties of Fully Transparent TiO2-Based Memory Devices. *J. Alloys Compd.* **2017**, *693*, 1180–1184.

(764) He, S.; Hao, A.; Qin, N.; Bao, D. Unipolar Resistive Switching Properties of Pr-Doped ZnO Thin Films. *Ceram. Int.* **2017**, *43* (xxxx), S474–S480.

(765) Hao, A.; He, S.; Qin, N.; Chen, R.; Bao, D. Ce-Doping Induced Enhancement of Resistive Switching Performance of Pt / NiFe 2 O 4 / Pt Memory Devices. *Ceram. Int.* **2017**, *43* (xxxx), S481–S487.

(766) Hao, A.; Ismail, M.; He, S.; Qin, N.; Chen, R.; Rana, A. M.; Bao, D. Enhanced Resistive Switching and Magnetic Properties of Gd-Doped NiFe 2 O 4 Thin Films Prepared by Chemical Solution Deposition Method. *Mater. Sci. Eng. B* **2018**, *229* (August 2017), 86–95.

(767) Kim, S. J.; Lee, H.; Hong, S. H. Solution-Processed Flexible NiO Resistive Random Access Memory Device. *Solid. State. Electron.* **2018**, *142* (February), 56–61.

(768) Hao, A.; Jia, D.; Ismail, M.; Huang, W.; Chen, R.; Bao, D. Electric Field Induced Manipulation of Resistive and Magnetization Switching in Pt/NiFe 1.95 Cr 0.05 O 4 /Pt

Memory Devices. *Appl. Phys. Lett.* **2019**, *114* (20), 203502.

(769) Chen, R.; Hu, W.; Zou, L.; Ke, Y.; Hao, A.; Bao, D. Bipolar Resistive Switching Effect and Mechanism of Solution-Processed Orthorhombic Bi2SiO5 Thin Films. *Curr. Appl. Phys.* **2019**, *19* (9), 987–991.

(770) Farooq, T.; Surana, K.; Mukherjee, S. Synthesis of Titanium Dioxide TiO2 Thin Film to Achieve Resistive Switching Property for the Application of Nonvolatile Memory. *Mater. Today Proc.* **2020**, No. xxxx, 2–6.

(771) Nauman, M. M.; Zulfikre Esa, M.; Zaini, J. H.; Iqbal, A.; Bakar, S. A. Zirconium Oxide Based Memristors Fabrication via Electrohydrodynamic Printing. In *2020 IEEE 11th International Conference on Mechanical and Intelligent Manufacturing Technologies (ICMIMT)*; IEEE, 2020; pp 167–171.

(772) Ismail, M.; Hao, A.; Huang, W.; Lee, J.; Kim, S.; Bao, D. Coexistence of Unipolar and Bipolar Switching in Nanocrystalline Spinel Ferrite ZnFe2O4 Thin Films Synthesized by Sol-Gel Method. *Appl. Phys. Lett.* **2018**, *113* (15), 2–7.

(773) Jang, K.; Park, J.-H.; Oh, S.-M.; Hwang, I.; Cho, W.-J. Superior Bipolar Resistive Switching Behaviors of Solution-Processed HfAlO x Thin Film for Nonvolatile Memory Applications. *Jpn. J. Appl. Phys.* **2014**, *53* (8S3), 08NE03.

(774) Jung, S.; Kong, J.; Kim, T. W.; Song, S.; Lee, K.; Lee, T.; Hwang, H.; Jeon, S. In-Depth Study on the Effect of Active-Area Scale-down of Solution-Processed TiO X. *IEEE Electron Device Lett.* **2012**, *33* (6), 869–871.

(775) Lin, C.-Y.; Wu, C.-Y.; Wu, C.-Y.; Lee, T.-C.; Yang, F.-L.; Hu, C.; Tseng, T.-Y. Effect of Top Electrode Material on Resistive Switching Properties of $\hbox{ZrO}_{2}$ Film Memory Devices. *IEEE Electron Device Lett.* **2007**, *28* (5), 366–368.

(776) Magyari-Köpe, B.; Nishi, Y. *Advances in Non-Volatile Memory and Storage Technology*, Second edi.; Elsevier, 2019.

(777) Stille, S.; Lenser, C.; Dittmann, R.; Koehl, A.; Krug, I.; Muenstermann, R.; Perlich, J.; Schneider, C. M.; Klemradt, U.; Waser, R. Detection of Filament Formation in Forming-Free Resistive Switching SrTiO 3 Devices with Ti Top Electrodes. *Appl. Phys. Lett.* **2012**, *100* (22), 223503.

(778) Yin, Y.; Pourtois, G.; Clima, S.; Goux, L.; Govoreanu, B.; Fantini, A. Hf Cap Thickness Dependence in Bipolar-Switching TiN\HfO2\Hf\TiN RRAM Device. *ECS Meet. Abstr.* **2012**, *50* (34), 3–9.

(779) Wedig, A.; Luebben, M.; Cho, D.-Y.; Moors, M.; Skaja, K.; Rana, V.; Hasegawa, T.; Adepalli, K. K.; Yildiz, B.; Waser, R.; Valov, I. Nanoscale Cation Motion in TaOx, HfOx and TiOx Memristive Systems. *Nat. Nanotechnol.* **2016**, *11* (1), 67–74.

(780) Do, Y. H.; Kwak, J. S.; Bae, Y. C.; Jung, K.; Im, H.; Hong, J. P. Oxygen Ion Drifted Bipolar Resistive Switching Behaviors in TiO2–Al Electrode Interfaces. *Thin Solid Films* **2010**, *518* (15), 4408–4411.

(781) Parreira, P.; Paterson, G. W.; McVitie, S.; MacLaren, D. A. Stability, Bistability and Instability of Amorphous ZrO 2 Resistive Memory Devices. *J. Phys. D. Appl. Phys.* **2016**, *49* (9), 095111.

(782) Zhang, T.; Chen, H.; Ni, M.; Su, Z.; Zhang, W. Resistance Switching Behaviors of V-Doped La0.67Ca0.33MnO3 Thin Films on F-Doped SnO2 Conducting Glass. *J. Appl. Phys.* **2009**, *105* (8), 083708.

(783) Lin, M. H.; Wu, M. C.; Lin, C. C.; Tseng, T. Y. Nonpolar Bistable Resistive Switching Behaviors of Bismuth Titanate Oxide Thin Film. *Ferroelectrics* **2009**, *380* (1 PART 1),

30–37.

(784) Wang, J.; Sun, B.; Gao, F.; Greenham, N. C. Memristive Devices Based on Solution-Processed ZnO Nanocrystals. *Phys. Status Solidi Appl. Mater. Sci.* **2010**, *207* (2), 484–487.

(785) Hsu, C. H.; Lin, J. Sen; He, Y. Da; Yang, S. F.; Yang, P. C.; Chen, W. S. Optical, Electrical Properties and Reproducible Resistance Switching of GeO2 Thin Films by Sol-Gel Process. *Thin Solid Films* **2011**, *519* (15), 5033–5037.

(786) Li, Y.; Zhao, G. Y.; Zhou, X. F.; Pan, L. N.; Ren, Y. A HRTEM Study of Resistive Switching Behaviour in SiO_2 Thin Films by Sol-Gel Process. *Mater. Sci. Forum* **2011**, *687*, 1–6.

(787) Kundozerova, T. V.; Grishin, A. M.; Stefanovich, G. B.; Velichko, A. A. Anodic $\hbox{Nb}_{2}\hbox{O}_{5}$ Nonvolatile RRAM. *IEEE Trans. Electron Devices* **2012**, *59* (4), 1144–1148.

(788) Kundozerova, T. V.; Stefanovich, G. B.; Grishin, A. M. Binary Anodic Oxides for Memristor-Type Nonvolatile Memory. *Phys. status solidi* **2012**, *9* (7), 1699–1701.

(789) Chang, Y. C.; Wei, C. Y.; Wang, Y. H. Sol-Gel Barium Titanate-Based RRAM by Inserting Graphene Oxide Interlayer. *2012 IEEE Int. Conf. Electron Devices Solid State Circuit, EDSSC 2012* **2012**, *2*, 4–5.

(790) Ramadoss, A.; Krishnamoorthy, K.; Kim, S. J. Resistive Switching Behaviors of HfO$_{2}$ Thin Films by Sol–Gel Spin Coating for Nonvolatile Memory Applications. *Appl. Phys. Express* **2012**, *5* (8), 085803.

(791) Koza, J. A.; Bohannan, E. W.; Switzer, J. A. Superconducting Filaments Formed During Nonvolatile Resistance Switching in Electrodeposited δ-Bi 2 O 3. *ACS Nano* **2013**, *7* (11), 9940–9946.

(792) Zou, S.; Xu, P.; Hamilton, M. C. Resistive Switching Characteristics in Printed Cu/CuO/(AgO)/Ag Memristors. *Electron. Lett.* **2013**, *49* (13), 829–830.

(793) Younis, A.; Chu, D.; Li, S. Tuneable Resistive Switching Characteristics of In2O3 Nanorods Array via Co Doping. *RSC Adv.* **2013**, *3* (32), 13422–13428.

(794) Lai, C. H.; Chen, C. H.; Tseng, T. Y. Resistive Switching Behavior of Sol-Gel Deposited TiO2 Thin Films under Different Heating Ambience. *Surf. Coatings Technol.* **2013**, *231*, 399–402.

(795) Hsu, C. H.; Lin, S. Y. Characterization of ZrTiO4 Thin Films Prepared by Sol-Gel Method. *Mater. Sci. Semicond. Process.* **2013**, *16* (5), 1262–1266.

(796) Zoolfakar, A. S.; Ab Kadir, R.; Rani, R. A.; Balendhran, S.; Liu, X.; Kats, E.; Bhargava, S. K.; Bhaskaran, M.; Sriram, S.; Zhuiykov, S.; O'Mullane, A. P.; Kalantar-zadeh, K. Engineering Electrodeposited ZnO Films and Their Memristive Switching Performance. *Phys. Chem. Chem. Phys.* **2013**, *15* (25), 10376.

(797) Kim, J. H.; Nam, K. H.; Ha, T. J.; Cho, W. J.; Chung, H. B. Rectifying Characteristics of Sol-Gel Derived TiOx Thin Films for 1D-1R Resistance Switching Memory Applications. In *Extended Abstracts of the 2014 International Conference on Solid State Devices and Materials*; The Japan Society of Applied Physics, 2014; pp 72–73.

(798) Kamarozaman, N. S.; Herman, S. H.; Mahmudin, M. A. Memristive Behaviour of Spin Coated Titania Thin Film. *IOP Conf. Ser. Mater. Sci. Eng.* **2014**, *64* (1), 012054.

(799) Zou, L.; Hu, W.; Fu, J.; Qin, N.; Li, S.; Bao, D. Uniform Bipolar Resistive Switching Properties with Self-Compliance Effect of Pt/TiO 2 /p-Si Devices. *AIP Adv.* **2014**, *4* (3),

037106.

(800) XU, J.; YANG, Z.; ZHANG, Y.; ZHANG, X.; WANG, H. Bipolar Resistive Switching Behaviours in ZnMn2O4 Film Deposited on P+-Si Substrate by Chemical Solution Deposition. *Bull. Mater. Sci.* **2014**, *37* (7), 1657–1661.

(801) Luo, J. M.; Chen, S. H.; Bu, S. L.; Wen, J. P. Resistive Switching and Schottky Diode-like Behaviors in Pt/BiFeO3/ITO Devices. *J. Alloys Compd.* **2014**, *601*, 100–103.

(802) Park, S. P.; Yoon, D. H.; Tak, Y. J.; Lee, H.; Kim, H. J. Highly Reliable Switching via Phase Transition Using Hydrogen Peroxide in Homogeneous and Multi-Layered GaZnOx-Based Resistive Random Access Memory Devices. *Chem. Commun.* **2015**, *51* (44), 9173–9176.

(803) Yazdanparast, S.; Koza, J. A.; Switzer, J. A. Copper Nanofilament Formation during Unipolar Resistance Switching of Electrodeposited Cuprous Oxide. *Chem. Mater.* **2015**, *27* (17), 5974–5981.

(804) Awais, M. N.; Choi, K. H. Resistive Switching Mechanism in Printed Non-Volatile Ag/ZrO2/ITO Sandwiched Structure. *Electron. Lett.* **2015**, *51* (25), 2147–2149.

(805) Kasim, S. M. M.; Shaari, N. A. A.; Bakar, R. A.; Aznilinda, Z.; Mohamad, Z.; Herman, S. H. Influence of Different Sol-Gel Spin Coating Speed on Memristive Behaviour of Pt/TiO 2 /ZnO/ITO Device. *IOP Conf. Ser. Mater. Sci. Eng.* **2015**, *99* (1), 012020.

(806) Shaari, N. A. A.; Kasim, S. M. M.; Sauki, N. S. M.; Herman, S. H. The Effect of the Sol-Gel Spincoating Deposition Technique on the Memristive Behaviour of ZnO-Based Memristive Device. *IOP Conf. Ser. Mater. Sci. Eng.* **2015**, *99* (1), 012022.

(807) Sohrabi Anaraki, H.; Gaponenko, N. V.; Litvinov, V. G.; Ermachikhin, A. V.; Kolos, V. V.; Pyatlitski, A. N.; Ivanov, V. A. Low-Resistance and High-Resistance States in Strontium Titanate Films Formed by the Sol–Gel Method. *Phys. Solid State* **2015**, *57* (10), 2030–2033.

(808) Shaari, N. A. A.; Mohd Kasim, S. M.; Muhamad Sauki, N. S.; Herman, S. H. Annealing Time Dependence of Zinc Oxide Thin Films Memristive Behavior. In *2015 International Symposium on Technology Management and Emerging Technologies (ISTMET)*; IEEE, 2015; pp 16–19.

(809) Velichko, A.; Pergament, A.; Putrolaynen, V.; Berezina, O.; Stefanovich, G. Effect of Memory Electrical Switching in Metal/Vanadium Oxide/Silicon Structures with VO2 Films Obtained by the Sol-Gel Method. *Mater. Sci. Semicond. Process.* **2015**, *29*, 315–320.

(810) Lee, K. J.; Wang, L. W.; Chiang, T. K.; Wang, Y. H. Effects of Electrodes on the Switching Behavior of Strontium Titanate Nickelate Resistive Random Access Memory. *Materials (Basel).* **2015**, *8* (10), 7191–7198.

(811) Sharma, B.; Rabinal, M. K. A Simple Dip Coat Patterning of Aluminum Oxide to Constitute a Bistable Memristor. *Mater. Res. Express* **2016**, *3* (12), 126302.

(812) Ali, S.; Bae, J.; Lee, C. H. Printed Non-Volatile Resistive Switches Based on Zinc Stannate (ZnSnO3). *Curr. Appl. Phys.* **2016**, *16* (7), 757–762.

(813) Kanao, K.; Nakata, S.; Arie, T.; Akita, S.; Takei, K. All Solution-Processed Flexible Memory Integrated with Tactile Sensor. In *2016 IEEE 29th International Conference on Micro Electro Mechanical Systems (MEMS)*; IEEE, 2016; Vol. 2016-Febru, pp 435–438.

(814) Saraei, A.; Eshraghi, M. J.; Massoudi, A. Investigation of Resistive Switching in Anodized Titanium Dioxide Thin Films. *Adv. Ceram. Prog.* **2016**, *2* (3), 34–37.

(815) Pawar, P. S.; Tikke, R. S.; Patil, V. B.; Mullani, N. B.; Waifalkar, P. P.; Khot, K. V.; Teli, A. M.; Sheikh, A. D.; Dongale, T. D. A Low-Cost Copper Oxide Thin Film Memristive Device Based on Successive Ionic Layer Adsorption and Reaction Method. *Mater. Sci. Semicond. Process.* **2017**, *71* (April), 102–108.

(816) Qu, B.; Du, H.; Wan, T.; Lin, X.; Younis, A.; Chu, D. Synaptic Plasticity and Learning Behavior in Transparent Tungsten Oxide-Based Memristors. *Mater. Des.* **2017**, *129* (May), 173–179.

(817) Thakre, A.; Kaswan, J.; Shukla, A. K.; Kumar, A. Unipolar Resistive Switching Behavior in Sol-Gel Synthesized FeSrTiO3 Thin Films. *RSC Adv.* **2017**, *7* (85), 54111–54116.

(818) Munjal, S.; Khare, N. Valence Change Bipolar Resistive Switching Accompanied with Magnetization Switching in CoFe2O4 Thin Film. *Sci. Rep.* **2017**, *7* (1), 1–10.

(819) Chu, J.; Li, Y.; Fan, X.; Shao, H.; Duan, W.; Pei, Y. Multistate Data Storage in Solution-Processed NiO-Based Resistive Switching Memory. *Semicond. Sci. Technol.* **2018**, *33* (11), 115007.

(820) Kumari, C.; Varun, I.; Prakash Tiwari, S.; Dixit, A. Robust Non-Volatile Bipolar Resistive Switching in Sol-Gel Derived BiFeO3 Thin Films. *Superlattices Microstruct.* **2018**, *120*, 67–74.

(821) Duan, W.; Tang, Y.; Liang, X.; Rao, C.; Chu, J.; Wang, G.; Pei, Y. Solution Processed Flexible Resistive Switching Memory Based on Al-In-O Self-Mixing Layer. *J. Appl. Phys.* **2018**, *124* (10), 1–10.

(822) She, Y.; Peng, Y.; Tang, B.; Hu, W.; Qiu, J.; Tang, X.; Bao, D. Bipolar Resistive Switching Effects with Self-Compliance and Multilevel Storage Characteristics in Ag/MgZnO/Si Structures. *Ceram. Int.* **2018**, *44* (xxxx), S11–S14.

(823) Aglieri, V.; Lullo, G.; Mosca, M.; Macaluso, R.; Zaffora, A.; Di Franco, F.; Santamaria, M.; Cicero, U. Lo; Razzari, L. Forming-Free and Self-Rectifying Resistive Switching Effect in Anodic Titanium Dioxide-Based Memristors. In *2018 IEEE 4th International Forum on Research and Technology for Society and Industry (RTSI)*; IEEE, 2018; pp 1–4.

(824) Yu, Y.; Yang, F.; Mao, S.; Zhu, S.; Jia, Y.; Yuan, L.; Salmen, M.; Sun, B. Effect of Anodic Oxidation Time on Resistive Switching Memory Behavior Based on Amorphous TiO2 Thin Films Device. *Chem. Phys. Lett.* **2018**, *706*, 477–482.

(825) Dongle, V. S.; Dongare, A. A.; Mullani, N. B.; Pawar, P. S.; Patil, P. B.; Heo, J.; Park, T. J.; Dongale, T. D. Development of Self-Rectifying ZnO Thin Film Resistive Switching Memory Device Using Successive Ionic Layer Adsorption and Reaction Method. *J. Mater. Sci. Mater. Electron.* **2018**, *29* (21), 18733–18741.

(826) Khan, M. U.; Hassan, G.; Raza, M. A.; Bae, J.; Kobayashi, N. P. Schottky Diode Based Resistive Switching Device Based on ZnO/PEDOT:PSS Heterojunction to Reduce Sneak Current Problem. *J. Mater. Sci. Mater. Electron.* **2019**, *30* (5), 4607–4617.

(827) Mukherjee, B. Resistive Switching and Nonvolatile Memory in TiO 2 /CuPc Nanocomposite Devices. *J. Electron. Mater.* **2019**, *48* (4), 2131–2136.

(828) Ghosh, A.; Kumar, K.; Dwivedi, S. M. M. D.; Ghosh, C.; Sushama, S.; Murkute, P.; Ghadi, H.; Chakrabarti, S.; Mondal, A. Bipolar Analog Memristive Switching of In 2 O 3 Using Al Nanoparticles . *J. Nanosci. Nanotechnol.* **2019**, *19* (12), 8126–8134.

(829) Liu, C.-F.; Tang, X.-G.; Wang, L.-Q.; Tang, H.; Jiang, Y.-P.; Liu, Q.-X.; Li, W.-H.; Tang, Z.-H. Resistive Switching Characteristics of HfO2 Thin Films on Mica Substrates Prepared by Sol-Gel Process. *Nanomaterials* **2019**, *9* (8), 1124.

(830) Nassar Moreira, E.; Kendall, J.; Maruyama, H.; Nino, J. C. Simplified Sol-Gel Processing Method for Amorphous TiOx Memristors. *J. Electroceramics* **2020**, *44* (1–2), 52–58.

(831) Kim, S.-E.; Lee, J.-G.; Choi, I.-Y.; Kim, H.-E.; Lee, H.-S. Resistive Switching Characteristic of Ce0.9Y0.1O2/TiO2 Bi-Layer Structure by Photochemical Metal-Organic Deposition. *J. Korean Ceram. Soc.* **2020**, *57* (1), 73–79.

(832) Kamat, R. K.; Dongale, T. D.; Kim, D. Resistive Switching Characteristics of Electrochemically Anodized Sub-Stoichiometric Ti6O Phase. *J. NANO- Electron. Phys.* **2020**, *12* (2), 2–5.

(833) Sahu, D. P.; Jammalamadaka, S. N. Bipolar Resistive Switching in HoCrO 3 Thin Films. *Nanotechnology* **2020**, *31* (35), 355202.

(834) Patil, A. A.; Khot, S. S.; Amate, R. U.; Kamble, P. N.; Patil, P. B.; Bulakhe, R. N.; In, I.; Dongale, T. D.; Kim, D. Bipolar-Resistive Switching and Memristive Properties of Solution-Processable Cobalt Oxide Nanoparticles. *J. Mater. Sci. Mater. Electron.* **2020**, *31* (12), 9695–9704.

(835) Rahman, K.; Mustafa, M.; Muhammad, N. M.; Choi, K. H. Electrohydrodynamic Printed TiO 2 Flexible Memory Device - Fabrication and Characterisation. *Electron. Lett.* **2012**, *48* (20), 1261–1263.

(836) Choi, K. H.; Awais, M. N.; Kim, H. C.; Doh, Y. H. Cost-Effective Printed Memristor Fabrication and Analysis. *Int. Work. Cell. Nanoscale Networks their Appl.* **2012**, 0–3.

(837) Lee, K.-J.; Chang, Y.-C.; Lee, C.-J.; Wang, L.-W.; Wang, Y.-H.; Chou, D.-W. Sol-Gel Strontium Titanate Nickelate Thin Films for Flexible Nonvolatile Memory Applications. In *2016 IEEE International Nanoelectronics Conference (INEC)*; IEEE, 2016; Vol. 2016-Octob, pp 1–2.

(838) Huber, B.; Popp, P. B.; Kaiser, M.; Ruediger, A.; Schindler, C. Fully Inkjet Printed Flexible Resistive Memory. *Appl. Phys. Lett.* **2017**, *110* (14), 143503.

(839) Wang, Z.; Jiang, Z.; Zheng, X.; Fong, S.; Chen, H.-Y.; Wong, H.-S. P.; Nishi, Y. Ultrafast Accelerated Retention Test Methodology for RRAM Using Micro Thermal Stage. *IEEE Electron Device Lett.* **2017**, *38* (7), 863–866.

(840) Wei, Z.; Kanzawa, Y.; Arita, K.; Katoh, Y.; Kawai, K.; Muraoka, S.; Mitani, S.; Fujii, S.; Katayama, K.; Iijima, M.; Mikawa, T.; Ninomiya, T.; Miyanaga, R.; Kawashima, Y.; Tsuji, K.; Himeno, A.; Okada, T.; Azuma, R.; Shimakawa, K.; Sugaya, H.; Takagi, T.; Yasuhara, R.; Horiba, K.; Kumigashira, H.; Oshima, M. Highly Reliable TaOx ReRAM and Direct Evidence of Redox Reaction Mechanism. In *2008 IEEE International Electron Devices Meeting*; IEEE, 2008; pp 1–4.

(841) Lee, H. Y.; Chen, Y. S.; Chen, P. S.; Gu, P. Y.; Hsu, Y. Y.; Wang, S. M.; Liu, W. H.; Tsai, C. H.; Sheu, S. S.; Chiang, P. C.; Lin, W. P.; Lin, C. H.; Chen, W. S.; Chen, F. T.; Lien, C. H.; Tsai, M. J. Evidence and Solution of Over-RESET Problem for HfOX Based Resistive Memory with Sub-Ns Switching Speed and High Endurance. *Tech. Dig. - Int. Electron Devices Meet. IEDM* **2010**, 7–10.

(842) Torrezan, A. C.; Strachan, J. P.; Medeiros-Ribeiro, G.; Williams, R. S. Sub-Nanosecond Switching of a Tantalum Oxide Memristor. *Nanotechnology* **2011**, *22* (48), 485203.

(843) Hansen, M.; Zahari, F.; Kohlstedt, H.; Ziegler, M. Unsupervised Hebbian Learning Experimentally Realized with Analogue Memristive Crossbar Arrays. *Sci. Rep.* **2018**, *8* (1), 8914.

(844) Ali, S.; Bae, J.; Lee, C. H.; Kobayashi, N. P.; Shin, S.; Ali, A. Resistive Switching Device with Highly Asymmetric Current–Voltage Characteristics: A Solution to Backward Sneak

Current in Passive Crossbar Arrays. *Nanotechnology* **2018**, *29* (45), 455201.

(845) Fei, W.; Yu, H.; Zhang, W.; Yeo, K. S. Design Exploration of Hybrid CMOS and Memristor Circuit by New Modified Nodal Analysis. *IEEE Trans. Very Large Scale Integr. Syst.* **2012**, *20* (6), 1012–1025.

(846) Valov, I. Interfacial Interactions and Their Impact on Redox-Based Resistive Switching Memories (ReRAMs). *Semicond. Sci. Technol.* **2017**, *32* (9), 093006.

(847) Hoffmann-Eifert, S.; Dittmann, R. Interface Effects on Memristive Devices. In *Advances in Non-Volatile Memory and Storage Technology*; Elsevier, 2019; pp 171–202.

(848) Pereira, M.; Deuermeier, J.; Nogueira, R.; Carvalho, P. A.; Martins, R.; Fortunato, E.; Kiazadeh, A. Noble-Metal-Free Memristive Devices Based on IGZO for Neuromorphic Applications. *Adv. Electron. Mater.* **2020**, *2000242*, 2000242.

(849) Pang, Y.; Gao, B.; Lin, B.; Qian, H.; Wu, H. Memristors for Hardware Security Applications. *Adv. Electron. Mater.* **2019**, *5* (9), 1800872.

(850) Sawa, A. Resistive Switching in Transition Metal Oxides. *Mater. Today* **2008**, *11* (6), 28–36.

(851) Yang, J. J.; Pickett, M. D.; Li, X.; Ohlberg, D. a a; Stewart, D. R.; Williams, R. S. Memristive Switching Mechanism for Metal/Oxide/Metal Nanodevices. Supp. *Nat. Nanotechnol.* **2008**, *3* (7), 429–433.

(852) Vogel, E. Technology and Metrology of New Electronic Materials and Devices. *Nat. Nanotechnol.* **2007**, *2* (1), 25–32.

(853) Waser, R.; Aono, M. Nanoionics-Based Resistive Switching Memories. *Nat. Mater.* **2007**, *6* (11), 833–840.

(854) Yanagida, T.; Nagashima, K.; Oka, K.; Kanai, M.; Klamchuen, A.; Park, B. H.; Kawai, T. Scaling Effect on Unipolar and Bipolar Resistive Switching of Metal Oxides. *Sci. Rep.* **2013**, *3* (c), 1–6.

(855) Kim, G. H.; Lee, J. H.; Ahn, Y.; Jeon, W.; Song, S. J.; Seok, J. Y.; Yoon, J. H.; Yoon, K. J.; Park, T. J.; Hwang, C. S. 32 × 32 Crossbar Array Resistive Memory Composed of a Stacked Schottky Diode and Unipolar Resistive Memory. *Adv. Funct. Mater.* **2013**, *23* (11), 1440–1449.

(856) Qian, K.; Nguyen, V. C.; Chen, T.; Lee, P. S. Novel Concepts in Functional Resistive Switching Memories. *J. Mater. Chem. C* **2016**, *4* (41), 9637–9645.

(857) Chen, Y. S.; Lee, H. Y.; Chen, P. S.; Wu, T. Y.; Wang, C. C.; Tzeng, P. J.; Chen, F.; Tsai, M. J.; Lien, C. An Ultrathin Forming-Free HfOx Resistance Memory with Excellent Electrical Performance. *IEEE Electron Device Lett.* **2010**, *31* (12), 1473–1475.

(858) Zhang, Y.; Wu, H.; Bai, Y.; Chen, A.; Yu, Z.; Zhang, J.; Qian, H. Study of Conduction and Switching Mechanisms in Al/AlOx/WOx/W Resistive Switching Memory for Multilevel Applications. *Appl. Phys. Lett.* **2013**, *102* (23), 1–5.

(859) Kim, K. M.; Choi, B. J.; Koo, B. W.; Choi, S.; Jeong, D. S.; Hwang, C. S. Resistive Switching in Pt/Al[Sub 2]O[Sub 3]/TiO[Sub 2]/Ru Stacked Structures. *Electrochem. Solid-State Lett.* **2006**, *9* (12), G343.

(860) Lee, M.-J.; Lee, C. B.; Lee, D.; Lee, S. R.; Chang, M.; Hur, J. H.; Kim, Y.-B.; Kim, C.-J.; Seo, D. H.; Seo, S.; Chung, U.; Yoo, I.; Kim, K. A Fast, High-Endurance and Scalable Non-Volatile Memory Device Made from Asymmetric Ta2O5−x/TaO2−x Bilayer Structures. *Nat. Mater.* **2011**, *10* (8), 625–630.

(861) Lee, H. Y.; Chen, P. S.; Wu, T. Y.; Chen, Y. S.; Wang, C. C.; Tzeng, P. J.; Lin, C. H.;

Chen, F.; Lien, C. H.; Tsai, M.-J. Low Power and High Speed Bipolar Switching with a Thin Reactive Ti Buffer Layer in Robust HfO2 Based RRAM. In *2008 IEEE International Electron Devices Meeting*; IEEE, 2008; pp 1–4.

(862) Kim, S.; Choi, Y.-K. K. Resistive Switching of Aluminum Oxide for Flexible Memory. *Appl. Phys. Lett.* **2008**, *92* (22), 223508.

(863) Dongsoo Lee; Hyejung Choi; Hyunjun Sim; Dooho Choi; Hyunsang Hwang; Myoung-Jae Lee; Sun-Ae Seo; Yoo, I. K. Resistance Switching of the Nonstoichiometric Zirconium Oxide for Nonvolatile Memory Applications. *IEEE Electron Device Lett.* **2005**, *26* (10), 719–721.

(864) Kittl, J. A.; Opsomer, K.; Popovici, M.; Menou, N.; Kaczer, B.; Wang, X. P.; Adelmann, C.; Pawlak, M. A.; Tomida, K.; Rothschild, A.; Govoreanu, B.; Degraeve, R.; Schaekers, M.; Zahid, M.; Delabie, A.; Meersschaut, J.; Polspoel, W.; Clima, S.; Pourtois, G.; Knaepen, W.; Detavernier, C.; Afanas'ev, V. V.; Blomberg, T.; Pierreux, D.; Swerts, J.; Fischer, P.; Maes, J. W.; Manger, D.; Vandervorst, W.; Conard, T.; Franquet, A.; Favia, P.; Bender, H.; Brijs, B.; Van Elshocht, S.; Jurczak, M.; Van Houdt, J.; Wouters, D. J. High-k Dielectrics for Future Generation Memory Devices (Invited Paper). *Microelectron. Eng.* **2009**, *86* (7–9), 1789–1795.

(865) Baek, I.-J.; Cho, W.-J. Resistive Switching Characteristics of Solution-Processed Organic-Inorganic Blended Films for Flexible Memory Applications. *Solid. State. Electron.* **2018**, *140* (xxxx), 129–133.

(866) Chen, S.; Lou, Z.; Chen, D.; Shen, G. An Artificial Flexible Visual Memory System Based on an UV-Motivated Memristor. *Adv. Mater.* **2018**, *30* (7), 1705400.

(867) Wu, Y. W. Y.; Lee, B. L. B.; Wong, H. P. Based RRAM Using Atomic Layer Deposition (ALD) With 1- RESET Current. *IEEE Electron Device Lett.* **2010**, *31* (12), 1449–1451.

(868) Yu, S.; Jeyasingh, R.; Yi Wu; Philip Wong, H.-S. Understanding the Conduction and Switching Mechanism of Metal Oxide RRAM through Low Frequency Noise and AC Conductance Measurement and Analysis. In *2011 International Electron Devices Meeting*; IEEE, 2011; pp 12.1.1-12.1.4.

(869) Kim, W.; Park, S. Il; Zhang, Z.; Yang-Liauw, Y.; Sekar, D.; Wong, H.-S. P.; Wong, S. S. Forming-Free Nitrogen-Doped AlO<inf>X</Inf> RRAM with Sub-μA Programming Current. *2011 Symp. VLSI Technol. - Dig. Tech. Pap.* **2011**, *31*, 22–23.

(870) Prakash, A.; Maikap, S.; Banerjee, W.; Jana, D.; Lai, C. S. Impact of Electrically Formed Interfacial Layer and Improved Memory Characteristics of IrOx/High-Kx/W Structures Containing AlOx, GdOx, HfOx, and TaOxswitching Materials. *Nanoscale Res. Lett.* **2013**, *8* (1), 1–12.

(871) Chen, Z.; Zhang, F.; Chen, B.; Zheng, Y.; Gao, B.; Liu, L.; Liu, X.; Kang, J. High-Performance HfO x /AlO y -Based Resistive Switching Memory Cross-Point Array Fabricated by Atomic Layer Deposition. *Nanoscale Res. Lett.* **2015**, *10* (1), 70.

(872) Park, K.; Lee, J.-S. Reliable Resistive Switching Memory Based on Oxygen-Vacancy-Controlled Bilayer Structures. *RSC Adv.* **2016**, *6* (26), 21736–21741.

(873) Jang, J.; Song, Y.; Cho, K.; Kim, Y.; Lee, W.; Yoo, D.; Chung, S.; Lee, T. Non-Volatile Aluminum Oxide Resistive Memory Devices on a Wrapping Paper Substrate. *Flex. Print. Electron.* **2016**, *1* (3), 034001.

(874) Yeom, S.-W.; Ha, H. J.; Park, J.; Shim, J. W.; Ju, B.-K. Transparent Bipolar Resistive Switching Memory on a Flexible Substrate with Indium-Zinc-Oxide Electrodes. *J. Korean Phys. Soc.* **2016**, *69* (11), 1613–1618.

(875) Trapatseli, M.; Cortese, S.; Serb, A.; Khiat, A.; Prodromakis, T. Impact of Ultra-Thin Al 2 O 3– y Layers on TiO 2– x ReRAM Switching Characteristics. *J. Appl. Phys.* **2017**, *121* (18), 184505.

(876) Yin Chen, Y.; Pourtois, G.; Adelmann, C.; Goux, L.; Govoreanu, B.; Degreave, R.; Jurczak, M.; Kittl, J. A.; Groeseneken, G.; Wouters, D. J. Insights into Ni-Filament Formation in Unipolar-Switching Ni/HfO 2 /TiN Resistive Random Access Memory Device. *Appl. Phys. Lett.* **2012**, *100* (11), 113513.

(877) Jung, K.-H.; Song, S.-G.; Park, K.-W.; Sok, J.-H.; Kim, K.-M.; Park, Y.-S. Observation of AlO x Material in Electrical Resistive Switching for Nonvolatile Random Access Memory Application. *J. Korean Phys. Soc.* **2017**, *70* (5), 489–493.

(878) Chang, T.-C.; Chang, K.-C.; Tsai, T.-M.; Chu, T.-J.; Sze, S. M. Resistance Random Access Memory. *Mater. Today* **2016**, *19* (5), 254–264.

(879) Sleiman, A.; Sayers, P. W.; Mabrook, M. F. Mechanism of Resistive Switching in Cu/AlO x /W Nonvolatile Memory Structures. *J. Appl. Phys.* **2013**, *113* (16), 164506.

(880) Nigo, S.; Kubota, M.; Harada, Y.; Hirayama, T.; Kato, S.; Kitazawa, H.; Kido, G. Conduction Band Caused by Oxygen Vacancies in Aluminum Oxide for Resistance Random Access Memory. *J. Appl. Phys.* **2012**, *112* (3), 033711.

(881) Águas, H.; Mateus, T.; Vicente, A.; Gaspar, D.; Mendes, M. J.; Schmidt, W. A.; Pereira, L.; Fortunato, E.; Martins, R. Thin Film Silicon Photovoltaic Cells on Paper for Flexible Indoor Applications. *Adv. Funct. Mater.* **2015**, *25* (23), 3592–3598.

(882) Sahu, V. K.; Das, A. K.; Ajimsha, R. S.; Misra, P. Studies on Transient Characteristics of Unipolar Resistive Switching Processes in TiO 2 Thin Film Grown by Atomic Layer Deposition. *J. Phys. D. Appl. Phys.* **2018**, *51* (21), 215101.

(883) Choi, K.-H.; Ahn, D. B.; Lee, S.-Y. Current Status and Challenges in Printed Batteries: Toward Form Factor-Free, Monolithic Integrated Power Sources. *ACS Energy Lett.* **2018**, *3* (1), 220–236.

(884) Somalu, M. R.; Muchtar, A.; Daud, W. R. W.; Brandon, N. P. Screen-Printing Inks for the Fabrication of Solid Oxide Fuel Cell Films: A Review. *Renew. Sustain. Energy Rev.* **2017**, *75* (November 2016), 426–439.

(885) Chen, A. A Review of Emerging Non-Volatile Memory (NVM) Technologies and Applications. *Solid. State. Electron.* **2016**, *125*, 25–38.

(886) Xu, L.; Yuan, R.; Zhu, Z.; Liu, K.; Jing, Z.; Cai, Y.; Wang, Y.; Yang, Y.; Huang, R. Memristor-Based Efficient In-Memory Logic for Cryptologic and Arithmetic Applications. *Adv. Mater. Technol.* **2019**, *4* (7), 1900212.

(887) Lee, T.-J.; Kim, S.-K.; Seong, T.-Y. Sputtering-Deposited Amorphous SrVOx-Based Memristor for Use in Neuromorphic Computing. *Sci. Rep.* **2020**, *10* (1), 5761.

(888) Abbas, H.; Abbas, Y.; Hassan, G.; Sokolov, A. S.; Jeon, Y.-R.; Ku, B.; Kang, C. J.; Choi, C. The Coexistence of Threshold and Memory Switching Characteristics of ALD HfO 2 Memristor Synaptic Arrays for Energy-Efficient Neuromorphic Computing. *Nanoscale* **2020**, *12* (26), 14120–14134.

(889) Wang, T.; Shi, Y.; Puglisi, F. M.; Chen, S.; Zhu, K.; Zuo, Y.; Li, X.; Jing, X.; Han, T.; Guo, B.; Bukvišová, K.; Kachtík, L.; Kolíbal, M.; Wen, C.; Lanza, M. Electroforming in Metal-Oxide Memristive Synapses. *ACS Appl. Mater. Interfaces* **2020**, *12* (10), 11806–11814.

(890) Stathopoulos, S.; Khiat, A.; Trapatseli, M.; Cortese, S.; Serb, A.; Valov, I.; Prodromakis, T. Multibit Memory Operation of Metal-Oxide Bi-Layer Memristors. *Sci. Rep.* **2017**, *7*

(1), 17532.

(891) Carlos, E.; Branquinho, R.; Martins, R.; Kiazadeh, A.; Fortunato, E. Recent Progress in Solution-Based Metal Oxide Resistive Switching Devices. *Adv. Mater.* **2020**, *2004328*, 2004328.

(892) Nayak, L.; Mohanty, S.; Nayak, S. K.; Ramadoss, A. A Review on Inkjet Printing of Nanoparticle Inks for Flexible Electronics. *J. Mater. Chem. C* **2019**, *7* (29), 8771–8795.

(893) Zhou, K.; Ding, G.; Zhang, C.; Lv, Z.; Luo, S.; Zhou, Y.; Zhou, L.; Chen, X.; Li, H.; Han, S.-T. A Solution Processed Metal–Oxo Cluster for Rewritable Resistive Memory Devices. *J. Mater. Chem. C* **2019**, *7* (4), 843–852.

(894) TaheriNejad, N.; Radakovits, D. From Behavioral Design of Memristive Circuits and Systems to Physical Implementations. *IEEE Circuits Syst. Mag.* **2019**, *19* (4), 6–18.

(895) Bid, A.; Bora, A.; Raychaudhuri, A. K. Temperature Dependence of the Resistance of Metallic Nanowires of Diameter <math Display="inline"> <mrow> <mo>⩾</Mo> <mn>15</Mn> <mspace Width="0.3em"/> <mi>nm</Mi> </Mrow> </Math> : Applicability of Bloch-Grüneisen Theorem. *Phys. Rev. B* **2006**, *74* (3), 035426.

(896) Rahman, M. T.; McCloy, J.; Ramana, C. V.; Panat, R. Structure, Electrical Characteristics, and High-Temperature Stability of Aerosol Jet Printed Silver Nanoparticle Films. *J. Appl. Phys.* **2016**, *120* (7), 075305.

(897) Tsuruoka, T.; Terabe, K.; Hasegawa, T.; Aono, M. Forming and Switching Mechanisms of a Cation-Migration-Based Oxide Resistive Memory. *Nanotechnology* **2010**, *21* (42), 425205.

(898) Valov, I.; Tsuruoka, T. Effects of Moisture and Redox Reactions in VCM and ECM Resistive Switching Memories. *J. Phys. D. Appl. Phys.* **2018**, *51* (41), 413001.

(899) Tappertzhofen, S.; Valov, I.; Tsuruoka, T.; Hasegawa, T.; Waser, R.; Aono, M. Generic Relevance of Counter Charges for Cation-Based Nanoscale Resistive Switching Memories. *ACS Nano* **2013**, *7* (7), 6396–6402.

(900) Milano, G.; Raffone, F.; Luebben, M.; Boarino, L.; Cicero, G.; Valov, I.; Ricciardi, C. Water-Mediated Ionic Migration in Memristive Nanowires with a Tunable Resistive Switching Mechanism. *ACS Appl. Mater. Interfaces* **2020**, *12* (43), 48773–48780.

(901) Yu, B.-S.; Jeon, J.-Y.; Kang, B.-C.; Lee, W.; Kim, Y.-H.; Ha, T.-J. Wearable 1 V Operating Thin-Film Transistors with Solution-Processed Metal-Oxide Semiconductor and Dielectric Films Fabricated by Deep Ultra-Violet Photo Annealing at Low Temperature. *Sci. Rep.* **2019**, *9* (1), 8416.

(902) Akkerman, A.; Boutboul, T.; Breskin, A.; Chechik, R.; Gibrekhterman, A.; Lifshitz, Y. Inelastic Electron Interactions in the Energy Range 50 EV to 10 KeV in Insulators: Alkali Halides and Metal Oxides. *Phys. status solidi* **1996**, *198* (2), 769–784.

(903) Seo, J. W.; Park, J. W.; Lim, K. S.; Yang, J. H.; Kang, S. J. Transparent Resistive Random Access Memory and Its Characteristics for Nonvolatile Resistive Switching. *Appl. Phys. Lett.* **2008**, *93* (22), 10–13.

(904) Won Seo, J.; Park, J. W.; Lim, K. S.; Kang, S. J.; Hong, Y. H.; Yang, J. H.; Fang, L.; Sung, G. Y.; Kim, H. K. Transparent Flexible Resistive Random Access Memory Fabricated at Room Temperature. *Appl. Phys. Lett.* **2009**, *95* (13), 1–4.

(905) Chen, M.-C.; Chang, T.-C.; Huang, S.-Y.; Chen, S.-C.; Hu, C.-W.; Tsai, C.-T.; Sze, S. M. Bipolar Resistive Switching Characteristics of Transparent Indium Gallium Zinc Oxide Resistive Random Access Memory. *Electrochem. Solid-State Lett.* **2010**, *13* (6), H191.

(906) Wang, Y. Resistive-Switching Mechanism of Transparent Nonvolatile Memory Device Based on Gallium Zinc Oxide. *Phys. Status Solidi* **2012**, *209* (2), 364–368.

(907) Yao, J.; Lin, J.; Dai, Y.; Ruan, G.; Yan, Z.; Li, L.; Zhong, L.; Natelson, D.; Tour, J. M. Highly Transparent Nonvolatile Resistive Memory Devices from Silicon Oxide and Graphene. *Nat. Commun.* **2012**, *3*, 1101–1108.

(908) Shang, J.; Liu, G.; Yang, H.; Zhu, X.; Chen, X.; Tan, H.; Hu, B.; Pan, L.; Xue, W.; Li, R. W. Thermally Stable Transparent Resistive Random Access Memory Based on All-Oxide Heterostructures. *Adv. Funct. Mater.* **2014**, *24* (15), 2171–2179.

(909) Wu, S.; Ren, L.; Qing, J.; Yu, F.; Yang, K.; Yang, M.; Wang, Y.; Meng, M.; Zhou, W.; Zhou, X.; Li, S. Bipolar Resistance Switching in Transparent ITO/$LaAlO_3$/$SrTiO_3$ Memristors. *ACS Appl. Mater. Interfaces* **2014**, *6* (11), 8575–8579.

(910) Yeom, S.-W.; Shin, S.-C.; Kim, T.-Y.; Ha, H. J.; Lee, Y.-H.; Shim, J. W.; Ju, B.-K. Transparent Resistive Switching Memory Using Aluminum Oxide on a Flexible Substrate. *Nanotechnology* **2016**, *27* (7), 07LT01.

(911) Tsai, T. L.; Chang, H. Y.; Lou, J. J. C.; Tseng, T. Y. A High Performance Transparent Resistive Switching Memory Made from ZrO2/AlON Bilayer Structure. *Appl. Phys. Lett.* **2016**, *108* (15), 2–6.

(912) Kim, M.; Choi, K. C. Transparent and Flexible Resistive Random Access Memory Based on Al 2 O 3 Film With Multilayer Electrodes. *IEEE Trans. Electron Devices* **2017**, *64* (8), 3508–3510.